DOC.20071106.0015

QA: QA

ANL-EBS-GS-000002 REV 01

September 2006

Geochemistry Model Validation Report: External Accumulation Model

THIS DOCUMENT CONTAINS THE FOLLOWING, LOCATED AT THE BACK OF THE DOCUMENT:
1) ADDENDUM 001, DATED 11/01/2007

Prepared for:
U.S. Department of Energy
Office of Civilian Radioactive Waste Management
Office of Repository Development
1551 Hillshire Drive
Las Vegas, Nevada 89134-6321

Prepared by:
Bechtel SAIC Company, LLC
1180 Town Center Drive
Las Vegas, Nevada 89144

Under Contract Number
DE-AC28-01RW12101

DISCLAIMER

This report was prepared as an account of work sponsored by an agency of the United States Government. Neither the United States Government nor any agency thereof, nor any of their employees, nor any of their contractors, subcontractors or their employees, makes any warranty, express or implied, or assumes any legal liability or responsibility for the accuracy, completeness, or any third party's use or the results of such use of any information, apparatus, product, or process disclosed, or represents that its use would not infringe privately owned rights. Reference herein to any specific commercial product, process, or service by trade name, trademark, manufacturer, or otherwise, does not necessarily constitute or imply its endorsement, recommendation, or favoring by the United States Government or any agency thereof or its contractors or subcontractors. The views and opinions of authors expressed herein do not necessarily state or reflect those of the United States Government or any agency thereof.

QA: QA

Geochemistry Model Validation Report: External Accumulation Model

ANL-EBS-GS-000002 REV 01

September 2006

2. Type of Mathematical Model

☒ Process Model ☐ Abstraction Model ☐ System Model

Describe Intended Use of Model

The results of the model will be used in external criticality risk assessments to support the postclosure safety case.

3. Title

Geochemistry Model Validation Report: External Accumulation Model

4. DI (including Rev. No.):

ANL-EBS-GS-000002 REV 01

	Printed Name	Signature	Date
5. Originator	Susan LeStrange	Susan LeStrange	9/28/06
6. Independent Technical Reviewer	Rob Howard	Robert Howard	28 SEPT 2006
7. Checker	William Downs	William Downs	9/28/06
8. QER	Paul Buenviaje	Paul Buenviaje	9/28/06
9. Responsible Manager/Lead	Ernest Hardin	E Hardin	9/28/06
10. Responsible Manager	Paul Dixon	Paul Dixon	9-28-06

11. Remarks

The contributing originators are as follows:
Susan LeStrange: all sections
Wendy Mitcheltree: all sections
Florie Caporuscio: 6.4.8, 7.2.3, Appendix B
Jim Houseworth: 7.2.5, Appendices C, D, E, F and G
Junghun Leem: 4.1.5, Appendix C
Paul Mariner: 6.4.3, 7.1.1, 7.2.4
Jean-Philippe Nicot: 6.4.7
James Schreiber: 6.4.6, 7:2.5
Kaveh Zarrabi: 6.5, 6.6.

Change History

12. Revision No.	13. Description of Change
REV 00	Initial Issue.
REV 01	Complete Revision. Revisions too extensive to use change bars. This revision will support resolution of key technical issue agreements CLST 5.04, ENFE 5.03, and RT 4.03 and Condition Report (CR) 5904.

CONTENTS

Page

CONTENTS (Continued)

Page

CONTENTS (Continued)

Page

CONTENTS (Continued)

Page

FIGURES

Page

FIGURES (Continued)

Page

FIGURES (Continued)

Page

INTENTIONALLY LEFT BLANK

TABLES

Page

TABLES (Continued)

Page

TABLES (Continued)

Page

INTENTIONALLY LEFT BLANK

ACRONYMS

AC	acceptance criteria
ANL	Argonne National Laboratory
CDSP	codisposed
CPU	central processing unit
CSNF	commercial spent nuclear fuel
DOE	U. S. Department of Energy
DTN	data tracking number
EBS	engineered barrier system
ESF	Exploratory Studies Facility
ECRB	Enhanced Characterization of the Repository Block (drift)
FEPs	features, events, and processes
FFTF	Fast Flux Test Facility
HLW	high-level waste
IED	information exchange drawing
KTI	key technical issues
MCO	multi-canister overpack
PWR	pressurized water reactor
SER	Safety Evaluation Report
SI	saturation index
SNF	spent nuclear fuel
STN	software tracking number
SZ	saturated zone
TIMS	thermal ionization mass spectrometry
TMI	Three Mile Island
TSPA-LA	total system performance assessment for the license application
TWP	technical work plan
USGS	United States Geological Survey
UZ	unsaturated zone
XRD	x-ray diffraction
YMP	Yucca Mountain Project
YMRP	*Yucca Mountain Review Plan, Final Report*

ELEMENTAL SYMBOLS

Ag	Silver
Al	Aluminum
Am	Americium
Ba	Barium
Be	Beryllium
C	Carbon
Ca	Calcium
Cl	Chlorine
Cm	Curium
Co	Cobalt
Cr	Chromium
Cs	Cesium
Cu	Copper
Eu	Europium
F	Fluorine
Fe	Iron
Gd	Gadolinium
H	Hydrogen
Ho	Holmium
In	Indium
K	Potassium
Kr	Krypton
La	Lanthanum
Li	Lithium
Mg	Magnesium
Mn	Manganese
Mo	Molybdenum
N	Nitrogen
Na	Sodium
Nb	Niobium
Nd	Neodymium
Ni	Nickel
Np	Neptunium
P	Phosphorus
Pa	Protactinium
Pb	Lead
Pd	Palladium
Pm	Promethium
Pr	Praseodymium
Rh	Rhodium
Rn	Radon
Ru	Ruthenium
S	Sulfur
Si	Silicon
Sm	Samarium
Tc	Technetium
Th	Thorium
Ti	Titanium
U	Uranium
V	Vanadium
W	Tungsten
Xe	Xenon
Y	Yttrium
Zn	Zinc
Zr	Zirconium

1. PURPOSE

The purpose of this report is to document and validate the external accumulation model that predicts accumulation of fissile materials in the invert, fractures and lithophysae in the rock beneath a degrading waste package containing spent nuclear fuel (SNF) in the monitored geologic repository at Yucca Mountain. (Lithophysae are hollow, bubblelike structures in the rock composed of concentric shells of finely crystalline alkali feldspar, quartz, and other materials (Bates and Jackson 1984 [DIRS 128109], p. 299.) A secondary purpose is to predict the quantity of non-fissile minerals that accumulate alongside the fissile materials. The results of the model will be used in external criticality risk assessments to support the post-closure safety case.

The scope of the report is to (1) describe the model and the parameters used to develop the model, (2) validate the model for use in criticality calculations, and (3) use the model to determine external accumulations from degrading waste packages. Commercial SNF (CSNF) waste packages and Department of Energy (DOE) SNF codisposed (CDSP) waste packages containing DOE SNF codisposed with high-level waste (HLW) glass are analyzed. The DOE SNF considered originates from Three Mile Island (TMI), the Fast Flux Test Facility (FFTF), and N-Reactor. The report considers (1) the nominal scenario, in which the drip shield is intact, and only diffusive losses of U and Pu can occur through a film of condensate, (2) the seismic-induced fault displacement scenario, in which the waste package and drip shield are damaged and pore water flows through the breached waste package, and (3) the igneous scenario, in which the drift is filled with basalt, the waste package and drip shield are damaged, and water flows through the basalt and through the breached waste package.

This report summarizes the releases from the waste package that could accumulate external to the waste package, either in the invert or the in the fractured host rock. The waste package releases are determined in *Geochemistry Model Validation Report: Material Degradation and Release Model* (BSC 2006 [DIRS 176911]) and the total system performance assessment (TSPA) (DTN: MO0506MWDTLVAC.000 [DIRS 174811]). The releases considered include (1) diffusive transport into the invert in a no-flow scenario, (2) dissolved constituents in the liquid phase flowing out of the waste package and into the invert or to the fractured rock, (3) solid particles flushed out of the waste package due to entrainment, that flow onto the top of the invert and possibly penetrate the invert, and (4) corrosion products from the bottom of a degrading waste package flowing as a slurry onto the top of the invert or possibly penetrating the invert due to a bottom failure of the waste package. The diffusive and solid losses are tabulated for use in criticality analyses.

The computer code PHREEQC (Section 3) is used to simulate the transport and interaction of the waste package effluent in an advective flow scenario (referred to as the source term) with the resident water and the crushed tuff in the invert or in the host rock. (Note that the phrase "source term" does not refer to the total waste package releases, but only refers to the dissolved releases subject to advective flow.) In these simulations the primary mechanisms for accumulation are (1) adsorption and (2) mixing of the actinide-laden source term with resident water, thus changing the chemistry sufficiently for fissile minerals to become insoluble and precipitate. The outputs from PHREEQC are processed to produce mass of accumulation, volume of accumulation, and the geometry of the accumulation zone for the invert and the host rock. The

geometry of the accumulation zone within the invert is inferred using TOUGHREACT, a numerical model describing two-dimensional steady-state flow and mixing within the unsaturated invert.

This model does not directly feed the assessment of system performance. The output from this model is used by several other models, such as the configuration generator, criticality, and criticality consequence models, prior to the evaluation of criticality FEPs in the report *Screening Analysis of Criticality Features, Events, and Processes for License Application* (BSC 2004 [DIRS 168556]).

This document has been prepared according to LP-SIII.10Q-BSC, *Models*, and prepared in accordance with *Technical Work Plan for External Accumulation for Criticality Evaluations* (BSC 2006 [DIRS 177153]).

2. QUALITY ASSURANCE

QA Program Applicability: Development of this report has been determined to be subject to the Yucca Mountain Project's Quality Assurance Program (BSC 2004 [DIRS 171583], Section 8) because the report involves investigations of the following barriers that are listed in *Q-List* (BSC 2005 [DIRS 175539]): the Engineered Barrier System (emplacement drift invert) and the Lower Natural Barrier.

Electronic Management of Data: The technical work plan (TWP) (BSC 2006 [DIRS 177153]) contains the process control evaluation used to evaluate the control of electronic management of data during the modeling and documentation activities, and this evaluation determined that the methods in the implementing procedures are adequate. No deviations from these methods were performed.

INTENTIONALLY LEFT BLANK

3. USE OF SOFTWARE

The controlled and baselined software used in this report is listed in Table 3-1; the operating environments are provided in Table 3-2, and the range of use for each piece of software is within that for which it was qualified. Each piece of software was selected because it is appropriate for use in geochemical modeling and uses the project-qualified thermodynamic database, and there are no limitations on the outputs due to the selected software. The limitation on the outputs due to the use of the project-qualified thermodynamic database is that some of the minerals found in nature are not represented in the database, such as the uranium minerals compreignacite, becquerelite, and K-boltwoodite. This is discussed in Section 7.2.3.1. The use of the software was consistent with the intended use and within the documented validation range of the software. No software was used prior to qualification to develop any preliminary output.

EXCEL, Mathcad, and Tecplot, commercially available software, are used in this report; however, the results are not dependent on the software programs used, so the software is exempt from requirements in IT-PRO-0011, *Software Management*.

For all software, the formulas and inputs used in this model are discussed in Section 4. The outputs are discussed in Section 6. No other information is required for an independent person to reproduce the work.

Table 3-1. Computer Software Used

Software Name	Version	Software Tracking Number (Qualification Status)	Description and Components Used
EQ6	7.2bLV	10075-7.2bLV-02 [DIRS 159731] (Qualified on Windows 2000 and NT)	A reaction path code which models water–rock interaction or fluid mixing in either a pure reaction progress mode or a time mode.
EQ3/6	8.1	10813-8.1-00 [DIRS 176889] (Qualified on Windows 2000)	A reaction path code which models water–rock interaction or fluid mixing in either a pure reaction progress mode or a time mode.
ASPRIN	1.0	10487-1.0-00 [DIRS 155712] (Qualified on Windows 2000)	Determines isotopic content of minerals and solution in EQ6 output files.
GetEQData	1.0.1	10809-1.0.1-00 [DIRS 173680] (Qualified on Windows NT 4.0 and Windows 2000)	A Microsoft Excel macro. It is used to extract data from EQ3/6 output files.
PHREEQC	2.3	10068-2.3-01 [DIRS 157837] (Qualified on Windows 2000)	A code for geochemical speciation, reaction path modeling, reactive transport, and surface complexation modeling.
PHREEQC	2.11	10068-2.11-00 [DIRS 175698] (Qualified on Windows 2000)	A code for geochemical speciation, reaction path modeling, reactive transport, and surface complexation modeling.

Table 3-1. Computer Software Used (Continued)

Software Name	Version	Software Tracking Number (Qualification Status)	Description and Components Used
PHREEQC_Post	1.1	10723-1.1-00 [DIRS 157839]	A Microsoft Excel macro. It is used to postprocess PHREEQC output information.
GetEqPhases	1.0	10725-1.0-00 [DIRS 157840]	A Microsoft Excel macro that determines the mineral phases likely to precipitate in PHREEQC simulations.
Acc_with_decay	1.2	10499-1.2-00 [DIRS 157838]	A Microsoft Excel macro. It is used to postprocess PHREEQC output information.
MinAcc	1.0	10724-1.0-00 [DIRS 157841]	A Microsoft Excel macro. It is used to postprocess PHREEQC output information.
TOUGHREACT	3.0	10396-3.0-00 [DIRS 161256]	Reactive transport code.
Microsoft Excel	97 SR-2	Commercial off-the-shelf software: Exempt	Used in this document for graphical representation and arithmetical manipulations.
Tecplot	10.0-2-24	Commercial off-the-shelf software: Exempt	Used in this document for graphical representation.
Mathcad	11.2a	Commercial off-the-shelf software: Exempt	Used in this document for arithmetical manipulations.

Table 3-2. Computers and Operating Systems Used

Computer Make (User)	CPU #	Operating System	Software Used
Dell Optiplex GX260 (Wendy Mitcheltree)	152383	Windows 2000	EQ6 V7.2bLV, ASPRIN, PHREEQC, PHREEQC _Post, GetEqPhases, Acc_with_decay, MinAcc
Dell Optiplex GX260 (Susan LeStrange)	152381	Windows 2000	EQ6 V7.2bLV, ASPRIN, PHREEQC V2.3, PHREEQC_Post, Acc_with_decay
DEC AlphaServer 8400 5/625 (Jim Schreiber)	S714355	OSF1 V5.1	TOUGHREACT V3.0
Dell Optiplex GX260 (Jim Houseworth)	150622	Windows 2000	Excel
Dell Optiplex GX280 (Jim Schreiber)	S867531	WindowsXP	Excel, Tecplot
Dell Latitude D610 (Paul Mariner)	S874043	Windows 2000	EQ6 V8.1, GetEqPhases, PHREEQCV2.11
Dell Optiplex GX260 (Junghun Leem)	152885	Windows 2000	Mathcad V. 11.2a
Dell Optiplex GX260 (Kaveh Zarrabi)	152388	Windows 2000	GetEQData, Excel

NOTE: CPU = central processing unit.

3.1 SOFTWARE APPROVED FOR QA WORK

3.1.1 Overview of Software Use

Figure 3-1 gives an overview of software usage for the geochemistry modeling portion. EQ3/6 and ASPRIN outputs are used as inputs to PHREEQC simulations in this report. GetEqPhases, PHREEQC_Post, Acc_with_decay, and MinAcc are then used to postprocess PHREEQC outputs. Section 6.4.1 details the use of pre-processing of inputs via EQ3/6 and ASPRIN, and Section 6.4.5 gives details of how PHREEQC was used in conjunction with all post-processing macros. TOUGHREACT is a separate software code that was used for modeling the flow and transport within the invert.

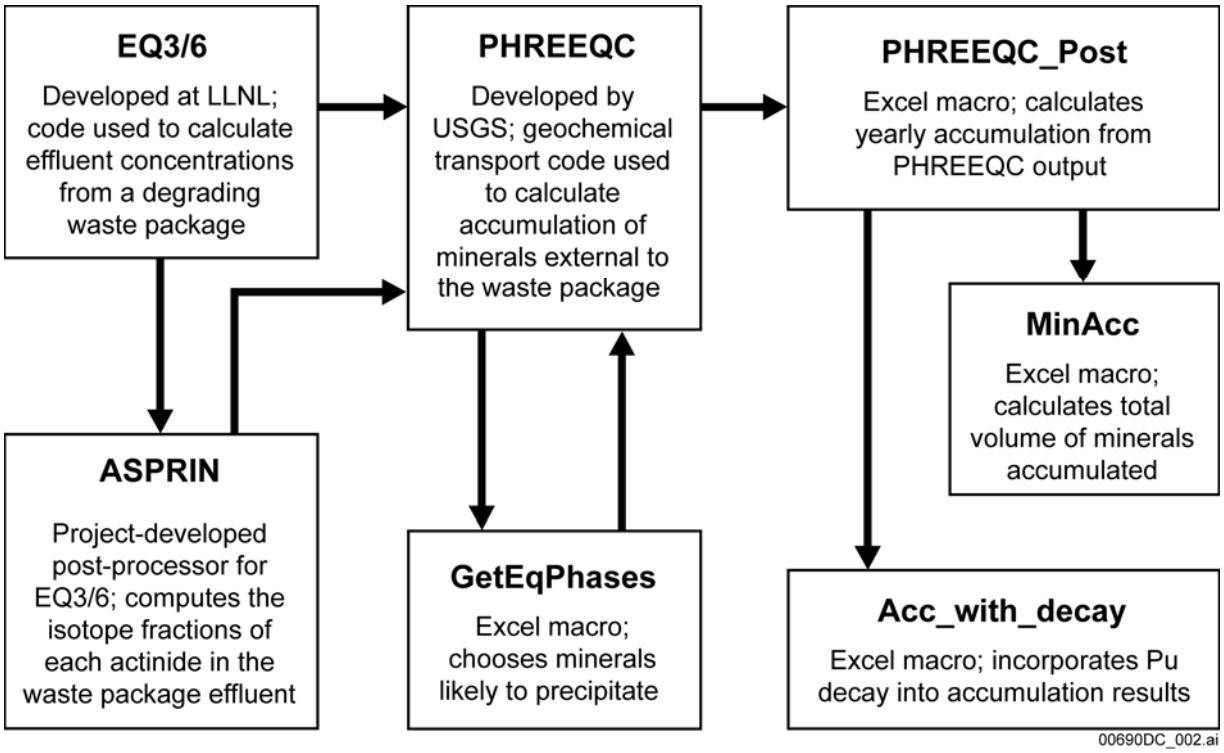

Figure 3-1. Overview of Software Use

3.1.2 Exempt Software

The computer programs Microsoft Excel 97 SR-2, Microsoft Excel XP Professional, Mathcad V.11.2a, and Tecplot Version 10.0-2-24 for Microsoft Windows were used in the preparation of this document. These software items are appropriate for this application. Microsoft Excel was used to perform support calculations and is not a controlled source of information. Thus, these are subject to software management per IT-PRO-0011. Microsoft Excel is a commercial spreadsheet program designed to assist in routine calculations. The program provides built-in mathematical functions that can be used together with user-defined formulas to automate the calculation process. Output formulae are automatically updated as input data are added or changed. Microsoft Excel also includes a graphics package to assist in data presentation. All plots and graphics of this document were produced on Microsoft Excel or Tecplot. Tecplot is

commercial off-the-shelf software used solely for visual display and graphical representation of data. Mathcad was used in the model validation of flow and transport in the invert. Mathcad was used to perform support calculations and is not a controlled source of information. Details on computers used and operating systems are given in Table 3-2.

3.1.3 PHREEQC Software Package

PHREEQC V2.3 (BSC 2002 [DIRS 157837]) has been qualified and baselined under software tracking number (STN) 10068-2.3-01. The software was obtained through Software Configuration Management. Table 3-2 indicates the platform and computer on which the software was installed and used. The software was used in Section 6.4 to simulate the one-dimensional transport of the source term, including mixing with the resident water and adsorption onto tuff in the invert or in the host rock. In Section 7.1.1, PHREEQC results were compared to EQ3/6 results for a confidence building exercise. PHREEQC V2.11 (BSC 2005 [DIRS 175698], STN: 10068-2.11-00) was used in Validation Method C: Simulation of Argonne UO_2 Drip Test (Section 7.2.4.1). The software is appropriate for use in this calculation and has been used within the range of parameters for which the software was qualified.

3.1.3.1 PHREEQC Description

The PHREEQC family of software products originated in the late 1970's and was developed by the U.S. Geological Survey. PHREEQC (V2.3 and V2.11) contains capabilities such as speciation-solubility and kinetically controlled reaction pathway features, which are found in many geochemical software packages, but also includes surface complexation, ion exchange, absorption and solid solutions, and a very versatile treatment of rate laws. In addition, PHREEQC has transport features with handling of dispersion and diffusion in a double-porosity medium. It also has inverse modeling capabilities. However, unlike EQ6, which is a similar geochemical modeling program, PHREEQC supports only the use of the Davies or B-dot equations for the activity coefficients in dilute systems. The thermodynamic database used by PHREEQC in this work is a direct transcription of the EQ6 database (*data0.ymp.R4*; see DTN: MO0604SPAPHR25.001 [DIRS 176868]).

PHREEQC models the consequences of reacting an aqueous solution with a set of reactants in accordance with equilibrium thermodynamics. It can also include kinetics laws through a BASIC interpreter coupled to the program. PHREEQC handles advective transport by moving aqueous solutions from one cell to the next, allowing the contents of each cell to reach equilibrium (or not) with the solids and surface features present in the cell. Diffusion and dispersion are handled by mixing the contents of cells in proportion to the diffusion (or dispersion) parameters. PHREEQC uses a finite-difference scheme and is therefore subject to numerical dispersion. Inclusion of dispersion-diffusion increases the run time of a particular set of parameters by several fold. PHREEQC uses a hybrid Newton-Raphson technique to solve the set of equations at each time step. It is restricted to a constant time step, unlike the dynamic time stepping of EQ6.

3.1.4 PHREEQC_Post V1.1

PHREEQC_Post V1.1 (BSC 2002 [DIRS 157839]) has been qualified and baselined under STN: 10723-1.1-00. The software was obtained through Software Configuration Management. Table 3-2 indicates the platform and computer on which the software was installed and used. The software is appropriate for use in this calculation and has been used within the range of parameters for which the software was qualified. The Excel macro PHREEQC_Post postprocesses geochemical code PHREEQC outputs and extracts actinide mineral accumulation rates.

3.1.5 GetEqPhases V1.0

GetEqPhases V1.0 (BSC 2002 [DIRS 157840]) has been qualified and baselined under STN: 10725-1.0-00. The software was obtained through Software Configuration Management. Table 3-2 indicates the platform and computer on which the software was installed and used. The software is appropriate for use in this calculation and has been used within the range of parameters for which the software was qualified. The Excel macro GetEqPhases postprocesses geochemical code PHREEQC outputs by collecting saturation index (SI) of all mineral phases throughout preliminary or screening simulations and processes the results in order to choose those minerals allowed to precipitate in actual accumulation PHREEQC simulations.

3.1.6 Acc_with_decay V1.2

Acc_with_decay V1.2 (BSC 2002 [DIRS 157838]) has been qualified and baselined under STN: 10499-1.2-00. The software was obtained through Software Configuration Management. Table 3-2 indicates the platform and computer on which the software was installed and used. The software is appropriate for use in this calculation and has been used within the range of parameters for which the software was qualified. The Excel macro Acc_with_decay V.1.2 applies decay to plutonium and uranium and variable enrichment to uranium to postprocess the geochemical code PHREEQC outputs.

3.1.7 MinAcc V1.0

MinAcc V. 1.0 (BSC 2002 [DIRS 157841]) has been qualified and baselined under the under STN: 10724-1.0-00. The software was obtained through Software Configuration Management. Table 3-2 indicates the platform and computer on which the software was installed and used. The software is appropriate for use in this calculation and has been used within the range of parameters for which the software was qualified. . The Excel macro MinAcc computes the volume of mineral accumulation by postprocessing the geochemical code PHREEQC outputs.

3.1.8 EQ6 V7.2bLV and EQ3/6 V8.1

EQ6 V7.2bLV (BSC 2002 [DIRS 159731], STN: 10075-7.2bLV-02) and EQ3/6 V8.1 (BSC 2005 [DIRS 176889], STN: 10813-8.1-00) have been qualified and baselined. The software was obtained through Software Configuration Management. Table 3-2 indicates the operating system and computer on which the software was installed and used. The major components of the EQ3/6 software package include EQ3NR, a speciation-solubility code; EQ6, a reaction path code which represents water–rock interaction or fluid mixing in either a pure

reaction progress mode or a time mode; EQPT, a data processor file; EQLIB, a supporting software library; and several (>5) supporting thermodynamic data files preprocessor. The waste package effluent concentrations (source terms) used as input in this calculation were computed with EQ3/6 in Section 6.4.1 of this report or within *Geochemistry Model Validation Report: Material Degradation and Release Model* (BSC 2006 [DIRS 176911]). In Section 7.1.1, EQ6 results were compared to PHREEQC results for a confidence building exercise.

3.1.9 GetEqData V1.0.1

GetEqData V1.0.1 (BSC 2002 [DIRS 173680]) has been qualified and baselined under STN: 10809-1.0.1-00. The software was obtained through Software Configuration Management. Table 3-2 indicates the platform and computer on which the software was installed and used. GetEqData is a software routine that operates as a Microsoft Excel macro to postprocess data in EQ3NR (**.3o*) or EQ6 (**.6o*) output files. The program was run on the Windows 2000 operating system on a PC platform. This macro is limited by the EQ3/6 output data and performs a specific extraction of data as directed at run time. The use of this software is consistent with its intended use, which is to postprocess the output files from EQ3/6 and used within its qualified range.

3.1.10 ASPRIN V1.0

ASPRIN V1.0 (BSC 2002 [DIRS 155712]) has been qualified and baselined under STN: 10487-1.0-00. ASPRIN, which stands for Automatic Software Processing of Inventories of Nuclides, performs postprocessing of an output data file created by EQ6 to calculate isotopic inventories for elements of interest. The software was obtained through Software Configuration Management. Table 3-2 indicates the platform and computer on which the software was installed and used. The software is appropriate for use in this calculation and has been used within the range of parameters for which the software was qualified.

3.1.11 TOUGHREACT V3.0

TOUGHREACT V3.0 (LBNL 2002 [DIRS 161256]) has been qualified and baselined under STN: 10396-3.0-00. This software solves mass balance and flow equations using an integral finite differences method. This formulation can handle regular and irregular geometries. In the problems described in Section 6.4.6, the grid is essentially regular (except near the bottom of the grid in the validation case); for regular grids, the integral finite differences method is equivalent to conventional finite differences. The flow geometry is defined by volume elements (or grid cells) and flow connections between them. The volume elements are defined by a label or identifier and an associated volume. The flow connections are defined entirely by the identifier of the volume elements that are connected, the half-distance between the element centers, and the angle from the vertical between the element centers. The TOUGHREACT simulations in this report do not involve dryout. TOUGHREACT was developed by introducing reactive geochemistry into the framework of an existing multiphase fluid and heat flow code, TOUGH2; much of the input for TOUGHREACT is described in the *TOUGH User's Guide, Version 2.0* (Pruess et al. 1999 [DIRS 160778]). TOUGHREACT is used for modeling two-dimensional flow and transport in the invert in Section 6.4.6 and Section 7.2.5.

4. INPUTS

This section lists the inputs used to develop this report.

4.1 DIRECT INPUT

This section identifies all technical product inputs that were used directly in the development of the model. The appropriateness of the inputs is also documented in this section.

4.1.1 Thermodynamic Database

Prior to running the software PHREEQC, the EQ6 software input files from DTN: MO0608MWDGEOMA.001 ([DIRS 177332], file: data0 files.zip) were rerun using EQ6 and a thermodynamic database (*data0.ymp.R4*), located in DTN: SN0410T0510404.002 [DIRS 172712]. (Table 4-4 contains the list of EQ6 input files that were rerun.) For the TMI_IG1 source term, the *data0.tmi* database (see DTN: MO0608MWDGEOMA.001, [DIRS 177332], file: data0 files.zip) was used. For the rest of the cases, the *data0.cr3* database (see DTN: MO0608MWDGEOMA.001, [DIRS 177332], file: data0files.zip) was used. The only difference between the two databases (*data0.tmi* and *data0.cr3*) is that *data0.tmi* contains the TMI fuel as a listed species. Since the TMI igneous simulations listed in Table 4-4 start with TMI fuel already corroded, either database could have been used for the TMI EQ6 cases. Both of these databases were created and used for running EQ6 in *Geochemistry Model Validation Report: Material Degradation and Release Model* (BSC 2006 [DIRS 176911]), and the EQ6 files are located in DTN: MO0608MWDGEOMA.001 [DIRS 177332]. Therefore, these databases are appropriate to use for rerunning EQ6 input files taken directly from the same source (DTN: MO0608MWDGEOMA.001, [DIRS 177332], file: data0 files.zip).

DTN: MO0604SPAPHR25.001 [DIRS 176868] contains the PHREEQC thermodynamic database (*phreeqcDATA025.dat*) at 25°C used in running PHREEQC. This database was developed by directly translating the qualified EQ3/6 database *data0.ymp.R4* (DTN: SN0410T0510404.002 [DIRS 172712]) at 25°C. However, due to the fact that *data0.cr3* was used in the prior EQ6 simulations, the PHREEQC database *phreeqcDATA025bdotCr3.dat*, (see output DTN: MO0609SPAINOUT.002), was actually used in the PHREEQC simulations. This is a modified version of the PHREEQC database (phreeqcDATA025.dat) and is located in DTN: MO0604SPAPHR25.001 [DIRS 176868]. The modified database *phreeqcDATA025bdotCr3.dat* contains the same data as the *phreeqcDATA025.dat* with the following changes*:* the suppression of Cr(II), Cr(V), and Cr(VI) species, modifications to specific log K values, and addition of $Cr(OH)_3$(am). These modifications to the Cr species are the same used in the EQ6 simulations using *data0.cr3* (see DTN: MO0608MWDGEOMA.001, [DIRS 177332], file: data0 files.zip) for the input source (BSC 2006 [DIRS 176911]). Thus, to be consistent with the input data that used the Cr corrected EQ6 database, these modifications were also done to the PHREEQC thermodynamic database.

While completing the validation exercise on the adsorption model in Section 7.2.2.2, it was discovered that there are several errors in the PHREEQC thermodynamic database for gamma 0,0 line, which incorrectly set the ion size parameter in the extended Debye Hückel (b-dot) to 0, instead of 4, for each uncharged species. This differs from how other software such as EQ6 uses

this ion size parameter, and this was how the error was discovered. The "-gamma 0.00 0.0410" was replaced with "-gamma 4.00 0.0410". This impacted 26 Np, 13 Pu, 2 Ti, and one U-Pu species. This error was discovered after all of the PHREEQC simulations had been completed. Thus, the simulations were redone for only source terms that contain the Np, Pu, Ti or the U-Pu, species. The corrections were made to the *phreeqcDATA025bdotCr3.dat*, a file described in the previous paragraph, the modified database is called *phreeqcDATA025bdotCr3az.dat* and is also located in output DTN: MO0609SPAINOUT.002. In summary, the source terms that used *phreeqcDATA025bdotCr3.dat* database are the TMI and CDSPIG and the source terms that used *phreeqcDATA025bdotCr3az.dat* database are the FFTF and CSFlux.

The database used in the TOUGHREACT simulations, *thermk1.01.dat*, was obtained from DTN: LB0302DSCPTHCS.001 [DIRS 164744]. The database was developed for TOUGHREACT V3.0 and previously used in *Drift-Scale THC Seepage Model* (BSC 2004 [DIRS 172862]) for a similar application.

4.1.2 Mixing Water Composition

There are two waters used in the PHREEQC simulations that are mixed with the waste package effluents. For the Igneous Scenario, basalt water is used as the mixing water and for the Seismic Scenario pore water from SD-9 was used. A third mixing water was used to do a sensitivity simulation in PHREEQC using J-13 well water.

4.1.2.1 Mixing Water: Basalt Water

The basaltic water composition used to model the waste package in the igneous scenario was obtained from *Dike/Drift Interactions* (BSC 2004 [DIRS 170028]). As described in Appendix E of that report (BSC 2004 [DIRS 170028]), the input and output files were obtained from cancelled document *Igneous Intrusion Impacts on Waste Packages and Waste Forms* (BSC 2004 [DIRS 168960], Attachment III, *b8b_3.6p* and *b8b_3.6o*). To calculate the basaltic water composition, Bin 8 seepage water from DTN: MO0310SPAEBSCB.003 [DIRS 166411] was reacted with basalt minerals in EQ6 (Table 4-1). Since the EQ6 simulations of water–basalt interaction were carried out at 25°C, Bin 8 (at 40.18°C) was chosen, as all other water types were for higher temperatures. A further justification of using the bin 8 seepage water was presented in *Dike/Drift Interactions* (BSC 2004 [DIRS 170028]), Section 6.8.4.1 in which sensitivity analyses were conducted using two other seepage water (bin 11 and J-13). These two water types represent seepage waters that are: 1) more concentrated, and 2) more dilute than the Bin 8 seepage water. The analyses show that the values for ionic strength and pH for the three water types are very similar. Therefore, the type of water percolating through the basalt will not have a meaningful impact on the final reacted water chemistry. More details of this are located in the report *Igneous Intrusion Impacts on Waste Packages and Waste Forms* (BSC 2004 [DIRS 168960], Sections 4.1 and 6.5.3).

Table 4-1. Basaltic Water Composition

EQ6 Input Composition Values		
Element	**Concentration**	**Units**
Al	6.46×10^{-7}	molal
Na	4.47×10^{-2}	molal
Si	6.74×10^{-5}	molal
Ca	4.76×10^{-6}	molal
K	1.24×10^{-9}	molal
Mg	4.69×10^{-5}	molal
H (pH)	9.02	Standard Units
Fe	1.43×10^{-12}	molal
F	2.96×10^{-13}	molal
Cl	5.61×10^{-4}	molal
P	9.87×10^{-3}	molal
C	2.19×10^{-2}	molal
N	3.97×10^{-5}	molal
S	3.55×10^{-4}	molal

Source: BSC 2004 [DIRS 168960], Attachment III, file *b8b_3.6p*; pH obtained from file *B8b_3.6o*, source has data in the units mol/kgw (moles per kg of water or moles aqueous) which is the same as molal

4.1.2.1.1 Justification for Use of Cancelled Document (BSC 2004 [DIRS 168960])

The basalt water composition listed in Table 4-1 is obtained from *Igneous Intrusion Impacts on Waste Packages and Waste Forms* (BSC 2004 [DIRS 168960]), which was cancelled when the technical content was incorporated into *Dike/Drift Interactions* (BSC 2004 [DIRS 170028]). *Dike/Drift Interactions* (BSC 2004 [DIRS 170028], Appendix E) provides an explanation and justification for the inclusion of the input and output files from the canceled document, that also applies to this report. A primary reason for the incorporation of the technical content is that it duplicates much of the technical scope of *Dike/Drift Interactions* (BSC 2004 [DIRS 170028]). Because the files have been incorporated into *Dike/Drift Interactions* (BSC 2004 [DIRS 170028]), the reliability of the input source is high. The citation of the input and output files in *Dike/Drift Interactions* (BSC 2004 [DIRS 170028]) is also an example of a prior use of the input data. Finally, the data provide the properties of interest: the composition of water that has interacted with basalt. Therefore, the basaltic water compositions provided by files *b8b_3.6p* and *b8b_3.6o* from *Igneous Intrusion Impacts on Waste Packages and Waste Forms* (BSC 2004 [DIRS 168960]) are appropriate for use as direct inputs by this report.

4.1.2.2 Mixing Water: SD-9 Pore Water

The water chosen as the mixing water for the seismic simulation for CSFlux9 is a pore water extracted from the tuff at the repository horizon from borehole SD-9 of the Tptpll unit. The rock units of the repository are located in the Topopah Spring Tuff and include the upper lithophysal (Tptpul), middle nonlithophysal (Tptpmn), lower lithophysal (Tptpll), and lower nonlithophysal (Tptpln). This exact SD-9 pore water sample has also been used as input water (labeled as "w6") in other analyses including the *Drift-Scale THC Seepage Model* (BSC 2005 [DIRS 172862] and *Engineered Barrier System: Physical and Chemical Environment* (BSC [DIRS 175083]). The

composition of the SD-9 pore water is similar to thermally perturbed seepage compositions used in the material degradation and release model for sensitivity cases (BSC 2006 [DIRS 176911], Table 4-3). The similarities are that the elemental concentrations are within the same order of magnitude. The chemical composition of the SD-9 pore water is presented in Table 4-2. This pore water was from the unit Tptpll, at a depth of 990.4 to 991.7 feet (DTN: GS020408312272.003 [DIRS 160899]). The water sample chosen for the analysis is one that originated from the stratigraphic rock units located at the depth of the repository horizon.

Table 4-2. SD-9 Pore Water Composition

EQ6 Input Composition Values		
Element	**Concentration**	**Units**
Na	3.65×10^{-3}	molal
Si	8.32×10^{-4}	molal
Ca	1.40×10^{-3}	molal
K	2.02×10^{-4}	molal
Mg	3.70×10^{-5}	molal
H (pH)	7.9	Standard Units
F	1.32×10^{-4}	molal
Cl	6.49×10^{-4}	molal
U	1.39×10^{-7}	molal
C as HCO_3	5.13×10^{-3}	molal
N as NO_3	2.74×10^{-4}	molal
S as SO_4	1.04×10^{-4}	molal
Mn	3.82×10^{-7}	molal
Mo	2.29×10^{-7}	molal

Source: DTN: GS020408312272.003 [DIRS 160899], sample SD-9/990.4-991.7/UC.

NOTE: All data were converted from mg/L in the source to molal (same as mol/kgw) for use in PHREEQC input file, with the exception of U, Mn, and Mo, which were converted from μg/L in the source to molal.

4.1.2.3 Sensitivity Analysis Mixing Water - J-13 Well Water

A sensitivity PHREEQC simulation was conducted for the CSFlux9 waste package to see the impact when the mixing water was changed from SD-9 pore water to J-13 well water from DTN: MO0006J13WTRCM.000 [DIRS 151029]. The chemical composition of the J-13 well water is presented in Table 4-3.

Table 4-3. J-13 Well Water Composition

EQ6 Input Composition Values		
Element	**Concentration**	**Units**
Ca	3.24×10^{-4}	molal
H (pH)	7.41	Standard Units
Mg	8.27×10^{-5}	molal
Na	1.99×10^{-3}	molal
K	1.29×10^{-4}	molal
Cl	2.01×10^{-4}	molal
S	1.92×10^{-4}	molal
N	1.42×10^{-4}	molal
F	1.15×10^{-4}	molal
Si	1.01×10^{-3}	molal

Source: DTN: MO0006J13WTRCM.000 [DIRS 151029].

NOTE: All data were converted from mg/L in the source to molal (same as mol/kgw) for use in the PHREEQC input file.

4.1.3 Waste Package Releases

The waste package releases include the following releases from the CSNF and DOE SNF waste packages:

1. Diffusive releases (dissolved U, dissolved Pu, and Pu-colloid) from the nominal scenario (no seepage) come from TSPA modeling. The data are preliminary and are used for scoping calculations only. The preliminary data are described in Section 6.3.

2. Dissolved releases from the seismic and igneous scenarios (seepage cases) come from *Geochemistry Model Validation Report: Material Degradation and Release Model* (BSC 2006 [DIRS 176911]; files listed below in Table 4-4)

3. Solid entrainment releases (mineral releases) from the seismic scenario (seepage case) come from *Geochemistry Model Validation Report: Material Degradation and Release Model* (BSC 2006 [DIRS 176911], file *Entrain5_CSNF.xls*, Sheet 1).

4. Solid releases from the bottom of the waste package for use in the bottom failure scenario come from *Geochemistry Model Validation Report: Material Degradation and Release Model* (BSC 2006 [DIRS 176911]; files listed below in Table 4-6).

4.1.3.1 Diffusive Releases from Waste Package

For the nominal case, there are no direct inputs. The diffusive releases of U and Pu from the waste package were taken from preliminary calculations performed for TSPA using GoldSim. The preliminary data can be used for scoping runs to see if the quantity of diffusive releases is high enough to cause criticality concerns. The preliminary data are described in Section 6.3.

4.1.3.2 Dissolved Losses

Table 4-4 contains the initial EQ6 simulations used as source terms for dissolved losses from the waste package from *Geochemistry Model Validation Report: Material Degradation and Release Model* (BSC 2006 [DIRS 176911], Tables 6-24, 6-34, and 6-38; DTN: MO0608MWDGEOMA.001 [DIRS 177332]). The contents of each waste package type listed in Table 4-4, including the SNF, are described in detail in *Geochemistry Model Validation Report: Material Degradation and Release Model* (BSC 2006 [DIRS 176911], Section 4.1.3).

Table 4-4. EQ6 Source Term File Inputs

EQ6 file Names Used for Input	Waste Package Type	Scenario	Conditions	Percent Remaining			Reason for Choice
				Pu	U	Years	
TMI_IG1a.6i	TMI	Igneous	1 L/yr	N/A	62.81	14,542	High U loss, low flow rate
TMI_IG2.6i	TMI	Igneous	1,000 L/yr	N/A	34.28	10,069	High U loss
CDSPIG2a.6i *CDSPIG2a.bin* *CDSPIG2a.min_info.txt* *CDSPIG2b.6i* *CDSPIG2b.bin* *CDSPIG2b.min_info.txt* *CDSPIG2c.6i*	N-Reactor	Igneous	1,000 L/yr	N/A	21.06	10,048	Highest U loss for igneous at 10,000 years
FFTFIG1adEhdec.6i *FFTFIG1adEhdec.bin* *FFTFIG1adEhdec.min_info.txt*	FFTF	Igneous	1 L/yr, adjusted Eh, Pu decay included	73.12	83.34	10,832	High Pu loss, low flow rate
FFTFIG2adEhdec.6i	FFTF	Igneous	1,000 L/yr, adjusted Eh, Pu decay included	72.86	57.04	10,076	Highest Pu loss at 10,000 years
CSFlux9.6i	CSNF	Seismic	1,000 L/yr	100.00	97.33	10,036	Highest U loss for seismic at 10,000 years

Source: DTN: MO0608MWDGEOMA.001 [DIRS 177332], folders: Igneous_Scenerio_TMI.zip (TMI waste package types); Igneous_Scenerio_FFTF.zip (FFTF waste package types); Igneous_Scenerio_CDSP.zip (N-reactor waste package type); and Seismic_Scenario.zip (CSNF waste package type).

4.1.3.3 Solid Entrainment Losses

Table 4-5 provides percent losses of major minerals by an entrainment process in a bathtub configuration as a function of seepage flow rate for the CSNF waste package for the seismic scenario. The table comes from the mass transfer model as applied in *Geochemistry Model Validation Report: Material Degradation and Release Model* (BSC 2006 [DIRS 176911]). Solid entrainment losses are not calculated for the igneous scenario because the material degradation and release model (BSC 2006 [DIRS 176911], Section 6.4.4.2) determined that the deposition of oxidized alteration products during an igneous event would form a filter pack preventing significant movement of particulate material (larger than colloidal) from the waste package.

Table 4-5 is used in Section 6.6 to determine the mass of material entrained out of the waste package at 20,000 years after breach, as a function of flow rate for the seismic case.

Table 4-5. Entrainment Percents for Major Minerals, CSNF, Bathtub

Flow Rate, Q (L/yr)	1	5	10	15	50	100	150
Gibbsite	0.000	0.461	1.554	2.389	6.101	9.435	11.951
Goethite	0.000	0.000	0.299	0.858	3.351	5.605	7.317
Schoepite	0.000	0.000	0.096	0.610	2.904	4.980	6.558
Pyrolusite	0.000	0.000	0.043	0.545	2.787	4.817	6.360
Trevorite	0.000	0.000	0.015	0.510	2.724	4.730	6.253
Eskolaite	0.000	0.000	0.000	0.491	2.690	4.681	6.195
$Fe_2(MoO_4)_3$	0.000	0.000	0.220	0.761	3.177	5.362	7.021

Source: DTN: MO0608MWDGEOMA.001 [DIRS 177332], folder: mass transfer.zip, file: *EntrainPercent.xls*.

4.1.3.4 Solid Losses from Bottom of Waste Packages

A set of the criticality scenarios presented in *Disposal Criticality Analysis Methodology Topical Report* (YMP 2003 [DIRS 165505], Section 3.3) refers to bottom failure as a mechanism for release of material out of the waste package. Bottom failure could happen by corrosion mechanisms such as degradation of the waste package bottom by water droplets hanging or dripping from the bottom.

In order to evaluate the effects of bottom failure, scenarios examined in *Geochemistry Model Validation Report: Material Degradation and Release Model* (BSC 2006 [DIRS 176911]) were used to select scenarios with maximum losses of Gd from the waste package. Those scenarios contained corrosion products with the lowest Gd content, and thus were more likely to cause an external criticality concern once the solids have been released to the invert. Preferential losses of Gd, primary neutron absorber, from the waste packages could affect the neutronics of the system and increase the likelihood of criticality events involving the remaining solids that are lower in Gd than the initial waste package contents. Table 4-6 is the listing of EQ6 files from degradation and release model that exhibit highest percent losses of Gd compared to fissile materials in the waste package. N-Reactor and TMI waste packages were not considered, as the amount of fissile materials in these waste packages does not require addition of neutron absorbers. In addition, FFTF waste packages were not considered here, as the loss of Gd from these packages did not occur in the EQ6 simulations reported in the degradation and release model.

Table 4-6. Selected EQ6 Simulations with Highest Percent Releases of Gd

Scenario	EQ6 Input File	Percent Gd Losses	Percent Np Losses	Percent Pu Losses	Percent U Losses	Time (years)
Seismic	*CS-S-Mx-C5_adEH.6i*	68.61	100.00	100.00	100.00	20,151
Igneous	*CSNFIG1.6i*	84.83	99.79	99.52	100.00	12,773
Nominal	*CSNF_Nominal.6i*	99.99	99.65	97.28	100.00	10,959

Source: DTN: MO0608MWDGEOMA.001 [DIRS 177332], folders: Nominal_Scenario.zip, Igneous_Scenario_CSNF.zip, Seismic_Scenario.zip.

4.1.3.5 Uranium and Plutonium Isotopic Content of Waste Forms

For criticality, one of the important inputs is the initial uranium and plutonium isotopic composition of the waste forms in the waste packages that are modeled. For each source term listed in Table 4-4, the starting uranium and plutonium isotopic fraction and masses were determined for each waste form contained in the waste packages. Those calculations are documented in spreadsheet *Fuel Isotopic Composition.xls* using the inputs listed in Table 4-7.

Table 4-7. Inputs for Fuel Isotopic Composition Calculations

Input	Source
Molecular weights	Parrington et al. 1996 [DIRS 103896], pp. 48 and 49 (Established Fact)
CSNF gram-atoms of each U and Pu isotope	BSC 2005 [DIRS 174583], Appendix F, *CSNF.xls*, sheet "Complete Fuel Composition"
CSNF total moles fuel	BSC 2006 [DIRS 176911], Appendix A, *CSNF WP.xls*, tab "WP Total Moles and SA"
CSNF moles U per mole of fuel	BSC 2005 [DIRS 174583]), Appendix F, *CSNF.xls*, sheet "Simplified Fuel Composition"
CSNF moles Pu per mole fuel	BSC 2005 [DIRS 174583]), Appendix F, *CSNF.xls*, sheet "Simplified Fuel Composition"
N-Reactor Mark IA fuel isotopic composition	DOE 2000 [DIRS 150095], Table 3-1
N-Reactor total moles fuel	BSC 2006 [DIRS 176911], Appendix A, spreadsheet *CDSP WP.xls*, tab "Bathtub"
N-Reactor moles U per mole of fuel	BSC 2006 [DIRS 176911], Appendix A, EQ6 input file *CDSPIG2.6i* (calculated from 100 g fuel divided by 238 g/mole)
TMI U-235 mole fraction	DOE 2003 [DIRS 164970], Section 3.1.2.2, p. 23 of 57
TMI total moles fuel	BSC 2006 [DIRS 176911], Appendix A, spreadsheet *CDSP_Long_WP_TMI.xls*, tab "TMI"
TMI moles U per mole of fuel	BSC 2006 [DIRS 176911], Appendix A, spreadsheet *CDSP_Long_WP_TMI.xls*, tab "TMI"
HLW glass mole fraction	BSC 2001 [DIRS 157640], Table 5
N-Reactor HLW glass total moles	BSC 2006 [DIRS 176911], Appendix A, *spreadsheet CDSP WP.xls*, tab “WP Total Moles & Surface Areas”
TMI HLW glass total moles	BSC 2006 [DIRS 176911], Appendix A, spreadsheet *CDSP_Long_WP_TMI.xls*, tab “SDM EQ6 Inputs”
FFTF HLW glass total moles	BSC 2006 [DIRS 176911], Appendix A, spreadsheet *CDSP_Long_WP_FFTF.xls*, tab “EQ6 Inputs”
HLW glass moles U per mole of glass	BSC 2001 [DIRS 157640], Table 5
FFTF mole fraction MOX and UOX	BSC 2001 [DIRS 157195], Table 4
FFTF total moles fuel	BSC 2006 [DIRS 176911], Appendix A, *CDSP_Long WP_FFTF.xls*, tab "FFTF"
FFTF moles U per mole of fuel	BSC 2001 [DIRS 157195], Table 4
FFTF moles Pu per mole fuel	BSC 2001 [DIRS 157195], Table 4

NOTE: For each waste form, one mole of fuel or HLW glass is defined as 100 grams.

4.1.3.6 Radioactive Half-Life of Plutonium-239

In the EQ6 simulation for FFTF, the radioactive decay of ^{239}Pu to ^{235}U was included in the calculations. No other source term contained ^{239}Pu. The half-life of ^{239}Pu is 24,100 years

(Parrington et al. 1996 [DIRS 103896], p. 48). The value is used in the software program Acc_with_decay. This source has been used extensively on the project in engineering documents as well as scientific reports and calculations and is considered Established Fact.

4.1.4 Waste Package Flow Rate

The flow rate through the waste package is consistent with flow rate used in source term. The values of flow rate are either 1 L/yr or 1,000 L/yr. This flow rate was established for each source term in *Geochemistry Model Validation Report: Material Degradation and Release Model* (BSC 2006 [DIRS 176911]), the source of the inputs listed in Table 4-4. The flow rate is indicated in the header of each input file for PHREEQC (see Appendix A for an example of the input file for PHREEQC).

4.1.5 Self-Diffusion Coefficient of Water

The self-diffusion coefficient of water at 25°C is 2.299×10^{-9} m^2 s^{-1} and comes from the paper "*Self-diffusion in Normal and Heavy Water in the Range 1-45°*" (Mills 1973 [DIRS 133392], Table III) in the *Journal of Physical Chemistry*. The diffusion coefficient is used in the TOUGHREACT flow and transport modeling described in Sections 6.4.6 and 7.2.5. The information from Mills (1973 [DIRS 133392], Table III) has been justified for intended use in this document in Section 4.1.14.4.

4.1.6 Tuff Composition

Tuff is the type of rock in the far-field and the type of rock planned for the invert ballast. The properties of tuff are required to model the interaction of the source term with the tuff. The description of the mineralogy used in this report is based on the main phenocryst constituents of the Topopah Spring Tuff member from Lipman et al. (1966 [DIRS 100773], pp. F28 through F33). These minerals are cristobalite (quartz), annite, phlogophite, anorthite, albite, and maximum microcline. The mnetal oxide composition of tuff is provided in Table 4-8 and converted to moles of the normative minerals in output DTN: MO0609SPAINOUT.002 (folder: Dissolution_Rates_of_ Tuff_Minerals, spreadsheet: *Tuff_minerals.xls*). The resulting composition of the tuff was entered into each PHREEQC input file as described in Appendix A.

Table 4-8. Tuff Composition

Oxide	Mean Tuff Composition (wt%)
SiO_2	76.29
Al_2O_3	12.55
FeO	0.14
Fe_2O_3	0.97
MgO	0.13
CaO	0.50
Na_2O	3.52
K_2O	4.83

Table 4-8. Tuff Composition (Continued)

Oxide	Mean Tuff Composition (wt%)
TiO_2	0.11
MnO	0.07
Total	99.11

Source: DTN: GS000308313211.001 [DIRS 162015].

NOTE: Values are the mean of 40 ECRB samples. The mean value is located in the second to last row of data in the source DTN.

4.1.7 Dissolution Rates for Tuff Minerals

The dissolution rate of cristobalite (SiO_2) is calculated based on the dissolution rate of quartz (see output DTN: MO0609SPAINOUT.002, folder: Dissolution_Rates_of_Tuff_Minerals, file: *cristobalite&quartz.xls*). This approach is based on findings by Rimstidt and Barnes (1980 [DIRS 101708]), who showed that all the silica polymorphs share the same growth rate at near-neutral pH when conditions are far from equilibrium.

Table 4-9. Quartz Dissolution Rate at 25°C

pH	log (dissolution rate) at 25°C (mol/cm^2 s)	Location in Source
2.15	−16.05	Table I
4.03	−16.23	Table I
4.09	−16.10	Table I
5.5	−16.44	Table I
6.9	−15.90	Table I
8.33	−15.85	Table III
9.02	−15.85	Table III
10.27	−15.47	Table III
10.3	−15.50	Table III
10.3	−15.51	Table III
10.9	−15.27	Table III
11	−15.14	Table III
11.04	−14.99	Table III
12.3	−14.78	Table III
12.3	−14.81	Table III

Source: Brady and Walther 1990 [DIRS 110754].

NOTE: Used in output DTN: MO0609SPAINOUT.002, folder: Dissolution_Rates_of_Tuff_minerals, file: *cristobalite&quartz.xls*.

Table 4-10. Quartz Dissolution Rate at 60°C

pH	log (dissolution rate) at 60°C (mol/cm^2 s)	Location in Source
2.15	−15.30	Table I
3.10	−15.47	Table I
4.70	−15.37	Table I
6.15	−15.14	Table I
7.61	−14.90	Table III
8.62	−14.68	Table III
9.30	−14.47	Table III
9.30	−14.47	Table III
10.80	−13.42	Table III
10.80	−13.42	Table III
11.50	−13.18	Table III
11.68	−13.69	Table III

Source: Brady and Walther 1990 [DIRS 110754].

NOTE: Used in output DTN: MO0609SPAINOUT.002, folder: Dissolution_Rates_of_Tuff_minerals, file: *cristobalite&quartz.xls*.

Table 4-11. Dissolution Rate Constants for Cristobalite and Quartz

Mineral	Log K	
	Temperature = 25°C	Temperature = 60°C
Cristobalite	−3.1922	−2.8670
Quartz	−3.7501	−3.3553

Source: DTN: SN0410T0510404.002 [DIRS 172712], file: *data0.ymp.R4*.

The dissolution rate for maximum microcline (one of the K-feldspars) comes from a study by Palandri and Kharaka (2004 [DIRS 175261]). The equation for the dissolution rate is a function of pH and contains three terms, representing the low pH (acid), neutral pH, and high pH (basic) mechanisms (Palandri and Kharaka 2004 [DIRS 175261], Section 2.2). The log of the rate for the acid mechanism in the study by Palandri and Kharaka (2004 [DIRS 175261], Equation 14, p. 9) is given by:

$$\log(rate) = \log k_{acid}^{298.15K} - n_{H^+} pH$$

where $\log k_{acid}^{298.15K}$ is the log of the rate constant calculated at pH=0 and 25°C and n_{H^+} is the reaction order with respect to H^+. The following equation at 25°C represents the dissolution rate for a mineral like maximum microcline, with acid, neutral, and basic mechanisms:

$$-\frac{dm}{dt} = rate = k_{acid}^{298.15K} a_{H^+}^{n_1} + k_{neutral}^{298.15K} + k_{basic}^{298.15K} a_{H^+}^{n_2}$$

The equation is based on Equation 13 from Palandri and Kharaka (2004 [DIRS 175261]), with the third term added for the basic mechanism of the rate. The values of *n* and log *k* are given in Table 4-12. Values of E are given in case different temperatures are needed. In Section 6.4.2, the values of dissolution rates versus pH presented in Table 4-12, which are based on three segments (acidic, neutral, and basic), are converted to expressions based on two segments (acidic and basic), which is compatible with EQ6. The results are in output DTN: MO0609SPAINOUT.002 (folder: Dissolution_rates_of_Tuff_ Minerals, file: *maximum microcline (k-feldspar).xls*).

Table 4-12. Dissolution Rate Constants for Maximum Microcline

Acidic Leg			Neutral		Basic Leg		
log k[a]	E[a]	n[a]	log k	E	log k	E	n
−10.06	51.7	0.500	−12.41	38.0	−21.20	94.1	−0.823

Source: Palandri and Kharaka 2004 [DIRS 175261], Table 15.

NOTES: [a] Rate constant k, computed by source at 25°C, pH=0, mol/m^2·s.
Arrhenius activation energy E, kJ/mol.
Reaction order n with respect to H^+.

The equation for the dissolution rate for albite_low and anorthite from *Dike/Drift Interactions* (BSC 2004 [DIRS 170028], Appendix B, Equation B-1) is given by:

$$\text{Total Dissolution Rate} = k_1[H^+]^{S1} + k_2[H]^+]^{S2} \text{ (mol/cm}^2\text{·s)}$$

where k_1 and k_2 represent the exponential of the log intercept and S1 and S2 values represent the slopes of the trend lines, with the values of the constants given in Table 4-13.

Table 4-13. Dissolution Rate Constants for Anorthite and Albite_low

	Acidic Leg		Basic Leg	
Mineral	k_1 (mol/cm^2·s)	S1	k_2 (mol/cm^2·s)	S2
Anorthite	1.58×10^{-11}	0.91	2.00×10^{-18}	−0.30
Albite_low	7.94×10^{-15}	0.33	5.01×10^{-19}	−0.32

Source: BSC 2004 [DIRS 170028], Table 6-20, Figure B-1, Figure B-2.

The dissolution rates of annite and phlogopite are calculated based on the dissolution rates of muscovite; see output DTN: MO0609SPAINOUT.002 (folder: Dissolution_rates_of_Tuff_ Minerals, file: *Annite and Phlogopite Dissolution (muscovite).xls*).

Table 4-14. Annite and Phlogopite Dissolution Rates at 70°C

pH	Limiting Dissolution Rates at 70°C (mol/cm^2 s)	log (dissolution rate) at 70°C (mol/cm^2 s)]
1.4	6.350×10^{-16}	−15.197
2.1	2.700×10^{-16}	−15.569
3	1.270×10^{-16}	−15.896
4.1	5.970×10^{-17}	−16.224
5.3	2.010×10^{-17}	−16.697
6.2	2.770×10^{-17}	−16.558
7.8	4.060×10^{-17}	−16.391
8.8	1.070×10^{-16}	−15.971
9.5	1.200×10^{-16}	−15.921
10.8	1.610×10^{-16}	−15.793
11.8	4.450×10^{-16}	−15.352

Source: Knauss and Wolery 1989 [DIRS 124300], Table 4.

4.1.8 Invert Properties

The invert ballast material is identified as crushed tuff (BSC 2004 [DIRS 168489]). Table 4-15 lists the invert properties, which come from *Estimation of Mechanical Properties of Crushed Tuff for Use as Ballast Material in Emplacement Drifts* (BSC 2004 [DIRS 168138], Table 5). This source is listed as the appropriate source of invert properties in *D&E / PA/C IED Emplacement Drift Configuration and Environment* (BSC 2004 [DIRS 168489]). The invert properties in Table 4-15 represent invert ballast with non-uniform particle sizes, referred to as poorly sorted. The values were used to calculate the capillary properties for the poorly sorted materials in Appendix G.

Table 4-15. Poorly Sorted Invert Properties

	Minimum	Average	Maximum
Grain Density (g/cm^3) (Specific Gravity)[a]	2.52	2.55	2.58
Total Porosity (inter- and intragranular)	27%	31%	39%
Permeability (K-sat)	2.5×10^{-4} cm/sec	0.13 cm/sec	1.3 cm/sec

Source: BSC 2004 [DIRS 168138], Table 5, Section 7.6.

[a] The maximum and minimum grain density values represent the average value plus and minus one standard deviation, based on measured densities of tuff samples.

Table 4-16 presents another set of invert properties that were used as the base case in *Multiscale Thermohydrologic Model* (BSC 2005 [DIRS 173944], Appendix X; diameter = 3 mm). These invert properties represent uniform particle size, referred to as well-sorted.

Table 4-16. Well-Sorted Invert Properties for 3 mm Particle Size

Invert Type	Inter-granular Porosity	Saturated Permeability (m^2)	van Genuchten α_{vG} (m^{-1})	van Genuchten (*m*)	Residual Saturation (for Relative Permeability)
Well-sorted, 3 mm Particle Size	0.450	1.51×10^{-8}	61.2	0.875	0.0853

Source: BSC 2005 [DIRS 173944], Appendix X; DTN: MO0307SPAVGSUM.000 [DIRS 164438].

Both sets of invert properties were used in Section 6.4.6, Appendix F, and Appendix G for the TOUGHREACT modeling. Additional sources for matrix properties of the invert materials are listed in Table 4-18.

4.1.9 Adsorption Coefficients

Table 4-17 contains the properties used to model adsorption, as described in Section 6.4.3. The K_d values were measured on tuff core samples that were crushed and typically sieved to a size fraction of 75 to 500 μm. Specific surface areas are thought to be independent of size fraction because tuffs are composed of fine grained minerals on the order of 10-20 μm (BSC 2004 [DIRS 164500], p. A-6). This is consistent with the observation that larger size fractions do not significantly affect K_d measurements on tuff samples (Rogers and Meijer 1993 [DIRS 123127], pp. 1511 to 1512). The observed tendency for the smallest size fraction to produce higher adsorption is likely due to a disproportionately large abundance of clay minerals in these fractions (BSC 2004 [DIRS 164500], p. A-6).

Table 4-17. Adsorption Parameters and Sources

Parameter	Source
Mean invert (inter- and intragranular) porosity (0.31)	BSC 2004 [DIRS 168138], Table 5
Mean invert tuff (grain density) specific gravity (2.55)	BSC 2004 [DIRS 168138], Table 5
Surface site density (2.3 sites/nm^2)	Davis and Kent 1990 [DIRS 143280], p. 227
Specific surface area measurements of crushed tuff samples	BSC 2004 [DIRS 164500], Table A-1
Avogadro's number (6.022×10^{23})	Weast and Astle 1981 [DIRS 100833], p. F-81
Cumulative distributions of Pu and U Kd measurements for devitrified tuff	BSC 2004 [DIRS 164500], Figures A-33b and A-63b
Minimum Kd values recommended for devitrified tuff (10 and 0 mL/g, respectively)	BSC 2004 [DIRS 164500], Table 6-3
Mean change in Pu and U Kd measurements between 25°C and 95°C (negligible and factor of 3.9 increase, respectively)	BSC 2004 [DIRS 164500], p. I-47

All BSC references are qualified. The source from Weast and Astle (1981 [DIRS 100833]) is a handbook and thus is established fact. Since the source from Davis and Kent (1990 [DIRS 143280]) is an external source and not considered established fact, it is justified for intended use in Section 4.1.12.

4.1.10 Characteristics of Fractures, Matrix, and Lithophysae

Fractures in the host rock and lithophysae in the vicinity of the proposed repository are potential locations for accumulation of fissile material. Table 4-18 contains a summary of the sources for the inputs that describe the host rock properties. The inputs are used in Section 6.4.8.

Table 4-18. Sources for Characteristics of Fractures, Matrix, and Lithophysae

Input	Source
Matrix Permeability and Porosity	BSC 2004 [DIRS 170038]
Matrix porosity and residual saturation data	DTN: LB0207REVUZPRP.002 [DIRS 159672]
Matrix permeability data	DTN: LB0207REVUZPRP.002 [DIRS 159672]
Fracture aperture	DTN: LB990501233129.001 [DIRS 106787]
Percent closed fractures	GS990408314224.001 [DIRS 108396]; DTN: GS990408314224.002 [DIRS 105625]
Fracture frequency	DTN: LB0205REVUZPRP.001 [DIRS 159525]
Fracture porosity	DTN: LB0205REVUZPRP.001 [DIRS 159525]
Lithophysae dimensions	DTN: GS980308315215.008 [DIRS 107355]
Lithophysae porosity and fracture intersections	BSC 2004 [DIRS 166107], Appendix O, Table O-10 (cavities, fitted value)
Lithophysae porosity	DTN: GS980308315215.008 [DIRS 107355]
Lithophysae fill depth	DTN: GS980308315215.008 [DIRS 107355]

4.1.11 Atomic Weights

Atomic weights of the elements and radionuclide isotopes used were taken from *Atomic Mass Adjustment, Mass List for Analysis* (Audi and Wapstra 1995 [DIRS 149625]) and *Nuclides and Isotopes, Chart of the Nuclides* (Parrington et al. 1996 [DIRS 103896], p. 50). These two sources are considered to be established fact. These documents have been used as a source for this information throughout the Yucca Mountain Site Characterization Project and are appropriate as a source for atomic weights in this analysis.

4.1.12 Waste Package Dimensions

Table 4-19 contains the lengths and diameters of the waste package types covered by this report: 21-PWR waste package containing CSNF; 5 DHLW/DOE SNF-Long waste package containing FFTF or TMI SNF; and 2-MCO/2-DHLW waste package containing N-Reactor SNF. In addition, Table 4-19 contains the dimensions for 5 DHLW/DOE SNF-Short, which is a waste package type covered by previous criticality geochemistry calculations (for example, BSC 2004 [DIRS 171809]). The values are used in estimating the distance between waste package effluent and diverted water locations in Section 6.4.6.

Table 4-19. Waste Package Dimensions

Waste Package Type	Nominal Length (mm)	Nominal Diameter (mm)
21-PWR	5,024.4	1,718.3
5 DHLW/DOE SNF-Short	3,452.8	2,126.0
5 DHLW/DOE SNF-Long	5,059.4	2,126.0
2-MCO/2-DHLW	5,059.4	1,830.7

Source: BSC 2005 [DIRS 173501], Table 1.

4.1.13 Log K values used in Sensitivity Analyses for Uncertainty

The log K values at 25°C are 11.6981 for uranophane, and 5.9649 for boltwoodite-Na, which are both located in the EQ3/6 thermodynamic database (data0.ymp.R4) in DTN: SN0410T0510404.002 [DIRS 172712]. This database does not contain the standard deviations of these log K values; however, the sources of the log K's are journal articles (Pérez et al. 2000 [DIRS 157910], p. 606 ; Nguyen et al. 1992 [DIRS 100809]), and these provide the standard deviations. The standard deviation is ± 0.6 for uranophane and ± 0.16 for boltwoodite-Na. Sensitivity analyses using variations of the log K values for the uranium minerals uranophane and boltwoodite-Na are presented in Section 6.8.1.2. The sources (Pérez et al. 2000 [DIRS 157910]; Nguyen et al. 1992 [DIRS 100809]) are external sources and are justified for intended use in Section 4.1.14.3.

4.1.14 Justification and Qualification of External Sources

4.1.14.1 Justification and Qualification of Dissolution Rates and Dissolution Rate Parameters

Justification for the external sources of dissolution rates and dissolution rate parameters of the minerals is provided as follows:

Brady and Walther 1990 [DIRS 110754]—*Description of Data:* Dissolution rates of quartz at 25°C and 60°C used in Tables 4-5 and 4-6. *Qualification Status:* Justified for intended use in this report.. *Extent to Which the Data Demonstrate the Properties of Interest*: This work presents a comprehensive study involving the experimental dissolution rate data as a function of pH at low temperatures (25°C and 60°C). *Reliability of Data Source:* These data were published in *Chemical Geology*, which is a peer-reviewed, well-respected scientific journal with a long record of publication (since 1966). Its articles are reviewed by other experts in the pertinent technical field, including individuals with experience in the subject matter who typically use such information in the course of their work. Technical problems identified by the review process are either resolved prior to publication or the article is rejected. This process provides an appropriate level of confidence that the information is suitable for use in the types of analyses for which it was intended. *Qualification of Personnel*: The lead author, Patrick V. Brady, has a Ph.D. from Northwestern University with an emphasis on the study of silicate mineral surface chemistry and geochemical kinetics. Brady has been published extensively on the subject of silicate mineral geochemistry.

Palandri and Kharaka 2004 [DIRS 175261]—*Description of Data:* Dissolution rate parameters of maximum microcline (K-feldspar) used in Table 4-12. *Qualification Status*:

Justified for intended use in this analysis. *Extent to Which the Data Demonstrate the Properties of Interest:* This work presents a comprehensive study of rate parameters of various minerals for application in geochemical modeling. *Reliability of Data Source*: These data were published in Open File Report 2004-1068 by the U.S. Geological Survey (USGS). Its articles are technically reviewed by other USGS experts in the pertinent technical field, including individuals with experience in the subject matter who typically use such information in the course of their work. Technical problems identified by the review process are resolved prior to publication by the USGS. The USGS is a nationally recognized scientific institution and is highly regarded among the scientific community for both quality and the reliability of scientific work. Scientists at USGS are among the most highly respected in their scientific fields. The USGS provides an appropriate level of confidence that the information is suitable for use in types of analyses for which it was intended. Both the lead author James Palandri and the co-author Yousif Kharaka are part of the USGS Water Resources Division as geochemists and hydrologists. Both have been extensively published both inside the USGS (Open File Reports (OFR) and Water-Resources Investigations Reports (WRIR)) and outside the USGS (various journals including the Journal of Geochemical Exploration and Chemical Geology) on various subjects in experimental geochemistry and geochemistry modeling.

Knauss and Wolery 1989 [DIRS 124300]—*Description of Data:* Annite and phlogopite dissolution rate at 70°C are based on the dissolution rates of muscovite; and are presented in Table 4-14. *Qualification Status:* Justified for intended use in this analysis. *Extent to Which the Data Demonstrate the Properties of Interest:* This work presents a comprehensive study involving the experimental dissolution rate of muscovite as a function of pH at 70°C. *Reliability of Data Source:* These data were published in *Geochimica et Cosmochimica Acta*, which is a well-respected scientific journal with a long record of publication. Its articles are peer-reviewed, i.e., reviewed by other experts in the pertinent technical field, including individuals with experience in the subject matter who typically use such information in the course of their work. Technical problems identified by the review process are either resolved prior to publication or the article is rejected. This process provides an appropriate level of confidence that the information is suitable for use in types of analyses for which it was intended.

4.1.14.2 Justification and Qualification of Adsorption Parameters

Davis and Kent 1990 [DIRS 143280]—*Description of Data:* Surface site density (2.3 sites/nm^2). *Qualification Status:* Justified for intended use in this analysis. *Extent to Which the Data Demonstrate the Properties of Interest:* This work presents a study involving surface complexation modeling in aqueous geochemistry. *Reliability of Data Source:* These data were published in *Reviews in Mineralogy* (published by Mineralogical Society of America), which is a respected journal with a long record of publication, with volume 1 dating to 1974. The successful series is now published jointly by the Mineralogical Society of America and the Geochemical Society. Volumes 1 through 38 were published as "Reviews in Mineralogy." Its articles are peer-reviewed, i.e., reviewed by other experts in the pertinent technical field, including individuals with experience in the subject matter who typically use such information in the course of their work. Technical problems identified by the review process are either resolved prior to publication or the article is rejected. This process provides an appropriate level of confidence that the information is suitable for use in types of analyses for which it was intended. The lead author Jim A. Davis is a hydrologist for the USGS in Menlo Park, California with a

specialty in geochemistry. He has published numerous journal articles on the subject of surface complexations and site density.

4.1.14.3 Justification for External Source for Log K Values Used in Sensitivity Analyses for Uncertainty

Pérez et al. 2000 [DIRS 157910]—*Description of Data:* Log K standard deviation for uranophane. *Qualification Status:* Justified for intended use in this analysis. This source was used as the source of the log K standard deviation for uranophane in the database *data0.ymp.R4*, located in DTN: SN0410T0510404.002 [DIRS 172712]. The standard deviation of this log K is used to evaluate the uncertainty of the results for the uranium mineral uranophane. Uranophane was the most common mineral accumulated in the geochemistry modeling done in this report. The log K data in the EQ 3/6 data0 database was previously qualified for intended use in the database in *Qualification of Thermodynamic Data for Geochemical Modeling of Mineral-Water Interactions in Dilute Systems* (BSC 2004 [DIRS 171916]); a justification is re-iterated here as well. *Reliability of Data Source:* The study by Pérez et al. (2000 [DIRS 157910]) is an article entitled "The Thermodynamics and Kinetics of Uranophane Dissolution in Bicarbonate Test Solutions," published in *Geochimica et Cosmochimica Acta*, though the results had been reported previously in a technical report (Casas et al. 1997 [DIRS 102432]). The article concerns an experimental study on uranophane dissolution thermodynamics and kinetics in bicarbonate solution. The starting material for this study at 25°C is synthesized uranophane and the average measured log K value at infinite dilution is 11.7 (± 0.6). These data were published in *Geochimica et Cosmochimica Acta*, which is a respected journal with a long record of publication (since 1950). This journal is sponsored by the Geochemical Society. Its articles are peer-reviewed, i.e., reviewed by other experts in the pertinent technical field, including individuals with experience in the subject matter who typically use such information in the course of their work.

Nguyen et al. 1992 [DIRS 100809]—*Description of Data:* Log K standard deviation for boltwoodite-Na. *Qualification Status:* Justified for intended use in this analysis. This source was used as the source of the log K standard deviation for boltwoodite-Na in the database *data0.ymp.R4*, located in DTN: SN0410T0510404.002 [DIRS 172712]. The standard deviation of this log K is used to evaluate the uncertainty of the results for the uranium mineral boltwoodite-Na. Boltwoodite-Na was accumulated in two of the simulations (TMI#1 and FFTF#1) for the geochemistry modeling done in this report. The log K data in the EQ 3/6 data0 database were previously qualified for intended use in the database in *Qualification of Thermodynamic Data for Geochemical Modeling of Mineral-Water Interactions in Dilute Systems* (BSC 2004 [DIRS 171916]); a justification is re-iterated here as well. *Reliability of Data Source:* The study by Nguyen et al. (1992 [DIRS 100809]) is an article entitled "Standard Gibbs Free Energies of Formation at the Temperature 303.15 K of Four Uranyl Silicates: Soddyite, Uranophane, Sodium Boltwoodite, and Sodium Weeksite," published in the *Journal of Chemical Thermodynamics*. The *Journal of Chemical Thermodynamics* exists primarily for dissemination of significant new measurements in experimental thermodynamics and thermophysics including calorimetry, phase equilibria, equilibrium thermodynamic properties and transport properties. Its articles are peer-reviewed, i.e., reviewed by other experts in the pertinent technical field, including individuals with experience in the subject matter who

typically use such information in the course of their work. The journal has been published since 1969, thus has over a 30-year history.

4.1.14.4 Justification for the Self-diffusion Coefficient of Water

Mills 1973 [DIRS 133392]—*Description of Data:* The value for the self-diffusion coefficient of water at 25°C is 2.299×10^{-9} m^2 s^{-1} and comes from the paper "Self-diffusion in Normal and Heavy Water in the Range 1-45" (Mills 1973 [DIRS 133392], Table III) in the *Journal of Physical Chemistry*. The diffusion coefficient is used in the TOUGHREACT flow and transport modeling described in Sections 6.4.6 and 7.2.5. *Qualification Status:* Justified for intended use in this analysis. *Reliability of Data Source:* The *Journal of Physical Chemistry* has been is a well-respected scientific journal with a long record of publication (since 1896). This journal is sponsored by the American Chemical Society. Articles are reviewed by experts (peers) in the field that use their data in their work. These data have been used in succeeding investigations for over 30 years.

4.2 CRITERIA

4.2.1 Regulatory Requirements

4.2.1.1 Yucca Mountain Review Plan

As identified in Section 3 of the TWP (BSC 2006 [DIRS 177153]), the acceptance criteria (AC) from *Yucca Mountain Review Plan, Final Report* (YMRP) (NRC 2003 [DIRS 163274]) that will be addressed in this report are as follows:

- Section 2.2.1.3.3.3, Quantity and Chemistry of Water Contacting Waste Packages and Waste Forms (AC 1 through AC 5)
- Section 2.2.1.3.4.3, Radionuclide Release Rates and Solubility Limits (AC 1 through AC 5)
- Section 2.2.1.3.7.3, Radionuclide Transport in the Unsaturated Zone (AC 1 through AC 5)
- Section 2.2.1.3.9.3, Radionuclide Transport in the Saturated Zone (AC 1).

For AC 1 (System Description and Model Integration Are Adequate), under each section listed above, the equivalent models in the TSPA will be used for comparison and differences will be addressed.

Section 8.2.1.1 quotes the full text of the applicable acceptance criteria with pointers to the information within this report that pertains to the criteria.

4.2.1.2 Key Technical Issues (KTI) Agreements

The KTI agreements that will be addressed in this report are CLST 5.04, ENFE 5.03, and RT 4.03 (Reamer and Williams 2000 [DIRS 155464], MOL.20001208.0097, Attachment 1). Each

of these agreements commits the DOE to submitting a validation report for external accumulation modeling for criticality.

Section 8.2.1.2 explains how the KTI agreements have been addressed.

4.2.1.3 Safety Evaluation Report

The Safety Evaluation Report (SER) contains acceptance criteria for how the near-field conditions could influence the occurrence of criticality and how nuclear criticality outside of the waste package affects the near-field environment (Reamer 2000 [DIRS 150765], Section 2.3.3). Many of the criteria are covered by the criteria listed in the YMRP (NRC 2003 [DIRS 163274]). Those acceptance criteria not covered in the YMRP (acceptance criteria 3, 7, and 15 and SER open items 3 and 16 (Reamer 2000 [DIRS 150765], Section 4)) are addressed by this report.

Section 8.2.1.3 quotes the full text of the applicable acceptance criteria and open items and provides pointers to the information within this report that pertains to the item of interest.

4.2.2 Other Requirements—Disposal Criticality Analysis Methodology Topical Report

The following sections of *Disposal Criticality Analysis Methodology Topical Report* (YMP 2003 [DIRS 165505]) are addressed in this report:

- Section 3.3, Figure 3.3a and Figure 3.3b, External Criticality Master Scenarios
- Section 3.3.2, External Scenarios
- Section 3.3.4, Effect of Volcanic Events
- Section 3.4.2, Configurations with the Potential for External Criticality.

Section 8.2.2 provides pointers to the information within this report that pertains to the items of interest.

4.3 CODES, STANDARDS, AND REGULATIONS

This model documentation was prepared to comply with the U.S. Nuclear Regulatory Commission high-level waste rule (10 CFR Part 63 [DIRS 173273]). Subparts of this rule applicable to data include Subpart B, Section 15 (Site Characterization), and Subpart E, Section 114 (Requirements for Performance Assessment). The subpart applicable to models is also Subpart E, Section 114. The sections applicable to FEPs are 10 CFR 63.114(d), (e), and (f) [DIRS 173273].

No additional codes, standards, or regulations are applicable to this report.

5. ASSUMPTIONS

5.1 DISCUSSION OF ASSUMPTIONS IN UPSTREAM DOCUMENTS

The assumptions listed in the primary modeling report that feeds this model, *Geochemistry Model Validation Report: Material Degradation and Release* (BSC 2006 [DIRS 176911], Section 5), have a significant impact on the inputs to this report and are listed below.

5.1.1 Bulk Water Chemistry (Assumption 5.1 of Material Degradation and Release Model)

Assumption—For the nominal case, in the absence of a thin-film model, it is assumed that the bulk water chemistry calculated by this batch reactor model is applicable to thin films of water.

Rationale—For liquid films thicker than 8 to 20 monolayers, the behavior is similar to bulk water (Sposito 1984 [DIRS 127253], pp. 57 to 70). Franks (1975 [DIRS 173728]) supports this observation by indicating that films with thicknesses greater than 10 nm (equivalent to approximately 30 monolayers) behave as bulk water.

1. The OH-bond distance in a water molecule is ~0.1 nm; the length of a hydrogen bond between water molecules is ~0.3 nm (Stumm and Morgan 1996 [DIRS 125332], p. 7).

2. The effect of a cation on the structure of bulk water is localized to a suite of no more than 6 to 20 water solvation molecules (Sposito 1984 [DIRS 127253], p. 57). About 10 molecular layers of water on clay minerals exist at 98% humidity (Sposito 1984 [DIRS 127253], p. 61). The spatial extent of adsorbed water on a phyllosilicate surface is, conservatively, whatever is included in the region bounded by a plane about 1.0 nm from the basal plane of the clay mineral. The bounding plane at 1.0 nm is expected to include all but a few percent of the siloxane surface effects on water structure (Sposito 1984 [DIRS 127253], pp. 69 to 70). A 1-nm layer of water is roughly 4 to 10 water molecules, depending on how they are arranged, so an 8 to 20 water-molecule layer is, therefore, around 2 nm. In addition, cation hydration is similar to hydration of surface complexation sites (Sposito 1984 [DIRS 127253], p. 64). The above clay observations and the magnitude of cation hydration shell radii both suggest that 1 nm to 2 nm of surface associated water is not structurally different than bulk water (Sposito 1984 [DIRS 127253], pp. 57, 61, 64, 69, and 70).

3. Experimental studies of a 20-nm-thick water layer adsorbed onto metal plates indicate that its physical characteristics are consistent with bulk water (Zhang and Grischkowsky 2004 [DIRS 173729]).

Confirmation Status—This modeling assumption, when combined with the diffusion implementation of the EBS radionuclide transport model (BSC 2005 [DIRS 173433]) within TSPA-LA, is conservative in its estimation of radionuclide release and is, therefore, justified, and does not require confirmation.

Use in the Model—This assumption is used in *Geochemistry Model Validation Report: Material Degradation and Release* (BSC 2006 [DIRS 176911], Section 6) in the development of the conceptual model.

5.1.2 Constant Surface Area and Corrosion Rates of Alloys (Assumption 5.2 of Material Degradation and Release Model)

Assumption—In the absence of a surface area function within a geochemistry-modeling tool, the surface areas of the reactants are fixed and assumed not to vary with time.

Rationale—As a material degrades, its surface area will certainly change, but how it varies with time and degree of degradation is extremely complex. Though the actual surface area will increase with time, the effective surface area will tend to decrease due to the formation of a protective layer of corrosion products. The corrosion rate itself also decreases with time due to the formation of oxide layers (DTN: MO0409SPAACRWP.000 [DIRS 172059]). However, the constant surface area simplification can only result in estimated faster degradation, which maximizes the impact of the degradation on the solution chemistry. .

Confirmation Status—The impact of this simplification is that reactants may not degrade as quickly as modeled, but this difference is accounted for by varying the range of degradation rates over three orders of magnitude (BSC 2006 [DIRS 176911], Table 4-12) and is, therefore, justified and requires no further confirmation.

Use in the Model—This assumption is used in *Geochemistry Model Validation Report: Material Degradation and Release* (BSC 2006 [DIRS 176911], Section 6.3).

5.1.3 Thermodynamic Equilibrium (Assumption 5.3 of Material Degradation and Release Model)

Assumption—In the absence of data on the long-term behavior of man-made materials in the waste package for the regulatory period, it is assumed that all homogeneous solution and gas reactions, and all heterogeneous gas–solution reactions, are reversible and at equilibrium. Heterogeneous reactions between solutions and precipitating solids are also assumed to be at equilibrium except for those by which waste and waste package components degrade and dissolve in the in-package fluids. These reactions are irreversible and described by various expressions for reaction kinetics. These assumptions are implicit in the EQ3/EQ6 reaction and reaction path codes used to model the evolution of the in-package chemistry. Some exceptions to this assumption are the suppression of certain minerals known only to form at high temperatures (as discussed in BSC 2006 [DIRS 176911], Table 6-9), and that the oxidation state of chromium is limited to Cr(III).

Rationale—The justification for equilibrium between solution and precipitating solids is that some solids might require longer times to reach equilibrium (even longer than the times considered in the modeling). These solids, which include high-temperature minerals, are explicitly excluded from consideration as described in *Geochemistry Model Validation Report: Material Degradation and Release Model* (BSC 2006 ([DIRS 176911], Section 6.3.1.1). In this model, kinetic factors do not control the reactions, even though it is unlikely that all reactions will actually reach equilibrium, even over the regulatory period.

Confirmation Status—This assumption is justified because it is implicitly applied when using any thermodynamic modeling software, or any other reasonable modeling methodology. Its necessity can be established by considering the opposite view that thermodynamic disequilibrium is applicable. Assuming thermodynamic disequilibrium, there would no methodology or mechanism to model how the waste package would degrade, or determine what products would be produced by the degradation. Therefore, no further confirmation of thermodynamic equilibrium is required.

Use in the Model—This assumption is used in *Geochemistry Model Validation Report: Material Degradation and Release Model* (BSC 2006 [DIRS 176911], Sections 6.2, 6.3, and 6.4).

5.2 ASSUMPTIONS INTERNAL TO EXTERNAL ACCUMULATION MODEL

5.2.1 Carbon Dioxide Conditions

Assumption—The water flowing out of the waste package and mixing in the invert and host rock of the repository are assumed to be in equilibrium with carbon dioxide gas at a fugacity equal to 10^{-3} bar.

Rationale—The fugacity of carbon dioxide is set equal to 10^{-3} bar, which is higher than current atmospheric levels ($10^{-3.5}$ bar) because ambient fluids drawn from boreholes near the repository horizon appear to be in equilibrium with above-atmospheric carbon dioxide levels (Yang et al. 1996 [DIRS 100194], Table 8).

Confirmation Status—The conditions used in this report are consistent with the material degradation and release model (BSC 2006 [DIRS 176911]), which used carbon dioxide levels of 10^{-3} bar in the calculations. Thus, further confirmation is not needed.

Use in the Model—This assumption is used in Section 6.2 and 6.4.

5.2.2 Oxidizing Conditions

Assumption—The repository and its vicinity are in an oxidizing condition and oxygen fugacity equals 0.2 bars (the atmospheric value). The exceptions to this are the calculations involving Pu, in which the fugacity of oxygen was set equal to $10^{-8.7514}$ bar to be consistent with the material degradation and release model (BSC 2006 [DIRS 176911]), as discussed in Section 6.2.

Rationale—The existence of reducing conditions in the repository has not been proven, except for transient and localized conditions. Also, because the repository is in the unsaturated zone, it is connected to the atmosphere. Therefore, atmospheric oxygen fugacity is used.

Confirmation Status—The conditions used in this report are consistent with the material degradation and release model (BSC 2006 [DIRS 176911]), which used atmospheric oxygen levels in the calculations. A series of sensitivity cases showed that when a waste package degraded under reducing conditions, all U and Pu were retained in the waste package and no releases occurred (BSC 2004 [DIRS 168405], Section 4.1.2.6). Therefore, for external criticality, reducing conditions within the waste package would be less conservative, therefore oxidizing conditions are justified. Thus, further confirmation is not needed.

Use in the Model—This assumption is used in Section 6.2 and 6.4.

5.2.3 Seepage Rates

Assumption—The seepage rates presented in Figure 5-1 and Figure 5-2 are applicable values to use in flow and transport modeling. The figures represent the predicted drift seepage flux for the only two cases in TSPA that predict water flux through damaged waste packages: the seismic-induced fault displacement model case and the igneous intrusion modeling case. The seepage rate is the rate of water that enters the area defined by the diameter of the emplacement drift (5.5 m; BSC 2004 [DIRS 168489], Table 1) and the longest waste package length (5.1 m, Table 4-19).

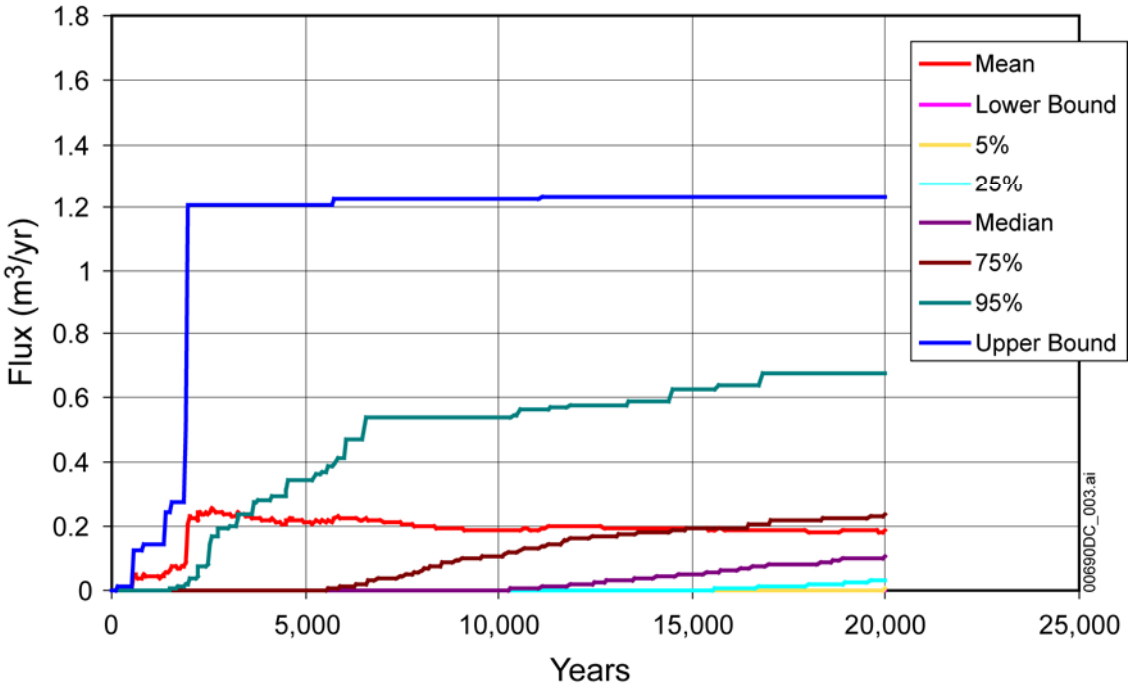

Figure 5-1. Predicted Seepage Flux into Drift from the Seismic-Induced Fault Displacement for CSNF

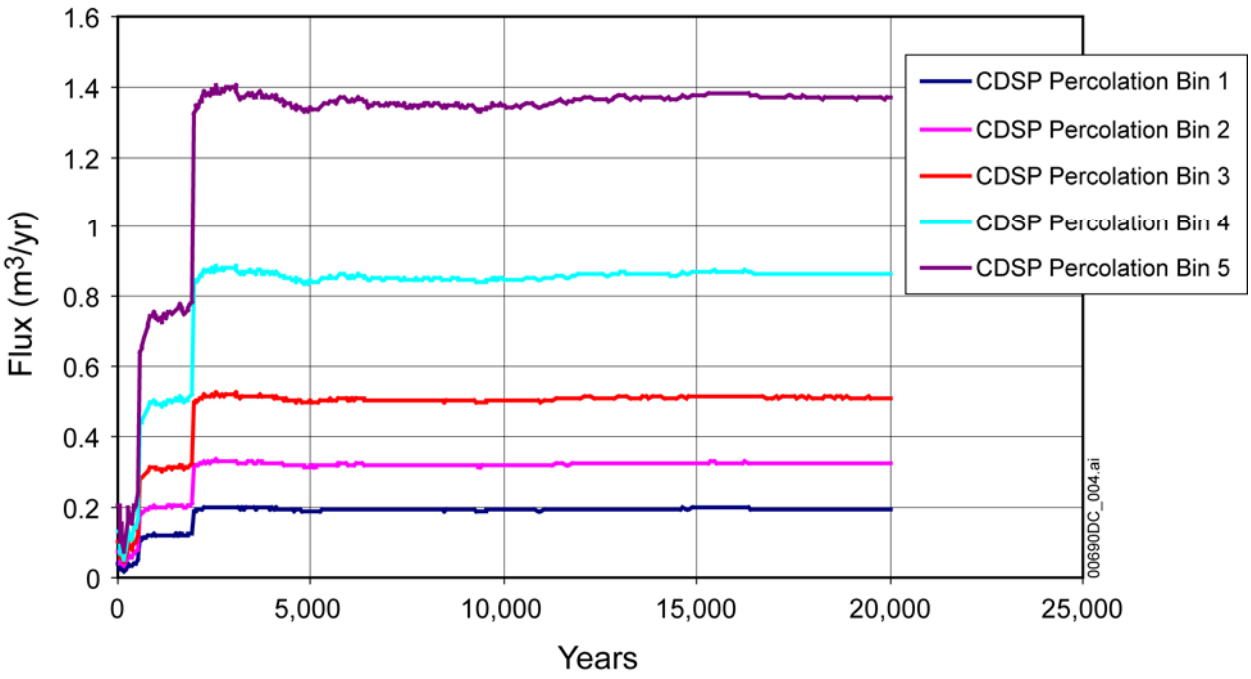

Figure 5-2. Predicted Seepage Flux into Drift from the Igneous Intrusion Modeling Case for CDSP

Rationale—The values plotted in Figures 5-1 and 5-2 were used in TSPA and documented in preliminary DTN: MO0506MWDTLVAC.000. The seepage rates used by TSPA have not been finalized and the DTN is currently unqualified and subject to change. However, the values are the best available in order to be consistent with TSPA modeling.

Confirmation Status—Once qualified values of seepage rates are available from TSPA, an impact analysis will be needed to determine the significance of the new seepage rates on the model results.

Use in the Model—This assumption is used in Section 6.4.6 and 6.4.7 to determine the diverted water flow rates.

INTENTIONALLY LEFT BLANK

6. MODEL DISCUSSION

6.1 OBJECTIVES

The objective of the external accumulation model is to determine the quantity of fissile material that could accumulate external to a degrading waste package in the invert or the underlying fractured tuff. Accumulation of fissile elements, such as ^{235}U and ^{239}Pu, is the primary interest for criticality; however, neutron absorbers (such as gadolinium) and minerals that may fill pore space or influence the water content (iron-oxides, calcite, etc.) are also of interest. The potentially accumulated material originates from a breached waste package that contains condensed water vapor or seepage water that has reacted with the waste package contents and caused degradation. The external accumulation model covers CSNF waste packages containing SNF and basket materials and DOE SNF waste packages containing DOE SNF, high-level waste glass, and basket materials.

6.2 CONCEPTUAL MODEL

Figures 6-1, 6-2, and 6-3 are flow charts of the three scenarios addressed in the external accumulation model: nominal, igneous, and seismic. The details of all cases for these three scenarios are provided in *Geochemistry Model Validation Report: Material Degradation and Release Model* (BSC 2006 [DIRS 176911], Section 6.2.2). In the nominal scenario, the drip shield remains intact and acts as a barrier to advective flow. The waste package is not affected by general corrosion, but may be breached by stress corrosion cracks. The stress corrosion cracks permit material to enter and exit the waste package by diffusion. After water vapor diffuses into the waste package, it will condense and react with internal components. The oxidation and corrosion reactions will produce alteration minerals in equilibrium with the condensed film of water. The releases from the waste package include diffusive transport, as calculated by TSPA, and bottom failure release of solids due to general corrosion, as calculated by the material degradation and release model (Figure 6-1). The external accumulation model does not simulate the movement of the diffusive releases or the solid releases. The releases are simply tabulated for use later in criticality calculations (Sections 6.3.1 and 6.5).

The igneous scenario applies to an igneous intrusion event in which magma enters the repository drift and encapsulates the waste packages. The details from *Geochemistry Model Validation Report: Material Degradation and Release Model* (BSC 2006 [DIRS 176911], Section 6.2.2-.3) are as follows:

> The magma flowing in the drift will "roll" over the invert without significant penetration into the ballast material (BSC 2004 [DIRS 170028]). The thermal effects caused by this intrusion are documented in *Dike/Drift Interactions* (BSC 2004 [DIRS 170028], Section 8.2.3). The elevated temperatures will cause the emplacement pallet underlying the waste package to fail and, as a result, the waste package will settle on the invert. In addition, the waste package will deform, and the interior will become over pressured due to the expanding interior gases. At some point, the waste package will rupture due to over-pressured gas. The failure is predicted to occur at the waste package's weakest point, which is the untempered end-cap welds. Once the waste package ruptures, it will deform

> and sag under the force of gravity depending on each component's thermal yield strength, and the weight of overlying materials. The elevated temperatures will also have a chemical effect on the waste package components. Because of its reactivity, uranium (uranium metal and UO_2) will preferentially and rapidly oxidize in a series of reactions that will produce fine-grained U_3O_8 precipitates (McEachern and Taylor 1997 [DIRS 101726]; 1998 [DIRS 113270]).

Due to the high temperatures and subsequent cool-down, some of the materials in the waste package will melt and resolidify (HLW glass and aluminum) and some materials will be sensitized (stainless steel), resulting in high corrosion rates (BSC 2006 [DIRS 176911], Section 6.2.2.3). Eventually, the drift temperature will drop below the boiling temperature of water, and water will reenter the drift. The drip shield will be displaced, allowing water to drip onto the waste package materials. Water will enter the waste package through ruptures in the waste package fed by fractures in the solidified magma. Water entry into the waste package will initiate corrosion reactions.

The releases from the waste package considered in this document include dissolved release of radionuclides and bottom failure release of solids (Figure 6-2). The quantity and description of the solids released are tabulated for external criticality calculations. The dissolved releases are modeled using PHREEQC. PHREEQC simulates waste package effluent mixing with seepage water (referred to as mixing water or resident water). The results produce the quantity of U and Pu accumulated due to precipitation and adsorption and apply to either the invert or the fractured host rock. The geometry of the accumulation within the invert is estimated using TOUGHREACT, which simulates flow and transport in the invert. The porosity and spacing between fractures (aperture), size of lithophysae, and matrix properties are presented to allow for criticality calculations within the host rock.

The seismic scenario, consistent with TSPA, considers the drip shield, waste package, and cladding to be failed and all the fuel exposed to seepage. Upon entry into the remnants of the waste package, water interacts with the internal components and causes corrosion. The releases from the waste package considered include dissolved release of radionuclides, waste package bottom failure release of solids, and entrained transport of solids (Figure 6-3). The quantity and description of the solids released are tabulated for external criticality calculations. In the same way as for the igneous scenario, the dissolved releases are modeled using PHREEQC.

For all scenarios, the external accumulation model begins with establishing the inputs to the model, including dissolved and solid releases from the waste package. The waste package effluent concentrations as functions of time, referred to as the source terms, are taken from the *Geochemistry Model Validation Report: Material Degradation and Release Model* (BSC 2006 [DIRS 176911]). The internal components of the waste packages that are subject to corrosion (such as the waste forms, basket materials, stainless steel inner barrier of the waste package) are described in BSC 2006 ([DIRS 176911], Section 4.1.4). The Alloy 22 outer barrier of the waste package is not included in the corrosion calculations because of its low corrosion rate (BSC 2006 ([DIRS 176911], Section 6.2.1.1). The diffusive releases for the nominal scenario come from TSPA (DTN: MO0506MWDTLVAC.000 [DIRS 174811]). The source for the quantity of entrained solids, which are solids flushed out of the waste package due to buoyant and drag forces of moving water, is the mass transfer model (BSC 2006 [DIRS 176911], Section

6.2.2.2.2). The sources for the composition of the slurry effluent that would result from a waste package bottom failure come from *Geochemistry Model Validation Report: Material Degradation and Release Model* (BSC 2006 ([DIRS 176911]) and are listed in Table 4-6.

The accumulation of the source term in the invert is as follows: The constituent-carrying fluid enters the invert and mixes with seepage water that does not contain any fissile elements. During the mixing, the processes modeled include adsorption of U and Pu onto the crushed tuff ballast, dissolution of the tuff, and precipitation of minerals within the voids of the invert. The geometry and location of the accumulation within the invert is inferred from 2-D flow and mixing calculations using TOUGHREACT, a numerical flow and transport code.

To simplify the calculations of accumulation in the fractured tuff, the source term is assumed to have no interaction with the invert materials. This simplification increases the likelihood of a criticality event, and is therefore conservative, as it maximizes the quantity of fissile material available to accumulate in the fractures and minimizes the spreading of that material between the invert and the host rock.

The accumulation of the source term in the fractured tuff is as follows: The constituent-carrying fluid flows through the invert, without any interaction with the invert materials, enters the fractured tuff, and mixes with water that was diverted around the drift. During the mixing, the processes modeled include adsorption of U and Pu onto the fractured tuff, dissolution of the tuff, and precipitation of minerals within the fractures and lithophysae. The location and shape of the accumulation within the fractured rock are not modeled, however the characteristics of the accumulation zone (fracture porosity, spacing, lithophysae, etc.) are described.

The results from the PHREEQC modeling are moles of U and Pu accumulated and adsorbed and the volume of other minerals that accumulate alongside the U and Pu minerals. The results apply to either the invert or the fractured tuff. The two-dimensional location and shape of the accumulation within the invert were estimated using TOUGHREACT, a numerical flow and transport code.

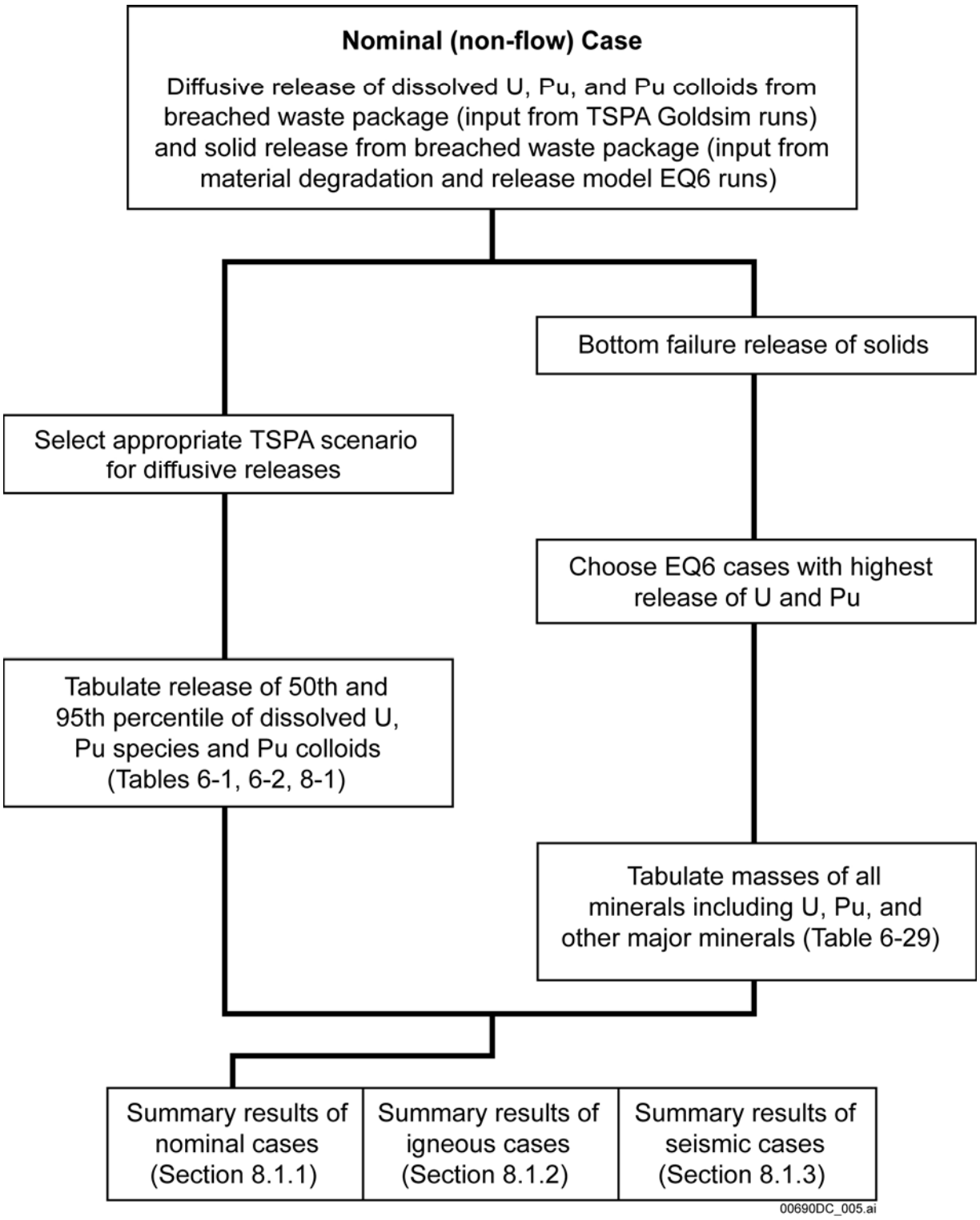

Figure 6-1. Flow Chart for Nominal Scenario

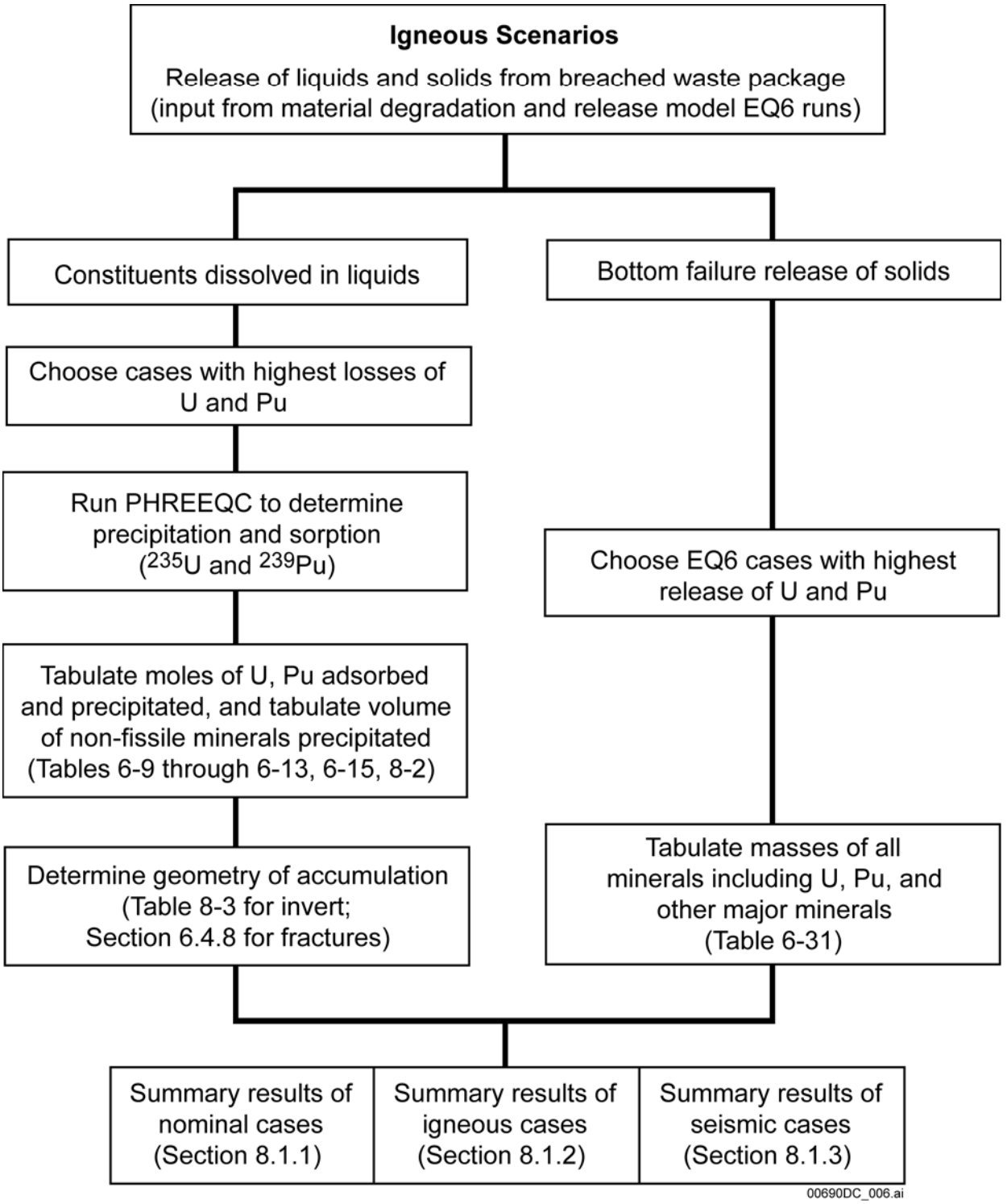

Figure 6-2. Flow Chart for Igneous Scenario

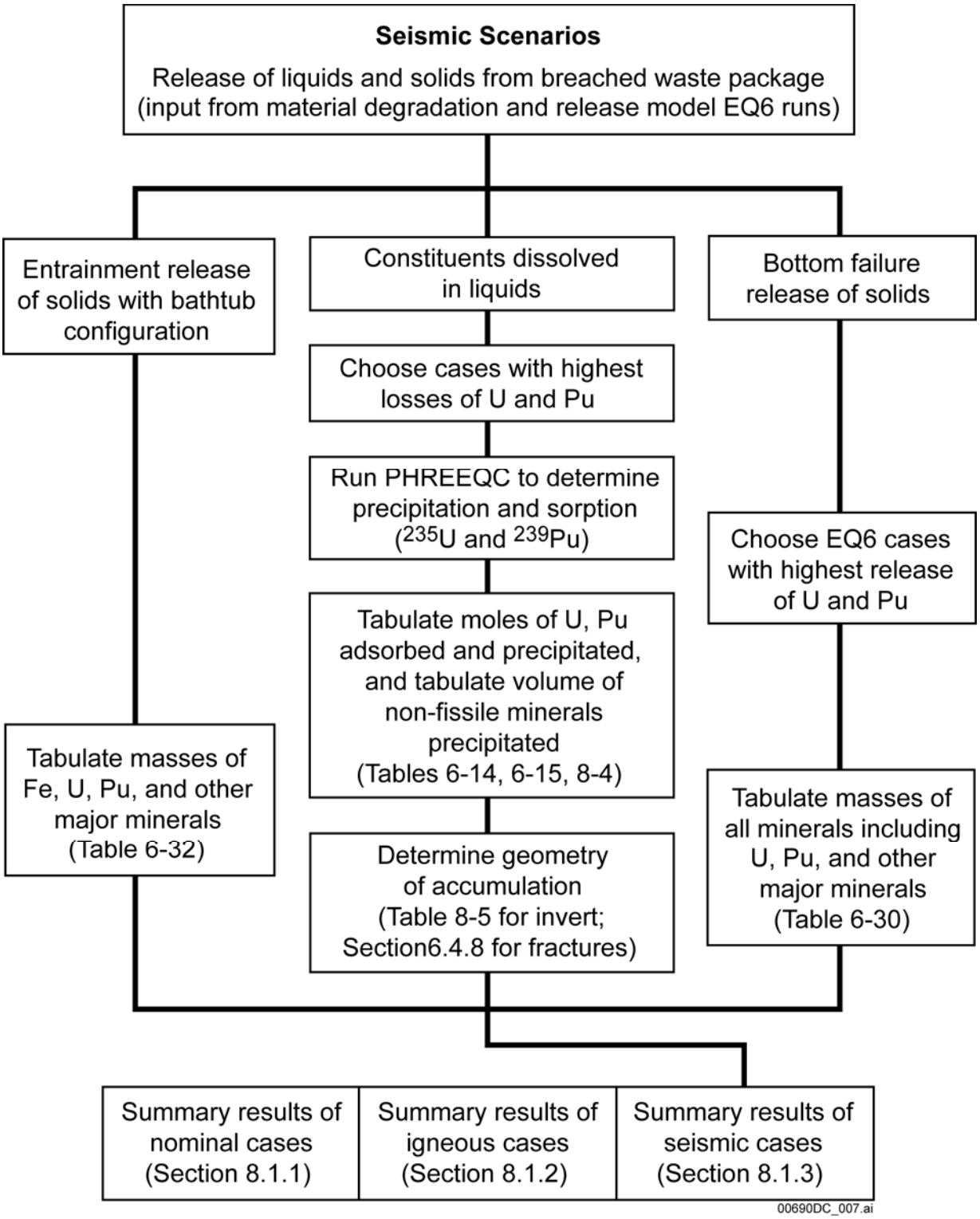

Figure 6-3. Flow Chart for Seismic Scenario

The important modeling concepts and assumptions associated with the modeling of accumulation are as follows:

Fugacity of Carbon Dioxide and Oxygen—The fugacity of carbon dioxide (CO_2) and oxygen (O_2) in the PHREEQC simulations is set equal to the conditions of the source term, as specified in *Geochemistry Model Validation Report: Material Degradation and Release Model* (BSC 2006 [DIRS 176911]). The fugacity of CO_2 is set equal to 10^{-3} bar (Assumption 5.2.1), which is higher than current atmospheric ($10^{-3.5}$ bar) because ambient fluids drawn from boreholes near the repository horizon appear to be in equilibrium with above-atmospheric carbon dioxide levels (Yang et al. 1996 [DIRS 100194], Table 8). The fugacity of oxygen (f_{O2}) is set equal to atmospheric levels (0.2 atm; Weast 1977 [DIRS 106266], p. F-210) for the TMI and N-Reactor waste packages that contain only uranium. For the CSNF and FFTF waste packages that contain both U and Pu, the adjusted-Eh model from *Dissolved Concentration Limits of Radioactive Elements* (BSC 2005 [DIRS 174566], Section 6.5.4) was used. The adjusted-Eh model was developed because the Pu-solubility modeling results using a redox potential calculated from the atmospheric values of oxygen did not represent Pu-solubility behavior in laboratory experiments (BSC 2005 [DIRS 174566], Figure 6.5-8). The differences are caused by the oxidation state of Pu, which has a large impact on the geochemical behavior of Pu in aqueous environments. The model using atmospheric levels of oxygen predicted the formation of Pu(VI) as the dominant dissolved species, whereas measurements in experiments and natural waters observed Pu(V) as the dominant dissolved species (BSC 2005 [DIRS 174566], Section 6.5.4.1.3). The adjusted-Eh model, which results in a lower oxygen fugacity, generates a Pu concentration that closely matches concentrations measured in equilibrium laboratory experiments (BSC 2005 [DIRS 174566], Figure 6.5-6). Based on the adjusted-Eh model, f_{O2} was calculated to be $10^{-8.7514}$ bar at 25°C (Output DTN: MO0609SPAINOUT.002, file *Adjusted_Eh.xls*), using:

pE = 20.78 - pH + 1/4 log(pO2) (Stumm and Morgan 1996 [DIRS 125332], Equation 58, p. 456)

pE = [nF] Eh ÷ 2.303 RT (Langmuir 1997 [DIRS 100051], Equation 11.12)

Eh = 1.1 - 0.0592 pH (BSC 2005 [DIRS 174566], Equation 6.5-7)

Thermodynamic Equilibrium—A thermodynamic chemical equilibrium approach is used in this report (Assumption 5.1.3). When conditions are thermodynamically favored, as determined by the database, a mineral is allowed to precipitate. The list of minerals allowed to form and the list of minerals suppressed are provided in Tables 6-7 and 6-8. The suppressed minerals are minerals that have not been observed in temperature and pressure conditions expected in the repository. The exception to thermodynamic equilibrium is the treatment of chromium. To be consistent with the source of the inputs for this report, *Geochemistry Model Validation Report: Material Degradation and Release Model* (BSC 2006 [DIRS 176911]), and to be consistent with other project reports (BSC 2005 [DIRS 174583], Section 6.6.3; BSC 2005 [DIRS 175083], Section 6.8.2), the model limits the oxidation state of chromium to Cr(III) rather than Cr(VI). *Engineered Barrier System: Physical and Chemical Environment* (BSC 2005 [DIRS 175083], p. 6-103) provides the following explanation:

Selection of Cr(III) over that of the more soluble Cr(VI) species is based on experimentally observed corrosion products, and on the kinetics and conditions required to obtain the fully oxidized Cr(VI) state (Smith and Purdy 1995 [DIRS 162976]). Smith and Purdy's (1995 [DIRS 162976], Figure 6) examination of the actual chromium speciation as a result of corrosion of Stainless Steel Type 316L demonstrated a predominance of the less soluble Cr(III) species, except under the conditions of hot concentrated nitric acid (111°C and >7 molar HNO_3).

Dissolution of Precipitated Minerals—Each source term represents concentration versus time of waste package effluent. Several points along the curve are chosen for PHREEQC simulations, since only one composition at a time can be run with PHREEQC. At each time step, the accumulation of minerals is determined. The total accumulation is computed by integrating under the accumulation curve (mol/year) versus time (year). Redissolution of the precipitated minerals is not allowed in the model. This is a simplification that overestimates the amount of material that precipitates, since minerals will dissolve if the chemistry of the water changes with time.

6.3 NOMINAL CASE—DIFFUSIVE RELEASES—SCOPING CALCULATIONS

The diffusive releases of U and Pu from the waste package were taken from preliminary calculations performed for TSPA using GoldSim (DTN: MO0506MWDTLVAC.000 [DIRS 174811], files *LA_v3.004_ne_00300_008.gsm* [DOE SNF waste package] and *LA_v3.004_ne_00300_018.gsm* [CSNF waste package]). The data extracted from the GoldSim files are identified within the spreadsheets in DTN: MO0604SPANOMIN.000. Appendix J provides a list of the values extracted from the GoldSim files, the exact location within the GoldSim files where the data was extracted, and the output excel spreadsheets that contain the data. The TSPA runs modeled 300 realizations of a single early-failure waste package in a drip environment in Bin 3, where Bin 3 represents the infiltration conditions most likely to occur at the repository. Since the drip shield was considered to be intact, only diffusive transport of the radionuclides occurred. For criticality, the releases of interest were dissolved U, Pu (dissolved and reversible colloids), and irreversibly sorbed Pu colloids, i.e., iron colloids (If) and glass colloids (Ic).

The diffusive loss for the nominal case for CSNF and for each DOE SNF (N-Reactor, FFTF, and TMI) was calculated in spreadsheets *CSNF Results.xls* and *DOE SNF Results.xls* in Output DTN: MO0604SPANOMIN.000. The following steps were taken:

1. Calculate the initial composition and mass of SNF used in TSPA calculations

2. Determine mass released to the invert in TSPA runs

3. Determine fraction of starting mass released to the invert in TSPA runs

4. Using the fraction released from step 3, calculate the mass released to the invert for CSNF waste package and for each DOE SNF waste package using the starting mass that was used in *Geochemistry Model Validation Report: Material Degradation and Release Model* (BSC 2006 [DIRS 176911]).

6.3.1 Scoping Results

The masses of U and Pu released into the invert by diffusion in the nominal case for the CSNF waste package are presented in Table 6-1. The diffusive releases from the DOE SNF waste packages are presented in Table 6-2.

Table 6-1. Diffusive Releases from CSNF Waste Package in Nominal Scenario

	Releases from the Waste Package to the Invert			
	TSPA, CSNF (fraction released)		CSNF (BSC 2006 [DIRS 176911])	
Isotope	50th Percentile (kg)	95th Percentile (kg)	50th Percentile (kg)	95th Percentile (kg)
^{232}U	2.58E-10	1.00E-09	N/A	N/A
^{233}U	5.24E-03	1.13E-01	N/A	N/A
^{234}U	5.05E-04	2.44E-03	1.97E-03	9.52E-03
^{235}U	3.82E-04	1.82E-03	3.98E-02	1.90E-01
^{236}U	4.43E-04	2.08E-03	2.88E-02	1.35E-01
^{238}U	2.80E-04	1.31E-03	2.61E+00	1.22E+01
Total U	6.85E-03	1.21E-01	2.68E+00	1.26E+01
^{239}Pu	4.93E-05	1.11E-08	1.24E-07	6.07E-07
If^{239}Pu	9.69E-07	5.23E-11	1.01E-08	2.86E-09
^{240}Pu	1.51E-05	2.86E-09	6.57E-09	2.82E-08
If^{240}Pu	2.58E-07	8.38E-13	1.12E-10	8.27E-12
^{241}Pu	0.00E+00	0.00E+00	0.00E+00	0.00E+00
^{242}Pu	6.86E-06	5.48E-09	8.12E-09	3.78E-08
If^{242}Pu	1.42E-07	1.44E-12	1.69E-10	9.94E-12
Total Pu	7.26E-05	1.95E-08	1.49E-07	6.76E-07

NOTES: ^{239}Pu (dissolved and reversibly adsorbed colloids).

If^{239}Pu (irreversibly sorbed onto iron colloids).

DTN: MO0604SPANOMIN.000, *CSNF Results.xls*.

Table 6-2. Diffusive Releases from DOE SNF Waste Packages

	Releases From the Waste Package to the Invert							
	TSPA, DSNF (fraction released)		N-Reactor		FFTF		TMI	
Isotope	50th Percentile (kg)	95th Percentile (kg)	50th Percentile (kg)	95th Percentile (kg)	50th Percentile (kg)	95th Percentile (kg)	50th Percentile (kg)	95th Percentile (kg)
^{232}U	2.03E-06	5.79E-06	N/A	N/A	N/A	N/A	N/A	N/A
^{233}U	2.88E-02	1.20E-01	N/A	N/A	N/A	N/A	N/A	N/A
^{234}U	3.12E-02	1.34E-01	1.14E-02	4.90E-02	2.39E-02	1.03E-01	2.39E-02	1.03E-01
^{235}U	3.09E-02	1.31E-01	5.32E+00	2.25E+01	8.31E-02	3.51E-01	4.92E-01	2.08E+00
^{236}U	3.90E-02	1.57E-01	2.18E-01	8.76E-01	2.82E-01	1.13E+00	1.81E-02	7.28E-02
^{238}U	2.40E-02	1.09E-01	3.26E+02	1.49E+03	9.96E+00	4.53E+01	1.71E+01	7.79E+01

Table 6-2. Diffusive Releases from DOE SNF Waste Packages (Continued)

Isotope	Releases From the Waste Package to the Invert							
	TSPA, DSNF (fraction released)		N-Reactor		FFTF		TMI	
	50th Percentile (kg)	95th Percentile (kg)	50th Percentile (kg)	95th Percentile (kg)	50th Percentile (kg)	95th Percentile (kg)	50th Percentile (kg)	95th Percentile (kg)
Total U	1.54E-01	6.50E-01	3.32E+02	1.51E+03	1.03E+01	4.69E+01	1.76E+01	8.01E+01
^{239}Pu	1.38E-07	7.19E-07	N/A	N/A	7.11E-06	3.70E-05	N/A	N/A
Ic^{239}Pu	5.03E-06	3.18E-05	N/A	N/A	2.59E-04	1.64E-03	N/A	N/A
If^{239}Pu	1.78E-06	1.11E-05	N/A	N/A	9.17E-05	5.73E-04	N/A	N/A
Total Pu	6.95E-06	4.36E-05	N/A	N/A	3.57E-04	2.25E-03	N/A	N/A

NOTES: ^{239}Pu (dissolved and reversibly adsorbed colloids).

Ic^{239}Pu (irreversibly sorbed, imbedded glass colloids).

If^{239}Pu (irreversibly sorbed onto iron colloids).

DTN: MO0604SPANOMIN.000, *DOE SNF Results.xls*.

6.4 SEISMIC FAULT DISPLACEMENT AND IGNEOUS CASES—DISSOLVED RELEASES

This section describes the modeling involved in determining the quantity and geometry of U and Pu that accumulates as a result of the source term flowing out of the waste package and mixing with seepage water in the invert or host rock. Sections 6.4.1 through 6.4.4 describe the major inputs to PHREEQC input files: source term compositions (Section 6.4.1), the dissolution rate of the tuff minerals as the waters flow through the invert or host rock (Section 6.4.2), U and Pu adsorption onto the tuff minerals (Section 6.4.3), and the minerals included during the PHREEQC simulations (Section 6.4.4). Section 6.4.5 gives the details of running PHREEQC and the post-processing macros and presents the accumulation results. The TOUGHREACT modeling effort, to infer the extent of mixing within the invert, is described in Sections 6.4.6 and 6.4.7. Section 6.4.8 provides characteristics of the host rock (such as fracture and lithophysae porosity) used for describing the geometry of accumulation within the fractured tuff.

6.4.1 Source Term Description

PHREEQC was used to determine accumulation due to mixing of waste package water effluent with mixing water in the invert. The source terms used are listed in Table 4-4. Two types of source terms were used for the PHREEQC simulations—igneous and seismic scenarios. In the seismic scenario, the waste package is breached and all the waste package internals are degraded by the incoming water (see BSC 2006 [DIRS 176911]). In the igneous scenario, the EQ6 simulations were conducted in two stages. The first stage has water vapor reacting with the fuel only, causing oxidation. In the second stage, the basalt-equilibrated water reacts with the remainder of the waste package contents and the oxidized fuel (see BSC 2006 [DIRS 176911]). For each source term, the software ASPRIN was used to calculate the enrichment fraction (ratio of ^{235}U to total uranium) in the effluent solution. The details of the ASPRIN calculations are provided in Appendix I. Table 6-3 lists the isotopic mole fraction for each waste form used in the ASPRIN calculations. Figures 6-4 through 6-9 provide plots of aqueous concentration of U

and Pu (when applicable) and the enrichment fraction for each source term. In addition, the points identified for PHREEQC simulations are marked on the figures.

Table 6-3. Isotopic Mole Fraction for Each Waste Form

Isotope	Mole Fraction for Each Waste Form				
	CSNF	N-Reactor	TMI	FFTF	HLW Glass
^{234}U	4.17E-04	N/A	N/A	N/A	2.92E-03
^{235}U	1.11E-02	1.27E-02	2.96E-02	2.20E-03	8.86E-03
^{236}U	6.88E-03	3.95E-04	N/A	4.28E-02	1.75E-03
^{238}U	9.82E-01	9.87E-01	9.70E-01	9.55E-01	9.87E-01
^{239}Pu	7.67E-01	N/A	N/A	1.00E+00	N/A
^{240}Pu	1.38E-01	N/A	N/A	N/A	N/A
^{242}Pu	9.56E-02	N/A	N/A	N/A	N/A

Source: DTN: MO0609SPAINOUT.002, file *Fuel_Isotopic_Composition.xls*. Inputs used to create the table are listed in Table 4-7.

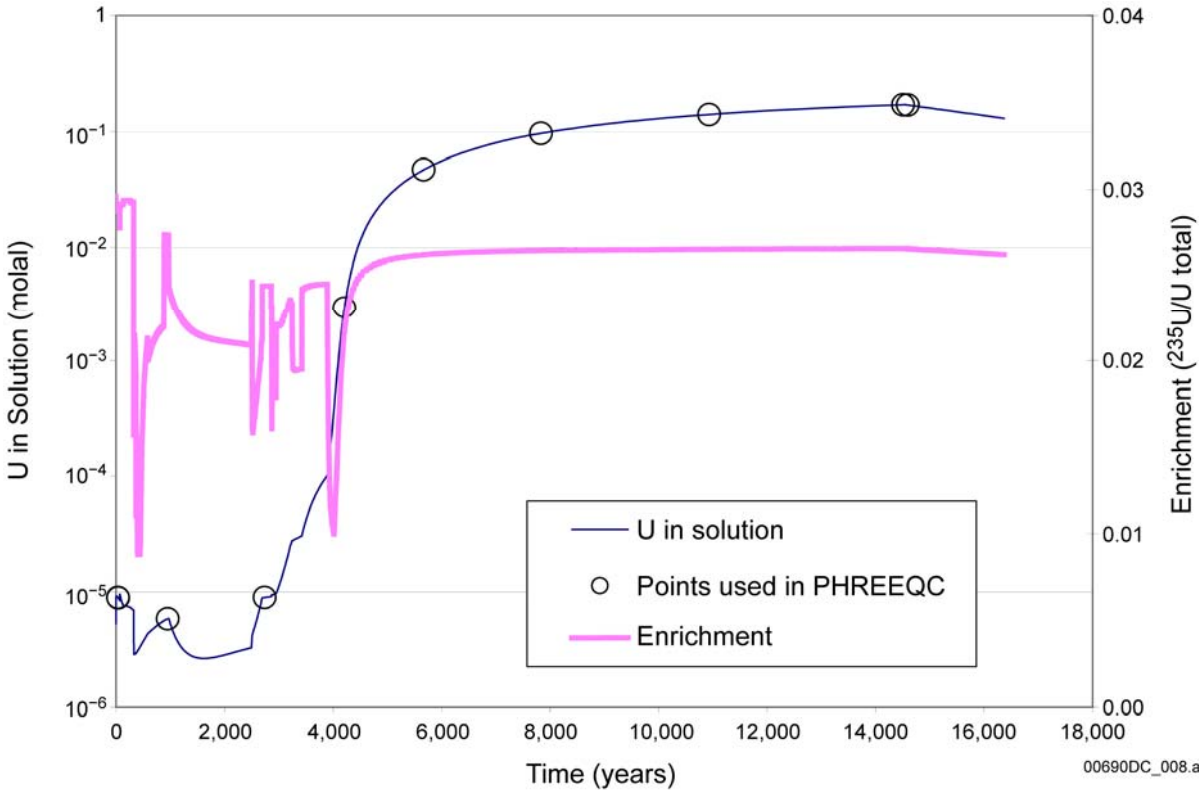

Source: Output DTN: MO0609SPAINOUT.002, folders: TMI_IG1\TMI_IG1_Asprin, file: *TMI_IG1A.xls*, tab: Chart2.

Source term description: TMI SNF, Igneous Scenario, 1 L/yr

Figure 6-4. TMI_IG1 Source Term, Uranium in Solution Versus Time

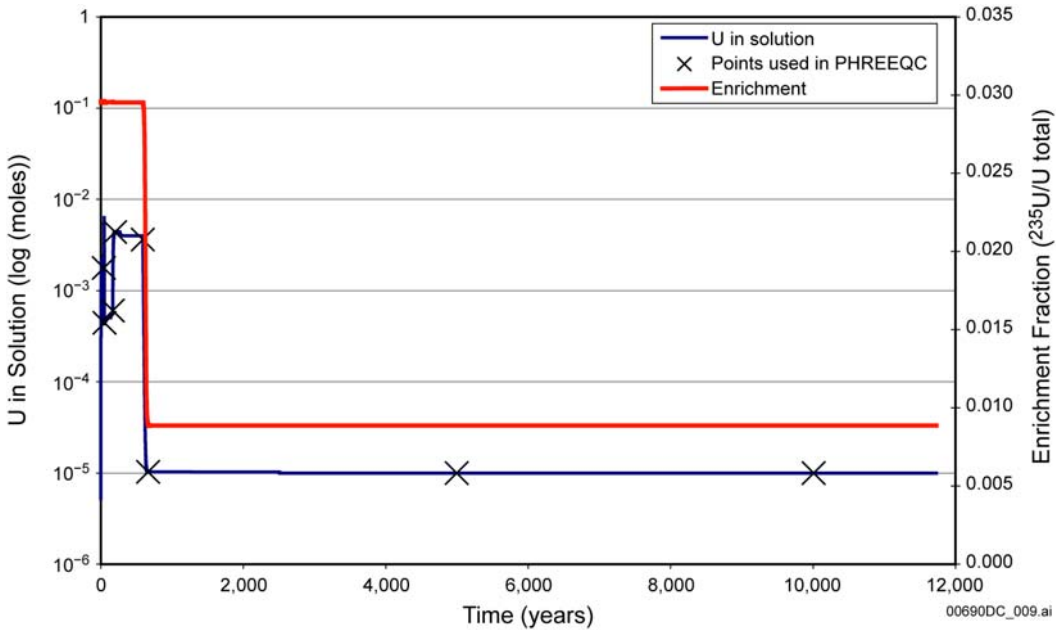

Source: Output DTN: MO0609SPAINOUT.002, folders: TMI_IG2\TMI_IG2_Asprin, file: *TMI_IG2_asprin_all.xls*, tab: Chart

Source term description: TMI SNF, Igneous Scenario, 1,000 L/yr.

Figure 6-5. TMI_IG2 Source Term, Uranium in Solution Versus Time

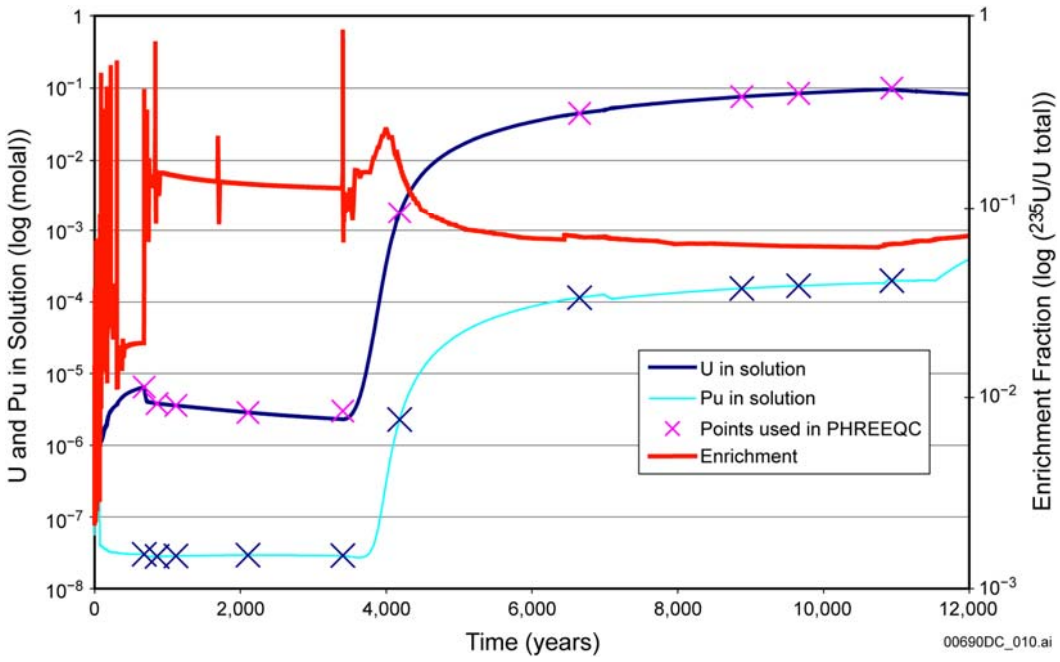

Source: Output DTN: MO0609SPAINOUT.002, folders: FFTFIG1adEhdec \ FFTFG1_Asprin_Sourceterm, file: *FFTFIG1adEhdec.xls*, tab: Chart1

Source term description: FFTF SNF, Igneous Scenario, 1 L/yr.

Figure 6-6. FFTFIG1adEhdec Source Term, Uranium and Plutonium in Solution Versus Time

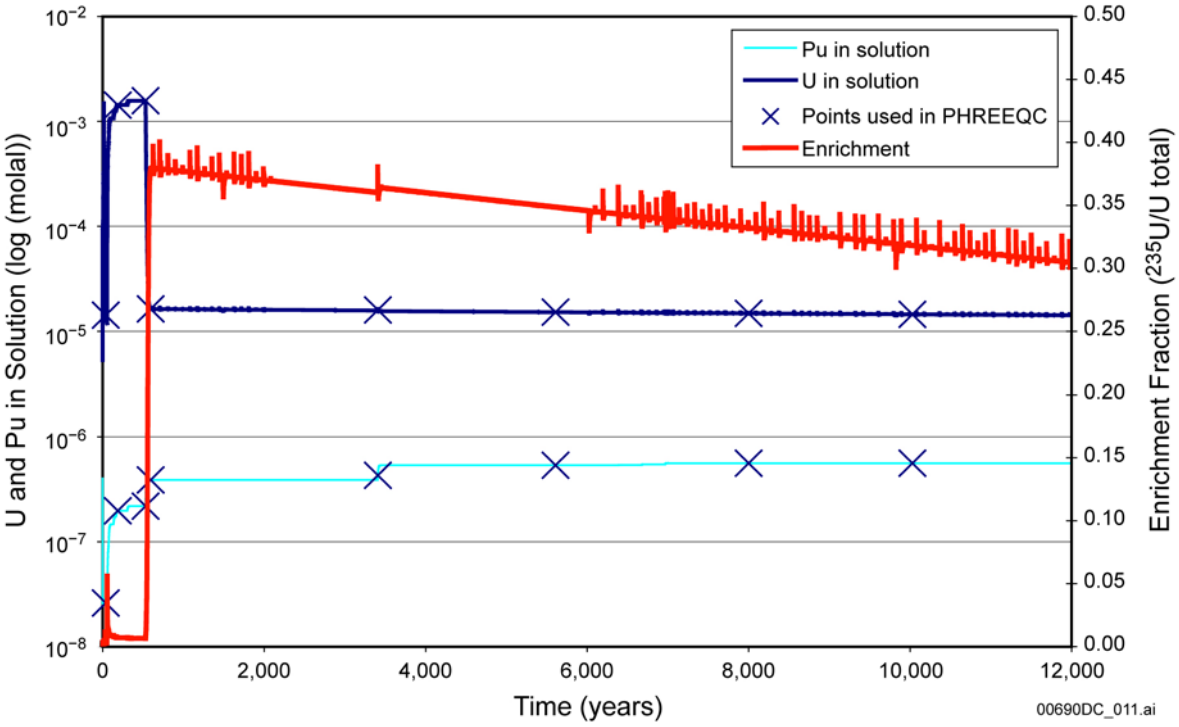

Source: Output DTN: MO0609SPAINOUT.002, folders: FFTFIG2adEhdec\FFTFG2_Asprin, file: *Aqueous_Species_FFTFIG2.xls*, tab: Chart1

Source term description: FFTF SNF, Igneous Scenario, 1,000 L/yr

Figure 6-7. FFTFIG2adEhdec Source Term, Uranium and Plutonium in Solution Versus Time

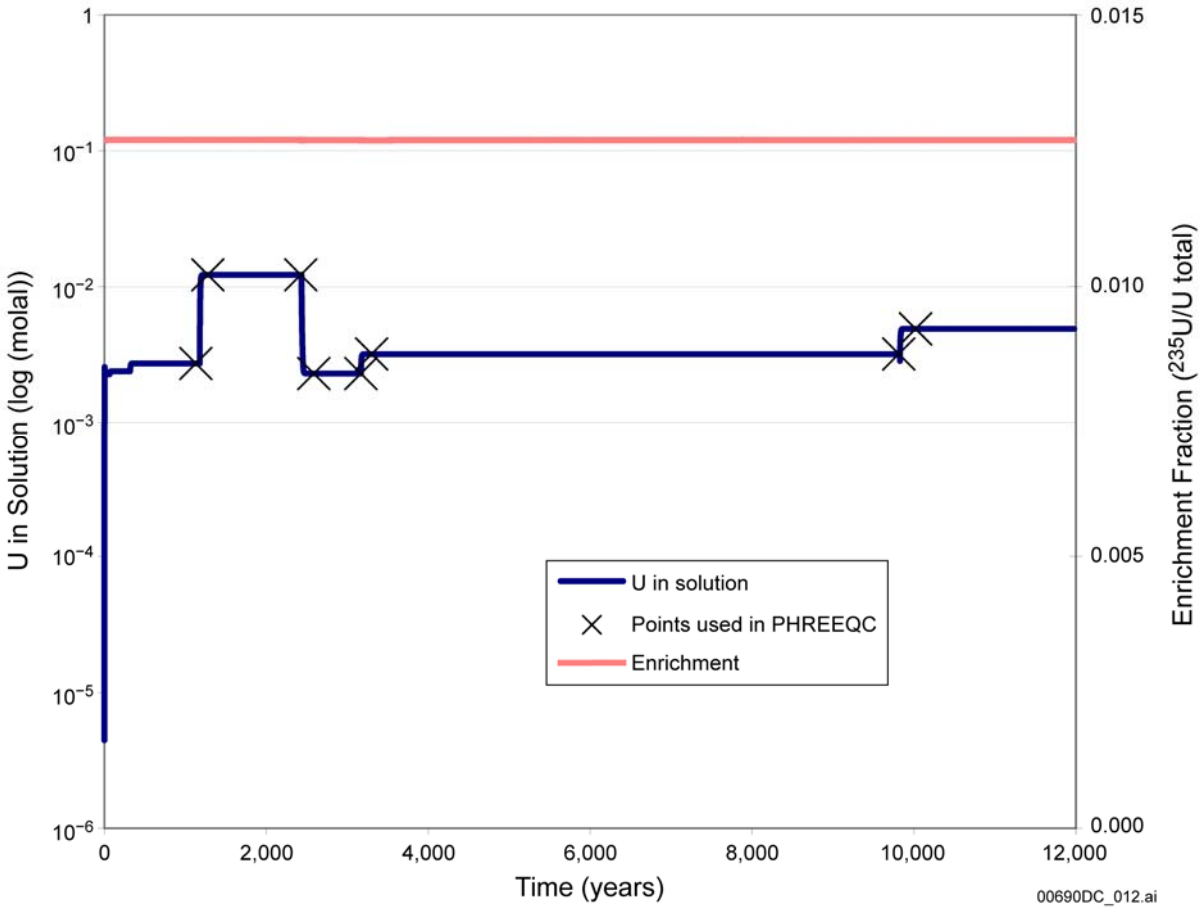

Source: Output DTN: MO0609SPAINOUT.002, folders: CDSPIG\CDSPIG_Asprin, file: *CDSPIG2_asprin_all.xls*, tab: Chart1.

Source term description: N-Reactor SNF, Igneous Scenario, 1,000 L/yr.

Figure 6-8. CDSPIG2 Source Term, Uranium in Solution Versus Time

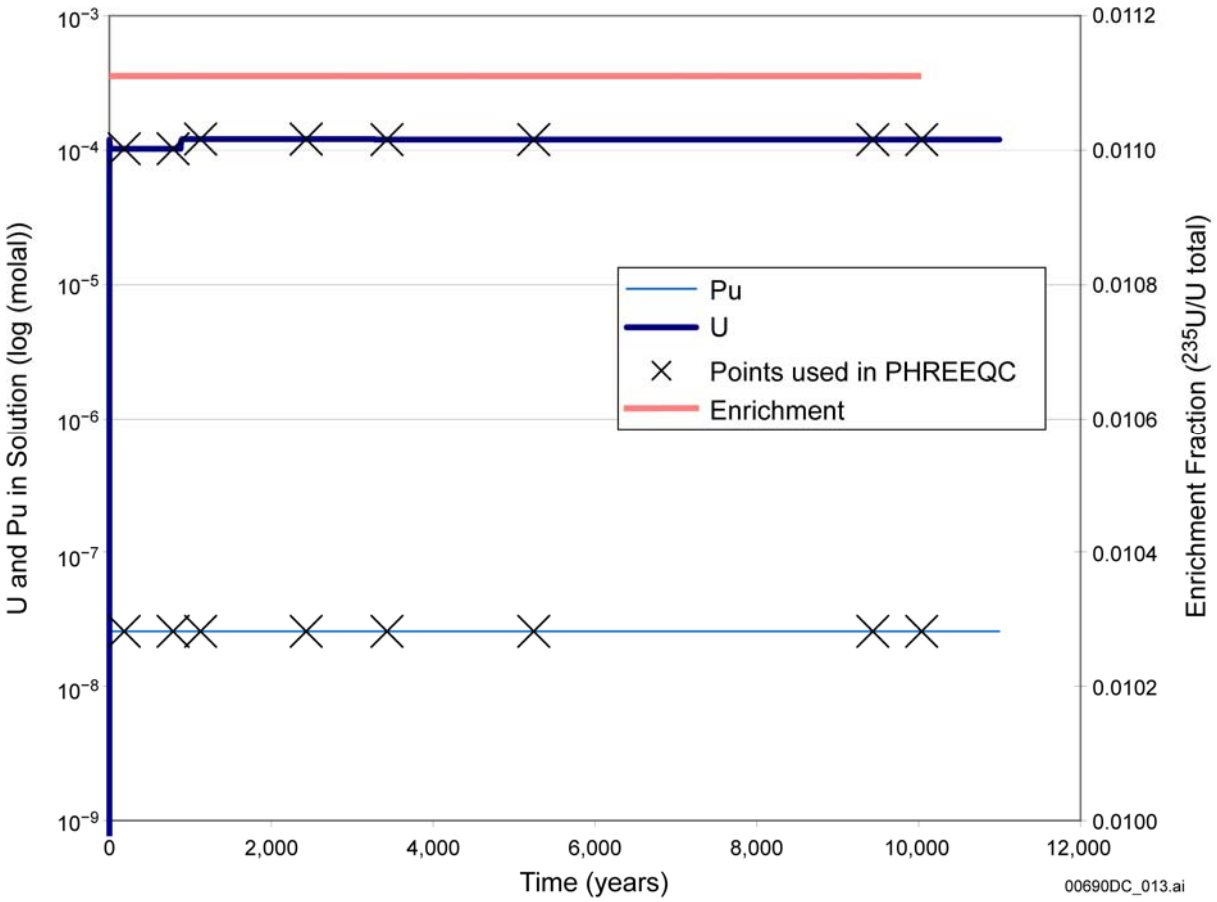

Source: Output DTN: MO0609SPAINOUT.002, folders: CSFlux9\CSFlux9_Asprin, file: *CSFlux9_asprin_all.xls*, tab: Chart1.

Source term description: CSNF, Seismic Scenario, 1,000 L/yr

Figure 6-9. CSFlux9 Source Term, Uranium and Plutonium in Solution Versus Time

6.4.2 Dissolution of Tuff Minerals

Table 6-4. Dissolution Rate Constants and Mole Fraction of Minerals in the Topopah Spring Tuff

Mineral	Dissolution Rate = $k_1[H^+]^{S1} + k_2[H^+]^{S2}$ (mol/cm^2·s)				Source	Mole Fraction (Source: *Tuff_minerals.xls*)	Temperature °C
	Acidic Leg		Basic Leg				
	k_1	S1	k_2	S2			
Cristobalite	3.94E-16	0.0594	6.93E-19	−0.318	*cristobalite&quartz.xls*	0.371	25
Annite	2.37E-15	0.426	7.34E-19	−0.231	*annite and phlogopite (muscovite).xls*	0.0140	70
Phlogopite						0.00459	70
Maximum microcline	5.50E-15	0.443	2.62E-17	−0.0214	*maximum microcline (k-feldspar).xls*	0.281	25
Albite_low	7.94E-15	0.33	5.01E-19	−0.32	BSC 2004 [DIRS 170028], Table 6-20, Figure B-1; *Albite & anorthite.xls*	0.304	25
Anorthite	1.58E-11	0.91	2.00E-18	−0.30	BSC 2004 [DIRS 170028], Table 6-20, Figure B-2; *Albite & anorthite.xls*	0.0254	25

Source: Output DTN: MO0609SPAINOUT.002, folder: Dissolution_Rates_of_Tuff_MInerals, files: *cristobalite& quartz.xls*, *Albite & anorthite.xls*, *maximum microcline (k-feldspar).xls*, and *annite and phlogopite (muscovite).xls*.

6.4.3 Adsorption onto Tuff Minerals

The external accumulation model simulates transport of water and dissolved solids from a leaking waste package through the invert. Immobilization and collection of radionuclides near the surface of the invert or in other places along the flow path might conceivably create conditions conducive to a criticality event. Precipitation and adsorption are the two primary mechanisms capable of immobilizing dissolved radionuclides. Both of these processes are implemented simultaneously in the model.

The external accumulation model simulates adsorption of U and Pu because of the potentially high concentrations of these radionuclides and their importance to criticality. This section describes how adsorption is simulated. Section 6.4.3.1 presents a brief discussion of alternative adsorption models, and Section 6.4.3.2 explains the adsorption approach implemented. Section 7.2.2.2 describes the validation of the adsorption model.

6.4.3.1 Alternative Adsorption Models

Adsorption can be modeled in a number of ways. The most rigorous approach is a surface complexation model. In surface complexation modeling, each adsorption reaction is defined stoichiometrically, and an electrical double layer is simulated. Such an approach requires well-characterized sorbents and a reliable sorption reaction database. For sorbents, the important parameters include specific surface area, surface charge, and surface site concentration. The database for such a surface complexation model includes the parameters of an electrostatic model and specific adsorption reactions for each type of surface site for each adsorbate. Because of the large uncertainties in the values of many of these parameters and the lack of sorption

reaction data for many mineral surfaces, surface complexation modeling is often limited to simple systems. New developments in the study of surface complexation show promise, such as the work of Sverjensky (2003, [DIRS 177119]) and Sverjensky (2006 [DIRS 177120]); however, surface complexation modeling as yet remains unproven for predicting radionuclide adsorption in the field. *NUREG/CR-6893* (Criscenti et al. 2006 ([DIRS 177117], p. 5-1); Section 3.2, and *NUREG/CP-0193,* Cygan et al. 2006 [DIRS177118]) also address the new developments in the modeling of surface complexation.

At the other end of the spectrum is the linear adsorption model, or distribution coefficient (K_d) approach. The ratio of adsorbed concentration to aqueous concentration at equilibrium is often constant over limited ranges of aqueous concentrations. For a given radionuclide, if a plot of the adsorbed versus aqueous concentration at a fixed temperature (i.e., isotherm) is a straight line that intersects the origin, adsorption is linear for that range and the slope of the line is the K_d. This K_d, however, is conditional. It is a function of temperature, pH, redox conditions (Eh), ionic strength, and the concentrations of competing and complexing aqueous components. Thus, using the strictest interpretation, K_d measurements apply only to the ground water composition, mineral samples, temperature, and aqueous concentration ranges of the conditions under which the experimental data were collected.

Many radionuclide K_d experiments have been conducted on crushed tuff samples from Yucca Mountain. These experiments and their results are summarized in *Radionuclide Transport Models Under Ambient Conditions* (BSC 2004 [DIRS 164500]). Appendix A of that report (BSC 2004 [DIRS 164500]) provides justification for using the linear K_d approach for modeling radionuclide adsorption in the tuffs of Yucca Mountain. The K_d experiments used Yucca Mountain tuff core samples that were crushed and sieved. The typical grain size fraction in the experiments was 75 to 500 μm. Larger size fractions are thought to have similar surface areas because tuffs are composed of fine-grained minerals (crystal sizes on the order of 10 to 20 μm) (BSC 2004 [DIRS 164500], p. A-6). This is consistent with the observation that larger size fractions do not significantly affect K_d measurements on tuff samples (Rogers and Meijer 1993 [DIRS 123127], pp. 1511 to 1512). Although smaller size fractions tend to produce higher adsorption, this tendency is discounted as the likely consequence of a disproportionately large abundance of clay minerals in these fractions (BSC 2004 [DIRS 164500], p. A-6).

The K_d experiments were performed by combining 1 gram of crushed tuff with 20 mL of groundwater in a test tube, spiking the mixture with the radionuclides of interest (at concentrations below their solubility limits), and shaking the mixtures for a predetermined period of time (BSC 2004 [DIRS 164500], p. A-7). The final aqueous concentrations of the radionuclides were measured and the adsorbed concentrations determined by subtraction.

Sections A8.4 and A8.9 in Appendix A of *Radionuclide Transport Models Under Ambient Conditions* (BSC 2004 [DIRS 164500]) present plots of numerous Pu and U K_d measurements on devitrified tuff, the type of tuff that will be used as ballast in the invert. Figures A-28, A-29, and A-60 in that report (BSC 2004 [DIRS 164500]) show slightly decreasing trends in K_d measurements on devitrified tuffs with increasing aqueous Pu and U concentrations; however, over large ranges of aqueous concentrations the mean values change little compared to the variation in the measurements. Desorption experiments generally yield larger K_d measurements than adsorption experiments (BSC 2004 [DIRS 164500], Figures A-29, A-30, A-61). This is

especially true for Pu, indicating the kinetic limitations of the short-term experiments and possibly Pu redox effects (BSC 2004 [DIRS 164500], pp. A-40 to A-44). The combination of adsorption and desorption data, as compiled in the report, is important in estimating mean K_d values and associated uncertainty. In some cases, negative K_d measurements were observed (e.g. BSC 2004 [DIRS 164500, Figure A-61). The negative values happened when the final equilibrated solution gave measured values of U that were greater than the initial values. The reason for the unexpected results is because the measurement of U in solution is imprecise and may also be inaccurate due to calibration errors. Ideally, the experiments would have been designed to achieve 30% to 70% adsorption, instead of the U experiments with <10% adsorbed and Pu experiments with >90% adsorbed. When experiments are conducted outside the optimum range of adsorption, uncertainty is higher. Regardless, the median value should still be a good measure of the representative K_d value.

No clear relationships are observed for Pu and U adsorption versus pH (BSC 2004 [DIRS 164500], Figures A-31, A-32, A-62, and A-63a). However, the surface complexation model simulations (plotted in Figure A-62 of BSC 2004 [DIRS 164500]) suggest a decrease in U K_d as pH increases from 6 to 8. Most of the U K_d experiments were performed in the 8 to 9 pH range where adsorption is lower; thus, the mean U K_d over a pH range of 6 to 9 may be biased towards a lower value. The K_d values presented in Appendix A of *Radionuclide Transport Models Under Ambient Conditions* (BSC 2004 [DIRS 164500]) are for ambient temperatures (~25°C). The effect of temperature is assessed in Appendix I of the same report (BSC 2004 [DIRS 164500]). Figures I-2(e) and I-3(a) in *Radionuclide Transport Models Under Ambient Conditions* (BSC 2004 [DIRS 164500]) show adsorption of U(VI) and Pu to crushed tuff as a function of the reciprocal of temperature. These data indicate that U(VI) adsorption increases by a factor of approximately 3.9 as temperature increases from 25°C to 95°C but that the increase observed for Pu is not statistically significant (BSC 2004 [DIRS 164500], p. I-47).

Many adsorption models fill the gap between the analytical surface complexation modeling approach and the empirical K_d approach. Slightly more parameterized than the K_d approach are the nonlinear Langmuir and Freundlich isotherms. The Langmuir isotherm model is essentially an extension of the K_d isotherm to higher aqueous concentrations. At low concentrations the Langmuir isotherm is equivalent to the K_d isotherm, but at high concentrations where adsorption begins to reduce the concentration of available adsorption sites considerably, the isotherm asymptotically bends toward the adsorption capacity limit of the solid phase. The Freundlich isotherm is nonlinear throughout and is represented by an exponential function. It is usually reserved for certain adsorbates, such as Cs, that exhibit nonlinear adsorption over large ranges of concentration.

Between the isotherm models and the surface complexation model are models such as the generalized composite model and the component additivity model (Davis et al. 1998 [DIRS 154436]). However, as is the case for the surface complexation models, these models are limited by their sensitivity to mineral surface properties and lack of experimental data.

As long as the chemical and environmental conditions in the drift during the modeling period are generally represented in the K_d experiments, the K_d approach is suitable and defensible for predicting adsorption in the invert. Based on the range of experimental conditions of the K_d experiments (BSC 2004 [DIRS 164500], Appendices A and I), the most important conditions

that could be different in the invert are pH values outside of the experimental pH ranges (pH 6 to 9 for U, pH 7 to 9.5 for Pu) and temperatures that are considerably higher than 25°C. Specifically, the pH could potentially alter the K_d values outside of the experimental pH range, and increased temperature could markedly increase the U K_d value. However, because the temperature effect on U K_d is quantified (BSC 2004 [DIRS 164500], p. I-47), the K_d approach for U and Pu adsorption in the invert is limited only by the experimental pH range.

Perhaps the most important reason for adopting the K_d approach for the external accumulation model is the abundance of relevant measurements. No other approach has sufficient supporting experimental data that its results will be more accurate than the K_d approach for modeling adsorption in the invert provided that simulation conditions are close to experimental conditions. Consequently, the K_d approach is chosen to represent adsorption in the external accumulation model.

6.4.3.2 Implementation of K_d Adsorption Model

The K_d distribution coefficient of a radionuclide is the equilibrium ratio of the adsorbed and aqueous concentrations:

$$K_d = \frac{S}{C} \qquad \text{(Eq. 6.4.3-1)}$$

where S is the total adsorbed concentration and C is the total aqueous concentration. When K_d is expressed in its traditional units of mL/g, S is the amount of adsorbed radionuclide per unit mass of rock and C is the amount of aqueous radionuclide per volume of water. The corresponding nondimensional distribution coefficient K'_d is represented by:

$$K'_d = \frac{S'}{C} \qquad \text{(Eq. 6.4.3-2)}$$

where S' is the adsorbed concentration in units of amount per liter water. For unsaturated porous media, S' and S are related by the following expression:

$$S' = S\frac{\rho_{db}}{\theta_w} \qquad \text{(Eq. 6.4.3-3)}$$

The parameter ρ_{db} is the dry bulk density (mass rock per volume of porous media) and θ_w is the water content of the porous media (the bulk volumetric water fraction). Substituting Equation 6.4.3-3 into Equation 6.4.3-2, and then substituting K_d for S/C (from Equation 6.4.3-1), results in:

$$K'_d = K_d\frac{\rho_{db}}{\theta_w} \qquad \text{(Eq. 6.4.3-4)}$$

To simulate U and Pu K_d adsorption in PHREEQC, specific surface reactions must be defined for each of the aqueous U and Pu species that comprise approximately one percent or more of the

total U and Pu aqueous concentrations. For example, $UO_2(CO_3)_2^{2-}$ is an important aqueous U species at near-neutral pH. The contribution of this species to K_d adsorption is represented in PHREEQC by the following reaction:

$$\text{Sor} + \text{UO}_2(\text{CO}_3)_2^{2-} = \text{SorUO}_2(\text{CO}_3)_2^{2-} + \text{Fb}^{2-} \quad \text{(Eq. 6.4.3-5)}$$

where Sor is an unoccupied surface site and Fb^{2-} is a fictitious divalent anion (explained later). The associated mass action equation is:

$$K = \frac{[\text{SorUO}_2(\text{CO}_3)_2^{2-}][\text{Fb}^{2-}]}{[\text{UO}_2(\text{CO}_3)_2^{2-}][\text{Sor}]} \quad \text{(Eq. 6.4.3-6)}$$

where brackets signify activities. Converting the activities to concentrations, the equation becomes:

$$K = \frac{(\text{SorUO}_2(\text{CO}_3)_2^{2-})(\text{Fb}^{2-})\gamma_{\text{Fb}^{2-}}}{(\text{UO}_2(\text{CO}_3)_2^{2-})\gamma_{\text{UO}_2(\text{CO}_3)_2^{2-}}(\text{Sor})} \quad \text{(Eq. 6.4.3-7)}$$

where γ_i denotes the activity coefficient of species i. There are no activity coefficients for the surface species because activities and concentrations of surface species are equivalent in this model.

The fictitious species Fb^{2-} is included in the reaction to offset the activity coefficient of $UO_2(CO_3)_2^{2-}$. Fictitious species do not contribute any real mass or charge to the system. Because γ_i values of aqueous species in the model are only a function of valency and ionic strength, the two γ_i parameters in Equation 6.4.3-7 are equal, which implies:

$$K = \frac{(\text{SorUO}_2(\text{CO}_3)_2^{2-})(\text{Fb}^{2-})}{(\text{UO}_2(\text{CO}_3)_2^{2-})(\text{Sor})} \quad \text{(Eq. 6.4.3-8)}$$

The ratio of $(SorUO_2(CO_3)_2^{2-})$ to $(UO_2(CO_3)_2^{2-})$ in Equation 6.4.3-8 is equivalent to K'_d; therefore, substituting Equation 6.4.3-4 for K'_d implies that:

$$K = (K_d \frac{\rho_{db}}{\theta_w}) \frac{(\text{Fb}^{2-})}{(\text{Sor})} \quad \text{(Eq. 6.4.3-9)}$$

The value of (Sor) can be estimated from the total concentration of surface sites $(Sor)_T$, often called the adsorption capacity. In fact, defining (Sor) in Equation 6.4.3-9 as $(Sor)_T$ effectively changes the adsorption model to a nonlinear Langmuir model at higher aqueous concentrations and prevents radionuclide adsorption from exceeding the adsorption capacity of the tuff. $(Sor)_T$ is estimated using the following equation:

$$(\text{Sor})_T = \frac{d_s a_s \rho_{db}}{N_A \theta_w} \quad \text{(Eq. 6.4.3-10)}$$

where d_s is the surface site density (number of sites per unit surface area), a_s is the specific surface area (surface area per mass rock), and N_A is Avogadro's number (6.022×10^{23} sites per mole of sites). Substituting Equation 6.4.3-10 into Equation 6.4.3-9 gives:

$$K = K_d \frac{(\mathrm{Fb}^{2-})}{\left(\frac{d_s a_s}{N_A}\right)} \qquad \text{(Eq. 6.4.3-11)}$$

which shows that the equilibrium constant is simply a function of K_d and the specific surface site concentration ($d_s a_s / N_A$) and is not a function of the water content. The aqueous concentration of the fictitious species Fb^{2-} is constant (set at 1.00×10^{-6} molal in the model). The fictitious concentrations are not allowed to change in the simulations.

The K in Equation 6.4.3-11 represents linear K_d partitioning at low radionuclide concentrations when (Sor) can be approximated by $(Sor)_T$. Only when (Sor) begins to decrease markedly from $(Sor)_T$ does the ratio of adsorbed to aqueous concentrations (S/C) begin to decrease. This decrease in S/C, which occurs at high aqueous concentrations, is automatically and analytically accomplished during the simulation by the mass action expression (Equation 6.4.3-8). As (Sor) decreases due to adsorption, the adsorbed and aqueous concentrations in the mass action expression must also adjust to ensure that the right hand side of the equation remains constant. These constraints imply that as (Sor) approaches zero, S approaches $(Sor)_T$. This limit is necessary because it prevents adsorbed concentrations from exceeding the total surface site concentration.

The values of the parameters in Equations 6.4.3-10 and 6.4.3-11 are either measured or known, which allows estimation of $(Sor)_T$ and K. The value used for d_s is 2.3 sites/nm^2, which is consistent with the value recommended by Davis and Kent (1990 [DIRS 143280], p. 227) for bulk composite geological materials. Measurements of specific surface areas (a_s) of the sieved fractions (75 to 500 μm) of the devitrified tuff samples used in the K_d experiments range from 1.8 to 6.4 m^2/g (BSC 2004 [DIRS 164500], Table A-1). Because these measurements are on samples where clays and other fines with large specific surface areas are removed (BSC 2004 [DIRS 164500], p. A-6), they are lower than would be expected for the invert. For comparison, the sieved zeolitic tuff samples used in the K_d experiments were measured to have average specific surface areas mostly in the 20 to 30 m^2/g range, owing to the presence of a larger proportion of clay minerals (BSC 2004 [DIRS 164500], Table A-1). Larger size fractions are thought to have surface areas similar to the 75 to 500 μm fraction because tuffs are composed of fine grained minerals (BSC 2004 [DIRS 164500], p. A-6). In consideration of the various factors above, the value of a_s used in the current model for the crushed devitrified (non-zeolitic) tuff of the invert is 9 m^2/g.

The value of ρ_{db} is calculated from the invert porosity (θ) and the rock density of the crushed tuff (ρ_s) using the equation:

$$\rho_{db} = (1 - \theta)\rho_s \qquad \text{(Eq. 6.4.3-12)}$$

As listed in Table 4-15, the porosity and density of the invert tuff are 31% and 2.55 (g/cm^3), respectively (BSC 2004 [DIRS 168138], Table 5); thus, ρ_{db} is approximately 1.8 (g/cm^3).

The water content (θ_w) can be estimated by multiplying the water saturation by the porosity. The water saturation is predicted to be around 0.6 (Appendix G). This value is higher than the residual saturation presented in Table 4-16, because it represents the water saturation that would occur during flow through the invert, as discussed in Appendix G. Therefore, the water content is approximately 0.19. Using these values, $(\mathrm{Sor})_T$ for the crushed invert tuff is approximately 0.33 molal.

The log K values are estimated from the various K_d values below. The empirical cumulative distributions of K_d measurements for Pu and U adsorption on devitrified crushed tuff are presented in Figures A-33b and A-63b in *Radionuclide Transport Models Under Ambient Conditions* (BSC 2004 [DIRS 164500], Appendix A). Based on these figures, the median, minimum, and 95th percentile values are as presented in Table 6-5. For 95°C, the Pu K_d values are unchanged and the U K_d values are increased by a factor of 3.9, as calculated in Appendix I (BSC 2004 [DIRS 164500], p. I-47,). The corresponding log K values, given a specific surface site concentration ($d_s a_s / N_A$) of 3.44×10^{-5} mol/g and fictitious species concentration of 1.00×10^{-6} molal, are presented in Table 6-6. The median value was used in the PHREEQC simulations.

Table 6-5. Pu and U K_d Measurement Distributions for Devitrified Tuff

Radionuclide	Experimental Conditions	Median K_d (mL/g)	Minimum K_d (mL/g)	95th Percentile K_d (mL/g)
Pu	25 to 95°C, 7 ≤ pH ≤ 9.5	200	10[a]	2500
U	25°C, 6 ≤ pH ≤ 9	2 (8 at 95°C)[b]	0[a] (0 at 95°C)[b]	6 (20 at 95°C)[b]

Source: BSC 2004 [DIRS 164500], Figures A-33b and A-63b.

[a] Minimum value in BSC 2004 [DIRS 164500], Table 6-3.

[b] U K_d values at 95°C are estimated by multiplying U K_d values at 25°C values by 3.9 (BSC 2004 [DIRS 164500], p. I-47). Pu K_d values at 95°C are not significantly different from 25°C values (BSC 2004 [DIRS 164500], p. I-47).

Table 6-6. Pu and U log K Values for Adsorption to Invert Tuff

Radionuclide	Experimental Conditions	Median log K	Minimum log K	95th Percentile log K
Pu	25 to 95°C, 7 ≤ pH ≤ 9.5	−2.24	−3.54	−1.14
U	25°C, 6 ≤ pH ≤ 9	−4.24 (−3.63 at 95°C)	N/A[a] (N/A at 95°C)	−3.76 (−3.24 at 95°C)

[a] N/A = no adsorption.

NOTE: Log K values are for reactions of the form of Equation 6.4.3-5, an invert tuff specific surface site concentration ($d_s a_s / N_A$) of 3.44e-5 mol/g, and a constant fictitious species concentration (Fx^z) of 1e-6 molal.

6.4.4 Minerals Included during PHREEQC Simulations

When running PHREEQC, the user must specify the minerals that are expected to form. For each PHREEQC input file, a preliminary PHREEQC run was performed to determine the minerals that were favored to form based on the saturated index (SI) of the mineral phases. All

minerals with a SI > −0.01, were included in the input file, except for those minerals that are not expected to form in the repository environment. A value of SI > 0 indicates supersaturation of a mineral phase and SI < 0 indicates undersaturation of a mineral phase. Setting the cutoff to −0.01, rather than 0, ensures that all the possible minerals are included. Table 6-7 contains a list of the minerals that were considered appropriate minerals to form in the PHREEQC run and were added if the SI > −0.01. The minerals listed in Table 6-7 are consistent with the minerals formed in the source term EQ6 calculations (BSC 2006 [DIRS 176911], Table 6-7 and 6-8) Table 6-8 contains a list of suppressed minerals for the EQ6 calculations that generated the source terms used in the PHREEQC simulations (BSC 2006 [DIRS 176911], Table 6-9). The justifications for the suppressions provided in Table 6-8 were expanded from the original table (BSC 2006 [DIRS 176911], Table 6-9) for a few of the minerals (bunsenite, $Ni(OH)_2$, PuO_2, and quartz). The table is provided because the minerals that were suppressed in the EQ6 calculations could have a significant influence on the source term. To be consistent with the source term input, the PHREEQC input files did not include any of the minerals listed in Table 6-8, even if the SI > 0.01. The rationales for inclusion or exclusion of the minerals from the PHREEQC and EQ6 calculations are included in each of the tables.

The most desirable evidence supporting formation was the precipitation of the mineral in nature at 0°C to 100°C, near-neutral pH (generally 5 to 9), and 1 atm pressure. Where natural information is scant or absent, experimental evidence of formation that is consistent with the noted temperature, pressure, and pH was accepted. In some cases, when log K values are not available for suitable low-temperature minerals, high temperature phases are allowed to form. For example, reasonable experimental evidence exists for the crystallization of trevorite ($NiFeO_4$) under repository conditions. Therefore, trevorite was allowed to form even though trevorite is in the spinel group, which typically forms at temperatures above repository conditions. In addition, the minerals allowed to form were chosen to be consistent with the minerals formed in the source term EQ6 calculations (BSC 2006 [DIRS 176911], Table 6-7 and 6-8).

Table 6-7. Minerals Included in PHREEQC Input Files

Mineral	Chemical Formula (Thermodynamic Database)	Justification
Alunite	$KAl_3(SO_4)_2(OH)_6$	Alunite is a low-temperature (i.e., on the order of 100°C) mineral that often forms as a result of the action of sulfuric acid derived from the oxidation of pyrite (Gaines et al. 1997 [DIRS 172360], p. 632). Data also indicates formation at 1 atm and mildly acidic conditions.
Amesite-14A	$(Mg_2Al)[SiAl]O_5(OH)_4$	Amesite forms during Ca metasomatism of biotite in granite (Ca to Mg); found with calcite, magnetite, clinochlore, diopside, clinozoisite, sometimes grossular, occasionally margarite (Gaines et al. 1997 [DIRS 172360], pp. 1422 to 1423). Amesite's precipitation with calcite and magnetite suggests possible formation under repository conditions.
Argonite	$CaCO_3$	Aragonite is a polymorph of calcite, which means that it has the same chemistry as calcite but it has a different structure, and more importantly, different symmetry and crystal shapes (see Calcite below).
Barite	$BaSO_4$	Barite has been found as a secondary precipitate in acid soils in coastal plains and associated river terrace soils (Doner and Lynn 1995 [DIRS 169277], p. 297); this indicates formation at temperatures at or below 100°C, near-neutral pH, and 1 atm.
Beidellite-Ca	$Ca_{0.165}Al_{2.33}Si_{3.67}O_{10}(OH)_2$	Beidellite-Ca is a clay mineral that forms in sedimentary environments and hydrothermal environments consistent with repository conditions (Gaines et al. 1997 [DIRS 172360], pp. 1481 to 1483).
Beidellite-H	$H_{0.33}Al_{2.33}Si_{3.67}O_{10}(OH)_2$	Beidellite-H is a clay mineral that forms in sedimentary environments and hydrothermal environments consistent with repository conditions (Gaines et al. 1997 [DIRS 172360], pp. 1481 to 1483).
Beidellite-K	$K_{0.33}Al_{2.33}Si_{3.67}O_{10}(OH)_2$	Beidellite-K is a clay mineral that forms in sedimentary environments and hydrothermal environments consistent with repository conditions (Gaines et al. 1997 [DIRS 172360], pp. 1481 to 1483).
Beidellite-Mg	$Mg_{0.165}Al_{2.33}Si_{3.67}O_{10}(OH)_2$	Beidellite-Mg is a clay mineral with the same properties and formation characteristics as Beidellite-Ca, Beidellite-H, and Beidellite-K; as such, Beidellite-Mg can form under repository conditions (Gaines et al. 1997 [DIRS 172360], pp. 1480 to 1485; see discussions of Mg content on pp. 1482 and 1484).
Beidellite-Na	$Na_{0.33}Al_{2.33}Si_{3.67}O_{10}(OH)_2$	Beidellite-Na is a clay mineral. Beidellite-Na is in solid solution with Beidellite-Ca; both form in sedimentary environments and hydrothermal environments consistent with repository conditions (Gaines et al. 1997 [DIRS 172360], pp. 1480 to 1483).
Bixbyite	$(Mn,Fe)_2O_3$	Bixbyite forms in lithophysae (a globular mass of crystals) in rhyolite (a felsic volcanic rock that is chemically similar to rocks at Yucca Mountain) (Gaines et al. 1997 [DIRS 172360], p. 230). Bixbyite is chemically similar to maghemite ($Fe_{2.67}O_3$), whose formation can occur from the slow oxidation of magnetite (Gaines et al. 1997 [DIRS 172360], pp. 229 to 230; Schwertmann and Cornell 1991 [DIRS 144629]). Bixbyite crystals have been observed in outcrop at Yucca Mountain, and their formation and crystal habit at Yucca Mountain is similar to vapor phase crystallization in lithophysae at Topaz Mountain in the Thomas Range in Utah (Gaines et al. 1997 [DIRS 172360], p. 230).

Table 6-7. Minerals Included in PHREEQC Input Files (Continued)

Mineral	Chemical Formula	Justification
Calcite	$CaCO_3$	Calcite forms in low-temperature environments consistent with repository conditions, such as in earthy crusts and in springs or streams in caves (Gaines et al. 1997 [DIRS 172360], p. 431).
Celadonite Ferro-celadonite	$K(Mg,Al)Si_4O_{10}(OH)_2K(Fe^{2+},Fe^{3+})Si_4O_{10}(OH)_2$	Celadonites are found in altered volcanic rocks (Roberts et al. 1990 [DIRS 107105], p. 113). Celadonites can form at low temperatures (on the order of 100°C) (Li et al. 1997 [DIRS 159034]). Celadonite can form in saline and alkaline lakes and lake margins from altered smectites (Hover and Ashley 2003 [DIRS 169212]).
Chabazite	$K_{0.6}Na_{0.2}Ca_{1.55}Al_{3.8}Si_{8.2}O_{24}:10H_2O$	Chabazite is a zeolite commonly found in sedimentary environments. Chabazite is an alteration product of volcanic glass in alkaline and saline lakes (Ming and Mumpton 1995 [DIRS 156843], p. 884). Basaltic glass is generally considered an appropriate natural analogue for nuclear waste glass (Ewing and Haaker 1979 [DIRS 161749]).
Chalcedony	SiO_2	A general term for fibrous, microcrystalline varieties of silica deposited from aqueous solutions, (Klein and Hurlbut 1985 [DIRS 105907], p. 442). Chalcedony forms at near-neutral pH and at 100°C, which is consistent with repository conditions.
Clinochlore-14A	$Mg_5Al_2Si_3O_{10}(OH)_8$	Clinochlore is in solid solution with daphnite (also known as chamosite) (Deer et al. 1992 [DIRS 163286], p. 335). Both minerals are in the chlorite group and may form authigenically (Deer et al. 1992 [DIRS 163286], p. 342), which indicates possible precipitation under repository conditions. While chlorite typically forms at elevated temperatures ($\geq$200°C), it is used in numerical simulations to represent the "mixed layer hydroxide" minerals commonly found in soils and that would be expected around the repository (Dixon 1995 [DIRS 159374]).
Clinoptilolite-Ca	$Ca_{1.7335}Al_{3.45}Fe_{0.017}Si_{14.533036}: 10.922H_2O$	Often present in saline, alkaline lake sedimentary deposits derived from volcanic material (Gaines et al. 1997 [DIRS 172360], p. 1673). As such, precipitation in the repository is possible.
Clinoptilolite-K	$K_{3.467}Al_{3.45}Fe_{0.017}Si_{14.533036}:10.922H_2O$	Often present in saline, alkaline lake sedimentary deposits derived from volcanic material (Gaines et al. 1997 [DIRS 172360], p. 1673). As such, precipitation in the repository is possible.
Clinoptilolite-Na	$Na_{3.467}Al_{3.45}Fe_{0.017}Si_{14.533036}: 10.922H_2O$	Often present in saline, alkaline lake sedimentary deposits derived from volcanic material (Gaines et al. 1997 [DIRS 172360], p. 1673). As such, precipitation in the repository is possible.
Co_2SiO_4	Co_2SiO_4	This structure most closely resembles Zn_2SiO_4, which is permitted to form due to its characteristics as a secondary mineral formed in oxidized zones with calcite and zincite; see discussion of Willemite (Zn_2SiO_4). In Zn_2SiO_4, Co^{2+} substitutes rarely for Zn in Zn_2SiO_4 (Gaines et al. 1997 [DIRS 172360], p. 1022); therefore, formation of $CoSiO_4$ is permitted.

Table 6-7. Minerals Included in PHREEQC Input Files (Continued)

Mineral	Chemical Formula	Justification
Dawsonite	$NaAl(CO_3)(OH)_2$	Dawsonite is a low-temperature hydrothermal mineral that forms from decomposing aluminous silicates (Gaines et al. 1997 [DIRS 172360], pp. 492 to 493). As such, formation in the repository is possible.
Diaspore	AlO(OH)	Diaspore is in partial solid solution with goethite (Gaines et al. 1997 [DIRS 172360], pp. 266 to 267), which is expected to readily form in the repository. Therefore, diaspore precipitation is considered possible.
Erionite	$K_{1.5}Na_{0.9}Ca_{0.9}Al_{44.2}Si_{13.8}O_{36}$:13.0$H_2O$	Rare zeolite, it is associated with chabazite and is an alteration product of volcanic glass in alkaline and saline lakes (Ming and Mumpton 1995 [DIRS 156843] p. 884). Basaltic glass is generally considered to be an appropriate natural analogue for nuclear waste glass (Ewing and Haaker 1979 [DIRS 161749]).
Eskolaite	Cr_2O_3	Swayambunathan et al. (1989 [DIRS 177221]) reported that aging of Cr(III) salt solutions could lead to formation of chromium (III) hydroxide at room temperature. However, eskolaite is the final product in the evolution of Cr(III) oxide even when exposed to short heating time (20 minutes at 100°C). In addition, eskolaite was allowed to form since the EQ6 database does not contain many other Cr phases.
$Fe(OH)_3$	$Fe(OH)_3$	$Fe(OH)_3$ has been allowed to form, due to its chemical similarities to gibbsite $Al(OH)_3$, which could form under repository conditions (Gaines et al. 1997 [DIRS 172360], pp. 280 to 281; Allen and Hajek 1995 [DIRS 159372]).
Fluorapatite	$Ca_5(PO_4)_3F$	May be formed from reaction of phosphate fertilizers with soils or soil constituents (Lindsay et al. 1995 [DIRS 169289], Table 22-3), which indicates formation at or below 100°C, 1 atm, and mildly basic conditions.
$GdPO_4$: $10H_20$	$GdPO_4$: $10H_20$	This mineral is reported at 100°C (Spahiu and Bruno 1995 [DIRS 103804], pp. 22 and 40). The database incorrectly lists the mineral with ten water molecules, whereas the source of the logK data shows the formula as GdPO4:xH2O. $GdPO_4$:$10H_2O$ was included in the database for sake of consistency with the model degradation and release report (BSC 2006 [DIRS 176911]). The inclusion of $GdPO_4$:$10H_2O$ compared to the correct form has no impact on the values of logK used in the EQ6 data base. The source used to obtain the logK values for the database (Spahiu and Bruno 1995 [DIRS 103804], pp. 22 and 40) presents the reaction and logK as: $GdPO_4.xH2O = Gd^{3+} + PO_4^{3-} + x\ H2O$ Log K = -24.3 Number of water hydration in cases that are not limiting in either hydrogen or oxygen, such as the cases in this report, would have no effect, on the values of logK. If the water activity is much lower than unity (e.g., in a brine), which is not the case in the report, the erroneously high water of hydration would make the solid appear much more soluble.
Gibbsite	$Al(OH)_3$	Most common $Al(OH)_3$ polymorph (Hsu 1995 [DIRS 105875]). AlOOH is rarer than hydroxides and are considered the product of weathering (Allen and Hajek 1995 [DIRS 159372]) so the $Al(OH)_3$ polymorphs will be the primary ones expected to form in the repository.

Table 6-7. Minerals Included in PHREEQC Input Files (Continued)

Mineral	Chemical Formula	Justification
Goethite	α-FeOOH	Goethite (α-FeOOH) and hematite (α-Fe_2O_3) are the two most thermodynamically stable and most widespread iron minerals occurring under oxidizing conditions (Schwertmann and Taylor 1995 [DIRS 105959]). Total suppression of the formation of hematite and goethite is not realistic considering the duration of the time frame of this analysis, until 20,000 years after waste package breach. Considering the temperature, solution and pH conditions in the waste package, a mixture of goethite and hematite would, eventually, be the most abundant iron oxides in the corrosion products (Schwertmann and Cornell 1991 [DIRS 144629], Chapters 4, 5, and 10). It is not possible to simulate the formation of such a mixture of iron oxides with EQ6 or PHREEQC since only the most thermodynamically stable solid is allowed to form. If hematite is not suppressed it will be the only iron oxide formed in a run. If hematite is suppressed and goethite is not, then goethite will be the only iron oxide that forms during a run. However, during waste package degradation, mixed Fe(II)-Fe(III) minerals, such as magnetite (Fe_3O_4) and green rusts (Fe hydroxy salts of chloride, sulfate or carbonate) as well as Fe(III) oxides such as maghemite (γ-Fe_2O_3) and lepidocrocite (γ-FeOOH) may also be the products of steel corrosion in the waste package (Schwertmann and Cornell 1991 [DIRS 144629], Introduction and Chapter 1; Furet et al. 1990 [DIRS 143296]). Of these minerals, only magnetite is in the database and magnetite will not form during most of the simulations because the assumption about O_2 fugacity (Section 6.2) has the effect of completely oxidizing Fe(0) to Fe(III), as well as Cr(0) to Cr(VI) and Mo(0) to Mo(VI). In conclusion, hematite is currently being suppressed and goethite is the only iron oxide currently forming.
Hopeite	$Zn_3(PO_4)_2\ 4H_2O$	This is a secondary (i.e., oxidizing environment), low-temperature (i.e., on the order of 100°C) mineral in zinc-bearing ore deposits (Roberts et al. 1990 [DIRS 107105], p. 374). Data also indicates formation at 1 atm and mildly basic conditions.
Hydroxylapatite	$Ca_5(PO_4)_3(OH)$	Hydroxylapatite is in complete solid solution with fluorapatite [$Ca_5(PO_4)_3F$] and incomplete solid solution with chlorapatite [$Ca_5(PO_4)_3Cl$] (Gaines et al. 1997 [DIRS 172360], pp. 854 to 861, especially p. 858). Precipitates as disseminated nodules in nearshore marine environments (Gaines et al. 1997 [DIRS 172360], p. 859), or as primary deposits in sedimentary rocks (Deer et al. 1992 [DIRS 163286], p. 668) indicating similarity to repository conditions.
Illite	$[K,(H_3O^+)]Al_2[Si_3AlO_{10}](OH)_2$	Like kaolinite, illite forms in oxidizing environments, and can precipitate at 100°C, near-neutral-pH, and 1 atm (Gaines et al. 1997 [DIRS 172360], p. 1472).
Kaolinite	$Al_2Si_2O_5(OH)_4$	Most common kaolin, formation at 25°C is usually slow; however, it can crystallize easily from the alteration of smectites (Dixon 1995 [DIRS 159374]).
K-Feldspar	$KAlSi_3O_8$	Abundant evidence exists supporting low-temperature precipitation (i.e., at or below approximately 100°C) at the earth's surface (Baskin 1955 [DIRS 175045], p. 150).

Table 6-7. Minerals Included in PHREEQC Input Files (Continued)

Mineral	Chemical Formula	Justification
Laumontite	$Ca_4[Al_8Si_{16}O_{48}]$ $16H_20$	Laumontite forms as an authigenic mineral in sedimentary rocks, which indicates that it precipitates at or below 100°C and standard pressure and pH at or near neutral (Deer et al. 1992 [DIRS 163286], p. 521).
Magnesite	$MgCO_3$	$MgCO_3$ forms in a variety of elevated concentration environments similar to repository conditions; therefore, $MgCO_3$ formation is allowed (Gaines et al. 1997 [DIRS 172360], pp. 434 to 435).
Magnetite	$Fe^{2+}Fe_2^{3+}O_4$	A corrosion product of steels (Ahn and Leslie 1998 [DIRS 159352]; Raman and Nasrazadani 1990 [DIRS 159354]; Marsh and Taylor 1988 [DIRS 100917]; Pednekar 1987 [DIRS 159329]; Brush and Pearl 1972 [DIRS 159355]).
Mesolite	$Na_{0.676}Ca_{0.657}Al_{1.99}Si_{3.01}O_{10}$:$2.647H_2O$	Mesolite is a zeolite that can precipitate as a hydrothermal mineral with (for example) calcite; it is isostructural with and forms incomplete solid solution with the zeolites, natrolite and scolecite, (Gaines et al. 1997 [DIRS 172360], p. 1688). Formation of these zeolites is consistent with repository conditions.
Montmorillonite-Ca	$Ca_{0.165}Mg_{0.33}Al_{1.67}Si_4O_{10}(OH)_2$	Montmorillonite is a member of the Smectite group and one of the three most common smectite minerals, along with nontronite and beidellite. Smectites are common in temperate and cold climates (Allen and Hajek 1995 [DIRS 159372], pg. 228).
Montmorillonite-K	$K_{0.33}Mg_{0.33}Al_{1.67}Si_4O_{10}(OH)_2$	See Montmorillonite-Ca
Montmorillonite-Mg	$Mg_{0.495}Al_{1.67}Si_4O_{10}(OH)_2$	See Montmorillonite-Ca
Montmorillonite-Na	$Na_{0.33}Mg_{0.33}Al_{1.67}Si_4O_{10}(OH)_2$	See Montmorillonite-Ca
Mordenite	$Ca_{0.2895}Na_{0.361}Al_{0.94}Si_{5.06012}$:$3.468H_2O$	Mordenite is a widespread zeolite that has been described in the Yucca Mountain tuffs (Chipera et al. 1998 [DIRS 101331]). Its formation in the repository is probable (Gaines et al. 1997 [DIRS 172360], p. 1688).
Boltwoodite-Na	$NaUO_2SiO_3OH$:$1.5H_2O$	A known alteration phase of synthetic or natural UO_2 (Wronkiewicz and Buck 1999 [DIRS 169286], Figure 3).
Natrolite	$Na_2Al_2Si_3O_{10}$:$2H_2O$	Natrolite is a zeolite that can precipitate as a hydrothermal mineral with (for example) calcite; it is isostructural with and forms incomplete solid solution with the zeolites mesolite and scolecite (Gaines et al. 1997 [DIRS 172360], pp. 1677 to 1679, p. 1688). Formation of these zeolites is consistent with repository conditions.
Nontronite-Ca	$Ca(Fe,Al)_2(Si,Al)_4O_{10}(OH)_2$:nH_2O	Nontronite is one of the three most common smectite minerals, along with montmorillonite and beidellite. Smectites are common in temperate and cold climates (Allen and Hajek 1995 [DIRS 159372], pg. 228).
Nontronite-H	$H_2(Fe,Al)_2(Si,Al)_4O_{10}(OH)_2$: nH_2O	See Nontronite-Ca
Nontronite-K	$K_2(Fe,Al)_2(Si,Al)_4O_{10}(OH)_2$:nH_2O	See Nontronite-Ca
Nontronite-Mg	$Mg(Fe,Al)_2(Si,Al)_4O_{10}(OH)_2$:nH_2O	See Nontronite-Ca
Nontronite-Na	$Na_2(Fe,Al)_2(Si,Al)_4O_{10}(OH)_2$:nH_2O	See Nontronite-Ca

Table 6-7. Minerals Included in PHREEQC Input Files (Continued)

Mineral	Chemical Formula	Justification
NpO_2	NpO_2	NpO_2 formation is possible in the repository. Its formation is justified in *Dissolved Concentration Limits of Radioactive Elements* (BSC 2004 [DIRS 174566]), where it is a solubility-controlling mineral used in the TSPA. In addition, the study by Roberts et al. (2003 [DIRS 162536]) supports the formation of NpO_2.
Phillipsite	$KCaAl_3Si_5O_{16}: 6H_2O$	A rare zeolite, it is associated with chabazite and is an alteration product of volcanic glass in alkaline and saline lakes (Ming and Mumpton 1995 [DIRS 156843], p. 884). Basaltic glass is generally considered to be an appropriate natural analogue for nuclear waste glass (Ewing and Haaker 1979 [DIRS 161749]).
Powellite	$Ca(Mo,W)O_4$	Occurs as a secondary mineral in the oxidation zones of ore deposits (Roberts et al. 1990 [DIRS 107105], p. 692). It is a secondary mineral, often formed by the alteration of molybdenite, in copper deposits (Palache et al. 1951 [DIRS 162280], p. 1080). As such, formation under repository conditions is possible.
Prehnite	$Ca_2Al_2Si_3O_{10}(OH)_2$	Prehnite precipitates as a late-forming mineral in veins and cavities, where it is associated with zeolites (Gaines et al. 1997 [DIRS 172360], p. 1522). Given its typical crystallization history and association with zeolites, which are allowed to form, it is possible that prehnite will form in the repository.
$Pu(HPO_4)_2$(am, hyd)	$Pu(HPO_4)_2$(am, hyd)	Solubility studies by Katz et al. (1986 [DIRS 106312], pp. 638 to 655); thermodynamic data (OECD 2001 [DIRS 159027], pp. 58 and 62); and data supporting crystallization at 25°C (Denotkina et al. 1960 [DIRS 175102], pp. 731 to 734; 1960 [DIRS 175103], pp. 387 to 389) indicate that precipitation of this solid is possible under repository conditions.
PuO_2 (hyd.,aged)	PuO_2 (hyd., aged)	Experimental plutonium solution concentrations during PuO_2 or PWR spent nuclear fuel degradation have been shown to be between the solubility of PuO_2 and that of a more soluble phase, $Pu(OH)_4$ (or PuO_2·hyd,aged) (Rai and Ryan 1982 [DIRS 112060]; Wilson and Bruton 1989 [DIRS 137607], Section 3.1 and Table 3). PuO_2(hyd, aged) has been allowed to form and crystalline PuO_2 has been suppressed.
$PuO_2(OH)_2:H_2O$	$PuO_2(OH)_2:H_2O$	Thermodynamic data at standard temperature and pressure suggests that formation under repository conditions is possible (OECD 2001 [DIRS 159027], pp. 338 and 339).
Pyrolusite	MnO_2	Pyrolusite is very common in high pH, oxidizing conditions; in bogs, lacustrine, or shallow marine deposits; as deep sea-floor nodules; and as deposits formed by circulating metoric waters (Gaines et al. 1997 [DIRS 172360], p. 239). Data indicates that formation under repository conditions is possible.
Saponite	$(Ca_{0.5},H,K,Mg_{0.5},Na)_{0.33}Mg_3(Si,Al)_4O_{10}(OH)_2$	Trioctahedral Mg-rich smectites (saponite or stevensite) can precipitate in saline and alkaline lakes and lake margins (Hover and Ashley 2003 [DIRS 169212]; Akbulut and Kadir 2003 [DIRS 169213]).

Table 6-7. Minerals Included in PHREEQC Input Files (Continued)

Mineral	Chemical Formula	Justification
Scolecite	$CaAl_2Si_3O_{10} \cdot 3H_2O$	Scolecite is a zeolite that can precipitate as a hydrothermal mineral with (for example) calcite; it is isostructural with and forms incomplete solid solution with the zeolites mesolites and natrolite (Gaines et al. 1997 [DIRS 172360], pp. 1677 to 1679, 1688, 1682 to 1683). Formation of these zeolites is consistent with repository conditions.
Sepiolite	$Mg_4Si_6O_{15}(OH)_2{:}6H_2O$	Sepiolite may form in lacustrine environments characterized by alkaline solutions with high activities of silicon and Mg (Singer 1995 [DIRS 169280], pp. 856 to 857). Precipitation in lacustrine environments is on the order of 100°C, slightly alkaline pH, and 1 atm. As such, formation is possible in the repository.
Smectite-high-Fe-Mg	$Ca_{0.025}Na_{0.1}K_{0.2}Fe^{2+}_{0.5}Fe_{0.2}{}^{3+}Mg_{1.15}Al_{1.25}Si_{3.5}H2O_{12}$	Smectites (which include saponite, beidellite/montmorillonite, and nontronite, noted elsewhere in this table) form in environments consistent with repository conditions, such as saline and alkaline lakes (Hover and Ashley 2003 [DIRS 169212]; Akbulut and Kadir 2003 [DIRS 169213]; Gaines et al. 1997 [DIRS 172360], pp. 1480 to 1490).
Smectite-low-Fe-Mg	$Ca_{0.02}Na_{0.15}K_{.2}Fe^{2+}_{0.29}Fe^{3+}_{.16}Mg_{0.9}Al_{1.25}Si_{3.75}H_2O_{12}$	See Smectite-high-Fe-Mg
Smectite-Reykjanes	$Ca_{0.66}Na_{0.33}K_{0.03}Fe^{2+}_{0.33}Fe^{3+}_{0.35}Mg_{1.29}Mn_{0.01}Al_{1.11}Si_{3.17}H_2O_{12}$	See Smectite-high-Fe-Mg
Stellerite	$CaAl_2Si_7O_{18}{:}7H_20$	A zeolite; occurs in low-temperature (on the order of 100°C) settings such as geothermal fields or in veins and geodes in basalts and other basic volcanic rocks, and on their fracture surfaces (Gaines et al. 1997 [DIRS 172360], p. 1676).
Stilbite	$Ca_{1.019}Na_{0.136}K_{0.006}Al_{2.18}Si_{6.82}O_{18}{:}7.33H_2O$	A zeolite; occurs in sedimentary tuffs, and hot-spring deposits, which indicates formation conditions similar to repository conditions (Gaines et al. 1997 [DIRS 172360], pp. 1674 to 1675). Forms an incomplete solid solution with stellerite (Gaines et al. 1997 [DIRS 172360], p. 1674), which is also allowed to form.
Trevorite	$NiFe_2O_4$	Although spinels are typically high pressure/temperature minerals (Roberts et al. 1990 [DIRS 107105], p. 881), there are low temperature spinel corrosion products (Fe_3O_4) that form on iron in oxygen poor environments. Thus, trevorite was allowed to form since nickel-substituted goethite, hematite, and $NiFe_2O_4$ can be synthesized at 70°C (Cornell et al. 1992 [DIRS 164025], p.78), and nickel-substituted iron oxides are not in the EQ6 database.
$(UO_2)_3(PO_4)_2{:}4H_2O$ and $UO_2HPO_4{:}4H_2O$	$(UO_2)_3(PO_4)_2{:}4H_2O$ and $UO_2HPO_4{:}4H_2O$	$(UO_2)_3(PO_4)_2{:}4H_2O$ and $UO_2HPO_4{:}4H_2O$ are reported as a solubility-controlling phases in groundwater at low temperature and pH values (Sandino 1991 [DIRS 113307], pp. 16 to 17).
Uranophane (alpha)	$Ca(UO_2)_2SiO_3(OH)_2{\cdot}5(H_2O)$	A known alteration phase of synthetic or natural UO_2 (Wronkiewicz and Buck 1999 [DIRS 169286], Figure 3).

Table 6-7. Minerals Included in PHREEQC Input Files (Continued)

Mineral	Chemical Formula	Justification
Wairakite	$CaAl_2Si_4O_{12}:2H_2O$	A zeolite, wairakite precipitates in geothermal wells at 60°C to 300°C (Gaines et al. 1997 [DIRS 172360], p. 1650), which indicates that formation in the repository is possible.
Weeksite-Na	$Na_2(UO_2)_2Si_5O_{13}:3H_2O$	Weeksite precipitated during a 10-year degradation study of dripping J-13 well water onto UO_2 (BSC 2004 [DIRS 174566], p. 6-103). Weeksite-Na precipitates in opal veinlets in rhyolite; with carbonates and gypsum (Gaines et al. 1997 [DIRS 172360], p. 1114); and with aragonite ($CaCO_3$) in a sandstone matrix (Barthelmy 2005 [DIRS 175135]). These occurrences indicate conditions of formation similar to those in the repository.
Willemite	Zn_2SiO_4	Zn_2SiO_4 precipitates in the oxidized zone of zinc deposits (Gaines et al. 1997 [DIRS 172360], p. 1022). At Franklin, Sussex County, New Jersey, Zn_2SiO_4 is associated with secondary minerals zincite and calcite (Barthelmy 2005 [DIRS 175137]), which suggests formation under repository conditions.

Table 6-8. Minerals Suppressed in EQ6 Source Term Calculations from BSC 2006 [DIRS 176911]

Mineral	Formula	Justification
Andradite	$Ca_3Fe_2(SiO_4)_3$	Andradite is a high pressure/temperature mineral found in metamorphic and igneous rocks (Deer et al. 1966 [DIRS 102773], p. 30).
Annite	$KFe^{+2}{}_3AlSi_3O_{10}(OH)_2$	An end member of biotite, a mica found only in igneous and metamorphic rocks (Deer et al. 1966 [DIRS 102773], pp. 211, 212, and 276).
Antigorite	$Mg_3Si_2O_5(OH)_4$	Antigorite is stable at temperatures above typical repository conditions (i.e., commonly associated with other serpentines, magnetite, magnetite-magnesiochromite, talc, magnesite, dolomite, amphiboles, and pyroxenes) (Gaines et al. 1997 [DIRS 172360], pp. 1415 to 1417).
Baddeleyite	ZrO_2	High pressure/temperature mineral. Found in sedimentary deposits as a detrital mineral (Roberts et al. 1990 [DIRS 107105], p. 47), also formed in metamict zircon (Deer et al. 1966 [DIRS 102773], p. 15). Hydrolysis of zirconium salts leads to precipitation of poorly crystalline oxides at low temperatures (Milnes and Fitzpatrick 1995 [DIRS 105911], pp. 1189 to 1190) and soluble zirconium may be incorporated in or sorb onto clay mineral surfaces (Milnes and Fitzpatrick 1995 [DIRS 105911], pp. 1185 to 1186). However, based on baddeleyite's typical crystallization at higher temperatures than those expected in the repository, it is unlikely that some of the zirconium released by degradation of waste package components will precipitate from solution.
Berlinite	$AlPO_4$	A phosphate mineral that is found in pegmatites and high-temperature iron ores (i.e., above 200°C); as such, there is no evidence that this mineral would form in the repository (Gaines et al. 1997 [DIRS 172360], p. 720; see attakolite, p. 966).
Bornite	Cu_5FeS_4	Bornite typically forms at temperatures above 200°C, and formation in the repository is not likely (Stanton 1972 [DIRS 153993], pp. 114 to 121).
Bunsenite	NiO	Bunsenite is the mineral form of NiO that could be formed by heating NiO at 1,000°C for at least 24 hrs (Hemingway 1990 [DIRS 177093]). Formation of bunsenite was suppressed, as formation of this mineral at ambient conditions is unlikely.
$CaUO_4$	$CaUO_4$	Not a known alteration phase of synthetic or natural UO_2 (Wronkiewicz and Buck 1999 [DIRS 169286], Figure 3).
Chromite	$FeCr_2O_4$	Chromite occurs in magmatic deposits at temperatures above 300°C, which precludes formation in the repository (Gaines et al. 1997 [DIRS 172360], p. 302).
Clinozoisite	$Ca_2Al_3Si_3O_{12}$ (OH)	Clinozoisite typically forms in regional metamorphic rocks, pegmatites, veins, and felsic volcanic rocks (Gaines et al. 1997 [DIRS 172360], p. 1198). Precipitation in these rock types indicates temperatures of formation above repository conditions.
Corundum	Al_2O_3	Corundum forms in syenites, pegmatites, and metamorphic rocks such as marbles, schists, and gneisses (Gaines et al. 1997 [DIRS 172360], p. 216). Corundum formation temperatures are higher than anticipated repository conditions.

Table 6-8. Minerals Suppressed in EQ6 Source Term Calculations from BSC 2006 [DIRS 176911] (Continued)

Mineral	Formula	Justification
Cristobalite (alpha)	SiO_2	Cristobalite is metastable at 300°C (Gaines et al. 1997 [DIRS 172360], pp. 1568 to 1569); therefore, it will not precipitate under repository conditions (on the order of 100°C).
Chromium dioxide	CrO_2	Chromium dioxide is most commonly a synthesized film on recording tape; formation will not occur in the repository. Rutile (TiO_2) displays a minor amount of Cr substitution for titanium; however, rutile is confined to igneous and metamorphic environments (Gaines et al. 1997 [DIRS 172360], pp. 235 to 237), which are inconsistent with repository conditions.
Copper	Cu	Copper forms from secondary origin, by reduction of Cu-bearing solutions by iron minerals (Gaines et al. 1997 [DIRS 172360], p. 4). The redox conditions in the repository are oxidizing, precluding the precipitation of copper metal.
Dolomite	$CaMg(CO_3)_2$	Dolomite is usually derived by secondary mineralization, from the replacement of calcium by Mg in the calcite crystal structure in Mg-rich waters (Klein and Hurlbut 1985 [DIRS 105907], p. 340). Because it rarely occurs as a primary mineral, dolomite was also suppressed.
Epidote	$Ca_2FeAl_2Si_3O_{12}OH$	Epidote forms in a wide variety of igneous and metamorphic environments, as well as in low-temperature veins, amygdules, fillings, and some hot-spring deposits (Gaines et al. 1997 [DIRS 172360], pp. 1200 to 1201). These occurrences are not consistent with repository conditions.
Ferrite-Ca Ferrite-Mg	$CaFe_2O_4MgFe_2O_4$	Magnesioferrite has been found in sintered magnesite of furnace linings and other refractories (Palache et al. 1944 [DIRS 163604], p. 705), and is not expected to form at low temperature.
Gd_2O_3	Gd_2O_3	Gd_2O_3 is a common and stable mineral form of gadolinium, which is typically refined from minerals such as bastanite (e.g., bastanite containing 0.01 wt % Gd_2O_3) (Hull et al. 2000 [DIRS 175241], pp. 100 to 101). Given bastanite's high melting point (i.e., 2,339°C) (Hull et al. 2000 [DIRS 175241], p. 100) and its precipitation within minerals that form in magmatic environments, formation under repository conditions is unlikely.
Hematite	α-Fe_2O_3	Goethite (α-FeOOH) and hematite (α-Fe_2O_3) are the two most thermodynamically stable and most widespread iron minerals occurring under oxidizing conditions (Schwertmann and Taylor 1995 [DIRS 105959]). Total suppression of the formation of hematite and goethite is not realistic considering the duration of the time frame of this analysis, up to 20,000 years after waste package breach. Considering the temperature, solution, and pH conditions in the waste package and repository environment, a mixture of goethite and hematite would, eventually, be the most abundant iron oxides in the corrosion products (Schwertmann and Cornell 1991 [DIRS 144629], Chapters 4, 5, and 10). It is not possible to simulate the formation of such a mixture of iron oxides with EQ6 since only the most thermodynamically stable solid is allowed to form. If hematite is not suppressed it will be the only iron oxide formed.. If hematite is suppressed and goethite is not, then goethite will be the only iron oxide that forms during an EQ6 simulation. However, during waste package degradation, mixed Fe(II)-Fe(III) minerals, such as magnetite (Fe_3O_4) and green rusts (Fe hydroxy salts of chloride, sulfate or carbonate), as well as Fe(III) oxides such as maghemite (γ-Fe_2O_3) and lepidocrocite (γ-FeOOH), may also be the products of steel corrosion in the waste package (Schwertmann and Cornell 1991 [DIRS 144629], Introduction and Chapter 1; Furet et al. 1990 [DIRS 143296]). Of these minerals, only magnetite is in the EQ6 database and magnetite will not form during most of the simulations because the assumption about O_2 fugacity (see Section 6.2) has the effect of completely oxidizing Fe(0) to Fe(III), as well as Cr(0) to Cr(VI) and Mo(0) to Mo(VI).

Table 6-8. Minerals Suppressed in EQ6 Source Term Calculations from BSC 2006 [DIRS 176911] (Continued)

Mineral	Formula	Justification
		In conclusion, hematite is currently being suppressed and goethite is the only iron oxide that is allowed to precipitate.
Hercynite	$FeAl_2O_4$	Hercynite typically forms in high temperature settings (>>300°C) with minerals such as sillimanite (which is a representative mineral for high-grade metamorphism) (Gaines et al. 1997 [DIRS 172360], p. 297).
Lawsonite	$CaAl_2Si_2O_7(OH)_2:H_2O$	Lawsonite's occurrences are confined to metamorphic rocks, which is dissimilar to repository conditions (Gaines et al. 1997 [DIRS 172360], p. 1157).
MnO_2(gamma)	MnO_2(gamma)	MnO_2(gamma) is suppressed because there are no high-temperature thermodynamic data for it and it is an alteration product of primary manganese minerals. The mineral did not form at 25°C. MnO_2 (gamma), known as nsutite (Bricker 1965 [DIRS 157873] pp. 1296 to 1354), is a widespread alteration mineral in most of the world's major manganese deposits. Manganoan nsutite (MnO_2) is typically derived from the oxidation of Mn carbonate minerals such as rhodochrosite ($MnCO_3$) (Gaines et al. 1997 [DIRS 172360], p. 248).
Muscovite	$KAl_2(Si_3Al)O_{10}(OH,F)$	Occurs in high temperature (>>300°C) and pressure (above 1 atm) mineral assemblages (Roberts et al. 1990 [DIRS 107105], p. 586).
$Ni(OH)_2$	$Ni(OH)_2$	This mineral is known as theophrastite, which forms in igneous environments with associated minerals (e.g., chlorite, vesuvianite, and andradite) that cannot precipitate under repository conditions (Gaines et al. 1997 [DIRS 172360], pp. 276 and 277). Other evidence suggests that $Ni(OH)_2$ could form under ambient conditions (Linke 1965 [DIRS 166191). However, to be consistent with the material degradation and release model (BSC 2006 [DIRS 176911], Table 6-9), $Ni(OH)_2$ was not allowed to precipitate in the calculations. As it turned out, though, inspection of the PHREEQC output files shows that the saturation index of $Ni(OH)_2$ stayed below –1 for all cases, indicating that it would not have formed even if it had been included in the input file. Instead, the Ni precipitated in Trevorite.
Phlogopite	$KMg_3AlSi_3O_{10}(OH)_2$	Occurs chiefly in metamorphic limestones and ultrabasic rocks (Roberts et al. 1990 [DIRS 107105], p. 671). Thus, it forms under more elevated temperature and pressure conditions than are estimated for the repository.
Polydymite	Ni_3S_4	Polydymite occurs under reducing conditions, in hydrothermal vein deposits with other sulfides (Roberts et al. 1990 [DIRS 107105], p. 689). Experimental evidence indicates typical precipitation/thermal stability at 353°C (Vaughan and Craig 1978 [DIRS 151482], p.357). Other experimental evidence indicates precipitation at 200°C, which is also above anticipated repository conditions (Kellerud and Yund 1962 [DIRS 175112], p. 168). The repository is expected to be oxidizing.
PuO_2	PuO_2	The solubilities of solid Pu(IV) oxide/hydroxide scatter within several orders of magnitude because of the difficulties of establishing equilibrium of Pu(IV), polymerization and disproportionation reactions and the strong sorption capacities of Pu^{4+} (Runde 1999 [DIRS 144800], p. 8). Experimental plutonium solution concentrations during PuO_2 or PWR spent nuclear fuel degradation have been shown to be between the solubility of PuO_2 and that of a more soluble phase, $Pu(OH)_4$ (or PuO_2·hyd,aged) (Rai and Ryan 1982 [DIRS 112060]); Wilson and Bruton 1989 [DIRS 137607], Section 3.1 and Table 3). PuO_2 was suppressed to be consistent with the material degradation and release model (BSC 2006 [DIRS 176911]) and with *Dissolved Concentration Limits of Radioactive Elements* (BSC 2005 [DIRS 174566], Section 6.5.3.1), which uses PuO_2·(hyd,aged) as the controlling solid for TSPA.

Table 6-8. Minerals Suppressed in EQ6 Source Term Calculations from BSC 2006 [DIRS 176911] (Continued)

Mineral	Formula	Justification
PuOF	PuOF	The conditions required for synthesis of this compound preclude its formation in the repository. Specifically, it forms through atomic hydrogen reduction of PuF_3 (Cleveland 1979 [DIRS 105754], pp. 331 and 332), which is unlikely in the repository because PuF_3 will not be present.
$PuPO_4$(s,hyd)	$PuPO_4$(s,hyd)	The conditions required for synthesis of this compound preclude its formation in the repository. Specifically, its precipitation is possible at a temperature of 950°C (Cleveland 1979 [DIRS 105754], pp. 436 to 439), which is well above repository conditions.
Pyrophyllite	$Al_2Si_4O_{10}(OH)_2$	Pyrophyllite forms in metamorphic terranes (Gaines et al. 1997 [DIRS 172360], p. 1440), which precludes formation under waste package conditions.
Quartz	SiO_2	Forms of SiO_2 that are less ordered than quartz are more likely to form as primary sedimentary minerals at low temperatures (such as chalcedony) (Klein and Hurlbut 1985 [DIRS 105907], p. 441 and 442). Therefore, the mineral quartz has been suppressed in the EQ6 simulations, allowing the less ordered (higher solubility) varieties of SiO_2 to form. It is possible that a high surface area of quartz minerals in the crushed tuff in the invert could lead to precipitation of quartz. However, suppressing quartz in the invert calculations is still appropriate because the surface area of the crushed tuff in the invert is not significantly greater than the tuff in the host rock because tuffs are composed of fine grained minerals as explained in Section 6.4.3.1.
Spinel-Co	$CoCo_2O_4$	This mineral occurs in magmatic deposits at temperatures above 300°C, which precludes formation in the repository (Gaines et al. 1997 [DIRS 172360], p. 303).
Talc	$Mg_3Si_4O_{10}(OH)_2$	Talc is characteristically associated with low-grade metamorphic rock and hydrothermal alteration of ultrabasic rocks (Kerr 1977 [DIRS 161606], p. 450), which is unlike repository conditions.
Tremolite	$Ca_2Mg_5Si_8O_{22}(OH)_2$	The amphiboles are high pressure/temperature minerals (i.e., >>300°C and 1 atm) that occur in igneous rocks (Huang 1995 [DIRS 169305], p. 1013).
Tridymite	SiO_2	Tridymite exists as both α and β types. The low-temperature α-tridymite forms only from preexisting β-tridymite, which forms in the temperature range of 870°C to 1,470°C (Roberts et al. 1990 [DIRS 107105], pp. 881 to 882).
$(UO_2)_3(PO_4)_2$:$6H_2O$	$(UO_2)_3(PO_4)_2$:$6H_2O$	$(UO_2)_3(PO_4)_2$:$6H_2O$ has been suppressed in favor of $(UO_2)_3(PO_4)_2$:$4H_2O$, which has been allowed to form since uranyl phosphates are associated with a wide range of weathered uranium deposits (Finch and Murakami 1999 [DIRS 145442]). Few uranyl phosphates are included in the EQ6 database.
Whitlockite	$Ca_3(PO_4)_2$	Based on whitlockite's occurrence in granite pegmatites with minerals such as siderite, quartz, and apatite (Gaines et al. 1997 [DIRS 172360], p. 715), it is unlikely that whitlockite will form under repository conditions.
Zircon	$ZrSiO_4$	High pressure/temperature mineral (i.e., >>300°C and 1 atm). Found in sedimentary deposits as a detrital mineral (Roberts et al. 1990 [DIRS 107105], p. 975).
Zoisite	$Ca_2Al_3Si_3O_{12}OH$	Zoisite primarily occurs in metamorphic rocks, and has been reported in quartz veins, pegmatites, and ecogite (Gaines et al. 1997 [DIRS 172360], p. 1205); therefore, it would not form under repository conditions.
$ZnCr_2O_4$	$ZnCr_2O_4$	$ZnCr_2O_4$, known as zincochromite, occurs with quartz and amorphous Cr-V-Fe oxides and hydroxides (Gaines et al. 1997 [DIRS 172360], p. 303). Like chromite, its temperature of formation (>500°C) is typically well above repository conditions.

Source: BSC 2006 [DIRS 176911], Table 6-9.

6.4.5 Use of PHREEQC and Post-Processing Macros for Geochemical Modeling

The following is a description of the use of geochemical modeling software PHREEQC v2.3 and the post-processing macros GetEqPhases v1.0, PHREEQC_Post v1.1, Acc_with_decay v1.2, and MinAcc v. 1.0. Figure 3-1 gives a flow chart overview of software usage for the geochemistry modeling portion.

6.4.5.1 Use of PHREEQC V2.3

The YMP qualified geochemical code PHREEQC V2.3 is a reaction-path and transport code (as described in Section 3) for tracing constituent accumulation. In this report, PHREEQC was used to estimate the concentrations remaining in the aqueous solution and the composition of the precipitated (accumulated) solids. PHREEQC handles advective transport by moving aqueous solutions from one cell to the next, allowing the contents of each cell to react with the solids and surface features present in the cell. This model uses 60 cells for 1 L/yr flow and 10 cells for 1,000 L/yr flow, which represents an idealized flow system through the invert or through the fractures. Diffusion and dispersion are handled by mixing the contents of cells in proportion to the diffusion (or dispersion) parameters. Precipitation and accumulation occur because the waste package aqueous effluent encounters chemical conditions different from those present inside the waste package, such as different pH. Of particular interest is the mixing of the waste package effluent water (source term) with resident natural waters. In the PHREEQC simulations in this report, the natural waters were either basalt water for the Igneous Case or pore water from SD-9 for the Seismic Case. The net result of mixing those two water types is mineral precipitation.

In the PHREEQC simulations within each cell, a 10% mixing ratio is implemented, where mixing ratio is defined as the mass fraction of added water to a cell relative to the final mass of water in that same cell. For example, adding 0.1 kg of mixing water in cell *n* to 0.9 kg of the water equilibrated in cell *n-1* to yield the 1 kg of water modeled in PHREEQC mimics the advection-mixing mechanism and corresponds to a mixing ratio of 10%. Mixing ratios of 5% and 20% were also examined in an earlier calculation and found to have a weak effect on the total accumulation estimates (BSC 2001 [DIRS 155771], Figure 6-7). The dilution factor is defined as the ratio of the total flux through the system to the flux going through the waste package (*seeprate*/*WPflux*). For a given dilution factor there corresponds a given number, *n*, of cells in the invert or the fracture system according to the following equation:

$$\left(1/\left(1-MixingRatio\right)\right)^{n} = \frac{seeprate}{WPflux} \qquad \text{(Eq. 6.4.5-1)}$$

Equation 6.4.5-1 was developed by noting that only 90% (i.e., 1-*MixingRatio*) of the water is transferred from one cell to the next to keep the self-imposed constraint of dealing with only one kg of water. In cell 1 (n=1), the true amount of water is 1/(1-*MixingRatio*) or 1/0.9 = 1.11 kg; in cell 2, the true amount of water impacted is $(1/0.9)^2$ = 1.23 kg, and so forth.

A PHREEQC run is executed for each of these user-selected EQ6 output times and a yearly accumulation rate valid only for that particular time is extracted. The EQ6 source terms (inputs) are described in Section 6.2.2. The accumulation rates are post-processed using several macros to get total accumulation at 10,000 years. For each EQ6 source term, up to 10 PHREEQC

simulations were performed, compared to the hundreds of EQ6 output times provided by EQ6. There are two reasons for such a treatment. First, EQ6 simulations deal with only one cell (the waste package + interior) while PHREEQC simulations have typically many cells with water advecting from one to the next. Second, the dynamic time-stepping that allows EQ6 to modulate the numerical time step as a function of the expected complexity of the aqueous system is not present in PHREEQC. PHREEQC uses a constant user-supplied time step. To mimic an EQ6 simulation, a single PHREEQC run would have to use a very small time step. This would preclude any PHREEQC simulation in a reasonable length of time, and therefore this report uses selected timesteps from the EQ6 simulations. Thus, PHREEQC simulations are carried out only for selected EQ6 output times. One PHREEQC simulation corresponds to one EQ6 selected output time, bounding the period leading to actinide mineral accumulation (i.e., with U and Pu concentrations high enough to sponsor actinide precipitation). Each EQ6 selected output time yields an accumulation valid only around that time. The EQ6 simulations were post-processed via ASPRIN v1.0 (Section 3.1.10). ASPRIN results give the enrichment fraction (ratio of ^{235}U to total U in solution and/or ratio of ^{239}Pu to total Pu in solution) versus time. ASPRIN also produces U and Pu concentration curves. EQ6 times were based on the U and Pu curves as shown in Figures 6-4 through 6-9.

Unlike EQ6, which automatically precipitates saturated phases, PHREEQC requires the user to specify them. This can be a challenging task in an unknown complex system. The minerals are given in the "EQUILIBRIUM_PHASES" field of the PHREEQC input file (Appendix A). Table 6-7 displays the list of minerals that were used for both of the EQ6 and PHREEQC simulations. Also, Table 6-8 contains the list of suppressed minerals, which were suppressed in both the EQ6 and PHREEQC simulations. In PHREEQC, there is not a suppressed mineral list in the input file; these minerals are simply left off the "EQUILIBRIUM_PHASES" field of the PHREEQC input file. To be consistent with the source term input, the PHREEQC input files did not include any of the minerals listed in Table 6-8, even if the SI was greater than 0.01. The rationales for inclusion or exclusion of the minerals from the PHREEQC and EQ6 calculations are included in each of the tables.

6.4.5.2 GetEQPhases

In order to determine which minerals will precipitate, a preliminary or screening PHREEQC run is done to obtain the saturation indices of all minerals that could precipitate. No minerals are given in the "EQUILIBRIUM_PHASES" field on the input file, thus no minerals are predicted to form and no minerals are suppressed. The saturation index gives the potential that a mineral will precipitate. A saturation index of 0 or more indicates that a mineral may form. The limited PHREEQC output files are post-processed via macro GetEqPhases V1.0 (Section 3.1.5). GetEqPhases scans the PHREEQC output files and extracts the saturation indices of minerals. When using GetEqPhases you list the output file names from PHREEQC simulations, indicate a list of suppressed minerals (same as the list in Table 6-8) and the SI cutoff. To limit the number of minerals to be placed on the "EQUILIBRIUM_PHASES" section of the input file, a SI cutoff of −0.01 has been chosen. Since only minerals with an SI of 0 or above can precipitate, a cutoff of −0.01 is a conservative number to choose. GetEqPhases produces a list minerals that have an SI of −0.01 or greater with the suppressed minerals missing, and this is the list used for the "EQUILIBRIUM_PHASES" section of the succeeding input file. Since all of the times chosen from the EQ6 simulations were post-processed via GetEqPhases at the same time, the same

minerals are used for the list of minerals under "EQUILIBRIUM_PHASES" for a particular source term.

6.4.5.3 Use of PHREEQC_Post V1.1

Each EQ6 selected output time yields an annual accumulation. The yearly accumulation at any given time is then obtained by linearly interpolating between two known yearly accumulations. The output files from PHREEQC were then post-processed via YMP qualified macro PHREEQC_Post (see Section 3.1.4). The Excel macro PHREEQC_Post computes the annual accumulation rate to be used in subsequent Excel macros Acc_with_decay and MinAcc. PHREEQC_Post post-processes the PHREEQC outputs and extracts actinide mineral yearly accumulation rates. The total accumulation is then calculated by summing all the yearly accumulation through time. The summation of the total U and Pu accumulations is completed via the macro Acc_with_decay. Acc_with_decay gives results in total U and Pu accumulation, as well as total ^{235}Uand ^{239}Pu accumulated using all PHREEQC times used for a source term. PHREEQC_Post produces a summary file, which gives the total U and Pu for each cell (60 for 1 L/yr simulations and 10 for 1,000 L/yr simulations), which is used as input to Acc_with_decay.

6.4.5.4 Use of Acc_with_decay V1.2

The macro Acc_with_decay V1.2 (see Section 3.1.6) gives results in total U and Pu accumulation, as well as total ^{235}U and ^{239}Pu accumulated using all PHREEQC times for a source term. PHREEQC_Post produces a summary file that gives the total U and Pu for each cell (60 for 1 L/yr and 10 for 1,000 L/yr), which is used as input into Acc_with_decay. Acc_with_decay applies decay to plutonium and uranium and variable enrichment to uranium to postprocess the PHREEQC output. The geochemical code PHREEQC gives annual accumulations of plutonium and uranium at selected times. All the plutonium is assumed to be ^{239}Pu while the uranium is made up of isotopes ^{234}U, ^{235}U, ^{236}U, and ^{238}U. The ratio of ^{235}U to the total uranium is called the enrichment fraction or enrichment. The enrichment varies with time and is provided as an input to Acc_with _decay and comes from the ASPIRIN output file, as described in the discussion of the source terms in Section 6.2.2. In addition, ^{239}Pu decays into ^{235}U with a half-life of 24,110 years (Parrington et al. 1996 [DIRS 103896], p. 48). The half-lives of the uranium isotopes are high enough for the assumption of no decay to be valid in the time span considered (20,000 years). The routine applies the decay equation to the ^{239}Pu and decays Pu continuously but adds the newly accumulated radionuclides. The input data for the Acc_with_decay macro consists of the summary file of outputs from PHREEQC_Post, for both elements U and Pu, for each cell for each PHREEQC run time, and of the ^{235}U enrichment data from the ASPRIN output file. The resulting output gives the moles of U, moles of ^{235}U, and moles of ^{239}Pu that accumulated in each cell; it then also gives the totals when each cell is added. The total accumulation of U, ^{235}U, and ^{239}Pu is presented in Table 6-15 for each source term.

6.4.5.5 Use of MinAcc v1.0

The macro MinAcc V1.0 (see Section 3.1.7) computes the volume of mineral accumulation by post-processing the geochemical code PHREEQC outputs. MinAcc is part of the suite of pre- and post-processing codes built around PHREEQC. The MinAcc macro integrates yearly accumulation through time assuming that the yearly rate varies linearly between two EQ6 output

times. MinAcc computes accumulation for all minerals while Acc_with_decay deals only with actinides but also takes into account decay. MinAcc contains calls to external codes written in the C programming language: GetMolVol.exe and SpeciesName.exe. GetMolVol.exe extracts molar volume information from the EQ6 thermodynamic database and SpeciesName.exe checks that all minerals listed in the Excel macro are present in the "EQUILIBRIUM PHASES" block of the PHREEQC input files. The output from MinAcc gives yearly accumulation of all minerals at selected times. To compute accumulation over a time range, the annual mineral accumulation is assumed to vary linearly. In using the MinAcc macro, the selected time (cell B35) gives the user the option to calculate accumulation results at any time; for the source terms in this report, 10,000 years was chosen. For accurate results, the minerals entered into the macro should correspond exactly to the list of minerals present in the "EQUIBRIUM_PHASES" block of the PHREEQC input files. The output provides the total mineral accumulation in the system at a given point in time (10,000 years) divided by the volume of water in the system (that is constant in time). In some cases (FFTFIG2adEhdec and CSFlux9), the volume of minerals calculated by MinAcc was scaled down so that the total volume of minerals did not exceed the void space available in the invert. The main point of this is to understand how open spaces can be plugged by mineral accumulation. The total volume of accumulation for each source term at 10,000 years is presented in Tables 6-9 through 6-14.

6.4.5.6 Results—Accumulation of Minerals

Deposition of minerals occurs over limited ranges of concentration. Because non-U/Pu minerals also take space in the invert, it is important to check the volume of all precipitated minerals. Table 6-10 through Table 6-15 tabulate the average volumes of minerals in the invert, including uranium and plutonium minerals. The post-processing macro Min_Acc, the tab Sorted Minerals, columns E & F for each source term give the volume of each mineral formed per 1 kg of solution in the invert or fractures. The equivalent volume of the invert that contains 1 kg of solution was calculated using invert properties used in the PHREEQC runs (Section 6.4.3.2) of 31 % porosity and 60% saturation: volume of invert with 1 kg water = (1 kg water) × (1 L water)/(kg water) ÷ (0.31 × 0.60) × 1000 cm^3/liter = 5376 cm^3. The maximum volume of minerals that could accumulate is equivalent to the unsaturated void volume, (100-60)% × 0.31 × 5376 = 667 cm^3. For two cases (FFTFIG2adEhdec and CSFlux9), the volume of minerals calculated by MinAcc had to be scaled down so that the total volumes did not exceed the capacity of 667 cm^3. The results indicate that a significant amount of non-fissile minerals form along with the uranium and plutonium minerals.

Table 6-9. Average Volume of Minerals Accumulated at 10,000 Years for Source Term TMI_IG1, Igneous Scenario, Flow at 1 L/yr

Type of Mineral	Mineral Name	Volume (cm^3/kg of solution) at 10,000 Years
Uranium Minerals	Boltwoodite-Na	35.93
Plutonium Minerals	N/A	N/A
Other Minerals	Celadonite	46.38
	Chabazite	8.82
	Dawsonite	2.70
	Erionite	27.04
	Fluorapatite	0.87
	Gibbsite	1.68
	Hydroxylapatite	0.38
	Magnesite	63.07
	$Ni_3(PO_4)_2$	0.02
	Nontronite-Na	0.81
	Powellite	0.93
	Saponite-Na	11.72
	Trevorite	0.03
	TOTAL:	200.4

Source: Output DTN: MO0609SPAINOUT.002, folders : TMI_IG1/ TMI_IG1_MinAcc, file: *tmi_Vol_Summary.xls*, tab: Sorted Minerals, columns E and F.

NOTE: Only volumes greater than or equal to 0.01 volume (cm^3/kg of solution) for non-uranium and non-plutonium minerals are presented.

Table 6-10. Average Volume of Minerals Accumulated at 10,000 Years for Source Term TMI_IG2, Igneous Scenario, Flow at 1,000 L/yr

Type of Mineral	Mineral Name	Volume (cm^3/kg of solution) at 10,000 Years
Uranium Minerals	None	0
Plutonium Minerals	N/A	N/A
Other Minerals	Chabazite	490.46
	Gibbsite	2.50
	Hydroxylapatite	3.20
	Laumontite	124.76
	Nontronite-Na	1.57
	Trevorite	0.01
	TOTAL:	622.5

Source: Output DTN: MO0609SPAINOUT.002, folders: TMI_IG2/ TMI_IG2_MinAcc, file: *tmi2_Vol_Summary.xls*, tab: Sorted Minerals, columns E and F.

NOTE: Only volumes greater than or equal to 0.01 volume (cm/kg of solution) for non-uranium and non-plutonium minerals are presented.

Table 6-11. Average Volume of Minerals Accumulated at 10,000 Years for Source Term FFTFIG1adEhdec, Igneous Scenario, Flow at 1 L/yr

Type of Mineral	Mineral Name	Volume (cm^3/kg of solution) at 10,000 Years
Uranium Minerals	Boltwoodite-Na	177.94
	$(UO_2)_3(PO_4)_2$:$4H_2O$	37.54
Plutonium Minerals	None	0
Other Minerals	Alunite	47.43
	Chalcedony	30.21
	Powellite	6.42
	Celadonite	2.15
	Hydroxylapatite	0.58
	Nontronite-Na	0.38
	$Fe_2(MoO_4)_3$	0.30
	Kaolinite	0.22
	Goethite	0.07
	TOTAL:	303.24

Source: Output DTN: MO0609SPAINOUT.002, Folder: FFTFIG1adEhdec/FFTF1-MinAcc, file: *fftfG1_Vol_Summary.xls*, tab: Sorted Minerals, columns E and F.

NOTE: Only volumes greater than or equal to 0.01 Volume (cm/kg of solution) for non-uranium and non-plutonium minerals are presented.

Table 6-12. Average Volume of Minerals Accumulated at 10,000 Years for Source Term FFTFIG2adEhdec, Igneous Scenario, Flow at 1,000 L/yr

Type of Mineral	Mineral Name	Volume (cm^3/kg of solution) at 10,000 Years
Uranium Minerals	None	0
Plutonium Minerals	None	0
Other Minerals	Dawsonite	307.26
	Analcime	298.57
	Kaolinite	57.56
	Celadonite	2.19
	Erionite	1.33
	Montmorillonite-Na	0.09
	TOTAL:	667

Source: Output DTN: MO0609SPAINOUT.002, folders: FFTFIG2adEhdec/FFTF2-Min_Acc, file: *fftfG2_Vol_Summary.xls*, tab: Sorted Minerals, columns E and F.

NOTE: Only volumes greater than or equal to 0.01 volume (cm^3/kg of solution) for non-uranium and non-plutonium minerals are presented.

Table 6-13. Average Volume of Minerals Accumulated at 10,000 Years for Source Term CDSPIG2, Igneous Scenario, Flow at 1,000 L/yr

Type of Mineral	Mineral Name	Volume (cm^3/kg of solution) at 10,000 Years
Uranium Minerals	None	0
Plutonium Minerals	N/A	N/A
Other Minerals	Gibbsite	131.85
	Hydroxylapatite	70.75
	Laumontite	2.88
	Nontronite-Na	0.01
	Trevorite	0.39
	Zn_2SiO_4	6.58
	TOTAL:	212.5

Source: Output DTN: MO0609SPAINOUT.002, folders: CDSPIG/CDSPIG-MinAcc, file: *CDSPIG_Vol_Summary.xls*, tab: Sorted Minerals, columns E and F.

NOTE: Only volumes greater than or equal to 0.01 volume (cm^3/kg of solution) for non-uranium and non-plutonium minerals are presented

Table 6-14. Average Volume of Minerals Accumulated at 10,000 Years for Source Term CSFlux9, Igneous Scenario, Flow at 1,000 L/yr

Type of Mineral	Mineral Name	Volume (cm^3/kg of solution) at 10,000 Years
Uranium Minerals	Uranophane(alpha)	662.3
Plutonium Minerals	N/A	N/A
Other Minerals	Laumontite	4.55
	Zn_2SiO_4	0.15
	Co_2SiO_4	0.02
	TOTAL:	667

Source: Output DTN: MO0609SPAINOUT.002, folders: CSFlux9/CSFlux9_Min_Acc, file: *CSFlux9_Vol_Summary.xls*, tab: Sorted Minerals, columns E and F.

NOTE: Only volumes greater than or equal to 0.01 volume (cm^3/kg of solution) for non-uranium and non-plutonium minerals are presented.

Table 6-15 contains the moles of U and Pu released from the waste package, accumulation within the crushed tuff of the invert or the host rock, and adsorbed onto the tuff.

Table 6-15. Uranium and Plutonium Flushed from Various Waste Packages, Accumulated and Adsorbed at Approximately 10,000 Years after Waste Package Breach

Source Term	Waste Package Type, Scenario, and Conditions	^{239}Pu Moles			Total U Moles			^{235}U Moles		
		Flushed from Waste Package	Accum-ulated	Adsorbed	Flushed from Waste Package	Accum-ulated	Adsorbed	Flushed from Waste Package	Accum-ulated	Adsorbed
TMI_IG1	TMI Igneous 1 L/yr	N/A	N/A	N/A	1.15E+03	14.5	1.12E+02	3.04E+01	0.4	2.97
TMI_IG2	TMI Igneous 1,000 L/yr	N/A	N/A	N/A	1.97E+03	0.0	9.45E-04	5.64E+01	0.0	8.36E-06
CDSPIG2	N-Reactor Igneous 1,000 L/yr	N/A	N/A	N/A	4.24E+04	0.0	4.59E-01	5.38E+02	0.0	5.83E-03
FFTFIG1adEhdec	FFTF Igneous 1 L/yr Adjusted Eh Pu decay included	0.58	4.01E-03	2.25E-02	3.04E+02	31.17	3.56E+01	1.99E+01	2.13	2.26
FFTFIG2adEhdec	FFTF Igneous 1,000 L/yr Adjusted Eh Pu decay included	4.83	0.0	5.62E-05	8.23E+02	0.0	1.37E-03	5.57E+01	0.0	4.37E-04

Table 6-15. Uranium and Plutonium Flushed from Various Waste Packages, Accumulated and Adsorbed at Approximately 10,000 Years after Waste Package Breach (Continued)

Source Term	Waste Package Type, Scenario, and Conditions	^{239}Pu Moles			Total U Moles			^{235}U Moles		
		Flushed from Waste Package	Accum-ulated	Adsorbed	Flushed from Waste Package	Accum-ulated	Adsorbed	Flushed from Waste Package	Accum-ulated	Adsorbed
CSFlux9	CSNF Seismic 1,000 L/yr Adjusted Eh	0.00	0.00	5.11E-07	1.15E+03	942.03	7.51E-04	1.27E+01	10.47	8.34E-06

Source: Output DTN: MO0609SPAINOUT.002.

NOTE: For each source term:

For the mole accumulated, under the folder for each source term, see folder *Acc_with_decay* and file *Acc_with_decay.xls* for total-U moles, ^{235}Umoles, and ^{239}Pu moles.

For the moles adsorbed, see file *adsoprtion_calc.xls*; use tab for each source term.

For the moles flushed from the waste package, under the folder for each source term, see the folder labeled “source_term” and the following files: *TMI1_U_loss.xls*, *TMI2_U_loss.xls*, *CDSPIG_U_loss.xls*, *FFTFIG1_U_Pu_loss.xls*, *FFTFIG2_U_Pu_loss.xls*, and *CSFlux9_U_Pu_loss.xls*.

6.4.6 Flow and Transport in the Invert Using TOUGHREACT

For criticality calculations, the extent of mixing and the location of the accumulation of fissile material within the invert is important. Two bounding cases are (1) complete mixing within the invert and accumulation is spread uniformly within the invert or (2) no mixing within the invert and all mixing occurs at the bottom of the invert, with accumulation along the boundary of the invert and the host rock. (Another possibility, which is discounted because it results in no criticality concern in the invert, is no mixing within the invert and the two aqueous streams flow through the invert and directly into the host rock without any mixing or accumulation.) Rather than assuming the bounding cases in the criticality calculations, a modeling effort was performed to infer the extent of mixing within the invert.

This section describes numerical modeling of mixing of flows in the invert using the reactive transport code TOUGHREACT. The objective of this modeling was to show whether it is possible for radionuclides released from a breached waste package to accumulate in the invert in such a way as to become critical. Figure 6-10 is a diagram of the system, showing the modeling grid. The approach taken was to simulate injection of water at two locations in the top of the invert: (1) directly beneath the waste package, where releases would occur, and (2) at a distance from the center of the invert where seepage water diverted by the remnants of the drip shield would enter the invert. (For the seismic and igneous scenarios, in which the seepage water contacts the waste package, the drip shield does not provide a barrier to flow.) Conservative tracers in the water at each injection point show where those waters move, and the concentration of the tracers indicates how releases from the waste package would be diluted and dispersed throughout the invert and where mixing of the two waters occurs. The mechanisms that impact the extent of mixing within the invert include random solute movement caused by pore water velocity variations (in both magnitude and direction) and molecular diffusion. Laboratory experiments on longitudinal mixing in unsaturated flow resulting from hydrodynamic dispersion and molecular diffusion are presented in the study by Toride et al. (2003 [DIRS 176906]).

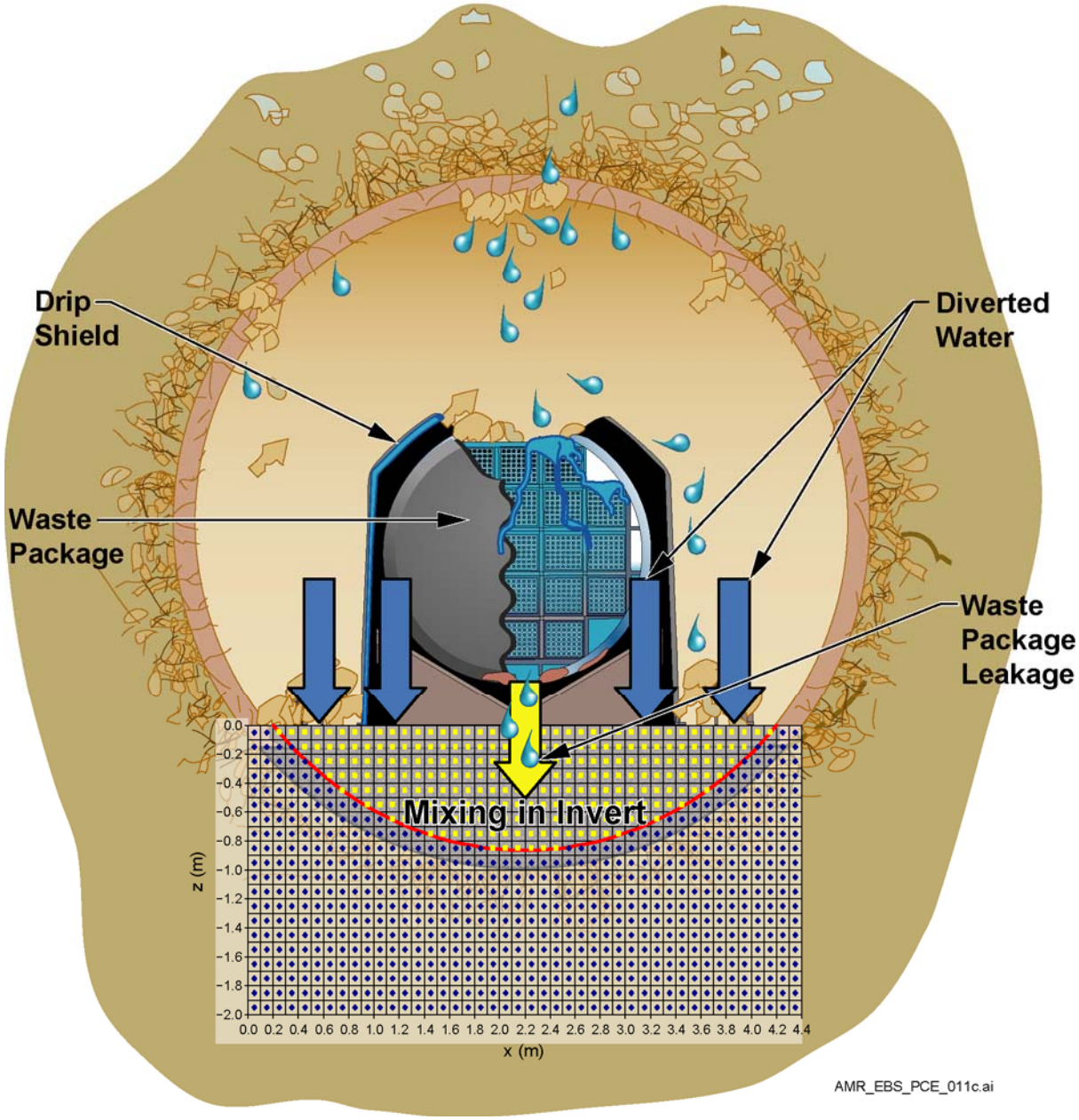

Figure 6-10. System Modeled for Mixing in the Invert

Two problems were modeled: (1) Validation Section 7.2.5 contains a validation case using a simple rectilinear geometry simulating a portion of the invert; the simple geometry and homogeneous properties allowed validation of the numerical model by comparison with an analytical model. (2) This section contains a set of six base case simulations using a larger region consisting of the invert as well as a portion of the unsaturated zone (UZ) host rock to the side of and below the invert, with the interface between the invert and host rock being curved to represent the drift wall; this problem allowed for more realistic treatment of invert geometry and the effects of host rock proximity and hydrologic behavior on invert flow behavior.

The region modeled in both problems was a two-dimensional vertical cross section of the invert. In effect, the waste package effluent water and the diverted water were injected as line sources, rather than as point sources. This simplified geometry (line sources) generates a larger mixing zone within the invert than would occur if point sources had been modeled, and therefore is conservative for criticality. (See Section 6.4.7.4 for additional discussion.)

In both problems, the invert was modeled as a single continuum. In the base case, the UZ host rock was modeled as a dual continuum consisting of the geologic formation Tptpll (UZ model layer tsw35) tuff matrix and fractures. The problems were both essentially multiphase fluid flow and solute transport simulations; using tracers that were as inert as possible intentionally minimized reactive geochemistry. The thermodynamic database used in the simulations, a file 'thermk1.01.dat,' which was obtained from DTN: LB0302DSCPTHCS.001 [DIRS 164744], was developed for TOUGHREACT V3.0 and used in *Drift-Scale THC Seepage Model* (BSC 2004 [DIRS 172862]). The problems were run isothermally at 25°C and atmospheric pressure to simulate conditions at late times, well after the thermal period, when waste package breaches will be most likely to have occurred. Although all simulations were transient, they were run to very late times so as to achieve steady state conditions.

6.4.6.1 Base Case Simulations Using TOUGHREACT

The base case involves simulations of flow and transport in the invert using a grid that reflects the actual geometry of the invert and a portion of the UZ host rock immediately adjacent to the invert. Calculations were done for three cases that represent various amounts of waste package and diverted flow. The flow conditions are summarized in Table 6-16. The flow rates through the waste package (1 and 1,000 L/yr) were the values used in the EQ6 simulations taken from the material degradation and release model as shown in Table 4-4. The diverted water flow values were chosen based on what would be considered reasonable values, given the flow through the waste package and given the assumed drift seepage, as presented in Figures 5-1 and 5-2. For Case 1 (igneous, 1 L/yr), the diverted source flow rates were set at 200 L/yr to represent the case with the lowest seepage flux in Figure 5-2, since the flow through the waste package was so low (1 L/yr). For Case 2 (seismic, 1,000 L/yr), the diverted source flow rate was set at 200 L/yr to represent the highest seepage rate in Figure 5-1 for the combined flows (1,200 L/yr). For Case 3 (igneous, 1,000 L/yr), the diverted source flow rate was set at 400 L/yr to represent the highest total seepage rate in Figure 5-2.

For each of the three cases, two types of invert hydrological properties are specified, representing well-sorted and poorly sorted granular material. Invert properties are summarized in Table 6-17. The well-sorted properties come from Table 4-16, with the exception of the residual saturation for capillary pressure, which was changed slightly from the residual saturation for relative permeability to avoid numerical problems, as instructed in the TOUGH2 user's manual (Pruess et al. 1999 [DIRS 160778], p. 189). The poorly sorted properties are calculated in Appendix G using values of total porosity and permeability in Table 4-15 and matrix porosity and residual saturation from Table 6-27. The invert is modeled as a single continuum, and the UZ is modeled as a dual continuum consisting of fractures and tuff matrix.

The model grid represents a vertical cross section of the invert and UZ. Figure 6-11 shows the numerical grid, with invert grid cells shown in yellow and the drift wall in red. The grid is a

regular rectangular grid with grid cell spacing of $\Delta x = \Delta z = 0.10$ m. The origin (0, 0) in the grid is the upper left corner of the outer boundaries of the upper left grid cell, whose center is at $(x, z) = (0.05, -0.05)$.

The waste package source is modeled as 1.0 molal Na^+, and the diverted source is modeled as 1.0 molal K^+. In all cases, the waste package source is located nominally at the top center of the invert, at $x = 2.15$ m in the numerical grid. The top surface of the invert is 4 m across, extending from $x = 0.20$ m to $x = 4.20$ m (these locations are at the interfaces between grid cells), so the invert center is at $x = 2.20$ m. Since water injection is modeled as occurring at a grid cell center, rather than at the interface between cells, the water is injected at one of the two grid cells closest to the center of the invert. The waste package source flux in Case 1 is nominally 1.0 L/yr (source term Table 4-4) from a 5.1-m-long waste package. To express the source flux in units of mm/yr (as used in model validation Section 7.2.5 and in Appendixes F and G), the width of the source region is specified as 2 cm, to be consistent with the width specified for model validation in Section 7.2.5. A source flux of 1.0 L/yr is equivalent to 9.8 mm/yr. In Cases 2 and 3, the nominal waste package flux is 1,000 L/yr (source term Table 4-4).

In Cases 1 and 2, the diverted source is 1 m to the right of the waste package source at $x = 3.15$ m. The distance between the waste package effluent and the diverted water could range from 0 (both sources at the same location) to greater than 5 meters (sources on opposite ends of the waste package), but a value of 1 m was chosen as roughly equal to the radius of a waste package (Table 4-19). A value of 1 m, a value on the low side of the range, was chosen because the sources need to be fairly close to each other if significant mixing and accumulation is going to occur. In Case 3, the diverted source is specified as 66 mm/yr divided over each side of the waste package and distributed over a region 0.59 m wide on either side of the waste package source, which corresponds to a nominal flow rate of 400 L/yr. In the numerical grid, diverted water in Case 3 is injected into six grid cell center locations on the left side of the invert, ranging from $x = 0.95$ m to 1.45 m, and six grid cell center locations on the right side of the invert, ranging from $x = 2.95$ m to 3.45 m. The total flux for each case is summarized in Table 6-16. The total flow rate for each case is summarized in Table 6-18, where the flow rate in kg/s is converted to mm^2/yr by dividing by the density (1000 kg/m^3) and 1.0 m, which is the length of the segment of a waste package that is modeled.

The TOUGHREACT input file 'GENER' specifies the water injection locations and rates, which are input in units of kg/s.

The input file 'chemical.inp' defines the geochemical system being modeled. Aqueous species included in the model are H_2O, SiO_2 (aq), O_2 (aq), Na^+, K^+, and Cl^-. One gas species, O_2, is included to provide a gas phase, which, in the modeled system, is relatively inert. Minerals that are included in the system and could potentially precipitate include SiO_2 (am), sylvite (KCl), and halite (NaCl). The water initially present contains SiO_2 (aq) at a concentration of 0.001 molal (mol/kg H_2O); O_2 (aq), Na^+, and K^+ each at a concentration of 1.0×10^{-12} molal; and Cl^- at a concentration of 2.0×10^{-12} molal. Na^+ serves as the tracer in the water from the waste package source, where the Na^+ and Cl^- concentrations are 1.0 molal. K^+ is the tracer in the water from the diverted source, where the K^+ and Cl^- concentrations are 1.0 molal.

The input file 'solute.inp' defines solute transport properties, including the locations where the tracer sources are injected (which must agree with the location of water injection locations specified in the 'GENER' file for the simulation to be correct).

The input file 'flow.inp' contains the invert hydrologic properties shown in Table 6-17, hydrologic properties of the UZ rock outside the invert, the initial conditions, and simulation control parameters. The convergence criterion for relative error is set at 10^{-3}. Time steps are automatically reduced whenever the convergence criterion is not met.

Input and output files for all TOUGHREACT simulations in this report are available in output DTN: SN0607T0504506.002.

Hydrodynamic dispersion is not considered; however, numerical dispersion is inherent in the calculations. For the regular rectangular numerical grid that is used, with a grid cell spacing of 10 cm, and with full upstream weighting of mobilities, numerical dispersion is approximately 0.05 m (Oldenburg 2003 [DIRS 176820], p. 244). Molecular diffusion is accounted for, with a diffusion coefficient of 2.3×10^{-9} m^2/s (Mills 1973 [DIRS 133392], Table III).

Table 6-16. Flow Conditions in Base-Case Simulations

Case	Scenario	Waste Package Flux		Diverted Flux		Size of Diverted Flow Source Region (m)
		(mm/yr)	(kg/s)	(mm/yr)	(kg/s)	
1	Igneous	9.8	6.21086×10^{-9}	2000	1.26752×10^{-6}	0.02
2	Seismic	9800	6.21086×10^{-6}	2000	1.26752×10^{-6}	0.02
3	Igneous	9800	6.21086×10^{-6}	66	1.23393×10^{-6}*	0.59**

Source: Hand calculations.

Sample calculation 1: Flux (mm/yr) = flow rate (L/yr) × 1000 (cm^3/L) ÷ 5.1 m ÷2 cm × (1 m/100cm) × (10 mm/cm).

Sample calculation 2: Flux (kg/s) = flow rate (mm/yr) × 10^{-3} (m/mm) × 0.02 m × 1.0 m × 1000 kg/m^3 ÷ 86400 s/day ÷365.25 day/yr.

* Total flux on one side of waste package, divided into 6 grid cells; same flux on the other side of waste package.
** Located on both sides of waste package flux source.

Table 6-17. Base Case Invert Properties

Invert Type	Porosity	Saturated Permeability (m^2)	van Genuchten α_{vG} (m^{-1})	van Genuchten *m*	Residual Saturation (for Rel. Perm.)	Residual Saturation (for Cap. Pres.)
Well-sorted	0.450	1.51×10^{-8}	61.2	0.875	0.0853	0.0850
Poorly sorted	0.224	1.33×10^{-10}	333.2	0.255	0.150	0.145

Source: Well-sorted properties come from Table 4-16, with the exception of the residual saturation for capillary pressure, which was changed slightly from the residual saturation for relative permeability to avoid numerical problems, as instructed in the TOUGH2 user's manual (Pruess et al. 1999 [DIRS 160778], p. 189). The poorly sorted properties are calculated in Appendix G based on properties in Tables 4-15 and 4-18.

Table 6-18. Total Flow Rates in Base-Case Simulations

Case	Total Injected Water Flow	
	(kg/s)	(mm^2/yr)
1	1.27373×10^{-6}	40,196
2	7.47838×10^{-6}	236,000
3	8.67878×10^{-6}	273,881

Source: Output DTN: SN0607T0504506.002.

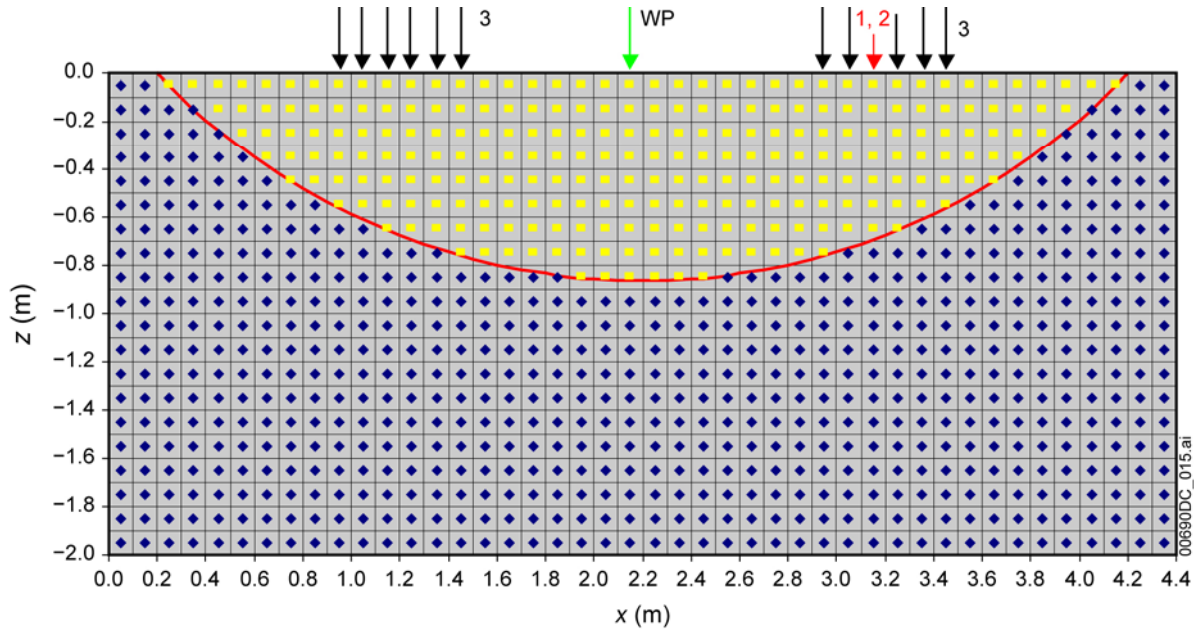

Source: Output DTN: SN0607T0504506.002.

NOTE: Green arrow indicates waste package effluent; red arrow indicates location of diverted water for Cases 1 and 2; black arrows (along with red arrow) indicate location of diverted water for Case 3.

Figure 6-11. Numerical Grid Used in Base Case TOUGHREACT Simulations (*x*-axis relative to edge of grid)

Boundary conditions are the TOUGHREACT default conditions of no flow and no transport at all boundaries. In order to maintain a constant pressure while water is injected into the top of the invert, the grid volume of each grid cell in the bottom row of a cell in the grid is set to a large value, 10^{10} m^3.

6.4.6.2 Grid Generation

For both the base case and the validation case, the grid is created using the MESHMAKER module in TOUGHREACT. To create the dual permeability (fracture and matrix) grid for the UZ portion of the grid, the initial grid created by invoking the MINC processing in

TOUGHREACT. The specific sequence of steps to create the dual permeability grid is as follows:

1. Run TOUGHREACT using input file 'flow.inp' containing the keyword MESHMAKER and the following set of inputs, which creates a 44×20 regular rectangular vertical grid with grid spacing of 10 cm:

```
MESHMAKER
XYZ
   0.0
NX      44   0.10
NY       1   1.00
NZ      20   0.10
```

2. Edit the resulting output file 'MESH' using Excel. First, in the ELEME data block, change the grid cell volume of each cell in the bottom row of cells to 10^{10} m^3. Second, identify all invert cells based on their location within a 5.5-m-diameter circle centered at (x, z) = (2.2 m, 1.8864 m), which is the center of the drift relative to the top center of the invert being designated as (x, z) = (2.2 m, 0.0 m). Third, move all grid cells identified as invert cells to the bottom of the ELEME data block. Fourth, make the grid cell volume of each invert grid cell negative; this tells the MINC process to leave these as single continuum while converting all other grid cells to dual continuum.

3. Rerun TOUGHREACT with the edited MESH file now being considered an input file, and with the input file 'flow.inp' containing the following set of inputs:

```
MESHMAKER
MINC
PART TWO-D     MMALL
  2  1OUT 0.3125
0.015
```

   This tells TOUGHREACT to create a 2-D dual permeability grid in which the fracture volume fraction in each original single continuum grid cell is 0.015. This run creates a new version of the MESH file, called 'MINC.'

4. Edit the ELEME data block in file 'MINC' to change the rock type labeled '2' to 'tswF5' (tsw35 fractures), type '3' to 'tswM5' (tsw35 matrix), and type '1' to 'invu' (upper invert). These rock type labels must agree with the corresponding rock type labels in input file 'flow.inp.' Change the grid cell volume for invert cells back to positive values. Rename the edited file 'MESH,' which is the input file for the flow and transport simulations.

By default, the MINC process results in connections between invert grid cells and UZ fracture cells, but not between invert grid cells and UZ matrix cells. In the UZ, fracture cells are connected to neighboring fracture cells, and matrix cells are connected to neighboring matrix cells. At each grid cell location, the UZ fracture cell is connected to its corresponding UZ matrix cell, but not to any other matrix cells. Similarly, a matrix cell is connected to its corresponding fracture cell, but not to any other fracture cells.

6.4.6.3 Base Case TOUGHREACT Simulations

The base cases for the poorly sorted invert are run in two steps. First, a flow calculation is run without reactive transport. Then, using the flow and saturation field obtained from the flow-only calculation, the reactive transport calculation is run.

The initial temperature and pressure is uniform everywhere at 25°C and 101.325 kPa. Since there is no heat source, the heat transfer calculation is turned off, and the temperature remains constant. The pressure remains nearly constant by virtue of the constant pressure boundary at the bottom of the grid coupled with the relatively high permeability and gas saturation of the UZ fractures and the invert.

For the simulations to complete successfully in a reasonable amount of time, the initial gas saturations need to be close to the final steady-state values. The initial gas saturation is set at 0.75 in the invert, 0.98 in UZ fractures, and 0.12 in UZ matrix. These initial conditions are based on trial simulations in which these saturations were found to result at late times.

The flow calculation is run to 1.0×10^6 years. The flow-and-transport calculation is also run to 1.0×10^6 years. Although the saturations and tracer concentrations continue to change slightly even after 2.0×10^6 years, the changes are so slight that the results are considered to be steady state.

The base cases for the well-sorted invert are also run in two steps, with one difference from the poorly sorted invert cases. The flow calculation, run without reactive transport, uses the results of the corresponding poorly sorted invert flow calculation as the initial condition. This is necessary because the well-sorted invert simulations appear to be much more sensitive to initial conditions than the poorly sorted invert cases. Using the poorly sorted invert flow results as initial conditions, the well-sorted invert cases reliably run to completion, whereas using the more uniform initial conditions as in the poorly-sorted invert cases, they fail to complete. Then, as with the poorly sorted invert cases, using the flow and saturation fields obtained from the flow-only calculation, the reactive transport calculation is run.

6.4.6.4 Base Case Results

Results for the base case calculations include the cumulative flow across the invert-UZ fracture boundary. This boundary is shown as the curved red line in Figure 6-11. In all plots (Figures 6-12 to 6-29), distances are shown relative to the left edge of the invert; thus, $X = 0$ m in Figures 6-12 to 6-29 corresponds to $x = 0.20$ m in Figure 6-11. Cumulative flow is calculated by starting at the left edge of the invert ($x = 0.2$ in Figure 6-11) and summing the flow across the invert-UZ fracture boundary (red line in Figure 6-11), proceeding from left to right. In other words, flows are summed across the width of the invert, as projected onto the surface of the invert, from the left edge of the invert to the right. In some instances, flow across the boundary has a horizontal component as well as a vertical component. Thus, in plots of these results, jumps in flows can be seen where the horizontal and vertical components of flux are accumulated at a single location. In Table 6-19, the two flow components are indicated by duplicate values in the column labeled "Distance from Edge of Invert." The results for the six simulations are shown in Figures 6-12

through 6-17. The numerical results, given in Table 6-19, are used in Section 6.4.7 to calculate the location of the accumulation zone within the invert.

Concentrations of tracers from the waste package (Na^+) and from the diverted flow (K^+) are shown in Figures 6-18 through 6-29. Results are shown as concentration profiles across the width of the invert, X, at each level or depth within the grid, Z (in meters).

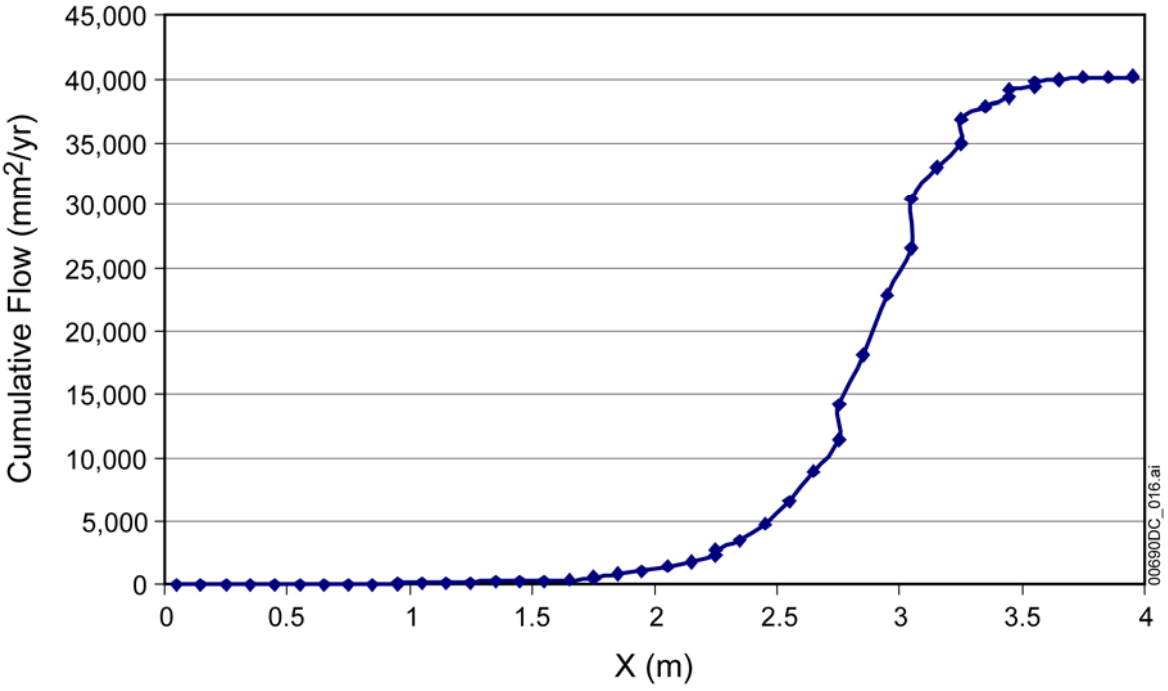

Source: Output DTN: SN0607T0504506.002.

Figure 6-12. Cumulative Water Flow out Bottom of the Invert: Case 1, Poorly Sorted

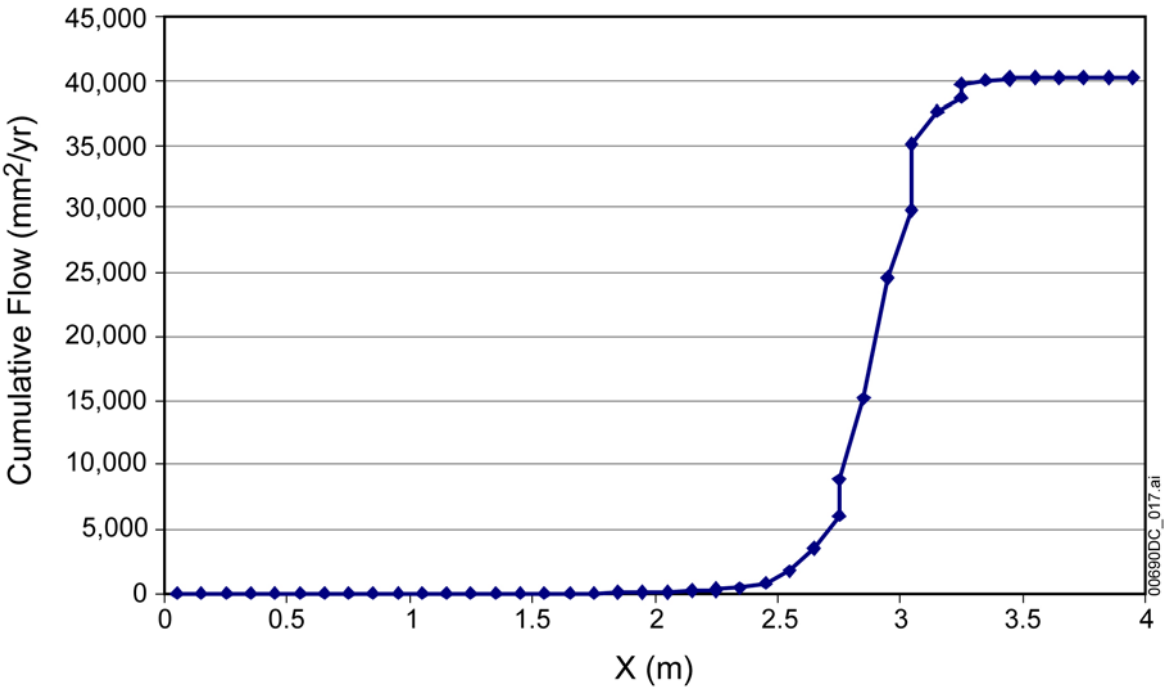

Source: Output DTN: SN0607T0504506.002.

Figure 6-13. Cumulative Water Flow out Bottom of the Invert: Case 1, Well-Sorted

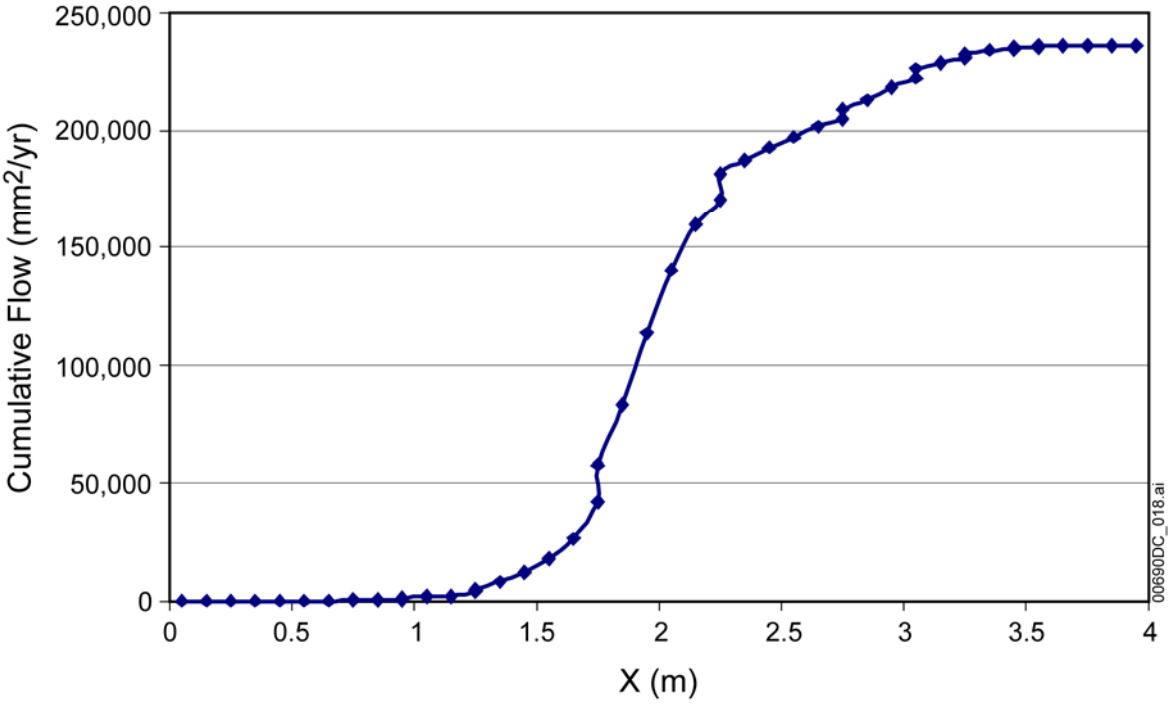

Source: Output DTN: SN0607T0504506.002.

Figure 6-14. Cumulative Water Flow out Bottom of the Invert: Case 2, Poorly Sorted

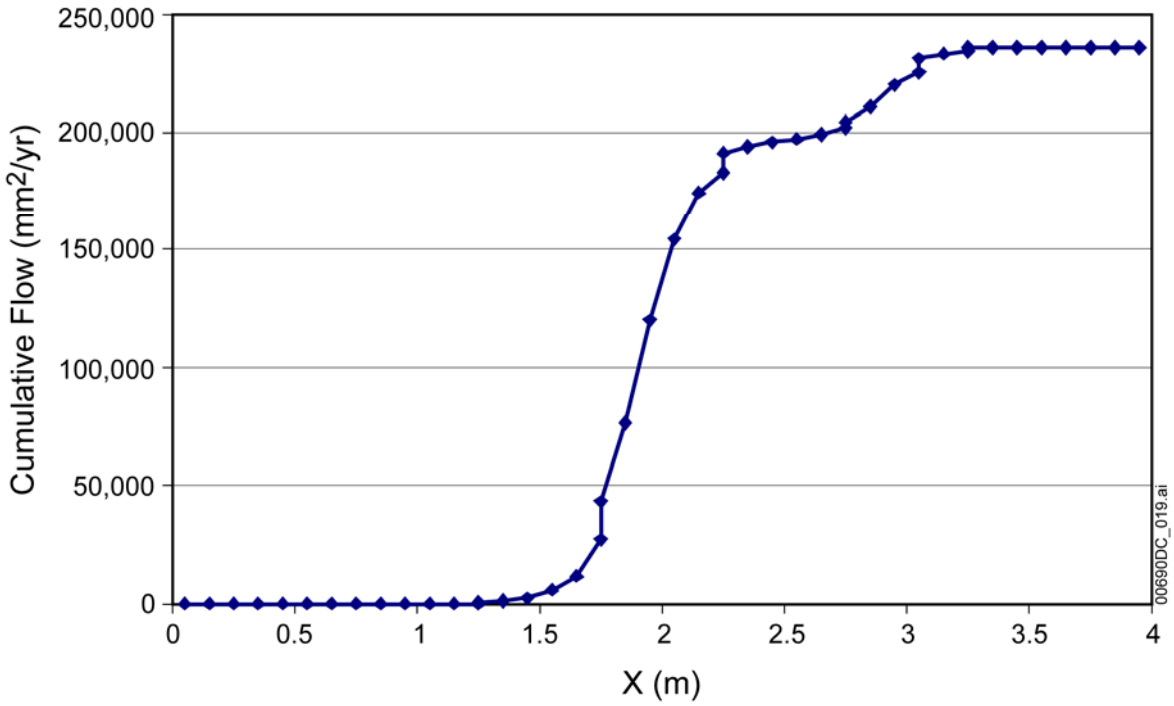

Source: Output DTN: SN0607T0504506.002.

Figure 6-15. Cumulative Water Flow out Bottom of the Invert: Case 2, Well-Sorted

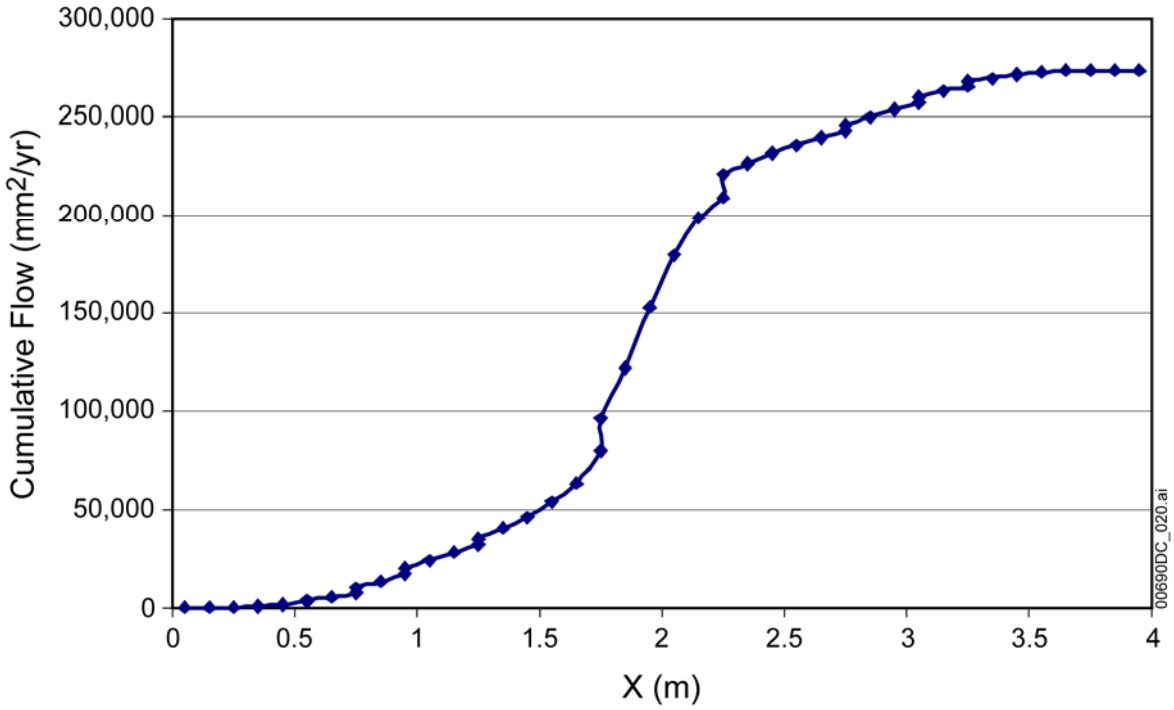

Source: Output DTN: SN0607T0504506.002.

Figure 6-16. Cumulative Water Flow out Bottom of the Invert: Case 3, Poorly Sorted

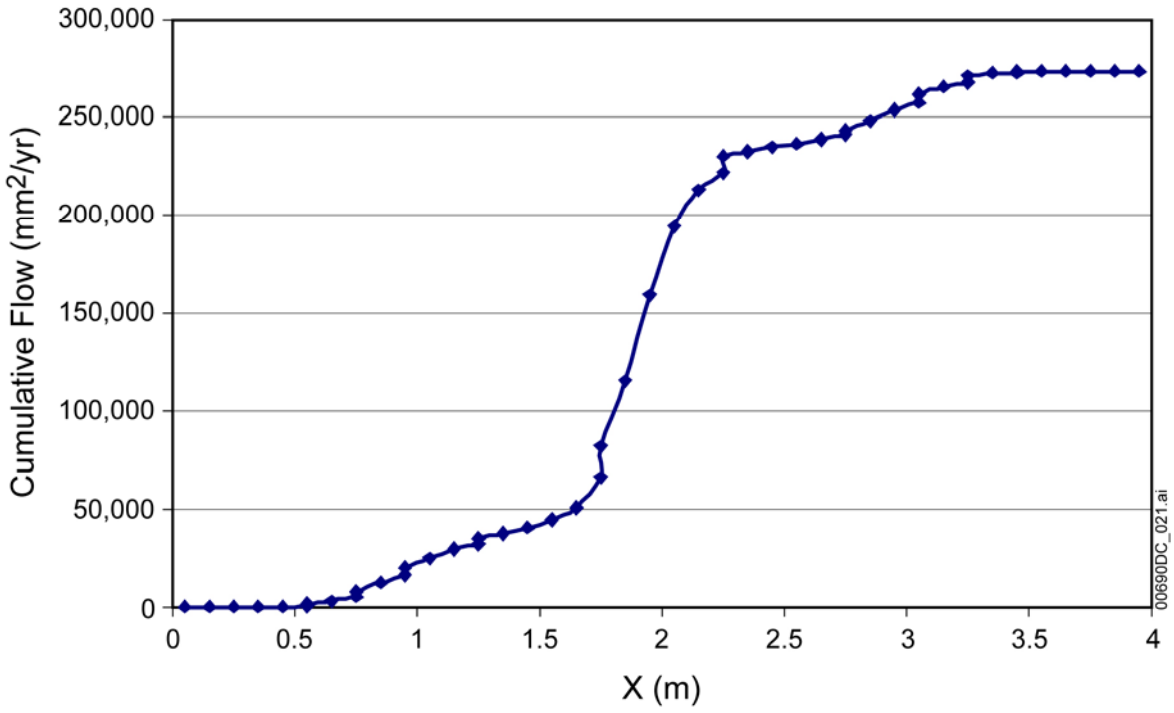

Source: Output DTN: SN0607T0504506.002.

Figure 6-17. Cumulative Water Flow out the Bottom of the Invert: Case 3, Well-Sorted

Table 6-19. Cumulative Flow out the Bottom of the Invert in Base-Case Simulations

Distance from Edge of Invert (m)	Cumulative Flow (mm^2/yr)					
	Case 1: Poorly Sorted	Case 1: Well-Sorted	Case 2: Poorly Sorted	Case 2: Well-Sorted	Case 3: Poorly Sorted	Case 3: Well-Sorted
0.05	1	0	3	0	31	0
0.05	1	0	7	0	61	0
0.15	2	0	11	0	104	0
0.25	3	0	19	0	216	2
0.25	5	0	26	0	327	5
0.35	6	0	39	0	585	26
0.35	8	0	52	0	839	47
0.45	11	0	75	0	1,378	166
0.45	13	0	98	0	1,908	282
0.55	17	0	139	0	3,032	882
0.55	21	0	180	0	4,147	1,462
0.65	25	0	233	0	5,709	2,908
0.75	31	0	339	0	8,068	5,532
0.75	37	0	442	0	10,453	8,157
0.85	45	0	581	0	13,415	12,310
0.95	57	0	896	3	16,756	16,088

Table 6-19. Cumulative Flow out Bottom of the Invert in Base Case Simulations (Continued)

Distance from Edge of Invert (m)	Cumulative Flow (mm^2/yr)					
	Case 1: Poorly Sorted	Case 1: Well-Sorted	Case 2: Poorly Sorted	Case 2: Well-Sorted	Case 3: Poorly Sorted	Case 3: Well-Sorted
0.95	68	0	1,200	6	20,197	20,012
1.05	83	0	1,637	15	24,259	25,315
1.15	100	0	2,245	39	27,862	29,713
1.25	128	0	3,892	245	31,565	32,327
1.25	157	0	5,497	440	35,368	35,051
1.35	193	1	8,131	1,053	40,285	37,718
1.45	238	2	12,261	2,562	46,354	40,301
1.55	296	6	18,452	5,853	54,061	44,186
1.65	370	13	26,814	11,883	63,441	50,519
1.75	505	29	42,143	27,548	79,229	66,211
1.75	640	43	57,939	43,387	95,611	82,182
1.85	823	78	83,354	76,376	121,605	115,255
1.95	1,070	124	113,815	120,419	152,447	159,334
2.05	1,397	166	140,440	154,779	179,285	193,722
2.15	1,817	205	159,580	174,846	198,547	213,824
2.25	2,252	247	170,690	183,264	209,737	222,281
2.25	2,724	293	182,084	191,651	221,193	230,702
2.35	3,494	435	187,978	194,202	227,099	233,341
2.45	4,721	812	193,054	195,788	232,136	235,084
2.55	6,526	1,703	197,490	197,148	236,427	236,739
2.65	8,969	3,557	201,651	199,205	240,262	239,054
2.75	11,457	6,062	205,184	201,864	243,373	241,550
2.75	14,165	8,868	208,863	204,718	246,589	244,184
2.85	18,040	15,196	213,147	211,012	249,971	248,576
2.95	22,858	24,593	218,234	220,368	253,891	253,879
3.05	26,583	29,775	222,156	225,589	257,146	257,643
3.05	30,458	35,082	226,177	230,895	260,512	261,567
3.15	33,120	37,616	228,867	233,419	263,457	265,726
3.25	35,007	38,687	230,784	234,492	265,802	268,348
3.25	36,896	39,719	232,693	235,525	268,178	270,974
3.35	37,850	39,987	233,648	235,792	269,738	272,421
3.45	38,515	40,080	234,318	235,885	270,860	273,022
3.45	39,169	40,170	234,975	235,975	271,974	273,601
3.55	39,462	40,182	235,268	235,987	272,513	273,720
3.55	39,750	40,193	235,556	235,998	273,043	273,836
3.65	39,884	40,195	235,690	236,000	273,301	273,857
3.65	40,017	40,196	235,822	236,001	273,556	273,878
3.75	40,076	40,196	235,881	236,001	273,668	273,881

Table 6-19. Cumulative Flow out Bottom of the Invert in Base Case Simulations (Continued)

Distance from Edge of Invert (m)	Cumulative Flow (mm^2/yr)					
	Case 1: Poorly Sorted	Case 1: Well-Sorted	Case 2: Poorly Sorted	Case 2: Well-Sorted	Case 3: Poorly Sorted	Case 3: Well-Sorted
3.75	40,135	40,196	235,940	236,001	273,779	273,883
3.85	40,160	40,196	235,964	236,001	273,822	273,883
3.95	40,178	40,196	235,983	236,001	273,853	273,883
3.95	40,197	40,196	236,001	236,001	273,883	273,883

Source: Output DTN: SN0607T0504506.002.

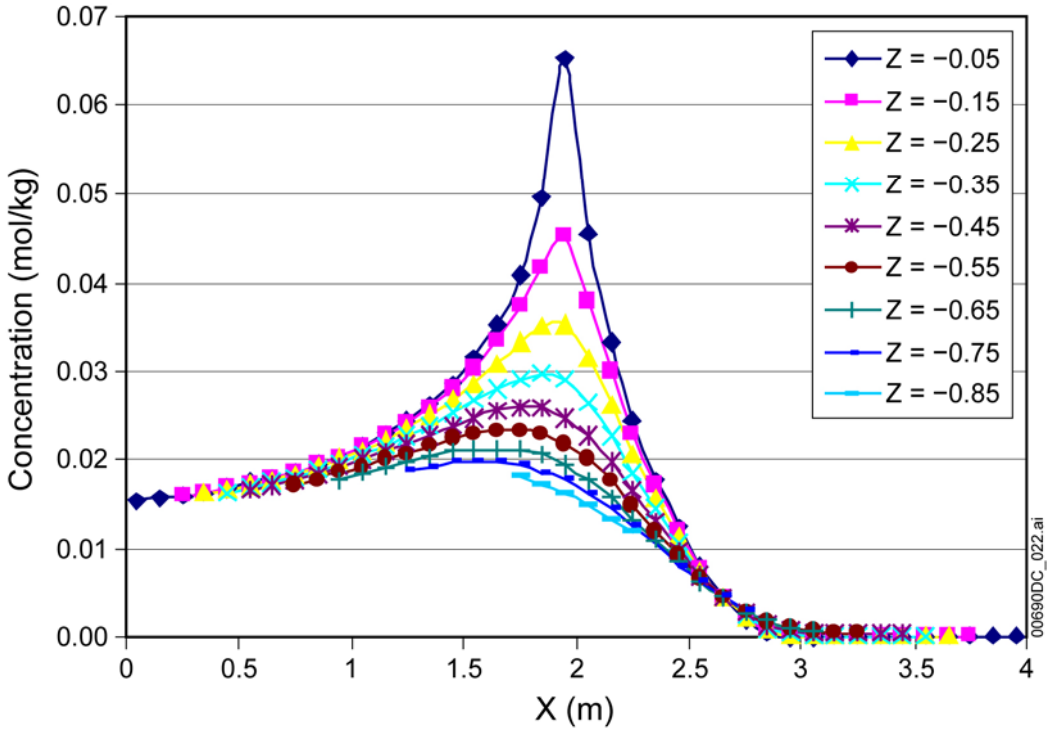

Source: Output DTN: SN0607T0504506.002.

Figure 6-18. Na^+ Tracer Concentration across the Invert: Case 1, Poorly Sorted

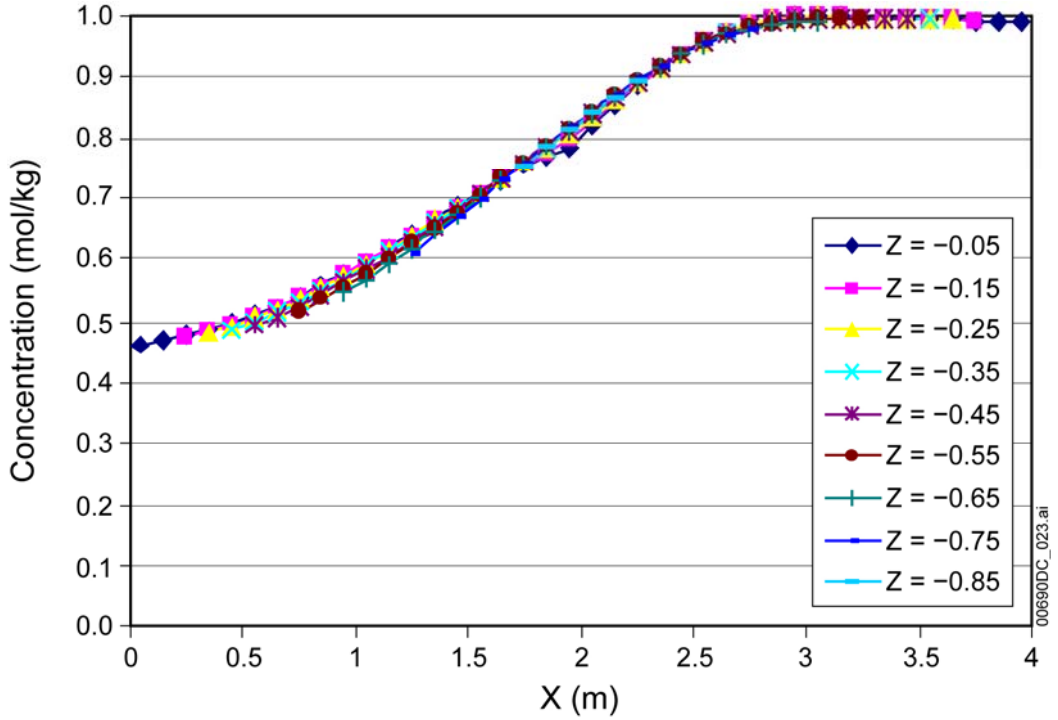

Source: Output DTN: SN0607T0504506.002.

Figure 6-19. K^+ Tracer Concentration across the Invert: Case 1, Poorly Sorted

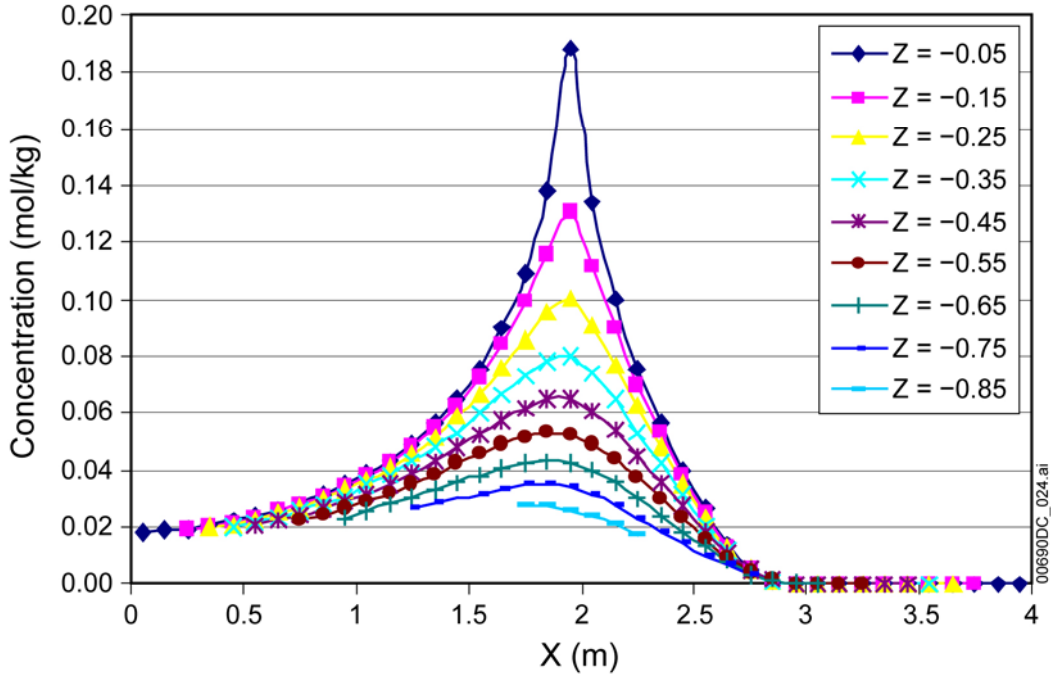

Source: Output DTN: SN0607T0504506.002.

Figure 6-20. Na^+ Tracer Concentration across the Invert: Case 1, Well-Sorted

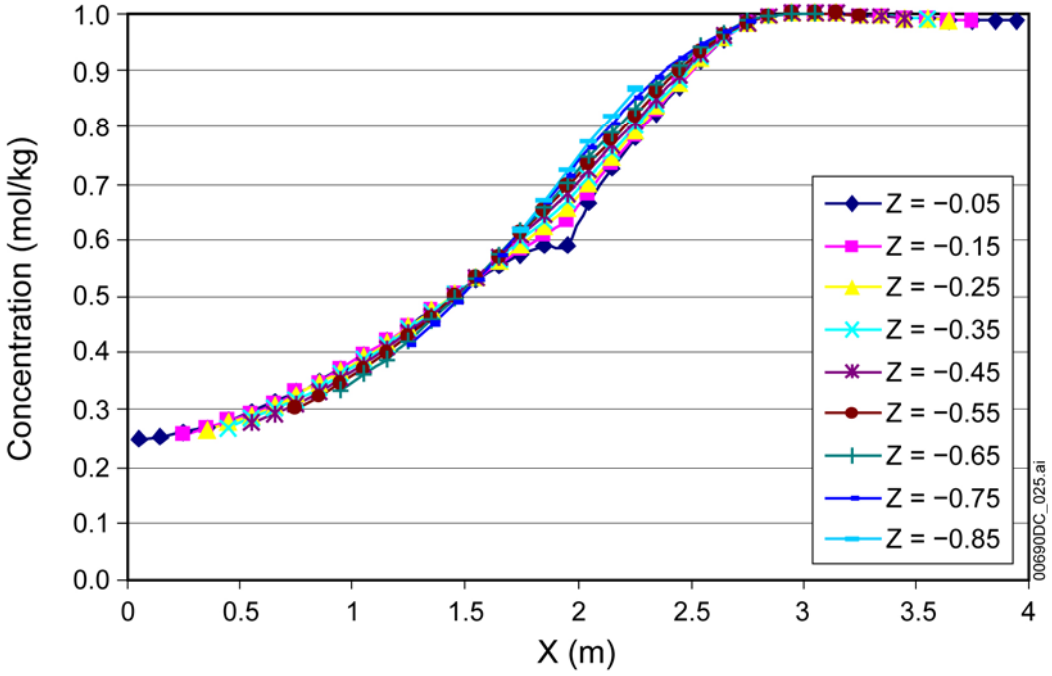

Source: Output DTN: SN0607T0504506.002.

Figure 6-21. K^+ Tracer Concentration across the Invert: Case 1, Well-Sorted

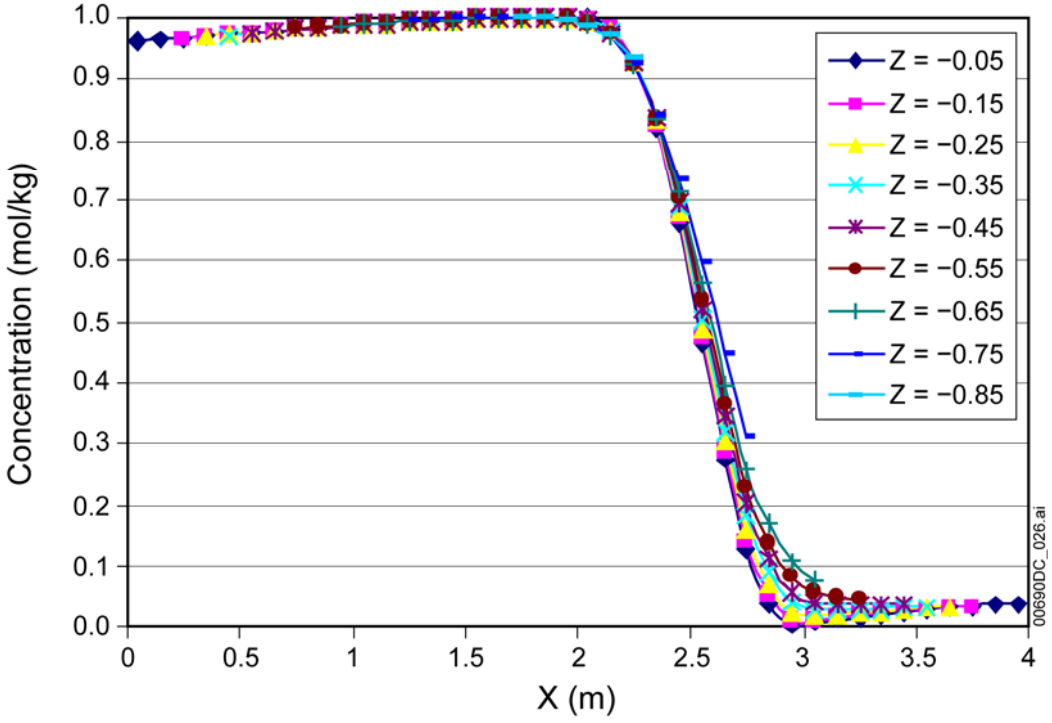

Source: Output DTN: SN0607T0504506.002.

Figure 6-22. Na^+ Tracer Concentration across the Invert: Case 2, Poorly Sorted

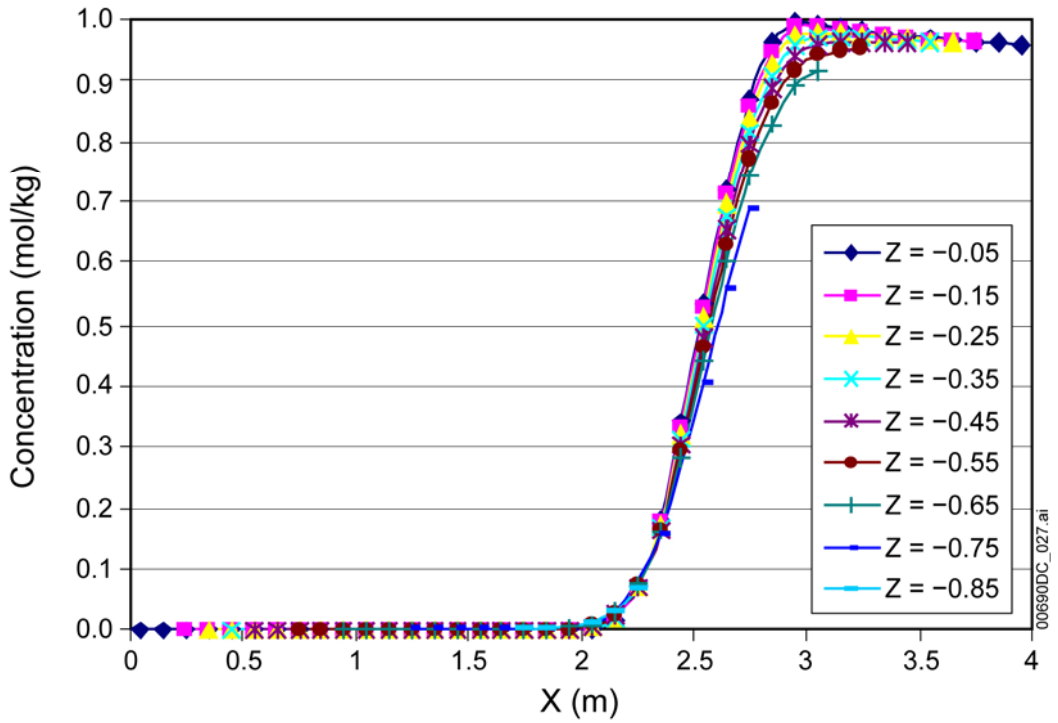

Source: Output DTN: SN0607T0504506.002.

Figure 6-23. K^+ Tracer Concentration across the Invert: Case 2, Poorly Sorted

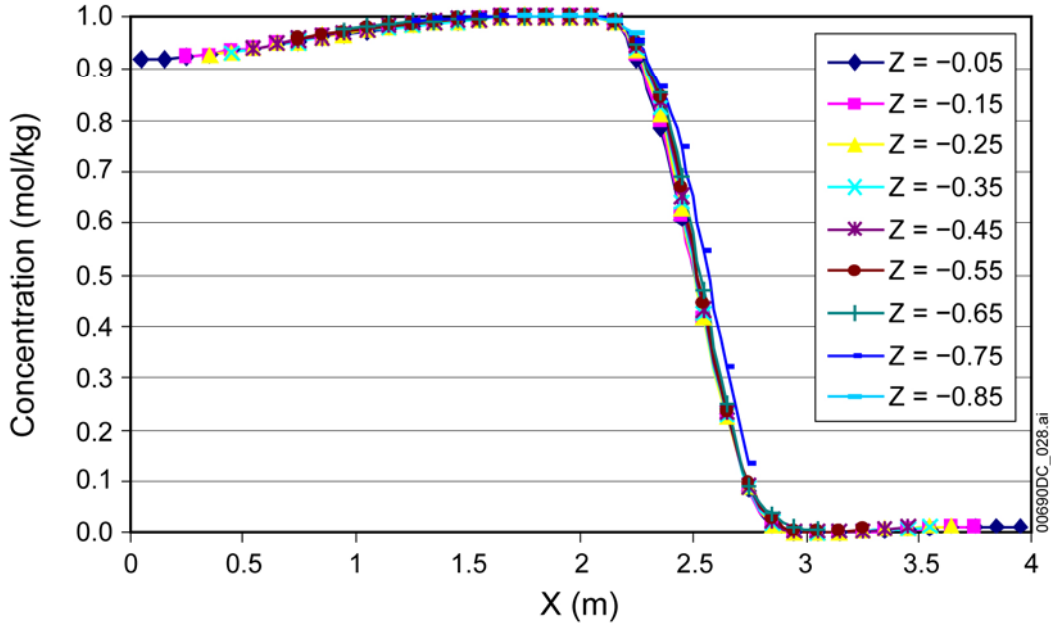

Source: Output DTN: SN0607T0504506.002.

Figure 6-24. Na^+ Tracer Concentration across the Invert: Case 2, Well-Sorted

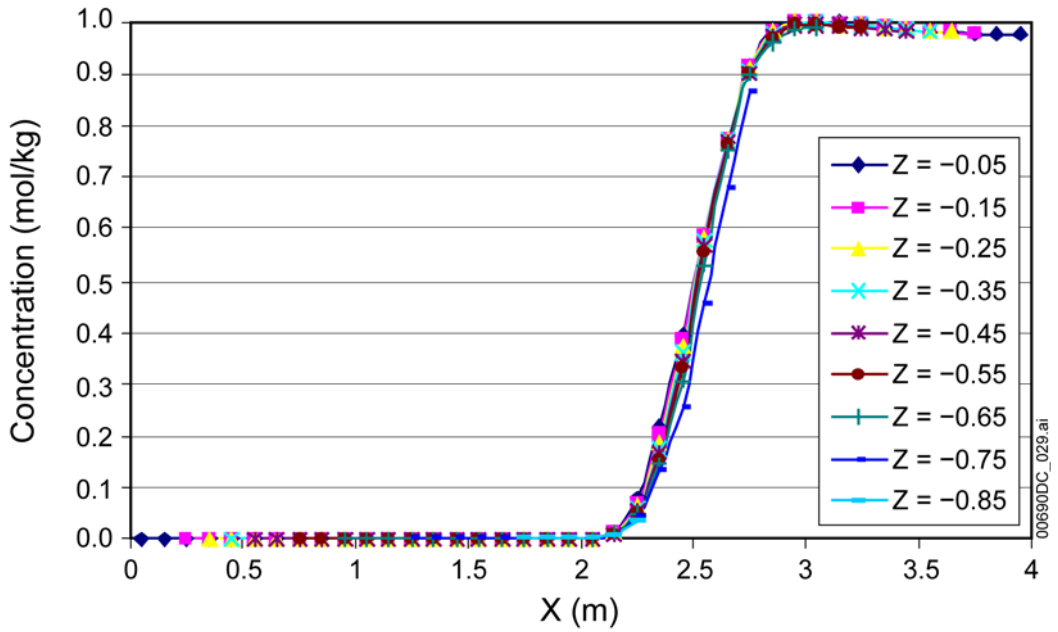

Source: Output DTN: SN0607T0504506.002.

Figure 6-25. K^+ Tracer Concentration across the Invert: Case 2, Well-Sorted

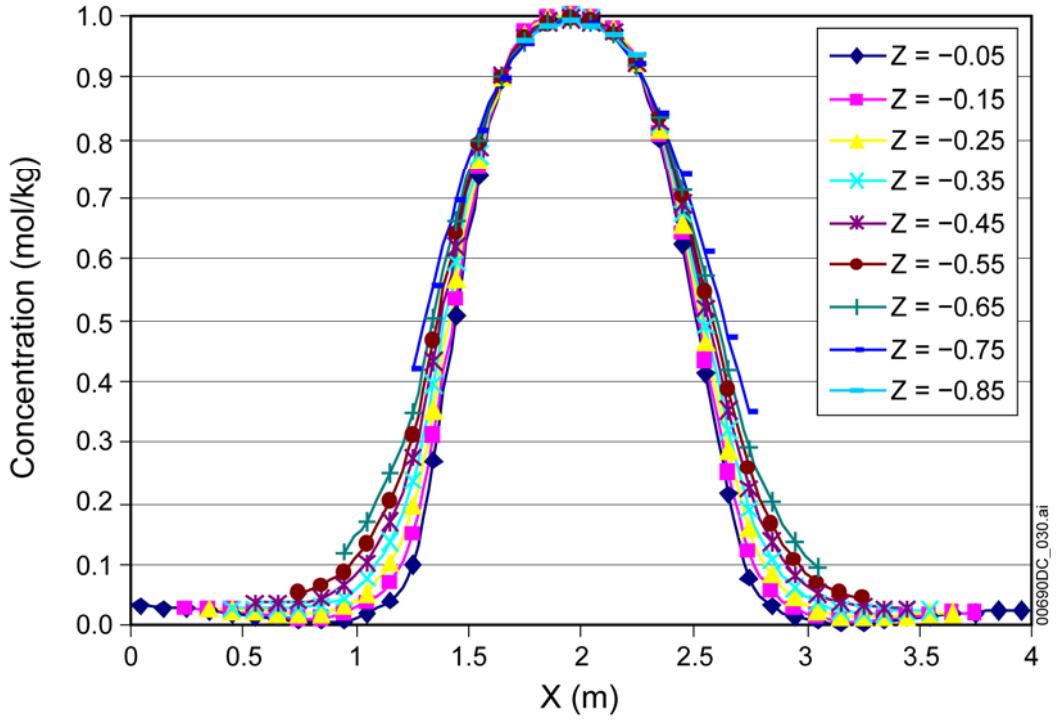

Source: Output DTN: SN0607T0504506.002.

Figure 6-26. Na^+ Tracer Concentration across the Invert: Case 3, Poorly Sorted

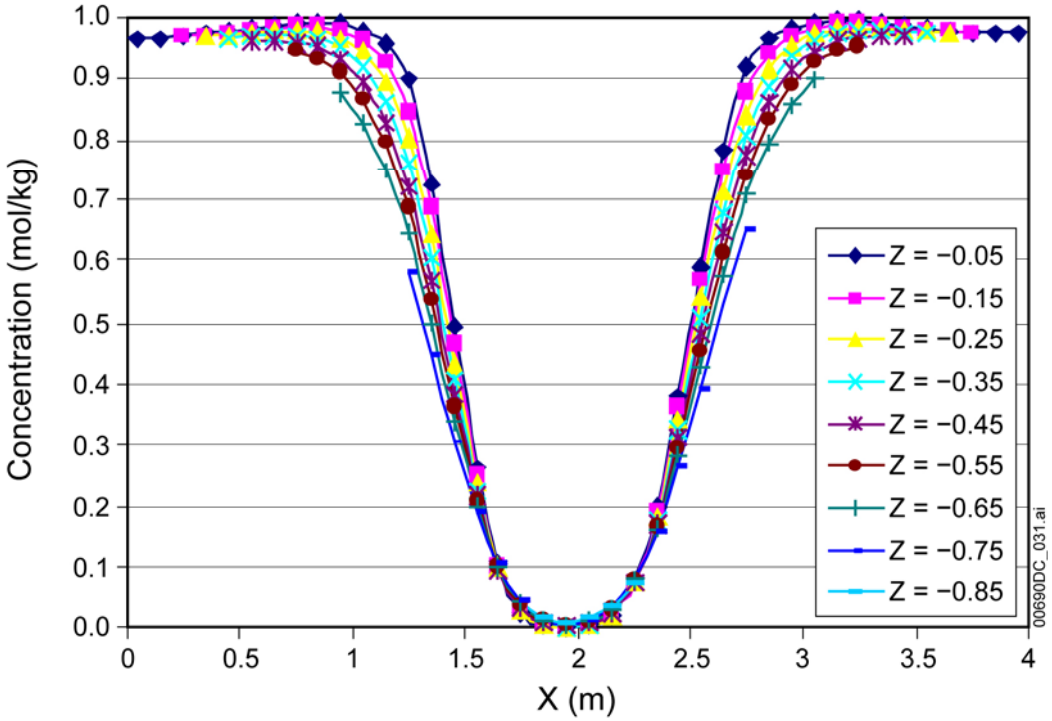

Source: Output DTN: SN0607T0504506.002.

Figure 6-27. K^+ Tracer Concentration across the Invert: Case 3, Poorly Sorted

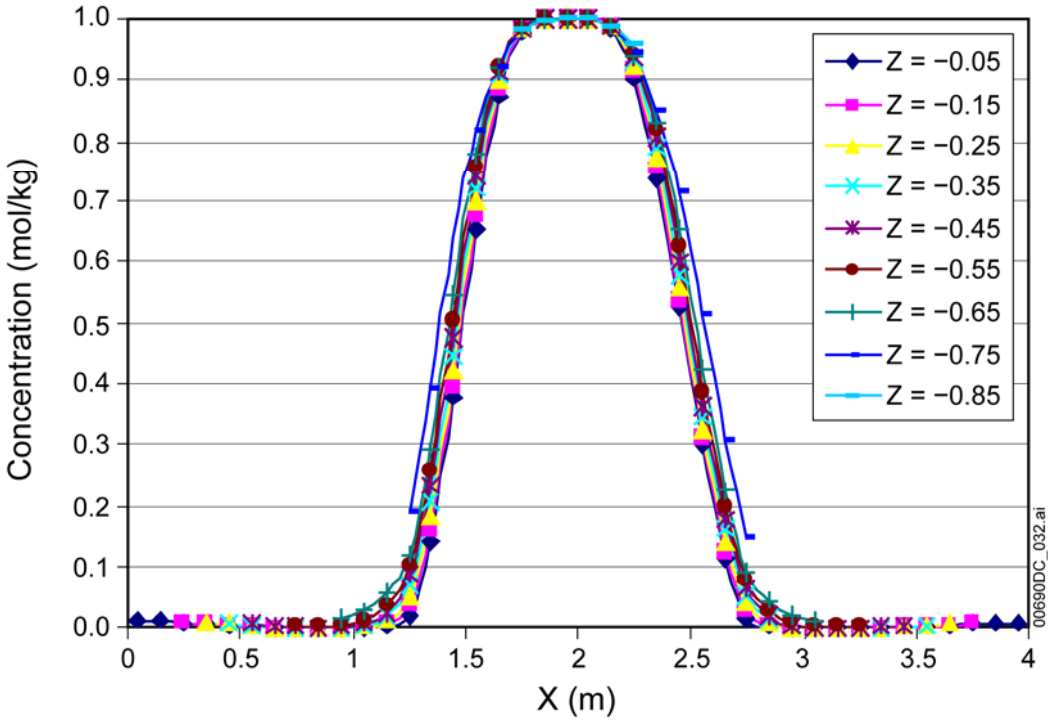

Source: Output DTN: SN0607T0504506.002.

Figure 6-28. Na^+ Tracer Concentration across the Invert: Case 3, Well-Sorted

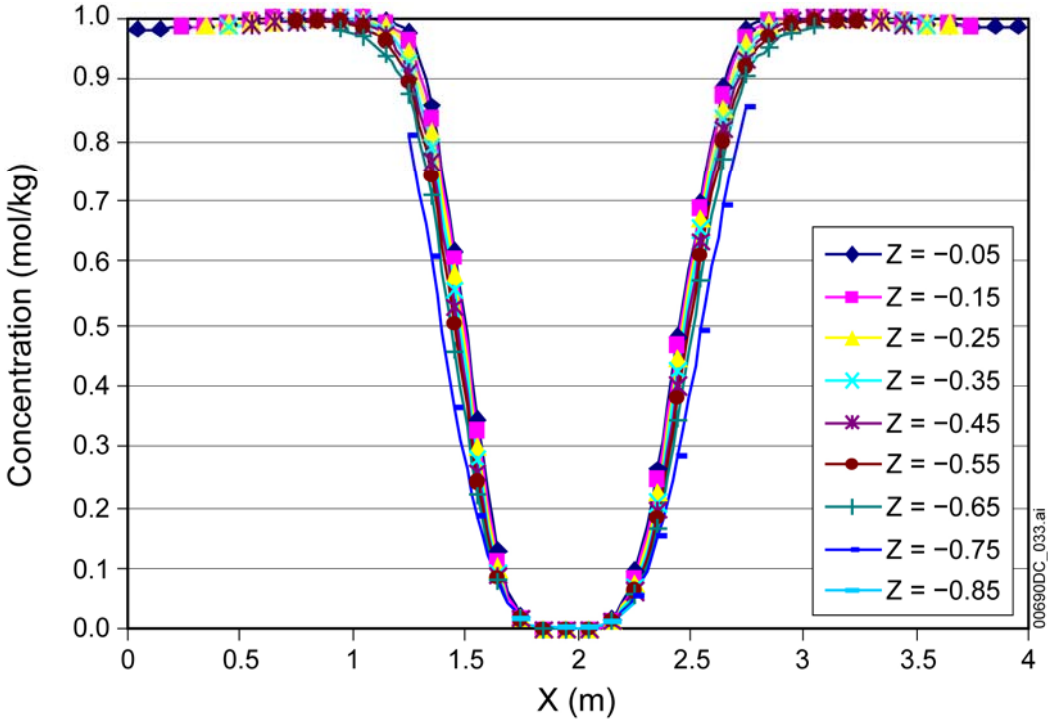

Source: Output DTN: SN0607T0504506.002.

Figure 6-29. K^+ Tracer Concentration across the Invert: Case 3, Well-Sorted

6.4.7 Location of Accumulation Zone within the Invert

Because PHREEQC lacks the spatial dimension needed to present a full 3-D distribution of mineral accumulation, the following approach has been developed. Each of the six cases described has four attributes that need to be determined: (1) how much mixing occurs in the bulk of the invert (in other words, what fraction of the waste package effluent contacts and mixes with "fresh" percolation/dripping water in the bulk of the invert); (2) what is the shape of the mixing zone in the bulk of the invert; (3) how much mixing occurs at the bottom of the invert; and (4) what is the shape of the mixing zone at the bottom of the invert. Detailed calculations are presented in DTN: MO0605SPAINVRT.000, files *Summaries - Poorly+Well Sorted Invert_1%_4.xls*, *Summaries - Poorly+Well Sorted Invert_3%_4.xls*, *Summaries - Poorly+Well Sorted Invert_5%_4.xls*, and *Summaries - Poorly+Well Sorted Invert_1+3+5%_4.xls*, tab "Cover" in each spreadsheet.

6.4.7.1 Methodology to Determine Shape of Mixing Zone in Bulk of the Invert

As described in Section 6.4.6, two tracers were used to determine the amount of mixing in the bulk on the invert. Waste package effluent water was tagged with Na^+ at an initial molal concentration of 1 mol/kg, while resident water flowing into the drift but diverted around the waste package uses K^+ as a tracer (at a concentration of 1 mol/kg). At steady state, areas within the invert where Na^+ concentrations are low would suggest that no mixing is likely to take place at those locations. Conversely, mixing also is not possible in areas with low K^+. The mixing zone can then be defined where both Na^+ and K^+ are above some concentration threshold. It

follows that not all incoming flow streams necessarily interact. At the top of the invert, both effluent and diverted water flows are spatially restricted. Depending on their relative flow rate strength, part of the Na^+ or K^+ flow may reach the bottom of the invert without reacting with each other. Consequently, mixing can also potentially occur at the bottom of the invert.

The tracer relative concentration threshold has been chosen at 1% of the source concentration. Relative concentration is defined as the ratio of tracer concentration in the invert water to its concentration in the source (waste package) water. Because the Na^+ tracer concentration in the waste package water in the numerical model was 1.0 molal, the relative concentration here is equal to the absolute Na^+ concentration. It follows that the mixing zone in the invert is defined as the intersection of the Na^+ and K^+ plumes where both concentrations are above 0.01 mol/kg. Figures 6-30 through 6-35 display the shape of the mixing zone for the 3 flow distribution and 2 types of invert properties described in Table 6-20. The plots were obtained by simply mapping the concentrations as given in DTN: SN0607T0504506.002 (worksheets "C*nX* Tracers"), where *n* and *X* represent the flow distribution case number (*n* = 1, 2, 3) and the invert properties (*X*= P (poorly sorted), W (well-sorted)), respectively.

Figures 6-30 and 6-33, depicting cases C1P and C1W (effluent and diverted water flow rates are 1 L/yr and 200 L/yr, respectively), suggest that mixing can take place in most of the invert side opposite to dripping area of the diverted water. The higher flow rate of the diverted water dominates the system and the diverted water is transported throughout the invert, but the low flow rate waste package water is restricted to the left side of the invert. Diffusion plays a large role in controlling the shape of the mixing zone that does not seem to be impacted by the capillary properties of the invert, as evidenced by the similar plots in Figures 6-30 and 6-33. Figures 6-31 and 6-34, depicting cases C2P and C2W (effluent and diverted water flow rates at 1,000 L/yr and 200 L/yr, respectively), show a mixing zone where effluent and diverted water flow rates are better balanced. In this case, capillary forces have a larger impact on the shape of the mixing zone. If those forces are weak enough, that is, with a well-sorted invert, the effluent and diverted water streams interact only in a narrow vertical slab located between the dripping areas (Figure 6-34). The mixing zone in Figure 6-31 is nearly opposite of Figure 6-30, because in this case the higher flow rate of the waste package effluent is spread throughout the invert and the lower flow rate of the diverted water is restricted to the right side of the invert. Figures 6-32 and 6-35, depicting cases C3P and C3W (effluent and distributed diverted water flow rates are 1,000 L/yr and 400 L/yr, respectively), display a similar pattern as the previous set.

6.4.7.2 Methodology to Determine Effluent Fraction Mixing in the Bulk of the Invert

In some cases, part of the dripping streams may flow directly to the bottom of the invert without interacting with one another. This is clear in cases C1P and C1W, where most of the diverted water stream bypasses the mixing zone in the bulk of the invert and flows directly to the bottom of the invert. One can compute the fraction of that flow by referring to DTN: SN0607T0504506.002 (worksheets "C*nX* Flows"), where *n* and *X* represent the flow distribution case number (*n* = 1, 2, 3) and the invert properties (*X* = P, W), respectively. Those worksheets present the total flow rate at the bottom of the invert as a function of the coordinate transverse to the drift axis. In the C1P case (Figure 6-30), interaction between the two streams is minimal beyond horizontal coordinate x = 2.40 m. A glance at the "C1P Flows" worksheet reveals that more than 90% of the diverted water flows directly to the bottom of the invert while

all of the effluent stream is somehow contacted by the diverted water and participates in the mixing. It follows that some mixing can still take place at the bottom of the invert. Case C1W (Figure 6-33) has a similar treatment.

Case C2P (Figure 6-31) is the reverse case compared to case C1P. All of the diverted water is used up in the mixing zone and no mixing can take place at the bottom invert. Case C2W (Figure 6-34) is similar to case C2P. However, some of the diverted water still reaches the bottom of the invert. It follows that mixing at the bottom of the invert is also possible in that case. Figure 6-32 (Case C3P) shows that the mixing zone covers most of the invert, except for a small vertical zone directly under the effluent dripping area. In that case, all of the mixing occurs in the bulk of the invert and none at the bottom. Case C3W (Figure 6-35) suggests that mixing will occur in two wide vertical slabs leaving a central zone as well as two zones on the edges with no mixing. In that case, too, mixing will occur in the invert.

Table 6-21 gives the total flow rate where mixing in the invert took place. Columns B to D are input to the TOUGHREACT simulations. Column E gives the range(s) of x-coordinate where there is no mixing. The coordinates are determined by a simple reading of Figures 6-30 through 6-35. Column F shows the total flux going through the invert mixing zone and is obtained through the "C*nX* Flows" worksheets. Column G information is simply the fraction of data in Column F relative to the total flux going through the system. Table 6-22 summarizes the results. Flow rates are now expressed in L/yr instead of mm^2/yr. The flow rates are computed from simple mass balances. For example, in Figure 6-35, it is clear that diverted water reaching the bottom of the invert between coordinate 0 and 0.9 did not mix with the effluent. The same thing can be said of the diverted water reaching the invert bottom between x-coordinate 3.1 and 4.0. Similarly, effluent water between x-coordinate 1.8 and 2.1 reaches the bottom of the invert without interacting with the diverted water. The mixing flow rate is then the remainder of the total flow rate.

6.4.7.3 Methodology to Determine Number of PHREEQC Cells to Consider

The number n of PHREEQC cells to consider for each case can be calculated using Equation 6.4.5-1, by solving for n:

$$n = \ln\left(\frac{seeprate}{WPflux}\right) \Big/ \ln\left(\frac{1}{1 - MixingRatio}\right) \qquad \text{(Eq. 6.4.7-1)}$$

Using total flow rate (column D) in Table 6-20 for the *seeprate* and 0.1 for the *MixingRatio*, the number of cells are calculated to be: 51 for Case 1, 2 for Case 2, and 4 for Case 3. So, even if the PHREEQC output files show accumulation in cells above the cutoff, those values are not considered in the total accumulation. The analyses of the location of the accumulation, as displayed in Table 6-22, cases C2P and C3P, are straightforward. There is no mixing in the bottom of the invert: 100% of the accumulation taking place in PHREEQC cells 1 through 2 (C2P) or cells 1 through 4 (C2P) should be applied to the mixing zone as defined in Figures 6-31 and 6-32, respectively. Cases C1P and C1W include mixing at the bottom of the invert, but those cases are a simple continuation of the mixing that already occurred in the invert, that is, the effluent is diluted further. In those cases, as given in Table 6-22, 100% of the accumulation given by PHREEQC cells 1-29 (C1P) or 1-25 (C1W) should be applied to the invert mixing zone

as defined in Figure 6-30. 100% of accumulation found in PHREEQC cell 30-51 (C1P) or 25-51 (C1W) should also be applied to the bottom of the invert.

Cases C2W and C3W are more complex. Neither the effluent nor the diverted water is exhausted in the invert mixing zone. It follows that mixing can start anew at the bottom of the invert. This is different from the previous C1P and C1W cases where the mixing at the bottom of the invert was a simple extension of the mixing in the bulk of the invert. When computing the number of PHREEQC cells to consider in the invert mixing zone for cases C2W and C3W, the approach is similar to the previous cases, but it is applicable only to a fraction of the accumulation as given by the fraction of the total flow rate mixing in the invert. The remainder of the effluent and diverted water can still mix and react at the bottom of the invert. Since they are both "fresh," it is legitimate to apply PHREEQC results starting from cell #1; the number of relevant cells being computed using Equation 6.4.7-1.

6.4.7.4 Where in the Mixing Zone Is the Precipitation?

The previous paragraphs develop the size and location of the mixing zone envelopes. One way to use the results would be to assume that the accumulation is uniformly distributed across the mixing zone by adding up accumulation of relevant PHREEQC cells. However, it is likely that the accumulation will not be uniform. To gain insight into the way to apply PHREEQC results of individual cells, Figures 6-36 through 6-41 depict additional results. The figures use a threshold of 0.03 and 0.05, in addition to the value of 0.01 assumed until now. The general shape implied by the different subdomains helps in distributing the PHREEQC results. Figures 6-36 and 6-39 suggest that the mineral accumulation will be deposited around the effluent dripping zone in somewhat concentric half-cylinders with horizontal axis. The shape of half-cylinders is caused by modeling the effluent and the diverted waters as line sources. If the waters were modeled as point sources, the accumulation would be hemi-spheres deposited around the effluent dripping zone. Similarly, for the higher flux cases, for the water inputs modeled as line sources, Figures 6-37, 6-38, 6-40, and 6-41 suggest that the accumulation will be in vertical slabs the length of the waste package. If the waters were modeled as point sources, instead, the accumulation would be concentric cylindrical layers with a vertical axis.

In addition to the material that accumulates within the bulk of the invert, as depicted in Figures 6-36 through 6-41, mineral accumulation also occurs along the drift-wall interface below the invert for some cases (Table 6-22). The shape of the accumulation zone along the drift-wall is unknown, but could range from a thick, crescent-moon shape to a thin, spread-out layer along the bottom of the curved interface. A range of possible shapes should be considered in criticality calculations.

As mentioned in Section 6.4.6, the 2D line-source approximation increases the extent of predicted mixing within the invert thickness, compared to discrete 3D point sources (which were not simulated for this report) because the 2D geometry is already better mixed at the source locations. The 2D approximation is therefore conservative for mixing, and therefore for the accumulation of fissile mass within the invert (see below for discussion of mixing at the drift-wall interface). This statement is supported by recognizing that if 3D point sources can be superposed to constitute 2D line sources, then the net effect is the same as if each individual incremental point source mixes only with the incremental point source directly opposite on the

other line, without 3D flow spreading as occurs with isolated 3D point sources. The net effect is the same because of the symmetry of mixing contributions from all the superposed point sources along each line.

Percolation through the invert is modeled by the Richards equation as implemented in TOUGHREACT. The van Genuchten characteristic equation, and the relative permeability relations typically used, are nonlinear functions so superposition does not apply. However, the Richards equation can be linearized as is done for the validation problem in Section 7.2.5, and in fact the 2D validation problem is mathematically equivalent to a superposition of 3D point sources to constitute 2D line sources. Thus the superposition analogy is valid to the extent that the validation problem agrees with the TOUGHREACT simulations used in this report. This agreement is discussed extensively in Section 7.2.5.9. This supports the argument above, that the 2D line-source approximation increases the extent of predicted mixing within the invert thickness, compared to discrete 3D point sources.

If mixing and accumulation within the invert thickness are over-predicted, then accumulation at the drift-wall interface below the invert is under-predicted. Although apparently non-conservative for representing potential criticality at the drift-wall interface, this condition is not significant to the intended use of the results from this model. This is because the results include cases for which most of the released mass breaks through to the drift-wall interface, and for which complete mixing at the interface (and the resulting accumulation) is assumed. The conservative 2D line-source approximation is most useful in representing the cases for which all accumulation occurs within the invert.

Table 6-20. Fraction of Total Flow Mixed in Bulk of Invert

A	B	C	D	E	F	G
Case ID*	Waste Package Thru-rate (L/yr)	Drift (no waste package) Flow Rate (L/yr)	Total Flow Rate (L/yr)	Horizontal Coordinates for Which There Is No Mixing**	Cumulative Flux of Mixing Zones at Bottom of Invert (mm^2/yr) **	Fraction of Total Flow Mixed in Invert**
C1P	1	200	201	>2.40	4,110	10.2%
C2P	1,000	200	1,200	<2.00	109,000	46.1%
C3P	1,000	400	1,400	>1.90 and <2.00	245,000	89.5%
C1W	1	200	201	>2.60	2,630	6.5%
C2W	1,000	200	1,200	<2.10 and >2.90	50,900	21.6%
C3W	1,000	400	1,400	<0.90 and (>1.80 and <2.10) and >3.10	152,000	55.6%

Output DTN: MO0605SPAINVRT.000, file: *Summaries Poorly_Well Sorted Invert_1_4.xls*.
* P = poorly sorted invert; W = well-sorted invert
** Using a relative concentration threshold of 1%.

Table 6-21. Distribution of Flow Streams at the Bottom of the Invert

A	B	C	D	E	F	G
Case ID*	Total Flow Rate (L/yr)	Flow Rate through the Mixing Zone (L/yr) **	Effluent Flow Rate through the Mixing Zone (L/yr) **	Effluent Flow Rate to the Invert Bottom with No Mixing (L/yr) **	Diverted Water Flow Rate through the Mixing Zone (L/yr) **	Diverted Water Flow Rate to the Invert Bottom with No Mixing (L/yr) **
C1P	201	20.54	1.00	0.00	19.54	180.46
C2P	1,200	553.59	353.59	646.41	200.00	0.00
C3P	1,400	1,252.58	852.58	147.42	400.00	0.00
C1W	201	13.15	1.00	0.00	12.15	187.85
C2W	1,200	258.70	161.98	838.02	96.72	103.28
C3W	1,400	778.87	462.99	537.01	375.96	24.04

Output DTN: MO0605SPAINVRT.000, file: *Summaries Poorly_Well Sorted Invert_1_4.xls*.
* P = poorly sorted invert; W = well-sorted invert.
** Using a relative concentration threshold of 1%.

Table 6-22. Conversion of Mixing Domains into PHREEQC-compatible Data

A	B	C	D	E
Case ID*	Number of Cells to Be Used in Invert**	Percent of PHREEQC Accumulation**	Number of Cells to Be Used at Bottom of Invert**	Percent of PHREEQC Accumulation**
C1P	1-29	100	30-51	100
C2P	1-2	100	N/A	N/A
C3P	1-4	100	N/A	N/A
C1W	1-25	100	25-51	100
C2W	1-2	21.6	1-2	78.4
C3W	1-4	55.6	1-4	44.4

Output DTN: MO0605SPAINVRT.000, file: *Summaries Poorly_Well Sorted Invert_1_4.xls*.

* P = poorly sorted invert; W = well-sorted invert.

** Using a relative concentration threshold of 1%.

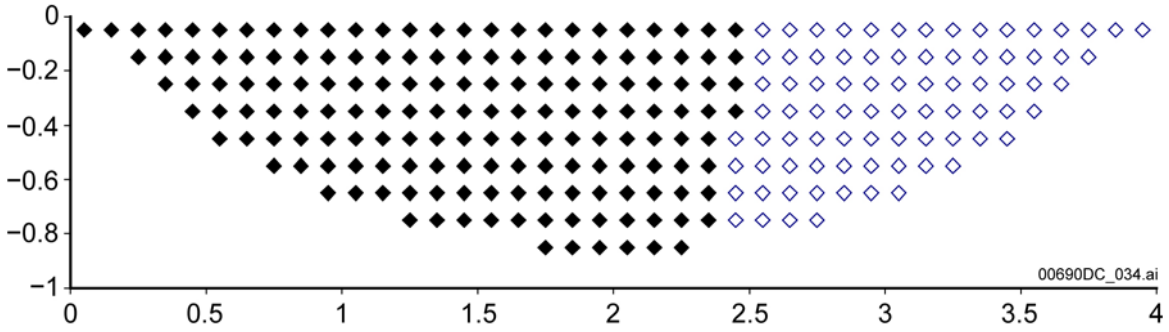

Output DTN: MO0605SPAINVRT.000, file: *Summaries Poorly_Well Sorted Invert_1_4.xls*.

NOTE: Relative concentration threshold of 1%. Waste package effluent flow 1 L/yr; diverted water 200 L/yr

Figure 6-30. Mixing Zone Shape (black diamonds), Case C1P

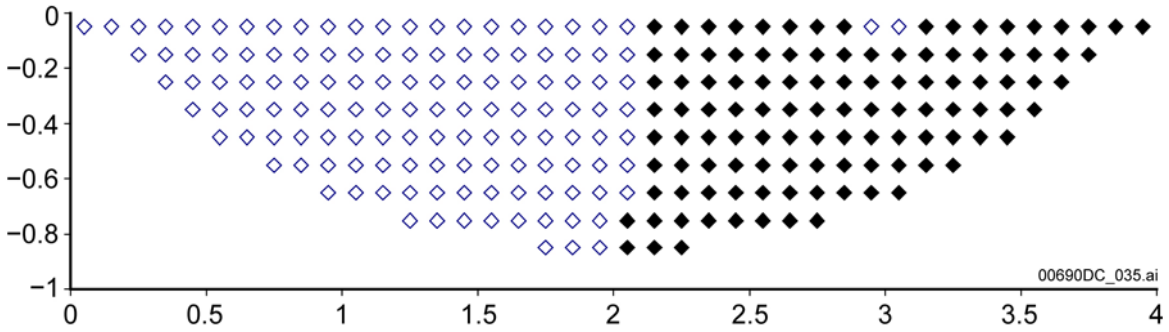

Output DTN: MO0605SPAINVRT.000, file: *Summaries Poorly_Well Sorted Invert_1_4.xls*.

NOTE: Relative concentration threshold of 1%. Waste package effluent flow 1,000 L/yr; diverted water 200 L/yr.

Figure 6-31. Mixing Zone Shape (black diamonds), Case C2P

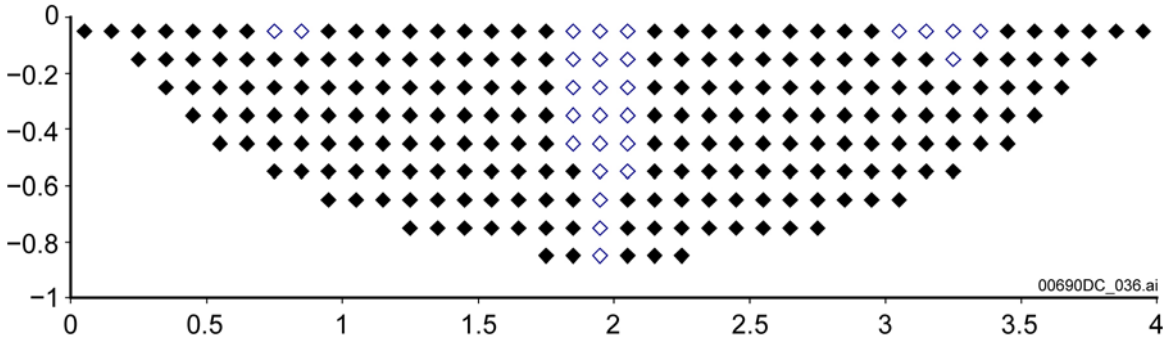

Output DTN: MO0605SPAINVRT.000, file: *Summaries Poorly_Well Sorted Invert_1_4.xls*.

NOTE: Relative concentration threshold of 1%. Waste package effluent flow 1,000 L/yr; diverted water 400 L/yr.

Figure 6-32. Mixing Zone Shape (black diamonds), Case C3P

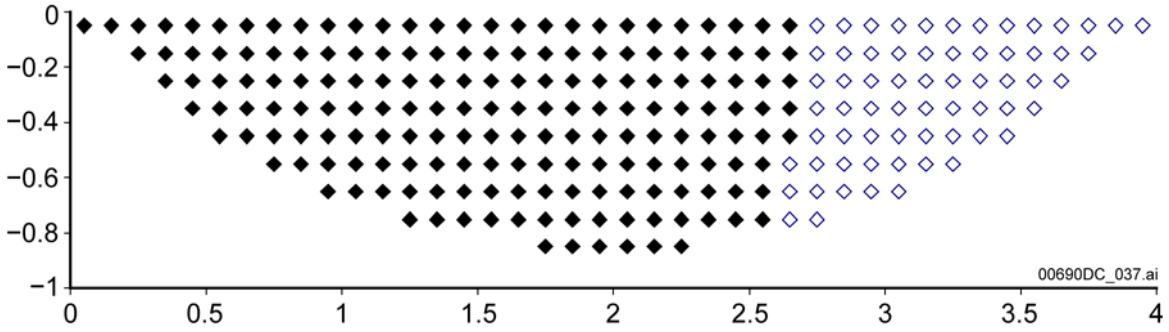

Output DTN: MO0605SPAINVRT.000, file: *Summaries Poorly_Well Sorted Invert_1_4.xls*.

NOTE: Relative concentration threshold of 1%. Waste package effluent flow 1 L/yr; diverted water 200 L/yr.

Figure 6-33. Mixing Zone Shape (black diamonds), Case C1W

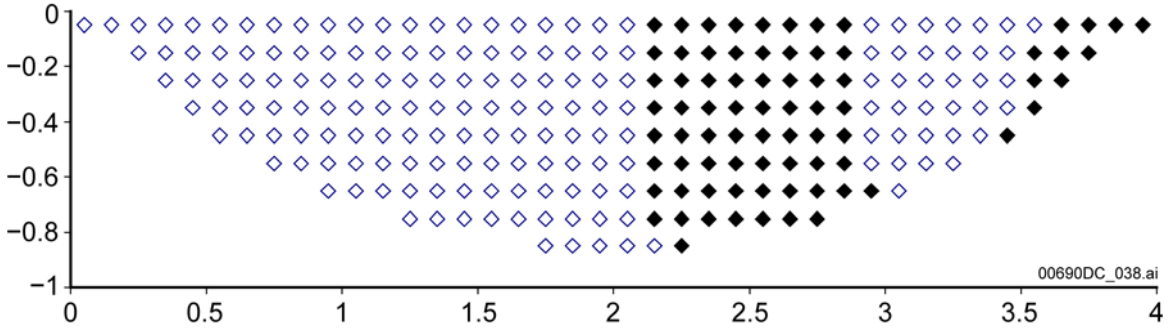

Output DTN: MO0605SPAINVRT.000, file: *Summaries Poorly_Well Sorted Invert_1_4.xls*.

NOTE: Relative concentration threshold of 1%. The few points on the right have not been considered part of the mixing zone. Waste package effluent flow 1,000 L/yr; diverted water 200 L/yr.

Figure 6-34. Mixing Zone Shape (black diamonds), Case C2W

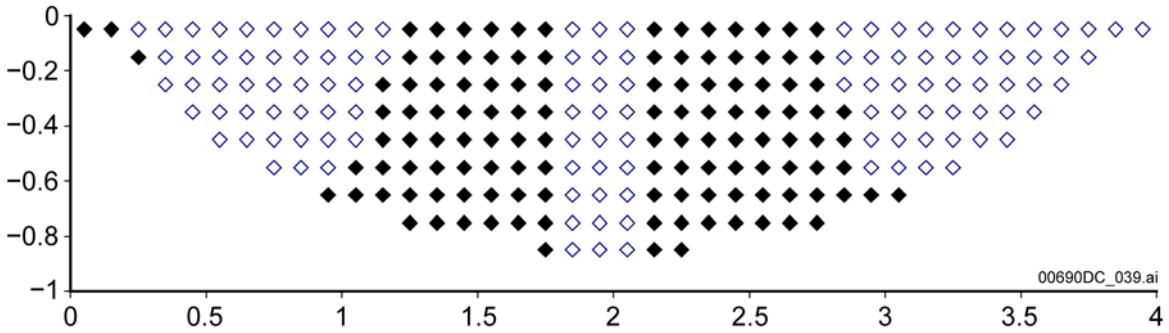

Output DTN: MO0605SPAINVRT.000, file: *Summaries Poorly_Well Sorted Invert_1_4.xls*.

NOTE: Relative concentration threshold of 1%. The few points on the left have not been considered part of the mixing zone. Waste package effluent flow 1,000 L/yr; diverted water 400 L/yr.

Figure 6-35. Mixing Zone Shape (black diamonds), Case C3W

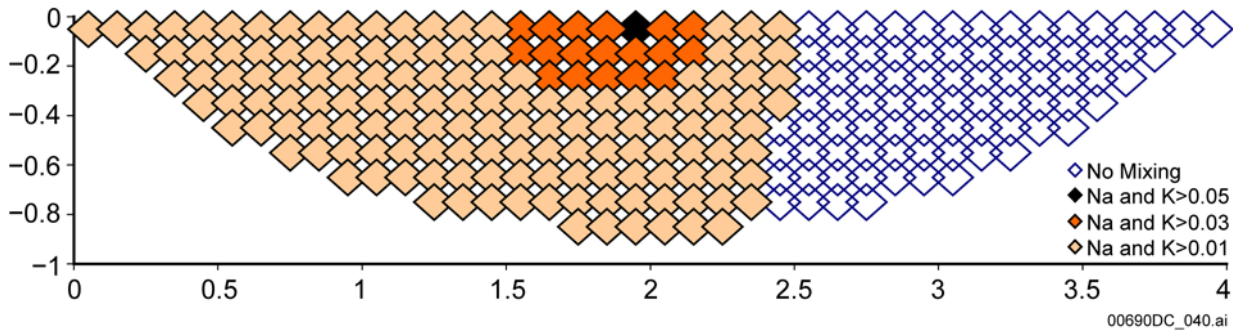

Output DTN: MO0605SPAINVRT.000, file: *Summaries Poorly_Well Sorted Invert_1_3_5_4.xls*.

NOTE: Relative concentration threshold of 1%. Waste package effluent flow 1 L/yr; diverted water 200 L/yr.

Figure 6-36. Nested Mixing Zones with Increasing Concentration Threshold, Case C1P

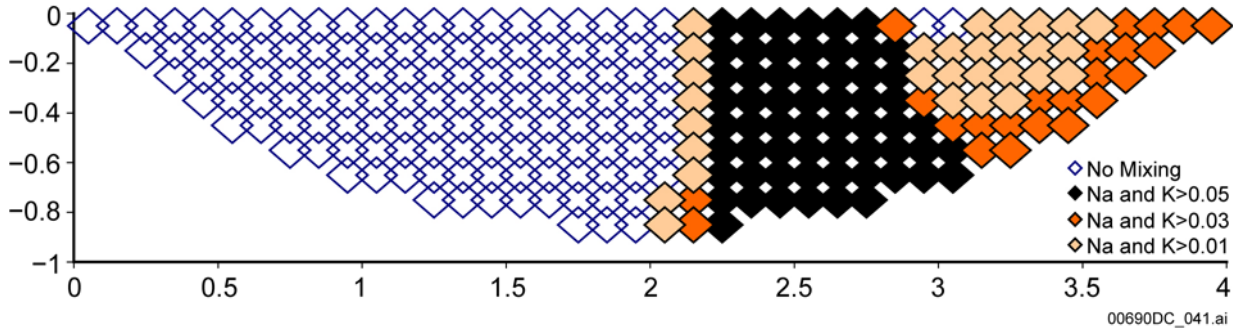

Output DTN: MO0605SPAINVRT.000, file: *Summaries Poorly_Well Sorted Invert_1_3_5_4.xls*.

NOTE: Relative concentration threshold of 1%. Waste package effluent flow 1,000 L/yr; diverted water 200 L/yr.

Figure 6-37. Nested Mixing Zones with Increasing Concentration Threshold, Case C2P

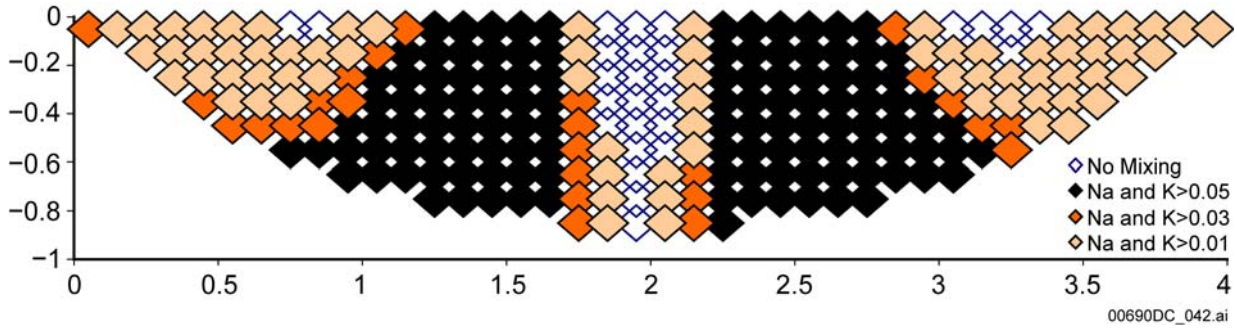

Output DTN: MO0605SPAINVRT.000, file: *Summaries Poorly_Well Sorted Invert_1_3_5_4.xls*.

NOTE: Relative concentration threshold of 1%. Waste package effluent flow 1,000 L/yr; diverted water 400 L/yr.

Figure 6-38. Nested Mixing Zones with Increasing Concentration Threshold, Case C3P

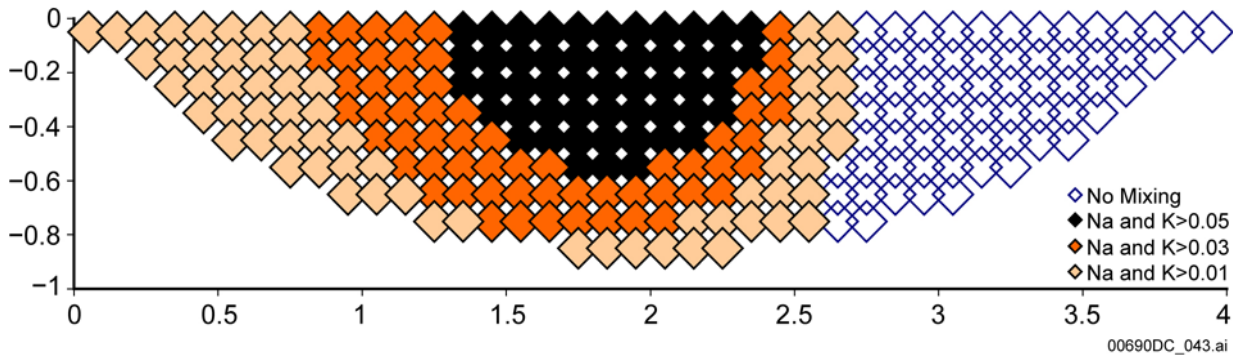

Output DTN: MO0605SPAINVRT.000, file: *Summaries Poorly_Well Sorted Invert_1_3_5_4.xls*.

NOTE: Relative concentration threshold of 1%. Waste package effluent flow 1 L/yr; diverted water 200 L/yr.

Figure 6-39. Nested Mixing Zones with Increasing Concentration Threshold, Case C1W

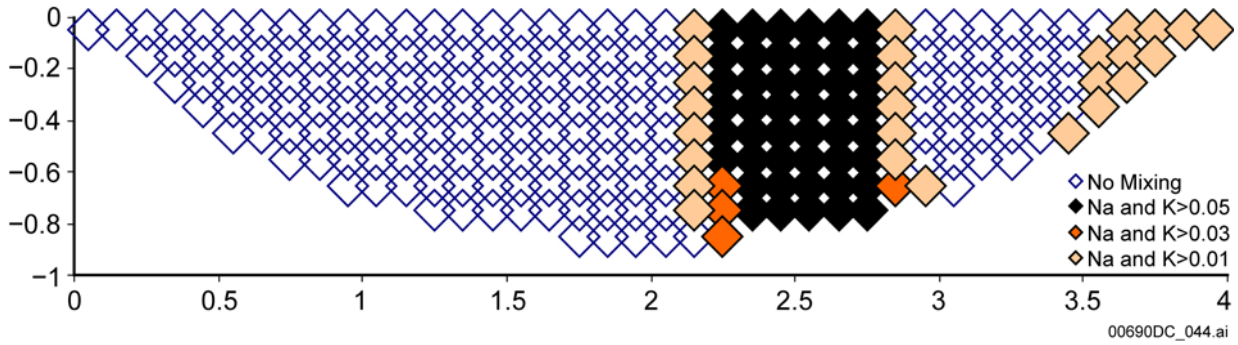

Output DTN: MO0605SPAINVRT.000, file: *Summaries Poorly_Well Sorted Invert_1_3_5_4.xls*.

NOTE: Relative concentration threshold of 1%. Waste package effluent flow 1,000 L/yr; diverted water 200 L/yr.

Figure 6-40. Nested Mixing Zones with Increasing Concentration Threshold, Case C2W

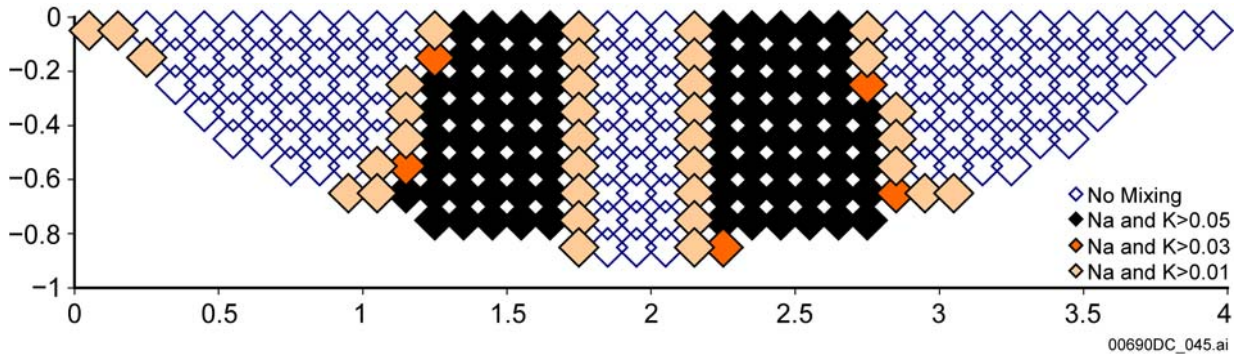

Output DTN: MO0605SPAINVRT.000, file: *Summaries Poorly_Well Sorted Invert_1_3_5_4.xls*.

NOTE: Relative concentration threshold of 1%. Waste package effluent flow 1,000 L/yr; diverted water 400 L/yr.

Figure 6-41. Nested Mixing Zones with Increasing Concentration Threshold, Case C3W

6.4.8 Accumulation within the Fractures and Lithophysae of the Host Rock

Accumulation in the fracture network depends on the fracture porosity, which is the product of two terms: the average fracture aperture (mm) and the fracture frequency (number of fractures in a unit distance in 1/m). Fracture frequency results from direct field measurements and is the simplest measure of fracture intensity. Because most fractures are near vertical (Mongano et al. 1999 [DIRS 149850], Table 7, p. 74), the fracture-only model invoked will consist of parallel plates of in-filled fractures separated by slabs of intact tuff.

6.4.8.1 Fracture Aperture

Fracture apertures in the repository horizon (Topopah Spring Tuff – Tpt) are invariably thin (median value across all repository units less than 0.16 mm) or non-measurable by hand tools in the field. The median aperture values are portrayed in Table 6-23. Measurements were taken on over 11,500 fractures in these three units and include all fractures over 30 cm. Of those fractures in the repository horizon with measurable apertures, the median values range from 0.23 mm (unit tsw33) down to 0.098 mm (tsw34). These data were obtained from DTN: LB990501233129.001 [DIRS 106787], file: *frac_prop_R00A2.xls*.

Table 6-23. Fracture Apertures in the Repository Units

UZ Model Layer	Geologic Formation	Median Aperture width
tsw33	Tptpul	0.23mm
tsw34	Tptpmn	0.098 mm
tsw35	Tptpll	0.15 mm
tsw36	Tptpln	0.16 mm

Source: DTN: LB990501233129.001 [DIRS 106787], file: *frac_prop_R00A2.xls*.

Furthermore, detailed line survey studies have been conducted by the USGS and archived in DTNs: GS990408314224.001 [DIRS 108396] and GS990408314224.002 [DIRS 105625], which contain fracture aperture data for stations 0 to 2,663 meters in the ECRB Cross Drift. These detailed line surveys are recorded fracture data along stations in the ECRB, including fracture aperture data. The fracture aperture data in DTNs: GS990408314224.001 [DIRS 108396] and DTN: GS990408314224.002 [DIRS 105625] (both minimum and maximum fracture apertures) indicate that over 60% of the fractures in Tptpul (tsw33) are closed (0 aperture), more than 80% of the fractures in Tptpmn (tsw34) are closed, more than 43% of the fractures are closed in unit Tptpll (tsw35), and more than 45% of the Tptpln (tsw36) unit fractures are closed (Table 6-24). Overall, for the entire data sets including all of the ECRB units, roughly 60% of fractures in the Cross Drift have zero aperture. The percentages were not presented in the DTNs; however, a percentage was easily deduced by summing the zero apertures fracture and dividing by the overall fractures noted in the dataset for each geologic formation. Mongano et al (1999 [DIRS 149850], Figures 16-20) also summarized the data presented in DTNs: GS990408314224.001 [DIRS 108396] and GS990408314224.002 [DIRS 105625] into five histograms and show the same percentages for the four geologic units as well as the overall ECRB, as stated above.

The fracture apertures presented in Table 6-23 are representative of the median values of the units in question and do not take into account the reported “closed” fractures or zero aperture

fractures. In light of the data on "closed" fractures presented in DTNs: GS990408314224.001 [DIRS 108396] and GS990408314224.002 [DIRS 105625], there is reason to believe that the median fracture aperture data in Table 6-23 are conservative and over-represent the median aperture spacing in the proposed repository units. Although these "closed" fractures have a high probability of transmitting water under favorable hydrologic conditions, the volume of secondary mineral phases that will be precipitated in such fractures will be insignificant relative to large (long length, aperture of at least 0.1 mm) fractures.

6.4.8.2 Fracture Spacing

Analysis of Hydrologic Properties Data (BSC 2004 [DIRS 170038]) contains fracture frequency and fracture spacing data, which are important characteristics when considering the amount of space available for secondary mineral phase precipitation within the fractures. Fracture frequency values were obtained from qualified fracture property data (DTN: LB990501233129.001 [DIRS 106787]) developed from field measurements. These include the detailed line survey fracture data (collected from the ESF North and South Ramps, Main Drift, and ECRB Cross-Drift, providing spatially varying frequency, length, and fracture dips and strikes) and fracture frequency data from boreholes. The fracture properties for a given hydrogeologic unit correspond to fractures that represent 80% of the fractures with trace lengths larger than 30 cm for that hydrogeologic unit.

The mean fracture frequency (BSC 2004 [DIRS 170038], Equation 6-2) is calculated as the inverse of the mean spacing (BSC 2004 [DIRS 170038], Equation 6-1) obtained from the detailed line surveys in the ESF and the ECRB Cross-Drift. *Analysis of Hydrologic Properties Data* (BSC 2004 [DIRS 170038], Equation 6-1) calculates the *apparent* spacing. This is not the normal distance between the fracture planes and is therefore a rough estimate of the *true* spacing. These values are not corrected for any possible bias in orientation in the detailed line survey due to a lack of fracture orientation information. Note that the detailed line surveys exclude small fractures that are considered not to connect the connective fracture networks in the large scale (i.e., site scale).

Borehole data were first processed to normalize for core recovery and corrected for orientation bias. To correct for orientation bias in vertical boreholes, dip distributions were appropriated as in *Analysis of Hydrologic Properties Data* (BSC 2004 [DIRS 170038], Equation 6-3). Because the borehole data include small fractures that are considered not to be connected to the conductive fracture networks in the large scale (i.e., site scale), the borehole fracture frequency values calculated are scaled to represent larger length fractures on the scale of those characterized in the ESF. A simple correction ratio (BSC 2004 [DIRS 170038], Equation 6-4) is used in calculating the final average fracture frequency for each model layer based on comparisons of ESF data with corresponding vertical boreholes for that model layer.

The characterization of units tsw34, tsw35, and tsw36 represented approximately 11,500 fractures from *Analysis of Hydrologic Properties Data* (BSC 2004 [DIRS 170038], Table 6-5). Table 6-24 provides the salient values for fracture spacing in these units. Note that all three main units of concern (tsw34, tsw35, and tsw36) have a fracture frequency between 3.95 and 5.40 per meter. The standard deviation in unit tsw34 is 3.42. To put this in perspective, units tsw34 and

tsw36 have fractures that are approximately 0.20 m apart on average, while unit tsw35 has the highest average fracture spacing, with fractures every 0.25 m (Table 6-24).

Table 6-24. Fracture Frequency in the Repository Units

UZ Model Layer (Geologic Formation)	Number of Fractures per Meter (80% Measured)	Number of Fractures per Meter (Calculated 100%)	Standard Deviation	Number of Samples	Average Fracture Spacing / (m)
tsw34 (Tptpmn)	4.32	5.40	3.42	10646	0.19
tsw35 (Tptpll)	3.16	3.95	NC	595	0.25
tsw36 (Tptpln)	4.02	5.03	NC	526	0.20

Source: DTN: LB0205REVUZPRP.001 [DIRS 159525], *FRACTURE_PROPERTY.xls*.

NC = Not Calculated.

6.4.8.3 Fracture Porosity

The porosity values listed in Table 6-25 summarize the relevant results from DTN: LB0205REVUZPRP.001 [DIRS 159525] (file: *fracture_property.xls*) for median values for repository units tsw34, tsw35, and tsw36.

Table 6-25. Fracture Porosity in the Repository Units

UZ Model Layer (Geologic Formation)	Median Air Porosity Test	Standard Deviation	CALC by Geologic data	CALC plus 1 cm Fracture
tsw34 (Tptpmn)	0.85%	0.25%	0.054%	
tsw35 (Tptpll)	0.96%	NC	0.081%	
tsw36 (Tptpln)	1.30%	NC	0.080%	1.06%

Source: DTN: LB0205REVUZPRP.001 [DIRS 159525].

NC = Not Calculated.

The fracture porosity reported in Table 6-25, measured with an air porosity test, measures the full void space and represents the space available for precipitation. In comparison, a scoping calculation was performed using the geologic data presented in Table 6-23 and Table 6-24 (fracture frequency) to estimate porosity. Rounding the tsw36 fracture frequency calculated value (5.03 / m) leads to 5 fractures per meter. The median aperture for unit tsw36 is 0.16 mm. If calculated on the basis of a 1 m^3 block and 1 m fractures, the following porosity is derived. The geologic data leads to an open fracture volume of 5 fractures × 0.16 mm × 1 m^2 in a 1 m^3 block, that is, 0.08% porosity. The geologic data derived porosity is within one order of magnitude of some of the measured air porosity test values. This is a reasonable scoping value, considering the following three factors. First, there are more fractures in the rock mass than taken into account in Table 6-24, namely those fractures less than 0.3 meters in length. Second, the larger fractures observed (greater than 5 mm and rarely ranging from 20 to 80 mm) in Figure 15 of the study by Mongano et al. (1999 [DIRS 149850], p. 79) were not taken into account in the scoping calculation. Third, fracture planes are not vertical and not normal to the drift and they may also be tortuous, adding more volume. Note that by substituting a single 1 cm aperture fracture for one of the 0.16 mm aperture fractures in unit tsw36 (well within the bounds of observed fractures in Mongano et al. 1999 [DIRS 149850], p. 79) scoping calculation, the newly

derived fracture porosity is 1.06%. As shown in Table 6-25, this value coincides well with the median fracture porosity determined by air tests. It is quite likely that the air tests for fracture porosity preferentially sampled the rare, larger fractures observed in the ECRB survey.

To summarize, the three potential contributing factors considered for the fracture porosity variance (one order of magnitude difference) are as follows. Factor number one, small thin fractures have been observed (for example, Mongano et al. 1999 [DIRS 149850]; BSC 2004 [DIRS 170038]), though their exact dimensions have not been documented. Factor number three, fractures that are non-vertical, non-normal to the drift, and perhaps tortuous, also have not been characterized fully in the field as to added volume. Even though both factors have been recognized in the drifts and ECRB, because there is a lack of documented field values, these factors will not be considered. The second factor, rare large aperture fractures (which have been documented Mongano, et al. 1999, figure 15), are most probably randomly mixed with the median aperture fractures as presented in Table 6-23. When one large fracture (1 cm aperture) was substituted into the scoping calculation above, the geologic data fracture porosity mimics the air test fracture porosity. This factor (some small aperture fractures (0.16 mm each) and one relatively large aperture fracture (1 cm) per meter of tuff is the most reasonable (and geologically substantiated) model for fracture apertures and therefore fracture porosity. Therefore, to provide conservatively large median fracture porosities, the air flow porosity test values quoted in Table 6-25would provide sufficiently high porosity values.

6.4.8.4 Lithophysal Porosity

Lithophysae vary in size from a fraction of a cm to over 0.7 m in horizontal dimension within the tuff tsw35 unit (average diameter is about 21.7cm) (DTN: GS980308315215.008, [DIRS 107355]). The lithophysal porosity in unit tsw35, as obtained from *Drift Degradation Analysis* (BSC 2004, [DIRS 166107] Appendix O, Table O-10, [cavities, fitted value]), is portrayed in Table 6-26. It should be noted that the lithophysae that are unfilled add porosity to the tuff.

Table 6-26. Lithophysal Porosity in Unit tsw35

UZ Model Layer (Geologic Formation)	Minimum	Median	Maximum	Std Dev.
tsw35 (Tptpll)	4.0 %	12.9%	29.2%	5.3

Source: BSC 2004 [DIRS 166107] Appendix O, Table O-10 (cavities, fitted value).

For lithophysae to be available for accumulation of fissile material, the lithophysae must be connected to fractures that could transport flow. Of particular interest is the statement in *Drift Degradation Analysis* (BSC 2004 [DIRS 166107], p. 6-15) that "the Tptpll (lower lithophysal zone)… shows few fractures that actually intersect the lithophysae." This may in part be due to the tight interlocking fabric of the quartz and feldspar rim material in the lithophysae (Byers and Moore 1987 [DIRS 101321], Figure 12d, p. 32) causing fractures to deflect around the cavities. Barr et al. (1996 [DIRS 100029], p. 118) describe such fractures refracting around and between lithophysal cavities. Barr et al. (1996 [DIRS 100029], p. 118) also state that "In many locations, fractures cut across lithophysal cavities," and that fractures terminating in such cavities are commonly coated with vapor phase minerals. The authors go on to state that since there are also concentric fractures around many cavities that the features suggest that the formation of

lithophysal cavities induced fracturing. The work of Barr et al. (1996 [DIRS 100029]) describes two types of fracture systems: (1) those fractures (lined by vapor phase minerals) induced by vapor phase created lithophysal cavities when the vapor phase gases exceed lithostatic pressure, and (2) subsequent tectonic fractures which refract around lithophysal cavities. Therefore, an unknown percentage of the lithophysal porosity listed in Table 6-26 is likely to be unavailable for accumulation due to the lack of fractures intersecting the cavities. However, in the absence of more accurate values, the values listed in Table 6-26 can be used as an upper limit on the lithophysae porosity available for fissile accumulation.

6.4.8.5 Lithophysae Fill Depth

Filling lithophysae is one potential mechanism for accumulating actinide secondary mineral phases to the necessary mass and geometry for criticality. Theoretically, the best geometry for actinide material to produce a critical mass is a sphere (Lamarsh 1983 [DIRS 149069]). To investigate the possibility that lithophysae could provide such a void space in the repository units, a review of the ECRB Cross Drift data was undertaken. Even though the mechanisms involved in the historical precipitation of calcite and opal in the lithophysal cavities (depressurization of high SiO_2-fCO_2 fluids), would be different from the mechanisms involved in the external accumulation model (mixing of solutions resulting in precipitation and adsorption), the existing infill quantities can be used as estimates of possible accumulation volumes.

Mongano et al (1999 [DIRS 149850]) provided an exhaustive study of lithophysae shapes and infill by secondary mineral phases. A total of 274 samples were measured and recorded for secondary fill material. Primarily, calcite thicknesses deposited in lithophysae were recorded in the ECRB study; minor opal was also observed. As shown in DTN: GS980308315215.008 [DIRS 107355], the median fill depth in the lithophysae was 0.4 cm and was commonly deposited along the bottom of the lithophysal cavity. In fact, 87.5 percent of all the fill depths in lithophysal cavities were less than 0.6 cm. None of the void spaces were filled entirely; the highest fill ratio observed was less than one-half filled (sample # 201). The maximum fill depth for a lithophysae was 2.5 cm (sample # 35), but the dimensions of that lithophysae were 18 cm high by 20 cm wide.

Although large, spherical lithophysae may be capable of creating conditions favorable to a criticality event (Lamarsh 1983 [DIRS 149069]), evidence from the ECRB Cross Drift does not indicate that would happen. From the detailed mapping of the ECRB, it is shown that most of the lithophysae were only minimally filled (averaging 0.4 cm depth) with secondary phases (calcite, opal) over a 12 million year period. In addition, the lithophysae with secondary phases form as shallow discs (or hemispheres) in the bottom of the voids rather than as spheres. In the unlikely event that fissile material did precipitate in the lithophysae, the fissile minerals would precipitate along with other non-fissile minerals as described in Section 6.4.5.6.

6.4.8.6 Matrix Properties

The proposed repository units of concern (tsw34-36) were investigated to determine both matrix porosity and permeability characteristics. The results are presented in *Analysis of Hydrologic Properties Data* (BSC 2004 [DIRS 170038]).

Matrix porosity was measured in core samples from the unsaturated zone (UZ). Porosity was determined after drying samples in a 105°C oven for at least 48 hours to obtain a standard dry weight (Flint 1988 [DIRS 100033], p.17). According to Flint (1988 [DIRS 100033], pp. 17 and 18), porosity is considered a normally distributed quantity, so the arithmetic mean of core measurements and standard deviation were used to characterize the porosity for a model layer. Matrix porosity values for the units in question range from approximately 10 to 13% and are presented in Table 6-27. These values are relatively low with respect to other rock units within Yucca Mountain (BSC 2004 [DIRS 170038], Table 6-6).

Table 6-27. Matrix Porosity and Residual Porosity in the Repository Units

UZ Model Layer (Geologic Formation, Hydro Unit)	Matrix Porosity, Mean	Matrix Porosity, Standard Deviation	Residual Saturation
tsw34 (Tptpmn,TMN)	11.1%	2.0%	19%
tsw35 (Tptpll, TLL)	13.1%	3.1%	12%
tsw36 (Tptpln, TM2)	10.3%	2.5%	18%

Source: DTN: LB0207REVUZPRP.002 [DIRS 159672]

Matrix permeability was measured on core samples from several boreholes at Yucca Mountain. Measurements are available for all units in the unsaturated zone (BSC 2004 [DIRS 170038], Table 6-6). Two different methods were used to measure permeability, with the detection limit of the first higher than the second. Most of the samples were tested using the first method; the second was used to test some new samples and retest some old samples originally tested using the first method, including some with permeabilities too low to measure (nondetect results). When the same sample was tested with both methods, the permeability measured on the one with the lower detection limit was used since it was expected to result in a more precise measurement.

The measured data was presented in terms of saturated hydraulic conductivity (m/s), K, which is converted to permeability (m^2), k, by the following relationship (BSC 2004 [DIRS 170038], Equation 6-27):

$$k = \frac{K\mu_w}{g\rho_w}$$

where μ_w is the viscosity of water (0.001 N s/m), g is the acceleration of gravity (9.81 m/s^2) and ρ_w is the density of water (998 kg/m^3). These parameter values correspond to a temperature of 25°C (room temperature at which the hydraulic conductivities were measured) (Lide 2002 [DIRS 160832], p.6-3). Permeability is a lognormally distributed quantity (Gelhar 1993 [DIRS 101388]). Therefore, the geometric mean was used to estimate the average permeability of each unit. The matrix permeability values for the three units of interest range from 3.7×10^{-17} to 2.3×10^{-20} m^2 and are listed in Table 6-28. Such permeability values are extremely low and would limit the extent of diffusion into the tuff matrix. Therefore, the potential for secondary phases to precipitate in the matrix is low. However, as a bounding case, precipitation in the matrix should be included along with precipitation in the fractures.

Table 6-28. Matrix Permeability in the Repository Units

UZ Model Layer (Geologic Formation, Hydro Unit)	Mean Upscaled k (m^2)	Number of Samples Tested
tsw34 (Tptpmn,TMN)	4.5E-19	74
tsw35 (Tptpll, TLL)	3.7E-17	51
tsw36 (Tptpln, TM2)	2.3E-20	21

Source: DTN: LB0207REVUZPRP.002 [DIRS 159672].

Physical evidence of the low permeability in the tuffs is observed in the study by Vaniman (1993 [DIRS 142216], Appendix 9). The microphotograph depicts coarse-grained calcite filling a fracture in borehole USW-G3 at a depth of 358 m. The calcite does not cross the boundary into the tuff matrix.

The calculation of the matrix permeability standard deviation is presented in Section 6.2.1 of *Analysis of Hydrologic Properties Data* (BSC 2004 [DIRS 170038]). The analysis considers the rock as a highly heterogeneous porous media, and takes into account the number of nondetect measurements *Analysis of Hydrologic Properties Data* (BSC 2004 [DIRS 170038], Eq. 6-38). However the authors do not take into consideration the existence of fractures, which may act as a capillary barrier that can increase tortuosity of liquid water flow in the matrix and therefore reduce the effective permeability compared to the case without fractures. To account for this, the upscaling (standard deviation) for unit tsw36 is capped at 1.5 orders of magnitude. For the other two units (tsw34 and tsw35) the upscaling is less than 1.5 orders of magnitude. Such upscaling of the matrix permeability values would still result in rock matrices with low permeability.

6.4.8.7 Fracture System Modeling Results

As one can see from the results of data presented in Sections 6.3.1 (fracture aperture) and 6.3.3 (fracture spacing), very little fissionable material can accumulate in units tsw34 – tsw36. With fracture apertures ranging from 0.16 mm to 0.98 mm (DTN: LB990501233129.001 [DIRS 106787]) and fracture spacing ranging from 0.25 m to 0.32 m in (BSC 2004 [DIRS 170038], Table 6-5) per fracture (0.3 m or longer), what little material can accumulate will be in thin vertical sheets bounded by thick plates of ash flow tuff. For a combination of fractures and small lithophysae filled with fissionable material, very few lithophysae were actually observed to be intersected by fractures (BSC 2004 [DIRS 166107], p. 6-15). This is due in part to the fracture spacing (Section 3.3.3), but also due to the extremely tough outer rind of microcrystalline material (quartz and feldspar) on the lithophysae (Byers and Moore 1987 [DIRS 101321]). Therefore, this conceptual model allows very little additional accumulation of fissionable material. Finally, larger lithophysae were averaging only 21.7 cm in width and had an average fill depth of 0.4 cm (DTN: GS980308315215.008 [DIRS 107355).

6.5 BOTTOM FAILURE AND SOLID RELEASE FOR ALL SCENARIOS

The mass of corrosion products that formed in the waste package, as a result of EQ6 calculations (see input files listed in Table 4-6, files: CSNF_Nominal.6i, CS-S-Mx-C5_adEH and CSNFIG1.6i), were extracted and tabulated in Table 6-29, Table 6-30, and Table 6-31 for time=0 and for the first EQ6 result for time after 10,000 years. For the igneous scenario (CSNFIG1.6i), the initial conditions (time=0) represent the beginning of the second stage of the igneous simulation. In the first stage, the CSNF was oxidized to schoepite and other minor minerals, as shown in Table 6-31 at time=0. The second stage exposes the remainder of the waste package contents to corrosion. The mass of corrosion products at the final time in Tables 6-29 through 6-31 represents the mass of material that could flow out of the waste package as a slurry if the bottom of the waste package failed due to corrosion.

Once the slurry is released from the waste package, the final geometry of the material would be determined by the extent of horizontal spreading on top of the invert and the extent of penetration into the invert. The horizontal spreading could range from low to high; where, low spreading results in a fairly compact mound on top of the invert and high spreading results in a thin layer of material spread over a large area on top of the invert. The extent of penetration could also range from low to high; where, low penetration would result in very little penetration of the slurry material in the invert and high penetration would result in the slurry filling the voids of the invert.

Table 6-29. Nominal Scenario, CSNF Waste Package (EQ6 run CSNF_Nominal.6i)

Component	Time (Years)	
	0	**15,524**
A516, kg	5,600	0
NiGd, kg	2,394	1992
Al_6061, kg	438	285
316 , kg	10,720	10717
CSNF_35at40_10K , kg	11,045	9746
Anatase (TiO_2), kg	0	0
$(UO_2)_3(PO_4)_2$:$4H_2O$,kg	0	3
Barite ($BaSO_4$),kg	0	3
Co_2SiO_4,kg	0	5
Eskolaite (Cr_2O_3),kg	0	31
$Fe_2(MoO_4)_3$, kg	0	39
$GdPO_4$:xH_2O, kg	0	25
Gibbsite ($Al(OH)_3$), kg	0	345
Goethite(FeOOH), kg	0	8492
Nontronite-Na ($Na_2(Fe,Al)_2(Si,Al)_4O_{10}(OH)_2$ nH_2O), kg	0	67
NpO_2, kg	0	3
PuO_2(OH)2:H_2O, kg	0	11
Pyrolusite (MnO_2), kg	0	93
RuO_2, kg	0	3
Schoepite(UO_3:$2H_2O$), kg	0	1399
Trevorite ($NiFe_2O_4$), kg	0	323

Table 6-29. Nominal Scenario, CSNF Waste Package (EQ6 run CSNF_Nominal.6i) (Continued)

Component	Time (Years)	
Total reactants and fuel remaining, kg	30,197	22,740
Corrosion products formed, kg	0	10,841
Total solids (remaining reactants, fuel, and formed minerals), kg	30,197	33,581

Source: For t=0, the source is DTN: MO0608MWDGEOMA.001 [DIRS 177332], /Spreadsheets/*CSNF WP.xls*; for t=15,524 years, see Output DTN: MO0608SPASOLID.002, file: *bfailf2.xls*.

Table 6-30. Seismic Scenario, CSNF Waste Package (EQ6 run CS-S-Mx-C5_adEH)

Component	Time (years)	
	0	**20,137**
A516, kg	5,600	0
NiGd, kg	2,394	1,649
Al_6061, kg	438	0
316, kg	10,720	0
CSNF_35at40_10K, kg	11,045	0
Anatase (TiO_2), kg	0	1
Chalcedony (SiO_2), kg	0	0
Barite ($BaSO_4$), kg	0	26
Co_2SiO_4, kg	0	20
Eskolaite (Cr_2O_3), kg	0	2,879
$Fe_2(MoO_4)_3$, kg	0	630
$GdPO_4$:$10H_2O$, kg	0	97
Gibbsite ($Al(OH)_3$), kg	0	1,210
Goethite (FeOOH), kg	0	14,734
Nontronite-Mg($Mg(Fe,Al)_2(Si,Al)_4O10(OH)_2$ nH_2O), kg	0	381
NpO_2, kg	0	27
Powellite ($CaMoO_4$), kg	0	2
$PuO_2(OH)_2$:H_2O, kg	0	82
Pyrolusite (MnO_2), kg	0	445
RuO_2, kg	0	29
Schoepite (UO_3:$2H_2O$), kg	0	12,881
Trevorite ($NiFe_2O_4$), kg	0	6,671
Total reactants and fuel remaining, kg	30,197	1,649
Corrosion products formed, kg	0	40,115
Total solids (remaining reactants, fuel, and formed minerals), kg	30,197	41,764

Source: For t=0, the source is DTN: MO0608MWDGEOMA.001 [DIRS 177332], /Spreadsheets/*CSNF WP.xls*; for t=20,137 years, see Output DTN: MO0608SPASOLID.002, file: *bfailf2.xls*.

Table 6-31. Igneous Scenario, CSNF Waste Package (EQ6 run CSNFIG1.6i)

Components	Time (Years)	
	0	12,764
A516 Mass, kg	5,600	0
NiGd Mass, kg	2,394	1,854
Al_6061 Mass, kg	438	0
316 Mass, kg	10,720	0
BaU_2O_7, kg	9	0
$CsTcO_4$, kg	4	0
$Gd_2(CO_3)_3$,kg	96	0
NpO_2, kg	27	27
$PuO_2(OH)_2:H_2O$, kg	98	97
RuO_2, kg	29	29
Schoepite ($UO_3:2H_2O$), kg	12,872	12,871
Anatase (TiO_2), kg	0	1
$(UO_2)_3(PO_4)_2:4H_2O$, kg	0	10
Barite ($BaSO_4$), kg	0	24
Co_2SiO_4, kg	0	13
Eskolaite (Cr_2O_3), kg	0	2,831
$Fe_2(MoO_4)_3$, kg	0	628
$GdPO_4:xH_2O$, kg	0	143
Gibbsite ($Al(OH)_3$),kg	0	1,210
Goethite (FeOOH), kg	0	15,139
Nontronite-Mg ($Mg(Fe,Al)_2(Si,Al)_4O_{10}(OH)_2 : nH_2O$),kg	0	359
Nontronite-Na ($Na_2(Fe,Al)_2(Si,Al)_4O_{10}(OH)_2 : nH_2O$),kg	0	51
Pyrolusite (MnO_2), kg	0	444
Trevorite ($NiFe_2O_4$), kg	0	6,134
Total reactants and minerals formed from oxidized fuel, remaining, kg	32,287	14,879
Corrosion products formed, kg	0	26,988
Total solids (remaining reactants, remaining minerals from oxidized fuel, and formed minerals), kg	32,287	41,867

Source: For t=0, the source of mass of reactants (A516, NiGd, Al_6061 and 316) is DTN: MO0608MWDGEOMA.001 [DIRS 177332], /Spreadsheets/*CSNF WP.xls*; for t=0 mass of minerals and all masses for t=12,764 years, see Output DTN: MO0608SPASOLID.002, file: *bfailf2.xls*.

6.6 SEISMIC SCENARIO—ENTRAINED RELEASES

In the seismic scenario, the mass transfer model (BSC 2004 [DIRS 172624]) was implemented in *Geochemistry Model Validation Report: Material Degradation and Release Model* (BSC 2006 [DIRS 176911], Section 6.2.2.2.2). The mass transfer model evaluates the loss of insoluble materials from the waste package due to entrainment transport in a fully flooded (bathtub) configuration. In a bathtub configuration, one mechanism that could lead to the necessary upward flow to cause entrainment losses is convective mixing from temperature gradients in the waste package (BSC 2006 [DIRS 176911], Section 6.2.2.2.2). The entrained solids exit the waste package at a rate depending on the flow velocity of water through the waste package.

Table 4-5 lists the entrainment percentages for major minerals that are formed during EQ6 degradation calculations in *Geochemistry Model Validation Report: Material Degradation and Release Model* (BSC 2006 [DIRS 176911]). To determine the entrained releases from the waste package, the entrainment percentages listed in Table 4-5 were multiplied by the masses of corrosion products present in the waste package at 20,000 years, as listed in Table 6-30. The entrained releases listed in Table 6-32 only apply to the bathtub scenario in which a bottom failure has not occurred.

Two scenarios are presented here to explain the entrainment of the solids from the waste packages into the invert. In the first scenario, effluent from the waste package encounters unsaturated materials on the invert floor. The entrained solids remain on the surface and water will seep through. The accumulated solids most likely will be shaped as a mound on top of the invert with only residual saturation water. In the second scenario, the effluent from the waste package encounters portions of the invert surface where draining through is slower than the effluent coming out of the waste package. In this case the effluent will pool until it finds a drain path, resulting in dispersion of entrained solids on the surface of the invert.

Table 6-32. Release of Major Minerals by Entrainment Process at 20,137 Years, Seismic Scenario, CSNF Waste Package (EQ6 run CS-S-Mx-C5_adEH), Bathtub Configuration

	Masses of Major Minerals Entrained (kg)						
	Flow Rate, q (L/yr)						
Minerals	1	5	10	15	50	100	150
Gibbsite ($Al(OH)_3$)	0	6	19	29	74	114	145
Goethite (FeOOH)	0	0	44	126	494	826	1078
Schoepite ($UO_3:2H_2O$)	0	0	12	79	374	642	845
Pyrolusite (MnO_2)	0	0	0	2	12	21	28
Trevorite ($NiFe_2O_4$)	0	0	1	34	182	316	417
Eskolaite (Cr_2O_3)	0	0	0	14	77	135	178
$Fe_2(MoO_4)_3$	0	0	1	5	20	34	44

Output DTN: MO0608SPASOLID.002, file: *ent_rel_bathtub.xls*.

6.7 ALTERNATIVE CONCEPTUAL MODELS

The *Disposal Criticality Analysis Methodology Topical Report* (YMP 2003 [DIRS 165505], Section 3.3.2) lists nine external criticality configuration classes to be addressed by criticality analyses. The nine classes are listed in Section 8.2.2. Two of the classes (Section 8.2.2, items (1) and (7)), that address accumulation in a reducing zone and accumulation in the saturated zone, are not covered in the external accumulation model. The next two sections discuss those methods of accumulation as alternative conceptual models.

6.7.1 Accumulation in Reducing Zone

In a previous document (CRWMS M&O 2000 [DIRS 135790]), a reducing zone in the invert resulted in uranium and plutonium accumulation. The assumptions were that fully oxidizing conditions existed inside the waste package, but that the iron oxide in the invert (gantry rail, etc.) was not fully oxidized and caused a local reducing zone. This is highly unlikely. The conditions outside of the waste package are expected to be oxidizing. If water is available to get inside the

waste package and cause corrosion, then water would be available outside the waste package to corrode the steel in the invert. Even if the steel was not totally converted from metal to an iron-oxide mineral, the oxidized layer on the outside surface of the steel would prevent unoxidized metal from being available to contact water exiting the waste package.

6.7.2 Accumulation in Saturated Zone

For accumulation in the saturated zone to be a criticality concern, a concentrated plume of plutonium or uranium would need to intercept a reducing zone at the water table. Reducing groundwaters have been detected in saturated zone waters in the Yucca Mountain area (BSC 2004 [DIRS 170036], Appendix F); however, the likelihood of a concentrated plume reaching the water table (depth approximately 1 km) is very low. As the source term fluids exit the waste package and flow through the invert and the unsaturated zone, many processes work to spread out the radionuclide plume. Diffusion and dispersion cause the contaminated zone to spread out. Adsorption causes material to be deposited along the travel path. Resident water present in the unsaturated zone provides a source of dilution as the plume moves toward the water table. By the time the radionuclide plume reaches the water table, it would be dispersed and the density of accumulation would be lower than the accumulation in the unsaturated zone. Therefore, accumulation in the saturated zone is not covered in this report as a separate model, because accumulation in the saturated zone is less likely to cause a criticality concern than accumulation in the unsaturated zone and invert. If downstream users of this report determine that criticality can occur in the unsaturated zone or invert, then accumulation in the saturated zone will need to be modeled.

6.8 SENSITIVITY ANALYSES

6.8.1 Sensitivity Analyses by Modification of Input Parameters

The following inputs parameters were evaluated for uncertainties:

- Composition of seepage water entering the drift. For the Seismic Scenario a pore water from SD-9 was chosen. This potential seepage water is from the unit Tptpll, at a depth of 990.4 to 991.7 feet (DTN: GS020408312272.003 [DIRS 160899]). The use of a different pore water or well water (J-13) with a different starting chemistry may impact the resulting accumulation in the invert.

- The log K values from the PHREEQC thermodynamic database. The log K is the log of the equilibrium constant of chemical reaction. A mineral dissolution reaction log K is a function of temperature. All of the PHREEQC simulations were conducted at 25°C. However, there is a standard deviation associated with measurements or estimates of each log K value that is not taken into consideration. The log K value for uranophane and the log K for boltwoodite-Na were modified by the standard deviation to see the impact on the resulting accumulation.

6.8.1.1 Variation of the Composition of Seepage Water Entering the Drift

The water chosen as the mixing water for the seismic run for CSFlux9 is a pore water extracted from the tuff at the repository horizon from unit Tptpll in borehole SD-9 at a depth of 990.4 to 991.7 feet (DTN: GS020408312272.003 [DIRS 160899]). The Tptpll is the major repository host rock unit and thus a good choice for representing mixing water in the invert. A PHREEQC sensitivity simulation was conducted for the CSFlux9 waste package to see the change when the mixing water was changed from the SD-9 pore water to a J-13 well water from DTN: MO0006J13WTRCM.000 [DIRS 151029]. The pore water simulation yielded uranium accumulation of 942.03 moles, and the J-13 well water yielded uranium accumulation of 858.05 moles. Thus, there is 9% less accumulation of uranium in using J-13 well water compared to SD-9 pore water as the mixing water. The starting chemistries of both the SD-9 pore water and the J-13 well water as included in the PHREEQC input files are presented in Table 6-33.

Table 6-33. Compositions of Mixing Waters, SD-9 Pore Water and J-13 Well Water

Pore Water from SD-9[a]		J-13 Water[b]	
Constituent	**Composition (mol/kgw)**	**Constituent**	**Composition (mol/kgw)**
pH	7.9 (standard units)	pH	7.41(standard units)
Ca	1.40E-03	Ca	3.24E-04
Mg	3.70E-05	Mg	8.27E-05
Na	3.65E-03	Na	1.99E-03
K	2.02E-04	K	1.29E-04
Cl	6.49E-04	Cl	2.01E-04
S	1.04E-04	S	1.92E-04
C	5.13E-03	N(5)	1.42E-04
N(5)	2.74E-04	F	1.15E-04
F	1.32E-04	Si	1.01E-03
Si	8.32E-04		
Mn	3.82E-07		
Mo	2.29E-07		
U	1.39E-07		

[a] From DTN: GS020408312272.003 [DIRS 160899], sample SD-9/990.4-991.7/UC.
[b] From DTN: MO0006J13WTRCM.000 [DIRS 151029].

NOTE: Both sources were converted to units mol/kgw. Both sources provided compositions of S as sulfate and N as nitrate.

The differing solute concentrations and pH values of 7.9 and 7.41 for the SD-9 pore water and J-13 well water, respectively, influenced the uranium accumulation. The total-U, ^{235}U, and ^{239}Pu accumulation for both the SD-9 pore water and the J-13 well water are presented in Table 6-34.

Table 6-34. Total Uranium and Plutonium Accumulated for Source Term CSFlux9, Seismic Scenario, Flow at 1,000 L/yr, Method: Separate Simulations Using Two Separate Mixing Waters, Pore Water SD-9 and J-13 Water

Details	Uranium Accumulation (moles)	^{235}U Accumulation (moles)	Uranium Adsorbed (moles)	Plutonium Accumulation (moles)	Plutonium Adsorbed (moles)
Original Mixing Water SD-9[a]	942.03	10.47	7.51E-04	0.00	5.11E-07
Sensitivity Mixing Water J-13[b]	858.5	9.54	7.77E-04	0.00	5.11E-07

[a] For SD-9 mixing water data, Output DTN: MO0609SPAINOUT.002, path: CSFlux9/CSFlux_Acc_with_decay/*CSFlux9_Acc_with_decay.xls* for accumulation; file *adsorption_calc.xls* for adsorption.
[b] For J-13 mixing water data, Output DTN: MO0609SPASENSI.003, path: CSFlux9_J-13/CSFlux__J-13_Acc_with_decay/*CSFlux9_J-13_ Acc_with_decay.xls* for accumulation; file *sens_adsorption_calc.xls* for adsorption.

6.8.1.2 Variation of the Values of log K for Uranium Minerals Uranophane and Boltwoodite-Na

Equilibrium thermodynamic-based geochemical codes like PHREEQC use log K to access the position of equilibrium for specific chemical reactions at specific conditions. In most cases, the uncertainty for the log K values is not reported in the databases. In order to evaluate the effects of log K uncertainty on precipitation and accumulation of uranium minerals, the log K's for uranophane and boltwoodite-Na were modified by the standard deviation. The log K values for uranophane and boltwoodite-Na are presented in Table 6-36. The log K value used in the PHREEQC thermodynamic database was previously qualified for the EQ 3/6 data0 databases in *Qualification of Thermodynamic Data for Geochemical Modeling of Mineral-Water Interactions in Dilute Systems* (BSC 2004 [DIRS 171916]). As discussed in Section 4.1.1, the EQ 3/6 data0.ymp.R4 database was translated for use in PHREEQC and presented in DTN: MO0604SPAPHR25.001 [DIRS 176868]. The sources of this log K value (Pérez et al. 2000 [DIRS 157910]; Nguyen et al. 1992 [DIRS 100809]) were also justified for intended use in this model in Section 4.1.14.3.

Table 6-35. Log K values for Uranophane and Boltwoodite-Na

Mineral	Source	Temperature C	log K value
Uranophane	Pérez et al. 2000 [DIRS 157910], p. 606	25	11.7 ± 0.6
Boltwoodite-Na	Nguyen et al. 1992 [DIRS 100809], Table 6, p. 374	30	5.82 ± 0.16

For the source terms CSFlux9 and FFTFIG1adEhdec, source term sensitivity simulations were done by changing the log K by ± the standard deviation for uranophane and boltwoodite-Na, respectively. The input files were modified to override the log K value in the PHREEQC thermodynamic database. The results of these simulations are presented in Tables 6-37 and 6-38. By changing the log K value of boltwoodite-Na by adding and substracting one standard deviation, which is 2.7% of the log K, the accumulation either decreased by 10% or increased by 17%. By changing the log K value of uranophane by the standard deviation (both up and down),

which is 5% of the log K, the accumulation either decreased by 24% or increased by 13%. The overall findings were that varying the log K value by the standard deviation did not impact the type of minerals that formed, but it did impact the amount of uranium accumulation.

Table 6-36. Comparison of Uranium Accumulation for CSFlux9 Source Term in the Invert with Changes in log K for Uranophane by Standard Deviation

Details	Uranophane log K Value	Total Uranium Accumulation (moles)	Moles of Uranium Adsorbed	Percentage Difference from Original Value of Total Uranium Accumulation
Original case	11.6981	942.03	7.51E-04	N/A
+0.6 (standard deviation)	12.2981	718.49	1.13E-03	−23.7%
−0.6 (standard deviation)	11.0981	1066.04	4.86E-04	+13.2%

Source: For original case, Output DTN: MO0609SPAINOUT.002, path: CSFlux9/CSFlux9_Acc_with_decay/*CSFlux9_Acc_with_decay.xls* for accumulation; file *adsorption_calc.xls* for adsorption.

For +0.6 sensitivity case, Output DTN: MO0609SPASENSI.003, path CSFlux9_logK_sens_12.2981/CSFlux9_logK_sens_12.2981_Acc_with_decay/ *CSFlux9_Acc_with_decay_logK_12.2981.zip* for accumulation; file *sens_adsorption_calc.xls* for adsorption. For −0.6 sensitivity case, follow similar path.

Table 6-37. Comparison of Uranium Accumulation for FFTFIG1adEhdec Source Term in the Invert with Changes in log K for Boltwoodite-Na by Standard Deviation

Details	Boltwoodite-Na, log K value	Uranium Accumulation (moles)	Moles of Uranium Adsorbed	Percentage Difference from Original Value
Original case	5.9649	31.17	3.56E+01	N/A
+0.16 (standard deviation)	6.1249	28.10	3.57e+01	−9.9%
−0.16 (standard deviation)	5.8049	36.53	3.53E+01	+17.2%

Source: For original case, Output DTN: MO0609SPAINOUT.002, path: FFTFIG1adEhdec / FFTFIG1adEhdec_Acc_with_decay/ *FFTFIG1adEhdec_Acc_with_decay.xls* for accumulation; file *adsorption_calc.xls* for adsorption.

For +0.16 sensitivity case, Output DTN: MO0609SPASENSI.003, path FFTFIG1adEhdec_logK_sens_6.1249/ FFTFIG1adEhdec_logK_sens_6.1249_Acc_with_decay/ *FFTFIG1adEhdec_logK_sens_6.1249_Acc_with_decay.zip* for accumulation; file *sens_adsorption_calc.xls* for adsorption. For −0.16 sensitivity case, follow similar path.

INTENTIONALLY LEFT BLANK

7. VALIDATION

The purpose of the external accumulation model is to estimate the quantity and geometry of the accumulation of fissile and non-fissile isotopes and corrosion products in the invert (near-field) and the surrounding fractured tuff (far-field) external to the waste package from a degrading waste package. The technical work plan (BSC 2006 [DIRS 177153], Section 2.2.1) states that validation will include a discussion of decisions and activities that were implemented during the model development process (Section 7.1) and post-development validation of the model will consist of four methods (Methods A through D), see Section 7.2. The first validation activity, Method A, is an independent model validation technical review of the entire model. The remaining validation activities address portions of the model. Method B compares the PHREEQC simulation estimates to the minerals observed in natural analogues and laboratory experiments. Method C uses the PHREEQC external accumulation model to estimate the accumulation of uranyl minerals observed in UO_2 degradation drip tests. Method D is a validation of the two-dimensional numerical flow and transport model by corroboration of model results with the results from a two-dimensional analytical model.

7.1 DOCUMENTED DECISIONS AND ACTIVITIES IMPLEMENTED DURING MODEL DEVELOPMENT PROCESS

The technical work plan (BSC 2006 [DIRS 177153], Section 2.2.1) indicates that the external accumulation model requires a low level of confidence (Level I) because the model is of limited or no importance to the calculation of mean annual dose.

Achieving Level I criteria requires discussion of documented decisions and activities that are implemented during the model development process that build confidence and verify that a reasonable, credible technical approach using scientific and engineering principles was taken.

The following items describe how Level I criteria have been satisfied during the model development efforts:

(a) *Evaluate and select input parameters and/or data*: Section 4.1 provides the inputs used in the external accumulation model, which include thermodynamic databases, mixing water and source water compositions, solid losses from the waste package, isotopic content of waste forms, flow rates, tuff composition, dissolution rates for tuff minerals, invert properties, adsorption coefficients, characteristics of fractures, and atomic weights. .

(b) *Formulate defensible assumptions and simplifications*: Assumptions that were necessary were included in Section 5. Modeling assumptions and simplifications are described in Sections 6.1, 6.2, and 6.4. All model assumptions and simplifications have been justified as reasonable or captured within the uncertainty of the model.

(c) *Ensure consistency with physical principles, such as conservation of mass, energy, and momentum*: All modeling efforts described in Sections 6.4.5 and 6.4.6 are based on conservation of mass. Both codes, PHREEQC and TOUGHREACT, are qualified and are consistent with conservation of mass.

(d) *Represent important future state (aleatoric), parameter, and alternative model uncertainties*: Future state conditions are addressed by modeling igneous events in which the drift is filled with basalt, resulting in a basalt-equilibrated mixing water. A range of flow rates (1 to 1000 L/yr) to represent future climates that may have a higher infiltration rate than today's climate. Uncertainties in seepage water composition and equilibrium constants are addressed in Section 6.8.1. Alternative model uncertainties that address the dissolution of minerals during the PHREEQC simulations are addressed in Section 6.8.2. Alternative models that address accumulation in a reducing zone and in the saturated zone are discussed and discounted in Section 6.7.

(e) *Ensure simulation conditions have been set up to span the range of intended use and the avoidance of inconsistent outputs*: The types and ranges of inputs described in Sections 4.1, 6.2, and 6.7 were developed to address the external accumulation mechanisms identified in *Disposal Criticality Analysis Methodology Topical Report* (YMP 2003 [DIRS 165505]). These mechanisms include accumulation due to precipitation, adsorption, mass loss due to bottom failure and entrained solids, and accumulation in a reducing zone or saturated zone.

(f) *Ensure that model predictions (performance parameters) adequately represent the range of possible outcomes, consistent with important uncertainties*: The important uncertainties equilibrium constant (log K), mixing water compositions, and mineral dissolution) are discussed in Section 6.8. The results presented in Section 8.1 incorporate the uncertainties.

7.1.1 Corroboration of PHREEQC and EQ3/6 Model Outputs

The mathematical calculations of the external accumulation process model are performed using PHREEQC. As a validation exercise to build confidence in the ability of PHREEQC to execute the mathematical model, two base case simulations were performed using comparable geochemical software, EQ3/6 V8.1 (see Section 3.1.8).

EQ3/6 V8.1 has many of the same features as PHREEQC, including capabilities for kinetic processes, mixing reactions, and flow of water through a cell. EQ3/6 was developed at Lawrence Livermore National Laboratories and is qualified for use on the Yucca Mountain Project. It was chosen for the validation because most of the processes simulated by the PHREEQC external accumulation model can be simulated using EQ3/6. One difference between the codes relevant to the model is that EQ3/6 cannot easily simulate advection through a multi-cell column. Instead, sequential EQ3/6 simulations are required to model each cell. Transfer of information from one cell to the next is not automatic in EQ3/6. Consequently, the EQ3/6 validation is limited to the first three cells, which is a minimum number of cells that still results in a thorough code-to-code comparison of PHREEQC and EQ3/6. Another difference between the software is that EQ3/6 cannot simulate adsorption. The adsorption aspect of the PHREEQC model, however, is easily checked by hand, and therefore separate software is not needed for corroboration of predicted adsorbed concentrations.

The treatment of pH and activities at high ionic strength is another difference between the codes. Although the B-dot equation is used by each code in this validation, the activity coefficients and

pH diverge as ionic strength increases above 0.1 molal. The divergence could be due to differences in pH scaling conventions. EQ3/6 offers three choices for pH scales: (1) no rescaling ("internal"); (2) National Bureau of Standards (Bates-Guggenheim equation); and (3) Mesmer (molality equals activity) scales. The National Bureau of Standards (NBS) scale is typically used in EQ3/6 calculations on the Yucca Mountain Project and is used in this validation. The treatment of pH and activities at high ionic strength is another difference between the codes. Although the B-dot equation is used by each code in this validation, the activity coefficients and pH diverge as ionic strength increases above 0.1 molal. This divergence is addressed in Section 7.1.1.3.2.

The EQ3/6 simulation in this section uses the fluid mixing approach because the solid-centered flow-through mode of EQ6 cannot be forced to perform a complete displacement (full flush) prior to its first equilibration like PHREEQC does. Without a full flush prior to equilibration, a portion of the initial water is retained in the cell, which affects water composition in the cell to a small degree for a number of subsequent flushes. Because the PHREEQC model fully flushes out the initial water, it does not retain a residual. The EQ6 fluid mixing approach avoids this conflict and therefore better replicates the PHREEQC model.

Two validation simulations are presented below. The first is performed at low ionic strength to show that the two codes produce essentially identical results at low ionic strength (Section 7.1.1.1). A second simulation is performed at higher ionic strength to assess the effects of high ionic strength on the calculations (Section 7.1.1.2). Results of these simulations are presented and discussed in Section 7.1.1.3.

7.1.1.1 Validation Simulation at Low Ionic Strength

The validation simulation at low ionic strength follows the igneous intrusion scenario described in Section 6.2.3.3. In this scenario, magma flows through the drift, encapsulates the waste package in basalt, and causes the waste package to rupture. Seepage water flows through the fractures in the basalt and is chemically altered by basalt minerals. Water that flows through and around the breached waste package mixes at the bottom of the invert. The PHREEQC and EQ6 validation simulations for this scenario are developed below.

7.1.1.1.1 Inputs

In the igneous intrusion scenario, the composition of the ambient water is a basalt water taken from calculations documented in *Igneous Intrusion Impacts on Waste Packages and Waste Forms* (BSC 2004 [DIRS 168960]). The calculations involved modeling the dissolution of basalt minerals in contact with a specified pore water. The resulting water, reproduced in Table 7-1, is taken from file *b8b_3.6p* (BSC 2004 [DIRS 168960]).

The waste package for this scenario is TMI and the waste package water is from a simulation with a flow rate of 1 L/yr and oxidizing conditions (*tmi_ig1.6i*). The composition at 38 years provides a low ionic strength validation test case. It is presented in Table 7-2.

The fugacities of oxygen and carbon dioxide were fixed at $10^{-0.7}$ and $10^{-3.0}$ bar, respectively. Nitrate was prevented from reducing to nitrogen gas, and chromium was limited to the (+3) oxidation state.

Table 7-1. Composition of Basalt Water Used in Igneous Scenario Validations

EQ6 Input Composition Values		
Element	**Concentration**	**Units**
Al	6.46×10^{-7}	molality
N	4.47×10^{-2}	molality
Si	6.74×10^{-5}	molality
Ca	4.76×10^{-6}	molality
K	1.24×10^{-9}	molality
Mg	4.69×10^{-5}	molality
pH	9.02	standard units
Fe	1.43×10^{-12}	molality
F	2.96×10^{-13}	molality
Cl	5.61×10^{-4}	molality
Mg	4.69×10^{-5}	molality
P	9.87×10^{-3}	molality
C	2.19×10^{-2}	molality
N	3.97×10^{-5}	molality
S	3.55×10^{-4}	molality

Source: BSC 2004 [DIRS 168960], Attachment III, file *b8b_3.6p*; pH obtained from File *B8b_3.6o*.

Table 7-2. Compositions of Waste Package Water Used in Igneous Scenario Validations

Constituent	Units	Low Ionic Strength Scenario	High Ionic Strength Scenario
pH (NBS)	standard units	6.75	8.75
Ca	molality	1.36E-04	1.28E-05
Mg	molality	5.46E-04	1.27E-04
Na	molality	3.48E-02	9.12E-01
K	molality	3.34E-03	9.33E-02
Si	molality	4.04E-05	1.78E-04
N	molality	1.86E-02	4.65E-02
C	molality	1.44E-04	4.68E-01
Cl	molality	3.81E-06	4.91E-04
F	molality	1.31E-04	1.06E-13
S	molality	9.27E-03	1.45E-02
Al	molality	1.27E-08	4.37E-08
Mn	molality	5.16E-13	1.21E-15
Fe	molality	4.96E-12	3.84E-12
U	molality	9.99E-06	1.49E-01
Cr(III)	molality	9.94E-13	3.22E-14
B	molality	2.24E-02	9.97E-02
Cu	molality	1.11E-16	1.84E-17
Zn	molality	1.11E-16	1.84E-17
Ni	molality	3.60E-05	7.38E-09

Table 7-2. Compositions of Waste Package Water Used in Igneous Scenario Validations (Continued)

Constituent	Units	Low Ionic Strength Scenario	High Ionic Strength Scenario
Mo	molality	1.05E-03	1.22E-01
Ba	molality	6.46E-08	6.99E-07
P	molality	4.39E-07	9.21E-03
Br (tracer)	molality	1.00E-06	1.00E-06

Source: BSC 2006 [DIRS 176911], Appendix A, folders Igneous Scenario and Seismic Scenario; DTN: MO0608MWDGEOMA.001 [DIRS 177332].

The databases used in the EQ3/6 and PHREEQC validation simulations are equivalent. The EQ3/6 database was *data0.cr3* (see DTN: MO0608MWDGEOMA.001, [DIRS 177332]), file: data0 files.zip) and the PHREEQC database was *phreeqcDATA025bdotCr3.dat*. The PHREEQC database *phreeqcDATA025bdotCr3.dat* (located in output DTN: MO0609SPAINOUT.002), is a modified version of the PHREEQC database (*phreeqcDATA025.dat*) located in DTN: MO0604SPAPHR25.001 [DIRS 176868]. The modifications contained in *phreeqcDATA025bdotCr3.dat* are the same as those in *data0.cr3* see DTN: MO0608MWDGEOMA.001, [DIRS 177332], file: data0 files.zip]). These changes, noted at the top of each database, included suppression of Cr(II), Cr(V), and Cr(VI) species, modifications to specific log K values, and addition of $Cr(OH)_3$(am).

Mineral reactants are listed in Table 7-3. The initial amount of each mineral in each cell was set at 100 moles. The exact quantity is irrelevant to the calculations as long as it is high enough to ensure an unending supply.

Table 7-3. Mineral Reactants and Dissolution Rates Used in Validation Simulations

Mineral	Abundance (mol)	Dissolution Rate (mol/s/L)
Cristobalite(alpha)	100	4.370e-12
Annite	100	2.493e-14
Phlogopite	100	1.511e-16
Maximum Microcline	100	3.914e-14
Albite Low	100	2.328e-12
Anorthite	100	5.142e-13

Source: Estimated using preliminary EQ6 output files that used pH-dependent rates.

The mineral dissolution rates were fixed at constant values to avoid the complications of synchronizing the timing of equilibrations in PHREEQC and EQ6. As mentioned in Section 7.1.1, the timing of equilibrations cannot be completely synchronized between the two codes. Dissolution rates are determined for each equilibration time step. If the dissolution rates are defined in terms of chemical parameters, such as pH, and the time steps are not synchronized, differences in time steps could cause differences in dissolution rates. The constant rates used in the validation simulations are listed in Table 7-3 and are based on preliminary EQ6 calculations that contained pH-dependent rates. The actual values that were used are not important to this

validation exercise. The important aspect is the exact same rates were used in the EQ6 and PHREEQC simulations.

7.1.1.1.2 PHREEQC Simulation

The input file for this PHREEQC validation simulation is *igb8lowv*. To reduce model output, this file was set up to model reactive transport through five one-liter cells over eight years at a flow rate of 1 L/yr. Reducing the number of cells and the modeling period has no effect on the calculations for these cells.

The input waters were defined in the PHREEQC input file as shown in Table 7-4 and Table 7-2 (low ionic strength). The basalt water is the dilution water (solution 999) and is also the initial solution in each cell (solutions 1 through 5). Solution 0 is the waste package water. The fugacities of oxygen and carbon dioxide were fixed at $10^{-0.7}$ and $10^{-3.0}$ bar, respectively, for each input water.

In the cells, a long list of potential minerals was defined to encompass potential equilibrium phases. At a minimum, this list must contain the minerals that become supersaturated during the simulation. It should not, however, contain minerals that are kinetically unfavored at the temperature and pressure of the simulation, such as those in Table 6-8, which are suppressed in the PHREEQC calculations.

The cells were further constrained by gas fugacities and mineral reactions. The fugacity of carbon dioxide was fixed at $10^{-3.0}$ bar and that of oxygen was fixed at $10^{-0.7}$ bar. Tuff minerals dissolving in each cell were defined by the dissolution rates listed in Table 7-3.

As in the general PHREEQC model in Section 6, reactive transport was defined by the `ADVECTION` keyword. Thus, no diffusion or dispersion was simulated. The time step was set at 3.1557 x 10^{+7} seconds (one year), and the number of shifts was set at 8 to simulate 8 years of advection.

The complete set of PHREEQC input and output files for this validation exercise are documented in DTN: MO0608SPACONFI.001. The file names are:

- Input file: *igb8lowv*
- Output file: *igb8lowv.out*
- Tabulated output: *igb8lowv.xls*.

7.1.1.1.3 EQ3/6 Simulation

The EQ3/6 validation simulation required a number of input and output files to predict mineral accumulation in the first three cells. The development of these files is described below. A summary of the input and output files is presented in Table 7-4 and Table 7-5.

Table 7-4. EQ3/6 Files Used to Define Basalt Water and Waste Package Water for the Low Ionic Strength Validation Simulation

Source Water	Input file	Output files	Pickup Source	Fluid Source
Basalt water (initial)	valbw.3i	valbw.3o, valbw.3p	NA	Table 7-1
Basalt water (equilibrated)	valbw.6i	valbw.6o, valbw.6p	valbw.3p	NA
Basalt water (equilibrated aqueous)	valbwsol.3i	valbwsol.3o, valbwsol.3p	NA	valbw.6o
Waste package water (initial)	valwp2.3i	valwp2.3o, valwp2.3p	NA	Table 7-2
Waste package water (equilibrated)	valwp2.6i	valwp2.6o, valwp2.6p	valwp2.3p	NA

Source: Output DTN: MO0608SPACONFI.001.

NA = not applicable.

Table 7-5. EQ3/6 Files Used to Simulate Cells 1, 2, and 3 for the Low Ionic Strength Validation Simulation

Simulation	Input file	Output files	Pickup Source	Fluid Reactant Source	Secondary Mineral Source
Cell 1 Time 1	igb8lo1.6i	igb8lo1.6o, igb8lo1.6p	valbwsol.3p	valwp2.6p	NA
Cell 2 Time 1	igb8lo2a.6i	igb8lo2a.6o, igb8lo2a.6p	valbwsol.3p	valbwsol.3p	NA
Cell 2 Time 2	igb8lo2.6i	igb8lo2.6o, igb8lo2.6p	valbwsol.3p	igb8lo1.6p	igb8lo2a.6o
Cell 3 Time 2	igb8lo3b.6i	igb8lo3b.6o, igb8lo3b.6p	valbwsol.3p	igb8lo2a.6p	igb8lo2a.6o
Cell 3 Time 3	igb8lo3.6i	igb8lo3.6o, igb8lo3.6p	valbwsol.3p	igb8lo2.6p	igb8lo3b.6o

Source: Output DTN: MO0608SPACONFI.001.

NA = not applicable.

Basalt Water—Basalt water was used both as a reactant and as the water that initially exists in the cells. Three EQ3/6 simulations were needed to prepare this water for the application. First, *valbw.3i* was created to define the basalt water composition as presented in Table 7-4. In this file, the following options were chosen:

- Mineral suppressions as needed in accordance with Table 6-8 presented in Section 6.4.4
- Suppression of paragonite, a high-temperature mineral similar to muscovite
- Suppression of N_2(aq) aqueous species to keep dissolved N as nitrate (important when simulating slightly reducing conditions)
- B-dot equation for activity coefficient model
- NBS pH scale.

EQ3NR execution of this input file produced the pickup file, valbw.3p, (note all files are found in output DTN: MO0608SPACONFI.001) which was used to build an EQ6 input file, valbw.6i. Input file valbw.6i was used to fix the CO_2 fugacity at $10^{-3.0}$ bar and the O_2 fugacity at $10^{-0.7}$ bar and to precipitate unsuppressed supersaturated minerals.

No minerals precipitated during the valbw.6i simulation (note that all files are found in output DTN: MO0608SPACONFI.001). The equilibrium aqueous solution from valbw.6o was entered into valbwsol.3i, a third input file that used valbw.3i as a template. Except for the slight changes in aqueous concentrations, the only other change from valbw.3i was the selection of the option to write an EQ6 input file with "fluid 1" set up for fluid mixing. This produced a valbwsol.3p pickup file that could be used as an EQ6 input file template for fluid mixing.

Waste Package Water—The water from the waste package was used as a reactant in cell 1. To generate the waste package water reactant for the EQ3/6 simulation, two EQ3/6 simulations were necessary. The first simulation defined the waste package water composition according to Table 7-2. The input file, named valwp2.3i (output DTN: MO0608SPACONFI.001), used the following options:

- Mineral suppressions as needed in accordance with Table 6-8 presented in Section 6.4.4
- Suppression of paragonite
- B-dot equation for activity coefficient model
- NBS pH scale.

The file valwp2.3p (found in output DTN: MO0608SPACONFI.001), generated by EQ3NR execution of valwp2.3i, was used as the pickup file for EQ6 simulation valwp2.6i. In this second input file, the CO_2 fugacity was fixed at $10^{-3.0}$ bar and the O_2 fugacity was fixed at $10^{-0.7}$ bar. The option of a fluid-centered flow-through system was selected, as was the option to generate an EQ6 input file with "fluid 1" set up for fluid mixing.

Cell 1—A flow rate of 1 L/yr implies that the full aqueous volume of cell 1 is flushed in exactly one year. To simulate a time step of one year, as PHREEQC does for this simulation, the fluid-mixing approach was required, as explained in Section 7.1.1. The EQ6 input file (igb8lo1.6i) used the basalt water from valbwsol.3p (note that all files are found in output DTN: MO0608SPACONFI.001) as the pickup file and the waste package water (fluid 2) reactant from valwp2.6p as a reactant. To achieve the correct ratio of basalt water to waste package water, 9 liters of waste package water reactant were mixed with the liter of basalt water from the pickup file. The one-year time step was defined by setting the equation for the waste package water reactant at a linear rate of 2.852×10^{-7} mol/sec, which was calculated by dividing 9 moles by the number of seconds in a year. The tuff minerals were added at the linear reaction rates listed in Table 7-3 multiplied by 10 to account for the final volume of 10 liters. Other settings in the igb8lo1.6i input file were:

- Starting time of 0 seconds
- Maximum time of $3.1557 \times 10^{+7}$ seconds (1 year)
- Starting and ending values for Xi, 0 and 10
- Zero order step size (in Xi) of 5
- Fugacity of carbon dioxide fixed at $10^{-3.0}$ bar

- Fugacity of oxygen fixed at $10^{-0.7}$ bar
- Titration system
- True kinetics
- Create EQ6 input file with fluid 1 set up for fluid mixing.

The inputs do not change from year to year for cell 1. Therefore, the results of this simulation can be used for any year in the simulation period. The only outputs that change over time are the total accumulations of precipitating minerals, which can be calculated by multiplying the moles precipitated in this simulation by the number of years. Note, however, that this simulation produces 10 times the precipitate as the PHREEQC model because it is scaled to 10 liters instead of 1.

Cell 2 Time 1—The first time step for cell 2 is not affected by waste package water. Instead, the water from cell 1 at time 0, which is also unaffected by waste package water, is diluted by basalt water at a 9:1 ratio. However, because the water in cell 1 at time 0 is also the basalt water, the water in cell 2 at time 1 is simply the basalt water with one year's worth of dissolved tuff minerals.

In keeping with the format for the cell 1 simulation, a fluid-mixing approach was used to simulate cell 2 at time 1. The input file, named igb8lo2a.6i (note that all files are found in output DTN: MO0608SPACONFI.001), used the pickup file from the valbwsol.3i basalt water simulation to provide both the bottom part (pickup) of the input file and the fluid-mixing reactant. Otherwise, the settings in igb8lo2a.6i were identical to igb8lo1.6i.

This simulation calculates the water and mineral composition for each cell except the first cell in the PHREEQC model at time 1. Thus, it simulates cell i at time 1 for $i \geq 2$.

Cell 2 Time 2—The second time step for cell 2 is affected by waste package water. The input file for cell 2 time 2, named igb8lo2.6i (note that all files are found in output DTN: MO0608SPACONFI.001); 2), the secondary minerals precipitated in the cell 2 time 1 simulation (igb8lo2a.6i); and 3) the basalt water pickup file, valbwsol.3p. Nine liters of the fluid reactant from igb8lo1.6p were entered with a linear reaction rate of 2.852×10^{-7} mol/sec (equivalent to 9 mol/yr). The secondary minerals were entered from igb8lo2a.6o as rapidly dissolving mineral reactants with linear rates of 0.01 mol/sec. The moles of these minerals were not divided by 10 because each simulation ends with 10 kg of water. The addition and rapid dissolution of these minerals ensure conservation of mass in the cell. If the forced rapid dissolution of the secondary mineral reactants causes these minerals to be supersaturated (which is usually the case), they will precipitate and there will be no net effect associated with their temporary absence at the beginning of the time step.

Other settings were identical to the cell 2 time 1 (igb8lo2a.6i) simulation except for the following:

- Starting time of $3.1557 \times 10^{+7}$ seconds (one year)
- Maximum time of $6.3114 \times 10^{+7}$ seconds (2 years)
- Starting and ending values for Xi, 0 and $1 \times 10^{+38}$.

This cell 2 time 2 simulation also calculates the water and mineral composition for cell 2 beyond two years. After two years, the inputs do not change. Therefore, this simulation is representative of cell 2 at time *j* for $j \geq 2$ years.

Cell 3 Time 1—The simulation for cell 3 time 1 is equivalent to cell 2 time 1 (see above).

Cell 3 Time 2—In this simulation, called *igb8lo3b.6i* (note that all files are found in output DTN: MO0608SPACONFI.001) progressed to cell 3. However, this cell at this time step begins with an initial amount of mineral precipitation from the first time step. The pickup file is *valbwsol.3p*, the mixing fluid is fluid 2 from *igb8lo2a.6p*, and the initial minerals are taken from *igb8lo2a.6o*. Other settings were the same as for cell 2 time 2. This simulation represents cell *i* at time 2 for $i \geq 3$.

Cell 3 Time 3—In the third time step, water affected by the waste package reaches cell 3. For this simulation, *igb8lo3.6i* (note that all files are found in output DTN: MO0608SPACONFI.001), the pickup file is *valbwsol.3p*, the mixing fluid is fluid 2 from *igb8lo2.6p*, and the initial minerals are taken from *igb8lo3b.6o*. Other settings were the same as for cell 2 time 2, except that the starting and ending times were $6.3114 \times 10^{+7}$ (2 years) and $9.467 \times 10^{+7}$ (3 years) seconds, respectively. This simulation represents cell 3 at time *j* for $j \geq 3$ years.

7.1.1.2 Validation Simulation at High Ionic Strength

The validation simulation at high ionic strength follows the low ionic strength scenario above, except that the waste package water is from a later time period when it has higher ionic strength. Its composition is compared to that of the low ionic strength simulation in Table 7-2.

7.1.1.2.1 PHREEQC Simulation

The input file for the PHREEQC validation simulation at high ionic strength is *igb8hiv* (note that all files are found in output DTN: MO0608SPACONFI.001). It is a copy of the low ionic strength simulation file *igb8lowv,* except for the low ionic strength water is replaced with the high ionic strength waste package water.

The complete set of PHREEQC input and output files for this validation exercise are documented in output DTN: MO0608SPACONFI.001. The file names are:

- Input file: *igb8hiv*
- Output file: *igb8hiv.out*
- Tabulated output: *igb8hiv.xls*.

7.1.1.2.2 EQ3/6 Simulation

The EQ3/6 simulations are nearly identical to the simulations described in Section 7.1.1.1.3 for the low ionic strength scenario. In fact, the valbw*.* files in Table 7-4 and Table 7-5 are identical (note that all files are found in output DTN: MO0608SPACONFI.001. Files valwp2.* differ only in the waste package water composition as presented in Table 7-2. The input files for the different cells at various times were built in the same way as described in Section 7.1.1.1.3 and Table 7-5; however, the file names were changed from igb8lo*.* to igb8hi*.*.

7.1.1.3 Comparison of EQ3/6 and PHREEQC Results

The largest changes in a cell in a given time step occur when the waste package water reaches the cell. Thus, for this validation exercise the results of the two codes are compared at the front of the plume, i.e., at cell 1 time 1, cell 2 time 2, and cell 3 time 3.

Spreadsheets called *Accumulation igb8lowv 4.xls* and *Accumulation igb8lhiv 4.xls* in output DTN: MO0608SPACONFI.001 were generated for graphical comparison of the PHREEQC and EQ3/6 results. Relevant graphs from these spreadsheets are reproduced and discussed below.

7.1.1.3.1 Low Ionic Strength Simulation

In the low ionic strength simulation, uranium minerals do not precipitate, but several other minerals do. Figure 7-1 shows the mineral assemblages at the front of the plume for the first three time steps. Not only did PHREEQC and EQ6 predict the same minerals to precipitate, but they also predicted nearly the same amounts of mineral precipitation. The largest relative differences are for pyrolusite, which is predicted to precipitate in extremely small quantities. Such low quantities have negligible effects on the primary purpose of the model; i.e., prediction of the accumulation and distribution of U, Pu, and neutron absorbers in the invert.

Another indication of corroboration is the comparison of predicted pH values at the front of the plume. As shown in Figure 7-2, the EQ6 predictions of pH match the PHREEQC predictions almost exactly. The predicted pH values in cells 1 through 3 (7.8, 8.2, and 8.3) are reasonable considering that the incoming waste package water has a pH of 6.75 and the background water has a pH of 9.0.

The external accumulation model is designed to predict the accumulation of components important to criticality at various distances along the flow path. The distances are represented by cell number in the model, and the accumulation in each cell is the sum of the components in all phases, whether aqueous, solid, or gas. In the model, components in the gas phase contribute negligibly to overall accumulation of the components of interest. In addition, in the validation simulation, adsorption is not included because EQ6 cannot model adsorption. Therefore, the accumulation of components in each cell in these validation simulations is the sum of the components in the aqueous and mineral phases.

The total accumulations of each component in the aqueous and mineral phases in cell 1 at time 1 and cell 3 at time 3 are presented in Figure 7-3 and Figure 7-4 as predicted by each code. The largest differences in these figures are the small differences in the components that have negligible concentrations (less than 1×10^{-12} molal).

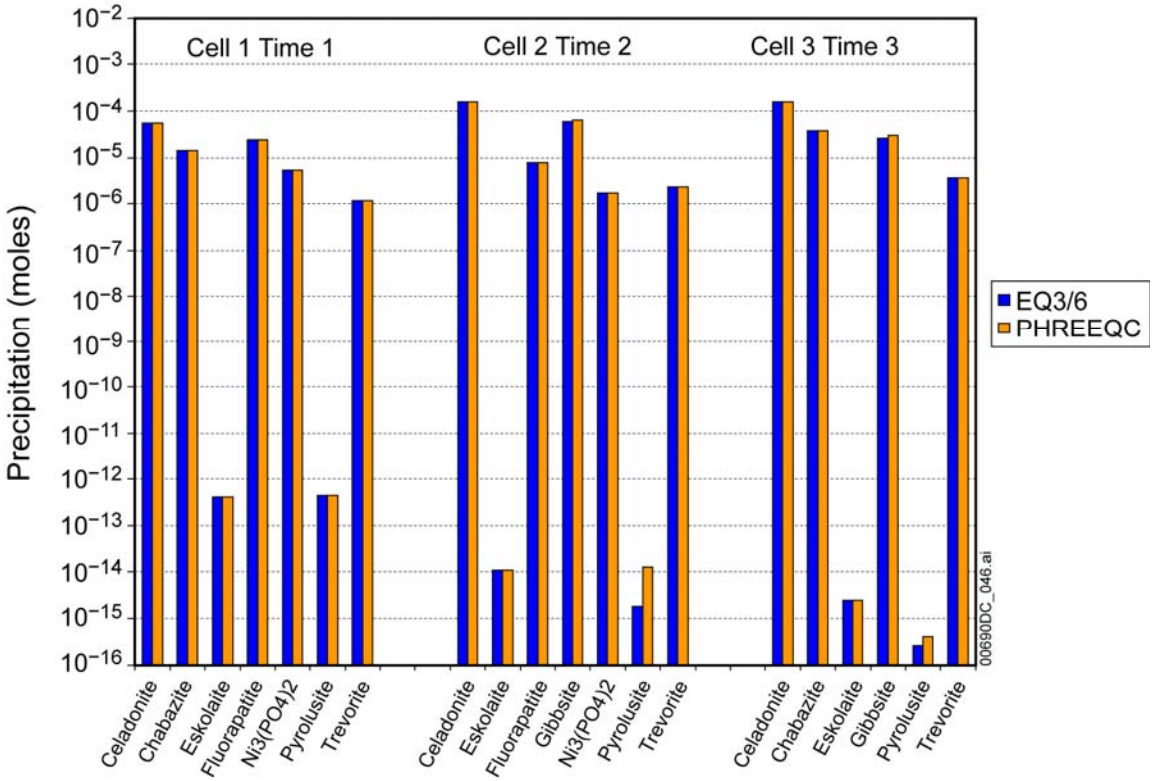

Source: Output DTN: MO0608SPACONFI.001, *Accumulation igb8lowv 4.xls*.

Figure 7-1. Comparison of Minerals Precipitated at Front for Low Ionic Strength Simulation

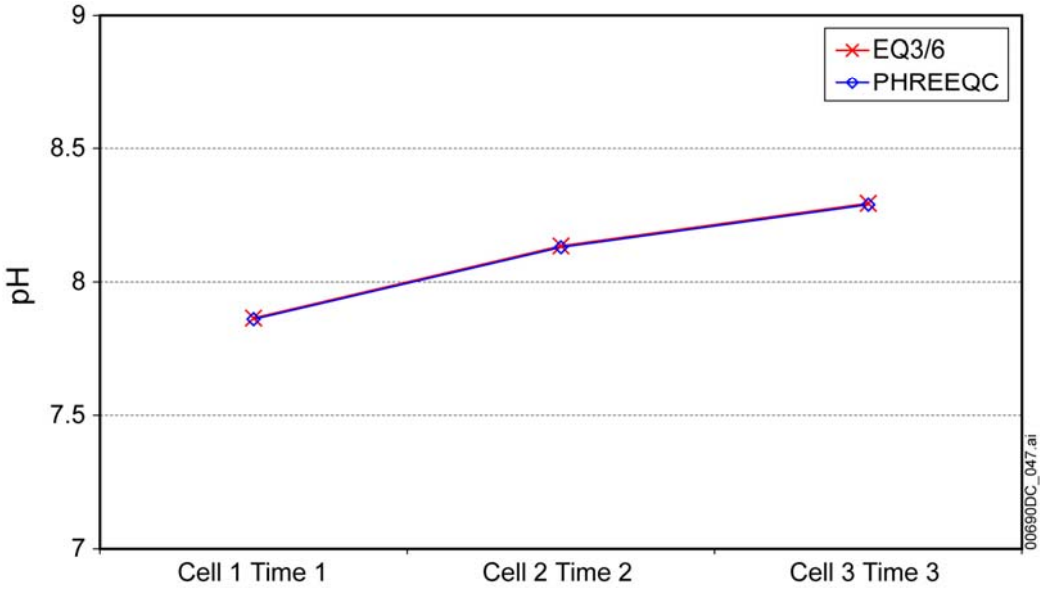

Source: Output DTN: MO0608SPACONFI.001, *Accumulation igb8lowv 4.xls*.

Figure 7-2. Comparison of Predicted pH at Front for Low Ionic Strength Simulation

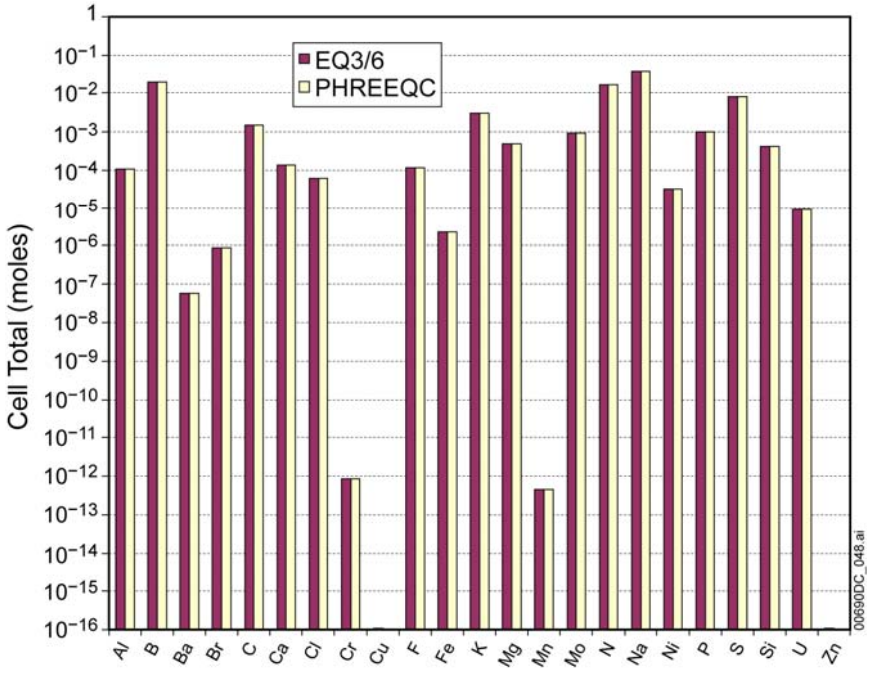

Source: Output DTN: MO0608SPACONFI.001, *Accumulation igb8lowv 4.xls*.

Figure 7-3. Comparison of Cell 1 Time 1 Accumulation for Each Component in the Low Ionic Strength Simulation

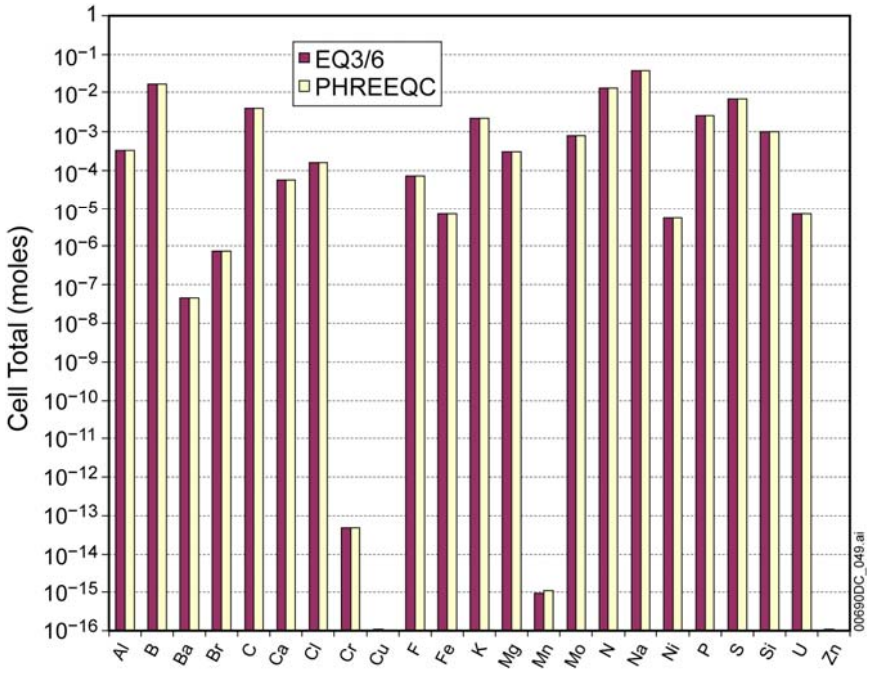

Source: Output DTN: MO0608SPACONFI.001, *Accumulation igb8lowv 4.xls*.

Figure 7-4. Comparison of Cell 3 Time 3 Accumulation for Each Component in the Low Ionic Strength Simulation

7.1.1.3.2 High Ionic Strength Simulation

In the high ionic strength simulation, U precipitates in the form of boltwoodite-Na. Figure 7-5 shows the mineral assemblages at the front of the plume for the first three time steps. The predictions between the codes are similar but two minerals that precipitate in the PHREEQC calculation in cell 3 at time 3 do not precipitate in the EQ6 calculation (fluorapatite and hydroxyapatite).

Differences in activity coefficients calculated by each code are likely responsible for the differences in mineral assemblages. These differences are larger in the high ionic strength simulation because activity coefficients become more sensitive to ionic strength as ionic strength increases. In each of the PHREEQC and EQ3/6 simulations in this report, the extended Debye-Hückel (B-dot) equation is used to calculate the activity coefficients (Parkhurst and Appelo 1999 [DIRS 159511], p. 11; SNL 2003 [DIRS 162494], p. B-32). PHREEQC uses the extended Debye-Hückel (B-dot) equation whenever the "-gamma" option is included for a given species (Parkhurst and Appelo 1999 [DIRS 159511], p. 157). In the database used (*phreeqcDATA025bdotCr3.dat*) this option is included for each dissolved species, so the B-dot equation is used for each species in the PHREEQC simulations.

The equilibrated waste package water provides a good example of the differences in calculated activity coefficients at high ionic strength. The activity coefficient of the dominant uranyl aqueous species in this water, $UO_2(CO_3)_3^{4-}$, was calculated by PHREEQC to be 1.112×10^{-4} (*igb8hiv.out*). EQ3/6 calculated it to be 0.967×10^{-4} (*valwp2.6o*), which is 13% lower. (Note that all files noted in this section are in output DTN: MO0608SPACONFI.001.) The activity coefficient for this species is especially low because of the high charge of the species (−4) and the high ionic strength of the solution (2.008 molal).

Much of the 13% difference is due to adjustments performed by EQ3/6 to ensure that activity coefficients are consistent with the NBS pH scale. PHREEQC does not perform this type of rescaling. This explanation was confirmed by rerunning the waste package water files in EQ3/6 (Table 7-4) with the "no-rescaling" option selected as the pH scaling choice. Using the "no-rescaling" option, the activity coefficient for $UO_2(CO_3)_3^{4-}$ increased to 1.080×10^{-4}, explaining 78% of the difference between the PHREEQC and original EQ3/6 simulations.

The remaining difference is due to small differences in the values of the Debye-Hückel A and B parameters. The Debye-Hückel "azero" (4.0) and "bdot" (0.0410) are identical in both databases. In the EQ3/6 database, the A and B parameters at 25°C are 0.5114 and 0.3288 (DTN: SN0410T0510404.002). Entering these values and the values for ionic strength, charge, "azero" and "bdot" from above into the extended Debye-Hückel equation gives an activity coefficient of 1.080×10^{-4} for $UO_2(CO_3)_3^{4-}$, which is the same value calculated by EQ3/6 when there is no pH rescaling. The PHREEQC values for A and B are calculated in the subroutine "model.c" of the PHREEQC code as a function of temperature. At 25°C, the calculated values for A and B are 0.5093 and 0.3283. Using these values in the extended Debye-Hückel equation gives the same 1.112×10^{-4} activity coefficient calculated by PHREEQC and explains the remaining difference in activity coefficient calculations.

While the mineral assemblages differ to a greater extent in the high ionic strength simulation, the predicted pH values and total accumulations nevertheless match well, as shown in Figure 7-6 through Figure 7-8. The largest differences in predicted cell accumulations are the small differences in the components that have negligible concentrations (less than 1×10^{-12} molal). The high degree of agreement in these figures suggests that marked differences in the mineral assemblages do not necessarily imply considerable differences in the total accumulations of the various components.

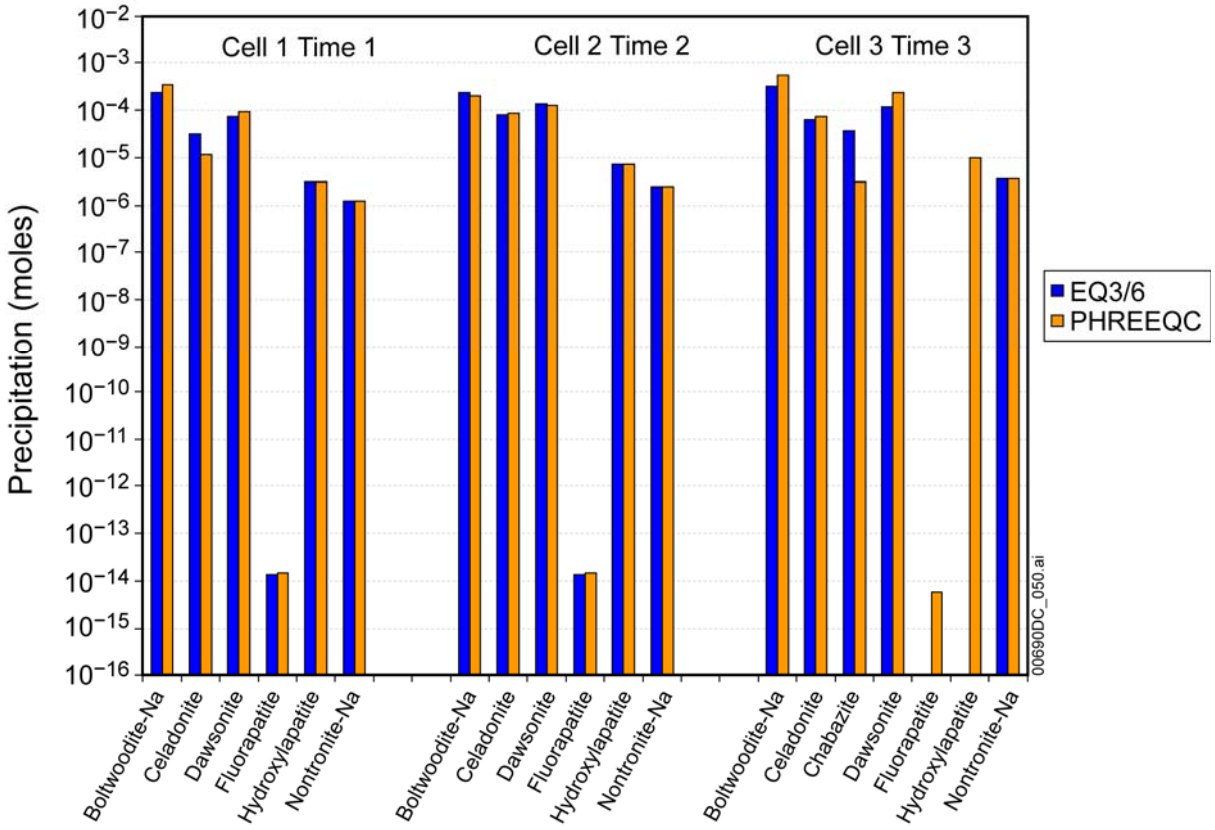

Source: Output DTN: MO0608SPACONFI.001 Accumulation igb8hiv 4.xls

Figure 7-5. Comparison of Minerals Precipitated at Front for High Ionic Strength Simulation

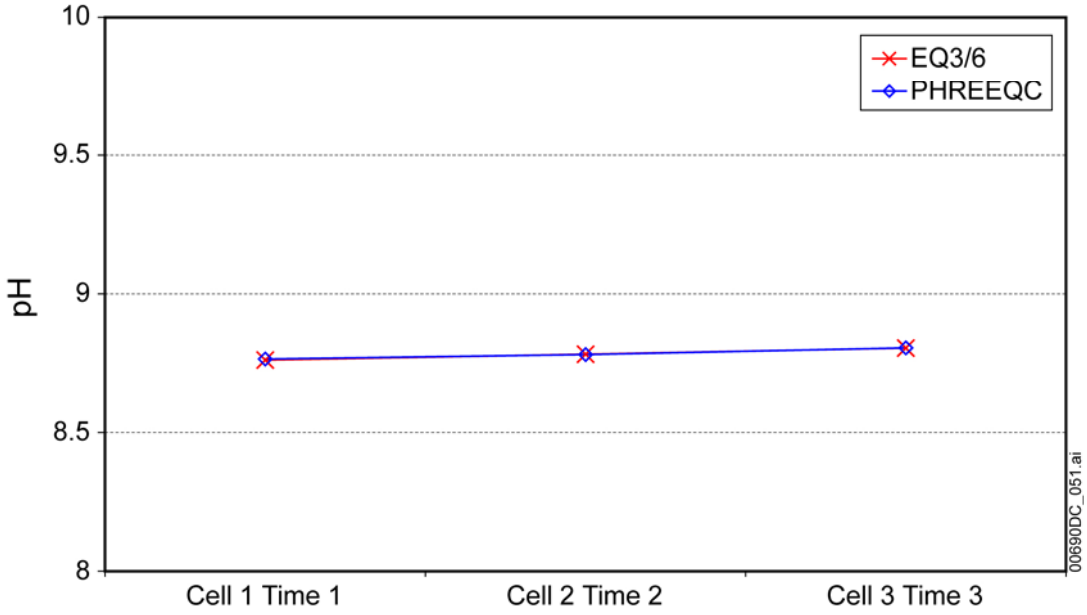

Source: Output DTN: MO0608SPACONFI.001 Accumulation igb8hiv 4.xls

Figure 7-6. Comparison of Predicted pH at Front for High Ionic Strength Simulation

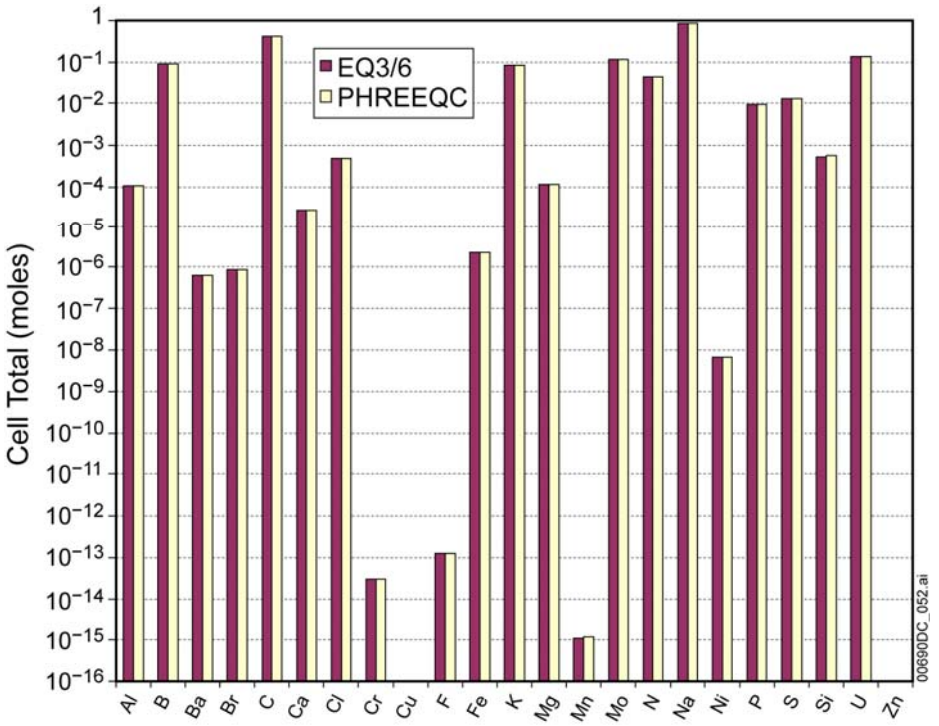

Source: Output DTN: MO0608SPACONFI.001 Accumulation igb8hiv 4.xls.

Figure 7-7. Comparison of Cell 1 Time 1 Accumulation for Each Component in the High Ionic Strength Simulation

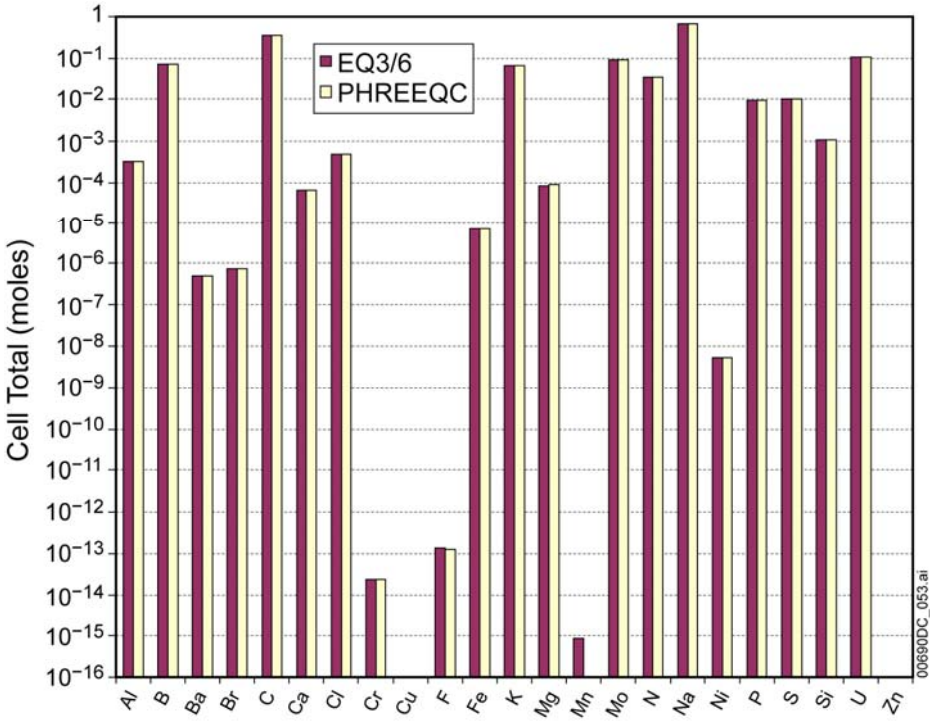

Source: Output DTN: MO0608SPACONFI.001 Accumulation igb8hiv 4.xls.

Figure 7-8. Comparison of Cell 3 Time 3 Accumulation for Each Component in the High Ionic Strength Simulation

7.1.1.3.3 Validation Conclusion

Overall, the differences observed between the EQ3/6 and PHREEQC validation simulations are small compared to model uncertainties and compared to the ranges of concentrations predicted for each of these components over the time period modeled. Although differences are observed, particularly in the mineral assemblages of the high ionic strength test case, the corroboration of predicted total elemental molalities in each cell supports the argument that the execution of the PHREEQC external accumulation model is valid. To be clear, this exercise validates the execution of the conceptual model with regard to advection and mineral precipitation. It does not validate the conceptual model itself.

7.2 POST-MODEL DEVELOPMENT VALIDATION METHODS

Level I validation requires one method of post-model development validation consistent with a model of limited importance to mean annual dose. To cover all aspects of the model, four methods of validation are employed.

7.2.1 Summary of Validation Methods

The TWP (BSC 2006 [DIRS 177153], Section 2.2.1) names four methods for validation, as listed in Table 7-6.

Table 7-6. Validation Activities and Criteria

Validation Method	Activities	Acceptance Criteria
A	Independent technical review.	1. The approach described in the document addresses all significant modes of accumulation in the near-field (invert) and far-field (unsaturated zone). 2. The adsorption of U and Pu on the invert materials (tuff), as implemented in the PHREEQC modeling, is based on sound scientific principles. 3. The use of the thermodynamic database in the PHREEQC modeling and the choice of mineral suppressions and formations are justified and appropriate for the intended use of the model. 4. Modeling assumptions are clearly defined, discussed, and justified as appropriate for the intended use of the model. 5. Uncertainties in parameters, processes, and assumptions are appropriately described, and impacts of these uncertainties on the intended use of the model are discussed. 6. The overall technical credibility of the approach, including assumptions, parameters, and equations are appropriate for the model's intended use.
B	The types of minerals that form (such as clays and Fe-oxides) and the radionuclide-bearing phases that form in the model are corroborated with natural analogues or experimental work published in peer-reviewed or industrial literature or both. (VA 3)	The activities are successful if (1) the mineral phases predicted by the model match the mineralogy observed in natural analogues or experiments; and (2) if the mineral phases do not match, then the differences can be explained by comparing aspects of the system, such as elemental chemistry of the host rock and the water chemistry.
C	Determine whether the PHREEQC external accumulation model can predict the accumulation of uranyl minerals observed in experiments in which the degradation of UO_2 was studied for ten years under unsaturated oxidizing conditions.	1. The model should predict that U(VI) minerals accumulate over time and throughout the column. Predicting the exact same mineral assemblages observed in the drip tests is not required, because the total uranium accumulation is what is important to criticality. 2. The uranium release rate measured in the drip tests is the total uranium released from the sample, including the uranium that precipitated on the vessel but excluding the portion that reprecipitates on the UO_2-Zircaloy assembly. That is, it is the sum of the aqueous uranium and the solid-phase uranium in the leachate and on the bottom of the stainless steel reaction vessel. The solid phase includes secondary minerals and UO_2 particles that detach from the sample surfaces. Because the model neither simulates entrainment of solid particles nor spallation of UO_2 particles, the predicted aqueous release rates should not exceed the mean measured cumulative uranium release rates.

Table 7-6. Validation Activities and Criteria (Continued)

Validation Method	Activities	Acceptance Criteria
C (continued)		3. Only toward the end of the experiments between 8 and 10 years was leachate filtered to separate suspended uranium from aqueous uranium. These measurements determined that approximately 2% of the uranium released was in the filtered <5 nm size fraction (Wronkiewicz et al. 1996 [DIRS 102047], p. 86). Experiments 3 and 6 were the only experiments that continued to 10 years with a flow rate (7.82 mL/yr) equal to the simulated flow rate (Wronkiewicz et al. 1996 [DIRS 102047], Table 1). Therefore, the predicted aqueous uranium release rates should be approximately 2% (plus or minus a factor of 10) of the mean measured cumulative uranium release rates between 8 and 10 years for the experiments 3 and 6. 4. Predicted leachate pH should be within the range observed in the experiments. 5. Predicted leachate concentrations of Na, Ca, and Si should be within the ranges observed in the experiments. Other than OH^-, the components Na, Ca, and Si are the primary controls on U(VI) solubility in the experiments.
D	The numerical flow and transport model will be validated by corroboration of model results with the results from a two-dimensional analytical model for flow and transport. Two of the major outputs of the numerical model, which will be corroborated using the analytical model, are the cumulative flux (flow out the bottom of the invert) and relative concentration (ratio of radionuclide or tracer concentration in invert water to its concentration in waste package water) as a function of horizontal distance along the cross section of the invert, where cross section is perpendicular to the centerline of the waste package.	The criterion used to demonstrate that the numerical model is sufficiently accurate is that for a given value of cumulative flux or relative concentration, the horizontal distance along the cross section of the invert calculated by the numerical model is within ±10 cm of the value calculated by the analytical model. This level of uncertainty was calculated using the analytical model and represents the expected variations due to the different equations used in the two models to describe the relationship of relative permeability to water potential: Gardner equation for the analytical model (Bear 1972 [DIRS 156269], p. 492) and van Genuchten equation for the numerical model (van Genuchten 1980 [DIRS 100610]).

7.2.2 Method A: Independent Technical Review

The TWP (BSC 2006 [DIRS 177153]) specifies that an independent model validation technical review will be conducted. The technical reviewer is assigned the following tasks:

1. Review the validation criteria in the TWP (BSC 2006 [DIRS 177153]) to determine if they are adequate for intended use of the model.

2. Review the external accumulation model report in draft.

3. Assess whether or not the model as documented in the report meets the validation criteria.

4. Assess whether or not the model is adequate for its intended use. Meet with the author to resolve comments, and recommend actions, as appropriate, to resolve any inadequacies found as part of the review.

5. Document this review process, and the final conclusion as to whether the model is valid for its intended use, as a memo to be included in the report.

In addition, the independent technical reviewer was tasked with confirming that the criteria listed in Table 7-6 were met.

7.2.2.1 Qualifications of Independent Technical Reviewer

Dr. Thomas J. Wolery, who is independent of the development and checking of the document conducted a technical review of the external accumulation model. Dr. Wolery has a B.S. in geochemistry, an M.S. in Geology with concentration on heavy metals in lacustrine sediments, and a Ph.D. in Geological Sciences with emphasis on marine hydrothermal geochemistry, global geochemical cycling, and numerical modeling. He has 28 years of experience, most of it in activities related to nuclear waste disposal and hazardous waste disposal and remediation. He is the author of EQ3/6, an internationally recognized code package for thermodynamic and kinetic modeling of rock/water interactions. He has conducted or participated in various studies for the Salt Repository Project, the Waste Isolation Pilot Plan, and the Yucca Mountain Project, addressing problems in rock–water interaction, aqueous speciation, radionuclide solubilities, and radionuclide migration. He is currently the Chemical Environment Modeling and Analysis Lead for the Yucca Mountain Project at Lawrence Livermore National Laboratory. He has particular interests in the fundamental theory and application of solution thermodynamics in aqueous solutions and solid solutions. He is the author of numerous technical papers and reports on the topics of radioactive waste disposal, actinide chemistry, environmental contamination and remediation, global geochemical cycles, thermodynamics, chemical kinetics, and electrolyte theory. He is on the editorial advisory board of the journal *Computers & Geosciences* and is a member of the Geochemical Society, the International Association for GeoChemistry, the American Chemical Society, and the American Geophysical Union. Dr. Wolery's report is presented in Appendix H.

The qualifications and training of Dr. Wolery to serve as the ITR were approved by a memo from the Technical Work Plan Manager (LeStrange 2006 [DIRS 177518]) as required in the TWP (BSC 2006 [DIRS 177153], Appendix A).

7.2.2.2 Validation of Adsorption Model

As listed in Table 7-6, Validation Method A, the second acceptance criteria to be addressed by the independent technical reviewer is to determine whether "adsorption of U and Pu on the invert materials (tuff), as implemented in the PHREEQC modeling, is based on sound scientific principles." This section presents that validation.

Section 7.2.2.2.1 explains that the PHREEQC adsorption model is based on scientific principles documented in standard textbooks and refereed journals. Section 7.2.2.2.2 shows quantitatively how this model works for various U/Pu ratios and examines the results with respect to uncertainty.

7.2.2.2.1 Scientific Basis

As indicated in Section 6.4.3.1, adsorption models vary widely in complexity. The model developed in this report for adsorption of U and Pu in the invert is based on the equilibrium K_d approach, an approach that is widely used for predicting adsorption and retardation of radionuclides in porous media (e.g., BSC 2004 [DIRS 164500]; McKinley and Scholtis 1993 [DIRS 170365], pp. 347 to 363). This approach was chosen for two main reasons. First, there is an extensive database of K_d values measured on crushed devitrified tuff (BSC 2004 [DIRS 164500], Sections A8.4.1 and A8.9.1), the material that will make up the bulk of the invert. Second, thermodynamic data and parameter characterization for crushed tuff are lacking for a more sophisticated surface complexation model.

In a simple K_d model, the ratio of adsorbed concentration to aqueous concentration is constant for any given aqueous concentration. To see if the simple model applies in the repository environment, plots of the experimental K_d data for U and Pu on crushed devitrified tuff were investigated. Measured K_d values show a wide scatter and show no clear dependence to aqueous concentrations (BSC 2004 [DIRS 164500], Sections A8.4.1 and A8.9.1). If there is any dependence to aqueous concentration within this data set, the scatter in measurements obscures it. Either way, the large uncertainty evident in these measurements does not justify adopting a more sophisticated adsorption model in place of the K_d model for these ranges of aqueous concentrations.

The U and Pu K_d measurements cited above were obtained from experiments in which the adsorption site concentrations greatly exceeded the aqueous concentrations. These conditions, which imply a low loading of adsorption sites, were maintained by design because adsorption of elements to the solid–water interface is limited at high concentrations by the total concentration of adsorption sites. Thus, linear adsorption (simple K_d model) cannot be justified at high aqueous concentrations that would cause the adsorbed concentration to approach or exceed the concentration of adsorption sites. Because of this limit, the partitioning ratio between the adsorbed and aqueous phases cannot remain constant at high loading.

Nonlinear behavior at high loading is typically represented by Langmuir adsorption (Stumm and Morgan 1996 [DIRS 125332], pp. 521 to 525). Langmuir adsorption is analytically and quantitatively described by the following generalized chemical reaction (Stumm and Morgan 1996 [DIRS 125332], pp. 521 to 524):

$$\mathrm{Sor} + \mathrm{R_i} = \mathrm{SorR_i} \qquad \text{(Eq. 7.2.2-1)}$$

and associated mass action equation:

$$K_i = \frac{(\mathrm{SorR_i})}{(\mathrm{R_i})(\mathrm{Sor})}. \qquad \text{(Eq. 7.2.2-2)}$$

Sor is an unoccupied surface site, R_i is aqueous adsorbate *i*, $SorR_i$ is adsorbed R_i, and concentrations are denoted by parentheses. The mass balance equation for the adsorption site is:

$$(\mathrm{Sor})_T = (\mathrm{Sor}) + \sum(\mathrm{SorR_i}) \qquad \text{(Eq. 7.2.2-3)}$$

where $(Sor)_T$ is the total adsorption site concentration. These equations represent an adsorption model in which numerous adsorbates compete for the same surface sites and all surface sites are in the same class. They also show that competition is negligible at low loading because at low loading (Sor) is abundant and remains essentially constant, consistent with linear (K_d) adsorption.

In the adsorption model adopted for this report, U and Pu compete for the available adsorption sites when loading is high. Competitive adsorption studies in the literature indicate that some ions compete for the same sites while others do not. For example, arsenate and phosphate compete for surface sites on goethite (Gao and Mucci 2001 [DIRS 173750]), cadmium and calcium compete for surface sites on amorphous iron hydroxide (Cowan et al. 1991 [DIRS 177177]), and molybdate, selenite, selenate, chromate, and sulfate compete for sites on aluminum oxide (Wu et al. 2000 [DIRS 177175]). The single-site Langmuir model validated here was specifically shown to accurately simulate the competition of nickel and zinc on goethite (Trivedi et al. 2001 [DIRS 173021]). Examples of ions that do not compete include calcium with either nickel or zinc on goethite (Trivedi et al. 2001 [DIRS 173021]) and phosphate with arsenate on goethite when pH exceeds 7 (Gao and Mucci 2001 [DIRS 173750]). The lack of competition in these instances is attributed to different types of adsorption reactions or chemical changes in reactants. For example, calcium adsorbs as an outer sphere complex whereas nickel and zinc adsorb as inner sphere complexes (Trivedi et al. 2001[DIRS 173021]).

Whether or not U and Pu compete for the same adsorption sites is unknown. A single-site model was chosen for U and Pu adsorption for simplicity. In this way, only one concentration of surface sites, $(Sor)_T$, required estimation. As explained in Section 6.4.3.2, $(Sor)_T$ was estimated from physical measurements of the specific surface area of crushed tuff and an approximated surface site density.

Solving the above equations for two competing adsorbates (U and Pu) gives (Stumm and Morgan 1996 [DIRS 125332], p. 524):

$$(\mathrm{SorU}) = \frac{(\mathrm{Sor})_\mathrm{T}(\mathrm{U})K_U}{1 + (\mathrm{U})K_U + (\mathrm{Pu})K_{Pu}} \quad \text{(Eq. 7.2.2-4)}$$

and

$$(\mathrm{SorPu}) = \frac{(\mathrm{Sor})_\mathrm{T}(\mathrm{Pu})K_{Pu}}{1 + (\mathrm{U})K_U + (\mathrm{Pu})K_{Pu}} \quad \text{(Eq. 7.2.2-5)}$$

For additional scientific basis, the equations above can be directly derived from surface complexation model equations (Stumm and Morgan 1996 [DIRS 125332], pp. 529 to 530). The following section shows how these equations represent the linear K_d model at low loading and how U and Pu compete for adsorption sites at high loading.

7.2.2.2.2 Quantitative Evaluation

According to Figures A-33b and A-63b in *Radionuclide Transport Models Under Ambient Conditions* (BSC 2004 [DIRS 164500]), the median values of U and Pu K_d measurements for crushed devitrified tuff at 25°C are approximately 2 and 200 mL/g, respectively. Given a dry bulk density of 1.8 g/mL and a water content equal to the average porosity (0.31) multiplied by the water saturation (0.6) (Section 6.4.3.2), the corresponding nondimensional U and Pu distribution coefficients (K'_d) are 19.4 and 1940 (Equation 6.4.3-4).

The K'_d values represent the ratios of the molal concentrations of $\mathrm{SorR_i}$ and $\mathrm{R_i}$ in Equation 7.2.2-2. Thus, factoring in the 0.33 molal concentration of total adsorption sites $(\mathrm{Sor})_T$ (Section 6.4.3.2) into Equation 7.2.2-2 provides K_U and K_{Pu} values of 58.7 and 5870 molal^{-1}.

These values were entered into Equations 7.2.2-4 and 7.2.2-5 to calculate adsorbed concentrations as a function of aqueous concentration at three aqueous U/Pu ratios: 1, 100, and 10,000. The results are plotted in Figures 7-9 and 7-10.

The figures show that linear adsorption prevails at low aqueous concentrations. They also show that adsorption cannot exceed the total adsorption site concentration, regardless of which radionuclide is the dominant adsorbate. In addition, they show that an aqueous U/Pu ratio greater than 100 is needed for higher adsorbed concentrations of U than Pu. This is consistent with the K_{Pu}/K_U ratio of 100. (Note that curves in these figures are vertically comparable only at an aqueous U/Pu ratio of 1. For vertical comparison at ratios of 100 and 10,000, Figure 7-10 should be shifted to the right by a factor of 100 and 10,000, respectively.)

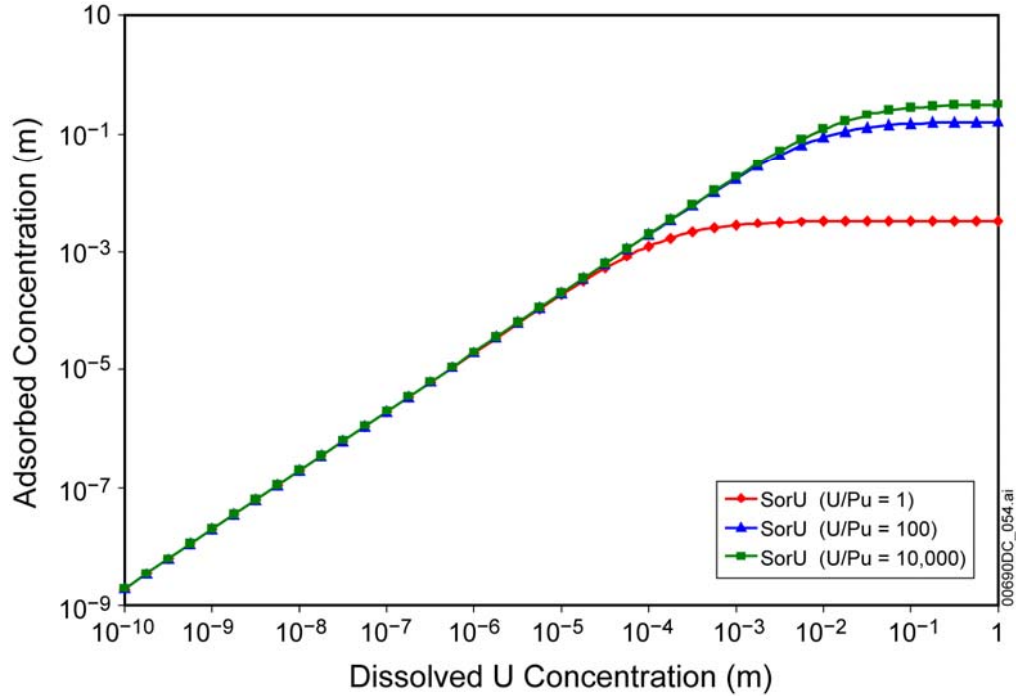

Output DTN: MO0607SPADSORP.000 file: *Isotherms.xls*.

Figure 7-9. Modeled U Adsorption versus Aqueous U for Three Aqueous U/Pu Ratios

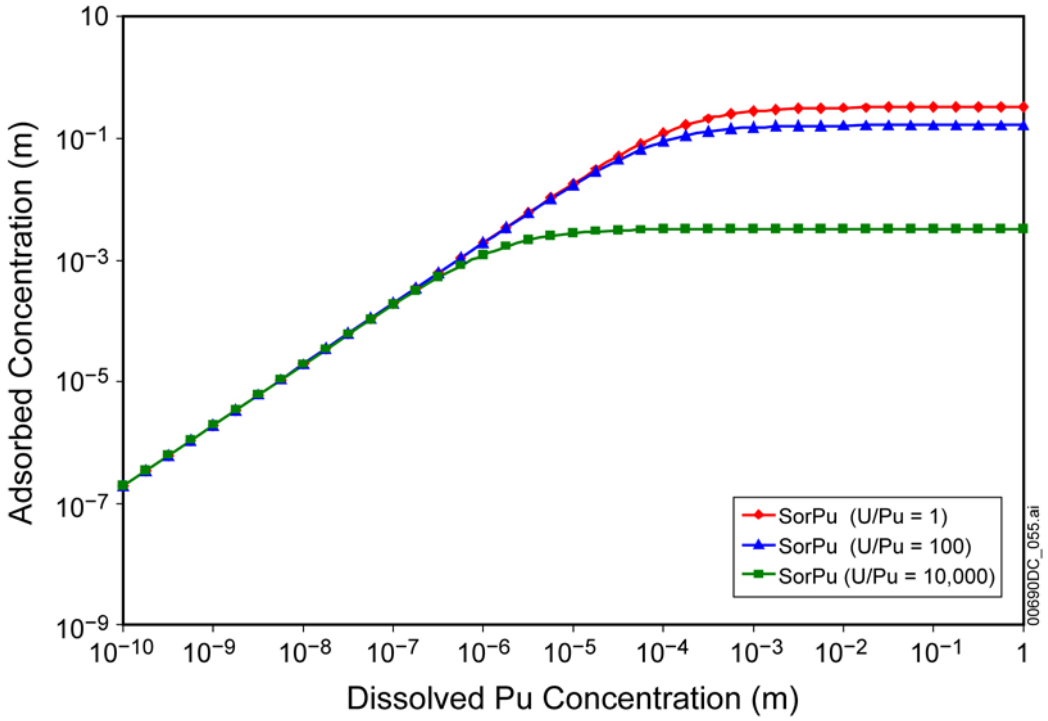

Output DTN: MO0607SPADSORP.000 file: *Isotherms.xls*.

Figure 7-10. Modeled Pu Adsorption versus Aqueous Pu for Three Aqueous U/Pu Ratios

The PHREEQC simulations described here comply with Equations 7.2.2-1 through 7.2.2-5 and thus maintain the relationships portrayed in Figures 7-9 and 7-10. The implementation is more complicated, however, because reactions have to be defined for each of the dominant aqueous U and Pu species, and the activities of these aqueous species must be converted to concentrations. Section 6.4.3.2 explains how the adsorption model is implemented in PHREEQC.

To verify that the PHREEQC approach obeys the Langmuir competitive model, a set of PHREEQC results was compared to calculations from the competitive adsorption equations. The selected set of PHREEQC model calculations is presented in Table 7-7. It is taken from simulation *fftfG110.936k.xls* (output DTN: MO0606SPAINOUT. 001, folder: FFTFIg1adEhdec, folder FFTFG1_Phreeqc_Post, folder: fftfG1_10.936, file: *fftfG110.936k.xls*) at 10 years and includes cells 1 through 10. The concentrations of U and Pu are highest in the first several cells. These high concentrations result in Langmuir competitive effects on K_d values. As shown in Table 7-7, the U K_d decreases from 2 mg/L at low aqueous U concentrations (cells 5 through 10) to 0.33 mL/g at the highest aqueous U concentration (cell 1). For the same cells, the Pu K_d decreases from 200 mL/g to 33 mL/g.

Calculations from the Langmuir competitive adsorption model equations (Equations 7.2.2-4 and 7.2.2-5) are presented in Table 7-8 for the same conditions as Table 7-7. These calculations corroborate the PHREEQC calculations, exceeding them by 2% or less. Considering the large uncertainty in U and Pu K_d values (Table 6.5), the RPD values are very small and verify that the prescribed adsorption model is functioning as intended in the PHREEQC model and easily within the limits of K_d uncertainty.

Table 7-7. PHREEQC Calculations from *fftfG1_10.936k.xls* Output File at 10 years.

Cell	U (aq) (molal)	Pu (aq) (molal)	SorU (molal)	SorPu (molal)	U K_d (mL/g)	Pu K_d (mL/g)
1	8.8E-02	5.9E-06	2.7E-01	1.8E-03	0.33	33
2	6.7E-02	5.2E-08	2.6E-01	2.0E-05	0.41	41
3	8.4E-03	4.9E-11	1.1E-01	6.3E-08	1.35	135
4	3.7E-04	1.7E-14	6.8E-03	3.2E-11	1.96	196
5	1.3E-05	5.5E-18	2.4E-04	1.0E-14	2.00	200
6	3.6E-07	2.0E-19	6.8E-06	3.8E-16	2.00	200
7	7.6E-09	2.0E-19	1.4E-07	3.8E-16	2.00	200
8	1.1E-10	2.0E-19	2.2E-09	3.8E-16	2.00	200
9	1.1E-12	2.0E-19	2.0E-11	3.8E-16	2.00	200
10	4.6E-15	2.0E-19	8.7E-14	3.8E-16	2.00	200

Source: Output DTN: MO0609SPAINOUT.002, folder: FFTFIg1adEhdec, folder FFTFG1_phreeqc_post, folder: fftfG1_10.936, file: *fftfG110.936k.xls.*

Table 7-8. Comparison of Langmuir Competitive Adsorption Equation Calculations to PHREEQC Calculations from *fftfG1_10.936k.xls* Output File at 10 Years

Cell	U (aq) (molal)	Pu (aq) (molal)	SorU (molal)[a]	SorPu (molal)[b]	SorU (RPD)[c]	SorPu (RPD)[c]
1	8.8E-02	5.9E-06	2.7E-01	1.8E-03	0.3%	0.4%
2	6.7E-02	5.2E-08	2.6E-01	2.0E-05	0.4%	0.5%
3	8.4E-03	4.9E-11	1.1E-01	6.4E-08	1.3%	1.3%
4	3.7E-04	1.7E-14	7.0E-03	3.3E-11	2.0%	2.0%
5	1.3E-05	5.5E-18	2.5E-04	1.1E-14	2.0%	2.0%
6	3.6E-07	2.0E-19	6.9E-06	3.9E-16	2.0%	2.0%
7	7.6E-09	2.0E-19	1.5E-07	3.9E-16	2.0%	2.0%
8	1.1E-10	2.0E-19	2.2E-09	3.9E-16	2.0%	2.0%
9	1.1E-12	2.0E-19	2.0E-11	3.9E-16	2.0%	2.0%
10	4.6E-15	2.0E-19	8.9E-14	3.9E-16	2.0%	2.0%

Source: Output DTN: MO0607SPADSORP.000; File: *fftfG1_10.936k adsval.xls.*

[a] Calculated from Equation 7.2.2-4.
[b] Calculated from Equation 7.2.2-5.
[c] RPD is relative percent difference (i.e., the difference between the equation value and PHREEQC output value divided by the PHREEQC output value).

7.2.3 Method B: Types of Minerals Accumulated Corroborated with Natural Analogues and Experimental Work

7.2.3.1 Introduction

As mentioned above, Method B model validation will corroborate the PHREEQC modeling results with information published from natural analogues and experimental data. In particular, the corroboration will be successful if the types of minerals that form (such as clays and Fe-oxides) and radionuclide-bearing phases that are estimated to form in the model are corroborated with natural analogues or experimental work published in peer-reviewed or industrial literature or both.

The minerals that are estimated to form by the model are controlled by the thermodynamic database. Whereas not all minerals that are known to form in nature are included in the database, a representative set of uranium minerals is included. The database includes single end member compositions (such as boltwoodite-Na) and does not include some intermediate, metastable phases. As an example, compreignacite (as seen at the Shinkolobwe Mine, Zaire) is a K-rich uranyl phase and would not be stable at Yucca Mountain due to differing rock major element chemistry (lack of potentially mobile K in the source rock). Another phase, becquerelite, is shown to be unstable in the experimental work of Wronkiewicz et al. (1996 [DIRS 102047]) and is described as such in Section B.4.1 of this report. It is also depicted as unstable in the long term experiments plotted in Figure B-1.

Considering the many potential end member compositions of a family of mineral phases, one must make a decision of the most likely end member to use. Numerical modeling of the stability and transport of dissolved inorganic constituents is limited to those components for which thermodynamic data are available for both the solid phases (minerals) and common complexes in solution. Thermodynamic data are usually collected on pure mineral phases. These data are used in simulations of the transport of a component in a given groundwater solution along a specified path through a reactive rock matrix. The result of these simulations provides a list of phases that should precipitate and the resulting concentrations of the constituents in solution. Because many of the minerals are isostructural (i.e., belong to a structural family such as boltwoodite), major ions of similar charge and size in solution will substitute for one another in a mineral and will form a solid solution. Thus, alkali metal constituents present in groundwater solutions in minor or trace concentrations will not form an individual mineral phase, but will be incorporated into a solid solution. There are minerals that have widely varying chemical compositions due to the incorporation of ions that are not present in sufficient concentrations to form their individual minerals. An example of this would be the widely variable compositions of boltwoodite. This mineral can contain weight percents of elements that are present as traces in solution. For example, boltwoodite-Na formed in oxidizing conditions often contains high concentrations of calcium or potassium. Because there are so many possibilities, the thermodynamic data for boltwoodite are limited to relatively pure $Na(UO_2)(SiO_4)\cdot 1.5(H_2O)$. One would expect, however, that under the conditions expected at the Yucca Mountain repository the trace amounts of the elements calcium and potassium would be coprecipitated with the dominant sodium in boltwoodite and would not form identifiable uranyl minerals on their own. The numerical simulation of the fate and transport of these constituents provides the saturation indicies for the individual oxides. However, the incorporation of the trace elements into the solid solution should provide lower actual concentrations in solution.

Natural uraninite (UO_2) is similar to nuclear fuel. The paragenesis of uraninite alteration phases depends on the age of the primary uraninite, the mineralogy of surrounding host rocks, and on groundwater composition, pH, and redox potential. In a general oversimplification, the progression of phases of uraninite alteration, in the absence of radiogenic lead in-growth, will be to uranyl silicates, culminating in uranophane ($Ca(UO_2SiO_3OH)_2\cdot 5H_2O$) in an oxidizing environment. Numerous compositional variations can be caused by trace elements present in the system. The composition of schoepite ($UO_3\cdot 2H_2O$) is often used to represent an alteration product in models of spent fuel alteration, but this is in the absence of common groundwater constituents such as silica. As shown by Finch and Ewing (1992 [DIRS 113030], p. 144), the formation of intermediate-phase schoepite may be favored early during the corrosion of uraninite. Schoepite is not, however, a long-term solubility-limiting phase for oxidized uranium in natural groundwaters containing dissolved silica or carbonate (e.g., the type of groundwaters at Yucca Mountain). Despite the analogy between uraninite and spent fuel, there are important differences between the two. For one thing, spent fuel is artificially enriched in ^{235}U and contains nuclear fission products that are not present in uraninite; in contrast, uraninite contains a higher proportion of nonradiogenic trace element impurities. Also, the thermal history of spent fuel, unlike that of natural uraninite, may cause lattice and structural crystallization defects in the spent fuel that are not present in the uraninite. In addition, geologically old uraninite contains in-grown radiogenic lead, which would not be found in younger uraninite or in spent fuel. Because the presence of lead effectively reduces the mobility of uranium in oxidizing waters, the concentration of uranium in groundwaters associated with oxidized uranium ore deposits will

depend in part on the age of the primary uraninite (Finch and Ewing 1992 [DIRS 113030], p. 133).

The experimentally determined mineral sequence that appears to be controlled by precipitation kinetics and is nearly identical to secondary uranium phases observed during the weathering of naturally occurring uraninite under oxidizing conditions, such as that which occurs at the Nopal I uranium deposit at Peña Blanca, Mexico (Wronkiewicz et al. 1996 [DIRS 102047], Figure 7). In laboratory UO_2 tests and in the natural uranium deposits at Nopal I, the alkali- and alkaline-earth uranyl silicates represent the long-term solubility-limiting phases for uranium (Stout and Leider 1997 [DIRS 100419], Section 2.1.3.5). Furthermore, at Nopal I, uranium concentrations in groundwater and seepage waters ranged from 170 parts per trillion (ppt) to 6 parts per billion (ppb) (Pickett and Murphy 1999 [DIRS 110009], Table 2). In general, the upper part of this range is similar to concentrations seen in filtered samples from spent fuel dissolution experiments (Stout and Leider 1997 [DIRS 100419], p. 2.1.3.5-4). This added similarity increases confidence that the experiments and the natural analogue reactions may simulate the long-term reaction progress of spent UO_2 fuel following disposal at Yucca Mountain.

Laboratory experiments have shown that UO_2 dissolution is accompanied by the formation of secondary phases on the fuel surface and that these corrosion products can retard further dissolution (Wronkiewicz et al. 1996 [DIRS 102047], p. 79). At the temperature and time scales of laboratory experiments, these phases are amorphous. However, natural sites where uraninite accumulations occur and where dissolution has taken place over long time periods could provide insights into the structure and mineralogy of the secondary passivating phases, and indicate whether they have been able to prevent further mobilization of radionuclides.

7.2.3.2 Natural Analogues and Experimental Data

There are three main natural analogue uranium deposits described in Appendix B: Oklo, Gabon (Section B.1), Peña Blanca, Mexico (Section B.2), and Shinkolobwe, Zaire (Section B.3). Of those three deposits, the main comparison for validation purposes will be with the uranium deposit at Peña Blanca, Mexico.

The natural reactor sites at Oklo, Gabon, can be excluded for the following reasons: differing rock types (Archean basement (granites, gneisses), sandstones, conglomerates, manganese-rich rocks, dolerites, and bitumen-rich black shale), age (2 billion years old), water content (6%, allowing for over-moderation), ^{235}U enrichment (3.5%), and quartz moderating layers.

The uranium deposit at Shinkolobwe, Zaire, can be excluded based on the rock type and the mineral assemblage produced by Na, K and Pb enrichment such as becquerelite ($Ca(UO_2)_6O_4(OH)_6 \cdot 8H_2O$), compreignacite ($K_2(UO_2)_6O_4(OH)_6 \cdot 8H_2O$), vandendriesscheite ($PbU_7O_{22} \cdot 22H_2O$), fourmarierite ($PbU_4O_{13} \cdot 6H_2O$), billietite ($Ba(UO_2)_6O_4(OH)_6 \cdot 8H_2O$), and schoepite ($UO_3 \cdot 2H_2O$). Becquerelite and schoepite (as fine-grained powder on becquerelite) are the most common hydrated uranyl oxides in the samples studied. Billietite and compreignacite occur as intergrowths with becquerelite. The Pb-uranyl oxide hydrates vandendriesscheite and fourmarierite are the most abundant Pb-uranyl minerals and are commonly associated with becquerelite and uraninite.

Peña Blanca is a good natural analogue for the following factors:

- Climatologically: both are located in semi-arid to arid regions.
- Structurally: both are parts of a basin-and-range host structure composed of Tertiary rhyolitic tuffs overlying carbonate rocks.
- Hydrologically: both are located in a chemically oxidizing environment within an unsaturated zone (UZ), 200 m or more above the water table (DOE 1998 [DIRS 100548], Section 2.2.4, and this study), and have broadly similar water chemistries.
- Chemically: Results indicate that in spent-fuel alteration experiments (Wronkiewicz et al. 1996 [DIRS 102047], Figure 7) the alteration of primary uraninite (Pearcy et al. 1994 [DIRS 100486], p. 714) to secondary uranium minerals at Nopal I may be similar to the eventual fate of uranium fuel rods in a geologic repository such as Yucca Mountain.

Therefore Oklo, Gabon, and Shinkolobwe, Zaire, will not be discussed further in the comparison of Yucca Mountain external accumulation PHREEC simulations. Comparisons for validation purposes will be restricted to Peña Blanca, Mexico, and the experiments of Wronkiewicz et al. (1996 [DIRS 102047]), Efurd et al. (1998 [DIRS 108015]), and the thermodynamic study of Kazuba and Runde (1999 [DIRS 122379]). The details of the experiments and the thermodynamic study are provided in Appendix B (Section B.4).

7.2.3.3 Comparison of Yucca Mountain and Peña Blanca Whole Rock and Trace Element Chemistry

The ignimbrites of Peña Blanca, Mexico, and the repository horizon (Topopah Springs Member) of Yucca Mountain are extremely similar in their major element compositions. As can be seen in Table 7-9, many of the major elements are virtually identical in weight percent amounts when comparing the Yucca Mountain values of Peterman and Cloke (2002 [DIRS 162576], Table 6) and the Peña Blanca average values (PB ave.) calculated by Goodell (1981 [DIRS 149484]) and George-Aniel et al. (1991 [DIRS 105636]). Elements such as silica, combined iron values, calcium, manganese, phosphorus, and aluminum are within 5% of each other at the respective ash flow sites. Magnesium is approximately twice as high at Peña Blanca. The alkali metals (sodium and potassium) closely balance each other at the two locations with sodium approximately 2 weight percent higher at Yucca Mountain, while potassium is 1.5 weight percent at Peña Blanca. This would indicate that perhaps more sodic minerals may be present at Yucca Mountain, while more potassic phases would occur at Peña Blanca. Accessory whole rock elements were analyzed for Yucca Mountain (F, S, Cl, and CO_2) but not for Peña Blanca. Water contents at Peña Blanca were higher than at Yucca Mountain.

Table 7-9. Peña Blanca / Yucca Mountain Igminbrite Whole Rock Analyses

Component	Yucca Mountain (Peterman and Cloke 2002 [DIRS 162576]), wt%	Peña Blanca (Goodell 1981 [DIRS 149484]), wt%	Peña Blanca (George-Aniel et al 1991 [DIRS 105636]), wt%	Peña Blanca Average, wt%
SiO_2	76.29	75.6	74.48	75.04
Al_2O_3	12.55	12.3	13.57	12.94
FeO	0.13	0.1	0.07	0.9
Fe_2O_3	0.97	1.3	1.38	1.34
MgO	0.12	0.08	0.42	0.25
CaO	0.5	0.29	0.52	0.41
Na_2O	3.52	0.75	2.43	1.59
K_2O	4.83	6.5	6.12	6.31
TiO_2	0.109	0.25	0.22	0.24
ZrOv	0.016	NA	NA	NA
P_2O_5	<0.05	0.07	0.07	0.07
MnO	0.068	0.06	NA	NA
Cl	0.017	NA	NA	NA
F	0.038	NA	NA	NA
S	<0.05	NA	NA	NA
CO_2	0.011	NA	NA	NA
H_2O^-	0.24	0.25	1.38	0.82
H_2O^+	0.4	NA	NA	NA
SUM	99.81	97.45	100.66	99.91

Trace element concentrations (Rb, Sr, Ba and Zr) appear to be almost twice as concentrated in the Peña Blanca ash flow tuffs as in the Topopah Springs Member of Yucca Mountain (see Table 7-10). An interesting observation is that select lanthanide series elements are virtually identical in concentration at the two sites.

Table 7-10. Peña Blanca / Yucca Mountain Igminbrite Trace Element Analyses

Trace Element	Yucca Mountain (Peterman and Cloke 2002 [DIRS 162576]) ppm	Peña Blanca (George-Aniel, et al 1991 [DIRS 105636]) ppm
Rb	188	277
Sr	25	38
Ba	55	146
Zr	116	344
La	51	50
Ce	84	103

Source: George-Aniel et al 1991 [DIRS 105636], Table 1, Average of 3 Nopal tuff samples; Peterman and Cloke 2002 [DIRS 162576], Table 6, Cross Drift sample.

7.2.3.4 Comparison of Yucca Mountain and Peña Blanca Host Rock Water Chemistry

In comparing major-element chemistry for SZ waters from Peña Blanca to SZ waters at Yucca Mountain in Table 7-11, both similarities and differences are apparent. The differences are due to host rock. Radionuclide transport from the Yucca Mountain repository would be predominantly through tuffaceous rock and alluvial deposits (Zyvoloski et al. 2003 [DIRS 163341], p. 745), whereas the regional aquifer at Peña Blanca is the carbonate aquifer (BSC 2004 [DIRS 169218], Figures I-1, I-4 and I-5). Components that are nearly identical include pH, silicon, potassium, and fluoride. Both water types are broadly similar in that the principal cations are sodium and calcium, and the principal anions are bicarbonate and sulfate. However, SZ waters at Peña Blanca are roughly two times as concentrated for both calcium and bicarbonate and show much larger ranges for sodium and sulfate. Alkalinity is twice as high in Peña Blanca carbonate groundwaters as in the tuff aquifer at Yucca Mountain. As is the case for waters from the Yucca Mountain area, calcium concentrations appear to be roughly limited by calcite solubility, and silicon concentrations are close to silica solubility (Pickett and Murphy 1999 [DIRS 110009]). Uranium concentrations are also broadly similar (0.2 to 20 ppb range), with the exception of the high uranium values in the newly drilled wells at Peña Blanca, which, as discussed above, are likely a result of drilling. In contrast, Peña Blanca SZ waters have significantly higher magnesium and strontium than Yucca Mountain SZ waters. In summary, although there are some exceptions, Peña Blanca SZ waters appear to be at least broadly similar to their counterparts at Yucca Mountain. However, the higher alkalinity in Peña Blanca groundwaters provides a greater solubility for uranium and its daughter products, and thus would provide more favorable conditions for transport than would Yucca Mountain groundwaters.

Table 7-11. Peña Blanca / Yucca Mountain SZ Water Chemistry Tables

Type	Parameter	pH field	pH lab	Ca ppm	Mg ppm	Na ppm	K ppm	HCO_3^- lab ppm	Cl ppm	SO_4^{2-} ppm	F ppm	Si ppm	Li ppm	Sr ppm	U ppb
YM-SZ	Mean	7.5	7.7	10.6	0.85	58.1	2.5	138.6	8.1	25.0	2.1	22.7	0.14	0.03	0.34 to 25.2
	Std. Dev.	0.33	0.36	5.5	0.75	15.4	1.2	22.9	2.2	9.8	1.1	2.0	0.21	0.02	N/A
PB-SZ-NF-Pump	Mean	7.4	7.9	49.2	12.3	102.9	5.9	278.8	8.1	131.4	2.8	9.7	0.17	1.0	381.7
	Std. Dev.	0.4	0.1	21.1	1.2	25.6	4.2	21.9	0.1	41.7	0.3	1.5	0.05	0.3	392.9
PB-SZ-NF-Bailer	Mean	9.9	9.8	31.8	5.2	160.1	28.6	283.0	9.3	191.8	2.7	15.4	0.16	0.7	2869.3
	Std. Dev.	2.0	2.4	27.6	4.4	107.4	29.4		3.6	121.3	0.4	8.0	0.06	0.4	5689.4
PB-SZ-FF	Mean	8.4	8.0	34.2	4.5	23.2	3.6	89.9	6.6	12.0	1.1	10.3	0.02	0.3	3.9
	Std. Dev.	1.5	1.1	17.3	3.2	23.4	2.3	103.6	5.1	0.7	0.9	7.8	0.02	0.2	4.0
PB-UZ-Adit	Mean			38.1	1.0	10.3	5.5	30.5	7.6	95.7	1.3	5.9	0.03	0.3	11.2
	Std. Dev.			44.0	1.7	14.6	6.0	25.9	8.4	137.3	1.4	6.1		0.3	12.9
PB-UZ-Borehole	Mean	7.3		98.3	5.2	18.5	5.4		7.6	29.7	1.1	18.3	0.03	0.3	7.0
	Std. Dev.	0.0		11.8	0.9	1.7	1.2		1.7	45.0	0.4	0.8			3.0

Sources: Benson et al. 1983 [DIRS 100727]; Pickett and Murphy 1999 [DIRS 110009]; BSC 2004 [DIRS 169218]; BSC 2004 [DIRS 169218], Table 10.4.2.

NOTE: NF = Near Field (PB1, PB2, PB3), FF = Far Field (PB4, Ranch Waters).

7.2.3.5 Comparison of Modeled Water Compositions to Yucca Mountain and Peña Blanca Groundwaters

Of the six PHREEQC runs, only three cases accumulated uranium due to precipitation (Table 6-15):

- TMI_IG1 (TMI SNF, igneous scenario, 1 L/year flow rate)
- FFTFIG1adEhdec (FFTF SNF, igneous scenario, 1 L/year flow rate)
- CSFlux9.(CSNF, seismic scenario, 1,000 L/year flow rate).

The CSFlux9 case involved an upper bound flow rate (1,000 L/yr) and therefore is not representative of cases experienced in the natural analogues and was not used in the comparison. The minerals formed in FFTFIG1adEhdec were very similar to TMI_IG1 (Table 6-9 and 6-11), but FFTF fuel contains plutonium, which is not an element in the analogues, and therefore the TMI_IG1 case was chosen for comparison in this section. TMI_IG1 is an igneous scenario with a seepage rate of 1 L/year. As shown in Table 7-12, the original source term and basalt water compositions were presented in moles per kilogram; however, to make comparisons to the host rock groundwater chemistries, the elemental compositions were converted to milligrams per kilogram (i.e., ppm). The Yucca Mountain saturated zone groundwater chemistry values were taken from *Natural Analogue Synthesis Report* (BSC 2004 [DIRS 169218], Table 10.4.2). The Peña Blanca groundwater most applicable for this comparison is the PB-SZ-FF values of Table 7-11. The other Peña Blanca values in the near field are suspect due to contamination in the drill hole. This hypothesis was supported by the changes in pH and uranium values between the pump (PB-SZ-NF-pump) and bailer (PB-SZ-NF-bailer) values. The Peña Blanca adit water value (PB-UZ-adit of Table 7-11) will also not be considered, due to potential evaporative and oxidation effects.

The TMI_IG1 waste package water used as input to the PHREEQC simulations (source term) is described in Section 6.2.2, and a plot of dissolved U versus time is presented in Figure 6-11. The Basalt water was used as the mixing water in the PHREEQC simulations. Therefore, the source term and the basalt mixing waters have significant differences when comparing compositions to the Peña Blanca or Yucca Mountain saturated zone waters. A comparison will give some insights as to which types of mineral classes should form by mixing of these two Yucca Mountain water types (as compared to those found at Peña Blanca).

The pH values of the mixing waters are at least one unit higher than the Yucca Mountain value, and similar to the Peña Blanca far field value. The CO_2 fugacity of the TMI_IG1 simulation is set at Log P CO_2 = −3, which is close to the atmospheric value of Log P CO_2 = −3.5. Calcium values for the natural analogue waters are two orders of magnitude higher than that of the TMI_IG1 simulation (tens of ppm vs. tenths of ppm). Magnesium values are comparable between the TMI_IG1 simulation and the Peña Blanca far field water composition, while the Yucca Mountain value is only slightly lower. Silica values in the mixing waters are approximately one order of magnitude lower than those of the natural analogue values, with the analogue values maximizing in the tens of ppm.

The major differences in cation concentration occur between the TMI_IG1 source term and the natural analogue waters for sodium (Na), potassium (K), and uranium (U). The sodium value in

the waste package water (20,965 ppm) is four orders of magnitude greater than that of either the Yucca Mountain value (58 ppm) or the Peña Blanca far field value (23 ppm). Similarly, potassium concentrations in the waste package water (3,639 ppm) are very elevated relative to Yucca Mountain (2.5 ppm) or Peña Blanca (3.6 ppm). Furthermore, the uranium in solution in this example of waste package water (35,385 ppm) is extremely elevated relative to waters at either Yucca Mountain (maximum of 25 ppm) or Peña Blanca (3.9 ppm). These elevated concentrations in the waste package water, upon mixing with the basalt water, should precipitate silicate minerals enriched in Na, K, and U relative to the Peña Blanca natural analogue mineral suite.

The anions (F^-, Cl^-, SO_4^{2-}) reported for both the TMI_IG1 source term and the natural waters at Yucca Mountain and Peña Blanca show the following characteristics. Fluorine concentrations are higher in Yucca Mountain (2.1 ppm) and Peña Blanca (1.1 ppm) than in the TMI_IG1 source term waters (approximately 10^{-9} ppm); however, all concentrations are insignificant in the ability to produce F-bearing mineral precipitates. Sulfur concentrations in the waste package water (464 ppm) are elevated relative to saturated zone water chemistry at either Yucca Mountain (25 ppm) or Peña Blanca (12 ppm). This could potentially lead to precipitation of sulfates in the TMI_IG1 PHREECQC simulations. Chloride values for both mixing waters (17 and 20 ppm) are slightly higher that those from the natural analogue systems (YM = 8 ppm, PB = 6.6 ppm) but can be considered roughly equivalent in that very little, if any, chloride minerals should precipitate from the mixing waters (and as validated from the natural systems considered).

Table 7-12. Comparisons of Waters for TMI_IG1 Scenario

	TMI_IG1 Source Term at 10,933 Years*	Basalt Water*	Waste Package Water*	Basalt Water	Peña Blanca (PB-SZ-FF)**	Yucca Mountain (YM-SZ)**
	mol/kg	mol/kg	mg/kg = ppm	mg/kg = ppm	ppm	ppm
PH (standard units)	8.75	9.02	8.75	9.02	8.4	7.5
Ca	1.28E-05	4.76E-06	0.512	0.1904	34.2	10.6
Mg	0.00012789	4.69E-05	3.06936	1.1256	4.5	0.85
Na	0.911515	4.47E-02	20964.85	1028	23.2	58.1
K	0.0933129	1.24E-09	3639.2	4.84E-05	3.6	2.5
Cl	0.00049054	5.61E-04	17.4	19.91	6.6	8.1
S	0.01450154	3.55E-03	464.0	113.6	12.0 (SO_4)	25.0 (SO_4)
F	1.06E-13	2.96E-13	2.01E-09	5.62E-09	1.1	2.1
Si	0.0001777	6.74E-05	4.98	1.89	10.3	22.7
U	0.148677	1.00E-16	35385.1	2.38E-11	3.9	0.34 to 25.2

* Output DTN: MO0609SPAINOUT.002, folder TMI_IG1\ TMI_IG1_phreeqc_runs\rlz9; file *tmi_10.933.in*.
** Sources: Benson et al. 1983 [DIRS 100727]; Pickett and Murphy 1999 [DIRS 110009]; BSC 2004 [DIRS 169218]

7.2.3.6 Predicted and Observed Mineralogy Comparison

The objective of this section is to compare the mineralogy of secondary minerals at Nopal, Peña Blanca, Mexico (Reyes-Cortes 2002 [DIRS 168028]; Pearcy et al. 1994 [DIRS 100486];

Wronkiewicz et al. 1996 [DIRS 102047]) with the mineralogy produced in the six PHREEQC simulations (Tables 7-5.1 to 7-5.6). Primary focus will be on uranium, clay, and oxide mineralogy to provide validation between the PHREEQC simulations and the observations of natural systems. Uranium mineralogy at Peña Blanca, Mexico, was identified by Pearcy et al. (1994 [DIRS 100486]), while other secondary mineralogy (clays, oxides, etc.) in the Coloradas and Pozos formations at Peña Blanca were characterized by Reyes-Cortes (2002 [DIRS 168028]).

The main mineralogy for the TMI_IG1 PHREEQC simulation compares quite favorably with both the natural analogue data at Peña Blanca and the experimental work of Wronkiewicz et al. (1996 [DIRS 102047]). The uranyl mineral boltwoodite-Na (Table 7-13) parallels the boltwoodite found at Peña Blanca (Section B.2.6) and the eight-year experiments of Wronkiewicz et al. (1996 [DIRS 102047]) shown in Figure B-1. Saponite clay is present in the TMI_IG1 simulation and alkali rich compared to the clays at Peña Blanca (Reyes-Cortes 2002 [DIRS 168028], pp. 323 to 324) and the palygorskite clay identified by Wronkiewicz et al. (1996 [DIRS 102047], p. 91). Such alkali enrichment for uranyl minerals, clays, zeolites, and micas in TMI_IG1 are due to the high alkali content in the source term and basalt waters, as described in the previous section. The high abundance of celadonite mica over saponite-Na clay is most likely due to the higher content of K and the lower content of Mg in the source term compared to the waters of Peña Blanca. Fe oxides are virtually absent in the TMI_IG1 simulation (as opposed to the natural analogue site at Peña Blanca), which is due to the low Fe content of the source term (with most Fe left in the waste package). Zeolites, in the form of erionite, formed in the TMI_IG1 simulation due to the high amount of Si available from the dissolution of the TMI_IG1 alkali-rich glass.

The occurrence of carbonate minerals magnesite and dawsonite predicted by the model is not reported to occur at the Peña Blanca natural analogue site or in the experimental simulations of Wronkiewicz et al. (1996 [DIRS 102047]). The source of the carbonates can be explained by the fact that during the PHREEQC simulations, the source term and the basalt water are equilibrated with a CO_2 partial pressure of 10^{-3} bar. When the high pH basalt water is mixed with the lower pH source term, the resulting pH is lower, causing carbonates to precipitate.

7.2.3.7 Summary

The validation criteria for Method B has been met since the types of minerals that formed during the model simulations (Table 7-13) were shown to match the natural mineralogy occurring at Peña Blanca and verified in the fuel degradation experiments of Wronkiewicz et al. (1996 [DIRS 102047]). In the case of carbonates, which were predicted to form by the model, but were not observed in the analogues, the differences were explained by the differences in chemistry.

Table 7-13. TMI_IG1 Accumulated Minerals at 10,000 Years

	Volume (cm^3/kg of solution)
Uranyl Minerals	
Boltwoodite-Na	35.93
Clays	
Celadonite (mica)	46.38
Saponite-Na	11.72
Zeolites	
Erionite	27.04
Chabazite	8.82
Carbonates	
Magnesite	63.07
Dawsonite	2.70
Oxides	
Gibbsite	1.68

Source: Output DTN: MO0609SPAINOUT.002, folders: TMI_IG1/ TMI_IG1_MinAcc, file: *tmi_Vol_Summary.xls*, tab: Sorted Minerals, columns E and F.

7.2.4 Method C: Simulation of Argonne UO_2 Drip Test

As directed in Method C of Section 2.2.1 of the TWP (BSC 2006 [DIRS 177153]), a validation exercise is performed to determine whether PHREEQC can be used to predict the accumulation of uranyl minerals and leachate compositions observed in the Argonne National Laboratory (ANL) UO_2 drip test (Wronkiewicz et al. 1996 [DIRS 102047]). A PHREEQC model is developed in the same manner as the external accumulation model to simulate the reactive transport of ground water through an unsaturated column containing UO_2 pellets over a ten-year period.

The ANL UO_2 drip test is not an ideal analogue for validation of the PHREEQC external accumulation model because it involves oxidation of uraninite, a process not simulated in the model. However, this test is better than any other experiment or natural analogue available for validation. The PHREEQC external accumulation model simulates U(VI) precipitation via advection and mixing of two waters. Similarly, a certain amount of mixing (or contact of two phases) is involved in the UO_2 oxidation analogues, and this mixing determines the various uranyl phases that form. Uranophane and becquerelite require a source of calcium, which can be provided by percolating ground water and nearby calcium minerals. Silica, which is needed for uranophane, weeksite, boltwoodite, and soddyite, can also be provided by the seeping ground water and nearby minerals. In this sense, the ANL UO_2 drip test presents a geochemical mixing process that causes precipitation of uranyl mineral phases.

The relevant materials, methods, and results of the ANL UO_2 drip test are described in Section 7.2.4.1. Section 7.2.4.2 lists the validation criteria from the TWP (BSC 2006 [DIRS 177153]). The PHREEQC model simulation is developed in Section 7.2.4.3, and the results are compared to experimental observations and the validation criteria in Section 7.2.4.4.

7.2.4.1 The Argonne UO_2 Drip Test

In the ANL UO_2 drip test, simulated ground water was slowly dripped onto UO_2 samples at 90°C, primarily to measure uranium release rates and degradation of UO_2. The experiments are documented by Wronkiewicz et al. (1991 [DIRS 176891]; 1992 [DIRS 100493]; 1996 [DIRS 102047]) and summarized here. The UO_2 samples were press sintered into wafered pellets from UO_2 powder and crushed into granules. They were prepared and arranged in the following configurations (Wronkiewicz et al. 1996 [DIRS 102047], p. 81):

- A stack of eleven wafered pellets, 13.9 mm in diameter and 1.8 mm thick (experiments 1 and 2)
- –60 to +80 crushed grains sandwiched between two wafers of the same dimensions as the first configuration (experiments 3 and 4)
- A stack of three wafered pellets, 13.9 mm in diameter and 10 mm thick (experiments 5 through 8).

The samples were held in place by eight Zircaloy metal tubes (13.9 mm ID) placed vertically so that water deposited on the top UO_2 wafer would eventually flow out the bottom. A crimp at the bottom of each tube prevented the samples from falling out and touching the Teflon stand below. The assemblies were sealed in reaction vessels made of 304L stainless steel. A port at the top of the vessel allowed injection of the simulated ground water. To maintain a temperature of 90°C, the reaction vessels were housed in an oven. Further details of the apparatus can be found in the work of Wronkiewicz et al. (1991 [DIRS 176891]; 1992 [DIRS 100493]; 1996 [DIRS 102047]).

The injectate, called EJ-13, was prepared by equilibrating J-13 well water with core samples from the Topopah Springs Member of the Paintbrush Tuff from Yucca Mountain (Wronkiewicz et al. 1996 [DIRS 102047], p. 82). Equilibration involved placing 10 grams of crushed tuff in one liter of J-13 well water at 90°C for two weeks, followed by filtering and dark storage. The composition of EJ-13 is presented in Table 7-14.

Table 7-14. Composition of EJ-13 water

Component	Units	Value
pH	standard units	8.2
Si	ppm	45.5
Na	ppm	54.1
K	ppm	8.08
Ca	ppm	8.81
Mg	ppm	0.96
Al	ppm	0.63
B	ppm	0.16
Sr	ppm	0.045
Li	ppm	0.044
Fe	ppm	0.01
Mn	ppm	0.005
U	ppm	0.0024
F^-	ppm	2.4
Cl^-	ppm	7.15
NO_3^-	ppm	7.60
NO_2^-	ppm	<0.5
SO_4^{2-}	ppm	17.3
HCO_3^-	ppm	135
C (organic)	ppm	5.0
C (inorganic)	ppm	26.5

Source: Wronkiewicz et al. 1996 [DIRS 102047], p. 82.

EJ-13 was injected at a rate of 0.075 mL every 3.5 days (7.82 mL/yr) for experiments 1 through 6 and at 0.0375 mL every 7 days (1.95 mL/yr) for experiments 7 and 8 (Wronkiewicz et al. 1996 [DIRS 102047], p. 82). To clear the injection line, 0.25 mL of air was injected after each EJ-13 injection. The injection process resulted in a buildup of pressure inside the reaction vessels, released only when leachate samples were collected. Sample collection times were 5 to 8 weeks for the first year, 23 to 28 weeks between years 1 and 4.6, and 52 to 67 weeks between years 4.6 and 10 (Wronkiewicz et al. 1996 [DIRS 102047], Table 1). Each experiment began with 0.2 mL of EJ-13 water in the bottom of the vessel to generate a humid atmosphere and prevent initial evaporation of the injectate. When leachate samples were collected, the UO_2 surfaces and accumulation of secondary minerals were analyzed and photographed.

7.2.4.2 Validation Criteria

The TWP (BSC 2006 [DIRS 177153], Section 2.2.1) specifies the following validation criteria for this validation exercise:

1. The model should predict that U(VI) minerals accumulate over time and throughout the column. Predicting the exact same mineral assemblages observed in the drip tests is not required, because the total uranium accumulation is what is important to criticality.

2. The uranium release rate measured in the drip tests is the total uranium released from the sample, including the uranium that precipitated on the vessel but excluding the portion that reprecipitates on the UO_2-Zircaloy assembly. That is, it is the sum of the aqueous uranium and the solid-phase uranium in the leachate and on the bottom of the stainless steel reaction vessel. The solid phase includes secondary minerals and UO_2 particles that detach from the sample surfaces. Because the model neither simulates entrainment of solid particles nor spallation of UO_2 particles, the predicted aqueous release rates should not exceed the mean measured cumulative uranium release rates.

3. Only toward the end of the experiments, between 8 and 10 years, was leachate filtered to separate suspended uranium from aqueous uranium. These measurements determined that approximately 2% of the uranium released was in the filtered <5 nm size fraction (Wronkiewicz et al. 1996 [DIRS 102047], p. 86). Experiments 3 and 6 were the only experiments that continued to 10 years with a flow rate (7.82 mL/yr) equal to the simulated flow rate (Wronkiewicz et al. 1996 [DIRS 102047], Table 1). Therefore, the predicted aqueous uranium release rates should be approximately 2% (plus or minus a factor of 10) of the mean measured cumulative uranium release rates between 8 and 10 years for experiments 3 and 6.

4. Predicted leachate pH should be within the range observed in the experiments.

5. Predicted leachate concentrations of Na, Ca, and Si should be within the ranges observed in the experiments. Other than OH^-, the components Na^+, Ca^{2+}, CO_3^{2-} and SiO_2 are the primary controls on U(VI) solubility in the experiments.

7.2.4.3 Drip Test Simulation

The five processes that the drip test simulation has in common with the external accumulation model are: (1) "mixing" of ambient water with a uranium source, (2) aqueous equilibration, (3) air-water equilibration of carbon dioxide, (4) precipitation of supersaturated minerals, and (5) advection of aqueous components. Minerals that are effectively allowed or suppressed in the drip test simulation are the same minerals effectively allowed or suppressed in the external accumulation model. Also, the PHREEQC databases used in the external accumulation model and the drip test simulation were directly translated from the same original thermodynamic database (*data0.ymp.R4*). The external accumulation model uses the *phreeqcDATA025bdotCr3.dat* database modified from the database (phreeqcDATA025.dat) located in DTN: MO0604SPAPHR25.001 [DIRS 176868], as explained in Section 4.1.1 and the drip test simulation uses *phreeqcDATA090.dat* (DTN: MO0604SPAPHR90.000 [DIRS 176909]). The only difference between the two databases, relevant to the drip test simulation, is that the former has log K values for 25°C and the latter has log K values for 90°C. When carbonate is present, the solubility of uranium decreases markedly as temperature increases from 25°C to 90°C. This retrograde solubility is due to the retrograde solubility of carbon dioxide and the stability of aqueous uranyl carbonate complexes.

The processes of the external accumulation model not modeled in the drip test simulation are: (1) the dissolution of tuff minerals, the injectate is J-13 water equilibrated with crushed tuff at 90°C for two weeks, but the model does not simulate this equilibration; (2) mixing of waste package

water with ambient water; and (3) uranium adsorption onto crushed tuff. These processes are not modeled because the EJ-13 injectate does not mix with ambient water and does not contact tuff after it is injected.

The UO_2/Zircaloy tube assembly is represented in the simulation by a one-dimensional six-cell column. The actual flow of water in the drip test experiments, however, was not one-dimensional. In addition to vertical percolation, water spread radially, as indicated by rings of secondary mineralization in photographs of the top surface (Wronkiewicz et al. 1996 [DIRS 102047], Figure 6). Effluent exited the lower end of the Zircaloy tube and collected at the bottom of the vessel. The six-cell one-dimensional representation used in the simulation, therefore, is meant to capture the general evolution of water and minerals along a flow path from the top of the tube to the bottom.

Cells 1 through 6 represent the UO_2/Zircoloy tube assembly in the crushed pellet configuration of experiments 3 and 4. The inner diameter was 13.7 mm and the height was 22.5 mm (19 mm of crushed UO_2 sandwiched between two 1.75 mm UO_2 wafers) (Wronkiewicz et al. 1991 [DIRS 176891], p. 4). Accordingly, the total volume per cell was set at 0.55 mL. The porosity was set at 0.3, which is in the range of unconsolidated sand (Freeze and Cherry 1979 [DIRS 101173], p. 37) and consistent with the estimated porosity (0.31) of crushed tuff in the external accumulation model (BSC 2004 [DIRS 168138], Table 5). Water saturation was set at 67 percent, implying a water volume of 0.11 mL per cell. The flow rate of water through the cells was based on the EJ-13 injection rate of 7.82 mL/yr (0.075 mL per 3.5 days) in experiments 1 through 6. Because each cell was defined to contain 0.11 mL of water, the time step for each shift (i.e., each complete flush of a cell) was set at 5.2 days.

Pressurization of the vessel was also modeled in the simulation. Injection of EJ-13 pressurizes the vessel by reducing the volume of air inside the vessel. In addition, purging of the injection lines with air adds additional pressure and CO_2. As the total pressure in the vessel increases, the partial pressure of CO_2 in the vessel increases, which in turn affects pH, water composition, and mineral solubilities.

The air volume in the reaction vessel was not reported. However, it was noted that 10 mL of liquid reached a level just above the Teflon stand (Wronkiewicz et al. 1991 [DIRS 176891], p. 5). Based on this information and the schematic drawing of the apparatus (Wronkiewicz et al. 1991 [DIRS 176891], p. 3), the void space in the vessel outside the Zircaloy tube was estimated to be between 20 and 25 mL when no water was present.

For the first year of the simulation, when leachate was collected for analysis every five to eight weeks, the air space surrounding the Zircaloy tube was set at 20 mL. Over the course of eight weeks, 1.2 mL of EJ-13 water (56 days * 0.075 mL/3.5 days) collected in the vessel. Because this volume is low compared to the estimated void space in the vessel (20 to 25 mL), a volume of 20 mL of air space was maintained in the vessel for the first year.

Between 1 and 4.5 years, the sampling periods ranged from 23 to 28 weeks. During these periods, 3.5 to 4.2 mL of EJ-13 water collected in the vessel. Reducing the air volume to 16 mL between 1 and 4.5 years simulated the resulting loss of air space. Incrementally reducing the air space as injectate is added between sampling periods would have been more realistic, but doing

so is unnecessary when model predictions are only compared to measurements at the end of sampling periods.

Beyond 4.5 years, sampling periods ranged from 52 to 67 weeks, implying 7.8 to 10 mL of EJ-13 water collected in the vessel by the end of the sampling periods. Accordingly, the air volume was reduced to 12 mL for this time period. Compression of the air space from 20 to 25 mL to 12 mL in a closed vessel due to injectate additions implies that the air pressure in the vessel approximately doubles.

Added to this pressurization is the air injected to purge the EJ-13 injection lines. At 0.25 mL per 3.5 days, air accumulates at a rate of 26 mL/yr. Thus, for the year-long sampling periods, in addition to the doubling of air pressure by injectate displacement of the air space, there is an additional doubling of pressure from the doubling of the mass of air in the vessel, implying an approximate four-fold overall increase in vessel pressure.

Cells 2 through 6 were defined to have a headspace of 0.055 mL (0.55 mL total per cell * 0.3 porosity * 0.67 water saturation). Cells 1 and 6 were directly exposed to the air space surrounding the UO_2/Zircoloy tube assembly. In the simulation, cell 1 was directly in contact with, and equilibrated with, this air space at all times. Cell 6 was equilibrated with this air space by setting the CO_2 partial pressure in its 0.055 mL headspace equal to the partial pressure in cell 1 at all times.

The injected air was added to the air space in the simulations by increasing the moles of air in the headspace over time. The temperature of the injected air was not reported and was taken to be 25°C. The ideal gas equation, PV=nRT (Mahan 1975 [DIRS 125331], p. 43) can be solved for the number of moles (n) of air per injection, where P is pressure, V is volume, R is the universal gas constant (0.08206 L-atm/mol-K), and T is temperature (K). For a 0.25 mL injection at 298 K and 1 atm, n is 1.0×10^{-5} moles of air, implying an injection rate of 3.3×10^{-11} mol/s ((1.0×10^{-5} mol/3.5 day)/(24 hr/day)/(3600 s/hr)). This injected air was distributed at each time step to each cell in proportion to the headspace defined for each cell. The air composition used was 0.04% CO_2, 1% Ar, 21% O_2, and 78% N_2. This composition was taken from the 62nd edition of the *CRC Handbook of Chemistry and Physics* (Weast and Astle 1982 [DIRS 100833], p. F-172), with CO_2 rounded up from 0.033%. In the simulation, argon (which is inert) was used in place of nitrogen to prevent nitrogen oxidation/reduction.

The original amount of UO_2 in each cell was set at 0.016 moles. This amount is equivalent to the initial UO_2 volume in each cell (0.39 mL) multiplied by the density (11 g/mL) divided by the molecular weight (270 g/mol) (Weast and Astle 1982 [DIRS 100833], p. B-161). A fixed UO_2 degradation rate of 1×10^{-13} mol/s per cell was chosen to approximately match the secondary mineralization observed in the experiments. This rate was the only parameter in the simulation that was adjusted to fit the observations. Degradation rates were not reported for the drip test; thus, the best choice was to adjust the degradation rate to match the experimental observations.

PHREEQC V2.11 was used to execute the simulation. The input file is *dt90h* and the output files are *dt90h.out* and *dt90h.xls*, located in output DTN: MO0604SPAPREDI.000. The *dt90h.xls* output file was post-processed in files *dt90h3.5yrfig.xls* and *dt90h8yrfig.xls*, which are

also located in output DTN: MO0604SPAPREDI.000. The latter two spreadsheets contain the same *dt90h.xls* output but are filtered for 3.5 and 8 years, respectively.

7.2.4.4 Results

The results of the drip test simulation are compared to observations as each validation criterion is addressed below. Each criterion is met, validating the PHREEQC external accumulation model for its ability to simulate: (1) mixing of ambient water with a uranium source, (2) aqueous equilibration, (3) air-water equilibration of carbon dioxide, (4) precipitation of supersaturated minerals, and (5) advection of chemical components.

Simulation results are presented in Table 7-15 and Figure 7-11 through Figure 7-14. The figures show model predictions for mineral phases, pH, partial pressure of carbon dioxide, and concentrations of aqueous components in each cell after 3.5 and 8 years. These times were chosen for the validation because mineral phases were analyzed in experiments that were terminated at these times.

Table 7-15. Comparison of Simulation to Drip Test Results

Component	Units	Range of Measurements[a]	Range of Predictions[b]
pH	pH units	5.8 to 7.9	7.5 to 7.8
Si	C/C_o[c]	0.01 to 1	0.13 to 0.24
Na	C/C_o	0.1 to 1.6	0.87 to 0.94
Ca[d]	C/C_o	0.001 to 1.0	0.00017 to 0.00019

[a] Wronkiewicz et al. 1996 [DIRS 102047], p. 88.
[b] See files *dt90h3.5yrfig.xls* and *dt90h8yrfig.xls* in output DTN: MO0604SPAPREDI.000, Cell 6, for corresponding measurements.
[c] C/C_o is the concentration relative to concentration in EJ-13 (Table 7-14).
[d] The bulk of the measured Ca release is likely colloidal or particulate which is not modeled in the simulation. Detection limits may also have prevented lower C/C_o measurements.

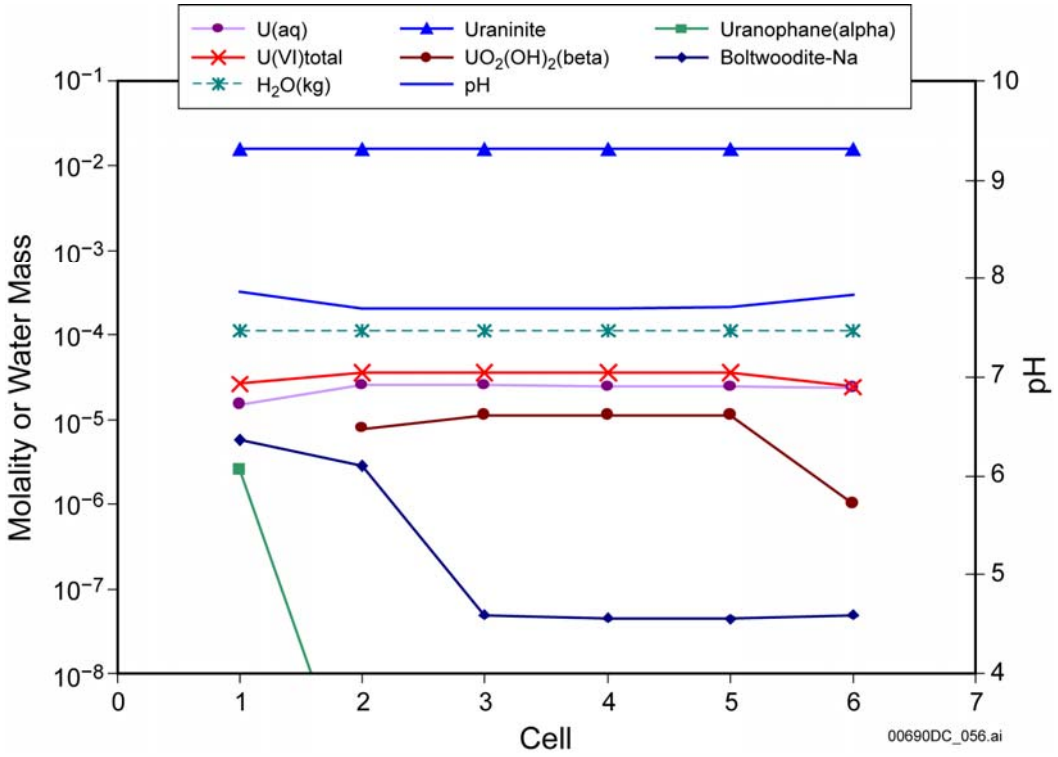

Figure 7-11. Predicted Drip Test Mineral Phases and pH at 3.5 Years

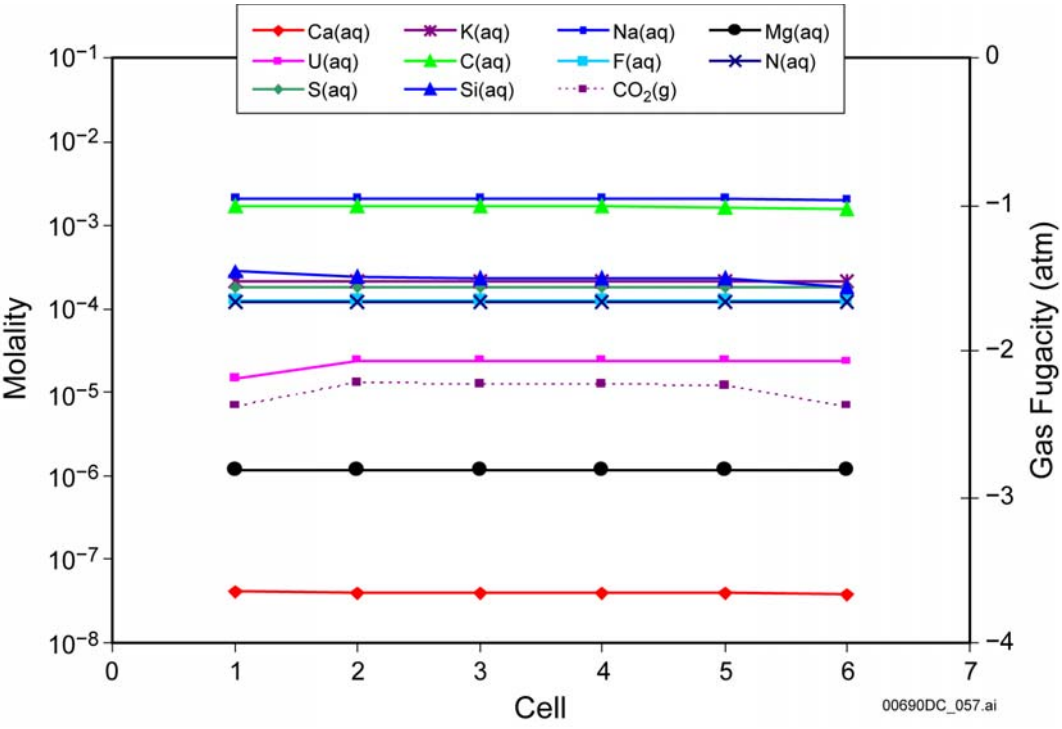

Source: Output DTN: MO0604SPAPREDI.000.

Figure 7-12. Predicted Drip Test Aqueous Concentrations at 3.5 Years

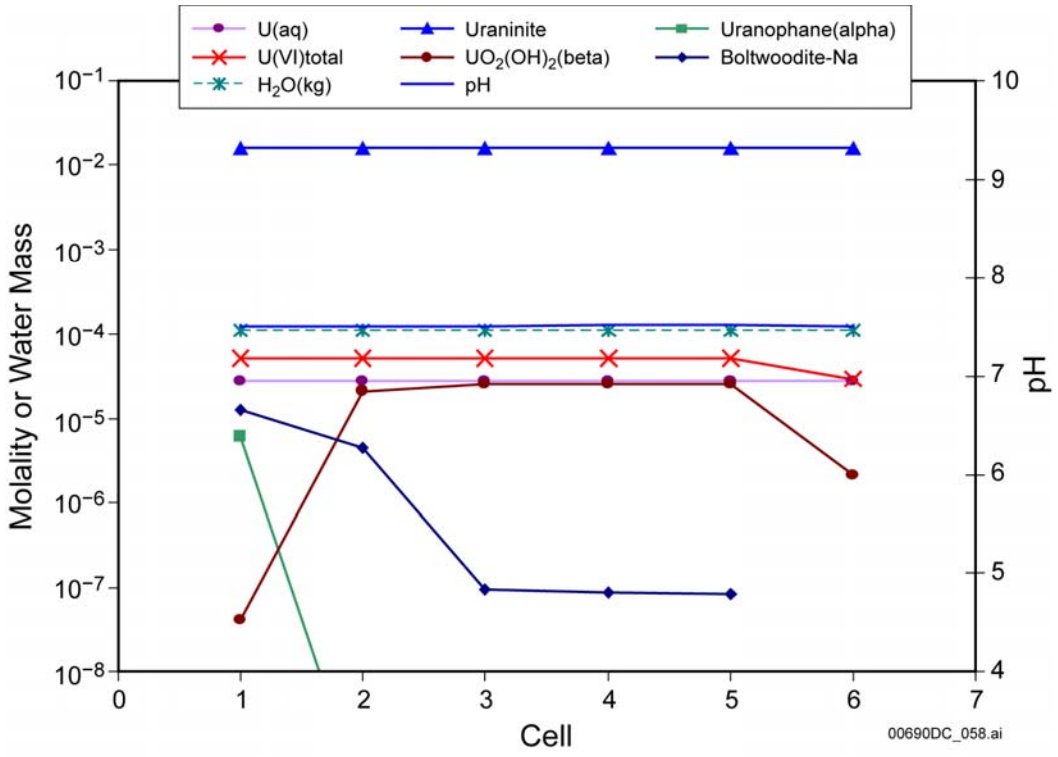

Figure 7-13. Predicted Drip Test Mineral Phases and pH at 8 Years

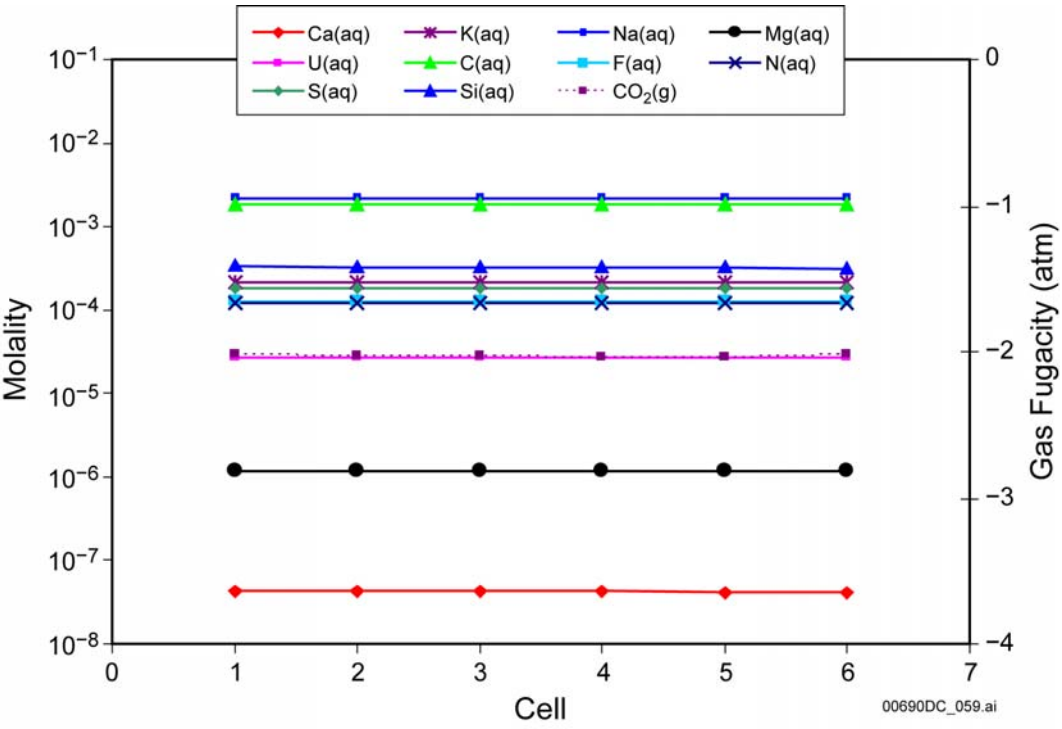

Source: Output DTN: MO0604SPAPREDI.000.

Figure 7-14. Predicted Drip Test Aqueous Concentrations at 8 Years

1. Accumulation of U(VI) minerals. The first validation criterion is to predict the accumulation of U(VI) minerals over time and throughout the column. Predicting the same mineral assemblages observed in the drip tests is not required because only the total uranium accumulation is important to criticality calculations.

Figure 7-11 and Figure 7-13 show accumulation of uranophane, boltwoodite-Na, and dehydrated schoepite (shown as $UO_2(OH)_2$(beta)) in the simulated 6-cell column at 3.5 and 8 years. Each of these phases was also observed in the drip tests (Wronkiewicz et al. 1996 [DIRS 102047], p. 87).

In the first cell, uranophane and boltwoodite-Na are the predominant U(VI) mineral phases. This prediction agrees strongly with observations, which show that these phases were primarily found on the surface of the top UO_2 pellet where EJ-13 water was injected. At 3.5 years, uranophane was the most common secondary phase observed on the top surface (Wronkiewicz et al. 1992 [DIRS 100493], p. 118). At 8 years, boltwoodite-Na became the dominant alteration phase on the surface while uranophane was confined to the periphery of the central mat of boltwoodite-Na (Wronkiewicz et al. 1996 [DIRS 102047], p. 89).

In cells 2 through 6 of the simulation, dehydrated schoepite (shown as $UO_2(OH)_2$(beta)) is the dominant uranyl phase, uranophane is absent, and a very small amount of boltwoodite-Na accumulates (Figure 7-11 and Figure 7-13). Uranophane disappears because, as indicated in Figure 7-12 and Figure 7-14, Ca is depleted due to uranophane precipitation in cell 1. These results also agree strongly with observations. In the drip tests, dehydrated schoepite occurred on the sides and bottom surfaces of the UO_2 samples and was virtually absent on the top surface (Wronkiewicz et al. 1992 [DIRS 100493], p. 122).

Other minerals observed in the drip tests were apparently transient. Soddyite, which was a predominant phase at 3.5 years (Wronkiewicz et al. 1992 [DIRS 100493]), was in such small quantities at 8 years that its presence was not discussed in the later paper (Wronkiewicz et al. 1996 [DIRS 102047]). Becquerelite was continuously replacing dehydrated schoepite and then being replaced by uranophane and boltwoodite-Na (Wronkiewicz et al. 1996 [DIRS 102047], p. 90). Becquerelite is not included in the PHREEQC thermodynamic database.

A mineral precipitate that apparently is not transient is palygorskite. This magnesium-hydroxyl clay does not contain uranium, so it does not affect the validation criteria. However, it should be noted that it also is not included in the PHREEQC thermodynamic database and therefore was not allowed to precipitate in the simulations.

Overall, the drip test simulation predicts accumulation of uranyl minerals throughout the column similar in assemblage and distribution to experimental observations. Therefore, the first validation criterion is met.

The paragenesis of UO_2 to uranyl oxide hydrates and uranyl alkali silicates in the drip test and simulation is similar to the paragenesis observed at Peña Blanca (Pearcy et al. 1994 [DIRS 100486]). For the last three million years, the Peña Blanca uraninite deposit has been exposed to an arid, oxidizing setting far above the water table, much like Yucca Mountain. Further, the groundwater at the site is broadly similar to the groundwater below Yucca Mountain (BSC 2004 [DIRS 169218], p. 10-31). Uraninite is oxidized at Peña Blanca to various U(VI)

secondary minerals, mainly uranophane and schoepite or dehydrated schoepite and to a lesser extent soddyite, weeksite, and boltwoodite (Pearcy et al. 1994 [DIRS 100486]).

2. Total uranium release rate. The second validation criterion is to predict aqueous release rates less than the mean measured cumulative uranium release rates. Predictions should be less than the measurements because the release rates measured in the drip tests are the total uranium released from the samples, including the uranium that precipitates on the vessel and UO_2 particles that detach from pellets and collect in the leachate. Both uranyl minerals and UO_2 particles collected in the leachate. In fact, less than two percent of the uranium released in years 8 through 10 passed through a 5 nm filter (Wronkiewicz et al. 1996 [DIRS 102047], p. 86). The model does not simulate entrainment of solid particles, spallation of UO_2 particles, or precipitation at the bottom of the vessel.

Based on the data in Table 1 of the study by Wronkiewicz et al. (1996 [DIRS 102047]), the mean measured release rate for experiments 1 through 6 was 0.96 mg/yr. This calculation is presented in the sheet *U release* of *dt90h8yrfig.xls* (output DTN: MO0604SPAPREDI.000). Experiments 7 and 8 were not included because their drip rates were 25% of the simulation drip rate (and of the drip rates of experiments 1 through 6).

The predicted release rate of dissolved uranium ranges from 0.039 to 0.051 mg/yr over the 10-year simulation period. These rates were calculated by multiplying the dissolved uranium concentration in cell 6 by the molecular weight of uranium and the flow rate. These values are approximately 4% to 5% of the mean measured cumulative uranium release rates; thus, the second validation criterion is met.

3. Aqueous uranium release rate. The third criterion is that the predicted aqueous uranium release rates be approximately 2% (plus or minus a factor of 10) of the mean measured cumulative uranium release rates between 8 and 10 years for experiments 3 and 6.

The release rates for experiments 3 and 6 between 8 and 10 years were approximately 0.29 mg/yr (see sheet *U release* of *dt90h8yrfig.xls* in output DTN: MO0604SPAPREDI.000). Of experiments 1 through 6, only 3 and 6 lasted beyond 8 years. Less than two percent of the uranium during this time period passed through a 5 nm filter, suggesting that the release rate of dissolved uranium was less than 0.0058 mg/yr. This calculation presumes that dissolved uranium was not lost by sorption to the filtration apparatus, complications of sample handling, or other mechanisms.

As indicated above, the simulation predicts a dissolved concentration in the effluent of 0.039 to 0.051 mg/yr. These values are 13% to 18% of the mean measured cumulative uranium release rates between 8 and 10 years for the experiments 3 and 6, which is within the 0.2% to 20% range of the criterion.

4. Predicted leachate pH. The fourth criterion is that the leachate pH values be predicted within the range observed in the experiments. Measurements for pH begin at 157 weeks (Wronkiewicz et al. 1996 [DIRS 102047], p. 88). The range of these measurements is 5.9 to 7.9.

The simulated sampling periods roughly correspond to the sampling periods defined in Table 1 of the study by Wronkiewicz et al. (1996 [DIRS 102047]) and are marked in red in the first

columns of files *dt90h3.5yrfig.xls* and *dt90h8yrfig.xls* (output DTN: MO0604SPAPREDI.000). For simulated sampling periods at 156 weeks and beyond, the predicted pH range in cell 6 is 7.5 to 7.8.

The simulations provide pH calculations at the end of the sampling periods and at intervals prior to the end of the sampling periods. Prior to the end of the sampling periods, pH calculations are generally closer to 8. By the end of the sampling periods, however, as air pressure builds in the vessel, pH calculations drop to the 7.5 to 7.8 range, which is within the pH range measured. Therefore, the pH criterion is met.

5. Predicted leachate concentrations of Na, Ca, and Si. The fifth criterion is that the predicted leachate concentrations of Na, Ca, and Si be within the ranges observed in the experiments. Na, Ca, and Si are important components of the major secondary uranyl phases observed in the drip tests. Therefore, their concentrations should be depleted in the leachate.

Table 7-15 lists the ranges of concentrations of Na, Ca, and Si observed in the leachate as well as the predicted leachate concentration ranges. As in the pH validation, predicted values are for simulated sampling periods corresponding to sampling periods represented in Figure 5 of the study by Wronkiewicz et al. (1996 [DIRS 102047]).

The depletion of Na and Si are in the range observed in the experiments, but the depletion of Ca is below the range reported. One reason might be a detection limit of approximately 2.2×10^{-7} ppm, as suggested by the numerous values plotted at a C/C_o value of 0.001 in Figure 5 of the study by Wronkiewicz et al. (1996 [DIRS 102047]). Nevertheless, most measurements are in the 0.01 to 1.0 range, indicating considerable mobility of Ca in the experiments that is not represented in the simulation.

The likely explanation is that the leachate contains uranophane. The simulation treats minerals as immobile, yet minerals are found in considerable quantities in the leachate. Some minerals are reported to precipitate on the Teflon stand beneath the UO_2/Zircoloy tube assembly (Wronkiewicz et al. 1996 [DIRS 102047], p. 86). Uranophane is shown in Figure 4 of the study by Wronkiewicz et al. (1996 [DIRS 102047]) to be trapped as a filtered residue of the leachate. Consequently, mobilization of uranophane could account for the vast majority of Ca in the leachate. As mentioned earlier, ultrafiltration revealed that less than two percent of uranium in the leachate between 8 and 10 years passed through a 5 nm filter (Wronkiewicz et al. 1996 [DIRS 102047], p. 88). The percentage of Ca that passed through a 5 nm filter is not reported but is expected to be very low based on the results of the simulation.

Although the Ca predictions are below the validation range, they do not invalidate the external accumulation model because the model does not simulate mobilization of colloidal or undissolved materials. The model assumes that uranium precipitation is immobile because doing so is conservative, i.e., it increases the chances of predicting a criticality. Observations of uranophane in the leachate prevent a meaningful comparison of predicted and observed Ca concentrations because observed Ca concentrations are likely dominated by undissolved Ca and predicted concentrations only include dissolved concentrations. Thus, while the fifth validation criterion is met for Na and Si, it is justifiably not applied to Ca.

7.2.5 Method D: Validate Numerical Model for Flow and Transport in Invert with Analytical Model

The objective of this validation activity is to show that the TOUGHREACT numerical model, which may be affected by limited convergence accuracy, roundoff errors, and numerical dispersion, agrees well with a two-dimensional analytical model for flow and transport, which is not afflicted with these limitations and potential errors. Two of the major outputs of the numerical model, which will be corroborated using the analytical model, are the steady-state cumulative flux (flow out the bottom of the invert) and relative concentration (ratio of radionuclide or tracer concentration in invert water to its concentration in waste package water) as a function of horizontal distance along the cross section of the invert, where cross section is perpendicular to the centerline of the waste package. The criterion used to demonstrate that the numerical model is sufficiently accurate (see Table 7-6) is that for a given value of cumulative flux or relative concentration, the horizontal distance along the cross section of the invert calculated by the numerical model is within ±10 cm of the value calculated by the analytical model. This level of uncertainty was calculated using the analytical model and represents the expected variations due to the different equations used in the two models to describe the relationship of relative permeability to water potential: Gardner equation for the analytical model (Bear 1972 [DIRS 156269], p. 492) and van Genuchten equation for the numerical model (van Genuchten 1980 [DIRS 100610]).

A validation case was developed in which the numerical model for invert flow and transport model could be validated with an analytical model for flow and transport in the invert. The analytical model, developed in Appendix C, is a direct solution of the steady-state flow and transport problem and uses the Gardner relationship between effective permeability and moisture potential (Bear 1972 [DIRS 156269], p. 492). The numerical model uses the software TOUGHREACT V3.0 (see Section 3.1.11).

The moisture potential and effective permeability relationships employed in the TOUGHREACT calculations were developed by van Genuchten (1980 [DIRS 100610]). The van Genuchten (1980 [DIRS 100610]) relationships are:

$$K(S_n) = K_s S_n^{1/2}\left(1-\left(S_n^{\frac{1+N(m-1)}{m(N-1)}} - S_n^{\frac{N}{N-1}}\right)^{\frac{N-1}{N}}\right)^2 \qquad \text{(Eq. 7.2.5-1)}$$

$$\psi(S_n) = -\frac{1}{\alpha_{vG}}\left(S_n^{-1/m}-1\right)^{1/N} \qquad \text{(Eq. 7.2.5-2)}$$

$$S_n = \frac{S - S_r}{1 - S_r} \qquad \text{(Eq. 7.2.5-3)}$$

where S is the water saturation, S_r is the residual water saturation, S_n is the normalized water saturation, and $N = \frac{1}{1-m}$, where m is the van Genuchten pore size distribution index. The Gardner relationship is:

$$K(\psi) = K_0 \exp\{\alpha(\psi - \psi_0)\} \quad \text{(Eq. 7.2.5-4)}$$

where, ψ is the water pressure head and α is a fitting parameter. It turns out that the van Genuchten (1980 [DIRS 100610]) parameterization can be fit more closely to the Gardner (Bear 1972 [DIRS 156269], p. 492) parameterization for larger values of the Gardner α. However, numerical precision errors in the analytical solution limit the value of Gardner α used to be less than about 4.08×10^{-3} Pa^{-1} (or in terms of water head, 40 m^{-1}). Problems associated with numerical precision preclude generating relative concentrations for high values of α. This is because of the nature of the concentration solution given in Equation C.2-36. For large values of α, large areas of the invert have very small values of both the transport potential, Θ, and flow potential, χ. These small potentials are generated from the summation of terms of much greater magnitude that nearly cancel. This situation leads to a loss in numerical precision. For the flow fields, the lack of precision is not critical because as χ becomes small, so do the fluxes. Therefore areas where χ loses precision also have very nearly zero flux. But for concentration this is not the case. As both Θ and χ become small, the relative concentration, which is computed as the ratio of these potentials, can be any value ranging between 0 and 1. The loss in precision can affect significant ranges of the relative concentration, not just values near zero. Therefore, the validation case was selected to have a Gardner $\alpha = 4.08 \times 10^{-3}$ Pa^{-1}. The van Genuchten capillary strength parameter, α_{vG}, the van Genuchten pore size distribution index, m, and the saturated permeability, k, were optimized manually to obtain a close fit between the relative permeability and moisture potential curves based on the Gardner and van Genuchten parameterizations. The best results are presented in Table 7-16.

Table 7-16. Best Fit Parameters for Gardner and van Genuchten Equations

Parameter	Value
α_{vG}	9.17×10^{-3} Pa^{-1}
m	0.805
k	1.62×10^{-11} m^2

Source: Output DTN: MO0604SPANUMER.000, *VG – Gardner fit for validation2.xls*

The fit between the Gardner and van Genuchten parameterizations is given in the Figure 7-15 below:

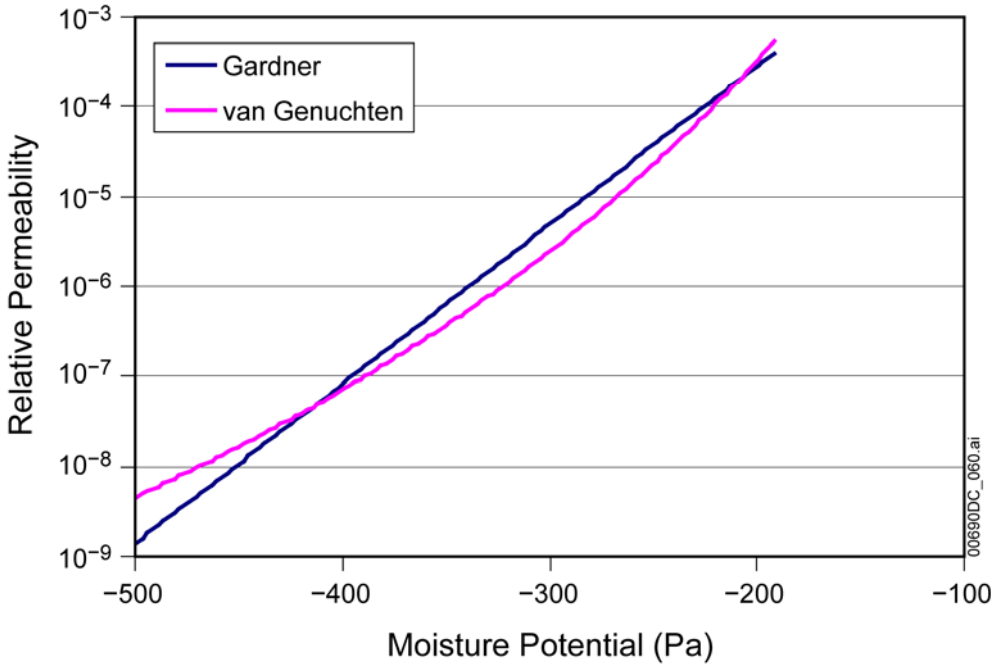

Figure 7-15. Fit between Gardner and van Genuchten Parameterization

Using Equations C.1-19, C.2-7, and C.2-9 from Appendix C, the dispersion coefficient is defined to be given by:

$$\overline{\overline{D}} = \left(\frac{1}{\alpha}\right)\frac{K}{\theta}$$

where α is in units of inverse length and the effective hydraulic conductivity, K, is in units of length per unit time. Theoretical descriptions of dispersion equate $\overline{\overline{D}}$ to the product of the pore velocity times a dispersion length scale called the dispersivity (Bear 1972 [DIRS 156269], Section 10.4.2). For an isotropic porous medium, the dispersion coefficient is a second rank tensor, the dispersivity is described by both longitudinal and transverse values, and pore velocity is a vector. However, in the analytical model, dispersion is approximated as isotropic and the pore velocity and dispersivity are scalar quantities. Approximating the pore velocity by $\frac{K}{\theta}$, the dispersivity is given by $\frac{1}{\alpha}$. Given the value of $\alpha = 40$ m^{-1}, the dispersivity is 0.025 m. The molecular diffusion coefficient is set equal to zero for the validation case, but a sensitivity case was run for the numerical model using 2.3×10^{-9} m^2/s (Mills 1973 [DIRS 133392], Table III).

The remaining parameters are taken from the well-sorted base case, as given in Table 7-17. These parameters have no effect on the results used for comparison between the analytical and base-case models, but are necessary to specify in TOUGHREACT.

Table 7-17. Analytical Parameters for Well-Sorted Base Case

Parameter	Value
porosity	0.45
maximum water saturation	1
residual water saturation	0.0853

Source: Table 4-16 and Table 6-17, except for maximum water saturation, which was set to 1 to represent fully saturated conditions.

The remaining specifications for source strength and other boundary conditions of the validation case are given below.

7.2.5.1 Parameterization of the Invert Flow and Transport Problem

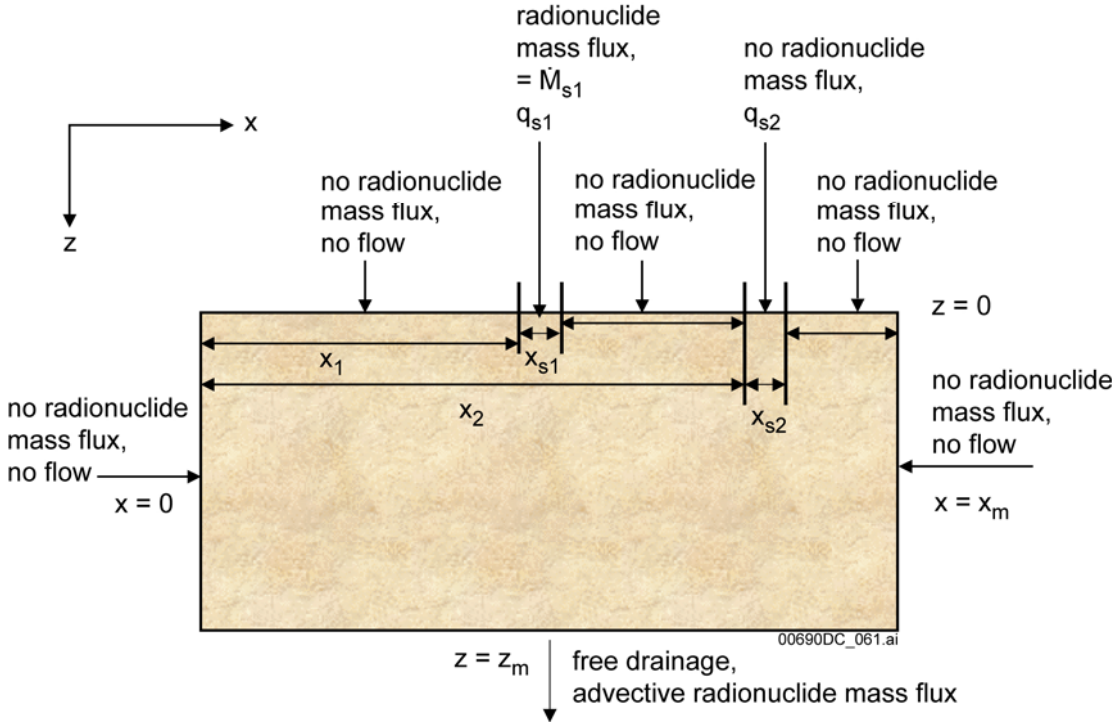

Figure 7-16. Analytical Model Parameters

The parameters required to characterize the invert for flow and transport calculations are:

- The depth and width of the invert, z_m and x_m, respectively.
- The locations of the two source regions, x_1 and x_2.
- The sizes of the two source regions, x_{s1} and x_{s2}.
- The water fluxes for the two source regions, q_{s1} and q_{s2}.
- The Gardner capillary strength parameter, α.

The radionuclide mass flux for the waste package source region, $\dot{M}_{s1}$, is also needed if mass concentrations are required from the transport calculation. However, in this analysis, only

relative concentrations are computed, so $\dot{M}_{s1}$ is not needed. Also, because the Gardner exponential form must be fit locally to the van Genuchten form, the saturated permeability and expected flow rates are needed to establish what range of the curve is to be fit with the Gardner relationship.

7.2.5.2 Invert and Source Geometries

In order to validate the numerical model, the invert geometry must be simplified so that it can be modeled analytically. The simplified geometry used for model validation captures the salient features of the invert, namely, the maximum depth and the effective width through which most of the flow will occur. The invert is represented by a two-dimensional rectangle with dimensions $z_m = 0.864$ m, which is the maximum invert depth, and $x_m = 3.18$ m in width (BSC 2004 [DIRS 169503]; BSC 2004 [DIRS 168489]). This width is the distance between the centers of the gantry crane rails and is considered representative of the effective portion of the invert.

The source location beneath the waste package is in the approximate center of the invert, with the left edge of the source at $x_1 = 1.57$ m from the left boundary. The source location for the diverted flow, x_2, is taken to be 2.57 m from the left boundary, or 1 m offset from the waste package source. The width of each of these source regions (x_{s1} and x_{s2}) is taken to be 2 cm. The length (along the axis of the drift) is 5.1 m, which is the drift length allocated to each waste package (BSC 2004 [DIRS 169131], Section 6.1.3).

7.2.5.3 Source Fluxes

Source flow rate is 1 liter per year for a 5.1-m-long drift segment through the waste package. One L/yr is the flow rate used in two of the source terms (TMI_IG1 and FFTFIG1adEhdec). Diverted flow is 200 L/yr, which corresponds to the mean seepage rate into the drift for the igneous and seismic fault displacement scenarios (Figure 5-1 and Figure 5-2). These flow rates, combined with the source geometries discussed above, correspond to fluxes as given in the following table:

Table 7-18. Flow Rates for Validation Case Seismic

	Waste Package	Diverted Flow
Flow rate (L/yr)	1	200
Flux (mm/yr)	9.8	1,960

NOTE: Flux (mm/yr) = flow rate (L/yr) × 1000 (cm^3/L) ÷ 5.1 m ÷2 cm × (1 m/100 cm) × (10 mm/cm).

The tracer mass flux is set by using unit tracer concentration in the waste package water and zero concentration in the diverted water. The remainder of the upper boundary has zero water and tracer mass flux.

7.2.5.4 Bottom Boundary Conditions

The capillary pressure and tracer concentration gradients in the vertical direction are set to zero.

7.2.5.5 Lateral Boundary Conditions

The capillary pressure and tracer concentration gradients in the horizontal direction are set to zero.

7.2.5.6 Exceptions to the Previous Specifications for Numerical Model

The previous specifications are the same for the analytical and numerical modeling, except for the following:

1. The water sources are modeled as point sources, rather than being spread over a 2-cm width, although the sources in the numerical model could also be interpreted as flowing in over the width of a grid cell.

2. The lateral boundary conditions are the default no-flow and no-transport conditions used in TOUGHREACT, rather than zero capillary pressure and tracer concentration gradients. Although the numerical simulation is therefore set up differently from the analytical model, the results are the same. Due to the high permeability and low water saturation in the simulations, the pressure is uniform throughout, so capillary pressure gradients are zero at the boundaries even though TOUGHREACT was run with no-flow boundary conditions. In addition, the numerical simulation results in horizontal tracer concentration gradients that are zero at steady state when no transport is allowed at the lateral boundary.

3. TOUGHREACT V3.0 does not model hydrodynamic dispersion; however, numerical dispersion does occur when upstream weighting is used. It has been found that for a rectangular grid and full upstream weighting, as used in these simulations, the numerical dispersion is approximately one-half of the grid spacing (Oldenburg 2003 [DIRS 176820], p. 244). In the validation case, the grid spacing is 0.05 m, so the numerical dispersion is approximately 0.025 m, equal to the dispersivity specified for the analytical model.

4. TOUGHREACT V3.0 does not have an option for a direct steady-state solution and does not have effective permeability-moisture potential relationships equivalent to the Gardner model. Therefore, to compare the analytical and numerical models at steady state, the numerical model is run through a transient period to a steady-state condition using parameterizations for moisture potential and effective permeability that approximate the Gardner relationship.

7.2.5.7 Numerical Grid Description

The numerical grid for the validation case is a regular rectangular grid consisting of 20 rows of 64 grid cells spaced $\Delta x = \Delta z = 5.0$ cm apart that represents a vertical two-dimensional cross section of a 3.2-m wide, 0.9-m deep portion of the invert. In the third dimension, horizontally in the axial direction of a drift, the grid is $\Delta y = 1.0$ m deep. The top of the grid is the top surface of the invert. The bottom of the invert is between the 18th and 19th rows. The vertical grid cell spacing (Δz) between the 19th and 20th (bottom) row is 20,000 m in order to achieve a vertical

concentration gradient boundary condition of zero; by making Δz very large, the gradient $\Delta C/\Delta z$ is maintained close to zero. The volume of each grid cell in the 20th row is set to an extremely large value (10^{10} m^3), which allows the pressure to remain constant while water is injected into the grid over long periods of time. The large grid cells also provide a sink for the tracers, which would otherwise accumulate unrealistically as water is injected.

Although TOUGHREACT does not utilize grid cell coordinates to define the grid, these are useful for plotting and describing results. For the validation case, the origin is taken to be the upper left corner of the upper leftmost grid cell boundary. The invert extends in the negative z-direction. Results (e.g., concentrations) are reported at grid cell centers. Thus, the grid cell closest to the origin is at (x, z) = (0.025, −0.025). The bottom of the invert is considered to be the row of grid cells at z = −0.875, which is the closest row to the specified invert depth of 0.864 m.

7.2.5.8 Validation Case TOUGHREACT Input

The grid is set up using the MESHMAKER capability of TOUGHREACT, which provides a convenient way to set up simple regular grids. The input file 'flow.inp' includes the following input lines specifying the number and size of grid cells in each direction. The keyword MESHMAKER signals TOUGHREACT to create a mesh instead of doing a flow and transport calculation. The last line tells MESHMAKER that the last grid cell increment in the z-direction is 20,000 m.

```
MESHMAKER
XYZ
   0.0
NX      64   0.05
NY       1   1.00
NZ      20   0.0
      0.10      0.10      0.10      0.10      0.10      0.10      0.10      0.10
      0.10      0.10      0.10      0.10      0.10      0.10      0.10      0.10
      0.10      0.10      0.10    20000.
```

When TOUGHREACT is run, it creates an output file 'MESH.' This will be the input file that defines the grid for the flow and transport simulations. First, however, 'MESH' must be manually edited to change the volumes of the bottom row of grid cells, from the volume computed by TOUGHREACT ($\Delta x \Delta y \Delta z$ = 0.0025 m^3) to the "infinite" values needed for the calculations (10^{10} m^3). Although the volumes of those cells are changed, the distances between these cells and connected cells are left unchanged, which is physically impossible but numerically acceptable.

The input file 'GENER' provides the water injection rates and locations. The specified source flow rates, in units of mm/yr, are input in units of kg/s. Using a water density of 1,000 kg/m^3, the specified width of the source region of 0.02 m, and Δy = 1.0 m, the source flow rates are:

Waste Package:

$$\frac{\left(9.8\,\frac{\text{mm}}{\text{yr}}\right)\left(10^{-3}\,\frac{\text{m}}{\text{mm}}\right)(0.02\text{ m})(1.0\text{ m})\left(1000\,\frac{\text{kg}}{\text{m}^3}\right)}{\left(86400\,\frac{\text{s}}{\text{day}}\right)\left(365.25\,\frac{\text{day}}{\text{yr}}\right)} = 6.21086\times10^{-9}\text{ kg/s}$$

Diverted: 1.26752×10^{-6} kg/s

The waste package source water is injected in the top (z = −0.025 m) grid cell centered at x = 1.575 m. The diverted source water is injected in the top grid cell at x = 2.575 m.

The input file 'chemical.inp' defines the geochemical system being modeled. The invert is modeled as being initially nonreactive. Aqueous species included in the model are H_2O, SiO_2 (aq), O_2 (aq), Na^+, K^+, and Cl^-. One gas species, O_2, is included. Minerals that could potentially precipitate include SiO_2 (am), sylvite (KCl), and halite (NaCl). The water initially present contains SiO_2 (aq) at a concentration of 0.001 molal (mol/kg H_2O); O_2 (aq), Na^+, and K^+ at a concentration of 1.0×10^{-12} molal; and Cl^- at a concentration of 2.0×10^{-12} molal. Na^+ serves as the tracer in the water from the waste package source, where the Na^+ and Cl^- concentrations are 1.0 molal. K^+ is the tracer in the water from the diverted source, where the K^+ and Cl^- concentrations are 1.0 molal.

The input file 'solute.inp' defines solute transport properties, including the specification of the diffusivity and the locations where the tracer sources are injected (which must agree with the location of water injection locations specified in the 'GENER' file for the simulation to be correct).

The input file 'flow.inp' contains the invert hydrologic properties and initial conditions. As specified for the analytical model, the permeability is 1.62×10^{-11} m^2, and the porosity is 0.45. The van Genuchten-Mualem relative permeability model is used, with the following parameters (using TOUGHREACT notation):

RP(1) = van Genuchten m = 0.805
RP(2) = residual water saturation = S_{lr} = 0.0853
RP(3) = maximum water saturation = S_{ls} = 1.0.

The van Genuchten capillary pressure model is used, with the following parameters:

CP(1) = van Genuchten m = 0.805
CP(2) = residual water saturation = S_{lr} = 0.0850 (chosen smaller than the corresponding relative permeability parameter, as recommended in the TOUGH2 User's Guide (Pruess et al. 1999 [DIRS 160778], p. 189)
CP(3) = van Genuchten α_{vG} = 0.000917 Pa^{-1}
CP(4) = P_{max} = 1.0×10^{10} Pa
CP(5) = maximum water saturation = S_{ls} = 1.0.

To achieve steady state conditions, the simulation is run to 10^9 years, using a maximum time step of 10^5 years. The convergence criterion for relative error is set at 10^{-3}. Time steps are automatically reduced whenever the convergence criterion is not met.

7.2.5.9 Results

The steady state concentrations of tracers across the bottom of the invert (z = −0.875 m) are shown in Figure 7-17. The results indicate a narrow zone of mixing less than 0.3 m wide. Due to the high value of the Gardner parameter α and no molecular diffusion, little dispersion occurs. (Molecular diffusion has a substantial effect, as shown below, where this same case is rerun with molecular diffusion included.)

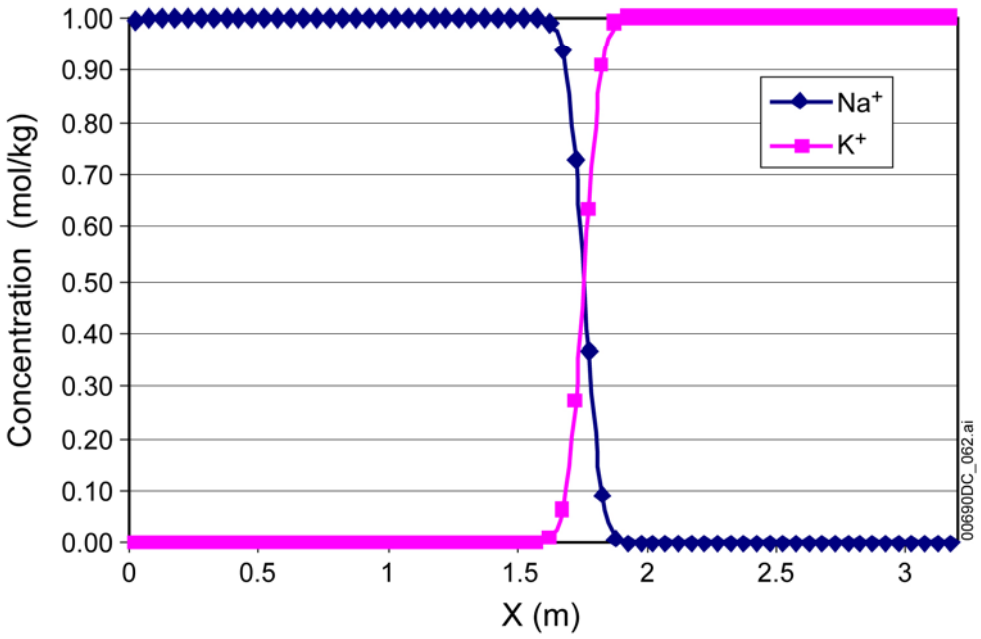

Source: Output DTN: SN0607T0504506.002.

Figure 7-17. Steady State Concentration of Na^+ and K^+ Tracers across Bottom of Invert

Fluxes out the bottom of the invert (from row z = −0.875 m to row z = −0.925 m) are shown in Figure 7-18. The fluxes are summed from x = 0 m across the bottom of the invert. The total cumulative flux is equal to the steady state water injection rate at the two sources: (9.8 mm/yr + 2,000 mm/yr)(0.02 m) = 40,196 mm^2/yr. The results confirm that the bulk of water flow is from the diverted source and tends to flow downward with little dispersion.

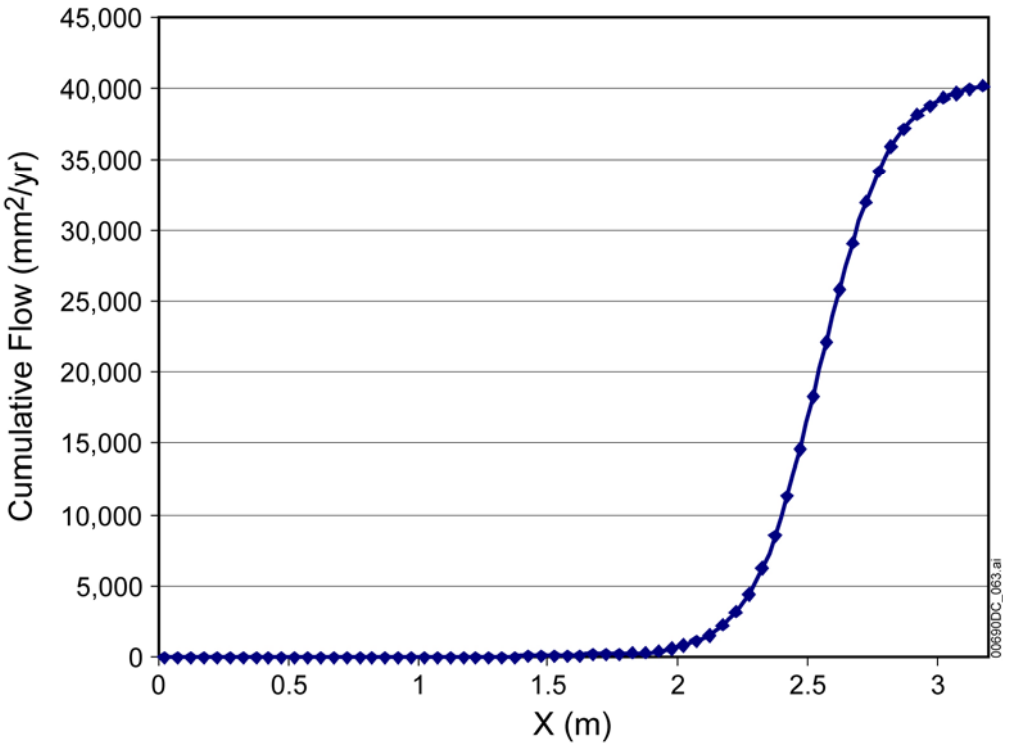

Source: Output DTN: SN0607T0504506.002.

Figure 7-18. Cumulative Steady State Flux of Water out Bottom of Invert

The objective of the validation case is to show that the numerical model, which may be affected by limited convergence accuracy, roundoff errors, and numerical dispersion, agrees well with the analytical model, which is not afflicted with these limitations and potential errors. The acceptance criterion for model validation, as given in Table 7-6, is that for a given value of cumulative flux or relative concentration, the horizontal distance along the cross section of the invert calculated by the numerical model is within ±10 cm of the value calculated by the analytical model. This is shown in Figure 7-19, which demonstrate acceptable agreement between the numerical model and the analytical model. The relative concentration results from the analytical model that are plotted in Figure 7-19 were calculated from Equations C.2-34, C.2-35, and C.2-36. The relative concentration is the ratio of tracer concentration in the invert water to its concentration in the waste package water. In the numerical model, because the Na^+ tracer concentration in the waste package water is 1.0 molal, the relative concentration is equal to the absolute Na^+ concentration. The cumulative flux results from the analytical model plotted in Figure 7-19 were calculated from Equation C.1-84. The files for the analytical model are provided in output DTN: MO0604SPANUMER.000.

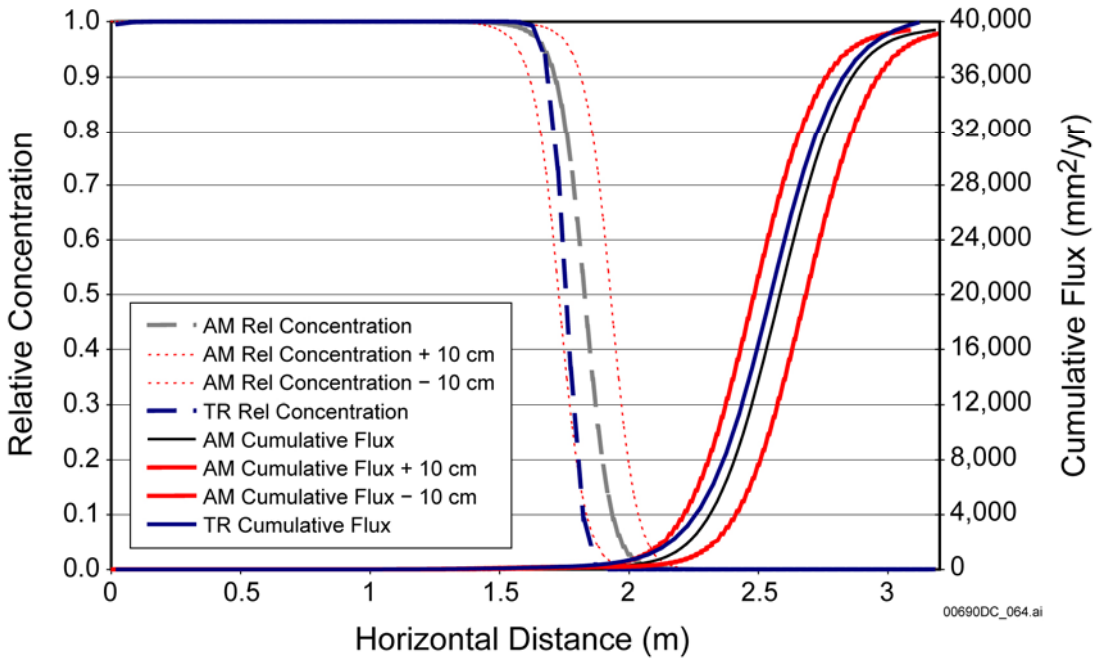

Source: Output DTN: MO0604SPANUMER.000.

NOTE: TR = TOUGHREACT; AM = Analytical Model.

Figure 7-19. Comparison of Cumulative Water Flux out Bottom of Invert and Tracer Concentration across Bottom of Invert

7.2.5.10 Validation Case Grid Convergence Study

As shown above, the validation case numerical model compares well with the analytical model. However, the base-case models differ from the validation case in several respects, including the invert hydrological properties, the invert geometry (having the shape of a circle segment instead of a rectangle), the presence of the UZ beneath the invert, and the grid cell spacing. The validation case gives confidence that the numerical model is capable of simulating the behavior of the invert. Changes in properties, geometry, and downstream flow characteristics are not expected to alter the ability to simulate invert behavior. However, the grid spacing can have significant impact on the accuracy of solutions. Whereas the validation case uses a 5-cm grid spacing, the larger, more complex base case models use a 10-cm grid spacing in order to keep run times reasonable. To gain confidence that the coarser grid will provide sufficiently accurate solutions, the validation case is repeated using both a coarser and finer grid, with 10-cm and 2.5-cm grid spacings.

Results are shown in Figure 7-20, Figure 7-21, and Figure 7-22, in which the 10-cm and 2.5-cm grid spacing results are compared with the validation case (5-cm grid spacing). The results are expected to be different if for no other reason than that the numerical dispersion in the 10-cm grid spacing is double that in the 5-cm grid spacing, and in the 2.5-cm grid spacing, the numerical dispersion is half that in the 5-cm grid spacing. The results show that the solution is converging as the grid is refined, which is expected if the numerical model is performing correctly. One noticeable exception is seen in the Na^+ tracer concentration results for the 2.5-cm

grid spacing. At the left end of the invert, the tracer concentration drops close to zero, whereas the coarser grid spacings and the analytical model show that the concentration is (and should be) 1.0 mol/kg. This behavior indicates that a steady state has not been reached in the 2.5-cm grid spacing calculation. The approach to steady state over time is much slower with the finer grid. The results shown are at 10^9 years.

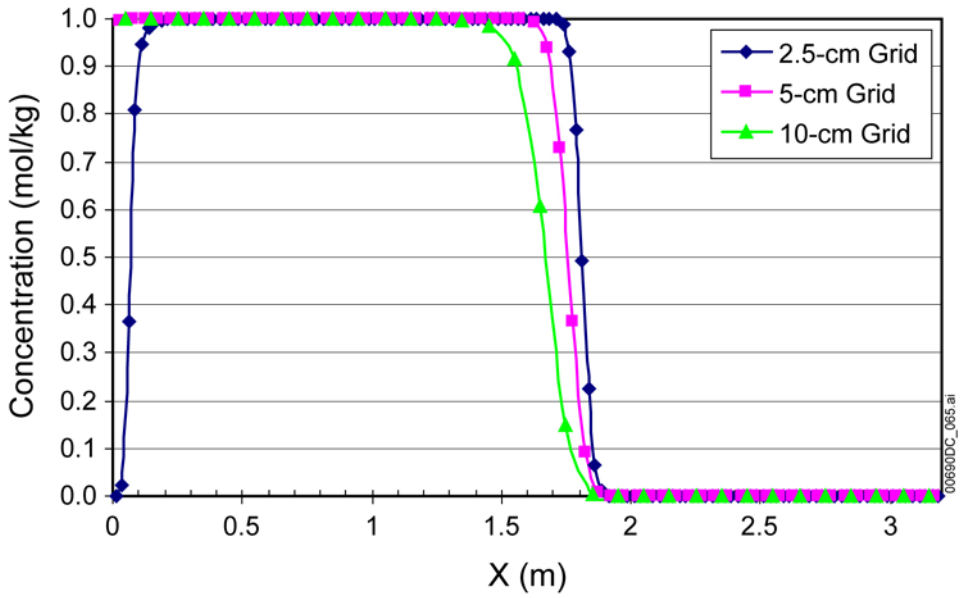

Source: Output DTN: SN0607T0504506.002.

Figure 7-20. Comparison of Waste Package Water Tracer (Na^+) Concentration across Bottom of Invert for Three Grid Spacings

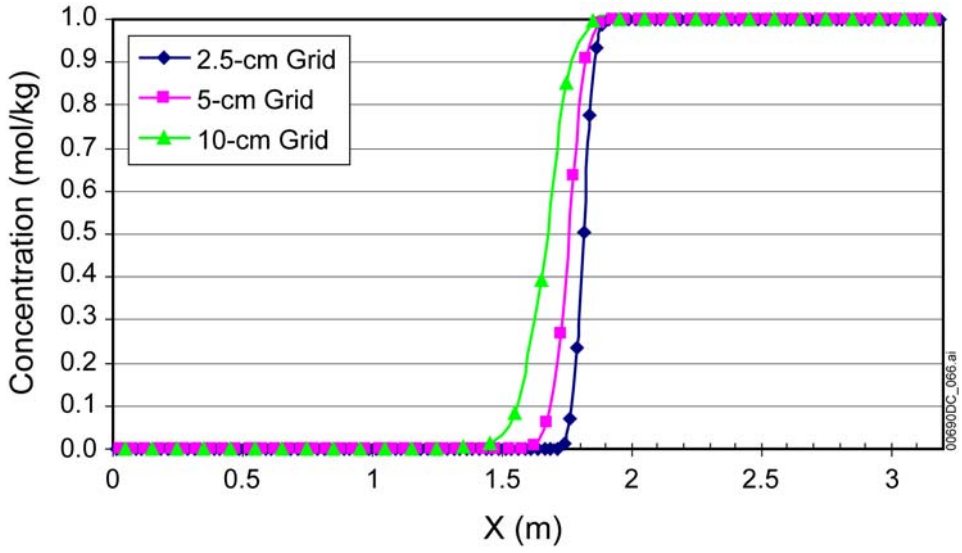

Source: Output DTN: SN0607T0504506.002.

Figure 7-21. Comparison of Diverted Water Tracer (K^+) Concentration across Bottom of Invert for Three Grid Spacings

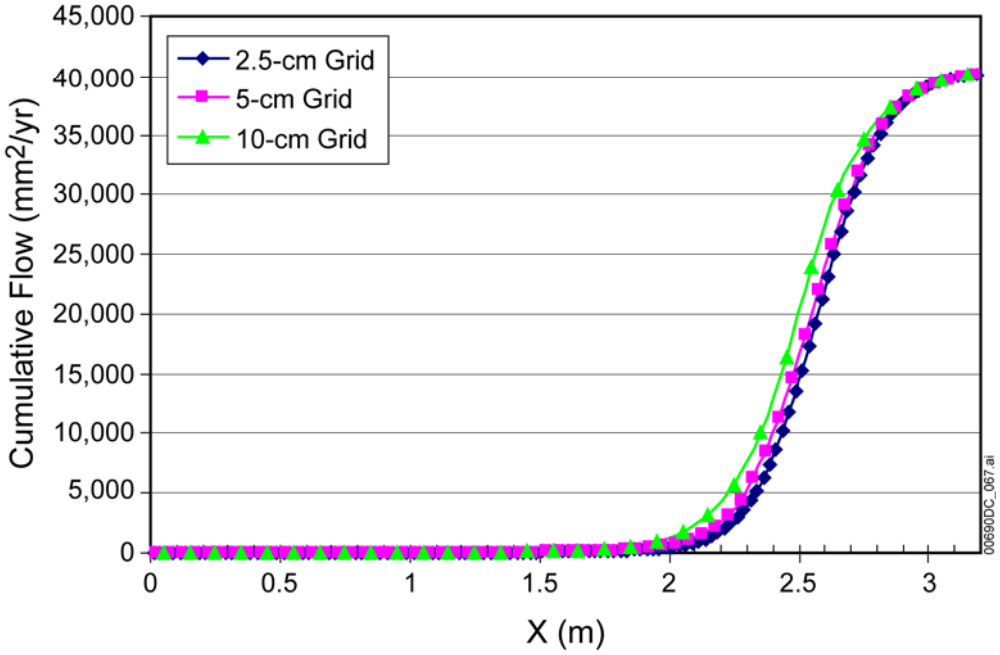

Source: Output DTN: SN0607T0504506.002

Figure 7-22. Comparison of Cumulative Steady State Flux of Water out Bottom of Invert for Three Grid Spacings

7.2.5.11 Validation Case with Diffusion

The validation case is rerun with diffusion of solutes turned on, using a diffusion coefficient of 2.3×10^{-9} m^2/s (Mills 1973 [DIRS 133392], Table III). The results are distinctively different from the case without diffusion. Tracer concentrations across the invert are shown in Figure 7-23 and Figure 7-24 at various levels in the invert. For comparison, the concentrations for the case with no diffusion are shown in Figure 7-25 and Figure 7-26.

Some of the base case calculations described earlier (Case 1, well-sorted, Figure 6-19) display the same behavior as the validation case with diffusion. This comparison in the validation case gives confidence that the base case calculations are showing the correct qualitative behavior.

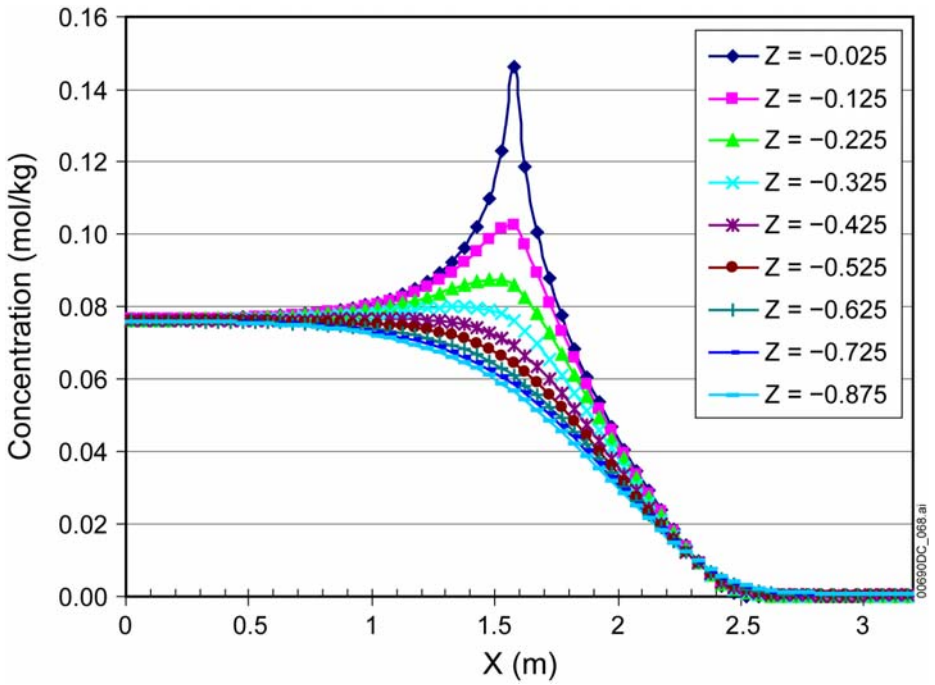

Source: Output DTN: SN0607T0504506.002.

Figure 7-23. Waste Package Water Tracer (Na^+) Concentration at Various Levels in the Invert for the Validation Case with Diffusion

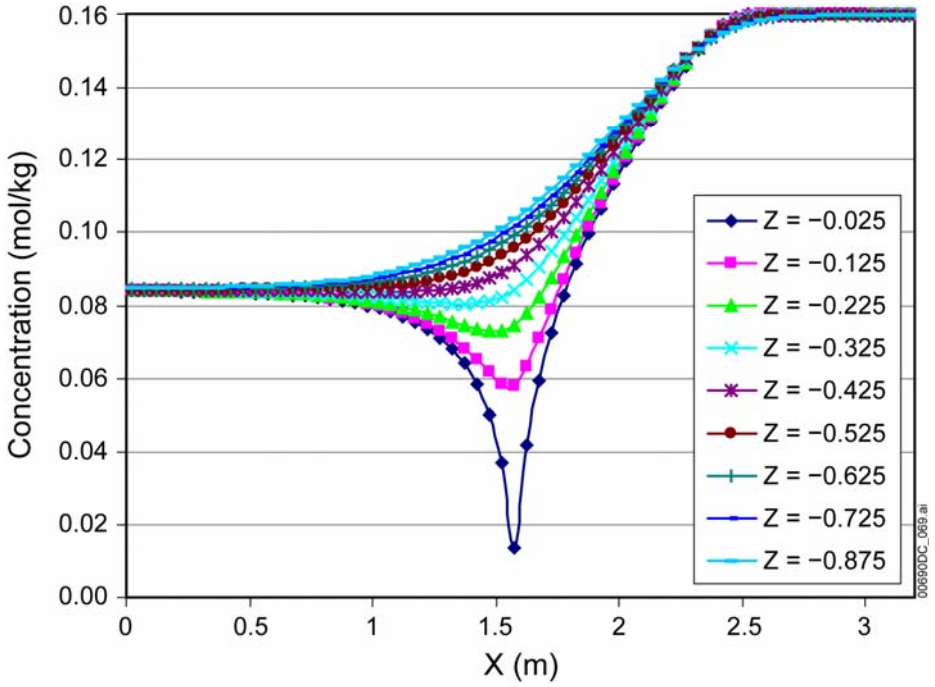

Source: Output DTN: SN0607T0504506.002.

Figure 7-24. Diverted Water Tracer (K^+) Concentration at Various Levels in the Invert for the Validation Case with Diffusion

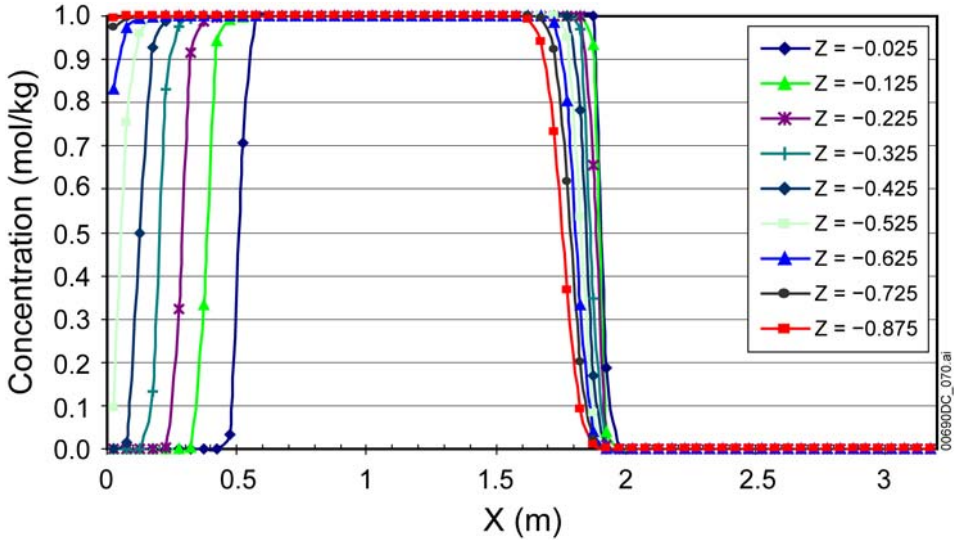

Source: Output DTN: SN0607T0504506.002.

Figure 7-25 Waste Package Water Tracer (Na^+) Concentration at Various Levels in the Invert for the Validation Case without Diffusion

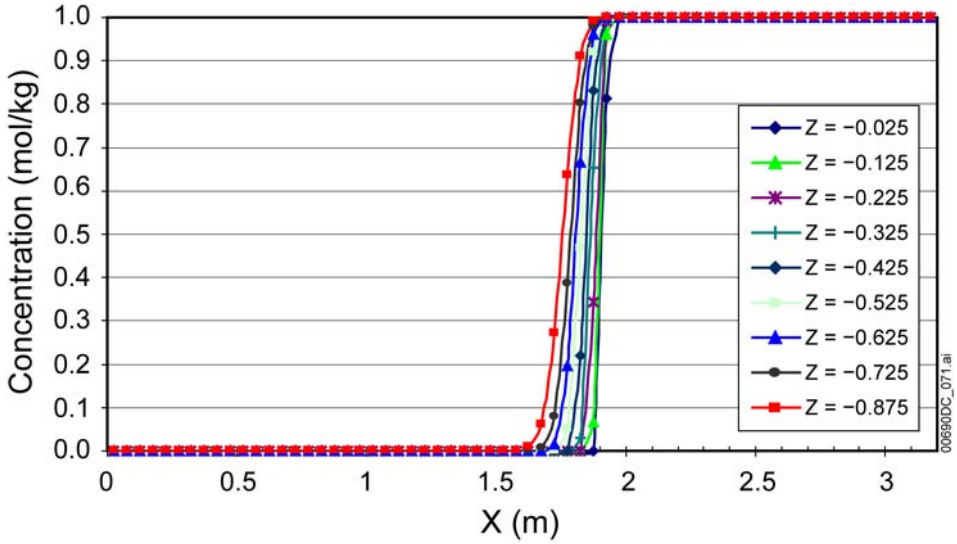

Source: Output DTN: SN0607T0504506.002.

Figure 7-26. Diverted Water Tracer (K^+) Concentration at Various Levels in the Invert for the Validation Case without Diffusion

7.2.5.12 Validation Case – Sensitivity of Steady State Solution to Time Step Size

The accuracy of *transient* TOUGHREACT solutions is sensitive to the time step size, Δt, due to time discretization errors and limitations on Courant number ($v\Delta t/\Delta x$, where v is water velocity, and Δx is the grid spacing). In theory, the Courant number should always be less than 1.0 for the numerical solution to be accurate. The amount of numerical dispersion may also be affected by time step size. The effect of Courant number and time step size at late times when the solution is

essentially at steady state is unknown. Therefore, the objective of this sensitivity study was to determine whether time step size has a significant effect on the steady state solution.

The steady state solution (at 10^9 years) from the validation run was continued for an additional 1,000 years in two runs: (1) One time step of 1,000 years, in which the maximum Courant number was about 155,000. (2) Time step limited to 2×10^5 s (about 2.3 days), thereby limiting the Courant number to less than 1.0, based on the magnitude of flow velocities at the end of the validation run; the small time step also reduced the time discretization error. In both runs, the convergence criterion was 10^{-3}, as used in all of the validation and base case runs. The duration of these runs was limited to 1,000 years due to the lengthy run times using the small time steps in the second continuation run, which required nearly 158,000 time steps to complete. The combined effects of time discretization errors and violation of the Courant number constraint were expected to result in differences in the steady state solution after the additional 1,000 years of simulation that indicate how sensitive the solution is to the time step size.

Table 7-19 compares the Na^+ concentrations along the bottom of the invert for the steady state validation run, the single-time-step continuation run, and the continuation run in which the time step was limited to 2×10^5 s. To the four digits shown in Table 7-19, the single-time-step run showed no change from the steady state solution after 1,000 years. The differences in concentration between the two continuation runs are shown in the last column. The maximum difference is about 6.6×10^{-3} mol/kg. Since the convergence criterion is 10^{-3}, the computed concentrations are only accurate to approximately three digits, so differences beyond the first three digits are insignificant. The largest and only significant differences occurred at $X < 1.5$ m, where the Na^+ concentrations should reach 1.0 at true steady state. In some grid cells, the numerical solution actually overshot that value. This overshoot occurred in more grid cells and to a greater degree in the small-time-step continuation run. Thus, the only significant differences between the two continuation runs occurred where the convergence errors and other numerical artifacts (e.g., roundoff and dispersion) resulted in the small-time-step continuation run actually being less accurate than when large time steps (with large Courant numbers) were used.

The results in Table 7-19 show that the time step size has essentially no impact on the accuracy of the steady state solution in the validation case. Since the base case runs are similar in scale, material properties, and flow rates, the same conclusion is expected to apply to the base-case runs.

Table 7-19. Comparison of Steady State Na^+ Concentrations in the Validation Case and in 1,000-Year Continuations from the Steady State Solution

X (m)	Na^+ Concentration (mol/kg)			
	Validation Case Steady State	Single 1000-yr Time Step	Time Step Limited to 2×10^5 s	Difference: Limited – Single Time Step
0.025	0.9953	0.9953	1.0018	6.5×10^{-3}
0.075	0.9990	0.9990	1.0054	6.6×10^{-3}
0.125	0.9997	0.9997	1.0061	6.4×10^{-3}
0.175	0.9999	0.9999	1.0063	6.4×10^{-3}

Table 7-19. Comparison of Steady State Na^+ Concentrations in the Validation Case and in 1,000-Year Continuations from the Steady State Solution (Continued)

X (m)	Na^+ Concentration (mol/kg)			
	Validation Case Steady State	Single 1000-yr Time Step	Time Step Limited to 2×10^5 s	Difference: Limited – Single Time Step
0.225	1.0000	1.0000	1.0064	6.4×10^{-3}
0.275	1.0000	1.0000	1.0065	6.5×10^{-3}
0.325	1.0000	1.0000	1.0065	6.5×10^{-3}
0.375	1.0001	1.0001	1.0065	6.4×10^{-3}
0.425	1.0001	1.0001	1.0065	6.4×10^{-3}
0.475	1.0001	1.0001	1.0065	6.4×10^{-3}
0.525	1.0001	1.0001	1.0065	6.4×10^{-3}
0.575	1.0000	1.0000	1.0065	6.5×10^{-3}
0.625	1.0000	1.0000	1.0064	6.4×10^{-3}
0.675	1.0000	0.9999	1.0064	6.5×10^{-3}
0.725	0.9999	0.9999	1.0064	6.5×10^{-3}
0.775	0.9999	1.0000	1.0064	6.4×10^{-3}
0.825	0.9999	1.0000	1.0064	6.4×10^{-3}
0.875	0.9999	1.0000	1.0061	6.1×10^{-3}
0.925	1.0000	1.0000	1.0054	5.4×10^{-3}
0.975	1.0000	1.0000	1.0041	4.1×10^{-3}
1.025	1.0000	1.0000	1.0024	2.4×10^{-3}
1.075	1.0001	1.0000	1.0007	7×10^{-4}
1.125	1.0000	1.0000	0.9993	-7×10^{-4}
1.175	1.0000	1.0000	0.9982	-1.8×10^{-3}
1.225	1.0000	1.0000	0.9973	-2.7×10^{-3}
1.275	1.0000	1.0000	0.9966	-3.4×10^{-3}
1.325	1.0000	1.0000	0.9962	-3.8×10^{-3}
1.375	1.0000	1.0000	0.9961	-3.9×10^{-3}
1.425	1.0000	1.0000	0.9963	-3.7×10^{-3}
1.475	1.0000	1.0000	0.9971	-2.9×10^{-3}
1.525	0.9999	0.9999	0.9983	-1.6×10^{-3}
1.575	0.9993	0.9993	0.9996	3×10^{-4}
1.625	0.9923	0.9923	0.9925	2×10^{-4}
1.675	0.9387	0.9387	0.9388	1×10^{-4}
1.725	0.7301	0.7301	0.7302	1×10^{-4}
1.775	0.3655	0.3655	0.3656	1×10^{-4}
1.825	9.102×10^{-2}	9.102×10^{-2}	9.110×10^{-2}	8×10^{-5}
1.875	7.898×10^{-3}	7.898×10^{-3}	7.914×10^{-3}	1.6×10^{-5}
1.925	3.837×10^{-5}	3.837×10^{-5}	3.854×10^{-5}	1.7×10^{-7}
1.975	1.000×10^{-12}	1.000×10^{-12}	7.270×10^{-13}	-2.7×10^{-13}

Table 7-19. Comparison of Steady State Na^+ Concentrations in the Validation Case and in 1,000-Year Continuations from the Steady State Solution (Continued)

X (m)	Na^+ Concentration (mol/kg)			
	Validation Case Steady State	**Single 1000-yr Time Step**	**Time Step Limited to 2×10^5 s**	**Difference: Limited – Single Time Step**
2.025	1.000×10^{-12}	1.000×10^{-12}	6.960×10^{-13}	-3.0×10^{-13}
2.075	1.000×10^{-12}	1.000×10^{-12}	6.645×10^{-13}	-3.4×10^{-13}
2.125	1.000×10^{-12}	1.000×10^{-12}	6.328×10^{-13}	-3.7×10^{-13}
2.175	1.000×10^{-12}	1.000×10^{-12}	6.019×10^{-13}	-4.0×10^{-13}
2.225	1.000×10^{-12}	1.000×10^{-12}	5.737×10^{-13}	-4.3×10^{-13}
2.275	1.000×10^{-12}	1.000×10^{-12}	5.508×10^{-13}	-4.5×10^{-13}
2.325	1.000×10^{-12}	1.000×10^{-12}	5.368×10^{-13}	-4.6×10^{-13}
2.375	1.000×10^{-12}	1.000×10^{-12}	5.367×10^{-13}	-4.6×10^{-13}
2.425	1.000×10^{-12}	1.000×10^{-12}	5.581×10^{-13}	-4.4×10^{-13}
2.475	1.000×10^{-12}	1.000×10^{-12}	6.138×10^{-13}	-3.9×10^{-13}
2.525	1.000×10^{-12}	1.000×10^{-12}	7.301×10^{-13}	-2.7×10^{-13}
2.575	1.000×10^{-12}	1.000×10^{-12}	1.000×10^{-12}	0
2.625	1.000×10^{-12}	1.000×10^{-12}	1.000×10^{-12}	0
2.675	1.000×10^{-12}	1.000×10^{-12}	1.000×10^{-12}	0
2.725	1.000×10^{-12}	1.000×10^{-12}	1.000×10^{-12}	0
2.775	1.000×10^{-12}	1.000×10^{-12}	1.000×10^{-12}	0
2.825	1.000×10^{-12}	1.000×10^{-12}	1.000×10^{-12}	0
2.875	1.000×10^{-12}	1.000×10^{-12}	1.000×10^{-12}	0
2.925	1.000×10^{-12}	1.000×10^{-12}	1.000×10^{-12}	0
2.975	1.000×10^{-12}	1.000×10^{-12}	1.000×10^{-12}	0
3.025	1.000×10^{-12}	1.000×10^{-12}	1.000×10^{-12}	0
3.075	1.000×10^{-12}	1.000×10^{-12}	1.000×10^{-12}	0
3.125	1.000×10^{-12}	1.000×10^{-12}	1.000×10^{-12}	0
3.175	1.000×10^{-12}	1.000×10^{-12}	1.000×10^{-12}	0

Source: Output DTN: SN0607T0504506.002.

7.3 SUMMARY

As required in the TWP, the model has been validated. The output DTNs for the validation exercises are as follows:

- Section 7.1.1, Confidence Building Exercise, DTN: MO0608SPACONFI.001
- Section 7.2.2.2, Validation of Adsorption Model, DTN: MO0607SPADSORP.000
- Section 7.2.4, Method C, Simulation of Argonne UO_2 Drip Test, DTN: MO0604SPAPREDI.000.
- Section 7.2.5, Method D, Validate Numerical Model for Flow and Transport in Invert with Analytical Model, DTN: MO0604SPANUMER.000; Modeling of Mixing in the Invert, DTN: SN0607T0504506.002.

8. CONCLUSIONS

8.1 MODEL OUTPUT

The following sections provide a summary of the results of the external accumulation model, including the output DTNs listed in Section 9.4. The output DTNs for the model validation are listed in Section 7.3 and 9.5.

8.1.1 Nominal Scenario-Scoping Results

The flow chart in Figure 6-1 shows that the nominal results include diffusive releases and solid releases from the waste package due to bottom failure. Table 8-1 provides the mass of U and Pu released from the waste package into the invert in the nominal case due to diffusion. The results in Table 8-1 are based on unqualified inputs and are therefore considered scoping results. The total Pu includes dissolved and colloidal. No additional modeling of these results was performed to determine the quantity of material that might diffuse out of the invert into the unsaturated zone. For bounding criticality calculations, the entire mass of U and Pu should be distributed through the invert.

Table 8-1. Scoping Results: Summary of Diffusive Releases from CSNF and DOE SNF Waste Packages (10,000 years)

	Releases from the Waste Package to the Invert							
	CSNF		N-Reactor		FFTF		TMI	
Isotope	50th percentile (kg)	95th percentile (kg)	50th percentile (kg)	95th percentile (kg)	50th percentile (kg)	95th percentile (kg)	50th percentile (kg)	95th percentile (kg)
^{235}U	3.98 E-02	1.90E-01	5.32 E+00	2.25E+01	8.31E-02	3.51E-01	4.92E-01	2.08E+00
Total U	2.68E+00	1.26E+01	3.32E+02	1.51E+03	1.03E+01	4.69E+01	1.76E+01	8.01E+01
Total Pu	1.49 E-07	6.76E-07	N/A	N/A	3.57E-04	2.25E-03	N/A	N/A

Source: Output DTN: MO0604SPANOMIN.000.

Note: These results are based on unqualified inputs and are therefore considered scoping results.

The masses of corrosion products in nominal case (files listed in Table 4-6) were extracted and tabulated in Table 6-29 and in output DTN: MO0607SPASOLID.001. These values represent mass of material that could flow out of the waste package as a slurry if the bottom of the waste package failed.

8.1.2 Igneous Scenario

The flow chart in Figure 6-2 shows that dissolved release of liquids and bottom failure of solids are possible mechanisms for material to enter the invert or host rock that are considered in the igneous scenario. The igneous cases produce the highest releases of dissolved material from the waste package, according to *Geochemistry Model Validation Report: Material Degradation and Release Model* (BSC 2006 [DIRS 176911], Section 8.1). The U and Pu releases from the CSNF igneous cases were much lower than the DOE SNF waste packages (BSC 2006 [DIRS 176911], Section 8.1), so only the accumulation of the releases from the DOE SNF waste packages were

calculated. Table 8-2 provides the U and Pu accumulation due to precipitation and adsorption on to the crushed tuff of the invert or in the fractures of the host rock for the igneous scenario. The low and high values are a result of the log K sensitivity results for boltwoodite-Na, the major uranium mineral forming in the DOE SNF waste package simulations (Section 6.8.1.2; DTN: MO0608SPASENSI.002). The cases in Table 8-2 that show no variation from low to high (e.g., TMI_IG2) are those cases that only had adsorption and no mineral precipitation.

Table 8-2. U and Pu Accumulated in the Igneous Scenario (10,000 years)

Source Term	Pu Accumulation (kg)	Total U Accumulation (kg)			U-235 Accumulation (kg)		
		Low	Medium	High	Low	Medium	High
TMI_IG1	N/A	2.98E+01	3.01E+01	3.07E+01	7.83E-01	7.92E-01	8.08E-01
TMI_IG2	N/A	2.25E-04	2.25E-04	2.25E-04	1.96E-06	1.96E-06	1.96E-06
FFTFIF1adEhdec	6.34E-03	1.52E+01	1.59E+01	1.72E+01	9.82E-01	1.03	1.12
FFTFIF2adEhdec	1.34E-05	3.26E-04	3.26E-04	3.26E-04	1.03E-04	1.03E-04	1.03E-04
CDSPIG2	N/A	1.09E-01	1.09E-01	1.09E-01	1.37E-03	1.37E-03	1.37E-03

Source: DTN: MO0609SPAINOUT.002, All PHREEQC runs, spreadsheet *Dissolved U and Pu acc total with sensitivities.xls*.

The accumulation results presented in Table 8-2 give a total amount, but it does not give a geometry of accumulation within the invert or host rock. The location within the invert where the accumulation occurs is presented in Table 8-3, based on Section 6.4.7 and developed in DTN: SN0607T0504506.002 and DTN: MO0605SPAINVRT.000. The geometry of the accumulation within the fractures and lithophysae of the host rock should be based on the properties presented in Section 6.4.8.

Table 8-3. Location of Accumulation within the Invert for Igneous Scenario

Source Term	Case	Accumulation in Poorly-Sorted Invert			Accumulation in Well-Sorted Invert		
		Percent within Invert	Location within Invert	Percent along Bottom of Invert	Percent within Invert	Location within Invert	Percent along Bottom of Invert
TMI_IG1	1	100%	Figure 6-36	0	100%	Figure 6-39	0
TMI_IG2	3	100%	Figure 6-38	0	55.6%	Figure 6-41	44.4%
FFTFIF1adEhdec	1	100%	Figure 6-36	0	100%	Figure 6-39	0
FFTFIF2adEhdec	3	100%	Figure 6-38	0	55.6%	Figure 6-41	44.4%
CDSPIG2	3	100%	Figure 6-38	0	55.6%	Figure 6-41	44.4%

NOTE: Case numbers corresponds to the cases mentioned in Sections 6.4.6 and 6.4.7.

The masses of corrosion products in the igneous case listed in Table 4-6 were extracted and tabulated in Table 6-31 and in output DTN: MO0607SPASOLID.001. These values represent mass of material that could flow out of the waste package as a slurry if the bottom of the waste package failed.

8.1.3 Seismic Scenario

The flow chart in Figure 6-3 shows that dissolved release of liquids and solid release due to entrained solids and bottom failure are possible mechanisms for material to enter the invert or host rock that are considered in the seismic scenario. The seismic cases produce low releases of dissolved U and Pu from the waste package (<1%), according to *Geochemistry Model Validation Report: Material Degradation and Release Model* (BSC 2006 [DIRS 176911], Section 8.1), for all cases except the high flux case (1,000 L/yr) for the CSNF and the DOE SNF N-Reactor waste packages, for which about 3% of U was released. The results for the CSNF high flux case (CSFlux9) are presented in Table 8-4. The total U and Pu accumulation is due to precipitation and adsorption on to the crushed tuff of the invert or in the fractures of the host rock. The low and high values in the table represent the 24% lower accumulation and 13% higher accumulation as a result of the log K sensitivity results for uranophane, the major uranium mineral forming in the PHREEQC simulation (Section 6.8.1.2; output DTN: MO0608SPASENSI.002).

Table 8-4. U and Pu Accumulation in CSNF Seismic Case (10,000 years)

Source Term	Pu Accumulation (kg)	Total U Accumulation (kg)			U-235 Accumulation (kg)		
		Low	Medium	High	Low	Medium	High
CSFlux9	1.22E-07	1.71E+02	2.24E+02	2.54E+02	1.88	2.46	2.79

Source: Output DTN: MO0609SPAINOUT.002, spreadsheet *Dissolved U and Pu acc total with sensitivities.xls*.

The accumulation results presented in Table 8-4 give a total amount, but this does not include a geometry of accumulation within the invert or host rock. The location within the invert where the accumulation occurs is presented in Table 8-5, based on Section 6.4.7 and developed in output DTNs: SN0607T0504506.002 and MO0605SPAINVRT.000. The geometry of the accumulation within the fractures and lithophysae of the host rock should be based on the properties presented in Section 6.4.8.

Table 8-5. Location of Accumulation Within the Invert for Seismic Case

Source Term	Case	Accumulation in Poorly Sorted Invert			Accumulation in Well-Sorted Invert		
		Percent within Invert	Location within Invert	Percent along Bottom of Invert	Percent within Invert	Location within Invert	Percent along Bottom of Invert
CSFlux9	2	100%	Figure 6-37	0	21.6%	Figure 6-40	78.4%

NOTE: Case number corresponds to the cases mentioned in Sections 6.4.6 and 6.4.7.

The masses of corrosion products in the seismic case listed in Table 4-6 were extracted and tabulated in Table 6-30 and in output DTN: MO0607SPASOLID.001. These values represent mass of material that could flow out of the waste package as a slurry if the bottom of the waste package failed.

The masses of minerals that could be entrained out of the waste package as a function of flow rate is provided in Section 6.6 and in output DTN: MO0607SPASOLID.001. The entrained losses only apply to a bathtub scenario that has not had a bottom failure.

8.2 CRITERIA

Section 4.2 lists the acceptance criteria and other requirements for this report. The subsections that follow indicate how the criteria and requirements were met.

8.2.1 Regulatory Requirements

8.2.1.1 Yucca Mountain Review Plan

The acceptance criteria in *Yucca Mountain Review Plan, Final Report* (NRC 2003 [DIRS 163274]) are intended for use by the NRC staff when reviewing the License Application submittal. The following criteria are applicable to the current report and are considered project requirements.

Section 2.2.1.3.3.3, Quantity and Chemistry of Water Contacting Waste Packages and Waste Forms

- **Acceptance Criterion 1 – System Description and Model Integration Are Adequate**

  (2) The abstraction of the quantity and chemistry of water contacting waste packages and waste forms uses assumptions, technical bases, data, and models, that are appropriate and consistent with other related U.S. Department of Energy abstractions.

  Response: The seepage rate is the same value used by TSPA. The chemistry of basalt water is the same as the igneous model. The oxygen and carbon dioxide fugacity values are consistent.

  (11) The abstraction of in-package criticality or external-to-package criticality, with in the emplacement drift, provides an adequate technical basis for screening these events. If either event is included in the assessment, then the U.S. Department of Energy uses acceptable technical bases for selecting the design criteria that mitigate the potential impact of in-package criticality on repository performance; identifies the features, events, and processes that may increase the reactivity of the system inside the waste package; identifies the configuration classes and configurations that have potential for nuclear criticality; and includes changes in thermal conditions and degradation of engineered barriers in the abstraction of the quantity and chemistry of water contacting waste packages and waste forms.

  Response: The changing chemistry of the water as it flows through the waste package is considered in Section 6.4.1, in which the source terms are discussed.

- **Acceptance Criterion 2 – Data Are Sufficient for Model Justification**

  (2) Sufficient data were collected on the characteristics of the natural system and engineered materials to establish initial and boundary conditions for conceptual models of thermal-hydrologic-mechanical-chemical coupled processes, that affect seepage and flow and the waste package chemical environment.

Response: The pore water composition used in the model was measured in one of the boreholes (Section 4.1.2.2). J-13 well water composition represents groundwater composition in the vicinity of Yucca Mountain (Section 4.1.2.3).

- **Acceptance Criterion 3 – Data Uncertainty Is Characterized and Propagated Through the Model Abstraction**

  (1) Models use parameter values, assumed ranges, probability distributions, and bounding assumptions that are technically defensible, reasonably account for uncertainties and variabilities, and do not result in an under-representation of the risk estimate.

  Response: The source terms were chosen as the cases with the highest losses from the waste package. Four fuel types are analyzed. Three mixing waters are used that have very different characteristics: dilute water (J-13), concentrated water (pore water), and high pH basalt water. The seepage rates range from the expected (1 L/yr) to 1,000 L/yr (>95% value).

- **Acceptance Criterion 4 – Model Uncertainty Is Characterized and Propagated Through the Model Abstraction**

  Response: This criterion does not apply because this report does not develop a model for the quantity and chemistry of water contacting waste packages and waste forms.

- **Acceptance Criterion 5 – Model Abstraction Output Is Supported by Objective Comparisons**

  Response: This criterion does not apply because this report does not develop a model abstraction for the quantity and chemistry of water contacting waste packages and waste forms.

Section 2.2.1.3.4.3, Radionuclide Release Rates and Solubility Limits

- **Acceptance Criterion 1 – System Description and Model Integration Are Adequate**

  (2) The abstraction of the radionuclide release rates and solubility limits uses assumptions, technical bases, data, and models, that are appropriate and consistent with other related U.S. Department of Energy abstractions.

  Response: The solubility limits are controlled by the thermodynamic database, which is the same database used in *In-Package Chemistry Abstraction* (BSC [DIRS 174566]) and *Dissolved Concentration Limits of Radioactive Elements* (BSC 2005 [DIRS 174566]), both of which support TSPA. The choices of solubility controlling phases are consistent with those reports and *Geochemistry Model Validation Report: Material Degradation and Release Model* (BSC 2006 [DIRS 176911]). The lists of suppressed and formed minerals in Table 6-7 and 6-8 are the same as those in *Geochemistry Model Validation Report: Material Degradation and Release Model* (BSC 2006 [DIRS 176911]). The use of the reduced Eh when considering Pu solubility is consistent with *Dissolved*

Concentration Limits of Radioactive Elements (BSC 2005 [DIRS 174566]) and *Geochemistry Model Validation Report: Material Degradation and Release Model* (BSC 2006 [DIRS 176911]).

(7) The abstraction of in-package criticality or external-to-package criticality, within the emplacement drift, provides an adequate technical basis for screening these events. If either event is included in the assessment, then the U.S. Department of Energy uses acceptable technical bases for selecting the design criteria that mitigate the potential impact of in-package criticality on repository performance; identifies the features, events, and processes that may increase the reactivity of the system inside the waste package; identifies the configuration classes and configurations that have potential for nuclear criticality; and includes changes in thermal conditions and degradation of engineered barriers in the abstraction of radionuclide release rates and solubility limits.

Response: The dissolution of the tuff ballast in the invert and the tuff of the host rock are included since the tuff is a potential source of elements necessary to form some of the important radionuclide-bearing secondary minerals.

- **Acceptance Criterion 2 – Data Are Sufficient for Model Justification**

(3) Where the U.S. Department of Energy uses data supplemented by models to support abstraction of solubility limits, the anticipated range of proportions and compositions of phases under the various physiochemical conditions expected are supported by experimental data.

Response: The reduced Eh conditions that control Pu concentrations used in *Dissolved Concentration Limits of Radioactive Elements* (BSC 2005 [DIRS 174566]) and in *Geochemistry Model Validation Report: Material Degradation and Release Model* (BSC 2006 [DIRS 176911]) are based on plutonium concentrations observed in experiments (BSC 2005 [DIRS 174566], Section 6.5.4), as discussed in Section 6.2, under the heading Fugacity of Carbon Dioxide and Oxygen.

- **Acceptance Criterion 3 – Data Uncertainty Is Characterized and Propagated Through the Model Abstraction**

(1) Models use parameter values, assumed ranges, probability distributions, and bounding assumptions that are technically defensible, reasonably account for uncertainties and variabilities, and do not result in an under-representation of the risk estimate.

Response: The uncertainty in the thermodynamic database is assessed by varying the log K of the main uranium minerals that form by plus and minus one standard deviation, as documented in Section 6.8.1.2.

- **Acceptance Criterion 4 – Model Uncertainty Is Characterized and Propagated Through the Model Abstraction**

  Response: This criterion does not apply because this report does not develop a model for the radionuclide release rates and solubility limits.

- **Acceptance Criterion 5 – Model Abstraction Output Is Supported by Objective Comparisons**

  Response: This criterion does not apply because this report does not develop a model abstraction for the radionuclide release rates and solubility limits.

Section 2.2.1.3.7.3, Radionuclide Transport in the Unsaturated Zone

- **Acceptance Criterion 1 - System Description and Model Integration Are Adequate**

  (3) The abstraction of radionuclide transport in the unsaturated zone uses assumptions, technical bases, data, and models, that are appropriate and consistent with other related U.S. Department of Energy abstractions.

  Response: The adsorption coefficients for U and Pu are consistent with those used in the TSPA model (Table 4-17). The invert properties are consistent with project values (Section 4.1.8). Characteristics of fractures, matrix, and lithophysae are consistent with the UZ model (Section 4.1.10).

- **Acceptance Criterion 2 – Data Are Sufficient for Model Justification**

  (1) Geological, hydrological, and geochemical values, used in the license application, are adequately justified (e.g., flow-path length, sorption coefficients, retardation factors, colloid concentrations, etc.). Adequate descriptions of how the data were used, interpreted, and appropriately synthesized into the parameters are provided.

  Response: The justification for the adsorption coefficients is provided in Section 4.1.9. The description of the adsorption aspect of the model is described in Section 6.4.3. The justification for the invert properties is provided in Section 4.1.8. The description of flow modeling is provided in Section 6.4.6.

- **Acceptance Criterion 3 – Data Uncertainty Is Characterized and Propagated Through the Model Abstraction**

  (1) Models use parameter values, assumed ranges, probability distributions, and bounding assumptions that are technically defensible, reasonably account for uncertainties and variabilities, and do not result in an under-representation of the risk estimate.

  Response: A range of invert properties is used in Section 4.1.8 (Appendices F and G). A median Kd is used as discussed in Section 6.4.3. The fracture void available for

accumulation, based on measured values, is increased to account for higher void observed in the air permeability test as described in Section 6.4.8.3.

- **Acceptance Criterion 4 – Model Uncertainty Is Characterized and Propagated Through the Model Abstraction**

  (2) Conceptual model uncertainties are adequately defined and documented, and effects on conclusions regarding performance are properly assessed.

  Response: Accumulation in a reducing zone and accumulation in the saturated zone were presented as alternative conceptual models in Section 6.7.

- **Acceptance Criterion 5 – Model Abstraction Output Is Supported by Objective Comparisons**

  (3) Well-documented procedures that have been accepted by the scientific community to construct and test the mathematical and numerical models are used to simulate radionuclide transport through the unsaturated zone.

  Response: The model was prepared according the procedures listed in Section 4 of the TWP (BSC 2006 [DIRS 177153]).

Section 2.2.1.3.9.3, Radionuclide Transport in the Saturated Zone

- **Acceptance Criterion 1 – System Description and Model Integration Are Adequate**

  (2) The description of the aspects of hydrology, geology, geochemistry, design features, physical phenomena, and couplings, that may affect radionuclide transport in the saturated zone, is adequate.

  Response: Accumulation in the saturated zone is not expected to cause a criticality concern, as discussed in Section 6.7.2, and therefore is not included in the model.

8.2.1.2 Key Technical Issue (KTI) Agreements

The KTI agreements that will be addressed in this report are CLST 5.04, ENFE 5.03, and RT 4.03 (Reamer and Williams 2000 [DIRS 155464], MOL.20001208.0097, Attachment 1). Each of these agreements commits the DOE to submitting a validation report for external criticality. After submittal of the previous version of the report, the NRC submitted a request for additional information (Schlueter 2002 [DIRS 159865]), as follows:

(1) Provide the complete validation approach for both models, to be consistent with discussions in both the Topical Report and the DOE RAI Response.

Response: Since submittal of the last version of the report in September 2001, the Topical Report has been revised and the approach to validation of the external accumulation report has been updated.

(2) Provide justification that the exercises in these reports constitute model validation independent of model development and calibration. If they do not, then provide model validation results.

Response: Section 7 of this report provides the validation methods that are independent of model development and calibration.

8.2.1.3 Safety Evaluation Report

The safety evaluation report contains acceptance criteria for how the near-field conditions could influence the occurrence of criticality and how nuclear criticality outside of the waste package affects the near-field environment (Reamer 2000 [DIRS 150765], Section 2.3.3). Those acceptance criteria not covered by the YMRP criteria that are addressed in this report are as follows:

3. DOE's evaluation of coupled THC processes properly considered site characteristics in establishing initial and boundary conditions for conceptual models and simulations of coupled processes that may affect nuclear criticality in the near-field environment.

   Response: The site characteristics considered in the model are seepage water compositions (Section 4.1.2), adsorption onto tuff (Section 4.1.9), dissolution of tuff (Section 4.1.7), fracture properties (Sections 6.4.8), matrix properties (Section 6.4.8.6), and invert properties (Section 4.1.8).

7. DOE's evaluation of coupled THC processes properly considered the uncertainties in the characteristics of the natural system and engineered materials, such as the type, quantity, and reactivity of material, in establishing initial and boundary conditions for conceptual models and simulations of THC coupled processes that affect potential nuclear criticality.

   Response: The uncertainties in the natural system that are considered include the seepage water composition (Section 6.8.1.1), equilibrium constants of the uranium minerals (Section 6.8.1.2), fracture porosity (Section 6.4.8.3), fracture aperture (Section 6.4.8.1), and fracture spacing (Section 6.4.8.2). The uncertainties in the engineered materials that are considered include the invert properties (Section 6.4.6, Table 6-17), the changing composition of the source term based on different fuel types and scenarios (Section 6.4.1). The uncertainties in the quantity of solids that may be transported into the invert are considered in Sections 6.5 and 6.6. The range of diffusive releases (50% and 95% percentile releases) is covered in Section 6.3.

15. Important mass transfer and mass transport processes and mechanisms considered for formation of both a critical mass and configuration are plausible for the YM near-field environment.

    Response: The model covers dissolved, diffusive, and solid releases (Sections 6.3, 6.4, 6.5, and 6.6). The model considers adsorption, advection, diffusion, and unsaturated flow characteristics (Section 6.4.3, Section 6.4.6).

The safety evaluation report open items (Reamer 2000 [DIRS 150765], Section 4) addressed in this report are as follows:

- Open item 3—The DOE needs to provide a modeling approach for igneous-activity-induced criticality;

  Response: The igneous and seismic scenarios are covered throughout this report.

- Open item 16—The DOE must present a validation methodology or work scope for external criticality models.

  Response: Validation is covered in Section 7.

8.2.2 Other Requirements—Disposal Criticality Analysis Methodology Topical Report

Disposal Criticality Analysis Methodology Topical Report (YMP 2003 [DIRS 165505]) contains sections applicable to external criticality.

Section 3.3, External Criticality Master Scenarios and Section 3.3.2, External Scenarios

The external criticality configuration classes are shown in Figure 3.3a and Figure 3.3b of *Disposal Criticality Analysis Methodology Topical Report* (YMP 2003 [DIRS 165505]) and are described as follows:

(1) Accumulation, by chemical reduction, of fissionable material by a mass of organic material (reducing zone). This covers fissile material that is transported to the water table. Such a deposit might be located beneath the repository, at a narrowing of the tuff aquifer, or at the surface outfall of the saturated zone flow (configuration classes FF-3c, 3d, 3e, respectively).

Response: Chemical reduction is not considered a likely mechanism as described in Sections 6.7.1 and 6.7.2.

(2) Accumulation, by sorption, onto clay or zeolite (configuration class FF-1b). Such material may be encountered beneath the repository.

Response: Adsorption onto the tuff of the invert and host rock are included as described in Section 6.4.3.

(3) Precipitation of fissionable material in fractures and other void spaces of the near field and the far field. This configuration is obtained from processes such as adsorption, from a reducing reaction, or from chemistry changes made possible by carrier plume interaction with surrounding rock and pore waters (configuration classes NF-1a, 1b, and FF-1a).

Response: Precipitation of minerals is included as described in Sections 6.2 and 6.4.4.

(4) Accumulation of fissionable material in water that has pooled in the drift. This configuration class, NF-4a, is reached from scenario E. This scenario involves waste packages that may not have been directly subjected to dripping water but are located in a local depression so that water from other dripping sites may collect around the bottom of the package during periods of high flow. A variant of this configuration class could have the intact, or nearly intact, waste form in a pool in the drift (configuration class NF-5a). Such a configuration class would be evaluated for waste forms that could be demonstrated to be more robust with respect to aqueous corrosion than their waste package.

Response: This scenario is not addressed by this report, since it does not involve transport of material away from the waste package.

(5) Accumulation by processes involving the formation, transport, and eventual breakup (or precipitation) of fissionable material containing colloidal particles. It has been suggested that the colloid-forming tendency of plutonium will enhance its transport capability, providing the potential for accumulation at some significant distance from the waste package. Such transport and accumulation could lead to far field configuration classes FF-2a, 2b, 2c, for final accumulation in dead-end fractures, clay or zeolites, and topographically low regions. It could also lead to the near field configuration classes NF-3b, 3c, for final accumulation in the invert in open fractures of solid material or pore space of granular material, respectively.

Response: Pu colloid transport is considered in the nominal scenario.

(6) Accumulation at the low point of the emplacement drift (or any connecting drift), configuration class NF-1c. The scenario leading to this configuration class must have a mechanism for sealing the fractures in the drift floor so that the effluent from individual waste packages can flow to, and accumulate at, a low point in the drift or repository, possibly in combination with effluent from other waste packages. As with the discussion of configuration class NF-4a above, such a pool would be expected to occur only within a short time (weeks or less) following a high infiltration episode.

Response: This scenario is not specifically addressed in this report, however criticality analyses can be performed using the accumulation quantities presented in Section 8.1, and using a geometry of accumulation based on the scenario of accumulation occurring in a low point of the drift.

(7) Accumulation of fissionable material by precipitation in the saturated zone at the contact between the waste-package plume and a hypothetical up welling fluid or a redox front (where the plume meets a different groundwater chemistry so that an oxidation-reduction reaction can take place), configuration classes FF-3a, 3b, respectively.

Response: Accumulation in the saturated zone is discussed as an alternative model in Section 6.7.2.

(8) Accumulation at the surface of the invert due to filtration by the degradation products, or remnants, of the waste package and its contents (configuration classes NF-2a, 3a, for the cases in which the fissionable material may be carried as a slurry or colloid, respectively).

Response: This is covered by the entrained releases (Section 6.6) and bottom failure releases (Section 6.5).

(9) Accumulation by precipitation from encountering perched water (groundwater deposit isolated from the nominal flow and not draining because of impermeable layer beneath) having significantly different chemistry from the fissionable material carrier plume (configuration class FF-1c).

Response: The model includes precipitation of fissionable materials caused by mixing of effluent waters with resident waters of significantly different chemistry. The resident water compositions include dilute, concentrated, and pH-basalt equilibrated waters as discussed in Section 4.1.2.

Section 3.3.4, Effect of Volcanic Events

The igneous and seismic scenarios are addressed throughout the report.

Section 3.4.2, Configurations with the Potential for External Criticality

Section 3.4.2 of the topical report (YMP 2003 [DIRS 165505]) provides the external criticality methodology approach and validation followed in the previous version of the external accumulation model report. The current version of the external accumulation report includes accumulation in the invert, in addition to accumulation in the fractures that was covered in the previous version, and has expanded the validation section to address NRC comments as mentioned in Section 8.2.1.2.

9. INPUTS AND REFERENCES

9.1 DOCUMENTS CITED

159352 Ahn, T.M. and Leslie, B.W. 1998. *Corrosion Products of Steels in High-Level Waste Management at the Proposed Yucca Mountain Repository.* Washington, D.C.: U.S. Nuclear Regulatory Commission. TIC: 242152.

169213 Akbulut, A. and Kadir, S. 2003. "The Geology and Origin of Sepiolite, Palygorskite and Saponite in Neogene Lacustrine Sediments of the Serinhisar-Acipayam Basin, Denizli, SW Turkey." *Clays and Clay Minerals, 51,* (3), 279-292. Aurora, Colorado: Clay Minerals Society. TIC: 256064.

159372 Allen, B.L. and Hajek, B.F. 1995. "Mineral Occurrence in Soil Environments." Chapter 5 of *Minerals in Soil Environments.* 2nd Edition. Dixon, J.B. and Weed, S.B., eds. SSSA Book Series, No. 1. Madison, Wisconsin: Soil Science Society of America. TIC: 237222.

149625 Audi, G. and Wapstra, A.H. 1995. *Atomic Mass Adjustment, Mass List for Analysis.* Upton, New York: Brookhaven National Laboratory, National Nuclear Data Center. TIC: 242718.

100029 Barr, D.L.; Moyer, T.C.; Singleton, W.L.; Albin, A.L.; Lung, R.C.; Lee, A.C.; Beason, S.C.; and Eatman, G.L.W. 1996. *Geology of the North Ramp — Stations 4+00 to 28+00, Exploratory Studies Facility, Yucca Mountain Project, Yucca Mountain, Nevada.* Denver, Colorado: U.S. Geological Survey. ACC: MOL.19970106.0496.

175135 Barthelmy, D. 2005. "Weeksite." Weeksite Mineral Data. Spring, Texas: David Barthelmy. Accessed October 6, 2005. TIC: 257785. URL: http://www.webmineral.com/data/Weeksite.shtml

175137 Barthelmy, D. 2005. "Willemite." Willemite Mineral Data. Spring, Texas: David Barthelmy. Accessed October 6, 2005. TIC: 257786. URL: http://www.webmineral.com/data/Willemite.shtml

175045 Baskin, Y. 1956. "A Study of Authigenic Feldspars." *Journal of Geology, 64,* (1), 132-155. Chicago, Illinois: University of Chicago Press. TIC: 257684.

128109 Bates, R.L. and Jackson, J.A., eds. 1984. *Dictionary of Geological Terms*. 3rd Edition. Garden City, New York: Anchor Books/Doubleday. TIC: 206591.

156269 Bear, J. 1972. *Dynamics of Fluids in Porous Media.* Environmental Science Series. Biswas, A.K., ed. New York, New York: Elsevier. TIC: 217356.

100727 Benson, L.V.; Robison, J.H.; Blankennagel, R.K.; and Ogard, A.E. 1983. *Chemical Composition of Ground Water and the Locations of Permeable Zones in the Yucca Mountain Area, Nevada.* Open-File Report 83-854. Denver, Colorado: U.S. Geological Survey. ACC: NNA.19870610.0028.

175262 Bonhomme, M.G.; Gauthier-Lafaye, F.; and Weber, F. 1982. "An Example of Lower Proterozoic Sediments: The Francevillian in Gabon." *Precambrian Research, 18,* 87-102. Amsterdam, The Netherlands: Elsevier. TIC: 257682.

175263 Bourrel, J. and Pfiffelman, J.P. 1972. "La Province Uranifère du Bassin de Franceville (République Gabonaise)." *Mineral Deposita, 7,* (1), 323-336. New York, New York: Springer-Verlag. TIC: 257690.

110754 Brady, P.V. and Walther, J.V. 1990. "Kinetics of Quartz Dissolution at Low Temperatures." *Chemical Geology, 82,* 253-264. Amsterdam, The Netherlands: Elsevier. TIC: 235349.

157873 Bricker, O. 1965. "Some Stability Relations in the System Mn-O $_2$-H_2O at 25° and One Atmosphere Total Pressure." *American Mineralogist, 50,* 1296-1354. Washington, D.C.: Mineralogical Society of America. TIC: 238855.

159355 Brush, E.G. and Pearl, W.L. 1972. "Corrosion and Corrosion Product Release in Neutral Feedwater." *Corrosion, 28,* (4), 129-136. Houston, Texas: National Association of Corrosion Engineers. TIC: 252684.

157640 BSC (Bechtel SAIC Company) 2001. *EQ6 Calculation of Source Terms for DOE Codisposal Waste Packages (Shippingport LWBR, N-Reactor, Melt and Dilute, and Fort St. Vrain).* CAL-EDC-MD-000017 REV 00. Las Vegas, Nevada: Bechtel SAIC Company. ACC: MOL.20020114.0316.

157195 BSC 2001. *EQ6 Calculations for Chemical Degradation of Fast Flux Test Facilities (FFTF) Waste Packages: Effects of Updated Design and Rates.* CAL-EDC-MD-000014 REV 00. Las Vegas, Nevada: Bechtel SAIC Company. ACC: MOL.20020102.0191.

155771 BSC 2001. *External Accumulation of Fissile Material from Waste Packages Containing Plutonium Ceramics.* CAL-EDC-GS-000004 REV 00. Las Vegas, Nevada: Bechtel SAIC Company. ACC: MOL.20011005.0153.

169131 BSC 2004. *Abstraction of Drift Seepage.* MDL-NBS-HS-000019 REV 01. Las Vegas, Nevada: Bechtel SAIC Company. ACC: DOC.20041103.0003.

170038 BSC 2004. *Analysis of Hydrologic Properties Data.* ANL-NBS-HS-000042 REV 00. Las Vegas, Nevada: Bechtel SAIC Company. ACC: DOC.20041005.0004; DOC.20050815.0003.

168489 BSC 2004. *D&E / PA/C IED Emplacement Drift Configuration and Environment.* 800-IED-MGR0-00201-000-00B. Las Vegas, Nevada: Bechtel SAIC Company. ACC: ENG.20040326.0001.

168208 BSC 2004. *Design and Engineering, 21 PWR Inner Vessel Sub-Assembly.* 000-MW0-DSU0-00701-000-00A. Las Vegas, Nevada: Bechtel SAIC Company. ACC: ENG.20040304.0023.

170028 BSC 2004. *Dike/Drift Interactions.* MDL-MGR-GS-000005 REV 01. Las Vegas, Nevada: Bechtel SAIC Company. ACC: DOC.20041124.0002; DOC.20050622.0002.

166107 BSC 2004. *Drift Degradation Analysis.* ANL-EBS-MD-000027 REV 03. Las Vegas, Nevada: Bechtel SAIC Company. ACC: DOC.20040915.0010; DOC.20050419.0001; DOC.20051130.0002.

168138 BSC 2004. *Estimation of Mechanical Properties of Crushed Tuff for Use as Ballast Material in Emplacement Drifts.* 800-CYC-SSE0-00100-000-00A. Las Vegas, Nevada: Bechtel SAIC Company. ACC: ENG.20040309.0023; ENG.20050817.0009; ENG.20050829.0017.

168405 BSC 2004. *Geochemistry Model Abstraction and Sensitivity Studies for the 21 PWR CSNF Waste Packages.* MDL-DSU-MD-000001 REV 00 [Errata 001]. Las Vegas, Nevada: Bechtel SAIC Company. ACC: MOL.20021107.0154; DOC.20040225.0005.

168960 BSC 2004. *Igneous Intrusion Impacts on Waste Packages and Waste Forms.* MDL-EBS-GS-000002 REV 01. Las Vegas, Nevada: Bechtel SAIC Company. ACC: DOC.20040421.0002.

171809 BSC 2004. *Impacts of Updated Design and Rates on EQ6 Calculations for Chemical Degradation of Fermi and TRIGA Codisposal Waste Packages.* CAL-DSD-MD-000001 REV 00A. Las Vegas, Nevada: Bechtel SAIC Company. ACC: DOC.20041006.0007.

172624 BSC 2004. *Mass Transfer Model.* MDL-EBS-NU-000004 REV 01. Las Vegas, Nevada: Bechtel SAIC Company. ACC: DOC.20040607.0003.

169218 BSC 2004. *Natural Analogue Synthesis Report.* TDR-NBS-GS-000027 REV 01. Las Vegas, Nevada: Bechtel SAIC Company. ACC: DOC.20040524.0008.

171916 BSC 2004. *Qualification of Thermodynamic Data for Geochemical Modeling of Mineral-Water Interactions in Dilute Systems.* ANL-WIS-GS-000003 REV 00. Las Vegas, Nevada: Bechtel SAIC Company. ACC: DOC.20041129.0006.

164500 BSC 2004. *Radionuclide Transport Models Under Ambient Conditions.* MDL-NBS-HS-000008 REV 02. Las Vegas, Nevada: Bechtel SAIC Company. ACC: DOC.20041101.0002; DOC.20050823.0003.

169503 BSC 2004. *Repository Subsurface Emplacement Drifts Steel Invert Structure Plan & Elevation.* 800-SS0-SSE0-00101-000-00B. Las Vegas, Nevada: Bechtel SAIC Company. ACC: ENG.20040520.0004.

168556 BSC (Bechtel SAIC Company) 2004. *Screening Analysis of Criticality Features, Events, and Processes for License Application.* ANL-EBS-NU-000008 REV 01. Las Vegas, Nevada: Bechtel SAIC Company. ACC: DOC.20041022.0001.

170036 BSC 2004. *Site-Scale Saturated Zone Transport.* MDL-NBS-HS-000010 REV 02. Las Vegas, Nevada: Bechtel SAIC Company. ACC: DOC.20041103.0004; DOC.20050405.0008.

171583 BSC 2004. *Technical Work Plan For: Regulatory Integration Modeling and Analysis of the Waste Form and Waste Package.* TWP-WIS-MD-000009 REV 00 ICN 01. Las Vegas, Nevada: Bechtel SAIC Company. ACC: DOC.20040910.0001.

169734 BSC 2004. *Yucca Mountain Site Description.* TDR-CRW-GS-000001 REV 02 ICN 01. Two volumes. Las Vegas, Nevada: Bechtel SAIC Company. ACC: DOC.20040504.0008.

174566 BSC 2005. *Dissolved Concentration Limits of Radioactive Elements.* ANL-WIS-MD-000010 REV 05. Las Vegas, Nevada: Bechtel SAIC Company. ACC: DOC.20050713.0006; DOC.20051006.0002.

172862 BSC 2005. *Drift-Scale THC Seepage Model.* MDL-NBS-HS-000001 REV 04. Las Vegas, Nevada: Bechtel SAIC Company. ACC: DOC.20050218.0001; DOC.20050801.0012.

173433 BSC 2005. *EBS Radionuclide Transport Abstraction.* ANL-WIS-PA-000001 REV 02. Las Vegas, Nevada: Bechtel SAIC Company. ACC: DOC.20050825.0008.

175083 BSC 2005. *Engineered Barrier System: Physical and Chemical Environment.* ANL-EBS-MD-000033 REV 05. Las Vegas, Nevada: Bechtel SAIC Company. ACC: DOC.20050829.0008.

176908 BSC 2005. *IED Subsurface Facilities Geological Data [Sheet 1 of 1].* 800-IED-WIS0-01801-000-00A. Las Vegas, Nevada: Bechtel SAIC Company. ACC: ENG.20051103.0002.

173501 BSC 2005. *IED Waste Package Configuration [Sheet 1 of 1].* 800-IED-WIS0-00601-000-00A. Las Vegas, Nevada: Bechtel SAIC Company. ACC: ENG.20050406.0005.

174583 BSC 2005. *In-Package Chemistry Abstraction.* ANL-EBS-MD-000037 REV 04. Las Vegas, Nevada: Bechtel SAIC Company. ACC: DOC.20050714.0003; DOC.20051130.0007.

173944 BSC 2005. *Multiscale Thermohydrologic Model.* ANL-EBS-MD-000049 REV 03. Las Vegas, Nevada: Bechtel SAIC Company. ACC: DOC.20050711.0001.

175539 BSC 2005. *Q-List.* 000-30R-MGR0-00500-000-003. Las Vegas, Nevada: Bechtel SAIC Company. ACC: ENG.20050929.0008.

176911 BSC 2006. *Geochemistry Model Validation Report: Material Degradation and Release Model.* ANL-EBS-GS-000001 REV 01. Las Vegas, Nevada: Bechtel SAIC Company.

177153 BSC 2006. *Technical Work Plan for External Accumulation for Criticality Evaluations.* TWP-MGR-PA-000025 REV 04. Las Vegas, Nevada: Bechtel SAIC Company. ACC: DOC.20060710.0004.

101321 Byers, F.M., Jr. and Moore, L.M. 1987. *Petrographic Variation of the Topopah Spring Tuff Matrix Within and Between Cored Drill Holes, Yucca Mountain, Nevada.* LA-10901-MS. Los Alamos, New Mexico: Los Alamos National Laboratory. ACC: NNA.19900510.0144.

102432 Casas, I.; Perez, I.; Torrero, E.; Bruno, J.; Cera, E.; and Duro, E. 1997. *Dissolution Studies of Synthetic Soddyite and Uranophane.* SKB TR-97-15. Stockholm, Sweden: Svensk Kärnbränsleförsörjning A.B. TIC: 237591.

101331 Chipera, S.J.; Vaniman, D.T.; and Bish, D.L. 1996. *Zeolite Abundances and the Vitric-to-Zeolitic Transition in Drill Holes USW SD-7, 9, and 12, Yucca Mountain, Nevada.* LA-EES-1-TIP-96-005. Los Alamos, New Mexico: Los Alamos National Laboratory. ACC: MOL.19970407.0339.

105754 Cleveland, J.M. 1979. *The Chemistry of Plutonium.* La Grange Park, Illinois: American Nuclear Society. TIC: 10231.

175264 Cohen, D. and Walter, A.J 1964. "Neptunium Pentoxide." *Journal of the Chemical Society,* Pages 2696-2699. London, England: Journal of the Chemical Society. TIC: 257688.

164025 Cornell, R.M.; Giovanoli, R.; and Schneider, W. 1992. "The Effect of Nickel on the Conversion of Amorphous Iron(III) Hydroxide into More Crystalline Iron Oxides in Alkaline Media." *Journal of Chemical Technology and Biotechnology, 53,* (1), 73-79. Oxford, England: Blackwell Scientific Publishing. TIC: 254448.

177177 Cowan, C.E.; Zachara, J.M.; and Resch, C.T. 1991. "Cadium Adsorption on Iron Oxides in the Presence of Alkaline-Earth Elements." *Environmental Science & Technology, 25,* 437-446. Washington, D.C.: American Chemical Society.

177117 Criscenti, L.J.; Eliassi, M.; Cygan, R.T.; Jové Cólón, C.F.; and Goldberg, S. 2006. *Modeling Adsorption Processes: Issues in Uncertainty, Scaling and Prediction.* NUREG/CR-6893. Washington, D.C.: U.S. Nuclear Regulatory Commission. ACC: MOL.20060710.0200.

135790 CRWMS (Civilian Radioactive Waste Management System) M&O (Management and Operating Contractor) 2000. *In-Drift Accumulation of Fissile Material from Waste Packages Containing Plutonium Disposition Waste Forms.* CAL-EDC-GS-000001 REV 00. Las Vegas, Nevada: CRWMS M&O. ACC: MOL.20001016.0008.

141407 CRWMS M&O 2000. *Natural Analogs for the Unsaturated Zone.* ANL-NBS-HS-000007 REV 00. Las Vegas, Nevada: CRWMS M&O. ACC: MOL.19990721.0524.

175243 CTDP (Common Thermodynamic Database Project) 2004. "Gadolinium." *Common Thermodynamic Database Project.* Paris, France: Common Thermodynamic Database Project. Accessed October 7, 2005. ACC: MOL.20051010.0168. URL: http://ctdp.ensmp.fr/

100438 Curtis, D.; Benjamin, T.; Gancarz, A.; Loss, R.; Rosman, K.; DeLaeter, J.; Delmore, J.E.; and Maeck, W.J. 1989. "Fission Product Retention in the Oklo Natural Fission Reactors." *Applied Geochemistry, 4,* 49-62. New York, New York: Pergamon Press. TIC: 237970.

177118 Cygan, R.T.; Siegel, M.D.; and Criscenti, L.J.; 2006. *Proceedings of the International Workshop on Conceptual Model Development for Subsurface Reactive Transport Modeling of Inorganic Contaminants, Radionuclides, and Nutrients.* NUREG/CP-0193. Washington, D.C.: U.S. Nuclear Regulatory Commission. ACC: MOL.20060710.0201.

143280 Davis, J.A. and Kent, D.B. 1990. "Surface Complexation Modeling in Aqueous Geochemistry." *Mineral-Water Interface Geochemistry.* Hochella, M.F., Jr. and White, A.F., eds. Reviews in Mineralogy Volume 23. Pages 177-260. Washington, D.C.: Mineralogical Society of America. TIC: 224085.

154436 Davis, J.A.; Coston, J.A.; Kent, D.B.; and Fuller, C.C. 1998. "Application of the Surface Complexation Concept to Complex Mineral Assemblages." *Environmental Science & Technology, 32,* (19), 2820-2828. Washington, D.C.: American Chemical Society. TIC: 249656.

100439 de Marsily, G. 1986. *Quantitative Hydrogeology: Groundwater Hydrology for Engineers.* San Diego, California: Academic Press. TIC: 208450.

102773 Deer, W.A.; Howie, R.A.; and Zussman, J. 1966. *An Introduction to the Rock-Forming Minerals.* New York, New York: John Wiley & Sons. TIC: 245492.

163286 Deer, W.A.; Howie, R.A.; and Zussman, J. 1992. *An Introduction to the Rock-Forming Minerals.* 2nd Edition. New York, New York: Prentice Hall. TIC: 221918.

175102 Denotkina, R.G.; Moskvin, A.I.; and Shevchenko, V.B. 1960. "The Composition and Dissociation Constants of Phosphate Complexes of Plutonium(IV) Determined by the Solubility Method." *Russian Journal of Inorganic Chemistry, 5,* (7), 731-734. London, England: Chemical Society. TIC: 257420.

159374 Dixon, J.B. 1995. "Kaolin and Serpentine Group Minerals." Chapter 10 of *Minerals in Soil Environments.* 2nd Edition. Dixon, J.B. and Weed, S.B., eds. SSSA Book Series, No. 1. Madison, Wisconsin: Soil Science Society of America. TIC: 237222.

100548 DOE (U.S. Department of Energy) 1998. *Introduction and Site Characteristics.* Volume 1 of *Viability Assessment of a Repository at Yucca Mountain.* DOE/RW-0508. Washington, D.C.: U.S. Department of Energy, Office of Civilian Radioactive Waste Management. ACC: MOL.19981007.0028.

150095 DOE 2000. *N Reactor (U-Metal) Fuel Characteristics for Disposal Criticality Analysis.* DOE/SNF/REP-056, Rev. 0. Washington, D.C.: U.S. Department of Energy, Office of Environmental Management. TIC: 247956.

164970 DOE 2003. *TMI Fuel Characteristics for Disposal Criticality Analysis.* DOE/SNF/REP-084, Rev. 0. Idaho Falls, Idaho: U.S. Department of Energy, Idaho Operations Office. ACC: MOL.20031013.0388.

169277 Doner, H.E. and Lynn, W.C. 1995. "Carbonate, Halide, Sulfate, and Sulfide Minerals." Chapter 6 of *Minerals in Soil Environments.* 2nd Edition. Dixon, J.B. and Weed, S.B., eds. SSSA Book Series, No. 1. Madison, Wisconsin: Soil Science Society of America. TIC: 237222.

108015 Efurd, D.W.; Runde, W.; Banar, J.C.; Janecky, D.R.; Kaszuba, J.P.; Palmer, P.D.; Roensch, F.R.; and Tait, C.D. 1998. "Neptunium and Plutonium Solubilities in a Yucca Mountain Groundwater." *Environmental Science & Technology, 32,* (24), 3893-3900. Easton, Pennsylvania: American Chemical Society. TIC: 243857.

161749 Ewing, R.C. and Haaker, R.F. 1979. *Naturally Occurring Glasses: Analogues for Radioactive Waste Forms.* PNL-2776. Richland, Washington: Pacific Northwest Laboratory. ACC: NNA.19900315.0277.

105591 Finch, R.J. and Ewing, R.C. 1991. "Alteration of Natural UO2 Under Oxidizing Conditions from Shinkolobwe, Katanga, Zaire: A Natural Analogue for the Corrosion of Spent Fuel." *Radiochimica Acta, 52/53,* 395-401. München, Germany: R. Oldenbourg Verlag. TIC: 237035.

113030 Finch, R.J. and Ewing, R.C. 1992. "The Corrosion of Uraninite Under Oxidizing Conditions." *Journal of Nuclear Materials, 190,* 133-156. Amsterdam, The Netherlands: Elsevier. TIC: 246369.

145442 Finch, R.J. and Murakami, T. 1999. "Systematics and Paragenesis of Uranium Minerals." Chapter 3 of *Uranium: Mineralogy, Geochemistry and the Environment.* Burns, P.C. and Finch, R.J., eds. Reviews in Mineralogy Volume 38. Washington, D.C.: Mineralogical Society of America. TIC: 247121.

100033 Flint, L.E. 1998. *Characterization of Hydrogeologic Units Using Matrix Properties, Yucca Mountain, Nevada.* Water-Resources Investigations Report 97-4243. Denver, Colorado: U.S. Geological Survey. ACC: MOL.19980429.0512.

173728 Franks, F. 1975. *Water, A Comprehensive Treatise.* Volume 5 of *Water in Disperse Systems.* New York, New York: Plenum Press. TIC: 257268.

101173 Freeze, R.A. and Cherry, J.A. 1979. *Groundwater.* Englewood Cliffs, New Jersey: Prentice-Hall. TIC: 217571.

143296 Furet, N.R.; Haces, C.; Corvo, F.; Diaz, C.; and Gomez, J. 1990. "Corrosion Rate Determination Using Fe-57 Mössbauer Spectra of Corrosion Products of Steel." *Hyperfine Interactions, 57,* 1833-1838. Basel, Switzerland: J.C. Baltzer, A.G. Scientific Publishing Company. TIC: 240940.

172360 Gaines, R.V.; Skinner, H.C.W.; Foord, E.E.; Mason, B.; and Rosenzweig, A. 1997. *Dana's New Mineralogy, The System of Mineralogy of James Dwight Dana and Edward Salisbury Dana.* 8th Edition. New York, New York: John Wiley & Sons. TIC: 256455.

173750 Gao, Y. and Mucci, A. 2001. "Acid Base Reactions, Phoshate and Arsenate Complexation, and Their Competitive Adsorption at the Surface of Goethite in 0.7 M NaCl Solution." *Geochimica et Cosmochimica Acta, 65,* (14), 2361-2378. New York, New York: Pergamon. TIC: 257331.

157542 Gauthier-Lafaye, F. 1996. "Introduction to the Oklo Problematic." *OKLO Working Group, Proceedings of the Fourth Joint EC-CEA Progress and Final Meeting held in Saclay, France, on 22 and 23 June 1995.* Blanc, P.L. and von Maravic, H., eds. EUR 16704 EN. Pages 5-16. Luxembourg, Luxembourg: Office for Official Publications of the European Communities. TIC: 251757.

124997 Gauthier-Lafaye, F.; Weber, F.; and Ohmoto, H. 1989. "Natural Fission Reactors of Oklo." *Economic Geology, 84,* (8), 2286-2295. El Paso, Texas: Economic Geology Publishing. TIC: 246605.

101388 Gelhar, L.W. 1993. *Stochastic Subsurface Hydrology.* Englewood Cliffs, New Jersey: Prentice-Hall. TIC: 240652.

105636 George-Aniel, B.; Leroy, J.L.; and Poty, B. 1991. "Volcanogenic Uranium Mineralizations in the Sierra Peña Blanca District, Chihuahua, Mexico: Three Genetic Models." *Economic Geology, 86,* (2), 233-248. El Paso, Texas: Economic Geology Publishing. TIC: 237050.

107880 Gertsch, R.E.; Fjeld, A.; Asbury, B.; and Ozdemir, L. 1993. *Construction Applications for TSw2 TBM Cuttings at Yucca Mountain.* Golden, Colorado: Colorado School of Mines. ACC: NNA.19940317.0013.

149484 Goodell, P.C. 1981. "Geology of the Peña Blanca Uranium Deposits, Chihuahua, Mexico." *Uranium in Volcanic and Volcaniclastic Rocks, Symposium held in El Paso, Texas, February 25-27, 1980.* Goodell, P.C. and Waters, A.C., eds. AAPG Studies in Geology No. 13. Pages 275-291. Tulsa, Oklahoma: American Association of Petroleum Geologists. TIC: 247861.

169212 Hover, V.C. and Ashley, G.M. 2003. "Geochemical Signatures of Paleodepositional and Diagenetic Environments: A STEM/AEM Study of Authigenic Clay Minerals from an Arid Rift Basin, Olduvai Gorge, Tanzania." *Clays and Clay Minerals, 51,* (3), 231-251. Aurora, Colorado: Clay Minerals Society. TIC: 256063.

105875 Hsu, P.H. 1995. "Aluminum Hydroxides and Oxyhydroxides." Chapter 7 of *Minerals in Soil Environments.* 2nd Edition. Dixon, J.B. and Weed, S.B., eds. SSSA Book Series, No. 1. Madison, Wisconsin: Soil Science Society of America. TIC: 237222.

169305 Huang, P.M. 1995. "Feldspars, Olivines, Pyroxenes, and Amphiboles." Chapter 20 of *Minerals in Soil Environments.* 2nd Edition. Dixon, J.B. and Weed, S.B., eds. SSSA Book Series, No. 1. Madison, Wisconsin: Soil Science Society of America. TIC: 237222.

176907 Hudson, D.B. 2000. Laboratory Measurements of Hydraulic Properties [final submittal]. Scientific Notebook SN-USGS-SCI-071-V1 & V2. Pages all V1 and all V2. ACC: MOL.20001116.0057; MOL.20001116.0058.

175241 Hull, L.; Pace, M.; Lessing, P.; Rogers, R.; Mizia, R.; Propp, A.; Shaber, E.; and Taylor, L. 2000. *Advanced Neutron Absorbers for DOE SNF Standardized Canister-Feasibility Study.* DOE/SNF/REP-057, Rev. 0. Idaho Falls, Idaho: U.S. Department of Energy, Idaho Operations Office. ACC: MOL.20051021.0173.

125207 IAEA (International Atomic Energy Agency) 1975. *The Oklo Phenomenon, Proceedings of a Symposium, Libreville, Gabon, 23 to 27 June 1975.* Vienna, Austria: International Atomic Energy Agency. TIC: 239176.

156284 Janeczek, J. 1999. "Mineralogy and Geochemistry of Natural Fission Reactors in Gabon." Chapter 7 of *Uranium: Mineralogy, Geochemistry and the Environment.* Burns, P.C. and Finch, R.J., eds. Reviews in Mineralogy Volume 38. Washington, D.C.: Mineralogical Society of America. TIC: 247121.

175266 Janeczek, J. and Ewing, R. 1996. "Phosphatian Coffinite with Rare Earth Elements and Ce-Rich Françoisite-(Nd) from Sandstone Beneath a Natural Fission Reactor at Bangombé, Gabon." *Mineralogical Magazine, 60,* (401), 665-669. London, England: Mineralogical Society. TIC: 257689.

157500 Jensen, K.A. and Ewing, R.C. 2001. "The Okélobondo Natural Fission Reactor, Southeast Gabon: Geology, Mineralogy, and Retardation of Nuclear-Reaction Products." *Geological Society of America Bulletin, 113,* (1), 32-62. Boulder, Colorado: Geological Society of America. TIC: 251743.

102010 Jury, W.A.; Gardner, W.R.; and Gardner, W.H. 1991. *Soil Physics.* 5th Edition. New York, New York: John Wiley & Sons. TIC: 241000.

122379 Kaszuba J.P. and Runde W.H. 1999. "The Aqueous Geochemistry of Neptunium: Dynamic Control of Soluble Concentrations with Applications to Nuclear Waste Disposal." *Environmental Science & Technology, 33,* (24), 4427-4433. Washington, D.C.: American Chemical Society. TIC: 246667.

106312 Katz, J.J.; Seaborg, G.T.; and Morss, L.R., eds. 1986. *The Chemistry of the Actinide Elements.* 2nd Edition. Two volumes. New York, New York: Chapman and Hall. TIC: 243942.

175112 Kellerud, G. and Yund, R.A. 1962. "The Ni-S System and Related Minerals." *Journal of Petrology, 3,* (1), 126-175. New York, New York: Oxford University Press. TIC: 257685.

161606 Kerr, P.F. 1977. *Optical Mineralogy.* 4th Edition. New York, New York: McGraw-Hill. TIC: 252886.

105907 Klein, C. and Hurlbut, C.S., Jr. 1985. *Manual of Mineralogy.* 20th Edition. New York, New York: John Wiley & Sons. TIC: 242818.

124300 Knauss, K.G. and Wolery, T.J. 1989. "Muscovite Dissolution Kinetics as a Function of pH and Time at 70°C." *Geochimica et Cosmochimica Acta, 53,* 1493-1501. Elmsford, New York: Pergamon Press. TIC: 236215.

152467 Kreyszig, E. 1970. *Introductory Mathematical Statistics, Principles and Methods.* New York, New York: John Wiley & Sons. TIC: 242632.

149069 Lamarsh, J.R. 1983. *Introduction to Nuclear Engineering.* 2nd Edition. Menlo Park, California: Addison-Wesley. TIC: 244841.

100051 Langmuir, D. 1997. *Aqueous Environmental Geochemistry.* Upper Saddle River, New Jersey: Prentice Hall. TIC: 237107.

101714 Leslie, B.W.; Pearcy, E.C.; and Prikryl, J.D. 1993. "Oxidative Alteration of Uraninite at the Nopal I Deposit, Mexico: Possible Contaminant Transport and Source Term Constraints for the Proposed Repository at Yucca Mountain." *Scientific Basis for Nuclear Waste Management XVI, Symposium held November 30-December 4, 1992, Boston, Massachusetts.* Interrante, C.G. and Pabalan, R.T., eds. *294,* 505-512. Pittsburgh, Pennsylvania: Materials Research Society. TIC: 208880.

177518 LeStrange, S. 2006. Approval of Tom Wolery as Independent Technical Reviewer for Geochemistry Model Validation Report: External Accumulation Model, ANL-EBS-GS-000002, Rev 01. Memo to file. ACC: MOL.20060905.0193.

159034 Li, G.; Peacor, D.R.; Coombs, D.S.; and Kawachi, Y. 1997. "Solid Solution in the Celadonite Family: The New Minerals Ferroceladonite, $K_2Fe^2{}_2+Fe^3{}_2+Si_8O_{20}(OH)_4$, and Ferroaluminoceladonite, $K_2Fe^2{}_2+Al_2Si_8O_{20}(OH)_4$." *American Mineralogist, 82,* (5-6), 503-511. Washington, D.C.: Mineralogical Society of America. TIC: 252472.

160832 Lide, D.R., ed. 2002. *CRC Handbook of Chemistry and Physics.* 83rd Edition. Boca Raton, Florida: CRC Press. TIC: 253582.

169289 Lindsay, W.L.; Vlek, P.L.G.; and Chien, S.H. 1995. "Phosphate Minerals." Chapter 22 of *Minerals in Soil Environments.* 2nd Edition. Dixon, J.B. and Weed, S.B., eds. SSSA Book Series, No. 1. Madison, Wisconsin: Soil Science Society of America. TIC: 237222.

166191 Linke, W.F. 1965. *Solubilities, Inorganic and Metal-Organic Compounds.* 4th Edition. Volume II, K–Z. Washington, D.C.: American Chemical Society. TIC: 222176.

100773 Lipman, P.W.; Christiansen, R.L.; and O'Connor, J.T. 1966. *A Compositionally Zoned Ash-Flow Sheet in Southern Nevada.* Professional Paper 524-F. Washington, D.C.: U.S. Geological Survey. TIC: 219972.

125331 Mahan, B.H. 1975. *University Chemistry.* 3rd Edition. Reading, Massachusetts: Addison-Wesley Publishing. TIC: 240721.

100917 Marsh, G.P. and Taylor, K.J. 1988. "An Assessment of Carbon Steel Containers for Radioactive Waste Disposal." *Corrosion Science, 28,* (3), 289-320. Oxford, England: Pergamon Press. TIC: 223393.

101726 McEachern, R.J. and Taylor, P. 1997. *A Review of the Oxidation of Uranium Dioxide at Temperatures Below 400°C.* AECL-11335. Pinawa, Manitoba, Canada: Atomic Energy of Canada Limited. TIC: 232575.

113270 McEachern, R.J. and Taylor, P. 1998. "A Review of the Oxidation of Uranium Dioxide at Temperatures Below 400°C." *Journal of Nuclear Material, 254,* 87-121. Amsterdam, The Netherlands: Elsevier. TIC: 246427.

170365 McKinley, I.G. and Scholtis, A. 1993. "A Comparison of Radionuclide Sorption Databases Used in Recent Performance Assessments." *Journal of Contaminant Hydrology, 13,* (1-4), 347-363. Amsterdam, The Netherlands: Elsevier. TIC: 256230.

133392 Mills, R. 1973. "Self-Diffusion in Normal and Heavy Water in the Range 1-45°." *Journal of Physical Chemistry, 77,* (5), 685-688. Washington, D.C.: American Chemical Society. TIC: 246404.

105911 Milnes, A.R. and Fitzpatrick, R.W. 1995. "Titanium and Zirconium Minerals." Chapter 23 of *Minerals in Soil Environments.* 2nd Edition. Dixon, J.B. and Weed, S.B., eds. SSSA Book Series, No. 1. Madison, Wisconsin: Soil Science Society of America. TIC: 237222.

156843 Ming, D.W. and Mumpton, F.A. 1995. "Zeolites in Soils." Chapter 18 of *Minerals in Soil Environments.* 2nd Edition. Dixon, J.B. and Weed, S.B., eds. SSSA Book Series, No. 1. Madison, Wisconsin: Soil Science Society of America. TIC: 237222.

149850 Mongano, G.S.; Singleton, W.L.; Moyer, T.C.; Beason, S.C.; Eatman, G.L.W.; Albin, A.L.; and Lung, R.C. 1999. *Geology of the ECRB Cross Drift - Exploratory Studies Facility, Yucca Mountain Project, Yucca Mountain, Nevada.* Deliverable SPG42GM3. Denver, Colorado: U.S. Geological Survey. ACC: MOL.20000324.0614.

100471 Naudet, R. 1975. "Mecanismes de Regulation des Reactions Nucleaires." *The Oklo Phenomenon, Proceedings of a Symposium, Libreville, Gabon, 23 to 27 June 1975.* Pages 589-601. Vienna, Austria: International Atomic Energy Agency. TIC: 238831.

100809 Nguyen, S.N.; Silva, R.J.; Weed, H.C.; and Andrews, J.E., Jr. 1992. "Standard Gibbs Free Energies of Formation at the Temperature 303.15 K of Four Uranyl Silicates: Soddyite, Uranophane, Sodium Boltwoodite, and Sodium Weeksite." *Journal of Chemical Thermodynamics, 24,* (1-6), 359-376. New York, New York: Academic Press. TIC: 238507.

163274 NRC (U.S. Nuclear Regulatory Commission) 2003. *Yucca Mountain Review Plan, Final Report.* NUREG-1804, Rev. 2. Washington, D.C.: U.S. Nuclear Regulatory Commission, Office of Nuclear Material Safety and Safeguards. TIC: 254568.

159027 OECD (Organisation for Economic Co-operation and Development, Nuclear Energy Agency) 2001. *Chemical Thermodynamics of Neptunium and Plutonium.* Volume 4 of *Chemical Thermodynamics.* New York, New York: Elsevier. TIC: 209037.

176820 Oldenburg, C.M. 2003. "Carbon Dioxide as Cushion Gas for Natural Gas Storage." *Energy & Fuels, 17,* (1), 240-246. Washington, D.C.: American Chemical Society. TIC: 258279.

163604 Palache, C.; Berman, H.; and Frondel, C. 1944. *Elements, Sulfides, Suffocates, Oxides.* Volume I of *The System of Mineralogy of James Dwight Dana and Edward Salisbury Dana, Yale University 1837–1892.* 7th Edition. New York, New York: John Wiley & Sons. TIC: 209331.

162280 Palache, C.; Berman, H.; and Frondel, C. 1951. *Halides, Nitrates, Borates, Carbonates, Sulfates, Phosphates, Arsenates, Tungstates, Molybdates, Etc.* Volume II of *The System of Mineralogy of James Dwight Dana and Edward Salisbury Dana, Yale University 1837–1892.* 7th Edition. New York, New York: John Wiley & Sons. TIC: 209332.

175261 Palandri, J.L and Kharaka, Y.K. 2004. *A Compilation of Rate Parameters of Water-Mineral Interaction Kinetics for Application to Geochemical Modeling.* Open File Report 2004-1068. Menlo Park, California: U.S. Geological Survey. ACC: MOL.20051110.0164.

103896 Parrington, J.R.; Knox, H.D.; Breneman, S.L.; Baum, E.M.; and Feiner, F. 1996. *Nuclides and Isotopes, Chart of the Nuclides.* 15th Edition. San Jose, California: General Electric Company and KAPL, Inc. TIC: 233705.

100486 Pearcy, E.C.; Prikryl, J.D.; Murphy, W.M.; and Leslie, B.W. 1994. "Alteration of Uraninite from the Nopal I Deposit, Peña Blanca District, Chihuahua, Mexico, Compared to Degradation of Spent Nuclear Fuel in the Proposed U.S. High-Level Nuclear Waste Repository at Yucca Mountain, Nevada." *Applied Geochemistry, 9,* 713-732. New York, New York: Elsevier. TIC: 236934.

159329 Pednekar, S.P. 1987. *Final Report on Corrosion of Carbon Steel in Aqueous Environments at Temperatures Below Boiling - A Literature Review to Electric Power Research Institute, February 24, 1987.* Columbus, Ohio: Battelle, Columbus Division. TIC: 224492.

157910 Pérez, I.; Casas, I.; Martín, M.; and Bruno, J. 2000. "The Thermodynamics and Kinetics of Uranophane Dissolution in Bicarbonate Test Solutions." *Geochimica et Cosmochimica Acta, 64,* (4), 603-608. New York, New York: Elsevier. TIC: 250919.

162576 Peterman, Z.E. and Cloke, P.L. 2002. "Geochemistry of Rock Units at the Potential Repository Level, Yucca Mountain, Nevada (includes Erratum)." *Applied Geochemistry, 17,* (6, 7), 683-698, 955-958. New York, New York: Pergamon. TIC: 252516; 252517; 254046.

105743 Philip, J.R.; Knight, J.H.; and Waechter, R.T. 1989. "Unsaturated Seepage and Subterranean Holes: Conspectus, and Exclusion Problem for Circular Cylindrical Cavities." *Water Resources Research, 25,* (1), 16-28. Washington, D.C.: American Geophysical Union. TIC: 239117.

110009 Pickett, D.A. and Murphy, W.M. 1999. "Unsaturated Zone Waters from the Nopal I Natural Analog, Chihuahua, Mexico - Implications for Radionuclide Mobility at Yucca Mountain." *Scientific Basis for Nuclear Waste Management XXII, Symposium held November 30-December 4, 1998, Boston, Massachusetts.* Wronkiewicz, D.J. and Lee, J.H., eds. *556,* 809-816. Warrendale, Pennsylvania: Materials Research Society. TIC: 246426.

168458 Porcelli, D. and Swarzenski, P.W. 2003. "The Behavior of U- and Th-Series Nuclides in Groundwater." *Uranium-Series Geochemistry.* Bourdon, B.; Henderson, G.M.; Lundstrom, C.C.; and Turner, S.P., eds. Reviews in Mineralogy and Geochemistry Volume 52. Pages 317-361. Washington, D.C.: Mineralogical Society of America. TIC: 256055.

160778 Pruess, K.; Oldenburg, C.; and Moridis, G. 1999. *TOUGH2 User's Guide, Version 2.0.* LBNL-43134. Berkeley, California: Lawrence Berkeley National Laboratory. TIC: 253038.

112060 Rai, D. and Ryan, J.L. 1982. "Crystallinity and Solubility of Pu(IV) Oxide and Hydrous Oxide in Aged Aqueous Suspensions." *Radiochimica Acta, 30,* 213-216. Munchen, Germany: R. Oldenbourg Verlag. TIC: 219107.

159354 Raman, A. and Nasrazadani, S. 1990. "Packing Corrosion in Bridge Structures." *Corrosion, 46,* (7), 601-605. Houston, Texas: National Association of Corrosion Engineers. TIC: 235061.

150765 Reamer, C.W. 2000. "Safety Evaluation Report for Disposal Criticality Analysis Methodology Topical Report, Revision 0." Letter from C.W. Reamer (NRC) to S.J. Brocoum (DOE/YMSCO), June 26, 2000, with enclosure. ACC: MOL.20000919.0157.

155464 Reamer, C.W. and Williams, D.R. 2000. Summary Highlights of NRC/DOE Technical Exchange and Management Meeting on Subissues Related to Criticality. Meeting held October 23-24, 2000, Las Vegas, Nevada. Washington, D.C.: U.S. Nuclear Regulatory Commission. ACC: MOL.20001208.0097; MOL.20001208.0098; MOL.20001208.0099; MOL.20001208.0100; MOL.20001208.0101; MOL.20001208.0102; MOL.20001208.0103; MOL.20001208.0104; MOL.20001208.0105; MOL.20001208.0106; MOL.20001208.0107; MOL.20001208.0108; MOL.20001208.0109; MOL.20001208.0110.

168028 Reyes-Cortés, I.A. 2002. "Geologic Setting and Mineralisation: Sierra Peña Blanca, Chihuahua, México." *Eighth EC Natural Analogue Working Group Meeting, Proceedings of an International Workshop held in Strasbourg, France from 23 to 25 March 1999.* von Maravic, H. and Alexander, W.R., eds. EUR 19118 EN. Pages 321-331. Luxembourg, Luxembourg: Office for Official Publications of the European Communities. TIC: 255689.

101708 Rimstidt, J.D. and Barnes, H.L. 1980. "The Kinetics of Silica–Water Reactions." *Geochimica et Cosmochimica Acta, 44,* 1683-1699. New York, New York: Pergamon Press. TIC: 219975.

162536 Roberts, K.E.; Wolery, T.J.; Atkins-Duffin, C.E.; Prussin, T.G.; Allen, P.G.; Bucher, J.J.; Shuh, D.K.; Finch, R.J.; and Prussin, S.G. 2003. "Precipitation of Crystalline Neptunium Dioxide from Near-Neutral Aqueous Solution." *Radiochimica Acta, 91,* (2), 87-92. München, Germany: Oldenbourg Wissenschaftsverlag. TIC: 254035.

107105 Roberts, W.L.; Campbell, T.J.; and Rapp, G.R., Jr. 1990. *Encyclopedia of Minerals*. 2nd Edition. New York, New York: Van Nostrand Reinhold. TIC: 242976.

123127 Rogers, P.S.Z. and Meijer, A. 1993. "Dependence of Radionuclide Sorption on Sample Grinding Surface Area, and Water Composition." *High Level Radioactive Waste Management, Proceedings of the Fourth Annual International Conference, Las Vegas, Nevada, April 26-30, 1993. 2,* 1509-1516. La Grange Park, Illinois: American Nuclear Society. TIC: 208542.

144800 Runde, W. 1999. "Letter Report on Plutonium Thermodynamic Database." Letter from W. Runde (LANL) to P. Dixon (LANL), August 1, 1999, with attachments. ACC: MOL.19991214.0624.

168432 Runde, W.; Conradson, S.D.; Efurd, D.W.; Lu, N.P.; VanPelt, C.E.; and Tait, C.D. 2002. "Solubility and Sorption of Redox-Sensitive Radionuclides (Np, Pu) in J-13 Water from the Yucca Mountain Site: Comparison between Experiment and Theory." *Applied Geochemistry, 17,* (6), 837-853. New York, New York: Pergamon. TIC: 254046.

113307 Sandino, A. 1991. *Processes Affecting the Mobility of Uranium in Natural Waters.* Ph.D. thesis. Stockholm, Sweden: Royal Institute of Technology. TIC: 246941.

159865 Schlueter, J. 2002. "Key Technical Issue Agreements Related to Criticality." Letter from J. Schlueter (NRC) to S. Brocoum (DOE/YMSCO), February 14, 2002, 0225021619, with enclosure. ACC: MOL.20020607.0085.

144629 Schwertmann, U. and Cornell, R.M. 1991. *Iron Oxides in the Laboratory: Preparation and Characterization.* New York, New York: VCH Publishers. TIC: 237942.

105959 Schwertmann, U. and Taylor, R.M. 1995. "Iron Oxides." Chapter 8 of *Minerals in Soil Environments.* 2nd Edition. Dixon, J.B. and Weed, S.B., eds. SSSA Book Series, No. 1. Madison, Wisconsin: Soil Science Society of America. TIC: 237222.

169280 Singer, A. 1995. "Palygorskite and Sepiolite Group Minerals." Chapter 17 of *Minerals in Soil Environments.* 2nd Edition. Dixon, J.B. and Weed, S.B., eds. SSSA Book Series, No. 1. Madison, Wisconsin: Soil Science Society of America. TIC: 237222.

162976 Smith, W.H. and Purdy, G.M. 1995. "Chromium in Aqueous Nitrate Plutonium Process Streams: Corrosion of 316 Stainless Steel and Chromium Speciation." *Waste Management, 15,* (7), 477-484. New York, New York: Pergamon. TIC: 254034.

162494 SNL (Sandia National Laboratories) 2003. *Software User's Manual, EQ3/6, Version 8.0.* SDN: 10813-UM-8.0-00. Albuquerque, New Mexico: Sandia National Laboratories. ACC: MOL.20030312.0084.

103804 Spahiu, K. and Bruno, J. 1995. *A Selected Thermodynamic Database for REE to be Used in HLNW Performance Assessment Exercises.* SKB TR-95-35. Stockholm, Sweden: Svensk Kärnbränsleförsörjning A.B. TIC: 225493.

127253 Sposito, G. 1984. *The Surface Chemistry of Soils.* New York, New York: Oxford University Press. TIC: 217687.

153993 Stanton, R.L. 1972. *Ore Petrology.* New York, New York: McGraw-Hill. TIC: 234764.

100419 Stout, R.B. and Leider, H.R., eds. 1997. *Waste Form Characteristics Report Revision 1.* UCRL-ID-108314. Version 1.2. Livermore, California: Lawrence Livermore National Laboratory. ACC: MOL.19980512.0133.

125332 Stumm, W. and Morgan, J.J. 1996. *Aquatic Chemistry, Chemical Equilibria and Rates in Natural Waters.* 3rd Edition. New York, New York: John Wiley & Sons. TIC: 246296.

177119 Sverjensky, D.A. 2003. "Standard States for the Activities of Mineral Surface Sites and Species." *Geochimica et Cosmochimica Acta, 67,* (1), 17-28. New York, New York: Pergamon. TIC: 258424.

177120 Sverjensky, D.A. 2006. "Prediction of the Speciation of Alkaline Earths Adsorbed on Mineral Surfaces in Salt Solutions." *Geochimica et Cosmochimica Acta, 70,* 2427-2453. New York, New York: Elsevier. TIC: 258425.

177221 Swayambunathan, V.; Liao, Y.X.; and Meisel, D. 1989. "Stages in the Evolution of Colloidal Chromium(III) Oxide." *Langmuir, 5,* (6), 1423-1427. Washington, D.C.: American Chemical Society. TIC: 258485.

131482 Thomas, G.B., Jr. 1972. *Calculus and Analytic Geometry.* Alternate Edition. Reading, Massachusetts: Addison-Wesley Publishing. TIC: 245088.

175267 Thomas, G.F. and Till, G. 1984. "The Dissolution of Unirradiated UO_2 Fuel Pellets under Simulated Disposal Conditions." *Nuclear and Chemical Waste Management, 5,* (2), 141-147. Elmsford, New York: Pergamon Press. TIC: 245790.

176906 Toride, N.; Inoue, M.; and Leij, F.J. 2003. "Hydrodynamic Dispersion in an Unsaturated Dune Sand." *Soil Science Society of America Journal, 67,* 703-712. Madison, Wisconsin: Soil Science Society of America. TIC: 258302.

173021 Trivedi, P.; Axe, L.; and Dyer, J. 2001. "Adsorption of Metal Ions onto Goethite: Single-Adsorbate and Competitive Systems." *Colloids and Surfaces, 191,* 107-121. New York, New York: Elsevier. TIC: 257088.

100610 van Genuchten, M.T. 1980. "A Closed-Form Equation for Predicting the Hydraulic Conductivity of Unsaturated Soils." *Soil Science Society of America Journal, 44,* (5), 892-898. Madison, Wisconsin: Soil Science Society of America. TIC: 217327.

142216 Vaniman, D.T. 1993. *Calcite Deposits in Drill Cores USW G-2 and USW GU-3/G-3 at Yucca Mountain, Nevada.* TWS-EES-1-7-92-2, Rev. 1. Los Alamos, New Mexico: Los Alamos National Laboratory. ACC: NNA.19931018.0075.

151482 Vaughan, D.J. and Craig, J.R. 1978. *Mineral Chemistry of Metal Sulfides.* Cambridge Earth Science Series. Harland, W.B., ed. New York, New York: Cambridge University Press. TIC: 248467.

176901 Vochten, R.; De Grave, E.; and Lauwers, H. 1990. "Transformation of Synthetic U_3O_8 into Different Uranium Oxide Hydrates." *Mineralogy and Petrology, 41,* 247-255. New York, New York: Springer-Verlag. TIC: 257681.

126924 Waber, N. 1991. *Mineralogy, Petrology and Geochemistry of the Pocos de Caldas Analogue Study Sites, Minas Gerais, Brazil. II. Morro do Ferro.* SKB TR-90-12. Stockholm, Sweden: Svensk Kärnbränsleförsörjning A.B. TIC: 206350.

100833 Weast, R.C. and Astle, M.J., eds. 1981. *CRC Handbook of Chemistry and Physics.* 62nd Edition. Boca Raton, Florida: CRC Press. TIC: 240722.

106266 Weast, R.C., ed. 1977. *CRC Handbook of Chemistry and Physics.* 58th Edition. Cleveland, Ohio: CRC Press. TIC: 242376.

128733 Weast, R.C., ed. 1978. *CRC Handbook of Chemistry and Physics.* 59th Edition. West Palm Beach, Florida: CRC Press. TIC: 246814.

137607 Wilson, C.N. and Bruton, C.J. 1989. *Studies on Spent Fuel Dissolution Behavior Under Yucca Mountain Repository Conditions.* PNL-SA-16832. Richland, Washington: Pacific Northwest Laboratory. ACC: HQX.19890918.0047.

169286 Wronkiewicz, D.J. and Buck, E.C. 1999. "Uranium Mineralogy and the Geologic Disposal of Spent Nuclear Fuel." Chapter 10 of *Uranium: Mineralogy, Geochemistry and the Environment.* Burns, P.C. and Finch, R., eds. Reviews in Mineralogy Volume 38. Washington, D.C.: Mineralogical Society of America. TIC: 247121.

176891 Wronkiewicz, D.J.; Bates, J.K.; Gerding, T.J.; Veleckis, E.; and Tani, B.S. 1991. *Leaching Action of EJ-13 Water on Unirradiated UO_2 Surfaces Under Unsaturated Conditions at 90°C: Interim Report.* ANL-91/11. Argonne, Illinois: Argonne National Laboratory. ACC: NNA.19910314.0091.

100493 Wronkiewicz, D.J.; Bates, J.K.; Gerding, T.J.; Veleckis, E.; and Tani, B.S. 1992. "Uranium Release and Secondary Phase Formation During Unsaturated Testing of UO2 at 90°C." *Journal of Nuclear Materials, 190,* 107-127. Amsterdam, The Netherlands: North-Holland Publishing Company. TIC: 236558.

102047 Wronkiewicz, D.J.; Bates, J.K.; Wolf, S.F.; and Buck, E.C. 1996. "Ten-Year Results from Unsaturated Drip Tests with UO_2 at 90°C: Implications for the Corrosion of Spent Nuclear Fuel." *Journal of Nuclear Materials, 238,* (1), 78-95. Amsterdam, The Netherlands: North-Holland. TIC: 243361.

177175 Wu, C.H.; Lo, S.L.; and Lin, C.F. 2000. "Competitive Adsorption of Molybdate, Chromate, Sulfate, and Selenate on gamma-Al2O3." *Colloids and Surfaces, 166,* 251-259. New York, New York: Elsevier. TIC: 258475.

100194 Yang, I.C.; Rattray, G.W.; and Yu, P. 1996. *Interpretation of Chemical and Isotopic Data from Boreholes in the Unsaturated Zone at Yucca Mountain, Nevada.* Water-Resources Investigations Report 96-4058. Denver, Colorado: U.S. Geological Survey. ACC: MOL.19980528.0216.

165505 YMP (Yucca Mountain Site Characterization Project) 2003. *Disposal Criticality Analysis Methodology Topical Report.* YMP/TR-004Q, Rev. 02. Las Vegas, Nevada: Yucca Mountain Site Characterization Office. ACC: DOC.20031110.0005.

173729 Zhang, J. and Grischkowsky, D. 2004. "Waveguide Terahertz Time-Domain Spectroscopy of Nanometer Water Layers." *Optics Letter, 29,* (4), 1617-1619. Washington, D.C.: Optical Society of America. TIC: 257234.

163341 Zyvoloski, G.; Kwicklis, E.; Eddebbarh, A.A.; Arnold, B.; Faunt, C.; and Robinson, B.A. 2003. "The Site-Scale Saturated Zone Flow Model for Yucca Mountain: Calibration of Different Conceptual Models and their Impact on Flow Paths." *Journal of Contaminant Hydrology, 62-63,* 731-750. New York, New York: Elsevier. TIC: 254340.

9.2 CODES, STANDARDS, REGULATIONS, AND PROCEDURES

173273 10 CFR 63. 2005 Energy: Disposal of High-Level Radioactive Wastes in a Geologic Repository at Yucca Mountain, Nevada. ACC: MOL.20050405.0118.

LP-SIII.2Q, Rev. 00, ICN 01. *Qualification of Unqualified Data*. Washington, D.C.: U.S. Department of Energy, Office of Civilian Radioactive Waste Management. ACC: DOC.20060601.0014.

LP-SIII.10Q-BSC, Rev 01, ICN 00. *Models*. Washington, D.C.: U.S. Department of Energy, Office of Civilian Radioactive Waste Management. ACC: DOC.20060518.0004.

IT-PRO-0011 Rev 00, ICN 00. *Software Management*. Las Vegas, NV, BSC (Bechtel SAIC Company). ACC: DOC.20060301.0007.

9.3 SOURCE DATA, LISTED BY DATA TRACKING NUMBER

162015 GS000308313211.001. Geochemistry of Repository Block. Submittal date: 03/27/2000.

160899 GS020408312272.003. Collection and Analysis of Pore Water Samples for the Period from April 2001 to February 2002. Submittal date: 04/24/2002.

107355 GS980308315215.008. Line Survey Information from the Exploratory Studies Facility Obtained to Estimate Secondary Mineral Abundance. Submittal date: 03/24/1998.

119916 GS980808312242.015. Water Retention and Unsaturated Hydraulic Conductivity Measurements for Various Size Fractions of Crushed, Sieved, Welded Tuff Samples Measured Using a Centrifuge. Submittal date: 08/21/1998.

108396 GS990408314224.001. Detailed Line Survey Data for Stations 00+00.89 to 14+95.18, ECRB Cross Drift. Submittal date: 09/09/1999.

105625 GS990408314224.002. Detailed Line Survey Data for Stations 15+00.85 to 26+63.85, ECRB Cross Drift. Submittal date: 09/09/1999.

159525 LB0205REVUZPRP.001. Fracture Properties for UZ Model Layers Developed from Field Data. Submittal date: 05/14/2002.

159672 LB0207REVUZPRP.002. Matrix Properties for UZ Model Layers Developed from Field and Laboratory Data. Submittal date: 07/15/2002.

161243 LB0208UZDSCPMI.002. Drift-Scale Calibrated Property Sets: Mean Infiltration Data Summary. Submittal date: 08/26/2002.

164744 LB0302DSCPTHCS.001. Drift-Scale Coupled Processes (THC Seepage) Model: Simulations. Submittal date: 02/11/2003.

168014 LB0402PBCORELG.001. Core Description for PB-1. Submittal date: 02/27/2004.

168018 LB0402PBMNRLGY.001. Petrographic Descriptions of Rock Samples from PB-1, PB-2, and PB-3. Submittal date: 02/27/2004.

106787 LB990501233129.001. Fracture Properties for the UZ Model Grids and Uncalibrated Fracture and Matrix Properties for the UZ Model Layers for AMR U0090, "Analysis of Hydrologic Properties Data". Submittal date: 08/25/1999.

151029 MO0006J13WTRCM.000. Recommended Mean Values of Major Constituents in J-13 Well Water. Submittal date: 06/07/2000.

164438 MO0307SPAVGSUM.000. van Genuchten Hydrologic Parameters. Submittal date: 07/26/2003.

166411 MO0310SPAEBSCB.003. EBS Chemistry Binning Abstraction Results of the THC Seepage Model. Submittal date: 10/15/2003.

172059 MO0409SPAACRWP.000. Aqueous Corrosion Rates For Non-Waste Form Waste Package Materials. Submittal date: 09/16/2004.

174811 MO0506MWDTLVAC.000. TSPA-LA Validation and Analysis Cases. Submittal date: 06/30/2005. Awaiting Final Publication

176868 MO0604SPAPHR25.001. PHREEQC Data 0 Thermodynamic Database for 25 Degrees C - File: PHREEQCDATA025.DAT. Submittal date: 04/10/2006. Imaging in Process

176909 MO0604SPAPHR90.000. PHREEQC Data 0 Thermodynamic Database for 90 Degrees C - File: PHREEQCDATA090.DAT. Submittal date: 04/10/2006.

177332 MO0608MWDGEOMA.001. Input Files and Model Output Runs: Geochemistry Model Validation Report: Material Degradation and Release Model. Submittal date: 08/07/2006.

172712 SN0410T0510404.002. Thermodynamic Database Input File for EQ3/6 - DATA0.YMP.R4. Submittal date: 11/01/2004.

9.4 OUTPUT DATA, LISTED BY DATA TRACKING NUMBER

MO0609SPAINOUT.002. PHREEQC Modeling Inputs and Outputs for Geochemistry Model Validation Report: External Accumulation Model. Submittal Date: 09/27/2006.

MO0604SPANOMIN.000. Nominal Case Diffusive Releases. Submittal Date: 04/26/2006.

MO0609SPASENSI.003. Sensitivity Analyses for PHREEQC Modeling for Geochemistry Model Validation Report: External Accumulation Model. Submittal Date: 09/27/2006.

MO0608SPASOLID.002. Solid Releases for all Scernarios. Submittal Date: 08/14/2006.

MO0605SPAINVRT.000. Accumulation in Invert. Submittal date: 05/02/2006.

SN0607T0504506.002. Modeling of Mixing in the Invert. Submittal date: 08/15/2006.

9.5 OUTPUT DATA FOR MODEL VALIDATION, LISTED BY DATA TRACKING NUMBER

MO0608SPACONFI.001. Model Validation – Confidence Building by Corroboration of PHREEQC and EQ3/6 Model Outputs. Submittal Date: 08/11/2006

MO0604SPANUMER.000. Model Validation – Validation of a Numerical Model for Mixing in Invert with an Analytical Model. Submittal Date: 04/25/2006.

MO0604SPAPREDI.000. Model Validation –PHREEQC Prediction of the Accumulation of Uranyl Materials and Leachate Compositions Observed in the Argonne UO2 Drip Test. Submittal Date: 04/25/2006.

MO0607SPADSORP.000. Model Validation- Comparasion of PHREEQC results to calculations from the competitive adsorption studies. Submittial Date: 07/18/2006

9.6 SOFTWARE CODES

155712 BSC 2001. *Software Code: ASPRIN.* V1.0. 10487-1.0-00.

157838 BSC 2002. *Software Code: Acc_with_decay.* V1.2. PC. 10499-1.2-00.

159731 BSC 2002. *Software Code: EQ6.* 7.2bLV. PC. 10075-7.2bLV-02. Windows NT, 2000.

173680 BSC 2002. *Software Code: GetEQData.* V. 1.0.1. PC, WINDOWS 2000. STN: 10809-1.0.1-00.

157840 BSC 2002. *Software Code: GetEqPhases.* V1.0. PC. 10725-1.0-00.

157841 BSC 2002. *Software Code: MinAcc.* V1.00. PC. 10724-1.0-00.

157837 BSC 2002. *Software Code: PHREEQC.* V2.3. PC. 10068-2.3-01.

157839 BSC 2002. *Software Code: PHREEQC_Post.* V1.1. PC. 10723-1.1-00.

176889 BSC 2005. *Software Code: EQ3/6.* 8.1. 10813-8.1-00. PC w/ Windows 95/98/2000/NT 4.0.

175698 BSC 2006. *Software Code: PHREEQC.* V. 2.11. PC, WINDOWS 2000. STN: 10068-2.11-00.

161256 LBNL (Lawrence Berkeley National Laboratory) 2002. *Software Code: TOUGHREACT.* V3.0. DEC ALPHA/OSF1 V5.1, DEC ALPHA/OSF1 V5.0, Sun UltraSparc/Sun OS 5.5.1, PC/Linux Redhat 7.2. 10396-3.0-00.

APPENDIX A

EXAMPLE OF PHREEQC V 2.3 INPUT FILE WITH KEY WORD DESCRIPTIONS

INTENTIONALLY LEFT BLANK

The following input file, **tmi_10.933k.in** (from Output DTN: MO0609SPAINOUT.002; folder TMI_IG1\TMI_IG1_phreeqc_runs\rlz8) will be used to illustrate a typical PHREEQC input file. An explanation will precede each of the keyword data blocks as they appear in the input file.

The TITLE data block is used to include comments about the simulation, for informational use only, PHREEQC does not use information from this block.

Note also, that any preceded by a " # ", is not read by PHREEQC and is for informational use only.

```
DATABASE  phreeqcDATA025.dat  - THERMODYNAMIC DATABASE USED

TITLE
From tmi                    -SOURCE TERM
SA=20000 cm2                -SURFACE AREA OF INVERT
Mixing=0.1                  -MIXING RATIO
mixing water=basalt         -MIXING WATER
timestep=1 years            -TIMESTEP
flowrate=1 L/y              -FLOWRATE
LogPCO2=-3                  -PCO2 VALUE
```

Fictitious anions are used to in the Kd equation to calculate adsorption. They were needed to offset activity coefficients in the mass law expressions because Kd values are ratios of concentrations, not activities. (It should be noted, however, that in the current model the “Kd equation” is actually a misnomer. In the model, Kd values and sorption capacities are used to generate Langmuir adsorption equations. These adsorption equations only reduce to Kd equations when there is a large excess of available adsorption sites at equilibrium.)

```
SOLUTION_MASTER_SPECIES
   Fa  Fa-1  0  1  1  # fictitious 1- charge anion used in Kd equation to compensate for act. coeff.
   Fb  Fb-2  0  1  1  # fictitious 2- charge anion used in Kd equation to compensate for act. coeff.
   Fd  Fd-4  0  1  1  # fictitious 4- charge anion used in Kd equation to compensate for act. coeff.
   Ff  Ff-5  0  1  1  # fictitious 5- charge anion used in Kd equation to compensate for act. coeff.
   Fo  Fo-0  0  1  1  # fictitious neutral ion used in Kd equation to compensate for act. coeff.
   Fp  Fp+1  0  1  1  # fictitious 1+ chargecation used in Kd equation to compensate for act.
coeff.
```

This SOLUTION data block begins the first data input set and is used to define the temperature and chemical composition of the initial solution. In this case, the initial solution, **SOLUTION 0,** is the TMI waste package water composition at time 10,933 years. The software APRIN V1.0 output file *TMI_IG1A.xls* in Output DTN: MO0609SPAINOUT.002; folder TMI_IG1\TMI_IG1_asprin is the sourceterm at 10,933 years.

```
SOLUTION 0  Waste Package Water
pH      8.752204
```

```
#pe      pe
 temp            25.
-units           mol/kgw
#Years           10933.13
#zi              zi
#pH              8.752204
#Eh              0.7012877
#fO2             0.1995262
#IonStr          2.097351
Na               0.911515
C                0.468116
B                0.09971127
Cr(3)            3.219781E-14
K                0.09331287
U                0.1486765
S                0.01450154
F                1.060372E-13
Si               0.0001777164
N(5)             0.04651195
Mo               0.1223714
Cl               0.0004905434
Ca               0.00001278942
Mg               0.0001270791
P                0.009207413
Al               0.00000004370317
Ni               0.000000007384461
Ba               0.000000699121
Fe(3)            3.838507E-12
Mn               1.210984E-15
Cu               1.844128E-17
#Gd              Gd
Zn               1.844127E-17
#Co              Co
#Pu              Pu
#Np              Np
        Fa       1 umol/kgw
        Fb       1 umol/kgw
        Fd       1 umol/kgw
        Ff       1 umol/kgw
        Fo       1 umol/kgw
        Fp       1 umol/kgw
```

The SOLUTION_SPECIES data block is used to add element or species data that is not in the database. It may be used to add an entirely new element or species as well as to change the parameters for species already in the database such as log k, activity coefficient, and delta h. In this case, a low log k for the formation of N2(aq) was entered to suppress nitrate reduction.

Also, a relationship between H2O and e- was defined as suggested in PHREEQC documentation to help with convergence. In additional SOLUTION_SPECIES data block, fictitious charged aqueous species were defined for the adsorption reactions defined in SURFACE_SPECIES.

```
SOLUTION_SPECIES       # used to suppress N2(aq)
1.5 O2 + 2. NH3 =N2 + 3. H2O
     log_k      -500.0
      -gamma 0 0
H2O + 0.01e- = H2O-0.01 # helps convergence
          log_k   -9.
```

Data used for the Adsorption calculations.

```
SOLUTION_SPECIES
   Fa-1 = Fa-1
   log_k     0
   -gamma    4.00   0.0410
   Fb-2 = Fb-2
   log_k     0
   -gamma    4.00   0.0410
   Fd-4 = Fd-4
   log_k     0
   -gamma    4.00   0.0410
   Ff-5 = Ff-5
   log_k     0
   -gamma    4.00   0.0410
   Fo-0 = Fo-0
   log_k     0
   -gamma    0      0
   Fp+1 = Fp+1
   log_k     0
   -gamma    4.00   0.0410
```

The following EQUILIBRIUM_PHASES data block is used to fix the partial pressure of gases in equilibrium with aqueous **SOLUTION 0**, the waste package water. The purpose of data block in this case is to fix the CO2(g) and O2(g) fugacities at 10^{-3} and $10^{-0.7}$ bar respectively. Here, each gas has a reservoir of 9.9 moles.

```
EQUILIBRIUM_PHASES  0
CO2(g)          -3        9.9
O2(g)           -0.7      9.9
```

The SAVE data block saves the composition of SOLUTION 0 for use in later calculations.

```
SAVE SOLUTION 0
END
```

To ensure that U and Pu adsorption concentrations do not exceed the surface site concentration of the crushed tuff, the adsorption equations included free adsorption sites as a reactant. Thus, the site had to be defined in the SURFACE_MASTER_SPECIES, SURFACE, and SURFACE_SPECIES blocks. Here, the total concentration of surface sites (0.33 molal) is defined for each of the 60 cells.

```
SURFACE_MASTER_SPECIES
   Sor Sor


Adsorption Section

SURFACE 1-60 Linear sorption
   Sor    0.33   1   0.33
# Value calculated from 9 m2/g; 2.3 sites/nm2; 0.31 porosity; 0.19 water content; 2.55 g/cc tuff
solid density
   -no_edl

SURFACE_SPECIES
   Sor = Sor
   log_k 0.0
```

To simulate U and Pu K_d adsorption in PHREEQC, specific surface reactions must be defined for each of the aqueous U and Pu species that comprise approximately one percent or more of the total U and Pu aqueous concentrations. The comment lines below explain how the log k values for each reaction were determined. The fictitious species do no more than offset the activity coefficients of the adsorbates. Note: in the case of the TMI source term there was no Pu in the waste package water, thus only the reactions for U are considered in this input file. The contribution of this species to U K_d adsorption is represented in PHREEQC by the following reactions.

```
# Adsorption reaction:  AqComp-1 + Sor  Fa-1= SorAqComp-1 + Fa-1
#     =>    k = [(SorAqComp-1)/(AqComp-1)]*(Fa-1)/(Sor)
#     =>    k = [(Kd(mL/g)*(drybulkdens(g/mL)/(water content))]*(Fa-
1)/(specificsurfacearea*sitedens*drybulkdens/(avagadro's number*water content))
#   Note that drybulkdensity and water content cancel out, which implies...
#     =>    k = [(Kd(mL/g)]*(Fa-1)/(specificsurfacearea*sitedens/avagadro's number)
#     =>    k = [(Kd(mL/g)]*(1e-6 mole/1000 mL) / (9 m2/g * 2.3e+18 sites/m2 / 6.02e+23
sites/mole)
#     =>    log_k = log[(Kd(mL/g) + log(1e-6/1000 / (9 * 2.3e+18 / 6.02e+23))
#     =>    log_k = log(Kd(mL/g)) - 4.54  (given above specific surface area and site density)

# U Kd = 2 mL/g
```

```
#    =>   log_k = 0.301 - 4.54 = -4.24 (given above specific surface area and site density)

        Sor + UO2(CO3)2-2 = SorUO2(CO3)2-2 + Fb-2
                log_k -4.24
                -no_check
                -mole_balance SorUO2(CO3)2
        Sor + UO2(CO3)3-4 = SorUO2(CO3)3-4 + Fd-4
                log_k -4.24
                -no_check
                -mole_balance SorUO2(CO3)3
        Sor + (UO2)2CO3(OH)3- = Sor(UO2)2CO3(OH)3- + Fa-1
                log_k -4.24
                -no_check
                -mole_balance Sor(UO2)2CO3(OH)3
        Sor + UO3 = SorUO3 + Fo-0
                log_k -4.24
                -no_check
                -mole_balance SorUO3
        Sor + HUO4- = SorHUO4- + Fa-1
                log_k -4.24
                -no_check
                -mole_balance SorHUO4
    Sor + UO2CO3 = SorUO2CO3 + Fo-0
                log_k -4.24
                -no_check
                -mole_balance SorUO2CO3
        Sor + UO2PO4- = SorUO2PO4- + Fa-1
                log_k -4.24
                -no_check
                -mole_balance SorUO2PO4
    Sor + UO2HPO4 = SorUO2HPO4 + Fo-0
                log_k -4.24
                -no_check
                -mole_balance SorUO2HPO4
    Sor + UO2F+ = SorUO2F+ + Fp+1
                log_k -4.24
                -no_check
                -mole_balance SorUO2F
```

This SOLUTION data block begins the second data input set and is used to define the temperature and chemical composition of **SOLUTION 1-60**, the pore water initially present in each of cells 1-60 before advection.

```
SOLUTION 1-60   BASALT WATER
 pH      9.02
 -units mol/kgw
```

Al	6.46e-7
Ca	4.76e-6
Cl	5.61e-4
F	2.96e-13
Fe(3)	1.43e-12
C	2.19e-2
P	9.87e-3
K	1.24e-9
Mg	4.69e-5
Mn	1.00e-16
N(5)	3.97e-5
Na	4.47e-2
S	3.55e-4
Si	6.74e-5
B	1e-16
Ba	1e-16
Br	1e-16
#Co	1e-16
Cr	1e-16
#Gd	1e-16
Mo	1e-16
Ni	1e-16
#Np(5)	1e-16
#Pu(6)	1e-16
U	1e-16
Fa	1 umol/kgw
Fb	1 umol/kgw
Fd	1 umol/kgw
Ff	1 umol/kgw
Fo	1 umol/kgw
Fp	1 umol/kgw

This EQUILIBRIUM_PHASES data block is similar to the previous one. **SOLUTION 1-60** is brought to equilibrium with CO2(g), O2(g), diaspore, pyrolusite and geothite before any further reactions take place.

EQUILIBRIUM_PHASES	1-60	
CO2(g)	-3	9.9
O2(g)	-0.7	9.9
Diaspore	0	10.0
Pyrolusite	0	10.0
Goethite	0	10.0

See above for SAVE and END data block descriptions.

```
SAVE SOLUTION 1-60
END
```

This SOLUTION data block begins the third data input set and is used to define the temperature and chemical composition of **SOLUTION 999**, the mixing water, basalt water in this case to be mixed with the water present in cells 1-60 and advecting downward. This water represents water that mixes with the source water as it flows downward. It is followed by the EQUILIBRIUM_PHASES, SAVE, and END data blocks as in the previous SOLUTION data blocks.

```
SOLUTION 999   BASALT WATER
 pH      9.02
-units mol/kgw
 Al                 6.46e-7
 Ca                4.76e-6
 Cl                 5.61e-4
 F                 2.96e-13
 Fe(3)              1.43e-12
 C                  2.19e-2
 P                  9.87e-3
 K                  1.24e-9
 Mg                  4.69e-5
 Mn                  1.00e-16
 N(5)                3.97e-5
 Na                 4.47e-2
 S                 3.55e-4
 Si                6.74e-5
 B               1e-16
 Ba              1e-16
 Br              1e-16
 #Co             1e-16
 Cr              1e-16
 #Gd             1e-16
 Mo              1e-16
 Ni              1e-16
 #Np(5)          1e-16
 #Pu(6)          1e-16
 U               1e-16
        Fa       1 umol/kgw
        Fb       1 umol/kgw
        Fd       1 umol/kgw
        Ff       1 umol/kgw
        Fo       1 umol/kgw
        Fp       1 umol/kgw
```

This EQUILIBRIUM_PHASES data block is similar to the previous blocks. **SOLUTION 999** is brought to equilibrium with CO2(g), O2(g), diaspore, pyrolusite and geothite before any further reactions take place.

```
EQUILIBRIUM_PHASES 999
CO2(g)          -3      9.9
O2(g)           -0.7    9.9
Diaspore        0       10.0
Pyrolusite      0       10.0
Goethite        0       10.0
```

See above for SAVE and END data block descriptions.

```
SAVE SOLUTION 999
END
```

The USE data blocks specify SOLUTION 0 and SOLUTION 999 to be used in the batch reaction calculation of the fourth simulation

```
USE SOLUTION 0
USE SOLUTION 999
```

In this example, the species that are allowed to precipitate in cells 1-60 (should they become chemically saturated in the water) are specified here. The values following each phase are the target saturation indices and the initial quantity present, respectively.

```
EQUILIBRIUM_PHASES 1-60
(UO2)3(PO4)2:4H2O 0       0
Amesite-14A     0       0
Barite          0       0
Boltwoodite-Na          0       0
Celadonite          0   0
Chabazite       0       0
Chalcedony      0       0
Chrysotile      0       0
Dawsonite       0       0
Erionite        0       0
Eskolaite       0       0
Fluorapatite    0       0
Gibbsite        0       0
Goethite        0       0
Hydroxylapatite         0       0
Kaolinite       0       0
Laumontite      0       0
Magnesite       0       0
Mesolite        0       0
```

```
Montmorillonite-Na  0       0
Ni3(PO4)2     0     0
Nontronite-Ca 0     0
Nontronite-K  0     0
Nontronite-Mg       0       0
Nontronite-Na 0     0
Phillipsite   0     0
Powellite     0     0
Pyrolusite    0     0
Saponite-Na   0     0
Sepiolite     0     0
Stellerite    0     0
Trevorite  0  0
Uranophane(alpha)   0       0
CO2(g)              -3      9.9
O2(g)         -0.7  9.9
```

The RATES data block is used to define general rate expressions for the kinetic reactions. The specific parameters used in the equations are defined later in the KINETCS data block. The rate laws are used to characterize the slow dissolution of the tuff minerals making up the invert. A Basic interpreter is embedded in PHREEQC, thus the Basic identifiers and numbered statement lines.

```
RATES
Cristobalite(alpha)
-start
300  SR_crst = SR("Cristobalite(alpha)")
310  ko=PARM(1)*ACT("H+")^PARM(2)+ PARM(3)*ACT("H+")^PARM(4)
320  moles = ko * PARM(5)*PARM(6)*(1 - SR_crst)* TIME
330 IF (moles<0) THEN moles=0
370 SAVE moles
-end

Annite
-start
300  SR_ant = SR("Annite")
310  ko=PARM(1)*ACT("H+")^PARM(2)+ PARM(3)*ACT("H+")^PARM(4)
320  moles = ko * PARM(5)*PARM(6)*(1 - SR_ant)* TIME
330 IF (moles<0) THEN moles=0
370 SAVE moles
-end

Phlogopite
-start
300  SR_phl = SR("Phlogopite")
```

```
310  ko=PARM(1)*ACT("H+")^PARM(2)+ PARM(3)*ACT("H+")^PARM(4)
320  moles = ko * PARM(5)*PARM(6)*(1 - SR_phl)* TIME
330 IF (moles<0) THEN moles=0
370 SAVE moles
-end

Maximum_Microcline
-start
200  SR_mxm = SR("Maximum_Microcline")
210  ko=PARM(1)*ACT("H+")^PARM(2)+ PARM(3)*ACT("H+")^PARM(4)
220  moles = ko * PARM(5)*PARM(6)*(1 - SR_mxm)* TIME
230 IF (moles<0) THEN moles=0
270 SAVE moles
-end

Albite_low
-start
200  SR_alb = SR("Albite_low")
210  ko=PARM(1)*ACT("H+")^PARM(2)+ PARM(3)*ACT("H+")^PARM(4)
220  moles = ko * PARM(5)*PARM(6)*(1 - SR_alb)* TIME
230 IF (moles<0) THEN moles=0
370 SAVE moles
-end

Anorthite
-start
200  SR_anh = SR("Anorthite")
210  ko=PARM(1)*ACT("H+")^PARM(2)+ PARM(3)*ACT("H+")^PARM(4)
220  moles = ko * PARM(5)*PARM(6)*(1 - SR_anh)* TIME
230 IF (moles<0) THEN moles=0
370 SAVE moles
-end
```

The KINETICS data block uses lines 1, 2, and 3 (below the comment lines), respectively, to specify the name of the rate expression, the current moles of reactant and the list of reaction parameters used in the RATES data block.

```
KINETICS 1-60
# second to last parameter is % volume of the mineral in tuff
#  last parameter is scaled surface area

Cristobalite(alpha)
        -m       100.0
        -parms 3.94e-16         0.0594 6.93e-19         -0.318  0.371   20000
Annite
        -m       100.0
```

```
        -parms 2.37e-15     0.426       7.34e-19        -0.231  0.0140 20000
Phlogopite
        -m      100.0
        -parms 2.37e-15     0.426       7.34e-19        -0.231  0.00459         20000
Maximum_Microcline
        -m      100.0
        -parms 5.50E-15         0.443           2.62E-17        -0.0214         0.281   20000
Albite_low
        -m      100.0
        -parms 7.94e-15         0.330           5.01e-19        -0.32           0.304   20000
Anorthite
        -m      100.0
        -parms 1.58e-11         0.91            2.00e-18        -0.30           0.0254 20000

-steps      1
-step_divide 1
-runge_kutta 3
#-cvode true
```

The ADVECTION data block specifies the number of cells, the number of shifts (time steps) for the simulation, the time step size, and the shifts for which results will be written to the selected output file, *TMI_10.933k.xls*

```
ADVECTION
        -cells              60
        -shifts             60
        -time_step      31557600    #1  years
        -punch_frequency      10
        -print_cells 1-60
        -print_frequency 60
```

The SELECTED_OUTPUT data block is used to create a file from the data produced after each calculation. The file will later processed with spreadsheet software programs (PHREEQC_Post V1.1, Acc_with_decay V1.2, and MinAcc V1.0) . The first line (-file) designates the file name that the data will be written to. The subsequent lines are user specified selections of the data to be written to the file and perform the following functions: line (totals) defines the list of total concentrations of elements contained in the phases of interest; line 3 (equilibrium_phases) defines the list of mineral phases for which total amounts in moles transferred will be written to the file; line 4 (kinetic_reactants) defines the list of tuff minerals and the saturation indices of phases of interest; lines 5 and 6 (-time and -step) provide information regarding cumulative time since the beginning of the simulation, advection shift numbers, and reaction steps; line 7 (-ionic_strength) prints ionic strength to the file.

```
SELECTED_OUTPUT
        -file      tmi_10.933k.xls
        -totals Al B Ba Ca Cl Cr Cu F Fe Gd C P K Mg Mn Mo N Na Ni S Si U Zn
```

```
        -equilibrium_phases   (UO2)3(PO4)2:4H2O Amesite-14A   Barite  Boltwoodite-Na
        Celadonite  Chabazite Chalcedony     Chrysotile       Dawsonite       Erionite
        Eskolaite       Fluorapatite    Gibbsite        Goethite        Hydroxylapatite
Kaolinite       Laumontite      Magnesite       Mesolite        Montmorillonite-Na  Ni3(PO4)2
        Nontronite-Ca Nontronite-K  Nontronite-Mg       Nontronite-Na Phillipsite
        Powellite       Pyrolusite      Saponite-Na     Sepiolite       Stellerite  Trevorite
         Uranophane(alpha)
        -kinetic_reactants  Cristobalite(alpha) Annite Phlogopite Maximum_Microcline
Albite_low
         Anorthite
        -time   true
        -step   true
        -ionic_strength true
```

The PRINT data block is used to select results to be written to the output file for the first simulation. For this example the output file is tmi_10.933k.out. The default switch is **true** for the print function. The saturation indices for each phase for which a saturation index is calculated as well as the distribution of aqueous species and will be printed to the output file. Any other print options that are set to **true** by default will be printed if chosen.

```
PRINT
        -saturation_indices     true
        -species        true
```

The USER_PUNCH data block is additional data to be printed to the output file tmi_10.933k.out, due to the addition of the adsorption function. SorU(m) is the total adsorbed concentration of U. UKd(mL/g) is a check on the partitioning of U between adsorbed and aqueous phases. This calculation is really only a Kd when aqueous U concentrations are very low compared to free sorption site concentrations (Sor). When free sorption site concentrations are considerably lower than total sorption site concentrations, the "UKd(mL/g)" calculation falls below the U Kd as dictated by the Langmuir adsorption equation used in this analysis.

```
USER_PUNCH
 -headings SorU(m) UKd(mL/g) #SI>0.01 - - - - '-0.01<SI<0.01
 -start
```

Adsorption calculations, see Section 6.2.5 for further explanation.

```
######  Check Adsorption  ###
10 Uaq = TOT("U")
#   add all Sorbed species:
20 SorU = mol("SorUO2(CO3)2-2") + mol("SorUO2(CO3)3-4")+ mol("Sor(UO2)2CO3(OH)3-
")+ mol("SorUO3")+ mol("SorHUO4-")+ mol("SorUO2CO3")+ mol("SorUO2PO4-") +
mol("SorUO2HPO4") + mol("SorUO2F+")
```

```
#   update water content and drybulkdens as needed in following lines:
30 watercontent = 0.19  # =0.31*0.6
35 dbdens = 1.8  # g/mL
#   check overall elemental Kd values
40 KdChk_U = SorU/Uaq*watercontent/dbdens
60 PUNCH SorU, KdChk_U
######  Identify Saturated and Supersaturated Minerals  ###
#100 max_si = SYS("phases", n, name$, type$, value)
#200 if (max_si < -0.01) then gosub 1000
#300 if (max_si >= -0.01) then gosub 2000
#400 end
#1000 REM  no saturated or supersaturated minerals
#1010 PUNCH "No phases are saturated or supersaturated"
#1020 return
#2000 REM saturated or supersaturated minerals
#2010 ssat = 0
#2020 FOR i = 1 to n
#2030 if (value(i) > 0.01) then PUNCH name$(i)
#2035 if (value(i) > 0.01) then ssat = ssat + 1
#2040 next i
#2050 spaces = 5 - ssat
#2055 FOR i = 1 to spaces
#2060 PUNCH " "
#2065 next i
#2070 PUNCH "SATD->"
#2075 FOR i = 1 to n
#2080 if (value(i) < -0.01) then return
#2085 if (value(i) < 0.01) then PUNCH name$(i)
#2090 next i
#2095 return
  -end
```

The KNOBS data block is used to redefine parameters that affect convergence for the numerical method during speciation, batch reaction, and transport calculations. In this example, the default for line 1 was used to aid convergence . The **false** option was chosen for line 2 so that information about each of the calculations would not be written to a separate log file. Log files contain information regarding the number of iterations and can be quite large. In this case, they are not needed. If the calculations do not converge with the default and user specified convergence parameters, PHREEQC attempts several combinations of the KNOBS data block features automatically before it will terminate the calculations due to nonconvergence. Warning messages appear by default in the output file, in this case it would appear in TMI_10.933k.out, as each attempt at convergence is made. If the numerical method will not converge, a statement appears at the end of the output file indicating the termination of the calculation.

```
KNOBS
        -logfile        false
```

```
    -diagonal_scale         true
```

The parameters in lines 1 and 2 of the MIX data blocks are the respective solution numbers and their mixing fractions. Previously, in the USE data block, SOLUTION 0 (waste package water), and SOLUTION 999 (basalt water), were specified to be used in this simulation. SOLUTION 0 enters cell one (the MIX 1 data block) and mixes with a fraction of SOLUTION 1 and SOLUTION 999 to form SOLUTION 2. SOLUTION 2 then advects to the second cell (MIX 2 data block) and so forth through the remaining cells (60 cells in total).

```
MIX 1
1  0.9
999   0.1
MIX 2
2  0.9
999   0.1
MIX 3
3  0.9
999   0.1
MIX 4
4  0.9
999   0.1
MIX 5
5  0.9
999   0.1
MIX 6
6  0.9
999   0.1
MIX 7
7  0.9
999   0.1
MIX 8
8  0.9
999   0.1
MIX 9
9  0.9
999   0.1
MIX 10
10  0.9
999   0.1
MIX 11
11  0.9
999   0.1
MIX 12
12  0.9
999   0.1
MIX 13
```

```
13  0.9
999   0.1
MIX 14
14  0.9
999   0.1
MIX 15
15  0.9
999   0.1
MIX 16
16  0.9
999   0.1
MIX 17
17  0.9
999   0.1
MIX 18
18  0.9
999   0.1
MIX 19
19  0.9
999   0.1
MIX 20
20  0.9
999   0.1
MIX 21
21  0.9
999   0.1
MIX 22
22  0.9
999   0.1
MIX 23
23  0.9
999   0.1
MIX 24
24  0.9
999   0.1
MIX 25
25  0.9
999   0.1
MIX 26
26  0.9
999   0.1
MIX 27
27  0.9
999   0.1
MIX 28
28  0.9
```

```
999   0.1
MIX 29
29  0.9
999   0.1
MIX 30
30  0.9
999   0.1
MIX 31
31  0.9
999   0.1
MIX 32
32  0.9
999   0.1
MIX 33
33  0.9
999   0.1
MIX 34
34  0.9
999   0.1
MIX 35
35  0.9
999   0.1
MIX 36
36  0.9
999   0.1
MIX 37
37  0.9
999   0.1
MIX 38
38  0.9
999   0.1
MIX 39
39  0.9
999   0.1
MIX 40
40  0.9
999   0.1
MIX 41
41  0.9
999   0.1
MIX 42
42  0.9
999   0.1
MIX 43
43  0.9
999   0.1
```

```
MIX 44
44  0.9
999   0.1
MIX 45
45  0.9
999   0.1
MIX 46
46  0.9
999   0.1
MIX 47
47  0.9
999   0.1
MIX 48
48  0.9
999   0.1
MIX 49
49  0.9
999   0.1
MIX 50
50  0.9
999 0.1
MIX 51
51  0.9
999   0.1
MIX 52
52  0.9
999   0.1
MIX 53
53  0.9
999   0.1
MIX 54
54  0.9
999   0.1
MIX 55
55  0.9
999   0.1
MIX 56
56  0.9
999   0.1
MIX 57
57  0.9
999   0.1
MIX 58
58  0.9
999   0.1
MIX 59
```

```
59  0.9
999   0.1
MIX 60
60  0.9
999  0.1
```

The INCREMENTAL_REACTIONS data block is used in this example to implement the same mixing ratios for each batch reaction step defined in the KINETICS data block.

```
INCREMENTAL_REACTIONS  false
END
```

APPENDIX B

DESCRIPTIONS OF NATURAL ANALOGUE SITES AND EXPERIMENTAL DATA

INTENTIONALLY LEFT BLANK

B.1 NATURAL REACTOR - DISCUSSION ON OKLO, GABON

General Geologic Setting

A natural fission reactor has been recognized in the Franceville basin in SE Gabon, Africa at the uranium deposits of Oklo. The sustained fission chain reaction occurred approximately 2 billion years ago. The rock types of the Francevillian Series consist of an Archean basement (granites, gneisses), sandstones, conglomerates, manganese-rich rocks, dolerites, and bitumen-rich black shale (Gauthier-Lafaye 1996 [DIRS 157542]). Despite an old age, the Francevillian Formation of the Franceville basin is practically unmetamorphosed and undeformed except for zones of early fracturing where uranium is concentrated Bonhomme, et.al., (1982 [DIRS 175262]). The uranium ore lenses lie interspaced between the sandstones and black shales of the formation. In total, there are 16 natural reactors at Oklo and a spatially close but distinct reactor at Okelobondo (Jensen and Ewing 2001 [DIRS 157500]). This uranium deposit is extraordinary in that it is the only location on earth where a criticality event has occurred in nature.

The natural fission reactors at Oklo are zoned bodies of high grade U-ore (the reactor core) enclosed by a mantle of clay minerals (clays of the reactor) composed mainly of chlorite or illite (Janeczek 1999 [DIRS 156284]). Uranium concentrations in the reactor core zones range from 20 to 87 wt. %. In the clays of the reactor, uranium concentrations vary from the ppm level to 3 wt % (Gauthier-Lafaye, et.al. 1996 [DIRS 157542]). The reactor core and the reactor clay mantle together form the reactor zone. The boundary between the reactor zone and the underlying sandstone is rather sharp and is marked by a thin layer of hematite and sometimes by the concentration of uraniferous organic matter and uraninite. Quartz in the sandstone adjacent to the reactor zone is quite corroded (Janeczek 1999 [DIRS 156284]).

The accepted model for the origin of the uranium deposits in the Franceville basin was described by (Gauthier-Lafaye 1996 [DIRS 157542]). The primary source of uranium was detrital uraniferous thorite deposited on fluvial conglomerates, now at the bottom of the FA formation (lower conglomerate grading upward to sandstone). The thorite was presumably derived from nearby Archean granites and gneisses. Uranium concentrations in the U-bearing thorite of the red conglomerates ranges from 0.3 to 5.9 wt. %. Apparently, uranium was preferentially removed from thorite by oxidizing fluids. The origin of the fluids is uncertain, however they may have been related to water trapped in closed porosity during deposition of the conglomerates, or they may be meteoric waters that descended along fractures and faults during uplift of the Franceville basin. These waters percolated through the U- and Th-bearing conglomerates and FA sandstones, dissolving sulfate and carbonates cements. Consequently, the oxidized and highly saline U(VI)-bearing fluids migrated upwards due to the convective circulation in the basin. The conglomerates were subsequently covered by thick deltaic and marine deposits, which now form the upper sandstones of the FA formation and the shales of the FB formation. The FB shales are organic rich and reached P,T conditions during burial of the Franceville series (up to 4 km depth) to produce petroleum. That petroleum migrated into the FA sandstones and accumulated in numerous traps. Uranium mineralization occurred at 2000+/- 50 Ma, when oxidized U (VI)-bearing fluids encountered the reduced hydrocarbon-bearing fluids. Uranium precipitated as uraninite in pores, as well as in hydraulically induced fractures that form an extensive network in the sandstones (Gauthier-Lafaye 1996 [DIRS 157542]). Soon after deposition of the uraninite, neutron induced chain fission reactions began in the richest uranium ore, resulting in the formation of the nuclear reactor zones.

Oklo Reactor Zone Specifics

Not all reactors in the Franceville basin are identical. They differ significantly in size geometry, U concentration, mineral composition, amount of organic material, and degree of depletion of ^{235}U, (Janeczek 1999 [DIRS 156284], Table 1). Although some of the differences were original, others were caused by processes related to the nuclear reactions and post-criticality geological events. The primary indicator of neutron induced fission reactions at Oklo is the depletion in fissile ^{235}U. The concentration of ^{235}U in uranium minerals not only varies amoung reactors, but also varies within a single reactor zone. Usually the central portions of the reactor cores are more deficient in ^{235}U than the outer parts of the reactor. Depleted uranium outside reactor cores provides strong evidence for migration of actinides out of reactor zones (Janeczek, 1999 [DIRS 156284]). Another aspect of the reactors that varies widely is the clay mantle zone around the reactors. At certain reactors (RZ-2, RZ -10, and Okelobondo) the clay mantle is a prominent feature, but the clay mantle is virtually non existent at RZ-13. The origin of the clay mantle is related to the desilicification of sandstone and its replacement by clay minerals. The desilicification of the sandstone was caused by hydrothermal fluids generated by heat released during the fission chain reactions Gauthier-Lafaye et. al., (1989 [DIRS 124997]). Silica released from the dissolved sandstone in the reactor zones migrated and may have precipitated in reactor cores again upon their cooling.

The ability for a uranium deposit to go critical and sustain a naturally occurring fission reactor is based on many parameters. From analogy to man made reactors, the minimum $^{235}U/^{238}U$ ratio required for operation of a natural reactor is approximately 1% Janeczek, (1999 [DIRS 156284]). Uranium 235 decays faster than ^{238}U because its half life is shorter by an order of magnitude ($t_{1/2} = 7.1X10^8$ a vs. $t_{1/2}=4.5X10^9$, respectively). Therefore the $^{235}U/^{238}U$ ratio was higher in the geologic past than today. Two billion years ago, the $^{235}U/^{238}U$ ratio was 3.5%, which is in the range of $^{235}U/^{238}U$ ratios in fuels artificially enriched in ^{235}U for man-made reactors using light water as a moderator.

Apart from the high ^{235}U concentration, the following conditions were necessary for self sustaining chain fission reactions to occur at the uranium deposits at Oklo, (Naudet 1991 [DIRS 100471]):

1. Total U concentration of at least 10% in a 2 meter thick layer.
2. Uranium ore seams at least 0.5 m thick (ideally > 63 cm).
3. A water moderator to uranium ratio of about 6%.
4. The presence of neutron reflectors (quartz in sandstone).
5. Low concentrations of neutron absorbers (i.e. elements with high neutron capture cross sections, such as B, Li, Mn, HREE and V)

Some of these constraints are not absolutely required, since the overall conditions at Oklo were especially favorable. Some of these include: First, an original porosity in the sediments 2 billion years ago of 40%, with the effect that the reactors may have even been overmoderated. Second, most ore lens were less than 0.5 m thick, but the presence of very effective neutron reflectors in the form of quartz-rich sandstones allowed criticality to occur. Third, the virtual absence of neutron poisons at Oklo allowed for sustained fission reactions.

The major minerals of the reactor zones at Oklo are uraninite, illite, chlorite, coffinite, and galena. There are two types of uraninite occurrences in the reactor cores: 1) massive uraninite and 2) euhedral, angular or rounded grains dispersed in clay matrix or solid bitumen (Janeczek and Ewing 1996 [DIRS 175266]). The uraninite crystals at Oklo commonly have trace amounts of Ti, Si, and Fe, which are incompatible with the uraninite structure. During the long duration of the fission reactions, the primary uraninite has altered and annealed allowing these otherwise incompatible elements to be incorporated (or intergrown) at the microscopic or even sub-microscopic level. Compatible elements found in trace levels in the uraninite structure are Ca, Th, and REE. Lead in uraninite can reach high levels (10-20 wt %) and is radiogenic in nature.

Coffinite ($USiO_4$) is the second most abundant uraniferous mineral encountered in and around the reactors at Oklo. Grain textures (overgrowths on uraninite cores) indicate that coffinite replaced primary uraninite at Gabon. The abundance of Si in the host rock allowed this uranium silicate to form readily.

Illite and chlorite are the major clay minerals of the reactor zones. High temperature 2M illite is related to heat generated by the criticality reaction. Otherwise, the remainder of the illite is the low temperature (< 200^{o}C) 1M polytype. Two main types of chlorite exist at Oklo; a Fe-rich chlorite in the sandstone matrix and an Mg-, Al-rich chlorite associated with the reactor cores (Janeczek 1999 [DIRS 156284]). Kaolinite occurs due to weathering of the reactors zones and are major constituents of the weathered FB shales.

Galena occurs ubiquitously in all the reactor cores. Its formation in close association with uraninite indicates that it was derived from radiogenic lead. Galena formed along grain boundaries, subgrain boundaries and in fractures, indicating that the sulfide probably derived from exsolution processes within the uraninite crystals.

Uranyl minerals in the reactor zones of Oklo are rare and their occurrences are limited to weathered zones and fractures accessible to oxidizing groundwaters. Uranyl minerals are abundant on exposed walls of the open pit mine and in tunnels and shafts (Janeczek 1999 [DIRS 156284]). Uranyl minerals identified in and around the natural reactors at Oklo include: alpha-uranotile, torbernite, fourmarierite, rutherfordine, and wolsendorfite (IAEA 1975 [DIRS 125207]) Francevillite was identified in the weathered zone at Oklo (Bourrel and Pfiffelman1972 [DIRS 175263]). Uranyl minerals recently described (Janeczek and Ewing 1996 [DIRS 175266]) from the sandstone beneath the Bangombe reactor include: francoisite -(Nd), zippeite, schoepite, and unnamed uranyl phosphates, and uranyl sulfates. Uranyl phosphates and sulfates are the most abundant uranyl minerals in and around the natural reactors. Their formation is apparently a product of water rock interactions. Deitrital monazite, florencite and apatite, all of which occur in the sandstone matrix, may have been the source of phosphorous for uranyl phosphate formation. The abundance of uranyl sulfates formed under ambient conditions suggests that the oxidation of pyrite is a significant source of oxidized sulfur.

Native lead and copper have been observed sparingly at Oklo, as have been Ru-, Rh- and Pd-bearing minerals. The latter phases occur as arsenides, sulf-arsenides, and as metals. Although extremely rare, these mimic Ru, Rh, Pd, Tc and Mo alloys found in spent nuclear fuel (Curtis, et. al. 1989 [DIRS 100438])

Pyrite has been commonly observed in the host rock sandstones at Oklo. In a few instances pyrite has also been identified in the reactor core zones. Hematite, Ti-oxides, and goethite are among the accessory oxides and oxyhydroxides identified in the reactor zones (Janeczek 1999 [DIRS 156284]). Anatase (TiO_2) is abundant in the reactor clay mantle of the Bangombe reactor. Goethite is found in reactors that have been affected by weathering processes. Colliform goethite occurs in fractures below the Bangombe reactor. Fibrous calcite occurs in veins at RZ10. The texture of the calcite indicates that it crystallized during dilation of veins. Apatite is a common accessory mineral in RZ-10 and RZ-16, as well as a detrital phase in the surrounding sandstones. Rare Crandallite group minerals have been identified at the RZ-10 and Bangombe reactors and in the Bangombe FA sandstone unit (Janeczek and Ewing 1996 [DIRS 175266]). The Crandallite group end member minerals are crandallite [$CaAl_3(PO_4)_2(OH)_5{\cdot}(H_2O)$], goyazite [$SrAl_3(PO_4)_2(OH)_5{\cdot}(H_2O)$ and florencite [$(REE)Al_3(PO_4)_2(OH)_6$].

B.2 DISCUSSION - NOPAL I, PENA BLANCA, CHIHUAHUA, MEXICO

B.2.1 Background

In the 1970s, the Peña Blanca region, approximately 50 km north of Chihuahua City, Mexico, was a major target of uranium exploration and mining by the Mexican government because the region contains numerous uranium deposits. Since that time, the Nopal I uranium deposit has been studied extensively because it is a good analogue for evaluating the fate of spent fuel, associated actinides, and fission products at a geologic repository in fractured, unsaturated volcanic tuff. Previous studies associated with Peña Blanca as well as a geologic description of the site were reviewed in the scientific analysis report *Natural Analogs for the Unsaturated Zone* (CRWMS M&O 2000 [DIRS 141407]). Briefly, the Nopal I uranium deposit at Peña Blanca represents an environment that closely approximates that of the Yucca Mountain high-level radioactive waste repository in the following ways:

- Climatologically: both are located in semi-arid to arid regions.
- Structurally: both are parts of a basin-and-range horst structure composed of Tertiary rhyolitic tuffs overlying carbonate rocks.
- Hydrologically: both are located in a chemically oxidizing environment within an unsaturated zone (UZ), 200 m or more above the water table (DOE 1998 [DIRS 100548], Section 2.2.4 and this study), and have broadly similar water chemistries.
- Chemically: the alteration of primary uraninite (Pearcy et al. 1994 [DIRS 100486], p. 714) to secondary uranium minerals at Nopal I may be similar to the eventual fate of uranium fuel rods in a potential geologic repository such as Yucca Mountain according to results of spent-fuel alteration experiments (Wronkiewicz et al. 1996 [DIRS 102047], Figure 7).

B.2.2 Previous Radionuclide Transport Studies at Peña Blanca

Previous uranium-series thermal ionization mass spectrometry (TIMS) work at Nopal I (CRWMS M&O 2000 [DIRS 141407], pp. 89–90) found closed-system behavior for many of the

long-lived uranium-series members in fracture-filling materials. Briefly, the TIMS results indicated that primary transport of uranium to fractures occurred more than 300 ka, see the *Natural Analogue Synthesis Report,* TDR-NBS-GS-000027 (BSC 2004 [DIRS 169218] Figure 10.4-1). Since that time there has been no significant ^{235}U or ^{238}U redistribution along the fractures.

B.2.3 Fieldwork

Recent fieldwork at Peña Blanca involved the drilling of three boreholes (BSC 2004 [DIRS 169218] Figures 10.4-4 and 10.4-9). A borehole with continuous core was drilled near the Nopal I deposit (PB-1) and two additional boreholes were drilled ~50 m uphill (PB-2) and downhill (PB-3) from PB-1. These boreholes were drilled out and completed to depths of approximately 20 m below the observed water table (total well depths of ~243-255 m). These wells were drilled to facilitate direct sampling of the ground water, to determine water chemistry, including the concentration of radionuclides possibly leached from the Nopal I uranium deposit.

B.2.4 Location of Peña Blanca Wells

The locations of the three drilled wells (PB-1, PB-2, and PB-3) and one reconditioned well (PB-4) were obtained using a hand-held Garmin GPS unit. In addition, the locations of two other wells and one spring, which were used in the geochemical characterization of regional waters, were also obtained. These locations are reported and shown in (BSC 2004 [DIRS 169218], Table 10.4-3 and Figure 10.4-4).Note that while the accuracy of these measurements when using the Wide Area Augmentation System correction feature is reported by Garmin to be about 3 m, the range of values for repeated measurements of the elevations of these features is up to 13 m.

B.2.5 Stratigraphy and Petrography of Peña Blanca Boreholes

The three new boreholes at Peña Blanca, PB-1, PB-2, and PB-3, are located within 100 m of each other and were drilled to similar depths and, thus, have very similar stratigraphic sections. Using the stratigraphic framework of Reyes-Cortes (2002 [DIRS 168028]), four distinct geologic units were intersected in the Peña Blanca wells. These are: (1) the Nopal Formation, (2) Coloradas Formation, (3) Pozos Formation, and (4) undifferentiated Cretaceous limestone. A description of the PB-1 core is provided in DTN: LB0402PBCORELG.001 [DIRS 168014]. Petrographic descriptions of thin sections prepared using core samples from PB-1 and cuttings samples from PB-2 and PB-3 are provided in DTN: LB0402PBMNRLGY.001 [DIRS 168018]. A description of each of these units, based primarily on the observations associated with the PB-1 core samples, is presented below. The stratigraphic sequences for these boreholes are summarized in BSC 2004 [DIRS 169218], Figures I-1, I-4, and I-5.

Nopal Formation. ~The Nopal Formation consists of a sequence of rhyolitic ash-flow tuffs Reyes-Cortes (2002 [DIRS 168028], p. 324). Within the PB-1 core, this unit is highly altered, with devitrification of the glassy matrix and kaolinite commonly replacing both feldspars and groundmass (BSC 2004 [DIRS 169218] Figure 10.4-10). Relict flattened pumice fragments and volcanic lithic fragments were also observed. Zeolite minerals have been observed locally in the Nopal Formation (Reyes-Cortes 2002 [DIRS 168208], p. 324) but were not identified in thin sections of core or cuttings taken from the PB-wells. The portion of the PB-1 core containing the

Nopal tuff contains zones of brecciation with fracture fillings of hematite, limonite and goethite. Other alteration minerals encountered in the Nopal tuff core samples include quartz, chlorite, and montmorillonite. A zone of intense clay alteration encountered at a depth of 17.45-19.15 m was interpreted to represent part of the highly altered vitrophyre that forms the base of this unit, and, thus, the contact with the underlying Coloradas Formation is thought to be located at or just below this interval. The precise location of the contact between the Nopal Formation and Coloradas Formation was not identified during the initial evaluation of the PB-1 core.

Coloradas Formation. The Coloradas Formation consists of a sequence of poorly to moderately welded lithic ash-flow tuffs (Reyes-Cortes 2002 [DIRS 168028], pp. 323-324). The unit contains ~10- 20% volcanic lithic fragments with some more pumice-rich intervals (up to 30%). The flattened pumice often exhibits good flow foliation (BSC 2004 [DIRS 169218] Figure 10.4-11). Like the Nopal tuff, the PB-1 core samples of this unit are also quite altered with much of the tuff exhibiting devitrification, oxidation (hematite, limonite, goethite) and clay alteration (kaolinite and montmorillonite), with quartz being another important secondary mineral. Many of these secondary minerals replace primary minerals and the devitrified matrix, and fill voids and fractures within the altered tuff. As indicated by the core photographs and televiewer logs through this sequence, there are numerous zones of fracturing and brecciation within the Coloradas tuff (BSC 2004 [DIRS 169218] Figure I-3). There is a sharp contact between the Coloradas tuff and the underlying Pozos conglomerate in the PB-1 core at a depth of 136.38 m, thus resulting in an approximate measured unit thickness for the Coloradas tuff of around 115 m.

Pozos Formation. The Pozos Formation consists mainly of interbedded, poorly sorted sandstones and conglomerates (Reyes-Cortes 2002 [DIRS 168028], p. 323). The conglomeratic clasts consist of subangular to subrounded fragments of volcanic rocks, limestone, and chert, with clasts ranging in size from a mm to over 10 cm in diameter (BSC 2004 [DIRS 169218] Figure 10.4-12). Thin (2-6 m) intervals of intercalated pumiceous tuffs were observed within this unit in the PB-1 core. Bleached and oxidized zones were observed within the sedimentary unit, and these have been interpreted to represent changes in oxidation state. Within the cored interval of this formation, there are a number of fractured and brecciated zones that are associated with secondary mineralization, most often limonite, hematite, silica, calcite, kaolinite, and clays. The contact between the Pozos conglomerate and the underlying Cretaceous limestone was observed in the PB-1 core at a depth of 244.4 m, thus resulting in a total measured unit thickness of 108 m.

Cretaceous Limestone. A fine-grained massive limestone was encountered at the base of PB-1; this unit is considered to be Cretaceous in age (Reyes-Cortes 2002 [DIRS 168028], pp. 321, 323). This limestone contains microfossils (foraminifera, ostrocodes, bryozoans, and gastropods) set in a fine-grained, micritic matrix (BSC 2004 [DIRS 169218] Figure 10.4-13). Minor thin veins of calcite cut the limestone, especially in zones with brecciation.

B.2.6 Secondary Phases of Uranium Found at Nopal I, Peña Blanca

At Nopal I, uraninite occurs in rhyolite tuff in a semi-arid environment, where it has been exposed to oxidizing groundwater conditions with nearly neutral pH. Uranium was initially deposited as uraninite at Nopal I approximately 8 Ma (Pearcy et al 1994 [DIRS 100486], p. 729). Geologic, petrographic, and geochemical analyses indicate that primary uraninite at Nopal I has been almost entirely altered to hydrated oxides and silicates containing uranium in the oxidized

(uranyl) form. Because of its young geologic age, the deposit is low in radiogenic lead. The sequence of formation of uranyl minerals by alteration of uraninite at Nopal I is shown in (BSC 2004 [DIRS 169218],Figure 4-2) and is similar in many geologically young uranium deposits located in oxidizing environments.

Leslie et al. (1993 [DIRS 101714]) and (Pearcy et al. 1994 [DIRS 100486], pg. 730) compared the alteration of uraninite at Nopal I to laboratory experiments of degradation of spent nuclear fuel potentially to be disposed of at Yucca Mountain, Nevada. They found that uraninite from the Nopal I deposit should be a good natural analogue to spent nuclear fuel because long-term experiments on spent fuel show alteration parageneses, intergrowths, and morphologies that are very similar to those observed at Nopal I (Wronkiewicz et al. 1996 [DIRS 102047]). Oxidation of the uraninite at Nopal I has produced an ordered suite of minerals, first forming schoepite, a uranyl oxyhydroxide, followed by hydrated uranyl silicates, such as soddyite (BSC 2004 [DIRS 169218] Figure 4-2). A higher calcium abundance, relative to other cations in Nopal I groundwater, supports the formation of uranophane, a hydrated calcium uranyl silicate as the dominant secondary uranium phase. Because of the abundance of calcite at Yucca Mountain, uranophane would be a potential secondary phase there as well. In comparison, laboratory experiments find that the general trend is to form mixed uranium oxides, followed by uranyl oxhydroxides, and finally uraniumm silicates, mostly uranophane with lesser amounts of soddyite (Wronkiewicz et al. 1996 [DIRS 102047], p. 92). In addition, uraninite at Nopal I has a low trace-element component (average of 3 wt%) that compares well with that of spent nuclear fuel (typically < 5 wt% (Pearcy et al. 1994 [DIRS 100486], p. 730)). The young age of the Nopal I deposit is another similarity to Yucca Mountain with respect to the absence of Pb-bearing secondary phases.

B.2.7 Groundwater Major Elements

Major element concentrations for different sample types at Peña Blanca and for SZ waters near Yucca Mountain (Benson et al. 1983 [DIRS 100727]) are summarized in Section 7.2.3.4, Table 7-9. Results for the 2003 drilled well waters are subdivided into those obtained before (PB-SZ-NF-bailer) and after (PB-SZ-NF-pump) well conditioning. While most of the major components were not influenced by drilling activities or fluids, pH, uranium, and potassium concentrations decreased significantly post-drilling. The pH values in the wells drilled in 2003 were characterized initially by more basic conditions (pH = 8.5 – 11.3), most likely resulting from drilling fluids. Since well conditioning and pumping, these have subsequently returned to values (pH = 7.0-8.0) more typical of natural groundwater. Much like the uranium concentrations, potassium concentrations have also decreased in the 2003 drilled wells post-drilling (29 to 6 ppm), probably due to a decreasing contribution from the bentonite drilling mud over time.

Most of the components of the YMP well waters are similar to the range of regional SZ waters near Peña Blanca (PB-SZ-FF). They have similar ranges in pH, calcium, potassium, chloride, fluoride, silicon, and strontium, but the YMP wells do have noticeably higher sodium, uranium, bicarbonate, and sulfate concentrations both before and after well pumping and conditioning. UZ adit waters are atypical in their low bicarbonate concentrations but are similar to the newly drilled wells with high sulfate concentrations. High sulfate concentrations appear to be characteristic of the vast majority of samples from near the deposit. YMP UZ borehole samples

have extremely high calcium and bicarbonate concentrations, perhaps due to effects of evaporation to the ground surface

B.2.8 Conceptual Model of Transport

Data collected to date for the long-lived U-series members through YMP studies indicate limited mobility of uranium and its daughters over 100 k.y. timescales (CRWMS M&O 2000 [DIRS 141407], p. 90). Transport from the uranium deposit at Nopal I, Peña Blanca, Mexico to surrounding fractures has occurred in the past. However, the main transport activity currently observed is elevated ^{226}Ra in water samples in proximity to the deposit. The large depletions of 226Ra seen in the fractures point to ^{226}Ra mobilization via recoil from fine-grained (sub-micron) U-bearing materials in the fracture coatings. The ^{226}Ra concentrations in waters sampled away from the deposit are quite low, which is typical for surface waters around the world (Porcelli and Swarzenski 2003 [DIRS 168458]). Hence, the mobilization of radium is a near-field event resulting from recoil of the ^{226}Ra from high-uranium regions into fluids. This mode of radionuclide mobilization would have a bearing on transport of uranium and its daughters from breached canisters at a high-level geologic storage system but would not have a bearing on transport of fission products such as ^{133}Ba, ^{135}Cs, ^{137}Cs, and ^{90}Sr. By analogy to the Peña Blanca observations, one would expect to see any mobilized uranium transported locally to fracture-filling materials. Recoil effects would raise local concentrations of daughters in the fluids to be redeposited/sorbed at some moderate distance away from the recoil site.

B.2.9 Conclusions

Some of the conclusions thus far include:

1. The Nopal I uranium deposit remained largely in place prior to mining operations,indicating limited uranium transport (CRWMS M&O 2000 [DIRS 141407], pp. 89, 94).
2. A conceptual model of transport has been developed that describes the timing of uranium transport from the deposit into near-field fractures, where it largely remains (CRWMS M&O 2000 [DIRS 141407], pp. 82-87).
3. Away from the deposit, low radium concentrations are observed in the waters. This indicates that other factors limit radium mobility over long distances, such as sorption onto mineral surfaces or co-precipitation with calcium fluoride or carbonate minerals (Porcelli and Swarzenski 2003 [DIRS 168458], p. 234). By analogy, it would be expected that similar limits apply to the transport of fission products such as ^{133}Ba, ^{135}Cs, ^{137}Cs, and ^{90}Sr.

B.3 SECONDARY URANYL PHASES FROM THE SHINKOLOBWE, ZAIRE OXIDIZED URANIUM DEPOSIT

Finch and Ewing (1991 [DIRS 105591]) and (Finch and Ewing 1992 [DIRS 113030]) performed an exhaustive mineralogic study of the uranyl phases at the Shinkolobwe, Katanga, Zaire uranium deposit. Their rationale was to study the secondary uranyl phases produced by the oxidative alteration of uraninite exposed at the surface from the Shinkolobwe mine. The authors state that the alteration of uraninite would provide a natural analogue for the corrosion of spent

nuclear fuels. The study was believed to be extremely useful in determining the U[VI] solubility controlling phases that would be produced due to oxidative corrosion of spent fuel in a geologic repository. They performed an integrated analysis of the uranyl alteration products using optical microscopy, scanning electron microscopy, analytical electron microscopy and X-ray diffraction techniques.

Finch and Ewing (1991 [DIRS 105591]) describe the geologic setting of the Shinkolowbe deposit in the Katanga District of southern Zaire as follows. The Katanga mining district is rich in copper, zinc, iron, lead, cobalt, cadmium, germanium, uranium, nickel, silver, barium and gold. The host rocks at the Shinkolobwe mine are dolomitic shales, siliceous dolostones, and chloritic shales. The host rocks contribute to significant concentrations of silica, carbonate and sulfate in the groundwater. Common uranyl complexes in solution are therefore expected to be $[UO_2(CO_3)_2]^{2-}$, $[UO_2(CO_3)_3]^{4-}$, $[UO_2(SO_4)_2]^{2-}$, and $[UO_2(SiO_4)]^{2-}$. Metal cations present are Ca^{2+}, Ba^{2-}, Mg^{2+}, Cu^{2+}, Pb^{2+}, Mo^{6+}, V^{5+}, and the lanthinides (Ce^{3+}, La^{3+}, Y^{3+}, Gd^{3+}, Dy^{3+}). Leaching of the radiogenic lead occurred 600 to 720 million years ago due to hydrothermal fluids and some alteration probably occurred at that time.

Finch and Ewing (1991 [DIRS 105591]) describe the genesis and sequence of the secondary uranyl phases at Shinkolowbe. The first phases to form from the alteration of uraninite are uranyl oxy-hydroxides. The minerals identified are : becquerelite $Ca(UO_2)_6O_4(OH)_6 \cdot 8H_2O$, compreignacite $K_2(UO_2)_6O_4(OH)_6 \cdot 8H_2O$, vandendriesscheite $PbU_7O_{22} \cdot 22H_2O$, fourmarierite $PbU_4O_{13} \cdot 6H_2O$, billietite $Ba(UO_2)_6O_4(OH)_6 \cdot 8H_2O$, and schoepite $UO_3 \cdot 2H_2O$. Becquerelite and schoepite (as fine grained powder on becquerelite) are the most common hydrated uranyl oxides in the samples studied. Billietite and compreignacite occur as intergrowths with becquerelite. The Pb-uranyl oxide hydrates vandendriesscheite and fourmarierite are the most abundant Pb-uranyl minerals and are commonly associated with becquerelite and uraninite. These earliest formed phases are often replaced by much finer grained phases such as curite $Pb_2U_5O_{17} \cdot 4H_2O$, clarkeite $(Na,Ca,Pb)U_2(O,OH)_7$, and masuyite $Pb_3U_8O_{27} \quad 10H_2O$. Subsequently, uranyl silicates were formed by the reaction of the hydrated oxides with silica rich groundwater, producing a majority of uranophane $(H_3O)_2Ca(UO_2)_2(SiO_4)_2 \cdot 3H_2O$ and minor cuprosklodowskite $(H_3O)_2Cu(UO_2)_2(SiO_4)_2 \cdot 4H_2O$. These uranyl silicates appear to be the last formed phases in the samples studied.

Finch and Ewing (1992 [DIRS 113030]), a subsquent article on the uranium minerals of Shinkolowbe focused on the important role of Pb in limiting further solubility of uranyl secondary phases. Finch and Ewing (1992 [DIRS 113030]) summarized the study in the following manner. “The pervasive alteration of the uranyl oxide hydrates observed in nature suggests that their ubiquity may be due to favorable kinetics of crystallization as compared to the uranyl silicates. Although most of the uranyloxide hydrates alter readily to uranyl silicates, because of the relative immobility of Pb^{2+} in most ground waters, the Pb-uranyl oxide hydrates alter incongruently, producing increasingly Pb-enriched uranyl oxide hydrates. Thus, the precipitation of phases such as curite, sayrite, or masuyite does not require high ambient activities of Pb in the groundwater as suggested by synthesis experiments. Radiogenic Pb may play a role similar to that of silica, reducing the mobility of U by fixing U in solid phases. Also, since kasolite cannot form readily from the Pb-poor uranyl oxide hydrates, the formation of curite may be an important mechanism for uranyl phosphate formation if curite plays an integral

role in their formation, as indicated….Therefore, in the absence of Pb-bearing phases, the mineralogical evolution of an oxidized uranium ore body may be substantially different, with uranyl silicates limiting U solubility."

B.4 EXPERIMENTAL STUDIES

B.4.1 Experimental Uranium solubility and secondary phase precipitation, (Wronkiewicz, et.al. 1996, [DIRS 102047])

Background

The authors wanted to evaluate the reaction of UO_2 pellets after exposure to limited amounts of simulated groundwater (J-13), oxidizing conditions, and elevated temperatures. The results of the experimental simulations were used to characterize the dissolution behavior of UO_2, formation of alteration products, and the rates and mechanisms of uranium release. The experiments focussed on UO_2 pellets, serving as spent nuclear fuel surrogates, encased in Zircaloy-metal sleeves. The assemblies were exposed to periodic drops of simulated silicate-bicarbonate groundwater. Elevated temperatures (90^oC) and low water / solids rations were used to accelerate the alteration rates of the samples. For example, dissolution of UO_2 in dionized and mildly oxidizing water has been shown to increase proportionally with temperature from 30 to 90^oC (Thomas and Till 1984 [DIRS 175267]). Temperature can also control the stability of individual phase polymorphs (Vochten, et.al. 1990 [DIRS 176901]).

Although uranium is sparingly soluble under reducing conditions, its solubility increases by many orders of magnitude under oxidizing conditions. Significant dissolution of uranium is expected to occur once the surface approaches a composition of $UO_{2.33}$. Kinetics of the oxidation of the samples would be further enhanced when the sample surface reaction takes place in a thin water film that is exposed to oxidizing conditions (Wronkiewicz, et.al. 1996 [DIRS 102047]) .

Experimental procedure

The samples were press sintered from uranium oxide powder and had less than 70 ppm total contaminants, of which Cl (10ppm), Th (15 ppm) and Fe (20 ppm) were the major contributors. Samples were then assembled into 0.38 mm thick Zircaloy-4 metal tubes. The resulting assemblies had the pellets exposed at the top and bottom, while their sides were enclosed by Zircaloy. The assemblies were housed in 304L stainless steel reaction vessels, the vessels were then connected to a leachate injection line and placed in an oven to maintain a temperature of 90 +/- 2^oC. Premeasured quantities of EJ-13 simulated groundwater were then injected onto the top of the samples at predetermined intervals (samples 1-6, 0.075 ml every 3.5 days; samples 7-8, 0.0375 ml every 7 days). Periodically, leachate aliquots were collected to analyse for anion, pH, carbon and filtered uranium. Tests were terminated at 1.5, 2.25, 3.5, 8.0 and 10 years. Altered sample surfaces and alteration phases were analyzed by SEM/EDS, optical microscopy, XRD, and EMP. Solution aliquots were analyzed by ICP-MS, Dohrman carbon analyses and ion chromatography.

Results—Uranium Release

Reaction progress can be catagorized into three different periods of reaction: Period I, initial period of low release, Period II, rapid release of uranium, and Period III, extended period of

moderate uranium release. Period I covers the first year of reactions, marked by low quantities and rates of uranium release. Small patches of alteration phases began to appear on the sample surfaces, suggesting the uranium released from the pellets was incorporated into their structures. Period II reactions (between one and two years of testing) mark a distinct departure from the other periods in which the release rate was an order of magnitude or more, higher than the other periods. Microscopic examination of the sample surface faces revealed numerous micrometer or smaller sized anhedral UO_2 particles lying on top of the secondary uranyl phases, indicating that the particles were migrating across the sample surface. The majority of the uranium released during Period II reaction could be attributed to grain boundary corrosion and spallation of particles from the sample surfaces. Period III of uranium release began after Period II release ended (from two to ten year time frame) and went to the end of the experiments. This period of release is marked by a constant release rate that is considerably lower than the previous period. A dense mat of alteration phases on the sample surface developed concurrently with the reduction in uranium release. Examination of the sample surfaces indicates that the layer of alteration phases act as a trap to restrict the migration of loosened UO_2 particles from the sample surface. Overall release rates for uranium during Period III range from 0.1 to 0.3 mg/m^2 day. This long-term release rate is both more uniform and substantially lower than the rates that characterize the uranium release from the Period II reactions (averaging from 1.3 to 15 mg/m^2 day).

Results—Other Cation Components

Analysis of cation components other than uranium indicates that leachate solutions are depleted in alkalis, alkaline earths and silica relative to the original EJ-13 leachant solution. This is consistent with the uranyl secondary phases being derived from both the dissolution of the UO_2 pellets and the sequestering of alkalis, alkaline earths and silica from the EJ-13 solution. Magnesium was depleted the most, with leachate concentrations reduced to 10% of the original EJ-13 solution. Concentrations of Ca and K were depleted to 30%, while Si was depleted to 50% of the original EJ-13 composition. Sodium concentrations were depleted the least, with leachate concentrations at 90% of the original EJ-13 leachant value.

Results—Anion and pH

Most anions were slightly enriched in the leachate relative to the original EJ-13 solution. Nitrate (NO_3^-) displayed the largest change, approximately a three-fold change. Nitride values, however, remained consistent with the original leachant composition. The nitrate may have been produced as a radiolysis product. Oxygen, even though consumed to create the secondary phases, was constantly replenished during air flushes of the injection tube. The remaining anions analysed, F^-, Cl^-, and SO_4^{2-}, displayed an average increase of 1.7, 2.2, and 2.5-fold, respectively over the original EJ-13 leachant composition. However, their overall abundance was in trace quantities and may have had the steel vessel and the Teflon stand as their sources.

Solution pH values generally decreased after reaction with the UO_2 samples, with a value at 7 +/- 1. The original pH for the EJ-13 solution was 8.1. The decreased pH trend is consistent with production of small amounts of nitric acid, through radiolysis reactions, and the incorporation of hydroxide within the secondary uranium phases and palygorskite clays.

Results—Solids analysis

Paragenetic reaction pathways were characterized by the following trends: uraninite to schoepite group (mostly dehydrated schoepite with minor schoepite), to alkali + alkaline earth uranyl-oxide

hydrates (becquerelite, and compreignacite) to uranyl silicates (soddyite) to alkali + alkaline earth uranyl silicates (uranophane and boltwoodite). After 8 years palygorskite clays beagan to appear. The spatial coverage and density of alteration phase growth changed with time. The central mat of alkali + alkaline earth uranyl silicates, uranophane and boltwoodite, which had covered 25% of the top surface of the samples at 3.5 years, increased to 90% after 8 years of reaction. Over that same time period, the density of the central mat changed from a relatively permeable mesh of crystals to a dense network of phases that nearly enveloped the top surface of the pellets. Furthermore, while the secondary phase mat was dominated by uranophane with lesser boltwoodite at 3.5 years, at 8 years the dominant phase was boltwoodite.

Uranyl-oxide hydrate phases were consumed during the extensive alkali + alkaline earth uranyl silicate growth on top of the 8-year sample. Becquerelite, which showed extensive pitting at 3.5 years, was completely absent in the 8-year sample, as were the dehydrated schoepite crystals. Meta-schoepite / compreignacite crystals were restricted to the outer perimeter of the sample top surface, along with uranophane. Finally, the clay phase palygorskite appeared on the 8-year-old samples in minor amounts. On the bottom surfaces of the pellets, the following similar paragensis occurred. Originally dehydrated schoepite developed on the uraninite pellets. By 2.5 years, becquerelite and compreignacite began to replace the schoepite. Finally, by 8 years, the becquerelite was completely replaced by uranophane and boltwoodite.

Results—Comparison With Natural Analogs

A natural analogue to the present UO_2 tests has been described at the Nopal I uranium mine located in the Peña Blanca Mountains, Chihuahua, Mexico. The deposit is hosted by a sequence of ash flow tuffs that are relatively young (8 million years). The uraninite at Nopal I, was initially precipitated under reducing conditions. Subsequently, the uraninite was exposed to oxidizing groundwater after regional tectonic forces elevated the deposit above the local water table. A comparison of the reaction paragenesis indicates that a close similarity exists between the two reaction pathways (Wronkiewicz, et.al., 1996, [DIRS 102047]), see figure B-1 below. The uraninite in both examples was progressively altered, first to uranyl-oxide hydrates, then to uranyl silicates and finally to alkali and alkaline earth uranyl silicates, as a result of exposure to oxidizing groundwater (Leslie, et.al. 1993 [DIRS 101714]). The minor differences noted in the two systems can be atributed to differences in the availibility of various cations. The predominance of uranophane as the long-term phase at Nopal I, relative to the boltwoodite-Na observed in the 8 year UO_2 tests may reflect differences in the leachant compositions for the respective systems. The predominance of uranophane at Nopal I may reflect the presence of fluids that are less evolved (i.e. more enriched in calcium) relative to the EJ-13 solution used in the present UO_2 tests. Conversely, the predominance of boltwoodite-Na in the UO_2 tests may reflect the Na-rich nature of the EJ-13 leachant. For spent fuel alterations, the relative abundance of one specific secondary uranyl phase over another may well reflect the degree of such fluid evolution, as well as local hetrogeneities that exist in the Yucca Mountain host-rock assemblage.

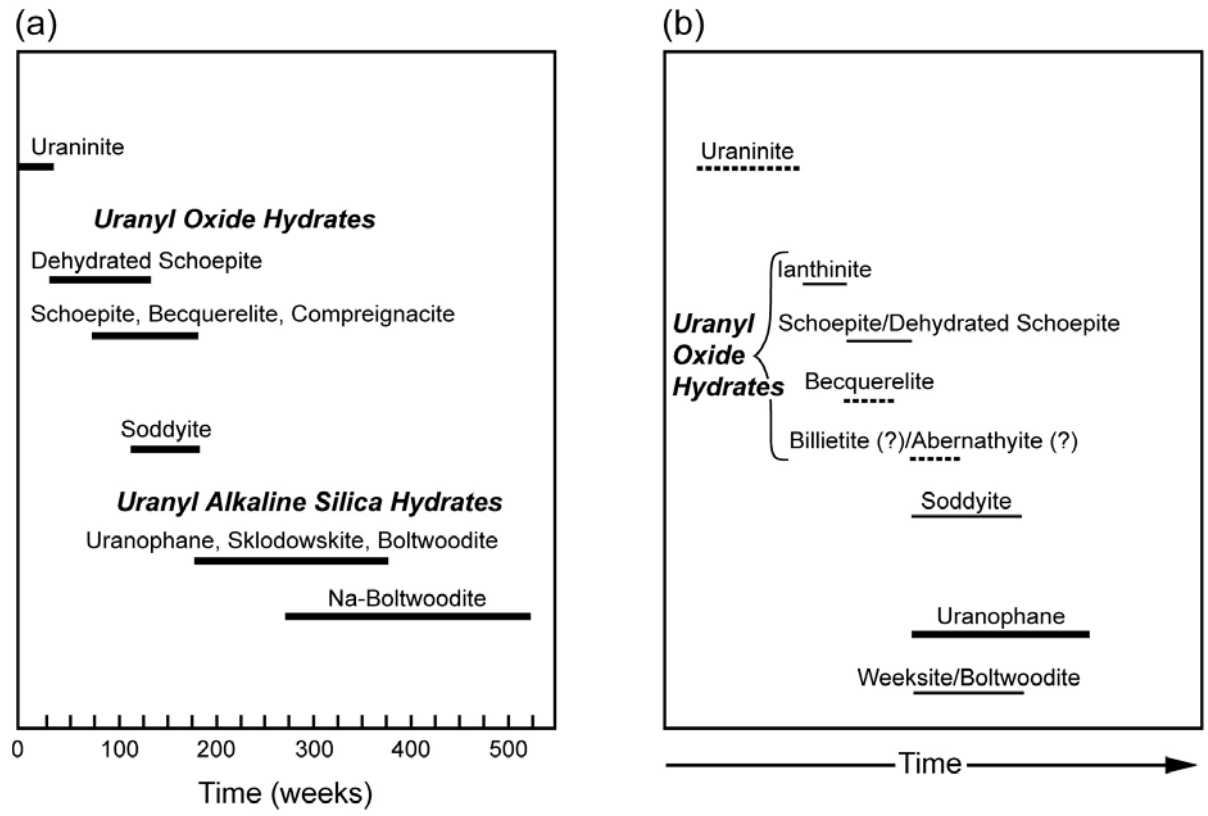

Source: (Wronkiewicz, et.al. 1996, [DIRS 102047]), Figure 7.

NOTE: Figure a) is interpretive experimental sequence developed on the samples from the present study over a ten year Interval. Figure b) sequence developed in the Nopal I natural analog uranium deposit, Mexico. Weigt of line indicates relative abundances of the phase, dashed = minor, thin line = abundant and thck line = very Abundant

Figure B-1. Comparative Reaction Paragenetic Sequences for Uranium Alteration Phases

Results—Summary of UO2 Dissolution Experiments

The experimentally determined mineral sequence appears to be controlled by precipitation kinetics and is nearly identical to secondary uranium phases observed during the weathering of naturally occurring uraninite under oxidizing conditions, such as that which occurs at the Nopal I uranium deposit, Peña Blanca, Mexico Wronkiewicz et al. 1996 [DIRS 102047], Figure 7). In laboratory UO_2 tests and in the natural uranium deposits at Nopal I, the alkali- and alkaline-earth uranyl silicates represent the long-term solubility-limiting phases for uranium (Stout and Leider (1997 [DIRS 100419], Section 2.1.3.5). Furthermore, at Nopal I, uranium concentrations in groundwater and seepage waters ranged from 170 parts per trillion (ppt) to 6 parts per billion (ppb) (Pickett and Murphy 1999 [DIRS 110009], Table 2). In general, the upper part of this range is similar to concentrations seen in filtered samples from spent fuel dissolution experiments (Stout and Leider 1997 DIRS 100419], p. 2.1.3.5-4). This added similarity increases confidence that the experiments and the natural analogue reactions may simulate the long-term reaction progress of spent UO_2 fuel following potential disposal at Yucca Mountain.

B.4.2 Efurd et al. (1998 [DIRS 108015]) - Pu, Np phases stable at Yucca Mt by experiments

Efurd et al. (1998 [DIRS 108015]) performed a series of experiments using J-13 groundwater to determine the solubility of neptunium and plutonium under Yucca Mountain conditions. The experimental conditions were derived to cover a specific range of temperatures and pH values pertinent to Yucca Mountain. Experimental conditions were as follows. Experiments were simulated at three separate pH values of 6, 7, and 8.5 at 25 and 90 ^{o}C. Since the J-13 water's natural CO_2 partial pressure would not be preserved during storage and filtration, the natural state of the well water's natural dissolved carbonate, 2.8 $X10^{-3}$M was induced by reequilibrating the water at each individual pH with defined argon/CO_2 gas mixtures. Adjustments to solutions to obtain the desired pH values were carried out such that the ionic strength of the J-13 water remained below 0.01 M. To be assured of the results for such solubility experiments, experiments were performed from both oversaturation and undersaturation conditions. The solubility experiments were allowed to equilibrate for several months. At the end of the solubility experiments, the neptunium and plutonium precipitates were dried under the corresponding CO_2 atmospheres and were analyzed using X-ray powder diffraction (XRD) and diffuse reflectance spectroscopy.

As expected, the average neptunium solubility generally decreased with increasing pH. With increasing temperature, a slight decrease in solubility is observed at pH 7 and pH 8.5, while at a pH of 6, the neptunium solubility remained relatively constant. For full solubility results from the experiments Efurd et al. (1998 [DIRS 108015], Table 3). The neptunium precipitates formed in the experiments were dark greenish brown. Low temperature solids (25 ^{o}C) produced only broad Bragg peaks in the XRD data. The powder patterns obtained from 90 ^{o}C experiments are generally consistent with the reported data for Np_2O_5 and Np_3O_8 (Cohen and Walter, 1964, [DIRS 175264]), however the existence of Np_3O_8 has been discounted. Therefore, Efurd et al. (1998 [DIRS 108015]) assign the principle XRD lines of the neptunium precipitates to $Np_2O_5 \cdot xH_2O$. While they assigned the additional peaks caused by intercalated water molecules and the further seperation of the neptunium oxide layers, they could not exclude the presence of amorphous neptunium (V) hydroxide by X-ray Diffraction.

The plutonium solubility was only studied from oversaturation (Efurd et. al., (1998 [DIRS 108015], Table 4). In general, plutonium was about 3 orders of magnitude less soluble than neptunium, and pH does not affect the soluble concentration as much as was seen in the neptunium solubility studies. Increasing temperature decreases the plutonium solubility below 10^{-8} $molL^{-1}$. The plutonium precipitates analyzed by XRD match patterns reported for PuO_2. However, this result does not exclude the potential presence of aged Pu(IV) polymer and/or amorphous $Pu(OH)_4$. Because of some fairly broad peaks in the resulting XRD data, plutonium hydroxides and/or plutonium colloids, aging toward $PuO_2 \cdot xH_2O$ are therefore interpreted to be the solubility controlling solids in these experiments (Efurd et al. 1998 [DIRS 108015]). Further experimental studies by (Runde et al. 2002 [DIRS 168432]) have refined the Pu (IV) phases that control Pu solubility. In the newer study, they have determined that either PuO_2 (s) or $Pu(OH)_4$ (s) are the controlling solid phases, primarily depending on Eh values.

B.4.3 Kazuba and Runde (1999 [DIRS 122379]) Thermodynamic studies of Neptunium

Kaszuba and Runde (1999 [DIRS 122379]) used thermodynamic databases to evaluate how redox potential and solid-phase stability interact and influence neptunium solubility and aqueous speciation in natural systems. The neptunium thermodynamic data for the most important valence states in natural waters (Np^{4+} and Np^{5+}) are updated to correct database inconsistencies. The four most significant changes developed from updating the database are as follows. One, Np_2O_5 is two orders of magnitude more stable than reported previously. Two, the stability of NpO_2OH (aq) is reduced. Three, $NpO_2(OH)_2^-$ and mixed Np(V) hydroxo-carbonato species become important at high pH. Four, $Np(OH)_5^-$ is disregarded as a valid species. Therefore, Np_2O_5 and $Np(OH)_4$ (am) are the stable species in low ionic strength aquifers.

INTENTIONALLY LEFT BLANK

APPENDIX C

ANALYTICAL MODEL FOR FLOW AND TRANSPORT IN THE INVERT

INTENTIONALLY LEFT BLANK

C.1 MATHEMATICAL FORMULATION FOR FLOW IN THE INVERT

An approximate analysis for steady dripping flow in the invert may be constructed based on unsaturated flow in a bounded domain with sources at the top of the invert. Because of the expected limited effects of the invert boundaries on the flow, the geometry of the invert boundaries are simplified to a rectangular cross-section. This expectation is based on the fact that flow in the unsaturated zone, including an unsaturated invert is primarily downward. Two sources are located along the upper boundary representing flow from the waste package and flow diverted around the waste package. Given these simplifications, the flow domain and boundary conditions are shown in Figure C.1-1.

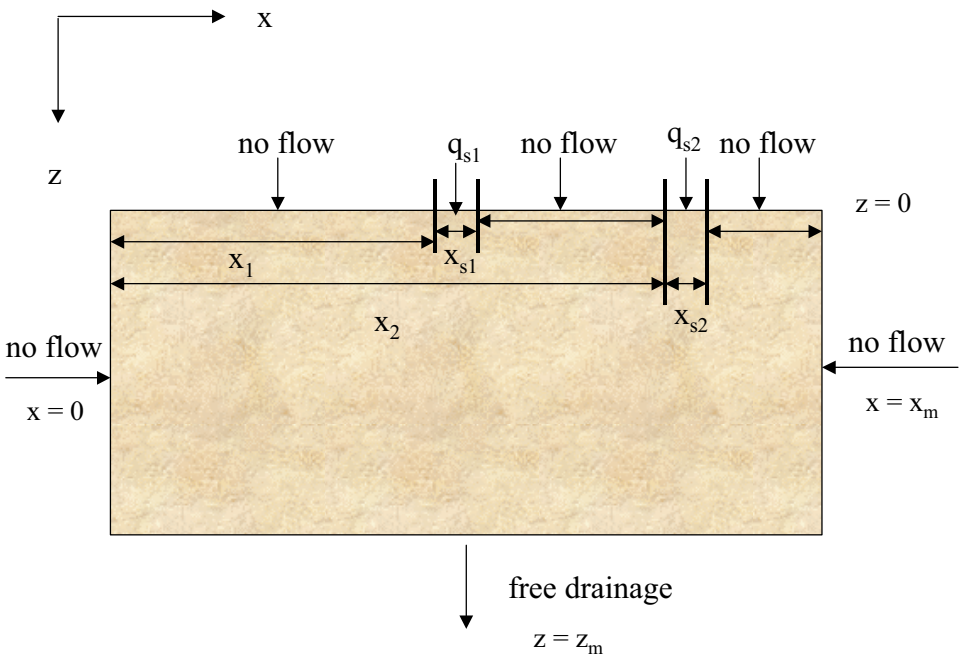

Figure C.1-1. Invert Domain and Boundary Conditions for Flow

Source 1 enters the invert beneath the waste package at a position x_1 with a flux, q_{s1}. Source 2 enters at a position x_2 where diverted flow around the waste package enters the invert with a flux of q_{s2}. The remainder of the top boundary is a no-flow boundary. Both side boundaries are no-flow boundaries. The bottom boundary is a free-drainage boundary, which means that the water pressure gradients are zero along the bottom boundary. The invert material is considered a homogeneous single-continuum, ignoring any effects of the intragranular porosity of the crushed tuff on the flow dynamics. Given these assumptions, the flow in the invert is governed by Darcy's law for unsaturated flow,

$$\vec{q} = -\frac{k_s k_{rw}(S_w)}{\mu_w}\nabla p_w(S_w) + \frac{k_s k_{rw}(S_w)}{\mu_w}\rho_w g\vec{k} \qquad \text{(Eq. C.1-1)}$$

where

$k_s \equiv$ saturated permeability
$k_{rw}(S_w) \equiv$ relative permeability to water
$S_w \equiv$ water saturation
$\mu_w \equiv$ viscosity of water
$p_w(S_w) \equiv$ water pressure (under tension, function of saturation)
$\rho_w \equiv$ density of water
$g \equiv$ acceleration of gravity
$\vec{q} \equiv$ darcy water flux
$\vec{k} \equiv$ unit vector in the z-direction

The form of Equation C.1-1 is close to that shown in Equation 9.4.21 of (Bear 1972 [DIRS 156269]). The difference is based the fact that capillary pressure is a function of saturation, as indicated in Section 9.4.3 of this text. The effective permeability in Equation 9.4.21 can be factored into a base (saturated) permeability times a relative permeability that is a function of saturation.

Let

$$\psi(S_w) = \frac{p_w(S_w)}{\rho_w g} \equiv \text{ water pressure head} \qquad \text{(Eq. C.1-2)}$$

$$K(S_w) = \frac{\rho_w g k_s k_{rw}(S_w)}{\mu_w} \equiv \text{ effective hydraulic conductivity} \qquad \text{(Eq. C.1-3)}$$

Then Equation (C.1-1) becomes,

$$\vec{q} = -K(S_w)\nabla\psi(S_w) + K(S_w)\vec{k} \qquad \text{(Eq. C.1-4)}$$

Now, because $K \equiv K(S_w)$ and $\psi \equiv \psi(S_w)$, then

$$K \equiv K(\psi) \qquad \text{(Eq. C.1-5)}$$

Then Equation (C.1-4) becomes,

$$\vec{q} = -K(\psi)\nabla\psi + K(\psi)\vec{k} \qquad \text{(Eq. C.1-6)}$$

Mass conservation for steady, incompressible flow is,

$$\nabla \bullet \vec{q} = 0 \qquad \text{(Eq. C.1-7)}$$

or, using Equation (C.1-6) in Equation (C.1-7),

$$\nabla \bullet K\nabla\psi = \frac{\partial K}{\partial z} \qquad \text{(Eq. C.1-8)}$$

The boundary condition for the top boundary specifies the flux entering the domain from the two sources,

$$-K\frac{\partial \psi}{\partial z}(x,0)+K(x,0)=q_{s1}H(x_{s1}+x_1-x)H(x-x_1)+q_{s2}H(x_{s2}+x_2-x)H(x-x_2)$$

(Eq. C.1-9)

where $H(x)$ is the step function $H(x)=1$ for $x>0$, $H(x)=0$ for $x<0$, and $H(0)=1/2$. The boundary condition on the bottom boundary is a "free gravity drainage" condition in which flow exits the bottom boundary by pure gravity flow, i.e., the vertical water pressure gradient along the bottom boundary is zero,

$$\frac{\partial \psi}{\partial z}(x,z_m)=0 \qquad \text{(Eq. C.1-10)}$$

Because flow in the x-direction requires a water pressure gradient, no flow conditions along each side boundary is obtained by setting the horizontal water pressure gradients along these boundaries to zero,

$$\frac{\partial \psi}{\partial x}(0,z)=0 \qquad \text{(Eq. C.1-11)}$$

$$\frac{\partial \psi}{\partial x}(x_m,z)=0 \qquad \text{(Eq. C.1-12)}$$

The solution to Equation C.1-8 subject to boundary conditions C.1-9 through C.1-12 follows the general solution method presented in (Philip et al. 1989 [DIRS 105743]) for unsaturated flow around a cylindrical cavity, modified to address the different domain geometry and boundary conditions for the drift invert problem. The left-hand side of Equation (C.1-8) is a nonlinear function of ψ. This may be linearized by introducing the Kirchhoff potential,

$$\Phi(\psi)=\int_{-\infty}^{\psi}K(\vartheta)d\vartheta \qquad \text{(Eq. C.1-13)}$$

Note that,

$$\nabla\Phi=\frac{d\Phi}{d\psi}\nabla\psi=K(\psi)\nabla\psi \qquad \text{(Eq. C.1-14)}$$

Using Equation (C.1-14) in Equation (C.1-8) gives,

$$\nabla^2\Phi=\frac{\partial K}{\partial z} \qquad \text{(Eq. C.1-15)}$$

Let ψ_0 be the (approximate) minimum potential in the problem and

$$\Phi_0 = \int_{-\infty}^{\psi_0} K(\vartheta) d\vartheta \qquad \text{(Eq. C.1-16)}$$

$$K_0 = K(\psi_0) \qquad \text{(Eq. C.1-17)}$$

The constitutive relationship used for the effective permeability is a variation on the Gardner relationship (Bear 1972 [DIRS 156269], Eq. 9.4.34),

$$K(\psi) = K_0 \exp\{\alpha(\psi - \psi_0)\} \qquad \text{(Eq. C.1-18)}$$

where α is the capillary strength of the material. The advantange of this constituitive relationship is that it linearizes the right-hand side of Equation (C.1-15) in terms of the Kirchhoff potential. The Gardner relationship in (Bear 1972 [DIRS 156269], Eq. 9.4.34) does not contain the term ψ_0. Introduction of ψ_0 is equivalent to multiplying the Gardner equation by a constant and leads to an effective permeability of K_0 when $\psi = \psi_0$. Therefore, this re-scales the equation such that K_0 is not the saturated permeability but the effective permeability when $\psi = \psi_0$.

Let

$$\ell_s = \frac{2}{\alpha} \qquad \text{(Eq. C.1-19)}$$

be the sorptive length scale.

From Equations (C.1-18) and (C.1-19),

$$\frac{\partial K}{\partial z} = \frac{2}{\ell_s} K_0 \exp\left\{\frac{2}{\ell_s}(\psi - \psi_0)\right\} \frac{\partial \psi}{\partial z} \qquad \text{(Eq. C.1-20)}$$

or,

$$\frac{\partial K}{\partial z} = \frac{2}{\ell_s} K \frac{\partial \psi}{\partial z} = \frac{2}{\ell_s} \frac{\partial \Phi}{\partial z} \qquad \text{(Eq. C.1-21)}$$

Also note, using Equations (C.1-18) and (C.1-19) in Equation (C.1-13) gives,

$$\Phi(\psi) = \int_{-\infty}^{\psi} K_0 \exp\left\{\frac{2}{\ell_s}(\vartheta - \psi_0)\right\} d\vartheta \qquad \text{(Eq. C.1-22)}$$

or,

$$\Phi = K_0 \exp\left(-\frac{2\psi_0}{\ell_s}\right) \int_{-\infty}^{\psi} \exp\left\{\frac{2\vartheta}{\ell_s}\right\} d\vartheta \qquad \text{(Eq. C.1-23)}$$

$$\Phi = K_0 \exp\left(-\frac{2\psi_0}{\ell_s}\right)\frac{\ell_s}{2}\int_{-\infty}^{\psi}\exp\left\{\frac{2\vartheta}{\ell_s}\right\}d\frac{2\vartheta}{\ell_s} \quad \text{(Eq. C.1-24)}$$

$$\Phi = \frac{\ell_s}{2}K_0 \exp\left\{\frac{2}{\ell_s}(\psi - \psi_0)\right\} = \frac{\ell_s}{2}K \quad \text{(Eq. C.1-25)}$$

Using Equation (C.1-21) in Equation (C.1-15) gives,

$$\nabla^2\Phi = \frac{2}{\ell_s}\frac{\partial\Phi}{\partial z} \quad \text{(Eq. C.1-26)}$$

Define the dimensionless coordinates,

$$\xi = \frac{z}{\ell_s} \quad \text{(Eq. C.1-27)}$$

$$\eta = \frac{x}{\ell_s} \quad \text{(Eq. C.1-28)}$$

$$\Phi_d = \frac{\Phi}{q_{s1}\ell_s} \quad \text{(Eq. C.1-29)}$$

and

$$\nabla_d \equiv \ell_s\nabla \quad \text{(Eq. C.1-30)}$$

Using Equations (C.1-27), (C.1-28), (C.1-29), and (C.1-30) in Equation (C.1-26) gives,

$$\nabla_d^2\Phi_d = 2\frac{\partial\Phi_d}{\partial\xi} \quad \text{(Eq. C.1-31)}$$

Introduce the following change of variables to transform Equation (C.1-31) to the Helmholtz equation,

$$\chi = \Phi_d \exp(-\xi) \quad \text{(Eq. C.1-32)}$$

or

$$\Phi_d = \chi\exp(\xi) \quad \text{(Eq. C.1-33)}$$

Evaluating the derivative of Equation (C.1-32),

$$\frac{\partial\Phi_d}{\partial\xi} = \chi\exp(\xi) + \frac{\partial\chi}{\partial\xi}\exp(\xi) \quad \text{(Eq. C.1-34)}$$

$$\frac{\partial^2 \Phi_d}{\partial \xi^2} = \chi \exp(\xi) + 2\frac{\partial \chi}{\partial \xi}\exp(\xi) + \frac{\partial^2 \chi}{\partial \xi^2}\exp(\xi) \quad \text{(Eq. C.1-35)}$$

$$\frac{\partial^2 \Phi_d}{\partial \eta^2} = \frac{\partial^2 \chi}{\partial \eta^2}\exp(\xi) \quad \text{(Eq. C.1-36)}$$

Using Equations (C.1-34), (C.1-35) and (C.1-36) in Equation (C.1-31) gives,

$$\nabla_d^2 \chi = \chi \quad \text{(Eq. C.1-37)}$$

Let the dimensionless boundary coordinates be

$$\omega = \frac{z_m}{\ell_s} \quad \text{(Eq. C.1-38)}$$

$$\sigma = \frac{x_m}{\ell_s} \quad \text{(Eq. C.1-39)}$$

The boundary condition (C.1-9) can be made dimensionless as follows:

By Equation (C.1-14), the z-component gives,

$$K(\psi)\frac{\partial \psi}{\partial z} = \frac{\partial \Phi}{\partial z} \quad \text{(Eq. C.1-40a)}$$

and by Equation (C.1-25),

$$K = \frac{2}{\ell_s}\Phi \quad \text{(Eq. C.1-40b)}$$

so

$$K(\psi)\frac{\partial \psi}{\partial z} + K(\psi) = \frac{\partial \Phi}{\partial z} + \frac{2}{\ell_s}\Phi \quad \text{(Eq. C.1-40c)}$$

Nondimensionalizing (using Equations (C.1-27) and (C.1-29)) and evaluating at coordinates (x, z) and dimensionless coordinates (η, ξ) gives,

$$K(x,z)\frac{\partial \psi}{\partial z} + K(x,z) = q_{s1}\frac{\partial \Phi_d}{\partial \xi}(\eta,\xi) + 2q_{s1}\Phi_d(\eta,\xi) \quad \text{(Eq. C.1-40d)}$$

Substituting from Equation (C.1-33) for Φ_d gives,

$$K(x,z)\frac{\partial \psi}{\partial z} + K(x,z) = q_{s1}\frac{\partial\{\chi(\eta,\xi)\exp(\xi)\}}{\partial \xi} + 2q_{s1}\chi(\eta,\xi)\exp(\xi) \quad \text{(Eq. C.1-40e)}$$

Differentiating gives,

$$K(x,z)\frac{\partial \psi}{\partial z} + K(x,z) = q_{s1}\chi(\eta,\xi)\exp(\xi) + q_{s1}\exp(\xi)\frac{\partial \chi}{\partial \xi}(\eta,\xi) + 2q_{s1}\chi(\eta,\xi)\exp(\xi \quad \text{(Eq. C.1-40f)}$$

or

$$K(x,z)\frac{\partial \psi}{\partial z} + K(x,z) = \exp(\xi)\begin{bmatrix} q_{s1}\left(\chi c + \frac{\partial \chi}{\partial \xi}(\eta,\xi)\right) \\ + 2q_{s1}\chi(\eta,\xi) \end{bmatrix} \quad \text{(Eq. C.1-40g)}$$

Evaluating at $(x,0$, or in dimensionless variables, $(\eta,0)$, gives,

$$K(x,0)\frac{\partial \psi}{\partial z} + K(x,0) = q_{s1}\left(\chi(\eta,0) + \frac{\partial \chi}{\partial \xi}(\eta,0)\right) + 2q_{s1}\chi(\eta,0) \quad \text{(Eq. C.1-40h)}$$

The boundary condition (C.1-9) becomes,

$$-q_{s1}\left(\chi(\eta,0) + \frac{\partial \chi}{\partial \xi}(\eta,0)\right) + 2q_{s1}\chi(\eta,0) = q_{s1}H(\eta_{s1}+\eta_1-\eta)H(\eta-\eta_1) + q_{s2}H(\eta_{s2}+\eta_2-\eta)H(\eta-\eta_2) \quad \text{(Eq. C.1-40i)}$$

or

$$\chi(\eta,0) - \frac{\partial \chi}{\partial \xi}(\eta,0) = H(\eta_{s1}+\eta_1-\eta)H(\eta-\eta_1) + \frac{q_{s2}}{q_{s1}}H(\eta_{s2}+\eta_2-\eta)H(\eta-\eta_2) \quad \text{(Eq. C.1-41)}$$

$$\frac{\partial \chi}{\partial \xi}(\eta,\omega) + \chi(\eta,\omega) = 0 \quad \text{(Eq. C.1-42)}$$

$$\frac{\partial \chi}{\partial \eta}(0,\xi) = 0 \quad \text{(Eq. C.1-43)}$$

$$\frac{\partial \chi}{\partial \eta}(\sigma,\xi) = 0 \quad \text{(Eq. C.1-44)}$$

Using the method of separation of variables (Kreyszig 1970 [DIRS 152467], p. 111), let

$$\chi(\eta,\xi)=\Gamma(\eta)\Psi(\xi) \quad \text{(Eq. C.1-45)}$$

Then, Equation (C.1-37) becomes,

$$\Psi\frac{d^2\Gamma}{d\eta^2}+\Gamma\frac{d^2\Psi}{d\xi^2}=\Gamma\Psi \quad \text{(Eq. C.1-46)}$$

and dividing each side by $\Gamma\Psi$,

$$1-\frac{1}{\Psi}\frac{d^2\Psi}{d\xi^2}=\frac{1}{\Gamma}\frac{d^2\Gamma}{d\eta^2}=-\lambda^2 \quad \text{(Eq. C.1-47)}$$

For Γ,

$$\frac{d^2\Gamma}{d\eta^2}+\lambda^2\Gamma=0 \quad \text{(Eq. C.1-48)}$$

The general solution for Γ is (Thomas 1972 [DIRS 131482], p. 914, Example 4),

$$\Gamma(\eta)=A\cos(\lambda\eta)+B\sin(\lambda\eta) \quad \text{(Eq. C.1-49)}$$

The next step is to satisfy boundary conditions (C.1-43) on $\eta=0$. Because $\chi(\eta,\xi)=\Gamma(\eta)\Psi(\xi)$ as given in Equation (C.1-45), then the boundary condition, Equation (C.1-43) gives,

$$\frac{\partial\chi}{\partial\eta}(0,\xi)=\Psi(\xi)\frac{d\Gamma}{d\eta}(0) \quad \text{(Eq. C.1-50a)}$$

and because we don't want the trivial solution $\Psi\equiv 0$, then

$$\frac{d\Gamma}{d\eta}(0)=0 \quad \text{(Eq. C.1-50b)}$$

Applying this to Equation (C.1-50e) gives,

$$\frac{d\Gamma}{d\eta}(0)=-A\lambda\sin(\lambda\bullet 0)+B\lambda\cos(\lambda\bullet 0)=0 \quad \text{(Eq. C.1-50c)}$$

Now, $\sin(0)=0$ and $\cos(0)=1$, therefore

$$\frac{d\Gamma}{d\eta}(0)=B\lambda=0 \quad \text{(Eq. C.1-50d)}$$

The only solution besides the trivial case of $\lambda=0$ is

$$B = 0 \qquad \text{(Eq. C.1-50e)}$$

and to satisfy boundary condition (C.1-44) on $\eta = \sigma$,

$$\sin(\lambda\sigma) = 0 \qquad \text{(Eq. C.1-51)}$$

which implies λ takes on a discrete set of values, λ_ℓ

$$\lambda_\ell = \frac{\ell\pi}{\sigma} \qquad \text{(Eq. C.1-52)}$$

where ℓ is an integer, $\ell = 0, 1, 2, 3, ...$

Therefore,

$$\Gamma_\ell(\eta) = A_\ell \cos(\lambda_\ell \eta) \qquad \text{(Eq. C.1-53)}$$

For Ψ_ℓ,

$$\frac{d^2\Psi_\ell}{d\xi^2} - (1 + \lambda_\ell^2)\Psi_\ell = 0 \qquad \text{(Eq. C.1-54)}$$

Solving for Ψ_ℓ (Thomas 1972 [DIRS 131482], Section 18-9, with a=0 and b=$-(1+\lambda_\ell^2)$) gives,

$$\Psi_\ell(\xi) = C_\ell \exp\left(\sqrt{1+\lambda_\ell^2}\,\xi\right) + D_\ell \exp\left(-\sqrt{1+\lambda_\ell^2}\,\xi\right) \qquad \text{(Eq. C.1-55)}$$

For convenience, let

$$\Lambda_\ell = \sqrt{1+\lambda_\ell^2} \qquad \text{(Eq. C.1-56)}$$

Then Equation (C.1-55) becomes,

$$\Psi_\ell(\xi) = C_\ell \exp(\Lambda_\ell \xi) + D_\ell \exp(-\Lambda_\ell \xi) \qquad \text{(Eq. C.1-57)}$$

To satisfy the boundary condition (C.1-42) on $\xi = \omega$,

$$C_\ell \Lambda_\ell \exp(\Lambda_\ell \omega) - D_\ell \Lambda_\ell \exp(-\Lambda_\ell \omega) + C_\ell \exp(\Lambda_\ell \omega) + D_\ell \exp(-\Lambda_\ell \omega) = 0 \qquad \text{(Eq. C.1-58)}$$

or

$$D_\ell = C_\ell \left(\frac{\Lambda_\ell + 1}{\Lambda_\ell - 1}\right) \exp(2\Lambda_\ell \omega) \qquad \text{(Eq. C.1-59)}$$

Therefore,

$$\Psi_\ell(\xi) = C_\ell \left\{ \exp(\Lambda_\ell \xi) + \left(\frac{\Lambda_\ell + 1}{\Lambda_\ell - 1} \right) \exp(2\Lambda_\ell \omega) \exp(-\Lambda_\ell \xi) \right\} \quad \text{(Eq. C.1-60)}$$

and,

$$\chi(\eta, \xi) = \sum_{\ell=0}^{\infty} a_\ell \cos(\lambda_\ell \eta) \left\{ \exp(\Lambda_\ell \xi) + \left(\frac{\Lambda_\ell + 1}{\Lambda_\ell - 1} \right) \exp(2\Lambda_\ell \omega) \exp(-\Lambda_\ell \xi) \right\} \quad \text{(Eq. C.1-61)}$$

where $a_\ell = A_\ell C_\ell$

To satisfy boundary condition (C.1-41) on $\xi = 0$, use Fourier decomposition.

Note that for $h \neq \ell$, the solution is (Weast 1978 [DIRS 128733], p. A-91, Equation 624)

$$\int_0^\sigma \cos(\lambda_\ell \eta) \cos(\lambda_h \eta) d\eta = \int_0^\sigma \cos\left(\frac{\ell \pi}{\sigma} \eta \right) \cos\left(\frac{h \pi}{\sigma} \eta \right) d\eta = \frac{\sigma}{\pi} \int_0^\pi \cos(\ell t) \cos(ht) dt = 0$$

(Eq. C.1-62)

and for $i \neq \ell$, $\ell \neq 0$

$$\int_0^\sigma \cos(\lambda_\ell \eta) \cos(\lambda_\ell \eta) d\eta = \int_0^\sigma \cos^2\left(\frac{\ell \pi}{\sigma} \eta \right) d\eta = \frac{\sigma}{\pi} \int_0^\pi \cos^2(\ell t) dt = \frac{\sigma}{2} \quad \text{(Eq. C.1-63)}$$

for $\ell = i = 0$

$$\int_0^\sigma \cos(\lambda_\ell \eta) \cos(\lambda_\ell \eta) d\eta = \int_0^\sigma d\eta = \sigma \quad \text{(Eq. C.1-64)}$$

and for the source term,

$$\begin{aligned} &\int_0^\sigma \cos(\lambda_\ell \eta) H(\eta_{s1} + \eta_1 - \eta) H(\eta - \eta_1) d\eta = \int_{\eta_1}^{\eta_{s1} + \eta_1} \cos\left(\frac{\ell \pi}{\sigma} \eta \right) d\eta \\ &= \frac{\sigma}{\ell \pi} \int_{\frac{\ell \pi \eta_1}{\sigma}}^{\frac{\ell \pi (\eta_{s1} + \eta_1)}{\sigma}} \cos(t) dt = \frac{1}{\lambda_\ell} \{ \sin[\lambda_n (\eta_{s1} + \eta_1)] - \sin(\lambda_n \eta_1) \} \end{aligned} \quad \text{(Eq. C.1-65)}$$

and

$$\frac{q_{s2}}{q_{s1}}\int_0^{\sigma}\cos(\lambda_\ell\eta)H(\eta_{s2}+\eta_2-\eta)H(\eta-\eta_2)d\eta=\frac{q_{s2}}{q_{s1}}\int_{\eta_2}^{\eta_{s2}+\eta_2}\cos\left(\frac{\ell\pi}{\sigma}\eta\right)d\eta$$
$$=\frac{q_{s2}}{q_{s1}}\frac{\sigma}{\ell\pi}\int_{\frac{\ell\pi\eta_2}{\sigma}}^{\frac{\ell\pi(\eta_{s2}+\eta_2)}{\sigma}}\cos(t)dt=\frac{q_{s2}}{q_{s1}}\frac{1}{\lambda_\ell}\{\sin[\lambda_\ell(\eta_{s2}+\eta_2)]-\sin(\lambda_\ell\eta_2)\}$$

(Eq. C.1-66)

$$a_\ell\frac{\sigma(1+2H(-\ell))}{2}\left\{1+\left(\frac{\Lambda_\ell+1}{\Lambda_\ell-1}\right)\exp(2\Lambda_\ell\omega)\right\}$$
$$-a_\ell\frac{\sigma(1+2H(-\ell))}{2}\left\{\Lambda_\ell-\Lambda_\ell\left(\frac{\Lambda_\ell+1}{\Lambda_\ell-1}\right)\exp(2\Lambda_\ell\omega)\right\}$$
$$=\frac{1}{\lambda_\ell}\{\sin[\lambda_\ell(\eta_{s1}+\eta_1)]-\sin(\lambda_\ell\eta_1)\}+\frac{q_{s2}}{q_{s1}}\frac{1}{\lambda_\ell}\{\sin[\lambda_\ell(\eta_{s2}+\eta_2)]-\sin(\lambda_\ell\eta_2)\}$$

(Eq. C.1-67)

$$a_\ell\left\{1-\Lambda_\ell+(1+\Lambda_\ell)\left(\frac{\Lambda_\ell+1}{\Lambda_\ell-1}\right)\exp(2\Lambda_\ell\omega)\right\}$$
$$=\frac{2}{(1+2H(-\ell))\lambda_\ell\sigma}\left[\sin[\lambda_\ell(\eta_{s1}+\eta_1)]-\sin(\lambda_\ell\eta_1)+\frac{q_{s2}}{q_{s1}}\{\sin[\lambda_\ell(\eta_{s2}+\eta_2)]-\sin(\lambda_\ell\eta_2)\}\right]$$

(Eq. C.1-68)

$$a_\ell=\frac{2\left[\sin[\lambda_\ell(\eta_{s1}+\eta_1)]-\sin(\lambda_\ell\eta_1)+\frac{q_{s2}}{q_{s1}}\{\sin[\lambda_\ell(\eta_{s2}+\eta_2)]-\sin(\lambda_\ell\eta_2)\}\right]}{(1+2H(-\ell))\lambda_\ell\sigma}\bullet$$
$$\frac{(\Lambda_\ell-1)\exp(-\Lambda_\ell\omega)}{(\Lambda_\ell+1)^2\exp(\Lambda_\ell\omega)-(\Lambda_\ell-1)^2\exp(-\Lambda_\ell\omega)}$$

(Eq. C.1-69)

$$a_\ell=\frac{\sin[\lambda_\ell(\eta_{s1}+\eta_1)]-\sin(\lambda_\ell\eta_1)+\frac{q_{s2}}{q_{s1}}\{\sin[\lambda_\ell(\eta_{s2}+\eta_2)]-\sin(\lambda_\ell\eta_2)\}}{(1+2H(-\ell))\lambda_\ell\sigma}\bullet$$
$$\frac{(\Lambda_\ell-1)\exp(-\Lambda_\ell\omega)}{(\Lambda_\ell^2+1)\sinh(\Lambda_\ell\omega)+2\Lambda_\ell\cosh(\Lambda_\ell\omega)}$$

(Eq. C.1-70)

Therefore, Equation (C.1-61) becomes,

$$\chi(\eta,\xi)=\sum_{\ell=0}^{\infty}\frac{\sin\left[\lambda_\ell(\eta_{s1}+\eta_1)\right]-\sin(\lambda_\ell\eta_1)+\frac{q_{s2}}{q_{s1}}\left\{\sin\left[\lambda_\ell(\eta_{s2}+\eta_2)\right]-\sin(\lambda_\ell\eta_2)\right\}}{(1+2H(-\ell))\lambda_\ell\sigma}\cos(\lambda_\ell\eta)\bullet$$
$$\frac{(\Lambda_\ell-1)\exp\{\Lambda_\ell(\xi-\omega)\}+(\Lambda_\ell+1)\exp\{-\Lambda_\ell(\xi-\omega)\}}{(\Lambda_\ell^2+1)\sinh(\Lambda_\ell\omega)+2\Lambda_\ell\cosh(\Lambda_\ell\omega)}$$

(Eq. C.1-71)

$$\chi(\eta,\xi)=\sum_{\ell=0}^{\infty}\frac{2\left[\sin\left[\lambda_\ell(\eta_{s1}+\eta_1)\right]-\sin(\lambda_\ell\eta_1)+\frac{q_{s2}}{q_{s1}}\left\{\sin\left[\lambda_\ell(\eta_{s2}+\eta_2)\right]-\sin(\lambda_\ell\eta_2)\right\}\right]}{(1+2H(-\ell))\lambda_\ell\sigma}\cos(\lambda_\ell\eta)\bullet$$
$$\frac{\Lambda_\ell\cosh\{\Lambda_\ell(\omega-\xi)\}+\sinh\{\Lambda_\ell(\omega-\xi)\}}{2\Lambda_\ell\cosh(\Lambda_\ell\omega)+(\Lambda_\ell^2+1)\sinh(\Lambda_\ell\omega)}$$

(Eq. C.1-72)

In terms of the dimensionless potential, χ, the flux field is,

$$\vec{q}=-K(\psi)\nabla\psi+K(\psi)\vec{k} \quad \text{(Eq. C.1-73)}$$

$$\vec{q}=-\nabla\Phi+\frac{2\Phi}{\ell_s}\vec{k} \quad \text{(Eq. C.1-74)}$$

$$\frac{\vec{q}}{q_{s1}}=-\nabla_d\Phi_d+2\Phi_d\vec{k} \quad \text{(Eq. C.1-75)}$$

$$\frac{\vec{q}}{q_{s1}}=-\exp(\xi)\left(\nabla_d\chi+\chi\vec{k}\right)+2\exp(\xi)\chi\vec{k} \quad \text{(Eq. C.1-76)}$$

$$\vec{q}=q_{s1}\exp(\xi)\left(\chi\vec{k}-\nabla_d\chi\right) \quad \text{(Eq. C.1-77)}$$

$$q_z = \exp(\xi)\left(\begin{array}{l}\displaystyle\sum_{\ell=0}^{\infty}\frac{2\left[q_{s1}\left\{\sin\left[\lambda_\ell\left(\eta_{s1}+\eta_1\right)\right]-\sin\left(\lambda_\ell\eta_1\right)\right\}+q_{s2}\left\{\sin\left[\lambda_\ell\left(\eta_{s2}+\eta_2\right)\right]-\sin\left(\lambda_\ell\eta_2\right)\right\}\right]}{\left(1+2H\left(-\ell\right)\right)\lambda_\ell\sigma}\cos\left(\lambda_\ell\eta\right)\bullet \\ \qquad\dfrac{\Lambda_\ell\cosh\left\{\Lambda_\ell\left(\omega-\xi\right)\right\}+\sinh\left\{\Lambda_\ell\left(\omega-\xi\right)\right\}}{2\Lambda_\ell\cosh\left(\Lambda_\ell\omega\right)+\left(\Lambda_\ell^2+1\right)\sinh\left(\Lambda_\ell\omega\right)} \\ +\displaystyle\sum_{\ell=0}^{\infty}\frac{2\left[q_{s1}\left\{\sin\left[\lambda_\ell\left(\eta_{s1}+\eta_1\right)\right]-\sin\left(\lambda_\ell\eta_1\right)\right\}+q_{s2}\left\{\sin\left[\lambda_\ell\left(\eta_{s2}+\eta_2\right)\right]-\sin\left(\lambda_\ell\eta_2\right)\right\}\right]}{\left(1+2H\left(-\ell\right)\right)\lambda_\ell\sigma}\cos\left(\lambda_\ell\eta\right)\bullet \\ \qquad\dfrac{\Lambda_\ell^2\sinh\left\{\Lambda_\ell\left(\omega-\xi\right)\right\}+\Lambda_\ell\cosh\left\{\Lambda_\ell\left(\omega-\xi\right)\right\}}{2\Lambda_\ell\cosh\left(\Lambda_\ell\omega\right)+\left(\Lambda_\ell^2+1\right)\sinh\left(\Lambda_\ell\omega\right)}\end{array}\right)$$

(Eq. C.1-78)

$$q_z = \exp(\xi)\sum_{\ell=0}^{\infty}\frac{2\left[q_{s1}\left\{\sin\left[\lambda_\ell\left(\eta_{s1}+\eta_1\right)\right]-\sin\left(\lambda_\ell\eta_1\right)\right\}+q_{s2}\left\{\sin\left[\lambda_\ell\left(\eta_{s2}+\eta_2\right)\right]-\sin\left(\lambda_\ell\eta_2\right)\right\}\right]}{\left(1+2H\left(-\ell\right)\right)\lambda_\ell\sigma}\cos\left(\lambda_\ell\eta\right)\bullet$$
$$\frac{2\Lambda_\ell\cosh\left\{\Lambda_\ell\left(\omega-\xi\right)\right\}+\left(\Lambda_\ell^2+1\right)\sinh\left\{\Lambda_\ell\left(\omega-\xi\right)\right\}}{2\Lambda_\ell\cosh\left(\Lambda_\ell\omega\right)+\left(\Lambda_\ell^2+1\right)\sinh\left(\Lambda_\ell\omega\right)}$$

(Eq. C.1-79)

$$q_x = \exp(\xi)\sum_{\ell=0}^{\infty}\frac{2\left[q_{s1}\left\{\sin\left[\lambda_\ell\left(\eta_{s1}+\eta_1\right)\right]-\sin\left(\lambda_\ell\eta_1\right)\right\}+q_{s2}\left\{\sin\left[\lambda_\ell\left(\eta_{s2}+\eta_2\right)\right]-\sin\left(\lambda_\ell\eta_2\right)\right\}\right]}{\left(1+2H\left(-\ell\right)\right)\sigma}\sin\left(\lambda_\ell\eta\right)\bullet$$
$$\frac{\Lambda_\ell\cosh\left\{\Lambda_\ell\left(\omega-\xi\right)\right\}+\sinh\left\{\Lambda_\ell\left(\omega-\xi\right)\right\}}{2\Lambda_\ell\cosh\left(\Lambda_\ell\omega\right)+\left(\Lambda_\ell^2+1\right)\sinh\left(\Lambda_\ell\omega\right)}$$

(Eq. C.1-80)

For computational purposes, the following forms are more convenient,

$$q_z = q_{s1}\exp(\xi)\sum_{\ell=0}^{\infty}\frac{2\left[\left\{\sin\left[\lambda_\ell\left(\eta_{s1}+\eta_1\right)\right]-\sin\left(\lambda_\ell\eta_1\right)\right\}+\dfrac{q_{s2}}{q_{s1}}\left\{\sin\left[\lambda_\ell\left(\eta_{s2}+\eta_2\right)\right]-\sin\left(\lambda_\ell\eta_2\right)\right\}\right]}{\left(1+2H\left(-\ell\right)\right)\lambda_\ell\sigma}\cos\left(\lambda_\ell\eta\right)\bullet$$
$$\exp\left(-\Lambda_\ell\xi\right)\frac{\left(\Lambda_\ell+1\right)^2-\left(\Lambda_\ell-1\right)^2\exp\left\{-2\Lambda_\ell\left(\omega-\xi\right)\right\}}{\left(\Lambda_\ell+1\right)^2-\left(\Lambda_\ell-1\right)^2\exp\left\{-2\Lambda_\ell\omega\right\}}$$

(Eq. C.1-81)

$$q_x = q_{s1}\exp(\xi)\sum_{\ell=0}^{\infty}\frac{2\left[\{\sin[\lambda_\ell(\eta_{s1}+\eta_1)]-\sin(\lambda_\ell\eta_1)\}+\frac{q_{s2}}{q_{s1}}\{\sin[\lambda_\ell(\eta_{s2}+\eta_2)]-\sin(\lambda_\ell\eta_2)\}\right]}{(1+2H(-\ell))\sigma}\sin(\lambda_\ell\eta)\bullet$$
$$\exp(-\Lambda_\ell\xi)\frac{(\Lambda_\ell+1)+(\Lambda_\ell-1)\exp\{-2\Lambda_\ell(\omega-\xi)\}}{(\Lambda_\ell+1)^2-(\Lambda_\ell-1)^2\exp\{-2\Lambda_\ell\omega\}}$$

(Eq. C.1-82)

Starting with Equation (C.1-81)

$$q_z = q_{s1}\exp(\xi)\sum_{\ell=0}^{\infty}\frac{2\left[\{\sin[\lambda_\ell(\eta_{s1}+\eta_1)]-\sin(\lambda_\ell\eta_1)\}+\frac{q_{s2}}{q_{s1}}\{\sin[\lambda_\ell(\eta_{s2}+\eta_2)]-\sin(\lambda_\ell\eta_2)\}\right]}{(1+2H(-\ell))\lambda_\ell\sigma}\cos(\lambda_\ell\eta)\bullet$$
$$\exp(-\Lambda_\ell\xi)\frac{(\Lambda_\ell+1)^2-(\Lambda_\ell-1)^2\exp\{-2\Lambda_\ell(\omega-\xi)\}}{(\Lambda_\ell+1)^2-(\Lambda_\ell-1)^2\exp\{-2\Lambda_\ell\omega\}}$$

(Eq. C.1-83)

Integrate over the transverse coordinate, $\eta\ell_s$, at the bottom of the invert, which has a dimensionless coordinate ω,

$$\ell_s\int_0^{\eta}q_z(\eta,\omega)d\eta = q_{s1}\exp(\omega)\sum_{\ell=0}^{\infty}\frac{2\left[\{\sin[\lambda_\ell(\eta_{s1}+\eta_1)]-\sin(\lambda_\ell\eta_1)\}+\frac{q_{s2}}{q_{s1}}\{\sin[\lambda_\ell(\eta_{s2}+\eta_2)]-\sin(\lambda_\ell\eta_2)\}\right]}{(1+2H(-\ell))\lambda_\ell\sigma}\bullet$$
$$\ell_s\int_0^{\eta}\cos(\lambda_\ell\eta)d\eta\bullet\exp(-\Lambda_\ell\omega)\frac{(\Lambda_\ell+1)^2-(\Lambda_\ell-1)^2\exp\{-2\Lambda_\ell(\omega-\omega)\}}{(\Lambda_\ell+1)^2-(\Lambda_\ell-1)^2\exp\{-2\Lambda_\ell\omega\}}$$

(Eq. C.1-84)

The result is the cumulative vertical flux at the bottom of the invert.

C.2 MATHEMATICAL FORMULATION FOR TRANSPORT IN THE INVERT

An approximate analysis for transport under dripping flow in the invert may be constructed using the same domain as used for the analysis of unsaturated flow. The source from the waste package carries radionuclides whereas the diverted flow does not carry radionuclides, as shown in Figure C.2-1.

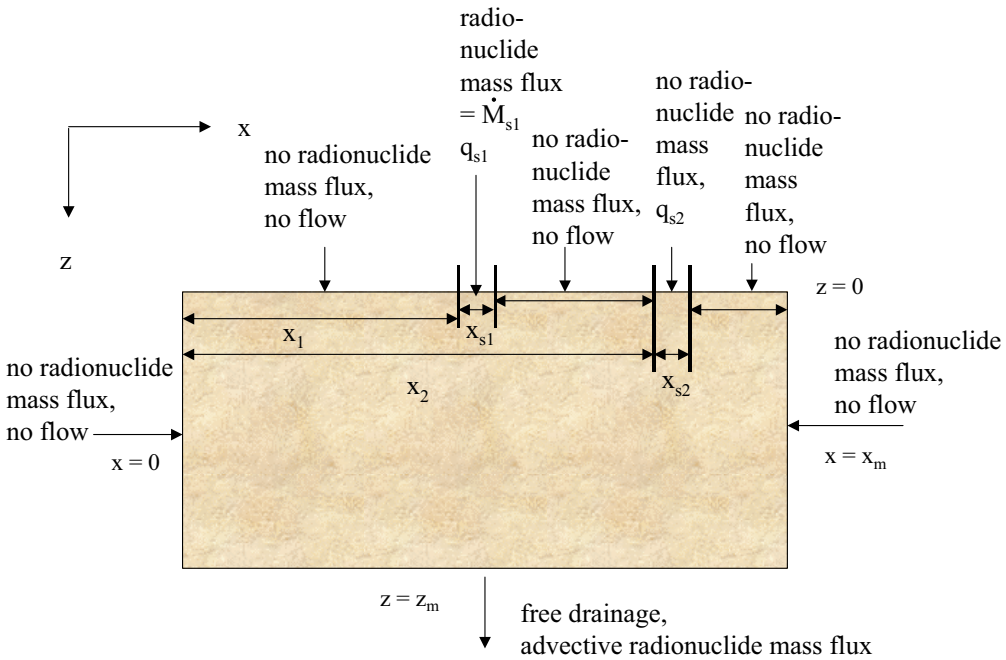

Figure C.2-1. Invert Domain and Boundary Conditions for Transport

The steady source of flow from the waste package has a darcy velocity, q_{s1} and a radionuclide concentration of C_{s1}. The steady source of flow diverted around the waste package has a darcy velocity, q_{s2} and radionuclide concentration $C_{s2} = 0$. The remainder of the top boundary is a no-flux boundary. Both side boundaries are no-flux boundaries. The bottom boundary is a no diffusive flux boundary (advection only), which means that the solute concentration gradients in the *z*-direction are zero along the bottom boundary. The invert material is considered a homogeneous single-continuum, ignoring any effects of the intragranular porosity of the crushed tuff on the dynamics of transport. Given these assumptions, the steady transport in the invert is governed by a balance of advective and dispersive fluxes,

$$\vec{q} \bullet \nabla C = \nabla \bullet \left\{ \theta \overline{\overline{D}} \nabla C \right\} \qquad \text{(Eq. C.2-1)}$$

where

$C \equiv$ solute mass concentration
$\theta = \phi S_w \equiv$ water content
$S_w \equiv$ water saturation
$\phi \equiv$ porosity

$\psi \equiv$ water pressure head
$\overline{\overline{D}} \equiv$ dispersion tensor
$\vec{q} \equiv$ darcy water flux

The top boundary conditions specifies the radionuclide mass flux entering the domain,

$$q(x,0)C(x,0) - \theta(x,0)\overline{\overline{D}}(x,0)\frac{\partial C(x,0)}{\partial z} = \dot{M}_{s1}H(x_{s1} + x_1 - x)H(x - x_1) \qquad \text{(Eq. C.2-2)}$$

where $H(x)$ is the step function $H(x) = 1$ for $x > 0$, $H(x) = 0$ for $x < 0$, and $H(0) = 1/2$. The radionuclide mass flux from the waste package is $\dot{M}_{s1} = q_{s1}C_{s1}$. The bottom boundary condition specifies that radionuclide mass exits the domain through advective transport only, i.e., that dispersive flux in the z-direction along the bottom boundary is zero. Therefore, the vertical concentration gradient along the bottom boundary is set to zero.

$$\frac{\partial C}{\partial z}(x, z_m) = 0 \qquad \text{(Eq. C.2-3)}$$

Radionuclide mass flux in the x-direction along the side boundaries is specified to be zero. This is accomplished by setting the concentration gradients in the x-direction along these boundaries to zero, i.e., zero dispersive flux in the x-direction along these boundaries. Note that advective flux is also zero because the flow analysis specifies zero flow across these boundaries (see boundary conditions in Equations (C.1-11) and (C.1-12)).

$$\frac{\partial C}{\partial x}(0, z) = 0 \qquad \text{(Eq. C.2-4)}$$

$$\frac{\partial C}{\partial x}(x_m, z) = 0 \qquad \text{(Eq. C.2-5)}$$

The Darcy water flux, $\vec{q}$, is defined by the flow solution. To proceed, the dispersion tensor needs to be specified. The dispersion tensor is derived by starting with Equation 10.4.17 from (Bear 1972 [DIRS 156269], Section 10.4.2) and noting the equivalence between ε_ℓ and a_I and ε_t and a_{II}. Bear states that g_{ij} in Cartesian coordinates is δ_{ij}. Also note that $\theta V = q$. That leaves the $\theta D_m \delta_{ij}$ term for molecular diffusion. This is from the Equation $D'_{ij} = D_{ij} + \left(D_d^*\right)_{ij}$ near the end of this Section 10.4.2 of (Bear 1972 [DIRS 156269]). Equation 4.8.29 of (Bear 1972 [DIRS 156269]) shows that the mass flux is proportional to the porosity time D_d^*. So, for an unsaturated porous medium, this becomes the water content times D_d^*. This is then multiplied by the identity tensor δ_{ij} because molecular diffusion is isotropic if the medium is isotropic (which is assumed). The resulting dispersion tensor is given by,

$$\theta\overline{\overline{D}} = \varepsilon_t |\vec{q}| \delta_{ij} + (\varepsilon_\ell - \varepsilon_t)\frac{q_i q_j}{|\vec{q}|} + \theta D_m \delta_{ij} \quad i, j = 1,2,3 \qquad \text{(Eq. C.2-6)}$$

where ε_ℓ and ε_t are the longitudinal and transverse dispersivities, respectively, D_m is the molecular diffusion coefficient in the porous medium, and

$$\delta_{ij} = 1 \text{ if } i = j$$

$$\delta_{ij} = 0 \text{ if } i \neq j$$

The dispersion tensor in general is anisotropic. For unsaturated flow, the dispersivities are also found to be functions of water saturation (Toride et al. 2003 [DIRS 176906]). Only a limited amount of experimental data is available for dispersion in unsaturated flow, and even less (perhaps none) has been developed for two or three-dimensional flow conditions. Given these uncertainties, the dispersion tensor will be simplified to be a scalar function of water saturation. The following simplification allows for analytical treatment of transport,

$$\theta \overline{\overline{D}} = \Phi \quad \text{(Eq. C.2-7)}$$

where Φ is the Kirchhoff potential. Given the Gardner relationship between hydraulic conductivity and water potential (Eq. C.1-25),

$$\Phi = \frac{\ell_s}{2} K \quad \text{(Eq. C.2-8)}$$

and $K(S_w)$ is the effective hydraulic conductivity and ℓ_s is the sorptive length scale. The validity of this approximation is discussed further in Section C.1.

Using Equation (C.2-7), Equation (C.2-1) becomes,

$$\vec{q} \bullet \nabla C = \nabla \bullet (\Phi \nabla C) \quad \text{(Eq. C.2-9)}$$

Putting Equation (C.2-9) into nondimensional form gives,

$$\vec{q}_d \bullet \nabla_d C_d = \nabla_d \bullet (\Phi_d \nabla_d C_d) \quad \text{(Eq. C.2-10)}$$

where

$$\nabla_d \equiv \ell_s \nabla \quad \text{(Eq. C.2-11)}$$

$$\vec{q}_d \equiv \frac{\vec{q}}{q_{s1}} \quad \text{(Eq. C.2-12)}$$

$$C_d \equiv \frac{q_{s1} C}{\dot{M}_{s1}} \quad \text{(Eq. C.2-13)}$$

$$\Phi_d = \frac{\Phi}{q_{s1} \ell_s} \quad \text{(Eq. C.2-14)}$$

and q_{s1} is the source strength for water flux.

Equation (C.2-10) may also be expressed as,

$$\nabla_d \bullet \left(\vec{q}_d C_d\right) = \nabla_d \bullet \left(\Phi_d \nabla_d C_d\right) \qquad \text{(Eq. C.2-15)}$$

because $\nabla_d \bullet \vec{q}_d = 0$ (see Equation (C.1-7))

Starting from Eq. C.1-6 and combining with Eq. C.1-14, C.2-12, C.2-11, C.2-14 and C.2-8, results in,

$$\vec{q}_d = -\nabla_d \Phi_d + 2\Phi_d \vec{k} \qquad \text{(Eq. C.2-16)}$$

Substituting Equation (C.2-16) into Equation (C.2-15) gives,

$$\nabla_d \bullet \left\{\left(-\nabla_d \Phi_d + 2\Phi_d \vec{k}\right) C_d\right\} = \nabla_d \bullet \left(\Phi_d \nabla_d C_d\right) \qquad \text{(Eq. C.2-17)}$$

or

$$\nabla_d \bullet \left(\Phi_d \nabla_d C_d + C_d \nabla_d \Phi_d\right) = 2\frac{\partial\left(\Phi_d C_d\right)}{\partial \xi} \qquad \text{(Eq. C.2-18)}$$

and finally,

$$\nabla_d^2 \left(\Phi_d C_d\right) = 2\frac{\partial\left(\Phi_d C_d\right)}{\partial \xi} \qquad \text{(Eq. C.2-19)}$$

Therefore, the transport problem is now expressed in terms of the dimensionless scalar potential,

$$\Omega \equiv \Phi_d C_d \qquad \text{(Eq. C.2-20)}$$

Equation (C.2-19) becomes,

$$\nabla_d^2 \Omega = 2\frac{\partial \Omega}{\partial \xi} \qquad \text{(Eq. C.2-21)}$$

The boundary conditions, Equations (C.2-2) through (C.2-5) become,

$$-\frac{\partial \Phi}{\partial z}(x,0) C(x,0) + \frac{2\Phi(x,0)}{\ell_s} C(x,0) - \Phi(x,0)\frac{\partial C(x,0)}{\partial z} = \dot{M}_s H\left(x_{s1} + x_1 - x\right) H\left(x - x_1\right)$$

(Eq. C.2-22)

or

$$-\frac{\partial \Phi_d}{\partial \xi}(\eta,0)C_d(\eta,0)+2\Phi_d(\eta,0)C_d(\eta,0)-\Phi_d(\eta,0)\frac{\partial C_d(\eta,0)}{\partial \xi}=H(\eta_{s1}+\eta_1-\eta)H(\eta-\eta_1)$$

(Eq. C.2-23)

or

$$2\Omega(\eta,0)-\frac{\partial \Omega(\eta,0)}{\partial \xi}=H(\eta_{s1}+\eta_1-\eta)H(\eta-\eta_1) \quad \text{(Eq. C.2-24)}$$

$$\frac{\partial \Omega}{\partial \xi}(\eta,\omega)=0 \quad \text{(Eq. C.2-25)}$$

$$\frac{\partial \Omega}{\partial \eta}(0,\xi)=0 \quad \text{(Eq. C.2-26)}$$

$$\frac{\partial \Omega}{\partial \eta}(\sigma,\xi)=0 \quad \text{(Eq. C.2-27)}$$

Using the transformation

$$\Theta=\Omega\exp(-\xi)=\chi C_d \quad \text{(Eq. C.2-28)}$$

Equation (C.2-21) transforms to the Helmholz equation,

$$\nabla_d^2\Theta=\Theta \quad \text{(Eq. C.2-29)}$$

and boundary conditions (C.2-22) through (C.2-25) become,

$$\Theta(\eta,0)-\frac{\partial \Theta}{\partial \xi}(\eta,0)=H(\eta_{s1}+\eta_1-\eta)H(\eta-\eta_1) \quad \text{(Eq. C.2-30)}$$

$$\frac{\partial \Theta}{\partial \xi}(\eta,\omega)+\Theta(\eta,\omega)=0 \quad \text{(Eq. C.2-31)}$$

$$\frac{\partial \Theta}{\partial \eta}(0,\xi)=0 \quad \text{(Eq. C.2-32)}$$

$$\frac{\partial \Theta}{\partial \eta}(\sigma,\xi)=0 \quad \text{(Eq. C.2-33)}$$

The problem given in Equations (C.2-29) through (C.2-33) is the same as for the dimensionless flow potential with $q_{s2}=0$ (Equations (C.1-37) and (C.1-41) through (C.1-44)). Therefore, the solution may be obtained from Equation (C.1-72) to give,

$$\Theta(\eta,\xi)=\sum_{\ell=0}^{\infty}\frac{2\left[\sin\{\lambda_\ell(\eta_{s1}+\eta_1)\}-\sin(\lambda_\ell\eta_1)\right]}{(1+2H(-\ell))\lambda_\ell\sigma}\cos(\lambda_\ell\eta)\frac{\Lambda_\ell\cosh\{\Lambda_\ell(\omega-\xi)\}+\sinh\{\Lambda_\ell(\omega-\xi)\}}{2\Lambda_\ell\cosh(\Lambda_\ell\omega)+(\Lambda_\ell^2+1)\sinh(\Lambda_\ell\omega)}$$

(Eq. C.2-34)

From the flow solution,

$$\chi(\eta,\xi)=\sum_{\ell=0}^{\infty}\frac{2\left[\sin[\lambda_\ell(\eta_{s1}+\eta_1)]-\sin(\lambda_\ell\eta_1)+\frac{q_{s2}}{q_{s1}}\{\sin[\lambda_\ell(\eta_{s2}+\eta_2)]-\sin(\lambda_\ell\eta_2)\}\right]}{(1+2H(-\ell))\lambda_\ell\sigma}\cos(\lambda_\ell\eta)\bullet$$
$$\frac{\Lambda_\ell\cosh\{\Lambda_\ell(\omega-\xi)\}+\sinh\{\Lambda_\ell(\omega-\xi)\}}{2\Lambda_\ell\cosh(\Lambda_\ell\omega)+(\Lambda_\ell^2+1)\sinh(\Lambda_\ell\omega)}$$

(Eq. C.2-35)

and,

$$C_d(\eta,\xi)=\frac{\Theta(\eta,\xi)}{\chi(\eta,\xi)}$$ (Eq. C.2-36)

For computational purposes, the following forms are more convenient,

$$\Theta(\eta,\xi)=\sum_{\ell=0}^{\infty}\frac{2\left[\sin\{\lambda_\ell(\eta_{s1}+\eta_1)\}-\sin(\lambda_\ell\eta_1)\right]}{(1+2H(-\ell))\lambda_\ell\sigma}\cos(\lambda_\ell\eta)\bullet$$
$$\exp(-\Lambda_\ell\xi)\frac{(\Lambda_\ell+1)+(\Lambda_\ell-1)\exp\{-2\Lambda_\ell(\omega-\xi)\}}{(\Lambda_\ell+1)^2-(\Lambda_\ell-1)^2\exp(-2\Lambda_\ell\omega)}$$ (Eq. C.2-37)

$$\chi(\eta,\xi)=\sum_{\ell=0}^{\infty}\frac{2\left[\sin[\lambda_\ell(\eta_{s1}+\eta_1)]-\sin(\lambda_\ell\eta_1)+\frac{q_{s2}}{q_{s1}}\{\sin[\lambda_\ell(\eta_{s2}+\eta_2)]-\sin(\lambda_\ell\eta_2)\}\right]}{(1+2H(-\ell))\lambda_\ell\sigma}\cos(\lambda_\ell\eta)\bullet$$
$$\exp(-\Lambda_\ell\xi)\frac{(\Lambda_\ell+1)+(\Lambda_\ell-1)\exp\{-2\Lambda_\ell(\omega-\xi)\}}{(\Lambda_\ell+1)^2-(\Lambda_\ell-1)^2\exp(-2\Lambda_\ell\omega)}$$

(Eq. C.2-38)

APPENDIX D

RELATIONSHIP BETWEEN THE KIRCHHOFF POTENTIAL AND THE DISPERSION COEFFICIENT

INTENTIONALLY LEFT BLANK

Longitudinal dispersion in unsaturated flow systems has been measured under conditions of uniform, one-dimensional, unsaturated flow (Toride et al. 2003 [DIRS 176906]). Hydraulic parameters for the granular media were based on the measured moisture potential as a function of water content fit with the (van Genuchten 1980 [DIRS 100610]) parameterization. The following hydraulic parameters were determined for the test system:

Table D-1. Hydrologic Parameters

Parameter	Value	Units
Maximum water content	0.35	na
Residual water content	0.05	na
van Genuchten *m*	0.808	na
van Genuchten α_{vG}	5	m^{-1}
Saturated hydraulic conductivity	6.37×10^{-05}	m/s

Source: Toride et al. 2003 [DIRS 176906].

The effective permeability and capillary pressures were computed from Toride's data for water content (θ) and the van Genuchten parameters given in Toride's Figure 1, using the van Genuchten equations and are plotted in Figure D-1 (DTN: MO0609SPAINOUT.002, File *Dispersion and Kirchhoff Potential_final.xls)*. Using the van Genuchten (1980 [DIRS 100610]) parameterizations for moisture potential and relative hydraulic conductivity, the relationship between relative hydraulic conductivity and moisture potential were fit to the same version of the Gardner exponential form (Bear 1972 [DIRS 156269], page 492) that was used in Appendix C (Eq. C.1-18),

$$K(\psi) = K_0 \exp\{\alpha(\psi - \psi_0)\} \qquad \text{(Eq. D-1)}$$

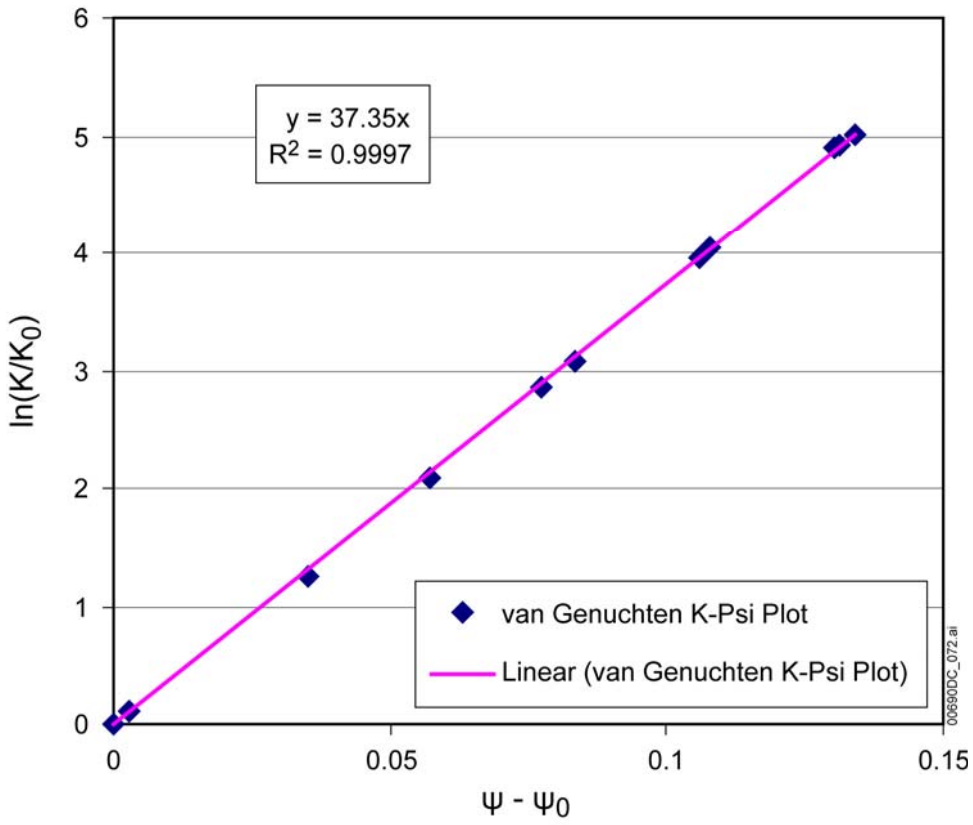

Source: DTN: MO0609SPAINOUT.002, File *Dispersion and Kirchhoff Potential_final.xls*

Figure D-1. Permeability – Water Pressure Plot

The fit of the Gardner equation to the van Genuchten properties in Figure D-1 (slope = 37.4 m^{-1}) gives the Gardner parameter, α, which may also be expressed as the sorptive length scale, $\ell_s = 2/\alpha$, as given in Table D-2.

Table D-2. Best Fit Gardner Parameters

Parameter	Value	Units
Gardner α	37.4	m^{-1}
Sorptive length	0.0535	m

The Kirchhoff potential is given by (see Equation (C.1-25)),

$$\Phi = \frac{\ell_s}{2} K \qquad \text{(Eq. D-2)}$$

which is dimensionally a diffusion or dispersion coefficient. A comparison of the magnitude of the Kirchhoff potential versus the measured longitudinal dispersion multiplied times the water content is given in Figure D-2 versus water pressure and in Figure D-3 versus water saturation. The saturation (S) in Figure D-3 is θ/θ_{max}, where θ_{max}=0.35 (Toride 2003 [DIRS 176906], caption of Figure 1) and θ is given in (Toride 2003 [DIRS 176906], Table 2). The capillary

pressure, ψ, was computed using the θ and the van Genuchten parameters given in (Toride 2003 [DIRS 176906], Figure 1). Lateral dispersion was estimated simply by reducing the measured longitudinal dispersion by a factor of 10 (de Marsily 1986 [DIRS 100439], p. 238).

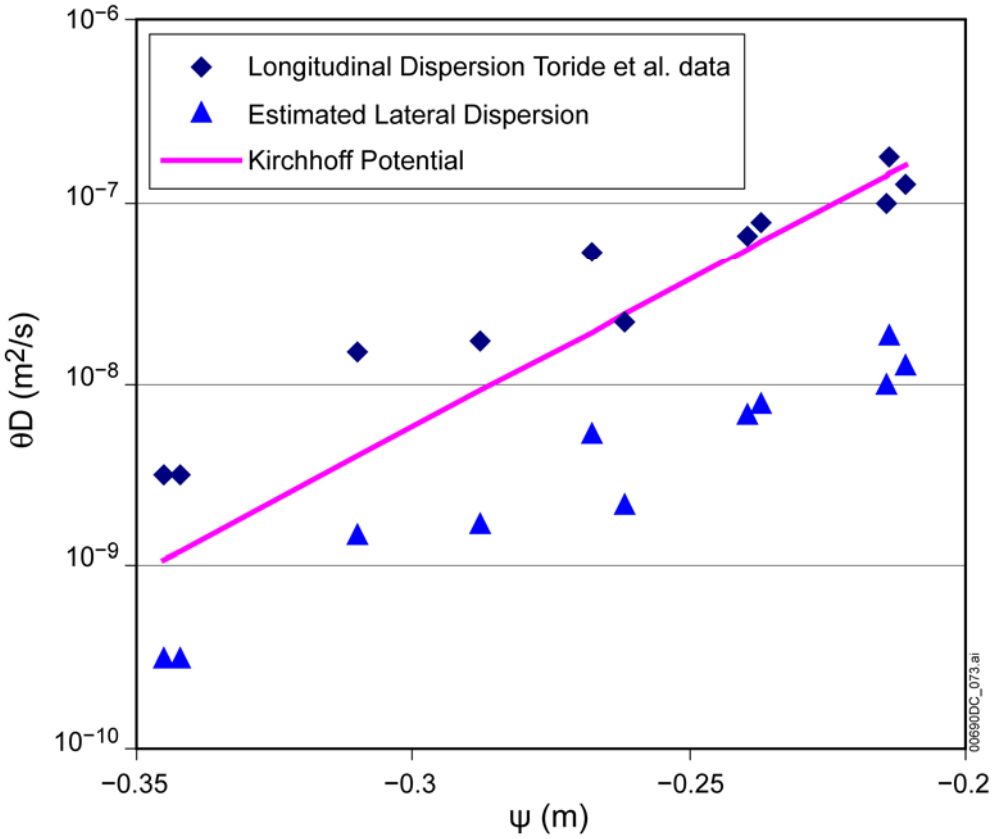

Source: DTN: MO0609SPAINOUT.002, File *Dispersion and Kirchhoff Potential_final.xls*

Figure D-2. Comparison of Kirchhoff Potential with Dispersion as a Function of Water Pressure

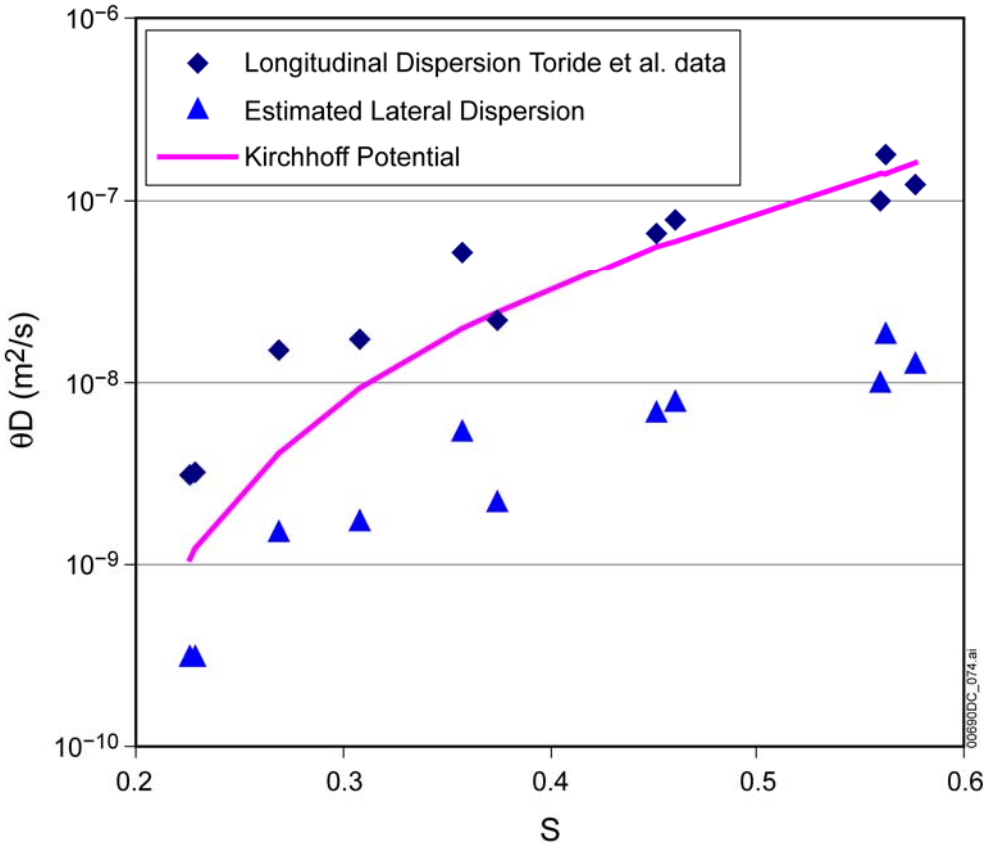

Source: DTN: MO0609SPAINOUT.002, File *Dispersion and Kirchhoff Potential_final.xls*

Figure D-3. Comparison of Kirchhoff Potential with Dispersion as a Function of Water Saturation

Figures D-2 and D-3 show that the Kirchhoff potential provides a reasonable estimate for the longitudinal dispersion as a function of hydrologic conditions and is likely to overestimate lateral dispersion (although no data for lateral dispersion were available). Also, note that data for dispersion under more complex unsaturated flow patterns are not available so that dispersion under these conditions remains uncertain.

APPENDIX E

RELATIONSHIPS FOR INVERT POROSITY AND SATURATION

INTENTIONALLY LEFT BLANK

The total pore volume of the invert consists of two kinds of pore volume: within particles (matrix pore volume) and between particles (fracture or intergranular pore volume). The total porosity, ϕ_T, is defined as the total pore volume divided by the bulk volume, i.e.,

$$\phi_T = \frac{V_p}{V_b} \quad \text{(Eq. E-1)}$$

where V_p is the total pore volume and V_b is the bulk volume. The bulk volume includes particles, the pore space within particles, and the pore space between particles. The intergranular (or "fracture") porosity, ϕ_f, is defined as the fracture pore volume divided by the bulk volume, i.e.,

$$\phi_f = \frac{V_{fp}}{V_b} \quad \text{(Eq. E-2)}$$

where V_{fp} is the fracture pore volume. The intrinsic intragranular (or "matrix") porosity, ϕ_m, of the tuff grains is defined as the matrix pore volume divided by the bulk volume of the matrix, i.e.,

$$\phi_m = \frac{V_{mp}}{V_{mb}} \quad \text{(Eq. E-3)}$$

where V_{mp} is the matrix pore volume and V_{mb} is the bulk volume of the matrix. Note that

$$V_p = V_{fp} + V_{mp} \quad \text{(Eq. E-4)}$$

$$V_b = V_{fp} + V_{mb} \quad \text{(Eq. E-5)}$$

Dividing Equation (E-4) by the bulk volume, V_b, and using the definitions in Equations E-1 and (E-2) gives,

$$\phi_T = \phi_f + \frac{V_{mp}}{V_{mb}}\frac{V_{mb}}{V_b} \quad \text{(Eq. E-6)}$$

Solving Equation (E-5) for V_{mb} and using the definitions in Equations E-1 and E-3 gives,

$$\phi_T = \phi_f + \phi_m\left(1-\phi_f\right) \quad \text{(Eq. E-7)}$$

The total water content, θ_T, is defined to be the total water volume, V_w, divided by the bulk volume, i.e.,

$$\theta_T = \frac{V_w}{V_b} \quad \text{(Eq. E-8)}$$

The intergranular (or "fracture") water content is defined to be the water volume in the intergranular pore space, V_{fw}, divided by the bulk volume, i.e.,

$$\theta_f = \frac{V_{fw}}{V_b} \quad \text{(Eq. E-9)}$$

The intrinsic intragranular (or "matrix") water content is defined to be the water volume in the intragranular pore space, V_{mw}, divided by the bulk volume of the matrix, i.e.,

$$\theta_m = \frac{V_{mw}}{V_{mb}} \quad \text{(Eq. E-10)}$$

The total water saturation is defined to be the total water volume divided by the total pore volume, i.e.,

$$S_T = \frac{V_w}{V_p} = \frac{\theta_T}{\phi_T} \quad \text{(Eq. E-11)}$$

The fracture water saturation is defined to be the fracture water volume divided by the fracture pore volume, i.e.,

$$S_f = \frac{V_{fw}}{V_{fp}} = \frac{\theta_f}{\phi_f} \quad \text{(Eq. E-12)}$$

The matrix water saturation is defined to be the matrix water volume divided by the matrix pore volume, i.e.,

$$S_m = \frac{V_{mw}}{V_{mp}} = \frac{\theta_m}{\phi_m} \quad \text{(Eq. E-13)}$$

Note that

$$V_w = V_{fw} + V_{mw} \quad \text{(Eq. E-14)}$$

Dividing Equation E-14 by the bulk volume and using definitions in Equations E-8 and E-9 gives,

$$\theta_T = \theta_f + \frac{V_{mw}}{V_{mb}} \frac{V_{mb}}{V_b} \quad \text{(Eq. E-15)}$$

Solving Equation E-5 for V_{mb} and using the definitions in Equations E-1 and E-10 gives,

$$\theta_T = \theta_f + \theta_m \left(1 - \phi_f\right) \quad \text{(Eq. E-16)}$$

Using the definitions for fracture and matrix water contents in Equations E-12 and E-13 gives,

$$\theta_T = S_f \phi_f + S_m \phi_m \left(1 - \phi_f\right) \quad \text{(Eq. E-17)}$$

and from Equation E-11, the total water saturation, S_T, is

$$S_T = \frac{\theta_T}{\phi_T} = \frac{S_f \phi_f + S_m \phi_m \left(1 - \phi_f\right)}{\phi_f + \phi_m \left(1 - \phi_f\right)} \quad \text{(Eq. E-18)}$$

INTENTIONALLY LEFT BLANK

APPENDIX F

PROPERTIES FOR THE WELL-SORTED INVERT

INTENTIONALLY LEFT BLANK

The well-sorted invert is characterized in the Multiscale Thermohydrologic Model (BSC 2005 [DIRS 173944], Appendix X; DTN: MO0307SPAVGSUM.000 [DIRS 164438]). Four cases were presented, having uniform grain diameters of 0.317 mm, 3 mm, 10 mm, and 20 mm. The 3 mm grain-size case is considered the base case (BSC 2005 [DIRS 173944], Section 6.3.11) and is the only one analyzed here. This invert is composed of crushed tuff from the Topopah Spring lower lithophysal unit (TLL). The intergranular porosity of the invert is 0.45 (BSC 2005 [DIRS 173944], p. IV-3), referred to as "Saturated Volumetric Moisture Content" in DTN: MO0307SPAVGSUM.000 [DIRS 164438] and the intrinsic intragranular porosity is 0.131 (DTN LB0208UZDSPMI.002, [DIRS 161243], File: *drift-scale calibrated properties for mean infiltration2.xls*; worksheet: Drift-scale Cal. Hydro Props). The saturated intergranular permeability of the invert is 1.51×10^{-8} m^2. The van Genuchten parameters capillary strength parameter (defined in Eq. 7.2.5-2), $\alpha_{vG} = 61.2$ m^{-1} and the pore size distribution index, $m = 0.875$.

The Gardner parameter is fit to the van Genuchten model over the applicable range of effective hydraulic conductivity for the cases described in Section 6.4.6. For Case 1, the maximum flux is 2000 mm/yr and the lower rate source is 9.8 mm/yr. The flux is approximately the same as K for all cases investigated, since flow is downward flow and the distance to the water table is large (Jury 1991 [DIRS 102010], p. 100). A range of flux from about 2000 mm/yr down to 2 mm/yr were chosen for the fit to the van Genuchten relationship (see Table F-1). The values of ψ and K in Table F-1 were calculated using the van Genuchten equation. S_n is the normalized saturation and is defined in Eq. 7.2.5-3. For cases 2 and 3, the maximum flux is 9800 mm/yr and the lower rates fluxes are 2000 and 66 mm/yr for Cases 2 and 3, respectively. Therefore, the same range from about 10000 mm/yr down to 10 mm/yr was used for Cases 2 and 3 (see Table F-2). Curve fits to establish the Gardner α (defined in Eq. 7.2.5-4) for Case 1 and Cases 2 and 3 are shown in Figures F-1 and F-2, respectively. The form of the Gardner equation used for the curve fitting is provided in Eq. C.1-18.

Table F-1. van Genuchten Values for Well-Sorted Invert, Case 1

S	S_n	ψ (m)	K (mm/yr)
0.0857	0.000	−4.93E-02	1.57E+00
0.086	0.001	−4.55E-02	7.46E+00
0.087	0.002	−4.01E-02	8.84E+01
0.088	0.003	−3.75E-02	3.21E+02
0.089	0.004	−3.59E-02	7.72E+02
0.09	0.005	−3.47E-02	1.50E+03

Table F-2. van Genuchten Values for Well-Sorted Invert, Cases 2 and 3

S	S_n	ψ (m)	K mm/yr
0.086	0.001	−4.55E-02	7.46E+00
0.087	0.002	−4.01E-02	8.84E+01
0.088	0.003	−3.75E-02	3.21E+02
0.089	0.004	−3.59E-02	7.72E+02
0.09	0.005	−3.47E-02	1.50E+03
0.091	0.006	−3.37E-02	2.57E+03
0.092	0.007	−3.30E-02	4.04E+03
0.093	0.008	−3.23E-02	5.95E+03
0.094	0.010	−3.17E-02	8.36E+03
0.095	0.011	−3.13E-02	1.13E+04

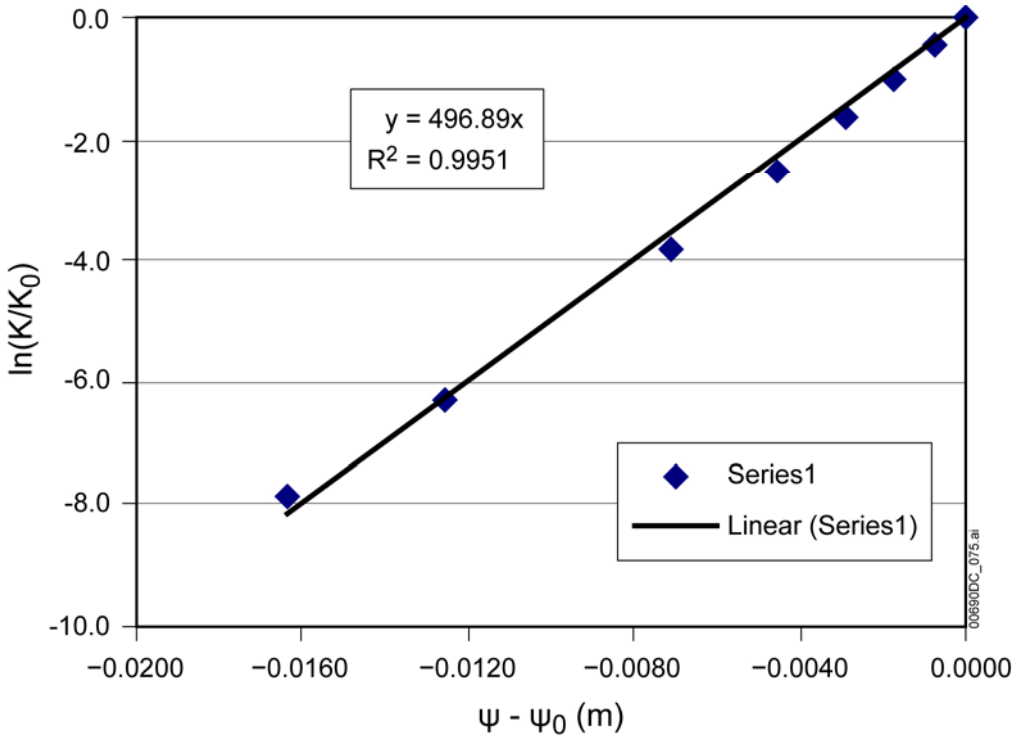

Figure F-1. Permeability – Water Pressure Plot for Well-Sorted Invert, Case 1

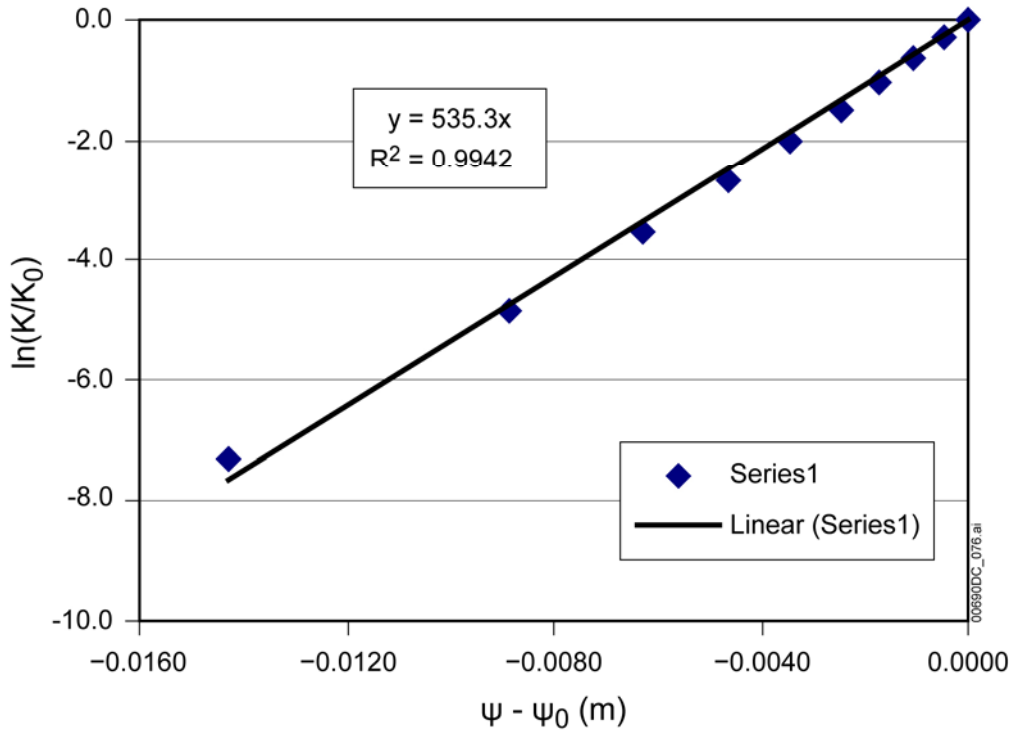

Figure F-2. Permeability – Water Pressure Plot for Well-Sorted Invert, Cases 2 and 3

INTENTIONALLY LEFT BLANK

APPENDIX G

PROPERTIES FOR THE POORLY SORTED INVERT

INTENTIONALLY LEFT BLANK

The intergranular porosity of the poorly-sorted invert must be evaluated from the total porosity of the invert, 0.31 (Table 4-15), and the intragranular porosity. The intergranular porosity of the invert may be computed from Equation (E-7) of Appendix E by solving for ϕ_f. Rock used to establish the porosity of crushed tuff was obtained from tunnel boring machine cuttings from the repository horizon of the Exploratory Studies Facility (BSC 2004 [DIRS 168138], Sections 7.1 and 7.8; (Gertsch et al. 1993 [DIRS 107880], Section 8). The main lithology excavated by the tunnel boring machine in the repository horizon was the tsw middle nonlithophysal unit (TMN). The value of ϕ_m for the TMN is 0.111 (BSC 2004 [DIRS 170038], Table 6-6, DTN: LB0207REVUZPRP.002 [DIRS 159672]). The resulting intergranular porosity is 0.224. The saturated intergranular permeability of the invert is 1.33×10^{-10} m^2, which is equivalent to the average saturated hydraulic conductivity of 0.13 cm/s (Table 4-15) reported in (BSC 2004 [DIRS 168138], Section 7.14).

Residual water saturations were determined from centrifuge experiments using TMN crushed tuff , DTN: GS980808312242.015 [DIRS 119916]; Hudson, D.B., (2000 [DIRS 176907, pp. 42A through 44A); and BSC 2004 [DIRS 169734], Section 7.2.2.2.5). For all cases, the residual saturation as determined from centrifuge tests are evaluated using Equation (E-17) from Appendix E. The total residual water content from the centrifuge experiments has been determined to be about 0.05. The matrix residual saturation for the TMN is 0.19 as given in (BSC 2004 DIRS [170038], Table 6-6, DTN: LB0207REVUZPRP.002 [DIRS 159672]). The residual water saturation may then be computed and is found to be 0.150. This is based on the assumption that both the intergranular and intragranular porosities attain residual saturation in the centrifuge experiments.

The van Genuchten properties were fit to the water pressure curve given in Table G-1 using the van Genuchten expression for water pressure to predict normalized water saturation for the given water pressures in the estimated curve. The differences in the expected water content and the van Genuchten water content were minimized using the Excel function "Solver" through adjusting the van Genuchten parameters α_{vG} and m as shown in Table G-2 and Figure G-1. The parameters used in the minimization and the results of the minimization are given here:

Table G-1. Estimated Water Pressure (Absolute Value) as a Function of Water Content

ψ (m)	Water Content	Normalized Water Content
9.767E+01	3.934E-02	3.000E-02
2.923E+01	4.314E-02	5.000E-02
9.266E+00	4.695E-02	7.000E-02
3.650E+00	5.265E-02	1.000E-01
1.157E+00	5.836E-02	1.300E-01
4.139E-01	7.167E-02	2.000E-01
1.467E-01	8.118E-02	2.500E-01
5.268E-02	1.040E-01	3.700E-01
1.707E-02	1.306E-01	5.100E-01
6.770E-03	1.725E-01	7.300E-01
2.170E-04	2.238E-01	1.000E+00

Table G-2. Fit of Water Pressure Data to van Genuchten Equation 7.2.5-2

van Genuchten α (m^{-1})	3.33E+02		
van Genuchten m	2.55E-01		
Sum of Residuals Squared	8.14E-05		
Retention Analysis Results			
Volumetric Moisture Content[1]	Moisture Potential (m)	Predicted Moisture Content[2]	Residuals Squared
3.93E-02	9.77E+01	3.91E-02	7.62E-08
4.31E-02	2.92E+01	4.18E-02	1.70E-06
4.69E-02	9.27E+00	4.58E-02	1.34E-06
5.27E-02	3.65E+00	5.04E-02	5.27E-06
5.84E-02	1.16E+00	5.84E-02	2.79E-09
7.17E-02	4.14E-01	6.89E-02	7.96E-06
8.12E-02	1.47E-01	8.38E-02	6.91E-06
1.04E-01	5.27E-02	1.05E-01	3.37E-07
1.31E-01	1.71E-02	1.36E-01	2.98E-05
1.72E-01	6.77E-03	1.67E-01	2.61E-05
2.24E-01	2.17E-04	2.22E-01	1.96E-06

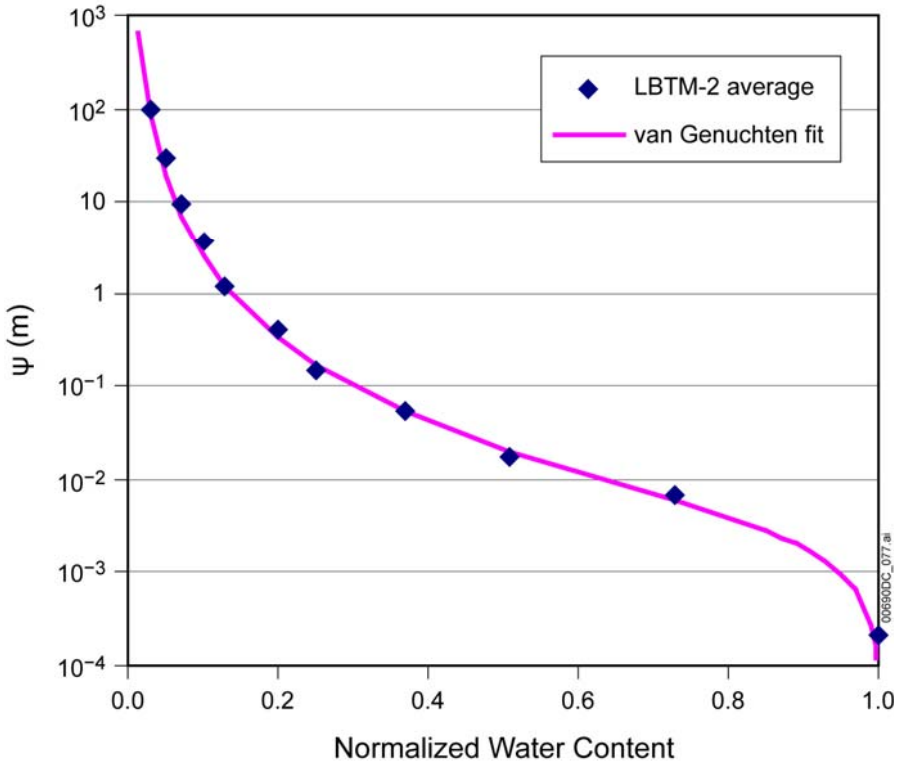

Figure G-1. Fit of van Genuchten Equation 7.2.5-2 to Water Pressure Data

The van Genuchten parameter capillary strength parameter is $\alpha_{vG} = 333.2\ \mathrm{m}^{-1}$ and the pore size distribution index is $m = 0.255$.

The Gardner parameter is fit to the van Genuchten model over the applicable range of effective hydraulic conductivity for the problem investigated. For Case 1, the maximum flux is 2000 mm/yr and the lower rate source is 9.8 mm/yr. Therefore a range of about 2000 mm/yr down to 2 mm/yr were chosen for the fit to the van Genuchten relationship as shown in Table G-3. For cases 2 and 3, the maximum flux is 9800 mm/yr and the lower rates fluxes are 2000 and 66 mm/yr for Cases 2 and 3, respectively. Therefore, the same range from about 10000 mm/yr down to 10 mm/yr was used for Cases 2 and 3 as shown in Table G-4. Curve fits to establish the Gardner α for Case 1 and Cases 2 and 3 are shown in Figures G-2 and G-3, respectively.

Table G-3. van Genuchten Values for Poorly Sorted Invert, Case 1

S	S_n	ψ (m)	K (mm/yr)
3.032E-01	1.800E-01	−4.496E-01	1.632E+00
3.117E-01	1.900E-01	−3.838E-01	2.563E+00
3.202E-01	2.000E-01	−3.303E-01	3.933E+00
3.287E-01	2.100E-01	−2.864E-01	5.911E+00
3.372E-01	2.200E-01	−2.499E-01	8.717E+00
3.457E-01	2.300E-01	−2.194E-01	1.264E+01
3.542E-01	2.400E-01	−1.936E-01	1.803E+01
3.627E-01	2.500E-01	−1.718E-01	2.536E+01
3.712E-01	2.600E-01	−1.531E-01	3.520E+01
3.797E-01	2.700E-01	−1.370E-01	4.825E+01
3.882E-01	2.800E-01	−1.231E-01	6.540E+01
3.967E-01	2.900E-01	−1.111E-01	8.771E+01
4.052E-01	3.000E-01	−1.005E-01	1.165E+02
4.137E-01	3.100E-01	−9.123E-02	1.533E+02
4.222E-01	3.200E-01	−8.307E-02	2.000E+02
4.307E-01	3.300E-01	−7.584E-02	2.588E+02
4.392E-01	3.400E-01	−6.942E-02	3.324E+02
4.477E-01	3.500E-01	−6.370E-02	4.239E+02
4.562E-01	3.600E-01	−5.858E-02	5.370E+02
4.647E-01	3.700E-01	−5.399E-02	6.760E+02
4.731E-01	3.800E-01	−4.986E-02	8.459E+02
4.816E-01	3.900E-01	−4.613E-02	1.052E+03
4.901E-01	4.000E-01	−4.275E-02	1.303E+03
4.986E-01	4.100E-01	−3.969E-02	1.604E+03
5.071E-01	4.200E-01	−3.691E-02	1.966E+03
5.156E-01	4.300E-01	−3.437E-02	2.398E+03

Table G-4. van Genuchten Values for Poorly Sorted Invert, Cases 2 and 3

S	S_n	ψ (m)	K (mm/yr)
3.372E-01	2.200E-01	−2.499E-01	8.717E+00
3.457E-01	2.300E-01	−2.194E-01	1.264E+01
3.542E-01	2.400E-01	−1.936E-01	1.803E+01
3.627E-01	2.500E-01	−1.718E-01	2.536E+01
3.712E-01	2.600E-01	−1.531E-01	3.520E+01
3.797E-01	2.700E-01	−1.370E-01	4.825E+01
3.882E-01	2.800E-01	−1.231E-01	6.540E+01
3.967E-01	2.900E-01	−1.111E-01	8.771E+01
4.052E-01	3.000E-01	−1.005E-01	1.165E+02
4.137E-01	3.100E-01	−9.123E-02	1.533E+02
4.222E-01	3.200E-01	−8.307E-02	2.000E+02
4.307E-01	3.300E-01	−7.584E-02	2.588E+02
4.392E-01	3.400E-01	−6.942E-02	3.324E+02
4.477E-01	3.500E-01	−6.370E-02	4.239E+02
4.562E-01	3.600E-01	−5.858E-02	5.370E+02
4.647E-01	3.700E-01	−5.399E-02	6.760E+02
4.731E-01	3.800E-01	−4.986E-02	8.459E+02
4.816E-01	3.900E-01	−4.613E-02	1.052E+03
4.901E-01	4.000E-01	−4.275E-02	1.303E+03
4.986E-01	4.100E-01	−3.969E-02	1.604E+03
5.071E-01	4.200E-01	−3.691E-02	1.966E+03
5.156E-01	4.300E-01	−3.437E-02	2.398E+03
5.241E-01	4.400E-01	−3.205E-02	2.913E+03
5.326E-01	4.500E-01	−2.993E-02	3.524E+03
5.411E-01	4.600E-01	−2.798E-02	4.246E+03
5.496E-01	4.700E-01	−2.619E-02	5.097E+03
5.581E-01	4.800E-01	−2.454E-02	6.097E+03
5.666E-01	4.900E-01	−2.302E-02	7.268E+03
5.751E-01	5.000E-01	−2.162E-02	8.636E+03
5.836E-01	5.100E-01	−2.031E-02	1.023E+04

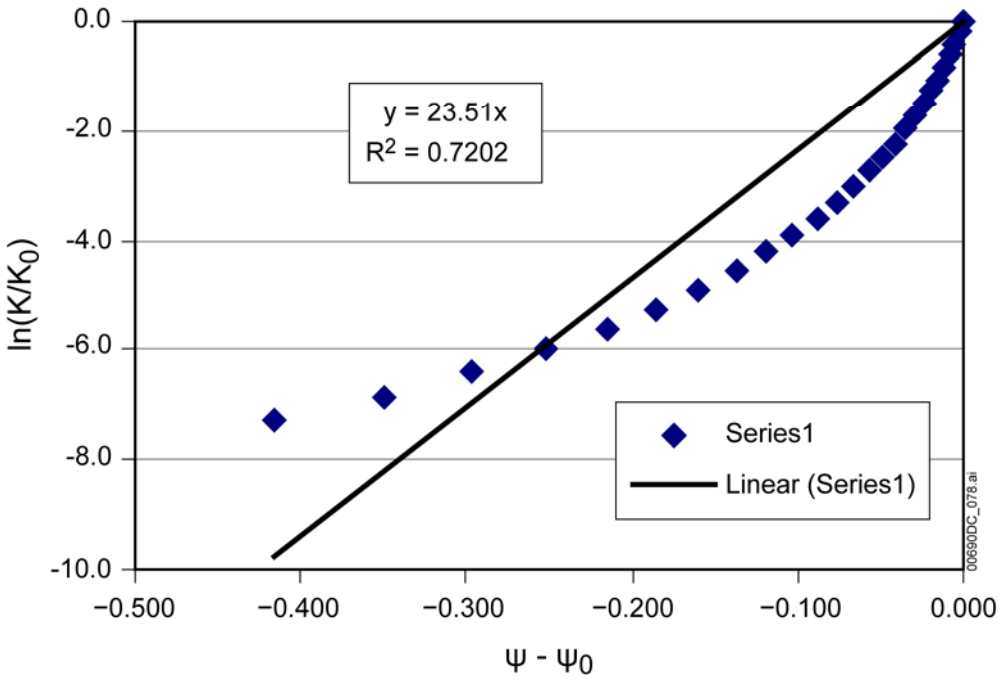

Figure G-2. Permeability – Water Pressure Plot for Poorly Sorted Invert, Case 1

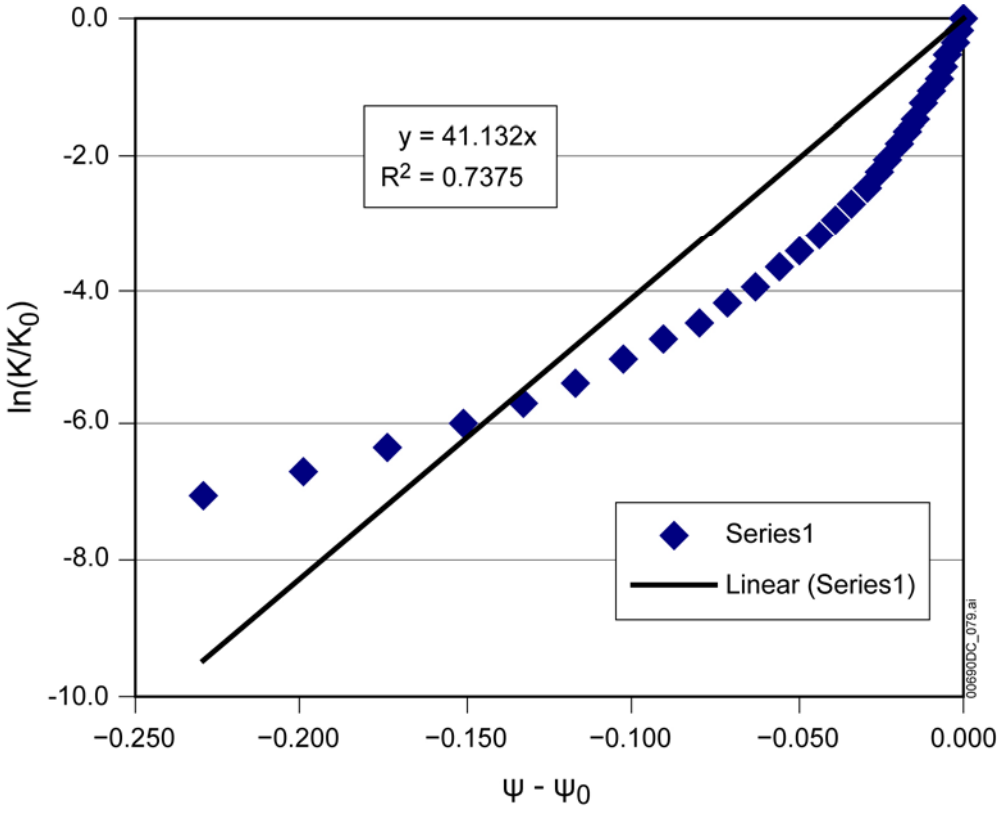

Figure G-3. Permeability – Water Pressure Plot for Poorly Sorted Invert, Cases 2 and 3

The maximum water saturation of the intergranular pores is about 0.6 for the cases considered in the criticality analyses for the poorly-sorted invert. This maximum saturation corresponds to a maximum flow rate of about 1000 liters per year into a footprint of about 1000 cm^2, or about 10,000 mm/year (see Table 6-7). This flux is compared with the effective hydraulic conductivity as a function of saturation. Although the saturated hydraulic conductivity for the invert is about 4×10^7 mm/yr, the normalized saturation needs to be about 0.51 to achieve a hydraulic conductivity of 10,000 mm/yr (see Table G-4). A normalized saturation of 0.51 corresponds to a physical saturation of about 0.584, given a residual saturation of 0.150. This high saturation is due to the strongly nonlinear effective hydraulic conductivity – saturation relationship, which is characteristic of the poorly sorted invert (and is substantially different than the well-sorted invert used in the current multiscale model).

Under flowing conditions, the water content of the intragranular pores is taken to be equal to the porosity, i.e., a water saturation of 1. The same intrinsic intragranular porosity, 0.131, as for the well-sorted invert (see Appendix F) is used here. This is the average matrix porosity of the Topopah Spring lower lithophysal (TLL) (BSC 2004 [DIRS 170038], Table 6-6) and accounts for more than 80% of the material expected to be excavated for waste emplacement drifts 800-IED-WIS0-01801-000-00A, (BSC 2005 [DIRS 176908]).

Therefore the range in total water saturation may be computed using Equation (E-18) from Appendix E to give,

$$S_{T,\min} = \frac{S_{fr}\phi_f + S_{m,\max}\phi_m\left(1-\phi_f\right)}{\phi_f + \phi_m\left(1-\phi_f\right)} = 0.42$$

$$S_{T,\max} = \frac{S_{f,\max}\phi_f + S_{m,\max}\phi_m\left(1-\phi_f\right)}{\phi_f + \phi_m\left(1-\phi_f\right)} = 0.71$$

Based on this range of saturation values, a representative total water saturation of 0.6 is appropriate for use in the criticality geochemical model.

APPENDIX H

INDEPENDENT TECHNICAL REVIEW

INTENTIONALLY LEFT BLANK

LAWRENCE LIVERMORE NATIONAL LABORATORY

P.O. Box 808, L-631
(925) 422-5789

LLYMP0607027
July 27, 2006

To: Susan LeStrange, Ernest Hardin
From: Tom Wolery (LLNL)
Subject: Independent Technical Review of ANL-EBS-GS-000002 REV 01

This memorandum was written pursuant to *Technical Work Plan for External Accumulation for Criticality Evaluations*, TWP-MGR-PA-000025 REV 03 (Section 2.2.1 and Appendix A, *Model Validation Technical Review*). It documents my independent technical review of *Geochemistry Model Validation Report: External Accumulation Model*, ANL-EBS-GS-000002 REV 01. Hereafter the Technical Work Plan (TWP-MGR-PA-000025 REV 03) will be referred to in places as the TWP; the report which is the subject of the present review (ANL-EBS-GS-000002 REV 01) will be variously referred to as the "Validation Report" or the AMR (Analysis/Model Report).

The stated purpose of ANL-EBS-GS-000002 REV 01 is (Technical Work Plan, p. 2);

> *To update, validate, and document the model for determining external accumulation of fissile material generated by a degrading waste package. The existing model (BSC 2001a), which covers accumulation in the fractured tuff, will be updated to include accumulation in the invert. The model will be used in the development of external configurations for use in criticality evaluations.*

The model approach and method is described as follows (TWP, p. 2):

> *The model estimates the quantity and geometry of accumulation of fissile and non-fissile isotopes and corrosion products in the invert (near-field) and the surrounding fractured tuff (far-field) external to the waste package.*

In actuality, the model is a complex of distinct models, most of which are developed and applied in other reports. Some of these models have themselves been individually validated and applied elsewhere. This Validation Report is intended to provide overall validation of the complex model, which includes previous results from some of the component models. The present report is somewhat constrained by this history, as its scope does not include modification of previous applications of components in response to present concerns. For example, the solid $Ni(OH)_2$ was suppressed in PHREEQC calculations cited in the Validation Report. This suppression was based on an understanding of mineralogical occurrences; however, physical chemistry data (e.g., the Linke 1965 solubility handbook) indicate that this phase can form readily enough given the necessary pH and concentration of dissolved nickel. In modeling an engineered system, this solid should not have been suppressed (at least in the opinion of this reviewer). The Validation Report, however, was able to show (see the entry for $Ni(OH)_2$ in Table 6-8) that this suppression had no consequence, as $Ni(OH)_2$ would not have formed anyway due to undersaturation caused by incorporation of nickel into another solid.

The Technical Work Plan (Section 2.2.1, p. 5) addresses the requisite level of confidence for the Validation Report:

Page 2

Since analyses using this model will not be used directly in performance assessment calculations, preclosure nuclear safety related issues, or license application design activities, the appropriate level of confidence assigned to the validation of this model is Level I (i.e., the model is of limited or no importance to the calculation of mean annual dose or to other repository objectives).

The TWP (again Section 2.2.1, p. 5) calls for application of four validation methods, each with a different scope:

...Method A, is an independent model validation technical review that reviews the entire model. This is appropriate because the model is an integrated approach that represents complex phenomenology and is only partly supported by laboratory testing and other analogues. The remaining validation activities address portions of the model.

Method B compares the PHREEQC results of the model to the minerals observed in natural analogues and laboratory experiments.

Method C uses the PHREEQC external accumulation model to predict the accumulation of uranyl minerals observed in UO_2 degradation drip tests.

[Method D] ... the TOUGHREACT-based model used to calculate the geometry in the invert is validated with an alternate model...

The scope of Method A (the present independent technical review) includes addressing Methods B, C, and D.

The TWP defined the following validation criteria for Methods B, C, and D (it also defined criteria for Method A itself; these will be addressed later in the present memo as I have elected to keep all the TWP Appendix A requirements and responses together):

Method B (Section 2.2.1, p. 6-7):

[1.] Are the types of minerals that form (such as clays and Fe-oxides) and the radionuclide-bearing phases that form in the model consistent with natural analogues or experimental work published in peer-reviewed or industrial literature, or both?

[2.] Before comparing the types of minerals formed in the analogues with the PHREEQC results, the following aspects of the analogue systems will be analyzed to identify differences in chemistry that could result in differences in minerals formed:

1. *Is the major and trace elemental chemistry (i.e., Si, Al, Na, K, Fe, Mg, Cr, V, Mn, Ba, P, rare earth elements) of the host rock and the invert in the model the same as with natural analogues or experimental work?*

2. *Are the major cations (Na^+, K^+, Ca^{2+}, Mg^{2+}) and anions (Cl^-, F^-, NO_3^-, SO_4^{2-}) of the water chemistry in the model the same as the natural analogues or experimental work?*

3. *Is the pH and alkalinity (HCO_3^-) of the model the same as with natural analogues or experimental work?*

4. *Are the partial pressures of CO_2 and O_2 used in the model similar to the natural analogues or experimental work?*

Page 3

The post model development activities are successful if (1) the mineral phases predicted by the model closely match the mineralogy observed in natural analogues or experiments; and (2) if the mineral phases do not match, then the differences can be explained by the aspects of the system listed above.

Method C (Section 2.2.1, p. 7-8):

1. The model should predict that U(VI) minerals accumulate over time and throughout the column. Predicting the exact same mineral assemblages observed in the drip tests is not required, because the total uranium accumulation is what is important to criticality.

2. The uranium release rate measured in the drip tests is the total uranium released from the sample, including the uranium that precipitated on the vessel but excluding the portion that reprecipitates on the UO_2-Zircaloy assembly. That is, it is the sum of the aqueous uranium and the solid-phase uranium in the leachate and on the bottom of the stainless steel reaction vessel. The solid phase includes secondary minerals and UO_2 particles that detach from the sample surfaces. Because the model neither simulates entrainment of solid particles nor spallation of UO_2 particles, the predicted aqueous release rates should not exceed the mean measured cumulative uranium release rates.

3. Only toward the end of the experiments between 8 and 10 years was leachate filtered to separate suspended uranium from aqueous uranium. These measurements determined that approximately 2% of the uranium released was in the filtered <5 nm size fraction (Wronkiewicz et al. 1996, p. 86). Experiments 3 and 6 were the only experiments that continued to 10 years with a flow rate (7.82 mL/yr) equal to the simulated flow rate (Wronkiewicz et al. 1996, Table 1). Therefore, the predicted aqueous uranium release rates should be approximately 2% (plus or minus a factor of 10) of the mean measured cumulative uranium release rates between 8 and 10 years for the experiments 3 and 6.

4. Predicted leachate pH should be within the range observed in the experiments.

5. Predicted leachate concentrations of Na, Ca, and Si should be within the ranges observed in the experiments. Other than OH^-, the components Na, Ca, and Si are the primary controls on U(VI) solubility in the experiments.

Method D (Section 2.2.1, p. 8):

[1.] The criterion used to demonstrate that the numerical model is sufficiently accurate is that for a given value of cumulative flux or relative concentration, the horizontal distance along the cross section of the invert calculated by the numerical model is within ±10 cm of the value calculated by the analytical model.

The Technical Work Plan (Appendix A) specified the following requirements for the qualifications of the independent model validation technical reviewer(s). A response or notation follows each requirement:

1. Reviewer shall not have contributed to the development, checking, and review of the model documentation.

This reviewer did not contribute to the development, checking, or review (in the 2.14 sense) of the Validation Report.

Page 4

2. *Reviewer shall have an appropriate technical background (i.e., advanced degree in an appropriate technical field) and demonstrated expertise in geochemistry, flow and transport in porous media.*

   The technical qualifications of this reviewer are documented in Section 7.2.2.1 (*Qualifications of Independent Technical Reviewer*) of the Validation Report.

3. *Qualifications and training of the reviewer shall be reviewed and approved by a memo from the Technical Work Plan Manager.*

   This reviewer has not seen the memo required in item (3). However, the fulfillment of this requirement need not be documented in the present review.

The Technical Work Plan (Appendix A) specified the following activities (*The independent model validation technical reviewer shall...)* for the present review. These activities follow the original numbering, here with "A" for activity preceding the number. A response follows each specified activity:

[A]1. *Review the validation criteria in this TWP to determine if they are adequate for intended use of the model.*

I find the validation criteria specified in the Technical Work Plan to be adequate for the intended use of the model. In making this finding, I considered the assigned level of confidence, Level I. If a higher level of confidence were required, I believe it would be necessary to tighten up validation criteria.

Specific validation criteria for Method A (independent technical review) are specified at the end of Appendix A in the TWP. They are also listed in Table 7-6 of the Validation Report as "acceptance criteria" for Method A (this table also includes the "acceptance criteria" for Methods A, B, and C which were identified in the TWP and previously in the present memo as the validation criteria for those methods). The Method A criteria will be reproduced later in the present memo along with corresponding specific findings of the present review. I found these criteria to be sufficiently encompassing and detailed in relation to the stated purpose and model approach and method and approach for this Validation Report. However, if the required level of confidence were to be raised to above Level I, I believe that tighter criteria would be appropriate.

The TWP provides specific validation criteria are given for Methods B, C, and D (also reproduced above in the present memo). The criteria for Method B (*compares the PHREEQC results of the model to the minerals observed in natural analogues and laboratory experiments)* appropriately focus on comparing computed and actual mineral assemblages. The criteria here appropriately require taking into account any differences in the chemistries of the modeled systems. I point out that the criteria do not require the computed models to provide a detailed match to the modeled systems. All models are approximations at one level or another. Given the required level of confidence and the intended use, I believe the present criteria are sufficient.

The criteria for Method C (uses the PHREEQC external accumulation model to predict the accumulation of uranyl minerals observed in UO_2 degradation drip tests) are similar in overall intent to those for Method C. The first criterion for this method is the most important: that the calculations make a reasonable prediction of the accumulation of uranium minerals, without requiring an exact match regarding the identities of the uranium minerals that precipitate. The second and third criteria appropriately address issues regarding the usage and interpretation of data from the drip tests, and are necessary to account for specific analytical issues, model limitations, and proper bookkeeping that are somewhat unique to these drip tests. The fourth and fifth criteria provide checks on important elements of the computed aqueous solution composition (a "sanity check"). These criteria appear to be sufficient

considering the required level of confidence and the intended use. I note that the representation of potential uranium minerals in the thermodynamic database is somewhat limited and that this could raise issues in the future. I understand that additional minerals are being added to this database and would be considered in future geochemistry calculations, including possible sensitivity calculations.

For Method D (... *the TOUGHREACT-based model used to calculate the geometry in the invert is validated with an alternate model...*) the single validation criterion of a 10 cm scale for differences between the two models in the position of a given value of cumulative flux or relative concentration appears adequate. In reality, the invert material will not be as ideal as it is represented in these calculations (the actual material will almost certainly have more heterogeneity). The processes of fluid flow and mixing of fluids in these models is also idealized. Furthermore, modifications of the shape and positions of waste isolation components in the drifts due to say seismic shaking are not considered. Consequently, any attempt to predict accumulation of uranium and plutonium in the invert material at a scale much finer than 10 cm is probably ingenuous. I have not considered the potential issue of how fine a scale might be required for some possible criticality scenarios, owing to a lack of pertinent information. I am assuming that when the relevant criticality analyses are performed, it will be recognized that the types of calculations validated by Method D carry some type of scale uncertainty of at least 10 cm.

[A]2. Review the external accumulation model report in draft.

This reviewer reviewed the Rev. 01A (Check Copy) draft and provided written comments to the AMR originator. These comments were resolved in the Rev. 01B (Preliminary Backcheck Copy) draft. Many of these comments dealt with transparency issues, particularly concerning the PHREEQC calculations. I note that additional validation information was requested regarding the application of the sorption model to the multi-component (competitive) case. This was included in Rev. 01B.

[A]3. Assess whether or not the model as documented in the report meets the validation criteria.

I find that the model as documented in the report (Rev. 01B draft) meets the validation criteria in regard to Methods A, B, C, and D. The validation (methods and results) is discussed in detail in Section 7 of the Validation Report.

[A]4. Assess whether or not the model is adequate for its intended use. Meet with the author to resolve comments, and recommend actions, as appropriate, to resolve any inadequacies found as part of the review.

I find the model adequate for its intended use. Following my examination of the Rev. 01A draft, I had a number of communications with the originator of record (Susan LeStrange) and other contributors to resolve inadequacies. One examples is the previously noted issue of suppressing $Ni(OH)_2$ solid (which should not have been on the suppressed list) and the inclusion of additional validation information for the multi-component sorption model. Another concerns issues involving the technical details of the PHREEQC calculations. These details were worked with Paul Mariner, one of the contributors to the Validation Report.

[A]5. Document this review process, and the final conclusion as to whether the model is valid for its intended use, as a memo to be included as an appendix in the report.

The present memo, once included in the Validation Report, meets this requirement.

Page 6

The Technical Work Plan (Appendix A) specified the following criteria for the present independent technical review (Method A). These activities follow the original numbering, here with "C" for activity preceding the number. A response follows each specified criterion:

[C]1. The approach described in the document addresses all significant modes of accumulation in the near-field (invert) and far-field (unsaturated zone).

The Validation Report addresses all likely modes of accumulation in the invert and unsaturated zone. These include precipitation, sorption, and movement of solid particulates out of a waste package. Precipitation is and sorption are dealt with as thermodynamically controlled processes. Thus, they are (or can be) controlled by processes such as gas exchange, temperature changes, and mineral-water and sorption interactions, including interactions that do not involve components of direct interest to criticality analyses.

[C]2. The adsorption of U and Pu on the invert materials (tuff), as implemented in the PHREEQC modeling, is based on sound scientific principles.

The adsorption model is not a perfect model. However, more elaborate sorption models used in geochemistry and environmental studies (for example, the triple-layer model) are not perfect either. The present model provides a sufficiently accurate approximation to support Level I criticality analyses. It accounts for the principal effects, including: an increase in the amount of adsorbed component with increasing aqueous concentration of the same component, following the usual sort of mass action form; substrate saturation due to finite substrate; and competition among adsorbing components for finite substrate. I note that basic Kd models have a long history of accepted use in groundwater transport modeling, although they often criticized by some geochemists (including the present reviewer). The modifications here to account for saturation and competitive effects are a major improvement over the "basic" Kd models.

[C]3. The use of the thermodynamic database in the PHREEQC modeling and the choice of mineral suppressions and formations are justified and appropriate for the intended use of the model.

In general, this was found to be the case. One exception, the improperly justified suppression of $Ni(OH)_2$ solid, has been noted previously in this memo. The Validation Report deals with that by showing that for the calculations examined, this solid would not have precipitated anyway. In my original comments provide to the originator, I also noted that the choice of neptunium solid (NpO_2) might be controversial, as some actinide chemists do not believe that this can form in oxidizing systems. I further noted that the same theoretical considerations that suggest NpO_2 for neptunium also suggest PuO_2 for plutonium (though there is no evidence for this from available experimental observations or field observations, of which I am aware). My sense though is that the potential formation of PuO_2 may be something that the people doing the criticality analyses should consider in evaluating their uncertainties. Of course, what I would really like to see is an appropriate experimental investigation of PuO_2 formation analogous to the limited NpO_2 studies, but I perhaps digress beyond the scope of the present memo.

[C]4. Modeling assumptions are clearly defined, discussed, and justified as appropriate for the intended use of the model.

I found this to be so for the stated intended use of the model (to feed Level I criticality analyses).

[C]5. Uncertainties in parameters, processes, and assumptions are appropriately described, and impacts of these uncertainties on the intended use of the model are discussed.

Page 7

Overall, within the context of this AMR and a Level I level of confidence, I found this to be true. It is not entirely clear how uncertainties in the present model will be dealt with in the criticality analyses that are intended to be fed by all this. This is a difficulty arising from the use of multiple AMRs to address a complex problem, when the linkages (and AMR timelines) are not "linear." There may be some risk of a "disconnect" when everything is put together, but that cannot be evaluated by reviewing the present AMR by itself.

[*C]6. The overall technical credibility of the approach, including assumptions, parameters, and equations, is appropriate for the model's intended use.*

The model basically pieces together other models. The geochemical models (including PHREEQC, EQ3/6, and TOUGHREACT, and associated qualified supporting databases) can probably be fairly said to have their own technical credibility owing to use elsewhere (both inside and outside the Yucca Mountain Project). The technical credibility of the overall model here seems more than adequate for the intended use (Level I criticality analyses). For a higher level of confidence, an integrated thermal-chemical-hydrologic model would be preferred, perhaps with an appropriately scaled field test.

In conclusion, I find this Validation Report to be adequate in light of the required level of confidence and intended use. I congratulate the originator and her team of contributors for doing an excellent job in pulling this complex effort together. If the required level of confidence and/or the intended use were to change, I believe that tighter requirements and additional work, including both model development and application and experimental work, would be necessary.

INTENTIONALLY LEFT BLANK

APPENDIX I
DETAILS OF ASPRIN CALCULATIONS

INTENTIONALLY LEFT BLANK

Source Term: TMI, Igneous, 1 liter/year

This source term (TMI_IG1) represents the second stage of an igneous simulation of the degradation of a Three Mile Island (TMI) codisposal waste package at a flow rate of 1 liter/year. The EQ6 input file located in Output DTN: MO0609SPAINOUT.002; folders: TMI_IG1\TMI_IG1_source_term, file: *TMI_IG1a.6i*, listed in Table 4-4, was rerun using data0.tmi (Section 4.1.1). This input file represents the second stage of an igneous simulations. ASPRIN was run using the following steps:

1. Updated the file defltsolids.txt located in Output DTN: MO0609SPAINOUT.002, folders: TMI_IG1\TMI_IG1_Asprin, with the file TMI_IG1a.min_info.txt , located in Output DTN: MO0609SPAINOUT.002, folders: TMI_IG1\TMI_IG1_Asprin. The file in defltsolids.txt contains the list of U solids appearing in the simulation and is needed to run ASPRIN. The file *.min_info.txt contains all the minerals that formed during the stage 1 simulation.

2. Input flushing rate from the EQ6 input file, TMI_IG1a.6i (5.01E-12 mol/sec), which is equivalent to 1 liter/year.

3. Input initial isotopic composition of aqueous solution and schoepite. This represents the composition after the first stage of the igneous scenario, when all the fuel has been oxidized to schoepite and the aqueous solution and schoepite have the same isotopic composition as the starting TMI fuel, as listed in Table 6-3.

4. Input isotopic composition of HLW Glass as listed in Table 6-3.

Based on a plot of the U concentration versus time from the ASPRIN output (Output DTN: MO0609SPAINOUT.002, folders: TMI_IG1\TMI_IG1_Asprin file: *TMI_IG1a.xls*), ten points were identified to be simulated with PHREEQC, as shown in Figure 6-4. Figure 6-4 also shows the ASPRIN results of enrichment fraction (ratio of U-235 to total U in solution) versus time.

Source Term: TMI, Igneous, 1,000 liter/year

This source term (TMI_IG2) represents the second stage of an igneous simulation of the degradation of a TMI codisposal waste package at a flow rate of 1,000 liter/year. The EQ6 input file TMI_IG2a.6i located in Output DTN: MO0609SPAINOUT.002, folders: TMI_IG2\TMI_IG2_source_term, listed in Table 4-4, was rerun using data0.cr3 (see Section 4.1.1). This input file represents the second stage of an igneous simulation at a flow rate of 1,000 liter/year. At this flow rate, the EQ6 output binary files are very large. If a binary file is too large, ASPRIN cannot read the file. For this case, six separate EQ6 simulations were required. For the first EQ6 run (TMI_IG2a.6i), ASPRIN was run with the following steps:

1. Updated defltsolids.txt with the TMI_IG2a.min_info.txt file (both files located in Output DTN: MO0609SPAINOUT.002, folders: TMI_IG2\TMI_IG2_Asprin\ Step1-TMI_IG2a)).

2. Input flushing rate from the EQ6 input file TMI_IG2a.6i (5.01E-9 mol/sec), which is equivalent to 1,000 liter/year.

3. Input initial isotopic composition of aqueous solution and schoepite. This is the composition after the first stage of the igneous scenario, when all the fuel has been oxidized to schoepite and the aqueous solution and schoepite have the same isotopic composition as the starting TMI fuel, as listed in Table 6-3.

4. Input isotopic composition of HLW Glass as listed in Table 6-3.

For the rest of the EQ6 simulation, see files TMI_IG2b.6i through TMI_IG2f.6i, located in Output DTN: MO0609SPAINOUT.002, folders: TMI_IG2\TMI_IG2_Asprin\Step#-TMI_IG2*, where # is 2-6 and 8 is b-f). ASPRIN was run according to the instructions listed above for steps 1, 2, and 4, but step 3 was slightly different. Step 3 requires the starting isotopic composition. In the first EQ6 simulation, the initial isotopic composition is the same as the isotopic composition of the fuel, and is listed in Table 6-3. But the second ASPRIN calculation requires the starting isotopic composition of the second EQ6 simulation. That value is calculated by running ASPRIN with the first EQ6 binary file. It differs from the fuel isotopic composition, because the EQ6 calculations include HLW glass degradation, which changes the isotopic composition of the aqueous solution. For each ASPRIN calculation, an output file was created that contains the isotopic composition at the end of the simulation, to be used in the subsequent ASPRIN calculation. In other words, the initial isotopic composition of the aqueous solution and uranium minerals (if present) for each ASPRIN calculation comes from the ASPRIN output of the previous EQ6 simulation. For example, for the second EQ6 simulation (TMI_IG2b.6i), the file *Isotopic fraction end step 1.xls* provides the values of enrichment that were taken from the ASPRIN output file (TMI_IG2a.txt).

Based on a plot of the U concentration versus time from the all the ASPRIN output files (*TMI_IG2_asprin_all.xls*, folder TMI_IG2), eight points were identified to be simulated with PHREEQC, as shown in Figure 6-5. Figure 6-5 also shows the ASPRIN results of enrichment fraction (ratio of U-235 to total U in solution) versus time.

Source Term: FFTF, Igneous, 1 liter/year

This source term (FFTFIG1adEhdec) represents the second stage of an igneous simulation of the degradation of an FFTF codisposal waste package at a flow rate of 1 liter/year. The adjusted Eh equivalent to oxygen fugacity of 1.77×10^{-9} bar, and Pu radioactive decay ($^{239}Pu \rightarrow ^{235}U$; half-life is 24,100 years) was included. ASPRIN was run according to the following steps:

1. Update defltsolids.txt with the FFTFIG1adEhdec.min_info.txt file, (both files located in Output DTN: MO0609SPAINOUT.002, folders: FFTFIG1adEhdec\FFTFG1_Asprin_Sourceterm).

2. Input flushing rate from the EQ6 input file, FFTFIG1adEhdec.6i (5.01E-12 mol/sec), equivalent to 1 liter/year.

3. Input initial isotopic composition of aqueous solution and schoepite. This represents same isotopic composition as the starting FFTF fuel, as listed in Table 6-3. Since

FFTF fuel is composed of UOX and MOX, which have different isotopic fractions, an average isotopic composition was calculated in Output DTN: MO0609SPAINOUT.002, file: *Fuel Isotopic Composition.xls* for use with ASPRIN.

4. Input isotopic composition of HLW Glass as listed in Table 6-3.

Based on a plot of the U and Pu concentrations versus time from the ASPRIN output (Output DTN: MO0609SPAINOUT.002, folders: FFTFIG1adEhdec\FFTFG1_Asprin_Sourceterm; file: *FFTFIG1adEhdec.xls*)), ten points were identified to be simulated with PHREEQC, as shown in Figure 6-6. Figure 6-6 also shows the ASPRIN results of enrichment fraction (ratio of U-235 to total U in solution) versus time.

Because this source term was estimated at a reduced Eh, the aqueous concentration in the PHREEQC input file needed more than just total concentration of N, Pu, and Np. The concentration of each dominant oxidation state for N, Pu, and Np needed to be specified. ASPRIN was used to extract the aqueous species for N, Pu, and Np, and the major species were summed in *Aqueous species.xls*, folder FFTFIG1_asprin.

Source Term: FFTF, Igneous, 1,000 liter/year

This source term (FFTFIG2adEhdec) represents the second stage of an igneous simulation of the degradation of an FFTF codisposal waste package at a flow rate of 1,000 liter/year. The EQ6 input file for this source term was rerun to create the binary files (Output DTN: MO0609SPAINOUT.002, folders: FFTFIG2adEhdec\FFTFG2_Asprin; file: *FFTFIG2adEhdec.bin*), needed to run the code ASPRIN. This input file represents the second stage of an igneous simulation at a flow rate of 1,000 liter/year. Four separate EQ6 simulations were required. For the first EQ6 simulation (Output DTN: MO0609SPAINOUT.002, folders: FFTFIG2adEhdec\FFTFG2_Asprin; file: *FFTFIG2adEhdec.6i*), ASPRIN was conducted according to the following steps:

1. Update defltsolids.txt with the FFTFIG2adEhdec.min_info.txt file (both files located in Output DTN: MO0609SPAINOUT.002, folders: FFTFIG2adEhdec\FFTFG2_Asprin\Step1- FFTFIG2adEhdec).

2. Input flushing rate from the EQ6 input file *FFTFIG2adEhdec.6i* (5.01E-9 mol/sec), which is equivalent to 1,000 liter/year.

3. Input initial isotopic composition of aqueous solution and schoepite. This represents the same isotopic composition as the starting FFTF fuel, as listed in Table 6-3. Since FFTF fuel is composed of UOX and MOX, which have different isotopic fractions, an average isotopic composition was calculated in in Output DTN: MO0609SPAINOUT.002, file: *Fuel_Isotopic_Composition.xls* for use with ASPRIN.

4. Input isotopic composition of HLW Glass as listed in Table 6-3.

For the rest of the EQ6 simulations, see files FFTFIG2adEhdeca.6i through FFTFIG2adEhdecc.6i), located in Output DTN: MO0609SPAINOUT.002, folders: FFTFIG2adEhdec\FFTFIG2adEhdec_Asprin\Step#-FFTFIG2adEhdec*, where # is 2-4 and 8 is

a-c)., ASPRIN was run according to the instructions listed above for steps 1, 2, and 4, but step 3 is slightly different. The initial isotopic composition of the aqueous solution and uranium minerals (if present) came from the ASPRIN output of the previous EQ6 simulations. For example, for the second EQ6 simulation (*FFTFIG2adEhdeca.6i*), the file *Isotopic fraction end step 1.xls* provides the values of enrichment that were taken from the ASPRIN output file (*FFTFIG2adEhdec.txt*).

Based on a plot of the U concentration versus time from the all the ASPRIN output files (folders: FFTFIG2adEhdec\FFTFG2_Asprin; file: *Aqueous_species_FFTFIG2.xls*)), eight points were identified to be simulated with PHREEQC, as shown in Figure 6-7. Figure 6-7 also shows the ASPRIN results of enrichment fraction (ratio of U-235 to total U in solution) versus time.

Like the previous FFTF source term, this source term was estimated at a reduced Eh, equivalent to oxygen fugacity of 1.77×10^{-9} bar. Because of this, the aqueous concentration in the PHREEQC input file must specify the concentration of each dominant oxidation state for N, Pu, and Np. ASPRIN was used to extract the aqueous species for N, Pu, and Np, and the major species were summed in the file: *Aqueous_species_FFTFIG2.xls*.

Source Term: N-Reactor, Igneous, 1,000 liter/year

This source term (CDSPIG2) represents the second stage of an igneous simulation of the degradation of an N-Reactor codisposal waste package at a flow rate of 1,000 liter/year. The first two EQ6 input files (see Output DTN: MO0609SPAINOUT.002, folder: CDSPIG_Asprin\Step1-CDSPIG2a and Step2-CDSPIG2b, files:CDSPIG2a.6i and CSDPIG2b.6i) had binary files from the *Geochemistry Model Validation Report: Material Degradation and Release Model* (BSC 2006 [DIRS 176911]) that were small enough to be read by ASPRIN. But, the binary file for the third EQ6 simulation (see Output DTN: MO0609SPAINOUT.002, folder: CDSPIG_Asprin\Step3-CDSPIG2c, file: *CDSPIG2c.bin*) was too large (448 Megabytes) and so the EQ6 input file had to be rerun with a shorter span of time to generate a smaller binary file. For the first EQ6 simulation (*CSDPIG2a.6i*), ASPRIN was run according to the following steps:

1. Update defltsolids.txt with the CDSPIG2a.min_info file, (both files located in Output DTN: MO0609SPAINOUT.002, folders: CDSPIG2\CDSPIG_Asprin\Step1-CDSPIG2a).

2. Input flushing rate from the EQ6 input file *CDSPIG2a.6i* (5.00E-9 mol/sec), equivalent to 1,000 liter/year.

3. Input initial isotopic composition of aqueous solution and U-minerals. This represents the same isotopic composition as the starting N-Reactor fuel, as listed in Table 6-3. The isotopic composition of Mark IA fuel, rather than Mark IV, was used in running ASPRIN since it has the highest U-235 content.

4. Input isotopic composition of HLW Glass as listed in Table 6-3.

For the rest of the EQ6 simulations, files *CDSPIG2b.6i* and *CDSPIG2c.6i*, (Output DTN: MO0609SPAINOUT.002, folders: CDSPIG\CDSPIG_Asprin\Step2-CDSPIG2b and Step3-

CDSPIG2c), ASPRIN was run according to the instructions listed above for steps 1, 2, and 4, but step 3 is slightly different. The initial isotopic composition of the aqueous solution and uranium minerals (if present) came from the ASPRIN output of the previous EQ6 run. For example, for the second EQ6 simulation (CDSPIGb.6i), the file *Isotopic fraction end step 1.xls* provides the values of enrichment that were taken from the ASPRIN output file of the first EQ6 simulations (CDSPIG2a.txt).

Based on a plot of the U concentration versus time from the all the ASPRIN output files (Output DTN: MO0609SPAINOUT.002, folder CDSPIG\CDSPIG_Asprin, file: *CDSPIG2_asprin_all.xls*), eight points were identified to simulate with PHREEQC, as shown in Figure 6-8. Figure 6-8 also shows the ASPRIN results of enrichment fraction (ratio of U-235 to total U in solution) versus time.

Source Term: CSNF, Seismic, 1,000 liter/year

This source term (CSFlux9) represents a CSNF waste package in the seismic scenario in which a pre-existing fault is reactivated and the displacement shears the drip shield, waste package, and fuel cladding (*Geochemistry Model Validation Report: Material Degradation and Release Model* (BSC 2006 [DIRS 176911], Section 6.2.3.2). The waste package is flooded and the flow rate is 1,000 liter/year. The EQ6 input file for this case was taken from *Geochemistry Model Validation Report: Material Degradation and Release Model* (BSC 2006 [DIRS 176911]), but was rerun to get the binary file. During the EQ6 simulation, two additional minerals were suppressed (PuO_2 and Spinel-Co), to be consistent with Table 6-8, the EQ6 suppressed minerals list. As was done for the FFTF source terms, a reduced Eh (oxygen fugacity of 1.77×10^{-9} bar) was used to more accurately reflect the Pu concentrations. Since the CSNF waste package only contains one waste form (as opposed to the co-disposal waste packages that contains both SNF and HLW glass), the enrichment fraction of the entire waste package contents is constant and equal to the starting enrichment of the CSNF as listed in Table 6-3. For the first EQ6 simulation (Output DTN: MO0609SPAINOUT.002, folders: CSFlux9\CSflux9_Asprin\Step1-CSFlux9a, file: *CSFlux9a.6i*), ASPRIN was executed not to determined the enrichment fraction, but to extract the aqueous species from the binary file according to the following steps:

1. Start ASPRIN and enter "N" to execute Read_Plt only. This choice is just for reading data from the binary file.

2. Choose all elements in aqueous species and all aqueous species containing N, Np, and Pu.

For the rest of the EQ6 simulations (*CSFlux9b.6i* and *CSFlux9c.6i*), Output DTN: MO0609SPAINOUT.002, folders: CSFlux9\CSflux9_Asprin\Step2-CSFlux9b and Step3-CSFlux9c, ASPRIN was run according to the instructions listed above. The ASPRIN outputs are contained in folder CSFlux9-asprin.

Based on a plot of the U concentration versus time from the all the ASPRIN output files (Output DTN: MO0609SPAINOUT.002, folder: CSFlux9_Asprin, file: *CSFlux9_asprin_all.xls*), eight points were identified to run with PHREEQC (Figure 6-9). Figure 6-9 also shows the enrichment fraction (ratio of U-235 to total U in solution), which comes from Table 6-3.

INTENTIONALLY LEFT BLANK

APPENDIX J

DIFFUSIVE RELEASE INPUT ROADMAP

INTENTIONALLY LEFT BLANK

Tables J-1 and J-2 provide roadmaps to the location within the TSPA source files (DTN: MO0506MWDTLVAC.000, [DIRS 174811]), for each value used in the diffusive release scoping calculations (Section 6.3).

Table J-1. Diffusive Release Input Roadmap for CSNF

Values	Source- DTN: MO0506MWDTLVAC.000, [DIRS 174811]),	Used in (Output DTN: MO0604SPANOMIN.000)
CSNF mass initial inventory without uncertainty term (g)	File: *LA_v3.004_ne_00300_018.gsm* Folder: Model/TSPA Model/ Engineered System/ Waste Form/ RN_Inventory/ Input_Params_RN_Inventory/ Input_Params_CSNF_Inventory In the TSPA runs, this value is multiplied by an uncertainty factor for each realization.	*CSNF Starting Inventory.xls*
CSNF mean uncertainty factor for 300 realizations	File: *LA_v3.004_ne_00300_018.gsm* Folder: \TSPA_Model\Results\Uncertainty_Results_Nominal\Inventory_uncert\Inventory_uncert\[5] Under "properties" it shows that Invert uncertainty [5] is CSNF, [6] is DSNF, and [7] is HLW.	*CSNF Starting Inventory.xls*
Invert release (g), 50th and 95th percentile	From File: *LA_v3.004_ne_00300_018.gsm* Folder: \TSPA_Model\Results\Results_1000rlz\ES_Results_Calcs\CSNF_Out_Cum_Species	*CSNF_Out_Cum_Species_Pu.xls* *CSNF_Out_Cum_Species_U.xls*
Waste package release (g), 50th and 95th percentile	From File: *LA_v3.004_ne_00300_018.gsm* Folder: \TSPA_Model\Results\Results_1000rlz\ES_Results_Calcs\WP_Release_Sel_RN	*CUM_CSNF_WP_Rel_Pu.xls* *CUM_CSNF_WP_Rel_U.xls*

Table J-2. Diffusive Release Input Roadmap for DOE SNF

Values	Source- DTN: MO0506MWDTLVAC.000, [DIRS 174811]),	Used in (Output DTN: MO0604SPANOMIN.000)
DSNF mass initial inventory without uncertainty term (g)	File: *LA_v3.004_ne_00300_008.gsm* Folder: Model/TSPA Model/ Engineered System/Waste Form/RN_Inventory/ Input_Params_RN_Inventory/ Input_Params_DSNF_Inventory In the TSPA runs, this value is multiplied by an uncertainty factor for each realization.	*CDSP Starting inventory.xls*
DSNF average uncertainty factor for 300 realizations	File: *LA_v3.004_ne_00300_008.gsm* Folder: \TSPA_Model\Results\Uncertainty_Results_Nominal\Inventory_uncert\Inventory_uncert\[6] Under "properties" it shows that Invert uncertainty [5] is CSNF, [6] is DSNF, and [7] is HLW.	*CDSP Starting inventory.xls*
HLW mass initial inventory (g)	File: *LA_v3.004_ne_00300_008.gsm* Folder: Model/TSPA Model/ Engineered System/Waste Form/RN_Inventory/ Model_Calcs_RN_Inventory/ HLW_Inventory_Calcs/ HLW_Source Unexposed_Mass, Time=0 This represents the actual mean of the starting inventory since the initial mass is multiplied by an uncertainty term.	*CDSP Starting inventory.xls*
Invert release (g), 50th and 95th percentile	From File: *LA_v3.004_ne_00300_008.gsm* Folder: \TSPA_Model\Results\Results_1000rlz\ES_Results_Calcs\CSNF_Out_Cum_Species	*CDSP_Out_Cum_Species_Pu.xls* *CDSP_Out_Cum_Species_U.xls*
Waste package release (g), 50th and 95th percentile	From File: *LA_v3.004_ne_00300_008.gsm* Folder: \TSPA_Model\Results\Results_1000rlz\ES_Results_Calcs\WP_Release_Sel_RN	*CUM_CDSP_WP_Rel_Pu.xls* *CUM_CDSP_WP_Rel_U.xls*

Addendum Cover Page

Complete only applicable items.

QA: QA

1. Total Pages: 84

2. Addendum to (Title): Geochemistry Model Validation Report: External Accumulation Model			
3. DI (including Revision and Addendum No.): ANL-EBS-GS-000002 REV 01 AD 01			
	Printed Name	Signature	Date
4. Originator	Susan LeStrange	Susan LeStrange	10/31/07
5. Independent Technical Reviewer	David Sassani	David Sassani	10/31/07
6. Checker	William Downs	William Downs	10/31/07
7. QCS / QA Reviewer	Brian Mitcheltree	Brian Mitcheltree	11/1/07
8. Responsible Manager / Lead	Cliff Howard	Cliff Howard	11/1/07
9. Responsible Manager	Kathryn Knowles	Kathryn Knowles	11/1/07
10. Remarks			

Change History

11. Revision and Addendum No.	12. Description of Change
REV 01 AD 01	The addendum was added to (1) incorporate revised inputs from ANL-EBS-GS-000001 REV 02, (2) address DOE comments submitted 1/16/07 on REV 01 of this report, and (3) add calculations to determine the mass of fissile material that would be required to accumulate in the invert or host rock in order to pose a significant probability that a critical event could occur. This addendum addresses CR-9424 (see Section 4.1.3.2[a]), which indicates that N_2(aq) should be suppressed in adjusted-Eh runs, and CR-8766 (see Section 6.4.5.1[a]), which indicates that the *azero* parameter in the PHREEQC database should be non-zero for charged species (Section 6.4.5.1[a]). This addendum supersedes CAL-DS0-NU-000004 REV00A [DIRS 170060], *Critical Mass Search Calculation in the Invert.*

ACKNOWLEDGEMENTS

The contributing originators are as follows: Wendy Mitcheltree (Section 6.4[a]), Pat McDaniel (Section 6.9[a], Appendix K[a]), Larry Sanchez (output DTN: MO0705SCALEGEO.000, folder: IO_ZIP, file: *Exter_crit.xls*), Harlan Stockman (output DTN: MO0705PHREEMOD.000, file: *activation_energy_multipliers.xls*).

The contributing checkers are as follows: Kaveh Zarrabi, John Scaglione.

INTENTIONALLY LEFT BLANK

CONTENTS

Page

CONTENTS (Continued)

Page

FIGURES

Page

INTENTIONALLY LEFT BLANK

TABLES

Page

INTENTIONALLY LEFT BLANK

ACRONYMS

CSNF	commercial spent nuclear fuel
DIRS	Document Input Reference System
DOE	U.S. Department of Energy
FFTF	Fast Flux Test Facility
HLWG	high-level waste glass
LWBR	light water breeder reactor
MDR	material degradation and release
MOX	mixed oxide
SNF	spent nuclear fuel
TMI	Three Mile Island
UO_X	uranium oxide

INTENTIONALLY LEFT BLANK

1[a]. PURPOSE

The purpose of this addendum is: (1) to perform accumulation analyses with revised inputs and (2) to add calculations to determine the mass of fissile material that would be required to accumulate in the invert or in the host rock of the repository (including fractures and lithophysae) in order to pose a significant probability of a critical event occurring. The output of this addendum is used to assess the potential for a criticality event outside the waste package due to the accumulation of radionuclides in the invert or the host rock.

The accumulation analyses in this addendum were performed because the main inputs (referred to as "source terms") to the external accumulation model were revised in *Geochemistry Model Validation Report: Material Degradation and Release Model* (MDR model) (SNL 2007 [DIRS 181165], Section 8). The accumulation analyses address source terms (defined in this report as estimates of dissolved releases of radionuclides from degrading waste packages) from a commercial spent nuclear fuel (CSNF) waste package and from a degrading codisposal waste package containing high-level waste glass (HLWG) and U.S. Department of Energy (DOE)-owned spent nuclear fuel (SNF) from the Fast Flux Test Facility (FFTF) at the Hanford site in Washington state. The source terms were recalculated in the MDR model due to changes in the waste package designs. The CSNF waste package design (SNL 2007 [DIRS 179394]) now includes a stainless steel transportation, aging, and disposal (TAD) canister within the waste package outer corrosion barrier and inner vessel, contains neutron absorber plates constructed of borated stainless steel rather than a gadolinium-bearing nickel alloy, and uses stainless steel in place of the carbon steel in the basket material specified in the old design. The major change to the codisposal waste package design is that a thick stainless steel shield plug has been added to the inner vessel (SNL 2007 [DIRS 179567]). The accumulation analyses were performed in accordance with the requirements in *Technical Work Plan for External Accumulation for Criticality Evaluations* (BSC 2006 [DIRS 177153], Sections 2.1.1, 2.1.2). To be more efficient, instead of preparing an analysis report, as specified in Section 2.1.2 of the TWP (BSC 2006 [DIRS 177153]), an addendum was prepared to address the CSNF TAD design. Another deviation from the TWP (BSC 2006 [DIRS 177153]) is that SCI-PRO-006, *Models*, was followed rather than the no longer applicable model procedure, which is listed in Section 2.1.1 of the TWP (BSC 2006 [DIRS 177153]).

In addition, this addendum contains new calculations to estimate the mass of fissile materials that would be required to accumulate in the invert or host rock in order to pose a significant probability of a critical event. The code system used for this analysis is SCALE (STN: 10129-5.1-00 [DIRS 181249]), which was developed at Oak Ridge National Laboratory. This qualified code package has been used to evaluate the criticality of uranium or plutonium minerals that may accumulate in the invert below the waste package or in the host rock below the invert. To mimic accumulation within the near field (invert) and far field (fractures and lithophysae), the uranium and plutonium minerals (also referred to as "waste" in the addendum) were mixed with Topopah Spring Tuff and pore water. The volume of interest was modeled as a spherical mass, reflected by an infinite amount of a similar rock–water composition. The spherical configuration was chosen, as it is the most reactive. The criticality calculations were developed in accordance with the requirements of *Technical Work Plan for: Postclosure Criticality* (SNL 2007 [DIRS 178869], Section 2.1.8).

The format of this addendum is patterned after the parent document, with the sections of the addendum numbered the same as the parent document except with "[a]" added to the end of each section number. Some sections have not been changed and are indicated as "No changes." Other sections contain information necessary to describe the new calculation inputs and results. A few sections contain additional information to improve clarity of the document.

2[a]. QUALITY ASSURANCE

Preparation of this addendum and its supporting technical activities has been performed in accordance with the appropriate requirements of the Yucca Mountain Project quality assurance program and are subject to the requirements of *Quality Assurance Requirements and Description* (DOE 2007 [DIRS 182051]). This addendum is prepared in accordance with SCI-PRO-006 and reviewed in accordance with SCI-PRO-003, *Document Review*. Input information for this addendum is identified and tracked in accordance with SCI-PRO-004, *Managing Technical Product Inputs*. The methods used to control the electronic management of data, as required by IM-PRO-002, *Control of the Electronic Management of Information*, are identified in Section 8 of the TWP (SNL 2007 [DIRS 177153]). Planning and preparation of the report were initiated under the Bechtel SAIC Company Quality Assurance Program. Therefore, forms and associated documentation (primarily the TWP (BSC 2006 [DIRS 177153])) prepared prior to October 2, 2006, the date this work was transferred to the Lead Laboratory, were completed in accordance with Bechtel SAIC Company procedures.

INTENTIONALLY LEFT BLANK

3[a]. USE OF SOFTWARE

The controlled and baselined software used in this report are listed in Table 3-1[a] and the operating environments are provided in Table 3-2[a]. The range of use for each software application is within that for which it was qualified. Each software code was selected because it is appropriate for use in geochemical or criticality modeling. The geochemistry software uses the project-qualified thermodynamic database. There are no limitations on the outputs due to the selected software. The use of the software was consistent with the intended use and within the documented validation range of the software. No software was used prior to qualification to develop any preliminary output.

Microsoft Excel, commercially available software, is used in this report; however, the results are not dependent on the software program used, so the software is exempt from requirements in IM-PRO-003, *Software Management*.

For all software, the formulas and inputs used in this model are discussed in Section 4 of the parent report and Section 4[a] of the addendum. The calculations and outputs are discussed in Section 6[a] and the appendices. No other information is required for an independent person to reproduce the work.

Table 3-1[a]. Computer Software

Software Name	Version	Software Tracking Number (Qualification Status)	Description and Components Used
ASPRIN	1.0	10487-1.0-00 [DIRS 179458] (Qualified on Windows 2000)	Determines isotopic content of minerals and solution in EQ6 output files
PHREEQC	2.3	10068-2.3-01 [DIRS 157837] (Qualified on Windows 2000)	A code for geochemical speciation, reaction path modeling, reactive transport, and surface complexation modeling
PHREEQC_Post	1.1	10723-1.1-00 [DIRS 157839] (Qualified on Windows 2000)	A Microsoft Excel macro that is used to postprocess PHREEQC output information and extracts actinide mineral accumulation rates
GetEqPhases	1.0	10725-1.0-00 [DIRS 157840] (Qualified on Windows 2000)	A Microsoft Excel macro that determines the mineral phases likely to precipitate in PHREEQC simulations
Acc_with_decay	1.2	10499-1.2-00 [DIRS 157838] (Qualified on Windows 2000)	A Microsoft Excel macro that applies decay to plutonium and uranium and variable enrichment to postprocess PHREEQC outputs
MinAcc	1.0	10724-1.0-00 [DIRS 157841] (Qualified on Windows 2000)	A Microsoft Excel macro that computes the volume of mineral accumulation by postprocessing PHREEQC outputs
transl	2.0	10251-2.0-00 [DIRS 155029] (Qualified on Windows 98)	Converts EQ3/6 formatted thermodynamic database to PHREEQC format
SCALE	5.1	10129-5.1-00 [DIRS 181249] (Qualified on Windows XP)	Performs light water reactor fuel depletion analyses, reactivity sensitivity analyses, and radiation transport calculations
Microsoft Excel	SP2	Commercial off-the-shelf software: Exempt	Used in this document for graphical representation and arithmetical manipulations

Table 3-2[a]. Computers and Operating Systems

Computer Make (Operator)	CPU #	Operating System	Software Used
Dell Optiplex GX260 (Wendy Mitcheltree)	S884987	Windows 2000	PHREEQC V. 2.3, PHREEQC_Post V.1.1, GetEqPhases V.1.0, Acc_with_decay V.1.2, MinAcc V.1.0
Dell Optiplex GX260 (Susan LeStrange)	S884966	Windows 2000	ASPRIN V.1.0
Dell Optiplex (William Downs)	X10-23533	Windows 98	Transl V. 2.0
Dell Optiplex GX260 (Larry Sanchez)	S884966	Windows XP	SCALE V. 5.1

NOTE: CPU = central processing unit.

4[a]. INPUTS

This section lists the additional inputs needed for the addendum calculations.

4.1[a] DIRECT INPUT

This section identifies the additional direct inputs that were used in the development of the addendum. (An exception is Table 4-1[a], which contains direct inputs used in the parent report, but is presented here to supplement the discussion in Section 4.1 of the parent report.)

4.1.1[a] Thermodynamic Database

Table 4-1[a] lists the databases that were used in the parent report. The table is provided as a supplement to the discussion in Section 4.1.1 of the parent report to improve transparency. The inputs were not used in the addendum and therefore are considered indirect inputs for the addendum. Table 4-2[a] lists the thermodynamic database that was used in the addendum.

Table 4-1[a]. Databases Used in Parent Report

Input Database	Input Database Description	Name of Output Database and Description of Output Database
data0.tmi; data0.cr3	These databases are based on file *data0.ymp.R4* (DTN: SN0410T0510404.002 [DIRS 172712]). Databases used in EQ6 simulations to generate source terms for external accumulation calculations (Section 6.4.1 of the parent report).	No changes
phreeqcDATA025.dat	PHREEQC database (DTN: MO0604SPAPHR25.001 [DIRS 176868]) converted from *data0.ymp.R4*. Database was changed for external accumulation analyses.	*phreeqcDATA025bdotCr3.dat* and *phreeqcDATA025bdotCr3az.dat*. Changes made to each database (to be consistent with *data0.cr3*) are listed in header of databases, as contained in DTN: MO0609SPAINOUT.002.
Thermk1.01.dat	Database developed for TOUGHREACT V3.0	No changes

NOTE: The table is provided as a supplement to the discussion in Section 4.1.1 of the parent report to improve transparency. The inputs were not used in the addendum and therefore are considered indirect inputs for the addendum.

Table 4-2[a]. Database Used in Addendum

Input Database	Source	Input Database Description	DTN and Name of Output Database
Data0.ymp.R5	DTN: SN0612T0502404.014 [DIRS 178850]	EQ3/6 thermodynamic database converted to PHREEQC format at 25°C, 50°C, and 90°C	Output DTNs: MO0704PHREEQ25.000, *phreeqcDATA0R525.dat;* MO0704PHREEQ50.000, *phreeqcDATA0R550.dat;* MO0709PHREEQ90.000, *phreeqcDATA0R590.dat*

4.1.2[a] Mixing Water Composition

4.1.2.1[a] Basalt Water

The composition of the mixing water used in the PHREEQC calculations in the addendum for the igneous scenario is taken from the Columbia Basin basalt groundwaters (Table 4-3[a]). This is the same basalt water composition used in the CSNF igneous case from the MDR model (SNL 2007 [DIRS 181165], Section 4.1.2). In the PHREEQC calculations, this water mixes with the waste package effluent (source term) within the invert or fractured rock.

Table 4-3[a]. Basalt Water Composition

pH, pE, and Elemental Composition	Value	Units
pH	8.3585	pH
pE	8.5603	pE
Calcium	$9.731024965 \times 10^{-5}$	Moles/kg
Chlorine	$3.666857706 \times 10^{-4}$	Moles/kg
Fluorine	$1.000084265 \times 10^{-4}$	Moles/kg
Carbon	$2.654332347 \times 10^{-3}$	Moles/kg
Potassium	$2.046124865 \times 10^{-4}$	Moles/kg
Magnesium	$2.057189976 \times 10^{-5}$	Moles/kg
Sodium	$3.305818354 \times 10^{-3}$	Moles/kg
Sulfur	$2.186051845 \times 10^{-4}$	Moles/kg
Silicon	$1.214959706 \times 10^{-3}$	Moles/kg

Source: DTN: MO0705GEOMODEL.000 [DIRS 181798], folder: EQ3\basalt waters\Columbia basin CSNF\Adjusted Eh, file: *b50_adeh.3o*.

4.1.2.2[a] SD-9 Pore Water

No changes.

4.1.2.3[a] J-13 Well Water

The composition of the mixing water used in the PHREEQC calculations for the seismic scenario is J-13 well water (Table 4-4[a]). This is the same base-case water composition used in the FFTF seismic case from the MDR model (SNL 2007 [DIRS 181165], Section 4.1.2).

Table 4-4[a]. J-13 Well-Water Composition, Adjusted-Eh, 50°C

pH, pE, and Elemental Composition	Value	Units
pH	8.2300	pH
pE	8.6888	pE
Calcium	$3.243674988 \times 10^{-4}$	Moles/kg
Chlorine	$2.013951078 \times 10^{-4}$	Moles/kg

Table 4-4[a]. J-13 Well-Water Composition, Adjusted-Eh, 50°C (Continued)

pH, pE, and Elemental Composition	Value	Units
Fluorine	$1.147465104 \times 10^{-4}$	Moles/kg
Carbon	$1.974634086 \times 10^{-3}$	Moles/kg
Potassium	$1.289058665 \times 10^{-4}$	Moles/kg
Magnesium	$8.269903705 \times 10^{-5}$	Moles/kg
Nitrogen	$1.416016275 \times 10^{-4}$	Moles/kg
Sodium	$1.992190534 \times 10^{-3}$	Moles/kg
Sulfur	$1.915397807 \times 10^{-4}$	Moles/kg
Silicon	$1.015240302 \times 10^{-3}$	Moles/kg

Source: DTN: MO0705GEOMODEL.000 [DIRS 181798], folder: EQ3\seismic pore waters\J13\CSNF\Adjusted Eh, file: *J-13-adeh.3o*.

4.1.3[a] Waste Package Releases

This addendum calculates the accumulation in the invert or fractured rock as a result of dissolved releases from CSNF and DOE SNF waste packages from igneous and seismic scenarios in which seepage drips on the waste packages. The source terms come from the MDR model (SNL 2007 [DIRS 181165]. The files are listed in Table 4-5[a]).

4.1.3.1[a] Diffusive Releases from Waste Package

No changes.

4.1.3.2[a] Dissolved Releases

Table 4-5[a] contains the EQ3/6 V. 8.1 (STN: 10813-81.-00 [DIRS 176889]) simulations used as source terms for dissolved losses from the waste packages from the MDR model (SNL 2007 [DIRS 181165]; DTN: MO0705GEOMODEL.000 [DIRS 181798]). For CSNF, the case with the highest uranium loss was the igneous scenario, with high seepage rate and adjusted-Eh, as shown in the MDR model (SNL 2007 [DIRS 181165], Tables 8.1-1 and 8.1-2). For DOE SNF waste packages, the case with the highest uranium loss was the FFTF waste package, igneous scenario with high seepage rate (Table 8.1-4). However, the results from the external accumulation presented in the parent report (Table 8-2) show that very little accumulation occurred for the high seepage cases (*TMI_IG2*, *FFTFIG2adEhdec*) compared to the low seepage cases (*TMI_IG1* and *FFTFIG1adEhdec*). The cases with the next highest release of uranium with a low seepage rate were the FFTF and Three Mile Island (TMI) waste packages, maximum HLWG corrosion rate. Since the FFTF waste packages contain both uranium and plutonium in the waste form, the FFTF waste package was chosen for the external accumulation analysis.

Table 4-5[a]. EQ6 Source Term File Inputs

EQ6 File Names Used for Input	Waste Package Type	Scenario	Conditions	Percent Remaining at 10,000 Years		Reason for Choice
				Pu	U	
CSIGAdEh.6i *CSIGAdEh.bin* *CSIGAdEh.min_info.txt* *CSIGAdE2.6i* *CSIGAdE2.bin* *CSIGAdE2.min_info.txt* *CSIGAdE3.6i* *CSIGAdE3.bin* *CSIGAdE3.min_info.txt*	CSNF	Igneous	1,000 L/yr seepage rate through the waste package, adjusted-Eh, 50°C	74.8	98.8	Highest uranium loss for CSNF of any cases listed in Section 8, *Conclusions* of SNL 2007 [DIRS 181165], Tables 8.1-1 and 8.1-2
FFTFMxGE.6i *FFTFMxGE.bin* *FFTFMxGE.min_info.txt*	FFTF	Seismic	1 L/yr seepage rate through the waste package, adjusted-Eh, "AugmentLogK" for gadolinium and plutonium species, 50°C	99.9	79.7	One of highest uranium losses for DOE SNF; contains both uranium and plutonium, low seepage flux

Source: DTN: MO0705GEOMODEL.000 [DIRS 181798], "Percent Remaining" values from folder: CSNF, file: *CSNF Igneous Summary.xls*; and folder: FFTF, file: *FFTF Seismic Summary.xls*; CSNF EQ6 files from folder: CSNF\CSNF Igneous\High Seepage Adj Eh; FFTF EQ6 files from folder: FFTF\Seismic\Max Glass Adj Eh.

NOTE: CSNF = commercial spent nuclear fuel; FFTF = Fast Flux Test Facility; SNF = spent nuclear fuel.

Both source terms used the adjusted-Eh model, in which the fugacity of oxygen is lower than atmospheric values. When preparing the PHREEQC input files, N_2(aq) was suppressed, as it is not expected to form. N_2(aq) was suppressed in the adjusted-Eh cases in the MDR model also (SNL 2007 [DIRS 181165], Section 6.3.14).

In the MDR model, the EQ3/6 source term from the FFTF waste package used the "AugmentLogK" option in the EQ3/6 input file, which adjusts the log K in the database for several gadolinium and plutonium aqueous species (SNL 2007 [DIRS 181165], Section 6.3.13). This adjustment was made because the EQ3/6 database only has log K values at 25°C for those aqueous species, not for 50°C conditions. The same adjustment to the log K in the PHREEQC runs were accomplished by calculating the log K at 50°C and entering the values in the PHREEQC input files. The inputs listed in Table 4-6[a] were used to calculate the log K values at 50°C. The calculations are presented in spreadsheet *Gd-Pu-augmentk.xls* (output DTN: MO0705PHREEMOD.000) and the results are presented in Section 6.4-1[a].

Table 4-6[a]. Augment Log K Input Values for FFTF PHREEQC Input File

Equation	Augment Log K Value (50°C)	log K (25°C)
$GdCO_3^+ + H^+ = Gd^{3+} + HCO_3^-$	−0.29949	2.5288
$Gd(CO_3)_2^- + 2H^+ = Gd^{3+} + 2HCO_3^-$	−0.51542	7.5576
$GdHCO_3^{2+} = Gd^{3+} + HCO_3^-$	−0.53328	−2.1000
$Gd_2(CO_3)_3$ (solid) + $3H^+ = 2\ Gd^{3+} + 3HCO_3^-$	−1.37366	−3.7136
PuO_2CO_3 (aq) + $H^+ = PuO_2^{2+} + HCO_3^-$	−0.24979	−1.2567

Sources: DTNs: SN0612T05024.014 [DIRS 178850], file: *data0.ymp.R5* (equation and log K at 25°C); MO0705GEOMODEL.000 [DIRS 181798], folder: Augment logK, file: *Gd-CO3-complex-augmentk.xls* (Augment Log K value).

4.1.3.3[a] Solid Entrainment Losses

The corresponding section in the parent report, Section 4.1.3.3, is deleted. Entrained releases are not estimated in the MDR model (SNL 2007 [DIRS 181165]), and therefore are not considered in the external accumulation model.

4.1.3.4[a] Solid Losses from Bottom of Waste Packages

No changes.

4.1.3.5[a] Uranium and Plutonium Isotopic Content of Waste Forms

An additional input for the addendum is the uranium and plutonium content of the HLWG as used in the MDR model (DTN: MO0705GEOMODEL.000 [DIRS 181798], folder: glass, file: *CDSP_HLWGlass_2004.xls,* tabs: "U content" and "HLWG Oxide Conversions"). The values are discussed in Section 6.4-1[a] and are used in the ASPRIN V. 1.0 (STN: 10487-1.0-00 [DIRS 179458]) code to determine the enrichment fraction of the source term (Appendix I[a]).

4.1.3.6[a] Radioactive Half-Life of ^{239}Pu

No changes.

4.1.4[a] Waste Package Flow Rate

No changes.

4.1.5[a] Self-Diffusion Coefficient of Water

No changes.

4.1.6[a] Tuff Composition

No changes.

4.1.7[a] Dissolution Rates for Tuff Minerals

4.1.7.1[a] Dissolution at 25°C for Parent Report

The dissolution rates of the tuff minerals (cristobalite, annite, phlogopite, maximum microcline, albite_low, and anorthite) used in the parent report did not change. The following paragraphs replace the discussion of the dissolution rates of cristobalite, annite, and phlogopite in the parent report.

The dissolution rate of cristobalite (SiO_2) is calculated based on the dissolution rate of quartz (see parent report output DTN: MO0609SPAINOUT.002, folder: Dissolution_Rates_of_Tuff_Minerals, file: *cristobalite&quartz.xls*). This approach is based on findings of Rimstidt and Barnes (1980 [DIRS 101708]), who showed that all the silica polymorphs share the same growth rate at near-neutral pH when conditions are far from equilibrium. Renders et al. (1995 [DIRS 107088]) further showed that the ratio of dissolution rate to precipitation rate should be proportional to the solubility of a silica polymorph. Thus, the ratio of dissolution rates for two different polymorphs is proportional to the ratio of solubilities. Table 4-11 of the parent report gives the solubility constants for cristobalite and quartz. Spreadsheet *cristobalite&quartz.xls* uses these data to calculate a solubility ratio that is multiplied by the quartz dissolution rate to obtain the cristobalite dissolution rate.

The dissolution rates of annite and phlogopite at 25°C are assumed to be the same as the dissolution rates of muscovite at 70°C (see parent report output DTN: MO0609SPAINOUT.002, folder: Dissolution_rates_of_Tuff_Minerals, file: *Annite and Phlogopite Dissolution (muscovite).xls*). Complete kinetic data for mica dissolution are available only for muscovite; very limited pH data are available for phlogopite and biotite (annite is the iron-rich end member of the latter). Nagy (1995 [DIRS 124361]) states that most sheet silicates have approximately the same dissolution rate on a mole-mineral basis at 25°C and near-neutral pH. Nagy (1995 [DIRS 124361], Table 6) gives dissolution rates for phlogopite and biotite as approximately 4 and 6 times those of muscovite at 25°C at a pH of 5. Activation energies for muscovite (Nagy 1995 [DIRS 124361], Table 8) are estimated to be from 22 to 54 kJ/mole, indicating that the dissolution rate of muscovite at 70°C should be from 3 to 17 times the value at 25°C (calculated in *activation_energy_multipliers.xls*, tab "Muscovite rates," output DTN: MO0705PHREEMOD.000). Thus, the 70°C muscovite rates should approximate the phlogopite and annite rates at 25°C, because the increase in rates expected for muscovite going from 25°C at 70°C is approximately equal to the increase in rates at 25°C expected for a change in mineral going from muscovite to phlogopite or annite.

4.1.7.2[a] Dissolution at 50°C for Addendum

The source terms listed in Table 4-5[a] were generated from EQ6 runs at 50°C. The dissolution rates for the tuff minerals developed in the parent report represent 25°C dissolution rates. Dissolution rates at 50°C were calculated using: (1) the activation energies from *A Compilation of Rate Parameters of Water-Mineral Interaction Kinetics for Application to Geochemical Modeling* (Palandri and Kharaka 2000 [DIRS 175261], pp. 15, 24, 26, and 38), (2) the universal gas constant of 8.31451 J/(mol·K) from *Nuclides and Isotopes, Chart of the Nuclides* (Parrington et al. 1996 [DIRS 103896], p. 59), and (3) the Arrhenius equation (Stumm and

Morgan 1996 [DIRS 125332], Equations 129 and 130). (The inputs from Palandri and Kharaka 2000 [DIRS 175261] and Parrington el al. 1996 [DIRS 103896] are classified as "Established fact" because they are sources that scientists would use in their normal work practices, containing a compilation of rate parameters and numerical constants.) The values of the activation energies and the calculations are contained in *activation_energy_multipliers.xls* (tab: "Tuff mineral rates 50," output DTN: MO0705PHREEMOD.000). The resulting dissolution rates of the tuff minerals at 50°C are tabulated in Section 6.4-2[a].

4.1.8[a] Invert Properties

No changes.

4.1.9[a] Adsorption Coefficients

No changes.

4.1.10[a] Characteristics of Fractures, Matrix, and Lithophysae

In addition to the references listed in Table 4-18 of the parent report, DTN: GS991108314224.015 [DIRS 151042] provided the sizes of lithophysae (5 cm to greater than 100 cm) and the void percentage of the lithophysae clusters (3% to 30%). The maximum value of infill thickness in lithophysae within the repository was observed to be 50-mm (DTN: GS980308315215.008 [DIRS 107355], values in column "Fracture Infill Thickness (cm)" for those entries with "Lithophysal Cavities" in column "Type"). The lithophysae data are used in Section 6.9[a].

4.1.11[a] Atomic Weights

No changes.

4.1.12[a] Waste Package Dimensions

No changes.

4.1.13[a] Log K Values Used in Sensitivity Analyses for Uncertainty

No changes.

4.1.14[a] Justification and Qualifications of External Sources

No changes.

4.1.15[a] Seepage Rates

The range of drift seepage flux expected for the seismic and igneous scenarios is presented in Figures 4-1[a] and 4-2[a]. The values represent locations in the repository with the lowest seepage (PS1) and the highest seepage (PS5). The drift seepage represents the water that enters the area defined by the diameter of the emplacement drift and the waste package length. The values shown are for the CSNF waste packages. Data is also available for codisposal waste

packages, but the values are approximately the same (see DTN: MO0705GEOMODEL.000 [DIRS 181798], file: *Igneous seepage.xls*, tabs: "25% Chart" and "95% Chart"). The values were calculated in the MDR model (DTN: MO0705GEOMODEL.000 [DIRS 181798]), based on Goldsim calculations for the total system performance assessment. The values are used to demonstrate that the flow rates used in Section 6.4.6 of the parent report are reasonable values. These values replace the seepage values that are presented in the parent report in Assumption 5.2.3, Section 5.

4.1.16[a] Atom Number Density Calculations

The density of crystalline PuO_2 (11.46 g/cm^3) and the iron nuclide atom percentages, as listed in *Exter_Crit.xls* (output DTN: MO0705SCALEGEO.000), come from *CRC Handbook of Chemistry and Physics* (Weast 1978 [DIRS 128733], p. B-148 and pp. B-284, B-285, respectively). Inputs from *CRC Handbook of Chemistry and Physics* (Weast 1978 [DIRS 128733]) are considered "established fact," as it is a handbook that scientists and engineers would use in their normal work practices, containing solid densities and isotope abundances. The inputs are used in the atom number density calculations described in Section K.3[a].

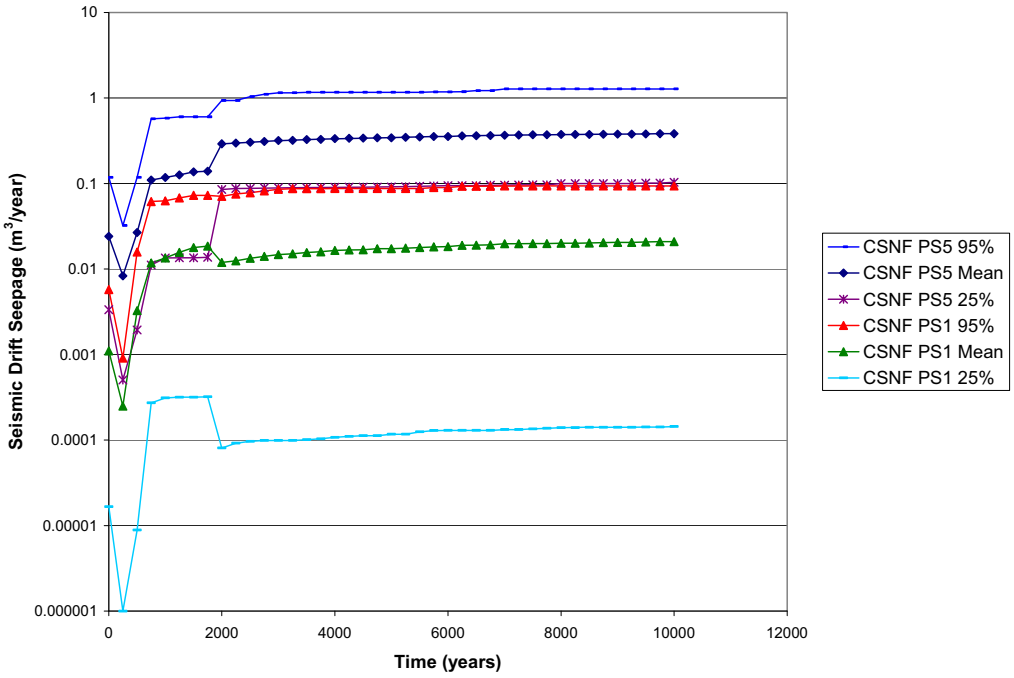

Source: DTN: MO0705GEOMODEL.000 [DIRS 181798], folder: seepage, file: *Seismic seepage.xls*.

Figure 4-1[a]. Seismic Drift Seepage

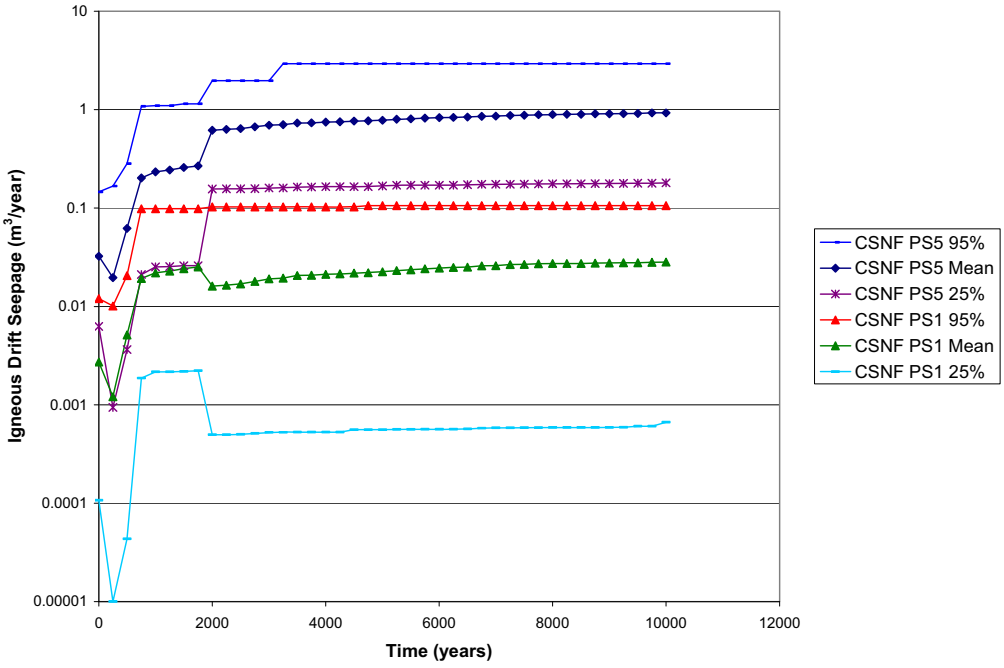

Source: DTN: MO0705GEOMODEL.000 [DIRS 181798], folder: seepage, file: *Igneous seepage.xls*.

Figure 4-2[a]. Igneous Drift Seepage

4.2[a] CRITERIA

No changes.

4.3[a] CODES, STANDARDS, AND REGULATIONS

No changes.

INTENTIONALLY LEFT BLANK

5[a]. ASSUMPTIONS

5.1[a] DISCUSSION OF ASSUMPTIONS IN UPSTREAM DOCUMENTS

No changes.

5.2[a] ASSUMPTIONS INTERNAL TO EXTERNAL ACCUMULATION MODEL

5.2.1[a] Carbon Dioxide Conditions

No changes.

5.2.2[a] Oxidizing Conditions

No changes.

5.2.3[a] Seepage Rates

The values for seepage rates are no longer an assumption. The seepage rates are presented in Section 4.1.15[a].

INTENTIONALLY LEFT BLANK

6[a]. MODEL DISCUSSION

6.1[a] OBJECTIVES

The objective of the addendum is to perform external accumulation analyses with revised inputs and to add calculations to determine the mass of accumulated fissile material that would be required in order to pose a significant probability of a critical event occurring. The revised inputs to the PHREEQC-based external accumulation model are described in Section 6.4[a] (including subsections) and Appendix I[a]. The criticality calculations are described in Section 6.9[a] (and subsections) and Appendix K[a]. When no additional information is needed for the calculations, the sections are marked as "No changes."

6.2[a] CONCEPTUAL MODEL

This addendum considers dissolved releases from the waste package due to an igneous or seismic event. As described in Section 6.2 of the parent document, in the external accumulation model, PHREEQC is used to determine accumulation in the invert or host rock due to precipitation and adsorption of uranium and plutonium contained in waste package effluent. The precipitation occurs in the invert or host rock due to mixing of the radionuclide-carrying waste package effluent with seepage water that does not contain fissile elements. The changes in chemistry of the resulting solution may result in lower solubilities of the fissile material, leading to precipitation.

6.3[a] NOMINAL CASE—DIFFUSIVE RELEASES—SCOPING CALCULATIONS

No changes.

6.4[a] SEISMIC FAULT DISPLACEMENT AND IGNEOUS CASES—DISSOLVED RELEASES

No changes.

6.4.1[a] Source Term Description

The source terms used in the PHREEQC simulations are listed in Table 4-5[a]. Two types of source terms were used for the PHREEQC simulations—igneous and seismic scenarios. For each source term, the software ASPRIN was used to calculate the enrichment fraction (ratio of ^{235}U to total uranium) in the effluent solution. The details of the ASPRIN calculations are provided in Appendix I[a]. Table 6.4-1[a] lists the isotopic mole fraction for each waste form used in the ASPRIN calculations. Figures 6.4-1[a] and 6.4-2[a] provide plots of aqueous concentration of uranium and plutonium and the enrichment fraction for each source term. In addition, the points identified for PHREEQC simulations are marked on the figures.

Table 6.4-1[a]. Isotopic Mole Fraction for Each Waste Form

Units	CSNF	FFTF Mixed Uranium and Plutonium Oxide (MOX)	FFTF Uranium Oxide (UO_X)	HLWG[a]
Moles uranium per mole of waste form	N/A[b]	2.75×10^{-1}	3.70×10^{-1}	6.90×10^{-3}
Moles plutonium per mole of waste form	N/A[b]	9.41×10^{-2}	0	1.00×10^{-4}
Moles ^{233}U per mole uranium	0	0	0	8.28×10^{-5}
Moles ^{234}U per mole uranium	4.17×10^{-4}	0	0	8.13×10^{-5}
Moles ^{235}U per mole uranium	1.11×10^{-2}	1.90×10^{-3}	7.00×10^{-3}	4.12×10^{-3}
Moles ^{236}U per mole uranium	6.88×10^{-3}	4.55×10^{-2}	0.00	4.70×10^{-4}
Moles ^{238}U per mole uranium	9.82×10^{-1}	9.53×10^{-1}	9.93×10^{-1}	9.95×10^{-1}
Moles ^{239}Pu per mole plutonium	7.67×10^{-1}	1.00	0	1.00
Moles ^{240}Pu per mole plutonium	1.38×10^{-1}	0	0	0
Moles ^{242}Pu per mole plutonium	9.56×10^{-2}	0	0	0

[a] The HLWG composition used in the EQ6 run that generated the FFTF source term (Table 4-5[a]) is based on a glass composition (Allison 2004 [DIRS 168734]) that differs slightly from the HLWG composition used in the parent report.

[b] Not applicable because it is not needed in the addendum calculations.

Sources: Parent report output DTN: MO0609SPAINOUT.002, file: *Fuel_Isotopic_Composition.xls* (CSNF and FFTF); DTN: MO0705GEOMODEL.000 [DIRS 181798], file: *CDSP_HLWGlass_2004.xls,* tabs: "HLWG Oxide Conversions," rows 52 to 53; "U content," rows 44 to 48 (HLWG).

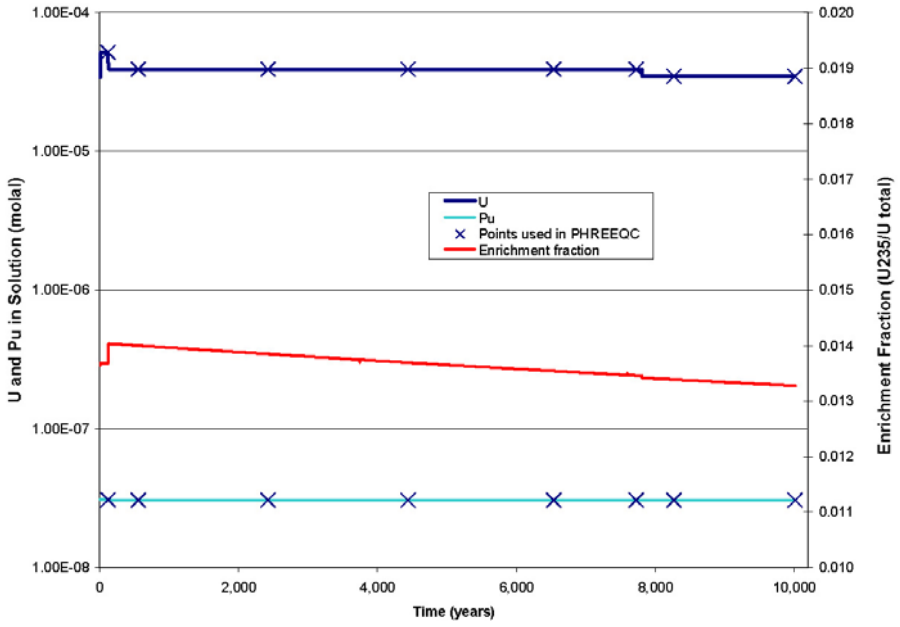

Source: Output DTN: MO0705PHREEMOD.000, folder: CSNF-Igneous\asprin, file: *CSIGAdEh U Pu.xls*.

Figure 6.4-1[a]. CSNF Source Term, 1000 L/yr, Uranium in Solution versus Time

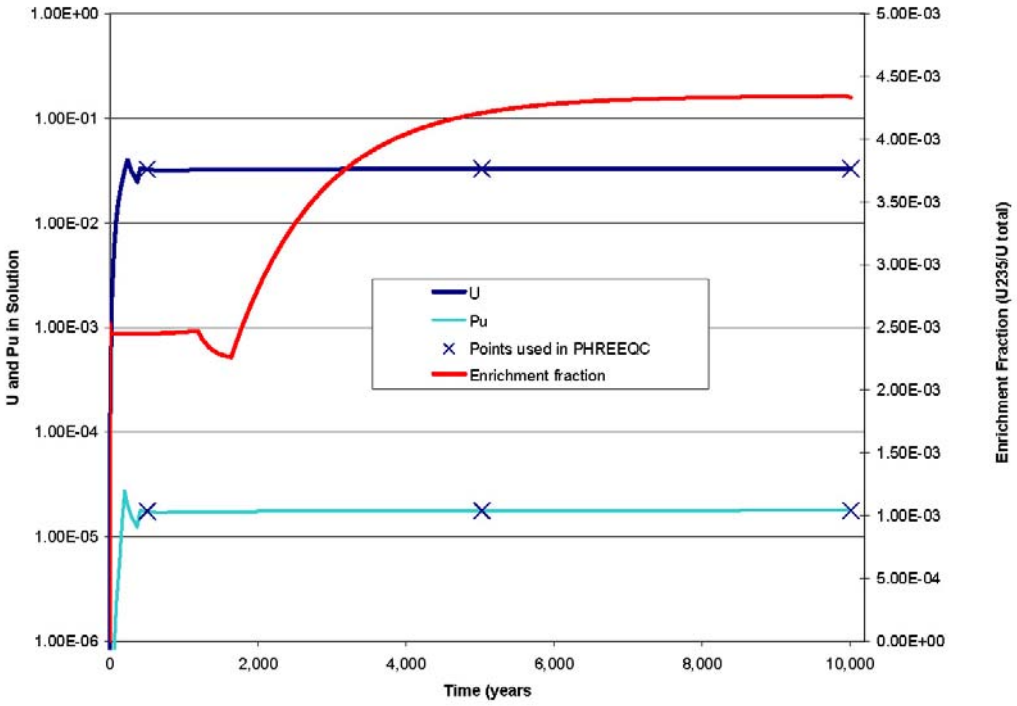

Source: Output DTN: MO0705PHREEMOD.000, folder: FFTF-Seismic\asprin, file: *FFTFMxGE U Pu.xls*.

Figure 6.4-2[a]. FFTF Source Term, 1 L/yr, Uranium and Plutonium versus Time

The EQ6 input file that generated the FFTF source term contained correction factors (Augment Log K) so that correct values of log K at 50°C for certain gadolinium and plutonium species were used in the simulations. Using the values listed in Table 4-6[a], the log K values at 50°C were calculated in *Gd-Pu-augmentk.xls* (output DTN: MO0705PHREEMOD.000). The resulting values are presented in Table 6.4-2[a]. The corrected values were included in each of the PHREEQC input files for the FFTF case (for example, see output DTN: MO0705PHREEMOD.000, folder: FFTF-Seismic\Phreeqc_Runs\rlz1, file: *FFTF_0.503k.in*). During checking, it was identified that the log K value used in the PHREEQC input files for the dissolution of $Gd_2(CO_3)_3$ (solid) was the value of −5.61822, rather than −5.08726. This small discrepancy (−0.53096) resulted in a lower solubility of $Gd_2(CO_3)$ than the conditions used in the EQ6 source term, which could have led to precipitation of the mineral simply due to the changes in the log K value. However, since the mineral did not form during the PHREEQC simulations (output DTN MO0705PHREEMOD.000, folder: FFTF-Seismic\Min_Acc, file: *FFTF_Vol_summary.xls*, tab: "Sorted Minerals"), the discrepancy has no impact on the results. Thus, the simulations were not rerun.

Table 6.4-2[a]. Augment Log K Values for FFTF PHREEQC Input File

Equation	log K, 50°C
$Gd^{3+} + HCO_3^- = GdCO_3^+ + H^+$	−2.22931
$Gd^{3+} + 2HCO_3^- = Gd(CO_3)_2^- + 2H^+$	−7.04218
$Gd^{3+} + HCO_3^- = GdHCO_3^{2+}$	2.63328
$Gd_2(CO_3)_3$ (solid) + $3H^+ = 2\ Gd^{3+} + 3HCO_3^-$	−5.08726
$PuO_2^{2+} + HCO_3^- = PuO_2CO_3$ (aq) + H^+	1.50649

Source: Output DTN: MO0705PHREEMOD.000, file: *Gd-Pu-augmentk.xls*.

6.4.2[a] Dissolution of Tuff Minerals

The dissolution rate constants for the tuff minerals were calculated for 50°C (Table 6.4-3[a]) based on the rate constants for 25°C developed in the parent report in Table 6-4. The calculations are presented in *activation_energy_multipliers.xls* (output DTN: MO0705PHREEMOD.000).

Table 6.4-3[a]. Dissolution Rate Constants of Minerals in the Topopah Spring Tuff for 50°C

	Dissolution Rate = $k_1[H^+]^{S1} + k_2[H^+]^{S2}$ (mol/cm^2·s)			
	Acidic Leg		Basic Leg	
Mineral	k_1	S1	k_2	S2
Cristobalite	3.00×10^{-15}	0.0594	5.28×10^{-18}	−0.318
Annite	4.71×10^{-15}	0.426	1.46×10^{-18}	−0.231
Phlogopite				
Maximum Microcline	2.77×10^{-14}	0.443	4.95×10^{-16}	−0.0214
Albite_low	6.05×10^{-14}	0.33	4.60×10^{-18}	−0.32
Anorthite	2.65×10^{-11}	0.91	3.49×10^{-18}	−0.30

Source: The values of S1 and S2 are unchanged from Table 6-4 in the parent report. The values of k_1 and k_2 are calculated in output DTN: MO0705PHREEMOD.000, file: *activation_energy_multipliers.xls*.

6.4.3[a] Adsorption onto Tuff Minerals

No changes.

6.4.4[a] Minerals Included during PHREEQC Simulations

In addition to the minerals listed in Table 6-7 of the parent report, the minerals listed in Table 6.4-4[a] were included in the PHREEQC simulations. (Minerals included in the PHREEQC input files will only form if the thermodynamic conditions are favorable.)

Table 6.4-4[a]. Minerals Included in PHREEQC Input Files

Mineral	Chemical Formula (Thermodynamic Database)	Justification
Becquerelite	$Ca(UO_2)_6O_4(OH)_6{:}8H_2O$	Occurs as a secondary uranium mineral usually closely associated with uraninite (Roberts et al. 1990 [DIRS 107105], p. 78).
$CaUO_4$	$CaUO_4$	Moroni and Glasser (1995 [DIRS 178395]) reported formation of $CaUO_4$ in high Ca environments.
Clinochlore-7A	$Mg_5Al_2Si_3O_{10}(OH)_8$	Clinochlore is in solid solution with daphnite (also known as chamosite) (Deer et al. 1992 [DIRS 163286], p. 335). Both minerals are in the chlorite group and may form authigenically (Deer et al. 1992 [DIRS 163286], p. 342), which indicates possible precipitation under repository conditions. While chlorite typically forms at elevated temperatures ($\geq$200°C), it is used in numerical simulations to represent the "mixed layer hydroxide" minerals commonly found in soils and that would be expected around the repository (Dixon 1995 [DIRS 159374]).
Compreignacite	$K_2(UO_2)_6O_4(OH)_6{:}8H_2O$	This phase was one of the uranium phases formed during laboratory degradation of UO_2 (Wronkiewicz et al. 1996 [DIRS 102047], Table 5). Also, found as a rare oxidation product of "pitchblende" in uranium deposits, along with other uranium minerals favorable to forming in the waste package, such as schoepite and uranophane.

NOTE: This table contains the minerals included in the PHREEQC modeling that are not listed in Table 6-7 of the parent report.

6.4.5[a] Use of PHREEQC and Postprocessing Macros for Geochemical Modeling

6.4.5.1[a] Use of PHREEQC V2.3

The EQ3/6 thermodynamic database (*Data0.ymp.R5*; DTN: SN0612T0502404.014 [DIRS 178850]) was converted into a format that can be used by PHREEQC. The conversion was accomplished using the YMP-qualified code *transl V2.0* (STN: 10251-2.0-00 [DIRS 155029]). The translation of the database contains the thermodynamic data for geochemical simulations valid at 25°C (output DTN: MO0704PHREEQ25.000), 50°C (output DTN: MO0704PHREEQ50.000), and 90°C (output DTN: MO0709PHREEQ90.000). Only the 50°C version of the database was used in the addendum calculations. During the translation, CR-8766 was addressed, in which the *azero* parameter in the PHREEQC database was checked to ensure it was correct.

6.4.5.2[a] GetEQPhases3

No changes.

6.4.5.3[a] Use of PHREEQC_Post V1.1

No changes.

6.4.5.4[a] Use of Acc_with_decay V1.2

No changes.

6.4.5.5[a] Use of MinAcc V1.0

No changes.

6.4.5.6[a] Results—Accumulation of Minerals

Tables 6.4-5[a] and 6.4-6[a] tabulate the volumes of minerals accumulated in the invert per one kilogram of solution, including the uranium and plutonium minerals. The volumes are scaled down so that the total volumes do not exceed the capacity of the invert, as described in Section 6.4.5.6 of the parent document. As mentioned in Section 6.2 of the parent report, redissolution of the precipitated minerals are not allowed in the model; therefore, the accumulated volumes at 10,000 years represent the maximum accumulation.

Table 6.4-5[a]. Average Volume of Minerals Accumulated at 10,000 Years for Source Term CSNF, Igneous Scenario, Flow at 1,000 L/yr

Mineral Type	Mineral Name	Volume (cm^3/kg of solution) at 10,000 Years
Uranium Minerals	Uranophane(alpha)	381.94
	$CaUO_4$	32.37
	Boltwoodite-Na	2.39
Plutonium Minerals	None	0
Other Minerals	Saponite-Mg	147.33
	Saponite-Ca	18.44
	Stellerite	66.79
	Chabazite	15.35
	Zn_2SiO_4 (Willemite)	2.24
	Nontronite-Mg	0.11
	Nontronite-Ca	0.04

Source: Output DTN: MO0705PHREEMOD.000, folders: CSNF-Igneous/CSNF_REV02_MinAcc, file: *CSNF_REV02_Vol_Summary.xls*, tab: "Sorted Minerals," columns E and H.

NOTE: Only values greater than 0.01 cm^3/kg of solution for all minerals are presented.

Table 6.4-6[a]. Average Volume of Minerals Accumulated at 10,000 Years for Source Term FFTF, Seismic Scenario, Flow at 1 L/yr

Mineral Type	Mineral Name	Volume (cm^3/kg of solution) at 10,000 Years
Uranium Minerals	Boltwoodite-Na	444.71
Plutonium Minerals	None	0
Other Minerals	Erionite	136.81
	Chabazite	49.76
	Phillipsite	19.60
	Mesolite	6.36
	Chalcedony	4.92
	Saponite-Na	2.72
	Nontronite-Na	2.12

Source: Output DTN: MO0705PHREEMOD.000, folders: FFTF-Seismic/ Min_Acc, file: *FFTF_Vol_summary.xls*, tab "Sorted Minerals," columns E and H.

NOTE: For all minerals, only values greater than 0.01 cm^3/kg of solution are presented.

Table 6.4-7[a] contains the moles of uranium and plutonium released from the waste package, moles precipitated within the crushed tuff of the invert or the host rock, and moles adsorbed onto the tuff. The moles of precipitated and adsorbed radionuclides were summed for total accumulation and converted to units of mass in *Mass accumulated.xls* (output DTN: MO0705PHREEMOD.000), using molecular weights from Audi and Wapstra (1995 [DIRS 149625], p. 60). (The inputs from Audi and Wapstra 1995 [DIRS 149625] are considered "established fact" since it is a source that scientists and engineers would use in their normal work practices, containing tables of the atomic mass for radioisotopes of the chemical elements.) The results are presented in Sections 8.1.2[a] and 8.1.3[a].

Both sets of results presented in Table 6.4-7[a] show no plutonium precipitation and very small amounts of adsorbed plutonium, which is similar to all of the cases analyzed in the parent report (Table 6-15). The results presented in Table 6.4-7[a] also show that about 80% of the uranium released from the waste package was precipitated, with very little adsorption. This is similar to the previous results for CSNF (Table 6-15 of the parent report), but differs for the previous FFTF case (Table 6-15 of the parent report, case *FFTFIG1adEhdec*) in which only about 10% precipitated and 10% was adsorbed. The differences are explained by the different compositions of the mixing waters used for the accumulation calculations. For the FFTF case from the parent report, the scenario is an igneous scenario in which the source term was mixed with basalt water with a pH of 9.02 (Table 4-1 of the parent report), whereas, for the FFTF case in the addendum, the scenario is a seismic scenario in which the mixing water was J-13 well water with a pH of 8.36 (Table 4-3[a]). When a mixing water with a higher pH (such as the basalt water) is combined with a source term, the resultant solution has a higher pH than the resultant solution would have if a lower pH solution (such as the J-13 well water) was mixed with the source term. The higher pH solution has a higher uranium solubility, which leads to less material precipitating. In addition, the higher uranium concentration of the higher pH solution leads to higher adsorption. Therefore, though some of the results presented in the addendum and the parent report are different, the differences are based on the different scenarios being modeled.

Table 6.4-7[a]. Uranium and Plutonium Flushed from Various Waste Packages, Precipitated and Adsorbed at Approximately 10,000 Years after Waste Package Breach

Source Term	Waste Package Type, Scenario, and Conditions	^{239}Pu Moles			Total U Moles			^{235}U Moles		
		Flushed from Waste Package	Precip-itated	Adsorbed	Flushed from Waste Package	Precip-itated	Adsorbed	Flushed from Waste Package	Precip-itated	Adsorbed
CSNF	CSNF Igneous 1000 L/yr	3.06×10^{-1}	0.00	3.06×10^{-6}	3.82×10^{2}	3.14×10^{2}	6.72×10^{-4}	5.19	4.13	8.93×10^{-6}
FFTF	FFTF Seismic 1 L/yr	1.78×10^{-1}	0.00	3.61×10^{-3}	3.30×10^{2}	2.71×10^{2}	2.63	1.38	1.16	1.14×10^{-2}

Source: Output DTN: MO0705PHREEMOD.000.

NOTE: For the total-U moles, ^{235}U moles, and ^{239}Pu moles precipitated, under the folder for each source term, see folder *Acc_with_decay* and file *CSNF_REV02_Acc_with_decay1.2_cell.xls* for CSNF, and file *FFTF_J-13_Acc_with_decay.xls* for FFTF.

For the moles adsorbed, see file *adsoprtion_calc.xls*; use tab for each source term.

For the moles flushed from the waste package, see folder CSNG-Igneous\asprin, file: *CSIGAdEh U Pu.xls*; folder FFTF-Seismic\asprin, file: *FFTFMxGE U Pu.xls*.

6.4.6[a] Flow and Transport in the Invert Using TOUGHREACT

No changes.

6.4.7[a] Location of Accumulation Zone within the Invert

No changes.

6.4.8[a] Accumulation within the Fractures and Lithophysae of the Host Rock

No changes.

6.5[a] BOTTOM FAILURE AND SOLID RELEASE FOR ALL SCENARIOS

No changes.

6.6[a] SEISMIC SCENARIO—ENTRAINED RELEASES

The corresponding section in the parent report, Section 6.6, is deleted. Entrained releases were not estimated in the MDR model (SNL 2007 [DIRS 181165], Section 8), and therefore are not considered in the external accumulation model.

6.7[a] ALTERNATIVE CONCEPTUAL MODELS

No changes.

6.8[a] SENSITIVITY ANALYSES

No changes.

6.9[a] EXTERNAL CRITICALITY CALCULATIONS

External criticality calculations are included in this addendum to estimate the mass of fissile materials that would be required to accumulate in the invert or host rock in order to pose a credible probability of a critical event occurring. When a system is "critical," the multiplication factor, k, is equal to 1, where k is defined as the number of neutrons in one generation divided by the number of neutrons in preceding generation (Duderstadt and Hamilton 1976 [DIRS 106070], p. 75). The infinite medium multiplication factor, k_{∞}, is a multiplication factor for an infinite system and the effective multiplication factor, k_{eff}, is a multiplication factor for a finite system (Duderstadt and Hamilton 1976 [DIRS 106070], pp. 81 and 84). The critical limit, which is the value of k_{eff} at which a configuration is considered potentially critical, is derived from the bias and uncertainties associated with the criticality code, nuclear data, and modeling process (YMP 2003 [DIRS 165505], Section 3.5.3.2.5). For this report, a value of k_{eff} equal to 0.96 was chosen as the critical limit, which is equivalent to or slightly lower than the lower critical limits calculated for CSNF (0.97) (BSC 2004 [DIRS 168553], Table 5, Waste Form: "IEU External" and "HEU External"), N-reactor (0.975) (BSC 2003 [DIRS 164419], Figure 31), FFTF (0.96) (BSC 2003 [DIRS 164419], Figure 19), and TMI (0.97) (BSC 2003 [DIRS 164419], Figure 33).

The resulting calculations can be used, along with the external accumulation model results, to establish the probability of achieving a critical event within the invert, or the host rock.

6.9.1[a] Basis of Calculations

Figure 6.9-1[a] provides diagrams of the external configurations considered in the criticality calculations. For the sake of simplicity and to increase reactivity of the system, the external criticality calculations were based on a sphere of a fissile-bearing mineral dispersed in a partially saturated rock matrix, surrounded by an infinite reflector (thickness greater than 300-mm) of a similar material. The computational steps required to get from the realistic depictions presented in Figure 6.9-1[a] to the spherical representation used in the criticality calculations are described in *Exter_Crit.xls* (output DTN: MO0705SCALEGEO.000, tab: "Introduction"). The small-scale heterogeneities of dispersal of the radionuclide-containing material into and through the rock matrix were modeled explicitly. Mass limits were based on a critical limit of $k_{eff} = 0.96$ for the reflected sphere configuration. The methodology used to determine the potential for criticality events external to waste packages is presented in detail in Appendix K[a].

All criticality calculations were performed with the SCALE V. 5.1 system (STN: 10129-5.1-00 [DIRS 181249]). The XSDRNPM module of the SCALE V. 5.1 system was used, along with the physical representation for this effort as a one-dimensional reflected sphere. XSDRNPM is a discrete-ordinates code that solves the one-dimensional Boltzmann transport equation in slab, cylindrical, or spherical coordinates. All calculations used the 238 group ENDF-VI criticality library of tabulated cross sections provided as a standard component of the SCALE code system (STN: 10129-5.1-00 [DIRS 181249]) and residing on the computers where the code is installed. The cross sections were self-shielded and resonance-processed with the BONAMI, CENTRM, and PMC modules (all qualified modules of the SCALE V.5.1 system) to treat the small-scale heterogeneity effects.

A deterministic method was chosen for these calculations in order to address the heterogeneity of the rock–liquid–fissile material system. The scale of the heterogeneity represented was on the order of less than a millimeter to several centimeters. The heterogeneity effect added on the order of 0.01 to 0.05 to k_{eff} versus a homogeneous representation.

The fissile material–rock–water configuration is not a homogeneous mixture. At low enrichments, heterogeneous mixtures can be more reactive than homogeneous mixtures, and this is true for the CSNF and some of the DOE SNF. At high enrichments the opposite is true. At low enrichments, the reactivity is increased because the neutrons released in fission can migrate through the rock and water media and miss the large resonances in the non-fissile isotopes of uranium. At high enrichments, lumping the uranium depresses the neutron flux at the centers of the lumps, and the fissile species are not as effectively utilized as they would be if the mixture were homogeneous. Therefore, detailed heterogeneity was considered for all enrichments, particularly those below 5% enriched in ^{235}U.

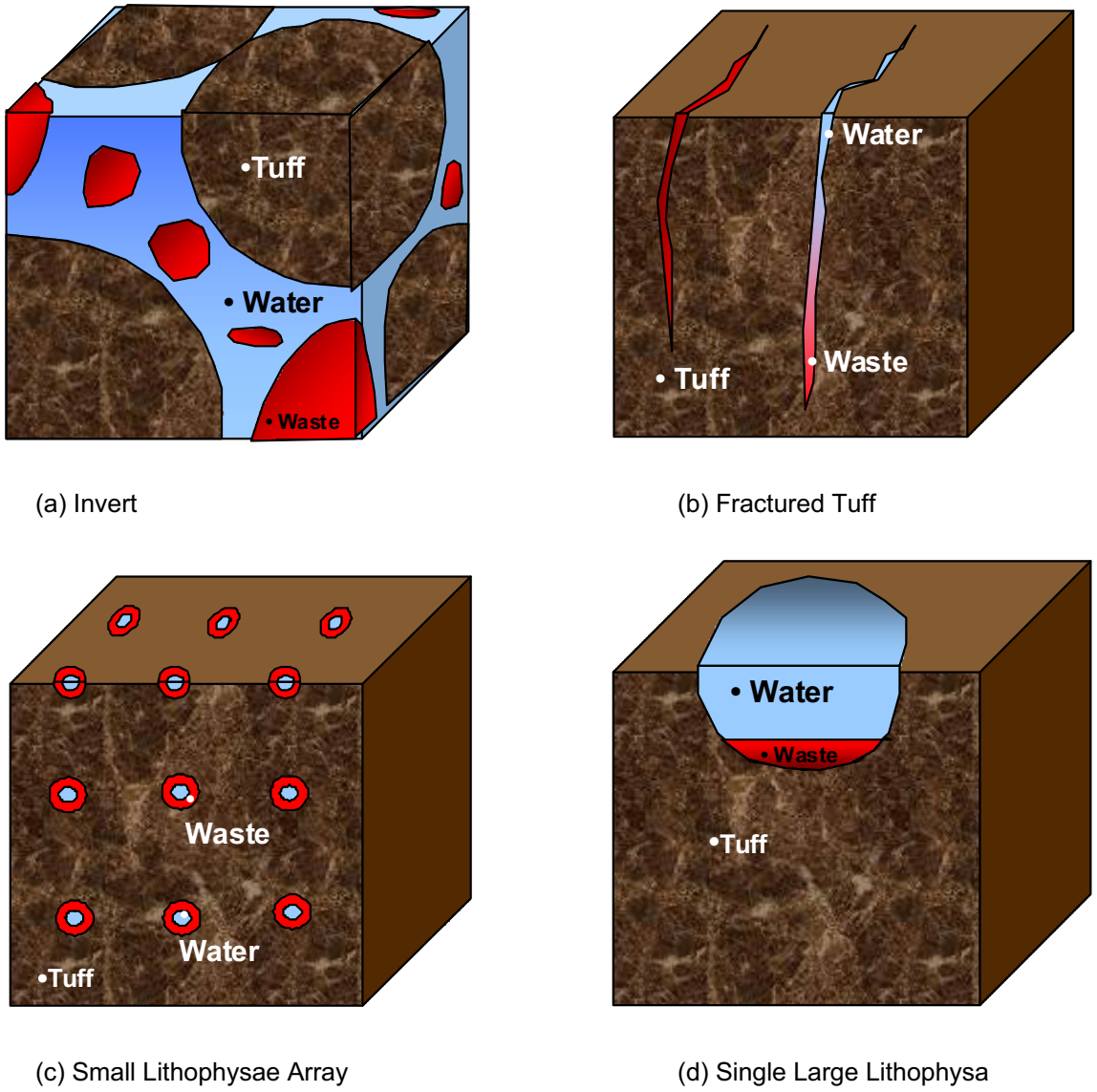

Source: Output DTN: MO0705SCALEGEO.000, file: *Exter_Crit.xls*.

NOTE: Red indicates the waste accumulated, where "waste" refers to precipitated minerals containing fissile material. The blue indicates the portion of the system filled 65.3% by volume with aqueous solution containing dissolved fissile material. The waste fraction is the volume of the waste (red) divided by the volume of the voids (red plus blue). The brown indicates the host rock, consisting of tuff.

Figure 6.9-1[a]. Diagrams of External Configurations for Criticality Calculations

The heterogeneity in the invert (near-field) was addressed as an array of spherical fuel particles surrounded by a mixture of water, rock, and void space. Three different environments were addressed for the analysis of heterogeneity effects in the far field. The first heterogeneity in the host rock was treated as an array of repeating slabs with interspersed fractures filled with fissile material, seepage water, and void space. The maximum water content filling the voids (0.653) was determined based on Appendix G in the parent report (details are given at the end of this section). The second and third heterogeneities in the host rock dealt with lithophysae partially filled with uranium or plutonium compounds and seepage water. These were treated in two

ways. Large lithophysae (> 200 mm, second heterogeneity) were treated as spherical voids filled with a fissile waste and seepage water mixture reflected by saturated tuff. In this case, a single lithophysa was treated as a separate entity. Small lithophysae (< 200 mm, third heterogeneity) were treated as an array of voids filled with a similar fissile waste/seepage water mixture (Figure 6.9-1[a], diagram (c)). The break point between large and small was chosen as 200 mm. Above 200 mm, the neutrons in one void are not able to communicate with adjacent voids, and the volume in the void is large enough to hold a critical mass for certain enrichments and fissile waste concentrations. Below 200 mm, the neutrons created in one void are able to communicate with fissile material in another void. To obtain a critical configuration with lithophysae below 200 mm in diameter, there must be more than one, and they need to be close together. While the arrays are random in nature, they were modeled as a regular arrangement. This simplification of the modeling captures the salient behavior of the system. Lithophysae that are located close together will have more interaction with each other, while those at greater separation will have less interaction, but in the aggregate, the effects would average out. The values of porosity of the rock containing the lithophysae and the lithophysae sizes were taken from DTN: GS991108314224.015 [DIRS 151042].

The main inputs to the external criticality calculations are the compositions of the rock matrix, the seepage water, the fissile material from the waste package effluent, and their mixing ratios. The rock matrix composition used for all of the external criticality calculations was Topopah Spring Tuff (Section 4.1.6 of the parent report). For the seismic cases, J-13 well water (Table 4-4[a]) filled the voids and pores in both the invert and the host rock. A sensitivity case using the concentration of SD-9 pore water gave nearly identical results to the J-13 water (output DTN: MO0705PHREEMOD.000, file: *CSNF.xls*, tab: "SSN5", columns M, N, O). For the igneous cases, basaltic water (Table 4-3[a]) filled the voids and pores in both the invert and the host rock. The uranium concentration for the seismic scenario was set equal to 1.21×10^{-4} moles/liter, the peak concentration observed in the CSNF seismic scenario from the parent document (output DTN: MO0609SPAINOUT.002, folder: CSFlux9\CSFlux9_Asprin, file: *Aqueous_Species_CSFlux9.xls*, column AJ). The uranium concentration for the all igneous scenarios (except TMI) was based on the peak concentration observed in the CSNF igneous scenario (5.17×10^{-5} molal) from the addendum (output DTN MO0705PHREEMOD.000, folder: CSNF-Igneous\asprin, file: *CSIGAdEh U Pu.xls,* tab: "phreeqc points, U Pu released"). The actual value used (5.43×10^{-5} molal) was taken from a preliminary simulation and was retained because it only slightly overestimates the uranium concentration and would only slightly overestimate the likelihood of a criticality. For the TMI igneous scenario, the highest uranium concentration (1.32×10^{-1} molal) predicted during the first 10,000 years for the TMI case in the parent report was used (parent report output DTN: MO0609SPAINOUT.002, folder: TMI_IG1\TMI_IG1_Asprin\TMI_IG1_Asprin, file: *TMI_IG1A.xls*).

Based on the results of the external accumulation model, the dominant uranium compounds that appear to form in the invert are uranophane and Na-boltwoodite (Tables 6-9, 6-11, and 6-14 of the parent report). The mineral $(UO_2)_3(PO_4)_2{:}H_2O$ formed for the FFTF igneous scenario at low flow rates (Table 6-11), but was not used in the criticality calculations because FFTF is only a concern for plutonium accumulation due to the low uranium enrichment in the fuel (Table 6.4-1[a]). Schoepite is found in spent fuel degradation experiments and could eventually form in the external environment (Section 7.2.3 of the parent report). Therefore, for the invert criticality calculations, schoepite was considered in addition to the primary minerals uranophane

and Na-boltwoodite. For the host rock analyses, only schoepite and uranophane were considered. Given the large ranges for the mixture variables that were considered, it is not likely that the exact waste form will have a big effect. Plutonium was considered to precipitate out as the compound PuO_2 rather than PuO_2(hyd,aged), which is listed in Table 6-7 of the parent report. This simplification has no impact on the reactivity of the system, since the waters of hydration on PuO_2(hyd,aged) would be overwhelmed by the abundance of water in the aqueous solution filling the voids.

Additional materials that are released from the waste packages, including neutron poisons and fission products, were neglected. This simplification increases the reactivity of the system.

Each fuel is modeled with its as-manufactured enrichment, which increases the reactivity of the system. In the case of CSNF, realistic burn-ups can easily be accounted for by comparing the results for fresh 5% enriched fuel, the 3% enriched TMI fuel, and the 1.3% enriched N-Reactor fuel.

Having identified the materials of interest, the next step is to identify how they are mixed. Since the waste packages will reside in drifts in the rock matrix over an invert filled with crushed rock, the mixing ratios and geometries must be split into three separate configurations. The first configuration deals with deposition in the crushed tuff in the invert. The second configuration deals with precipitation of the fissile material and water into the fractures in the rock matrix beneath the invert. The third configuration deals with the accumulation of waste in the spherical cavities of the lithophysae.

In the parent report (Section 4.1.8), two types of invert properties were addressed: The well-sorted (uniform particle size) and the poorly sorted (non-uniform particle sizes). The well-sorted crushed rock is identified as having a diameter of 3 mm (base case in Appendix F of the parent report), with an intergranular porosity of 0.45 (Table 4-16 of the parent report). The poorly sorted crushed rock specification indicates that the maximum size of the rock particles will be 50 mm, or less, and a distribution of sizes with less than 5% below a U.S. No. 200 sieve size (SNL 2007 [DIRS 179354], Table 4-1, Parameter 02-08, which points to BSC 2007 [DIRS 179897], Table 1 and Figure 1). The average particle diameter is estimated to be about 10 mm. The bed will be compacted to 95% of its maximum density. There is no simple way to model this random bed. Traditional nuclear engineering practice represents heterogeneities with regular or well-sorted arrays. Intergranular porosities for regular or well-sorted arrays tend to be larger than those for mixed arrays, as there are no smaller particles to fill in the spaces between the bigger particles. To estimate the performance of the invert then, a well-sorted array with particles of 10 mm diameter would be the first choice. However, due to the limitation on the ultra-fine particles (< than 200 sieve size), a regular array with a smaller diameter is a better representation for coming closer to the maximum intergranular porosity. The 3 mm regular array was chosen, as it meets this criteria, and matches the base case in the parent report. Another approach would be to self-shield cross sections for a number of different regular array particle sizes and then to combine them based on the distribution of particle sizes expected. There are no examples of this type of approach being taken in the nuclear engineering literature, and therefore it is not a validated approach. The 3 mm regular array with 45% maximum intergranular porosity is the best approximation to bound the reactivity of accumulations in the invert.

For the fractured tuff calculations, the heterogeneities were represented as repeating slabs of fissile minerals, liquid, and porous rock. The equivalent void fractions for the fractures in the rock matrix varied from 0.0075 to 0.0135 (slightly larger range than values in Table 6-25 of the parent report). The spacing between fractures was varied from 15 cm to 25 cm (slightly larger range than values in Table 6-24 of the parent report). For the filled lithophysae calculations in the far field, the lithophysae were represented first as spheres filled with a fissile mineral-liquid mixture that was limited to no more than 50% by volume (Section 6.4.8.5 of the parent report) of fissile waste, or to no more fissile waste than the amount required to build up a 50-mm layer on the internal bottom surface of the void (DTN: GS980308315215.008 [DIRS 107355], maximum value of infill thickness). The size of the void was allowed to vary so as to obtain the conditions for the minimum fissile mass required for k_{eff} = 0.96. For the repeating array of small lithophysae spheres, the diameter was varied from 50 to 200 mm, and the void fraction in the matrix was varied from 3% to 20%, based on values given in Section 6.4.8.4 of the parent report. Many of the voids observed were lenticular and not very spherical (Mongano et al. 1999 [DIRS 149850], Table 4). However, by treating the voids as spherical and allowing them to be completely filled, the calculations are conservative for criticality. No attempt has been made to justify how the voids could be filled with liquid, nor how they could retain this liquid once filled. The porosity of the rock matrix was set at 13% (Table 6-27 of the parent report).

The rock matrix pores were always considered saturated. A maximum saturation ($S_{f,max}$) of the void space in the invert, tuff, and lithophysae was chosen as 0.653, calculated from the final equation in Appendix G of the parent report, by setting total saturation ($S_{T,max}$) = 0.71, intergranular or fracture porosity (ϕ_f) = 0.4, matrix saturation ($S_{m,max}$) = 1.0, and matrix porosity ϕ_m = 0.131.

Each of the calculation sequences used in the SCALE input and output files (output DTN: MO0705SCALEGEO.000, folder: IO_ZIP) is identified by a code of three letters followed by a number. The first letter refers to the radionuclide containing material:

U = uranophane, B = Na-boltwoodite, S = schoepite, and P = PuO_2.

The second letter refers to the water type:

J = J-13 well water, B = basalt, and S = SD-9 pore water.

The third letter refers to the heterogeneity model employed:

N = invert, F = fractures, L = lithophysae arrays, and V = single lithophysa.

The number refers to the enrichment, where the higher-enriched DOE SNF does not correspond directly to any of the DOE SNF fuel groups, but are added for sensitivity cases:

1 = N-Reactor SNF (1.27 wt % enriched ^{235}U)
3 = TMI SNF (3 wt % enriched ^{235}U)
5 = CSNF (5 wt % enriched ^{235}U)
20 = DOE SNF (20 wt % enriched ^{235}U)
50 = DOE SNF (50 wt % enriched ^{235}U)

70 = DOE SNF (70 wt % enriched ^{235}U)
93 = DOE SNF (93 wt % enriched ^{235}U, Fort St. Vrain uranium and thorium dicarbide fuel)
98 = DOE SNF (98 wt % enriched ^{233}U, light water breeder reactor (LWBR) fuel)
10 = FFTF SNF (100 % enriched ^{239}Pu).

Thus, UBL20 would be uranophane with basalt water in the lithophysae array with 20 wt % enriched fuel.

6.9.2[a] Criticality Calculations Results

6.9.2.1[a] Critical Mass Bounds in the Invert (Near-Field)

CSNF in the Invert (Near-Field)—Since the greatest volume of material stored in the repository will be CSNF, it is appropriate to consider this waste form first. Once the compositions of the mineral waste form and filling liquid have been identified, there are seven parameters that can affect the maximum mass of fissile waste that can safely be accumulated without exceeding $k_{eff} = 0.96$. These are:

ε = fissile enrichment, set to 5 wt % enriched ^{235}U for CSNF
V_f = the fraction of total invert volume not occupied by rock (void fraction)
W_f = the volume fraction of the void (V_f) that is occupied by fissile waste (waste fraction)
S_l = saturation of remaining extra-granular spaces
D_w = diameter of rock particles
ϕ_m = rock matrix porosity
S_m = matrix saturation.

Once the matrix porosity and saturation, the enrichment, and the saturation of the remaining extra-granular spaces have been set, the fissile mass allowed to remain sub-critical depends on the particle diameter, D_w the void fraction, V_f, and the waste fraction, W_f. For all of the invert analysis performed here, the particle diameter was set to 3 mm. In the actual calculation, this becomes the diameter of the spherical waste particles as opposed to the rock particles. Since k_∞ increases very slightly with increased waste particle diameter for low enrichments, this choice of value increases reactivity. (For higher enrichments, 3-mm heterogeneity has a negligible effect on k_∞.) Then the maximum mass allowed to remain sub-critical depends simply on the waste fraction and the invert void fraction. The value for the invert void fraction has been identified as 0.45. This value provides the space for fissile waste and liquid to accumulate in the invert. In all calculations, this void fraction produced the minimum mass required to remain sub-critical. So in the following plots, curves for void fractions of 0.35 and 0.45 (and sometimes 0.4) are provided, though void fractions as low as 0.15 were calculated to ensure that no unusual effects were observed. The following plots then give the total mass of uranium fissile waste in the invert required to achieve $k_{eff} = 0.96$ as a function of the fraction of void space filled by the fissile waste, W_f.

The minimum fissile waste mass calculations proceed by estimating a radius for the waste containing spherical core, nominally 25 cm for CSNF. (The size of this core estimate is allowed to depend on the enrichment of the fissile waste for other fuels. It was always desirable to start

the search for the minimum critical size with a core size less than the actual minimum critical size due to a limitation in the XSDRNPM search algorithm. If the search algorithm predicts a negative radius, it quits rather than simply choosing a smaller radius than the current iteration.) The total fissile mass is then estimated for this initial core size. A spherical reflector, 100-cm thick, is then added to the core. This reflector has the same composition as the core, but replaces the fissile mass component with additional liquid. The core-plus-reflector sphere is then expanded (or contracted) until XSDRNPM calculates a k_{eff} equal to 0.96. The ratio of the radius calculated for this expansion (or contraction) to the initial radius is used to estimate the minimum critical mass. The value for the minimum critical mass is simply the value for the initial critical mass multiplied by the radius ratio cubed.

Because the invert has a finite depth, if the final core radius calculated for k_{eff} equal to 0.96 produces a core plus reflector that has a greater diameter than the depth of the invert, the calculated critical mass will be slightly more reactive. That is, a reflected sphere has the minimum volume (and fissile mass). Any permutation such as a smaller reflector or a non-spherical configuration will require a larger fissile mass to approach criticality. Even though the spherical representation used to estimate the minimum mass does not completely fit into the depth of the invert, the estimated mass is a lower bound for the mass that could be deposited in the invert and achieve a critical configuration. When the size of the configuration approaches or exceeds the depth of the invert, additional neutrons will leak out into the drift, and the tuff below the fissile mass will become part of the reflector. Both of these effects will tend to reduce the k_{eff} of the configuration. Therefore, the minimum mass calculated with the simple spherical model is a good lower bound for the minimum mass required to go critical. It is also simple to calculate and easily demonstrates its bounding properties.

The first scenario considered was the seismic scenario. The fissile mineral considered here is schoepite and the filling liquid is J-13 well water. The critical mass search results are given in Figure 6.9-2[a].

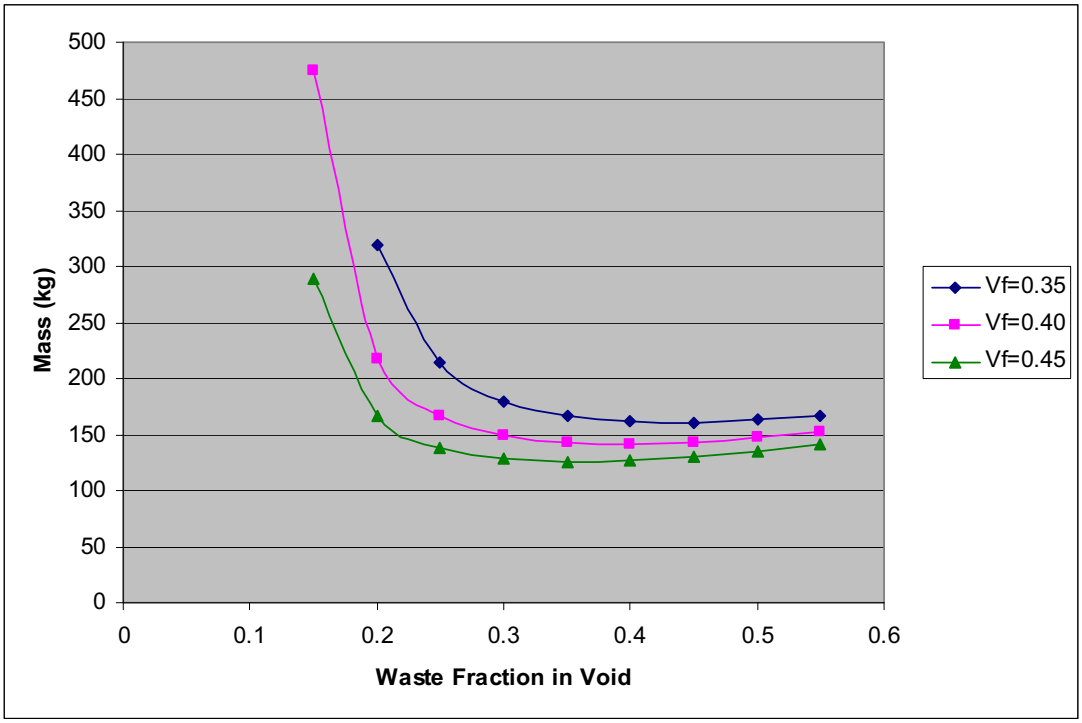

Source: Output DTN: MO0705SCALEGEO.000, file: *CSNF.xls*.

Figure 6.9-2[a]. Critical Masses of Uranium for SJN5 (schoepite, J-13 well water, CSNF)

The minimum mass of uranium for this case is 126 kilograms and occurs for a waste fraction in the void of 0.35. At 5 wt % enrichment, this gives 6.3 kilograms of ^{235}U. In calculating this total mass, the uranium in the liquid in the spherical core has a concentration of 1.21×10^{-4} moles/L. The uranium in the liquid outside of the core was included in the transport calculation but not in the mass estimate.

The second scenario considered was the igneous scenario. Two radionuclide-containing minerals were considered here, and the results are different. The void filling liquid was basalt water with a uranium concentration of 5.43×10^{-5} moles/L. The first radionuclide-containing mineral was Na-boltwoodite. The critical mass search results are presented in Figure 6.9-3[a].

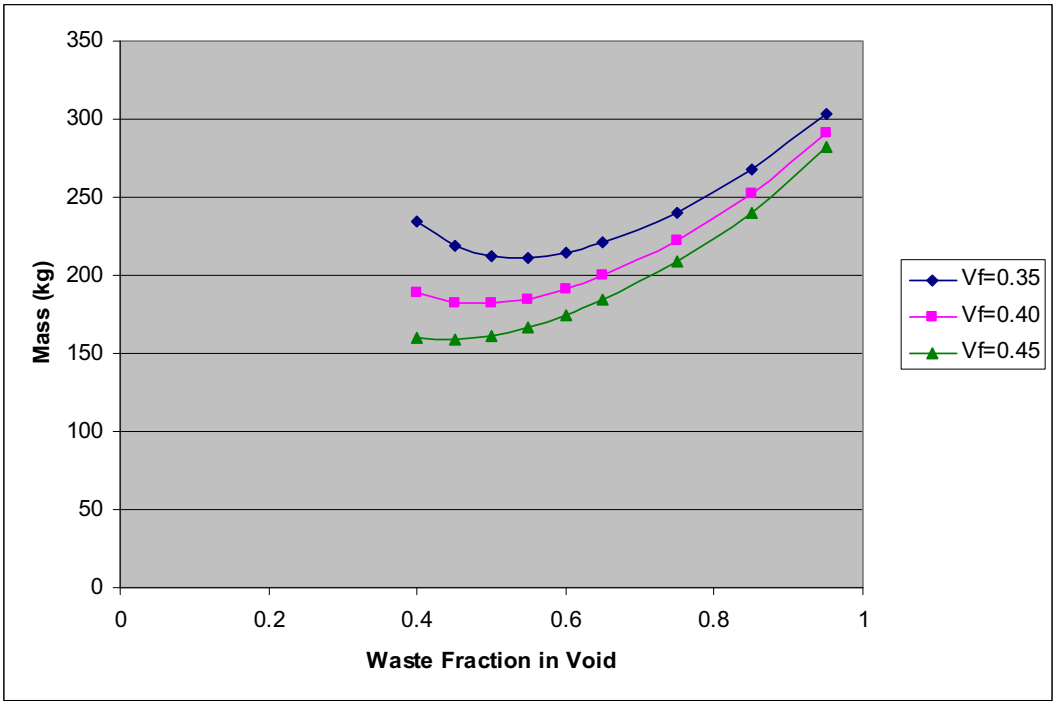

Source: Output DTN: MO0705SCALEGEO.000, file: *CSNF.xls*.

Figure 6.9-3[a]. Critical Masses of Uranium for BBN5 (Na-boltwoodite, basalt water, CSNF)

For this case, the minimum mass of 5 wt % enriched uranium is 159 kilograms, at a waste fraction of 0.45. The two sets of curves have a very similar structure. The second waste mineral considered was uranophane. The results for this waste form mineral are presented in Figure 6.9-4[a].

The results for this case are shifted to the right. This is due to the lower concentration of the uranium in the uranophane mineral. At theoretical density, uranophane has a uranium number density of 4.80×10^{21} atoms/cm^3, Na-boltwoodite has a uranium number density of 6.21×10^{21} atoms/cm^3, and schoepite has a uranium number density of 9.1×10^{21} atoms/cm^3. The minimum mass for uranophane is 158 kg, and it occurs at a waste fraction in the void of 0.45.

TMI Fuel in the Invert (Near-Field)—For this SNF, there is a significantly larger amount of uranium released into the invert. It is approximately 3 wt % enriched and provides a reasonable upper bound for the actual enrichment of most of the CSNF with any burnup of consequence.

In all of the analyses performed here, uranium and plutonium were considered totally separately. The reason for this approach is that the processes transporting these elements out of the fuel are different, and it is unlikely that the two elements would move together.

The seismic scenario for the TMI fuel is graphed in Figure 6.9-5[a].

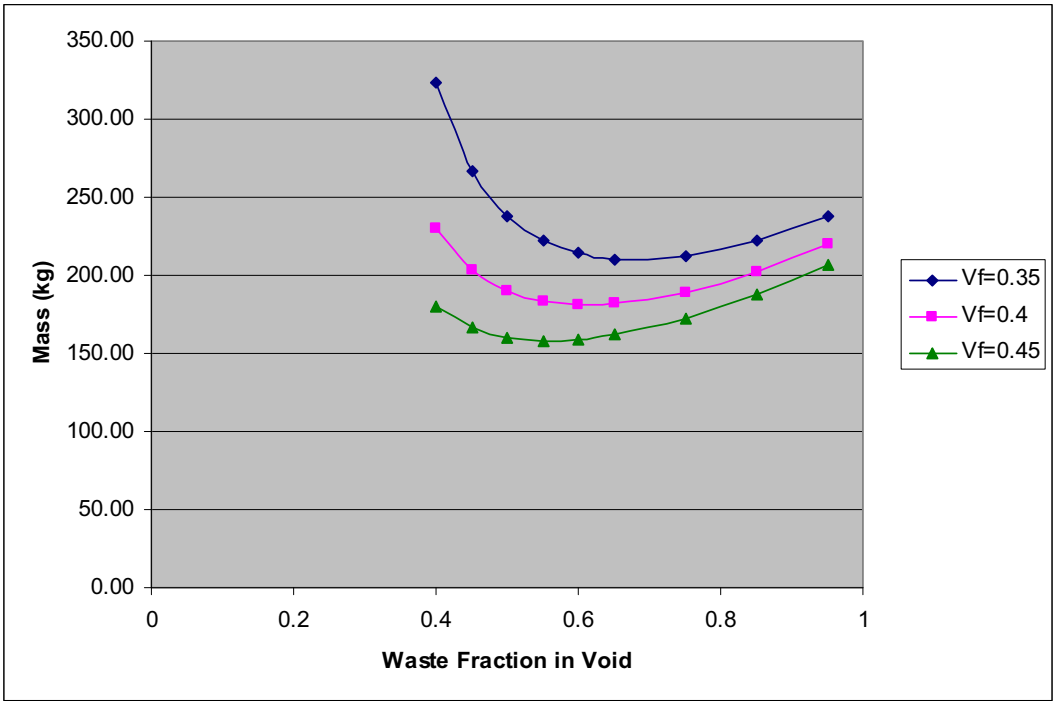

Source: Output DTN: MO0705SCALEGEO.000, file: *CSNF.xls*.

Figure 6.9-4[a]. Critical Masses of Uranium for UBN5 (Uranophane, basalt water, CSNF)

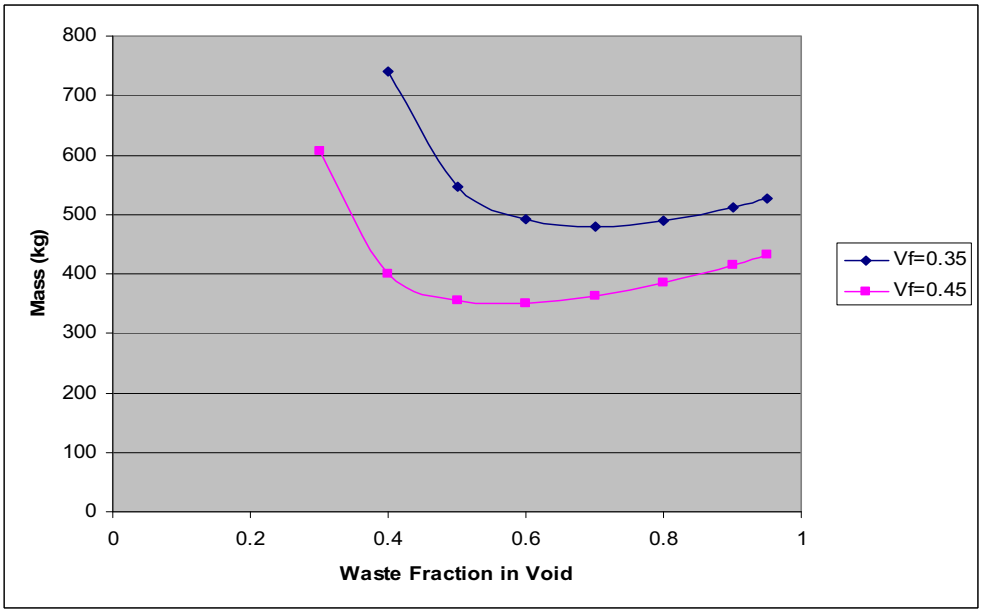

Source: Output DTN: MO0705SCALEGEO.000, file: *TMI.xls*.

Figure 6.9-5[a]. Critical Masses of Uranium for SJN3 (schoepite, J-13 well water, TMI)

The minimum critical mass is 349.6 kilograms. This includes the uranium in the water at a concentration of 1.21×10^{-4} moles/L.

Once again two minerals were considered for the igneous scenario. The results for the first, Na-boltwoodite, are presented in Figure 6.9-6[a].

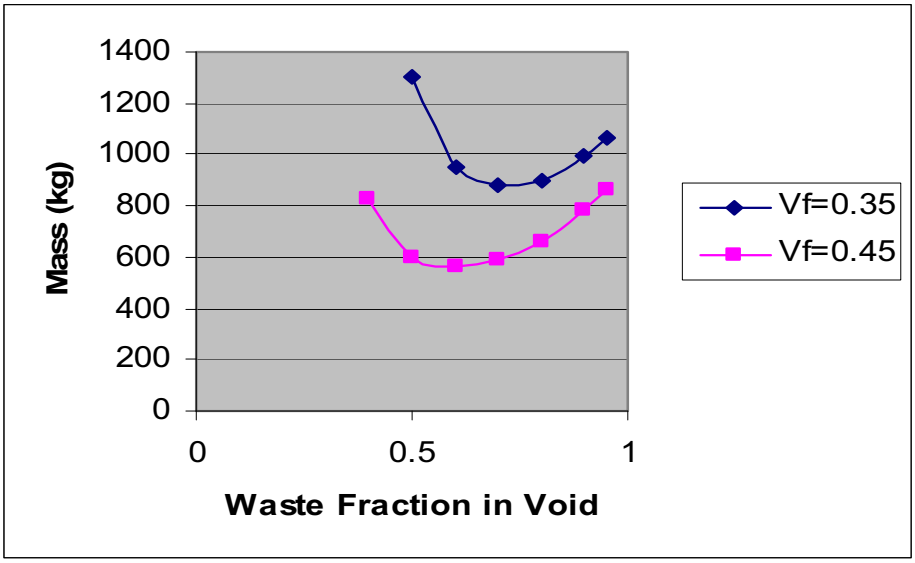

Source: Output DTN: MO0705SCALEGEO.000, file: *TMI.xls*.

Figure 6.9-6[a]. Critical Masses of Uranium for BBN3 (Na-boltwoodite, basalt water, TMI)

The minimum mass of uranium for this case to reach the critical limit is 560 kilograms. This occurs at a waste fraction in the void of 0.6 and includes the uranium in the water at a concentration of 0.132 moles/L, which is the peak uranium concentration observed from the TMI igneous case (TMI_IG1) presented in the parent report (output DTN: MO0609SPAINOUT.002, folder: TMI_IG1\TMI_IG1_Asprin\TMI_IG1_Asprin, file: *TMI_IG1A.xls*). The results for the second mineral, uranophane, are presented in Figure 6.9-7[a]. The minimum mass for this case is 538 kilograms of uranium at a waste fraction in the void of 0.8, including the uranium in the water at a concentration of 0.132 moles/L.

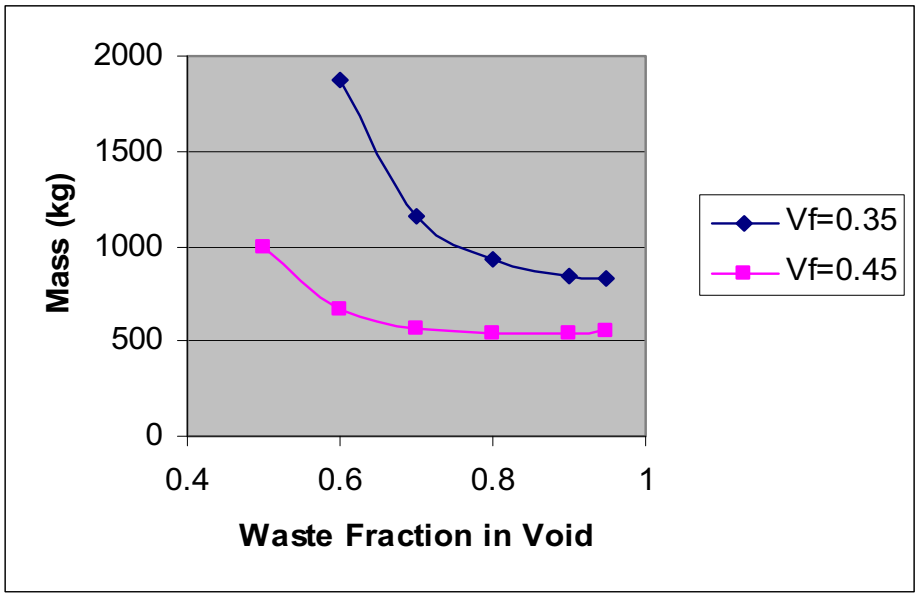

Source: Output DTN: MO0705SCALEGEO.000, file: *TMI.xls*.

Figure 6.9-7[a]. Critical Masses of Uranium for UBN3 (uranophane, basalt water, TMI)

N-Reactor Fuel in the Invert (Near-Field)—The next fuel type of interest is the N-Reactor fuel with an enrichment of 1.27 wt % ^{235}U. For this fuel, the igneous scenarios of interest in the invert with 3-mm-diameter fuel particles and void fractions from 0.15 to 0.45 yielded a k_∞ less than 0.96. The seismic scenario reached a k_∞ slightly greater than 0.96 and gave a minimum mass of 266,000 kg to approach a k_{eff} of 0.96 (SJN1). Thus, virtually any amount of this fuel could be accumulated in the invert, and there would not be a criticality. For the seismic scenario, the greatest k_∞ was 0.966 at a void fraction of 0.45 and a waste fraction of 0.95. For the igneous scenario with uranophane and basalt water, the largest k_∞ was 0.85 at a void fraction of 0.45 and waste fraction of 0.90.

	Peak k_∞	Void Fraction	Waste Fraction in Void
Seismic Scenario	0.966	0.45	0.95
Igneous Scenario	0.85	0.45	0.90

FFTF Fuel in the Invert (Near-Field)—For the FFTF fuel, two fissile materials were considered. The plutonium oxide fuel is 87% enriched in ^{239}Pu, and the uranium oxide fuel is either natural uranium or depleted uranium with enrichment between 0.2% and 0.7%. The plutonium oxide fuel was treated as 100% ^{239}Pu, since after 10,000 years, nearly all of the ^{240}Pu and ^{241}Pu will have decayed away. This increases reactivity, but not excessively so. The uranium oxide fuel was ignored, as these low enrichments are bounded by the N-Reactor fuel and not of any consequence for criticality.

Considering only the plutonium oxide mineral form, the seismic scenario with J-13 well water (PJN) gave a minimum critical mass of 1.66 kg at a waste fraction in the void of 0.004 and a void fraction of 0.45. For the igneous scenario with basalt water (PBN), the minimum critical mass

was 1.66 kg at a waste fraction of 0.004 and a void fraction of 0.45. As a sensitivity case, when a void fraction of 0.35 was used, the system was found to be less reactive, with a minimum critical mass increase of 283 grams. These results are tabulated in output DTN: MO0705SCALEGEO.000, file: *FFTF.xls*.

For both of these cases, the uranium in the water is of little consequence and is actually a poison, so neglecting it increases reactivity. There is essentially zero plutonium dissolved in the liquid for any cases considered to date**.** Plutonium dioxide is essentially insoluble in water and all PHRREQC calculations show a very small fraction released.

Other DOE SNF in the Invert (Near-Field)—In order to evaluate how other waste forms with higher fissile-material concentrations might accumulate and react, the following set of sensitivity cases were represented in order to observe the change in minimum critical mass as a function of fissile concentration. Since these fuels were not modeled explicitly in this study, it is difficult to say what enrichment the specific waste streams will have. So a generic plot was developed for ^{235}U fuels as a function of enrichment. These results are presented in Figure 6.9-8[a] for the seismic scenario.

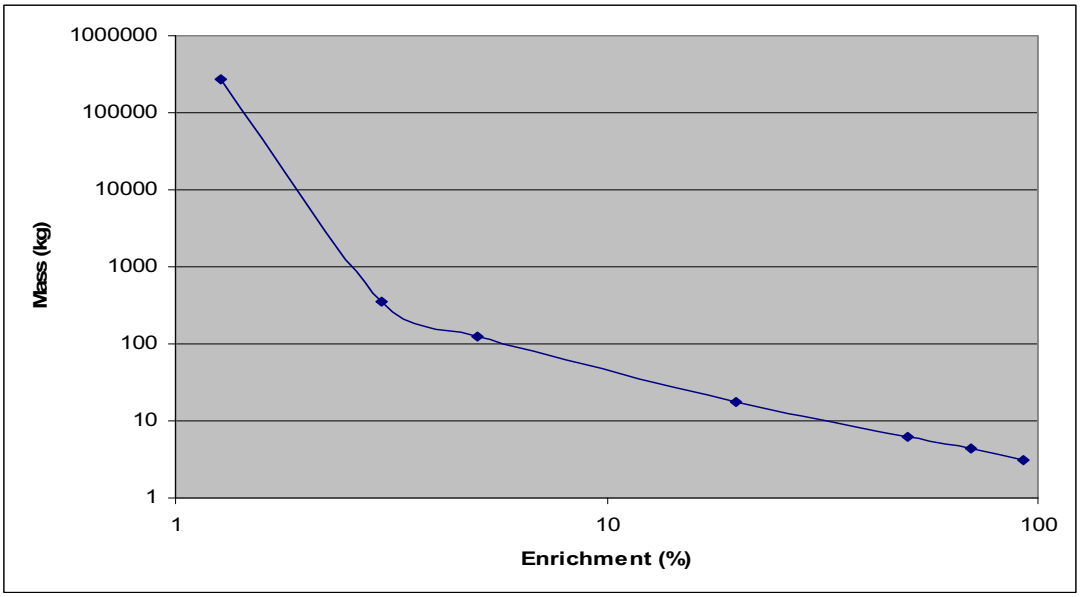

Source: Output DTN: MO0705SCALEGEO.000, file: *DOEF.xls.*

Figure 6.9-8[a]. Critical Masses of Uranium for SJN-All Enrichments (schoepite, J-13 well water, DOE SNF)

Note that the minimum uranium mass for 93% enriched fuel (SJN93) is 3.0 kilograms, and it occurs at a waste fraction of 0.02 and void fraction of 0.45**.**

The igneous scenario is covered by Figure 6.9-9[a]. These results are based on uranophane and basalt water and use uranium concentration in the liquid of 5.43×10^{-5} moles/L. This gives a minimum mass for 93% enriched fuel at 3.0 kg (UBN93).

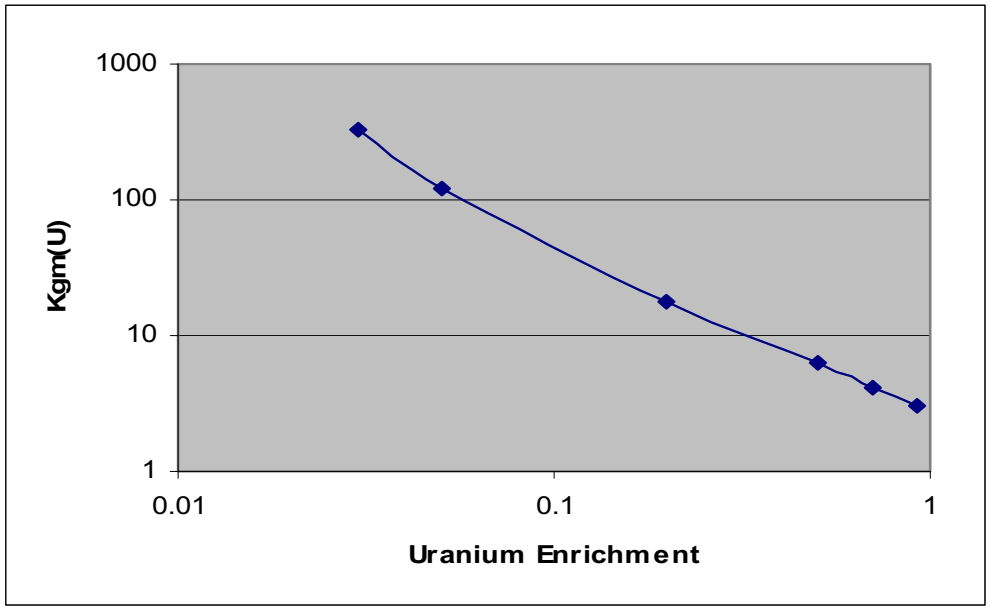

Source: Output DTN: MO0705SCALEGEO.000, file *DOEF.xls*.

Figure 6.9-9[a]. Critical Masses of Uranium for UBN-All Enrichments (uranophane, basalt water, DOE SNF)

One DOE SNF of interest is the LWBR fuel. It is 98% enriched in ^{233}U (DOE 1999 [DIRS 105007], Table 3-1). Typically, ^{233}U produces minimum critical masses closer to ^{239}Pu than to ^{235}U. The minimum critical mass for the seismic scenario is 1.89 kg at a waste fraction of 0.02 and a void fraction of 0.45. For the igneous scenario, the critical mass is 1.91 kg, which includes the uranium in the liquid at 5.43×10^{-5} moles/L. These results are summarized in output DTN: MO0705SCALEGEO.000, file: *DOEF.xls*.

The LWBR critical mass calculations in the preceding paragraph, however, do not take into account the high corrosion resistance of the LWBR fuel. A number of the studies have indicated that both air and water oxidation of uranium and thorium oxide fuel pellets ($(Th, U)O_2$) proceed more slowly than with pure uranium oxide (UO_2), and these processes decrease with decreasing UO_2 content in the fuel (DOE 2003 [DIRS 166027], p. 33). This lower solubility would lead to lower release of uranium from the waste package.

Another example of a fuel with a high enrichment that could cause concern for external criticality is the Fort St. Vrain fuels, with 93.5% enrichment (Taylor 2001 [DIRS 154726], Section 1.1). These fuels are also a corrosion-resistant waste form. The Fort St. Vrain fuels have an integral silicon carbide (SiC) protective layer that not only retains the fission products but also protects the uranium and thorium dicarbide ($(U,Th)C_2$) from oxidation and hydrolysis (DOE 2003 [DIRS 166027], p. 48). Comparative analysis has indicated that the Fort St. Vrain fuels have the lowest degradation rate of all DOE SNF and should behave significantly better in terms of fissile material dissolution.

Therefore, the high corrosion resistance of the LWBR and Fort St. Vrain fuels indicates that, even though the uranium enrichment content is high, the low solubility of the waste form is expected to result in much smaller quantities of accumulation in the invert or fractured rock than the DOE SNF analyzed in this report (N-Reactor, TMI, and FFTF).

6.9.2.2[a] Critical Mass Bounds in the Fractured Tuff (Far-Field)

CSNF in Fractured Tuff (Far-Field)—Upon exiting the invert, any waste will likely migrate into fractures in the tuff below the invert. The tuff has been characterized as large blocks of rock penetrated by fractures separated by an average spacing from 0.19 m to 0.25 m (Table 6-24 of the parent report). The fractures were too narrow to measure accurately in the field, but median air porosities measured between 0.85% and 1.30% (Table 6-25 of the parent report). So the tuff was modeled as a plane parallel structure with radionuclide-containing material in the center of the fracture, surrounded by the appropriate liquid, and contained in the rock matrix. The rock porosity was maintained fully saturated at 13% as before for the invert rock. The liquid in the fractures remained at 65.3% saturation as before. The fracture spacing was varied from 0.15 m to 0.25 m. The void fraction for the fractures was varied from 0.0075 to 0.0135. The waste fraction in the fractures was varied from 0.1 to 0.9.

Based on this representation, k_∞ never exceeded 0.96 for schoepite and J-13 well water, the most reactive mixture (schoepite has the largest theoretical number density). Thus, the rock matrix fractures could be filled with CSNF for as large a volume as possible and never approach criticality. Values of k_∞ for 0.15-m spacing are presented in Figure 6.9-10[a]. k_∞ values for 0.25-m spacing are presented in Figure 6.9-11[a].

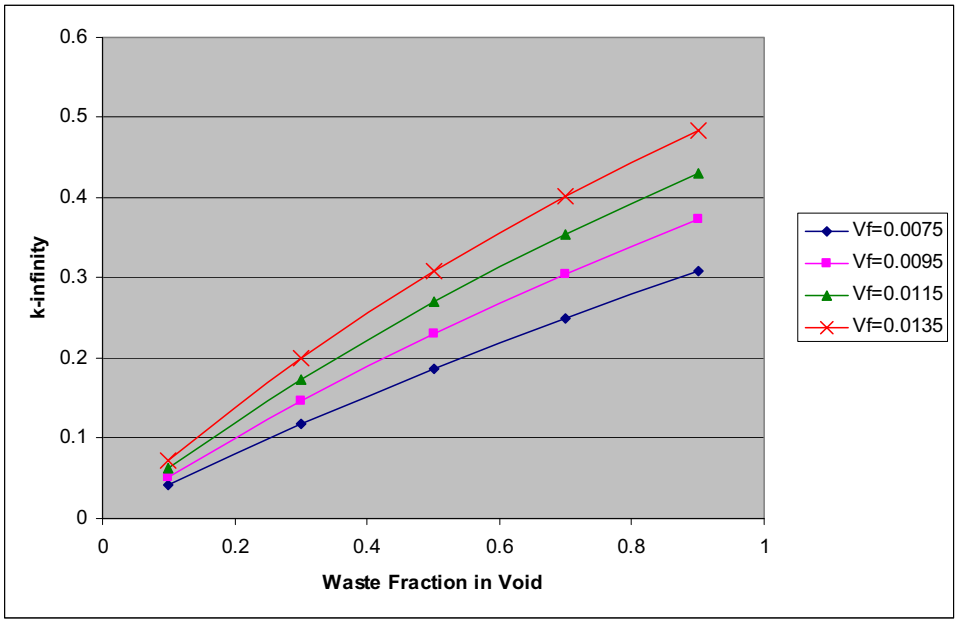

Source: Output DTN: MO0705SCALEGEO.000, file: *CSNF.xls*.

NOTE: Values of k_∞ for 0.15-m spacing are shown in this plot.

Figure 6.9-10[a]. k_∞ in Fractured Tuff for SJF5 (schoepite, J-13 well water, CSNF)

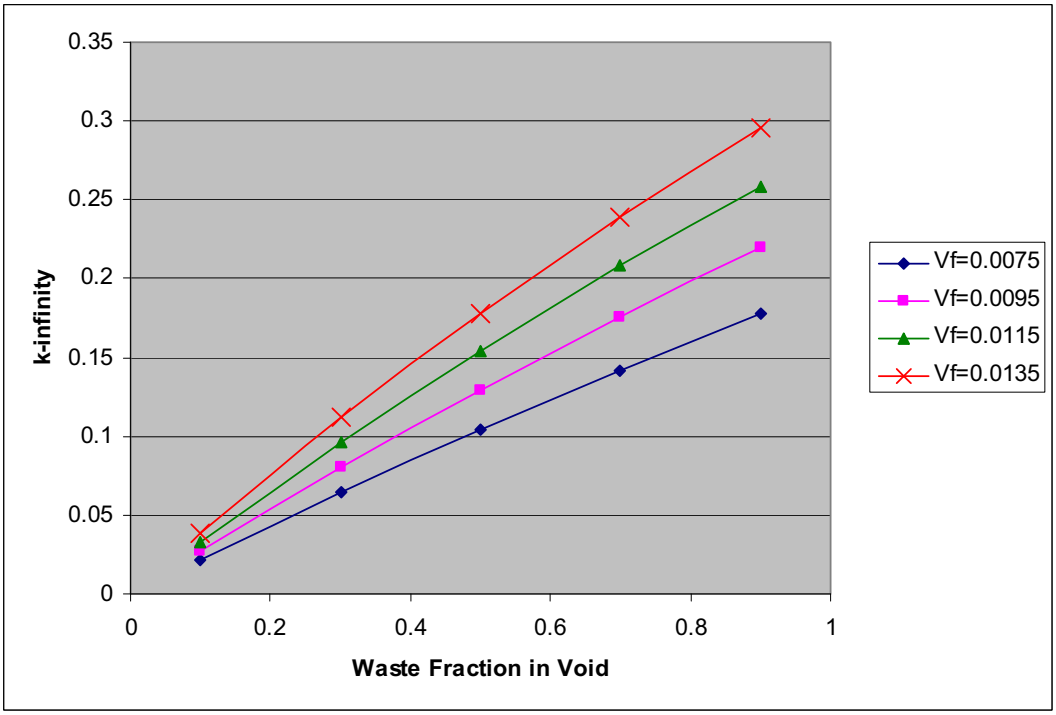

Source: Output DTN: MO0705SCALEGEO.000, file: *CSNF.xls*.

NOTE: Values of k_∞ for 0.25-m spacing are shown in this plot.

Figure 6.9-11[a]. k_∞ in Fractured Tuff for UBF5 (uranophane, basalt water, CSNF)

The values for the igneous scenario (Figure 6.9-11[a]) are a little less than for the seismic scenario due to the lower uranium number density in the uranophane mineral. For both cases, the difference between 0.15-m spacing of fractures and 0.25-m spacing of fractures was negligible. Even at 0.15-m spacing, there is very little communication between fractures neutronically.

TMI and N-Reactor Fuels in Fractured Tuff (Far-Field)—Given the results for the CSNF at the maximum 5% enrichment, it is obvious that the lower enrichments of N-Reactor and TMI fuels (1.27% and 2.98% enrichment, respectively) will not produce k_∞ values greater than 0.96.

FFTF Fuel in Fractured Tuff (Far-Field)—For the seismic scenario, the minimum mass of ^{239}Pu required to reach k_{eff} = 0.96 is 4.3 kg for a fracture porosity of 1.35%, a 0.15-m fracture spacing, and a waste fraction of 0.1 (PJF10). For the igneous scenario, the minimum mass is 4.3 kg at the same porosity and waste fraction (PBF10). These results are tabulated in output DTN: MO0705SCALEGEO.000, file: *FFTF.xls*.

Other DOE SNF in Fractured Tuff (Far-Field)—Higher enriched uranium fuels will produce k_∞ values that eventually exceed 0.96. At 20% enrichment, the seismic scenario can give a critical mass as little as 186 kg (output DTN: MO0705SCALEGEO.000, file: *DOEF.xls*, tab: "SJF20"). As the enrichment is increased to 93%, the mass of uranium required to reach a k_{eff} of 0.96 decreases substantially. The minimum uranium mass required to reach a k_{eff} of 0.96 as a function

of waste enrichment for both the seismic and igneous scenarios is presented in Figure 6.9-12[a]. In all cases, the minimum critical mass did not depend on fracture spacing for a given porosity.

The LWBR fuel was once again treated as a special case and the minimum critical mass for this material at k_{eff} = 0.96 was 4.7 kg for the seismic scenario and 4.8 kg for the igneous scenario. These results are tabulated in output DTN: MO0705SCALEGEO.000, file: *DOEF.xls* (tabs: "UBF98" and "SJF98").

As mentioned in Section 6.9.2.1[a], the high corrosion resistance of the DOE SNF with high enrichments, such as the LWBR and Fort St. Vrain fuels, is likely to result in low releases of uranium to the invert and far field, and therefore low quantities of accumulation.

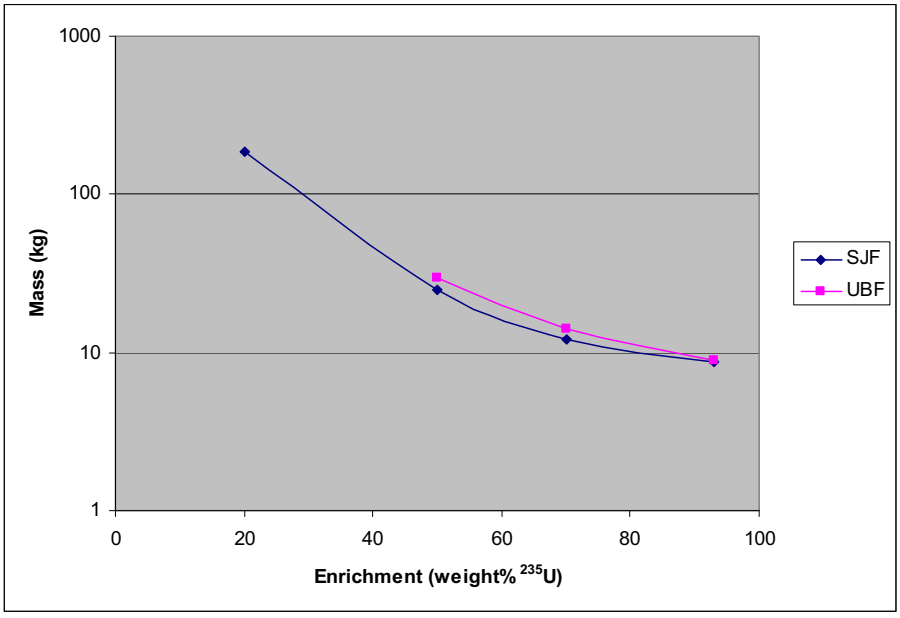

Source: Output DTN: MO0705SCALEGEO.000, file: *DOEF.xls*.

Figure 6.9-12[a]. Critical Masses of Uranium in Fractured Tuff for SJF and UBF-All Enrichments

6.9.2.3[a] Critical Mass Bounds in Lithophysae Formations (Far-Field)

The second far-field scenario of interest is the lithophysae filled with fissile-containing minerals and liquid. The analysis for this scenario was broken down into two separate configurations. The first was a single large lithophysa. The scenario that would lead to accumulation in a large lithophysa is as follows: The waste package effluent containing dissolved uranium and plutonium flows into the invert, and flows through a fracture that leads to a large lithophysa, without interacting with any fluids on the path. Once the effluent reaches the lithophysa, it mixes with uncontaminated seepage water that flows into the lithophysa via another fracture. The mixing of the two solutions causes the chemistry to change and the fissile minerals are precipitated. More realistically, the waste package effluent would be adsorbed or precipitated in the invert and fractures before it ever reached the lithophysa. Many of the fractures observed in the repository are deflected around lithohysae (Section 6.4.8.4 of the parent report), and therefore the chances are low of two fractures intersecting a large lithophysa, each carrying different water

solutions. In addition, *UZ Flow Models and Submodels* (SNL 2007 [DIRS 175177], Section 6.1.5) states that little water is expected to flow through lithophysal cavities, owing to the strong capillary barrier effect on seepage into cavities. Therefore, the accumulation in a large lithophysa is not considered a likely event. However, in order to determine the criticality potential of accumulation in a large lithophysa, the scenario is addressed in this addendum.

The second lithophysae configuration addressed is a regular array of small lithophysae. "Small" was defined as any lithophysa that had a diameter less than 200 mm, and "large" was a diameter greater than 200 mm. The rationale for this division was that the average mean free path in the Topopah Spring Tuff for neutrons above 0.1 MeV (fission range) was 48.3 mm based on the data available in the SCALE V. 5.1 cross-section libraries (STN: 10129-5.1-00 [DIRS 181249]). When arrays of lithophysae have spacings between voids that are greater than a mean free path, it is difficult for them to neutronically communicate with each other. In Figure 6.9-13[a], the minimum thickness of tuff that a neutron must travel to go from one lithophysa to its nearest neighbor is plotted as a function of the diameter of the lithophysae in the array. For diameters above 130 mm, the tuff thickness is greater than an average mean free path for neutrons in the fission range. So 200 mm diameter and larger was taken as the size of lithophysae that should be considered as single entities, rather than components of an array.

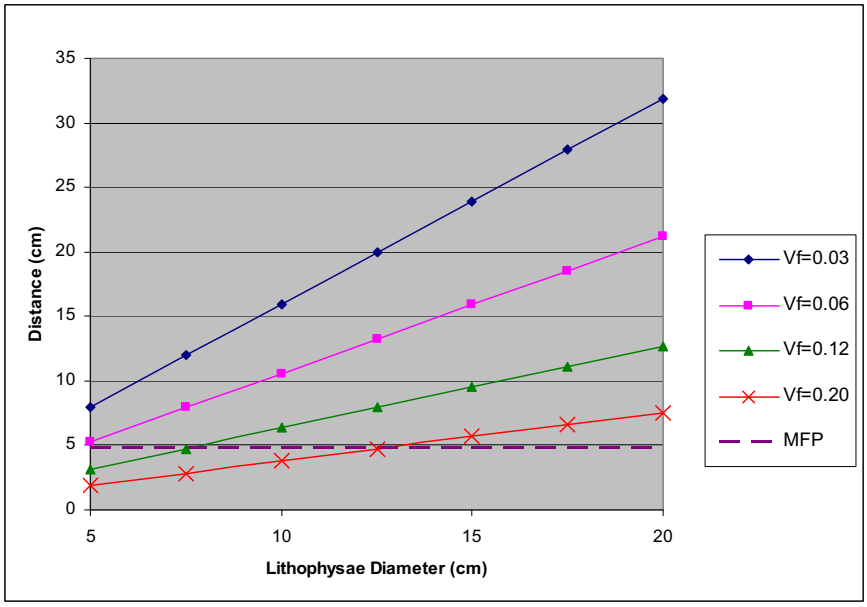

Source: Output DTN: MO0705SCALEGEO.000, file: *Lith_MFP.xls*.

Figure 6.9-13[a]. Minimum Distance between Lithophysae in Arrays

CSNF in Lithophysae (Far-Field)—The significant characteristics of the lithophysae that are important for far-field criticality analysis are as follows:

1. Sizes for lithophysae that occur in clusters were varied from 50 mm to 200 mm in diameter.

2. Void fractions for the lithophysae clusters varied from 0.03 to 0.20 (total lithophysal void volume divided by the total volume of the rock mass).

3. The maximum fill fraction for any lithophysa was 0.5, including the large single voids.

4. The maximum deposit depth in any lithophysa was 50 mm, including the large single voids (see the waste layer shown in Figure 6.9-1[a], diagram (d)). This depth is based on the data in DTN: GS980308315215.008 [DIRS 107355], which gives depths of secondary phases deposited over a 12-million-year period. Even though the mechanisms involved in the historical precipitation of calcite and opal in the lithophysal cavities (depressurization of high SiO_2-fCO_2 fluids) would be different from the mechanisms involved in the external accumulation model (mixing of solutions resulting in precipitation), the existing infill quantities can be used as a starting estimate of possible accumulation volumes.

5. The shapes of the deposits were not particularly regular.

Characteristics 3 and 4 were used to represent the maximum concentrations of waste and matrix liquid that could accumulate in a single large lithophysa of any size. The waste fraction was limited to a value of 0.5, and was further limited to the total amount of waste that could form a deposit layer on the bottom inner surface of the lithophysa no more than 50 mm in depth.

The single large lithophysa was represented as a large spherical void in the saturated tuff filled with basalt water and various volume fractions of uranophane waste. The results of this analysis are presented in Figure 6.9-14[a] for CSNF. (The bend-over in the curve is caused by hitting the 50 mm layer thickness limit for maximum waste depth.)

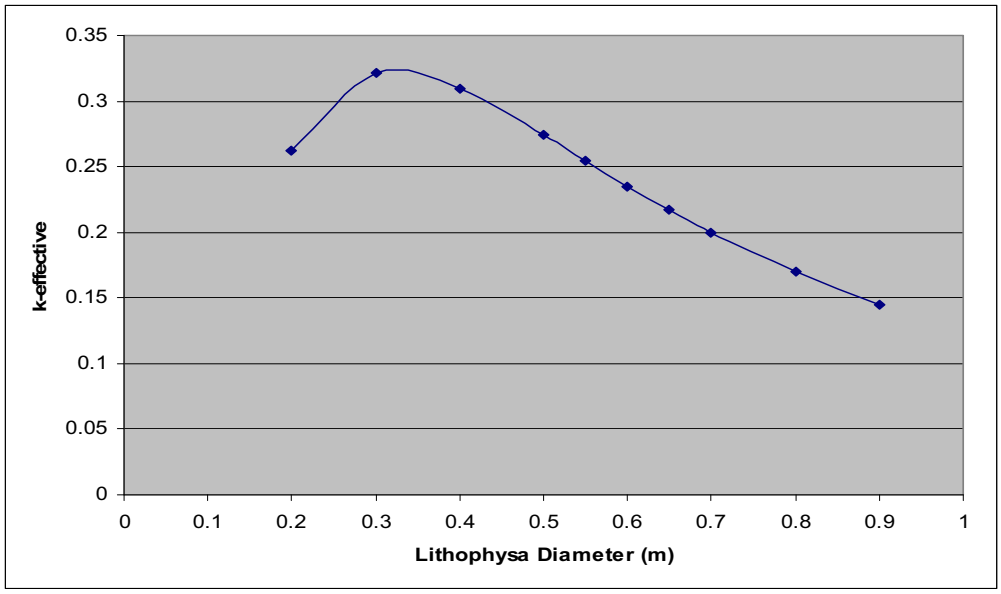

Source: Output DTN: MO0705SCALEGEO.000, file: *CSNF.xls*.

Figure 6.9-14[a]. Maximum k_{eff} for a Single Lithophysa (UBV5)

For arrays of lithophysae filled with CSNF (5% enrichment) and waste fractions up to 0.5, k_∞ can exceed 1.0 slightly. This occurs for smaller diameters, ~50 mm, when the void fraction approaches 0.2 and the waste fraction in the voids is 0.5. The values of k_∞ for a 0.2 void

fraction as a function of lithophysae diameter are plotted in Figure 6.9-15[a]. Calculating an array of 50-mm-diameter lithophysae with a void fraction of 0.2 is fairly reactive. For this case, the minimum fissile waste mass required to reach k_{eff} = 0.96 is 1,390 kg (UBL5). The results for this case are tabulated in output DTN: MO0705SCALEGEO.000, file: *CSNF.xls*.

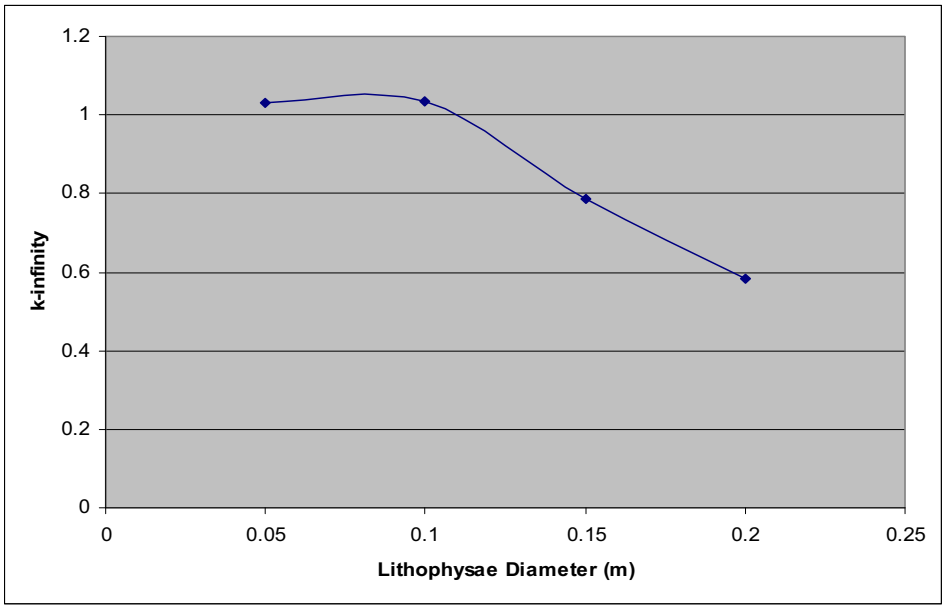

Source: Output DTN: MO0705SCALEGEO.000, file: *CSNF.xls*.

Figure 6.9-15[a]. Lithophysae Arrays with Waste Fraction of 0.5 (UBL5)

TMI Fuel in Lithophysae (Far-Field)—At a maximum of 3% enrichment for the TMI fuel, a single lithophysa cannot produce a critical sphere. Likewise, the lithophysae arrays filled with TMI fuel waste will not achieve k_{eff} = 0.96, because they are both bounded by the results for the CSNF fuel.

N-Reactor Fuel in Lithophysae (Far-Field)—Since the enrichment for the N-Reactor fuel is approximately 1.27%, the criticality results for CSNF in the lithophysae bound this case also. Essentially any amount could be leaked to the far field without presenting a criticality problem.

FFTF Fuel in Lithophysae (Far-Field)—The fuel from the FFTF can potentially release dissolved plutonium and uranium to the far-field lithophysae. The uranium released is not a problem because its enrichment is even lower than that of the N-Reactor. The plutonium waste is essentially not soluble in the typical liquids considered. The plutonium was treated as PuO_2, and 100% enriched as before. For a single large lithophysa, the minimum critical mass is 2.2 kg in a lithophysa with a diameter of 0.5 m and a waste fraction of 0.005 (PBV). For an array of lithophysae, the minimum mass is 4.0 kg in an array of 0.05-m-diameter voids, with a void fraction of 0.03 and a waste fraction in the void of 0.05 (PBL). These results are summarized in output DTN: MO0705SCALEGEO.000, file: *FFTF.xls*.

Other DOE SNF in Lithophysae (Far-Field)—For a single large lithophysa, a uranium waste form at 20% enrichment reached k_{eff} = 0.96 with a mass of 8.11 kg and a waste fraction of 0.074 in a void with a 0.45-m diameter (UBV20). At higher enrichments, the minimum mass required

drops below 1 kg, and the representations will need to be refined to give a truly realistic estimate. Since the 0.20-m-diameter void is at the upper end of the range considered for an array, array data were not calculated. The minimum masses for an array should be bounded by the minimum mass for a single lithophysa. An array model is not relevant when a single element can produce the bounding k_{eff}.

6.9.3[a] Summary

To summarize all of the above calculations and the predicted releases to the invert and the far-field host rock, a direct comparison is provided in Table 6.9-1[a]. None of the cases showed an accumulated mass higher than the mass required to achieve k_{eff} = 0.96. The DOE SNF addressed in this report (N-Reactor, TMI, and FFTF) make up approximately 90% of the mass of heavy metal in the DOE SNF inventory expected to be stored in the repository. Some of the other DOE SNF with high enrichments, such as LWBR and Fort St. Vrain, are also not expected to be a concern due to the corrosion resistance of the waste form (see Section 6.9.2.1[a]).

Table 6.9-1[a]. Summary of External Criticality Results—Minimum Mass for k_{eff} = 0.96

Scenario	Waste Package Type	Calculated Accumulation or Mass Released from Waste Package		Mass of U or Pu (for FFTF) required to achieve k_{eff} = 0.96			
		Uranium Mass, Unless Otherwise Noted (kg)	Location of Value	Invert (kg)	Fractured Tuff	Lithophysae Array	Large Lithophysa
Seismic	N-Reactor	Not calc[a]	Not calc	266,000	Inf[b]	Not calc	Not calc
	TMI Fuel	Not calc	Not calc	350	Inf	Not calc	Not calc
	CSNF	90.3[c]	Folder: CSNF-Seismic, File: *U released.xls* (output DTN: MO0705PHREEMOD.000)	126	Inf	Not calc	Not calc
	FFTF (Plutonium mass)	0	Table 8-2[a]	1.66	4.3	Not calc	Not calc
Igneous	N-Reactor	0.109	Parent report, Table 8-2, CDSPIG2	Inf	Inf	Inf	Inf
	TMI	30.7	Parent report, Table 8-2, TMI_IG1	538	Inf	Inf	Inf
	CSNF	74.8	Table 8-1[a]	159	Inf	1390	Inf
	FFTF (Plutonium mass)	6.34×10^{-3}	Parent report, Table 8-2, FFTFIG1adEhdec	1.66	4.3	4.0	2.2

[a] "Not calc" means that this scenario was of little interest given that it was bounded by another scenario. In most cases, this simply meant that, if CSNF waste was very sub-critical, then TMI and N-Reactor had to be also.

[b] "Inf" means that an infinite amount of fissile waste released in this model will not produce an arrangement that can reach k_{eff} = 0.96 (k_{∞} < 0.96).

[c] Maximum mass released from the waste package. This value supersedes the value in the parent report (Table 8-4) due to the new CSNF waste package design.

Source: The mass required to achieve k_{eff} = 0.96 is found in Output DTN: MO0705SCALEGEO.000.

7[a]. VALIDATION

No changes.

INTENTIONALLY LEFT BLANK

8[a]. CONCLUSIONS

8.1[a] MODEL OUTPUT

The conclusions in the parent report are still valid (except for the seismic scenario as indicated below) and are considered qualified. The following sections provide a summary of the addendum results. The output DTNs are listed in Section 9.4[a].

8.1.1[a] Nominal Scenario—Scoping Results

No changes.

8.1.2[a] Igneous Scenario

Table 8-1[a] provides the mass of uranium and plutonium accumulated in the invert or host rock for the CSNF igneous scenario.

Table 8-1[a]. Uranium and Plutonium Accumulation in the Igneous Scenario (10,000 years)

Source Term	Plutonium Accumulation (kg)	Total Uranium Accumulation (kg)	^{235}U Accumulation (kg)
CSNF	7.31×10^{-7}	7.48×10^{1}	9.72×10^{-1}

Source: Output DTN: MO0705PHREEMOD.000, file: *Mass Accumulated.xls*.

8.1.3[a] Seismic Scenario

Table 8-2[a] provides the mass of uranium and plutonium accumulated in the invert or host rock for the FFTF seismic scenario.

Table 8-2[a]. Uranium and Plutonium Accumulation in the Seismic Scenario (10,000 years)

Source Term	Plutonium Accumulation (kg)	Total Uranium Accumulation (kg)	^{235}U Accumulation (kg)
FFTF	8.63×10^{-4}	6.50×10^{1}	2.74×10^{-1}

Source: Output DTN: MO0705PHREEMOD.000, file: *Mass Accumulated.xls*.

Corrections to Seismic Scenario Results from Parent Report—The following two sets of results from the parent report are no longer valid:

- The mass accumulated in the CSNF seismic scenario presented in Table 8-4 of the parent report (ranging from 171 to 254 kg) were based on the results of the previous waste package design and are now considered too high. Using the results from the latest revision of the MDR model (SNL 2007 [DIRS 181165]), as presented in Table 6.9-1[a], the maximum uranium released from the waste package for the CSNF seismic scenario was found to be 90.3 kg. Therefore, the maximum accumulation that could occur would be less than or equal to 90.3 kg.

- The results discussed in Section 8.1.3 of the parent report regarding the entrained releases from the waste package are no longer valid. As mentioned in Section 6.6[a], the entrained releases are no longer considered in the external accumulation model because estimates of entrained releases were deleted from the MDR model.

8.1.4[a] Criticality Calculations

Plots showing the fissile mass needed for a k_{eff} of 0.96 are presented in Section 6.9.2[a]. The summary of the results is listed in Table 6.9-1[a]. The results show that none of the CSNF or DOE SNF (N-Reactor, TMI, FFTF) waste package scenarios investigated resulted in accumulation above the criticality threshold of $k_{eff} = 0.96$.

8.2[a] CRITERIA

No changes.

9[a]. INPUTS AND REFERENCES

9.1[a] DOCUMENTS CITED

168734 Allison, J.M. 2004. "Request for Referenceable Information on High-Level Waste (HLW) Radionuclide Inventories in Support of Preparation of the Yucca Mountain Project License Application (Your Letter, JCP-0445, 1/28/04)." Memorandum from J.M. Allison (DOE/SR) to J. Arthur, III (OCRWM), February 26, 2004, 0303040661, with attachment. ACC: MOL.20040317.0265.

149625 Audi, G. and Wapstra, A.H. 1995. *Atomic Mass Adjustment, Mass List for Analysis.* Upton, New York: Brookhaven National Laboratory, National Nuclear Data Center. TIC: 242718.

103805 Beyer, W.H., ed. 1987. *CRC Standard Mathematical Tables.* 28th Edition. 3rd Printing 1988. Boca Raton, Florida: CRC Press. TIC: 240507.

164419 BSC (Bechtel SAIC Company) 2003. *Analysis of Critical Benchmark Experiments and Critical Limit Calculation for DOE SNF.* CAL-DSD-NU-000003 REV 00A. Las Vegas, Nevada: Bechtel SAIC Company. ACC: DOC.20030724.0002; DOC.20050728.0006.

168553 BSC 2004. *Criticality Model.* CAL-DS0-NU-000003 REV 00A. Las Vegas, Nevada: Bechtel SAIC Company. ACC: DOC.20040913.0008; DOC.20050728.0007.

177153 BSC 2006. *Technical Work Plan for External Accumulation for Criticality Evaluations*. TWP-MGR-PA-000025 REV 04. Las Vegas, Nevada: Bechtel SAIC Company. ACC: DOC.20060710.0004.

179897 BSC 2007. *IED Emplacement Drift Invert.* 800-IED-MGR0-00601-000 REV 00A. Las Vegas, Nevada: Bechtel SAIC Company. ACC: ENG.20070716.0008.

163286 Deer, W.A.; Howie, R.A.; and Zussman, J. 1992. *An Introduction to the Rock-Forming Minerals.* 2nd Edition. New York, New York: Prentice Hall. TIC: 221918.

159374 Dixon, J.B. 1995. "Kaolin and Serpentine Group Minerals." Chapter 10 of *Minerals in Soil Environments.* 2nd Edition. Dixon, J.B. and Weed, S.B., eds. SSSA Book Series, No. 1. Madison, Wisconsin: Soil Science Society of America. TIC: 237222.

105007 DOE (U.S. Department of Energy) 1999. *Shippingport LWBR (Th/U Oxide) Fuel Characteristics for Disposal Criticality Analysis.* DOE/SNF/REP-051, Rev. 0. Washington, D.C.: U.S. Department of Energy, Office of Environmental Management. TIC: 245631. ACC: DOC.20030905.0016.

166027 DOE 2003. *Review of Oxidation Rates of DOE Spent Nuclear Fuel Part 2. Nonmetallic Fuel.* DOE/SNF/REP-068, Rev. 0. Idaho Falls, Idaho: U.S. Department of Energy, Idaho Operations Office. ACC: DOC.20030905.0009.

182051 DOE 2007. *Quality Assurance Requirements and Description.* DOE/RW-0333P, Rev. 19. Washington, D. C.: U.S. Department of Energy, Office of Civilian Radioactive Waste Management. ACC: DOC.20070717.0006.

106070 Duderstadt, J.J. and Hamilton L.J. 1976. *Nuclear Reactor Analysis.* New York, New York: John Wiley & Sons. TIC: 245454.

149850 Mongano, G.S.; Singleton, W.L.; Moyer, T.C.; Beason, S.C.; Eatman, G.L.W.; Albin, A.L.; and Lung, R.C. 1999. *Geology of the ECRB Cross Drift - Exploratory Studies Facility, Yucca Mountain Project, Yucca Mountain, Nevada*. Deliverable SPG42GM3. Denver, Colorado: U.S. Geological Survey. ACC: MOL.20000324.0614.

178395 Moroni, L.P. and Glasser, F.P. 1995. "Reactions Between Cement Components and U(VI) Oxide." *Waste Management, 15,* (3), 243-254. New York, New York: Pergamon. TIC: 258804.

124361 Nagy, K.L. 1995. "Dissolution and Precipitation Kinetics of Sheet Silicates." Chapter 5 of *Chemical Weathering Rates of Silicate Minerals*. White, A.F. and Brantley, S.L., eds. Reviews in Mineralogy Volume 31. Washington, D.C.: Mineralogical Society of America. TIC: 222496.

175261 Palandri, J.L and Kharaka, Y.K. 2004. *A Compilation of Rate Parameters of Water-Mineral Interaction Kinetics for Application to Geochemical Modeling*. Open File Report 2004-1068. Menlo Park, California: U.S. Geological Survey. ACC: MOL.20051110.0164.

103896 Parrington, J.R.; Knox, H.D.; Breneman, S.L.; Baum, E.M.; and Feiner, F. 1996. *Nuclides and Isotopes, Chart of the Nuclides.* 15th Edition. San Jose, California: General Electric Company and KAPL, Inc. TIC: 233705.

107088 Renders, P.J.N.; Gammons, C.H.; and Barnes, H.L. 1995. "Precipitation and Dissolution Rate Constants for Cristobalite from 150 to 300°C." *Geochimica et Cosmochimica Acta, 59*, 77-85. New York, New York: Elsevier. TIC: 226987.

101708 Rimstidt, J.D. and Barnes, H.L. 1980. "The Kinetics of Silica–Water Reactions." *Geochimica et Cosmochimica Acta, 44*, 1683-1699. New York, New York: Pergamon Press. TIC: 219975.

107105 Roberts, W.L.; Campbell, T.J.; and Rapp, G.R., Jr. 1990. *Encyclopedia of Minerals.* 2nd Edition. New York, New York: Van Nostrand Reinhold. TIC: 242976.

181165 SNL (Sandia National Laboratories) 2007. *Geochemistry Model Validation Report: Material Degradation and Release Model*. ANL-EBS-GS-000001 REV 02. Las Vegas, Nevada: Sandia National Laboratories. ACC: DOC.20070928.0010.

178869 SNL 2007. *Technical Work Plan for: Postclosure Criticality*. TWP-EBS-MD-000018 REV 01. Las Vegas, Nevada: Sandia National Laboratories. ACC: DOC.20070206.0003.

179567 SNL 2007. *Total System Performance Assessment Data Input Package for Requirements Analysis for DOE SNF/HLW and Navy SNF Waste Package Overpack Physical Attributes Basis for Performance Assessment*. TDR-TDIP-ES-000009 REV 00. Las Vegas, Nevada: Sandia National Laboratories. ACC: DOC.20070921.0009.

179354 SNL 2007. *Total System Performance Assessment Data Input Package for Requirements Analysis for Engineered Barrier System In-Drift Configuration*. TDR-TDIP-ES-000010 REV 00. Las Vegas, Nevada: Sandia National Laboratories. ACC: DOC.20070921.0008.

179394 SNL 2007. *Total System Performance Assessment Data Input Package for Requirements Analysis for TAD Canister and Related Waste Package Overpack Physical Attributes Basis for Performance Assessment*. TDR-TDIP-ES-000006 REV 00. Las Vegas, Nevada: Sandia National Laboratories. ACC: DOC.20070918.0005.

175177 SNL 2007. *UZ Flow Models and Submodels.* MDL-NBS-HS-000006 REV 03. Las Vegas, Nevada: Sandia National Laboratories. ACC: DOC.20070907.0001.

125332 Stumm, W. and Morgan, J.J. 1996. *Aquatic Chemistry, Chemical Equilibria and Rates in Natural Waters.* 3rd Edition. New York, New York: John Wiley & Sons. TIC: 246296.

154726 Taylor, L.L. 2001. *Fort Saint Vrain HTGR (Th/U Carbide) Fuel Characteristics for Disposal Criticality Analysis.* DOE/SNF/REP-060, Rev. 0. Washington, DC: U.S. Department of Energy, Office of Environmental Management. TIC: 249783. ACC: DOC.20030905.0002.

128733 Weast, R.C., ed. 1978. *CRC Handbook of Chemistry and Physics.* 59th Edition. West Palm Beach, Florida: CRC Press. TIC: 246814.

102047 Wronkiewicz, D.J.; Bates, J.K.; Wolf, S.F.; and Buck, E.C. 1996. "Ten-Year Results from Unsaturated Drip Tests with UO_2 at 90°C: Implications for the Corrosion of Spent Nuclear Fuel." *Journal of Nuclear Materials, 238,* (1), 78-95. Amsterdam, The Netherlands: North-Holland. TIC: 243361.

165505 YMP (Yucca Mountain Site Characterization Project) 2003. *Disposal Criticality Analysis Methodology Topical Report.* YMP/TR-004Q, Rev. 02. Las Vegas, Nevada: Yucca Mountain Site Characterization Office. ACC: DOC.20031110.0005.

9.2[a] CODES, STANDARDS, REGULATIONS, AND PROCEDURES

IM-PRO-002, *Control of the Electronic Management of Information*.

IM-PRO-003, *Software Management*.

SCI-PRO-003, *Document Review*.

SCI-PRO-004, *Managing Technical Product Inputs*.

SCI-PRO-006, *Models*.

9.3[a] SOURCE DATA, LISTED BY DATA TRACKING NUMBER

107355 GS980308315215.008. Line Survey Information from the Exploratory Studies Facility Obtained to Estimate Secondary Mineral Abundance. Submittal date: 03/24/1998.

151042 GS991108314224.015. Geology of the ECRB Cross Drift: Tabular Data. Submittal date: 11/05/1999.

176868 MO0604SPAPHR25.001. PHREEQC Data 0 Thermodynamic Database for 25 Degrees C - File: PHREEQCDATA025.DAT. Submittal date: 04/10/2006.

181798 MO0705GEOMODEL.000. Input Files and Model Output Runs: Geochemistry Model Validation Report: Material Degradation and Release Model. Submittal date: 05/23/2007.

172712 SN0410T0510404.002. Thermodynamic Database Input File for EQ3/6 - DATA0.YMP.R4. Submittal date: 11/01/2004.

178850 SN0612T0502404.014. Thermodynamic Database Input File for EQ3/6 - DATA0.YMP.R5. Submittal date: 12/15/2006.

9.4[a] OUTPUT DATA

MO0705PHREEMOD.000. PHREEQC Input and Output Files for Geochemistry Model Validation Report: External Accumulation Model in Support of Criticality. Submittal date: 05/30/2007.

MO0705SCALEGEO.000. SCALE Input and Output Files for Geochemistry Model Validation Report: External Accumulation Model in Support of Criticality Calculations. Submittal date: 05/30/2007.

MO0704PHREEQ25.000. PHREEQC Thermodynamic Database from DATA0 REV. 05 for 25 C. Submittal date: 05/16/2007.

MO0704PHREEQ50.000. PHREEQC Thermodynamic Database for 50 C (323.15K) from DATA0 REV. 05. Submittal date: 05/16/2007.

MO0709PHREEQ90.000. PHREEQCDATA0R590.DAT. Submittal date: 09/25/2007.

9.5[a] OUTPUT DATA FOR MODEL VALIDATION, LISTED BY DATA TRACKING NUMBER

No changes.

9.6[a] SOFTWARE CODES

157838 Acc_with_decay. V1.2. PC. 10499-1.2-00.

179458 ASPRIN V. 1.0. 2004. Windows 2000. STN: 10487-1.0-00.

176889 EQ3/6 V. 8.1. 2005. WINDOWS 2000. STN: 10813-8.1-00.

157840 GetEqPhases V. 1.0. 2002. PC. 10725-1.0-00.

157841 MinAcc V. 1.00. 2002. PC. 10724-1.0-00.

157837 PHREEQC V. 2.3. 2002. PC. 10068-2.3-01.

157839 PHREEQC_Post V. 1.1. 2002. PC. 10723-1.1-00.

181249 SCALE V. 5.1. 2007. WINDOWS XP. STN: 10129-5.1-00.

155029 transl V. 2.0. 2001. PC Windows98. 10251-2.0-00.

INTENTIONALLY LEFT BLANK

APPENDIX I[a]
DETAILS OF ASPRIN CALCULATIONS

APPENDIX I[a]—DETAILS OF ASPRIN CALCULATIONS

I.1[a] SOURCE TERM: CSNF, IGNEOUS, 1,000 L/YR

This source term (*CSIGAdEh*) represents the second stage of an igneous simulation of the degradation of a CSNF waste package at a flow rate of 1,000 L/yr. Three separate EQ3/6 (V. 8.1. STN: 10813-8.1-00 [DIRS 176889]) simulations were required to reach 10,000 years. For the first EQ3/6 simulation (output DTN: MO0705PHREEMOD.000, folder: CSNF-Igneous\asprin\CSNF Step 1, file: *CSIGAdEh.6i*), ASPRIN (V. 1.0. STN: 10487-1.0-00 [DIRS 179458]) was conducted according to the following steps:

1. Update file *defltsolids.txt* (which is a file provided along with the ASPRIN software package (STN: 10487-1.0-00 [DIRS 179458]) with the list of minerals formed during the EQ6 run, as listed in *CSIGAdEh.min_info.txt* (DTN: MO0705GEOMODEL.000 [DIRS 181798], folder: CSNF\CSNF Igneous\High Seepage Adj Eh). The revised file *deftlsolids.txt* is located in output DTN: MO0705PHREEMOD.000, folder: CSNF-Igneous\asprin\CSNF Step 1.

2. Begin running ASPRIN (STN: 10487-1.0-00 [DIRS 179458]), with the file *CSIGAdEh.bin* (DTN: MO0705GEOMODEL.000 [DIRS 181798], folder: CSNF\CSNF Igneous\High Seepage Adj Eh) and the updated *defltsolids.txt* in the same directory. [Since the **.bin* file was too large for ASPRIN (659 megabytes), the command line for running ASPRIN was revised as follows: "asprin.exe CSIGAdEh.bin 7," where the value "7" indicates that every 7th data point is read by ASPRIN.]

3. When prompted, input the normalized flushing rate (4.13×10^{-9} mol/s) from the EQ6 input file *CSIGAdEh.6i* (DTN: MO0705GEOMODEL.000 [DIRS 181798], folder: CSNF\CSNF Igneous\High Seepage Adj Eh), which is equivalent to 1,000 L/yr.

4. When prompted, input initial isotopic composition of aqueous solution and all uranium-bearing minerals. This represents the same isotopic composition as the starting CSNF, as listed in Table 6.4-1[a].

For the rest of the EQ3/6 simulations, see ASPRIN output files *CSIGAdE2.txt* and *CSIGAdE3.txt* (located in output DTN: MO0705PHREEMOD.000, folders: CSNF-Igneous\asprin\CSNF Step #, where # is 2 or 3). ASPRIN was run according to the instructions listed above for steps 1, 2, and 3, but step 4 is slightly different. In step 4, the initial isotopic composition of the aqueous solution and uranium minerals comes from the ASPRIN output of the previous EQ6 simulation. For example, for the second EQ6 simulation (*CSIGAdE2.txt*), *Isotopic fraction end step 1.xls* provides the values of enrichment that were taken from the ASPRIN output file from the first step (*CSIGAdEh.txt*).

Based on the ASPRIN output files (output DTN: MO0705PHREEMOD.000, folder: CSNF-Igneous\asprin*CSIGAdEh U Pu.xls*), eight points were identified to be simulated with PHREEQC, as shown in Figure 6.4-1[a]. Figure 6.4-1[a] also shows the ASPRIN results of enrichment fraction (ratio of ^{235}U to total uranium in solution) versus time. This source term was estimated at a reduced Eh, equivalent to oxygen fugacity of 1.77×10^{-9} bar (or $10^{-8.7514}$ bar)

(SNL 2007 [DIRS 181165], Section 6.3.14). Because of this, the aqueous concentration in the PHREEQC input file must specify the concentration of each dominant oxidation state for neptunium and plutonium. ASPRIN was used to extract the aqueous species for plutonium and neptunium, and the major species were summed in *CSIGAdEh U Pu.xls*.

I.2[a] SOURCE TERM: FFTF, SEISMIC, 1 L/YR

This source term (*FFTFMxGE*) represents the seismic simulation of the degradation of an FFTF waste package at a flow rate of 1 L/yr. ASPRIN was conducted according to the following steps:

1. Update *defltsolids.txt* with *FFTFMxGE.min_info.txt* (DTN: MO0705GEOMODEL.000 [DIRS 181798], folder: FFTF\Seismic\Max Glass Adj Eh). In addition, add waste forms UO_X, mixed oxide (MOX), and HLWG to *defltsolids.txt*. The uranium and plutonium contents of the MOX, UO_X, and HLWG are found in Table 6.4-1[a]. The revised file *deftlsolids.txt* is located in output DTN: MO0705PHREEMOD.000, folder: FFTF-Seismic\asprin\FFTF Step 1.

2. Begin running ASPRIN, with *FFTFMxGE.bin* and the updated *defltsolids.txt* in the same directory.

3. When prompted, input the normalized flushing rate (4.93×10^{-12} mol/s) from the EQ6 input file *FFTFMxGE.6i* (DTN: MO0705GEOMODEL.000 [DIRS 181798], folder: FFTF\Seismic\Max Glass Adj Eh), which is equivalent to 1 L/yr.

4. When prompted, input initial isotopic composition of aqueous solution, which can be assumed to be 100% ^{238}U, since it is just the starting composition. Next, when prompted, add the isotopic composition of the UO_X, MOX, and HLWG as listed in Table 6.4-1[a].

For the second EQ6 simulation, see ASPRIN output file *FFTFMxG2.txt* (located in output DTN: MO0705PHREEMOD.000, folder: FFTF-Seismic\asprin\FFTF Step 2). ASPRIN was run according to the instructions listed above for steps 1, 2, and 3, but step 4 is slightly different. In step 4, the initial isotopic composition of the aqueous solution and uranium minerals comes from the ASPRIN output of the previous EQ6 simulation. For example, for the second EQ6 simulation (*FFTFMxG2.txt*), *Isotopic fraction end step 1.xls* provides the values of enrichment that were taken from the ASPRIN output file from the first step (*FFTFMxGE.txt*).

Based on the ASPRIN output files, three points were identified to be simulated with PHREEQC, as shown in Figure 6.4-2[a]. Figure 6.4-2[a] also shows the ASPRIN results of enrichment fraction (ratio of ^{235}U to total uranium in solution) versus time. This source term was estimated at a reduced Eh, equivalent to oxygen fugacity of 1.77×10^{-9} bar. Because of this, the aqueous concentration in the PHREEQC input file must specify the concentration of each dominant oxidation state for neptunium and plutonium. ASPRIN was used to extract the aqueous species for Np and Pu, and the major species were summed in *FFTFMxGE U Pu.xls* (output DTN: MO0705PHREEMOD.000).

APPENDIX K[a]
EXTERNAL CRITICALITY CALCULATION APPROACH

APPENDIX K[a]—EXTERNAL CRITICALITY CALCULATION APPROACH

K.1[a] CALCULATION FLOW

All of the external criticality analyses depend on the materials likely to be found external to the waste packages. As indicated in Section 6.9[a], all external criticality calculations were performed for a spherical representation of the accumulated fissile-containing minerals (referred to as "waste") embedded in a tuff-water mixture and reflected by an infinite amount of the same tuff-water mixture, as shown graphically in *Exter_Crit.xls* (output DTN: MO0705SCALEGEO.000, tab: "Introduction"). The heterogeneity effects were taken into account with four different representations for the unit cells. After cell-weighted cross sections were developed by the BONAMI, CENTRM, and PMC modules of SCALE5.1 for these unit cells, the cells were homogenized and the critical sizes were estimated based on a mixed homogeneous sphere inside an infinite reflector. This configuration will produce the minimum fissile mass required to reach a specified multiplication constant, k_{eff}. (In this case, the k_{eff} limit was chosen as 0.96.)

The material mixtures are defined in terms of the atomic concentrations per unit volume in the zones of interest. To compute these atomic concentrations, the concentrations for each of the components are computed based on the full density for the component, for instance water. The components are then mixed based on the fractions of a unit volume that they occupy. When mixing components, the small scale heterogeneity of the components can influence the potential for criticality. That is, if the fissile material is arranged in lumps, it can be more or less reactive than if it is just homogeneously mixed on an atom by atom basis. A homogeneous mixture of natural uranium and carbon can not achieve a k_{eff} greater than 1.0 (Duderstadt and Hamilton 1976 [DIRS 106070], p. 400); however, by lumping natural uranium, Enrico Fermi was able to achieve the first critical pile in a matrix of graphite. For low enrichments, the configuration becomes more reactive due to a decrease in resonance self-shielding. For high enrichments, the lumped configuration can be less reactive due to flux suppression at the center of the lumps. Therefore, each of the external critical configuration possibilities was represented with a lumped configuration that best describes the likely physical situation that could occur.

The standard method for dealing with lumping or heterogeneity effects is to process the nuclear cross sections with a repeating cell representation to take into account the effects of lumping (adjusting resonance absorption and flux depressions). The industry standard code for performing this type of processing is the SCALE V. 5.1 (STN: 10129-5.1-00 [DIRS 181249]) code system and in particular the BONAMI, CENTRM, and PMC modules, which are described in the users manual provided with the electronic media containing the SCALE V. 5.1 software (STN: 10129-5.1-00 [DIRS 181249]) Once the repeating array heterogeneity is taken into account, the nuclear cross sections are rewritten in a file as a set of self-shielded cross sections. Each set of self-shielded cross sections is only valid for the array geometry for which it was processed. Then these cross sections are used in a large scale calculation as if the array were homogeneous. This large scale calculation attempts to determine the size of a reflected sphere that will require the minimum waste mass to achieve $k_{eff} = 0.96$. The SCALE module that performs this calculation is called XSDRNPM.

There are four heterogeneity representations that have been used in this analysis. The first applies to the near field in the invert. In the invert, the waste is represented as small spheres dispersed in water and tuff. As discussed in Section 6.9.1[a], the nominal size for the tuff particles is 3.0 mm. Based on the way the SCALE system is set up, the fissile material must be in a central spherical particle surrounded by the other materials. The fissile waste particles were chosen to have a diameter of 3.0 mm for calculation purposes. This may overestimate the likely size, based on 3.0 mm tuff fill. However, in this case, a larger than actual fissile waste particle increases reactivity. In preliminary calculations, smaller waste particles were analyzed and in fact k_{eff} did go down slightly. The volume fraction of voids in the invert between the tuff particles was varied from 0.15 to 0.45. The volume fraction of the fissile waste within these voids was varied from 0.0 to 1.0. The porosity of the tuff used to fill the invert was taken as 13% and fully saturated. The fluid that filled the remaining void volume was 65% of full saturation.

The second heterogeneity representation was used for the far-field host rock. In this representation, monolithic blocks of tuff are penetrated by fractures that occur in a semiregular pattern. As mentioned in Section 6.9.1[a], values of fracture porosity range from 0.75% to 1.35%. The fractures occur in a semi-regular fashion with a spacing in the range of 0.15 to 0.25 m. This geometry was represented as a repeating slab, with fissile waste in the middle of the fracture, surrounded by the appropriate liquid, followed by the tuff matrix. The tuff was fully saturated at 13% porosity. The waste fraction within the fracture was allowed to vary from 0.0 to 1.0 times the available volume.

The third heterogeneity representation was used to address a repeating array of small lithophysae, with voids that vary from 0.05 m to 0.2 m in diameter and void fractions of the media between 0.03 and 0.20. As discussed in Section 6.9.2.3[a], observations indicated that voids were always less than half filled with deposits and never had a deposit coating depth greater than 50 mm. These arrays were represented as repeating spheres of liquid and waste embedded in a matrix of tuff. The tuff had the same properties as above. In this case, the waste fraction on the void space was allowed to vary between 0.0 and 0.5, not to exceed the amount that could create a 50-mm coating on the bottom surface of the void.

The fourth heterogeneity representation simply extended the small lithophysae representation to large lithophysae. It dealt with lithophysae with a diameter of 0.2 m to over 1.0 m. For all of the cases considered, it was never necessary to extend much beyond 1.0 m in diameter, because a core mixture with a slightly different fraction of fissile waste was likely to produce a $k_{eff} = 0.96$ at a smaller diameter. The goal was always to find the minimum fissile mass that gave $k_{eff} = 0.96$. The waste in the central cavity was mixed homogeneously with the cavity water and restricted by the two bounds identified above. The waste fraction could never exceed 0.5 of the available void volume, or a quantity of full density waste that could form a layer equal to 50 mm on the bottom surface of the void.

The calculation procedure was:

1. Select materials of interest and calculate full density atomic number densities

2. Build a heterogeneity representation for the BONAMI, CENTRM, and PMC modules

3. Make a self-shielded cross section set for this representation

4. Use the self-shielded cross section set in XSDRNPM to search for the size of a reflected sphere that will give $k_{eff} = 0.96$.

K.2[a] CALCULATION OF MATERIAL ATOMIC NUMBER DENSITIES

Material atomic number densities were calculated from partial densities, atomic masses, and Avogadro's number. The real units are atoms per cubic centimeter. However, an alternative unit is defined, called the barn. A barn is 1.0×10^{-24} square centimeters, or 1.0×10^{-28} square meters. Then atomic number densities are expressed as atoms per barn-cm or atoms per barn-m. If Avogadro's number is taken as 6.022×10^{23} (Parrington et al. 1996 [DIRS 103896], p. 59), the choice of the unit atoms per barn-cm eliminates carrying a big exponent in all of the data input and documentation.

Consider

$$N_m = \rho_p N_a / A$$

where

N_m = material atomic number density in atoms/cc
ρ_p = the density of the element or compound in grams/cc
N_a = Avogadro's number – 6.022×10^{23}
A = atomic mass for the molecule or atom.

Consider water as an example. The density of water is 1.0 gm/cc and the water molecule has an atomic mass of 2(1.00794 [hydrogen]) +1(15.9994 [oxygen]) =18.015. This gives:

$$\begin{aligned} N_w &= 1.0 \times 6.022 \times 10^{23} / 18.015 \\ &= 3.343 \times 10^{22} \text{ molecules/cubic centimeter} \\ &= 3.343 \times 10^{28} \text{ molecules/ cubic meter} \\ &= 0.03343 \text{ molecules/barn/cm.} \end{aligned}$$

This translates into 0.03343 atoms/barn/cm for oxygen and 0.06686 atoms/barn/cm for hydrogen.

K.3[a] MATERIAL ATOM NUMBER DENSITIES

The material atom number densities were calculated in output DTN: MO0705SCALEGEO.000, file: *Exter_Crit.xls*. The formulas for the minerals come from *data0.ymp.R5* (DTN: SN0612T0502404.014 [DIRS 178850]). The densities for the minerals are calculated in *density.xls*, based on molar volumes from *data0.ymp.R5* (DTN: SN0612T0502404.014 [DIRS 178850]). The values of atomic mass come from Parrington et al. (1996 [DIRS 103896], p. 60). The density of crystalline PuO_2 and the iron nuclide atom percentages come from *CRC Handbook of Chemistry and Physics* (Weast 1978 [DIRS 128733], p. B-148 and pp. B-284 to B-285, respectively).

The compositions of the three uranium minerals, the tuff, the J-13 well water, and the basalt water were converted to number densities in *Exter_Crit.xls* (output DTN: MO0705SCALEGEO.000).

K.4[a] Heterogeneity Representations

K.4.1[a] Representation for the Single Large Lithophysa

The simplest of the heterogeneity representations is the far-field single lithophysa scenario. For this scenario, there are two homogeneously mixed material zones. For the central zone containing the fissile waste and liquid, the full atom number densities are mixed according to the following formula.

$$N_i^c = W_f\, N_w^0 + (1.0\text{-}W_f)\, S_v\, N_l^0 \qquad \text{(Eq. K-1[a])}$$

where

N_i^c = the number density in the central void for the fissile waste and liquid
W_f = the waste fraction (by volume) in the central void
N_w^0 = the full number density for the fissile waste
S_v = the liquid saturation of the void spaces
N_l^0 = the full number density for the liquid.

The first term in Equation K-1[a] represents the number density of the fissile waste and the second term in Equation K-1[a] represents the number density of the liquid.

For the tuff reflector, the full number density, N_i^r, is given by:

$$N_i^r = (1.0 - P_t)\, N_t^0 + P_t\, S_p\, N_l^0 \qquad \text{(Eq. K-2[a])}$$

where

P_t = the number porosity of the tuff
N_t^0 = the full number density for the tuff
S_p = the saturation of the pores in the tuff
N_l^0 = the full number density for the liquid.

The first term in Equation K-2[a] represents the number density of the tuff and the second term in Equation K-2[a] represents the number density of the saturating liquid.

The waste fraction in the void is limited by the maximum amount of waste that could precipitate to give a layer on the bottom of the void up to 50-mm thick. The volume of a spherical segment is given by (Beyer 1987 [DIRS 103805], p. 130):

$$V_{layer} = (1/3)\, \pi\, h^2\, (3R - h) \qquad \text{(Eq. K-3[a])}$$

where

h = the height of the layer at the bottom of the sphere
R = radius of the sphere.

Substituting h = 5 cm (50 mm) and R = D/2 into Equation K-3[a], where D is the diameter (cm) of the lithophysa, gives the volume (cm^3) of the deposit in the bottom of the spherical lithophysa:

$$V_{layer} = \pi (25/2\ D - 125/3) \quad \text{(Eq. K-4[a])}$$

Where D is the diameter of the void (cm). The volume of the void is given by (Beyer 1987 [DIRS 103805], p. 130):

$$V_{void} = 4/3\ \pi (D/2)^3 \quad \text{(Eq. K-5[a])}$$

The waste fraction in the void is then limited by the ratio V_{layer}/V_{void}.

K.4.2[a] Representation for the Lithophysae Arrays

The SCALE representation (STN: 10129-5.1-00 [DIRS 181249]) used for the cross section self-shielding for the lithophysae arrays is the LATTICECELL, SPHSQUAREP representation. This represents the unit cell as an internal fuel region composed of the mixed fissile waste and liquid in the central region surrounded by a tuff moderator. The formulas for calculating the number densities for these two regions are exactly the same as given for the single lithophysa representation above. The difference here is that the dimension of the void region is smaller and a reflecting boundary condition is placed on the outside of the reflector. The diameter of the void, or fissile waste and liquid region, is set as a parameter. Then the outside radius of the tuff reflector is calculated based on the void fraction that the lithophysae represent of the total matrix. The arrangement of spheres on a square pitch was used to calculate array pitch. The spherical voids are represented as spheres located in the center of a regular array of cubes with side of length P. Then:

$$V_f = \{\ 4/3\ \pi (D/2)^3\ \}/\ P^3 \quad \text{(Eq. K-6[a])}$$

is the defining equation. V_f is the array void fraction, D is the void diameter, and P is the pitch of the cubes. The only unknown is P. The equation is solved for pitch providing all of the geometric model input data required to run the SPHSQUAREP model for a LATTICECELL calculation in SCALE. The maximum waste fraction in the voids is also limited by the 50-mm layer on the bottom of the voids as above.

K.4.3[a] Representation for the Invert

The representation for the invert is very similar, once again using the LATTICECELL SPHSQUAREP sequence in SCALE (STN: 10129-5.1-00 [DIRS 181249]). In this case, the fissile waste is assumed to form a full density particle in the invert with a diameter of 3 mm. It is surrounded by a liquid layer that performs the classic geometric function of a "clad" in reactor terminology. Outside of the clad is the tuff matrix moderator. The tuff number densities are calculated as shown in Section K.4.1[a]. The fuel kernel number densities and the liquid density numbers are taken as the full density values. The remaining data required are the geometric data necessary to run the cell calculation. The diameter of the tuff particles and the void fraction are combined to give a relationship for the tuff as a moderator in a fuel particle centered cell. For a square pitch arrangement, the pitch P can be solved for from the following equation:

$$(1-V_f)\, P^3 = 4/3\ \pi\ (D_t/2)^3 \qquad \text{(Eq. K-7[a])}$$

where V_f is the invert void fraction and D_t is the tuff particle diameter. The clad diameter can then be calculated based on:

$$V_f\, P^3 = 4/3\ \pi\ (D_c/2)^3 \qquad \text{(Eq. K-8[a])}$$

where D_c is the clad diameter (liquid outer diameter). Then the waste diameter is calculated from:

$$W_f = \{4/3\ \pi\ (D_f/2)^3\}/\{4/3\ \pi\ (D_c/2)^3\} = (D_f/D_c)^3$$

where D_f is the fuel particle diameter. This gives all of the required geometric data required to run the LATTICECELL SPHSQUAREP model in SCALE.

K.4.4[a] Representation for the Fractured Tuff

The fractured tuff representation uses the LATTICECELL SYMMSLABCELL model in SCALE (STN: 10129-5.1-00 [DIRS 181249]) to perform the self-shielding. For this representation the fracture spacing is essentially the required pitch. The void fraction is then the width of the liquid and fuel layer and becomes the dimension for the clad overall thickness (CLADD). The waste fraction is then the fraction of this fracture width that contains the full density fissile waste. Or the thickness of the fissile waste region is given by:

$$T_w = W_f\ V_f\ S_f \qquad \text{(Eq. K-9[a])}$$

where

T_w = width of the fissile waste region
S_f = fracture mean spacing
W_f = waste fraction (by volume)
V_f = void fraction in the tuff matrix.

This becomes the fuel dimension for the SCALE5.1 calculation. The number densities in the tuff are calculated as in Section K.4.1[a].

K.5[a] Neutron Transport Calculations

The transport calculations were performed in two parts. First, the cross sections from the 238 group ENDF/B/VI data set were self-shielded with the BONAMI, CENTRM, and PMC modules from SCALE (STN: 10129-5.1-00 [DIRS 181249]). These cross sections were saved to disk so that the transport could be run several times if necessary. Then, the XSDRNPM module performed the minimum critical mass calculations. Instead of two parts, the calculations could have been incorporated into a single XSDRNPM run, but in order to facilitate the ability to perform sensitivity studies, the XSDRNPM module was run separately from the BONAMI, CENTRM, and PMC modules. In many cases both an infinite medium calculation and a finite medium calculation were run. So for each scenario there are two sets of input and output files (output DTN: MO0705SCALEGEO.000, folder: IO_ZIP). If the title is SJN5, then the input and

output for the self-shielding run are SSJN5.INP and SSJN5.OUT. The input and output files for the XSDRNPM run are *XSJN5.INP* and *XSJN5.out*. Each scenario is maintained in a separate directory.

INTENTIONALLY LEFT BLANK